Machine Learning methods and Land Use/Land Cover (LULC) in the coastal Pays de Brest

Guanyao Xie

COLLEGE SCIENCES DOCTORAL DE LA MER BRETAGNE ET DU LITTORAL

Université de Bretagne Occidentale

THESE DE DOCTORAT DE

L'UNIVERSITE
DE BRETAGNE OCCIDENTALE

ECOLE DOCTORALE N° 598
Sciences de la Mer et du Littoral
Spécialité : *Géomatique*

Par

Guanyao XIE

Machine Learning methods and Land Use/Land Cover (LULC) in the coastal Pays de Brest

Méthodes d'apprentissage automatique et les changements de l'occupation du littoral du Pays de Brest

Thèse présentée et soutenue à Plouzané, le 10 février 2023
Unité de recherche : LETG – UMR CNRS 6554

Rapporteurs avant soutenance :

Antoine COLLIN Maître de conférences, École Pratique des Hautes Études
Sébastien GADAL Professeur des Universités, CNRS ESPACE UMR 7300, Université Aix-Marseille

Composition du Jury :

Président :	Christophe CLARAMUNT	Professeur des Universités, Ecole Navale de Lanvéoc-Poulmic
Examinateurs :	Antoine COLLIN	Maître de conférences, École Pratique des Hautes Études
	Thomas CORPETTI	Directeur de Recherche CNRS, LETG-Rennes UMR 6554, CNRS
	Sébastien GADAL	Professeur des Universités, CNRS ESPACE UMR 7300, Université Aix-Marseille
	Vincent RODIN	Professeur des Universités, Lab-STICC, Département Informatique, Université Bretagne Occidentale
Dir. de thèse :	Simona NICULESCU	Maître de conférence, LETG-Brest UMR 6554, Université Bretagne Occidentale

Acknowledgement

In the beginning, I would like to express my special gratitude to my Ph. D. supervisor Dr. Simona NICULESCU, who gave me this opportunity and precise advice for my work. The thesis could not have been accomplished without her guidance throughout this research. I am also grateful for her kindness and empathy.

I would like to express my sincere appreciation to the members of my thesis jury, Prof. Christophe CLARAMUNT, Dr. Thomas CORPETTI, Prof. Vincent RODIN, and the rapporteurs, Dr. Antoine COLLIN and Prof. Sébastien GADAL, not only for taking the time to assess my work, but also for being comprehensive when I had to reschedule the defense because of my health issues.

I would like to extend my sincere thanks to Dr. Thomas CORPETTI and Dr. Dino IENCO for being on my thesis committee, evaluating my works, and providing advice and guidance during these four years of study.

I thank my dear work colleagues of UMR LETG Brest, thank you for taking me in and all the beautiful times. In particular, Soumia, Chi-Nguyen, Nina, and Laurianne, thank you so much for bringing me joy over these four years; I could not have undertaken this journey without you.

I would like to acknowledge the medical team of Cavale Blanche hospital for being professional and performing the surgeries quickly every time so that I could go back to work and submit the thesis on time (with some delays, although).

I am also very grateful to my dear partner Hassan and my lovely family-in-law for supporting and taking care of me when I was under the stress of writing, moreover, a special thanks to Daniel for the help in the layout of my thesis. I am so lucky to call you my family, and I will never forget your support and kindness.

At last, to my beloved parents and family, whom I have not seen for three years, there are no words to express my deep and sincere gratitude for what you have done for me. **Now I dedicate this thesis to you. I love you, three thousand!**

Table of contents

ACKNOWLEDGEMENT **3**

TABLE OF CONTENTS **4**

LIST OF FIGURES **8**

LIST OF TABLES **11**

LIST OF EQUATIONS **12**

LIST OF ABBREVIATIONS **13**

GENERAL INTRODUCTION **19**

General context 19

Problematic 21

Objective 22

Outline of thesis 24

CHAPTER 1. DETECTION OF LAND USE/LAND COVER CHANGES IN COASTAL AREA WITH REMOTE SENSING **27**

1.1. Definition of land use/land cover 27

1.1.1. Land cover and land use *27*

1.1.2. LULC changes and the importance of management *28*

1.2. LULC mapping and detecting changes with remote sensing techniques 31

CHAPTER 2. GEOGRAPHIC LOCALIZATION AND MAJOR LAND USE / LAND COVER IN PAYS DE BREST **46**

2.1. Geographical localization 46

2.2. Geographical condition 49

2.3. Land use / land cover in Pays de Brest 51

2.3.1. CORINE Land Cover (CLC) *51*

2.3.2. Main activities and protected natural areas *52*

2.4. Major LULCC issues 55

2.4.1. Imbalance of development between intercommunalités *59*

2.4.2. Imbalance between different land uses *61*

2.5. Research objectives and study sites 63

CHAPTER 3. DATA STRUCTURE AND FIELD RESEARCH **68**

3.1. Satellite imagery 69

3.1.1. Optical image *69*

3.1.1.1. Very high spatial resolution image (Pléiades-1, SPOT-5) ... 72
3.1.1.2. High-spatial-resolution open-source image (Sentinel-2) ... 76
3.1.2. Synthetic-aperture RaDAR image (Sentinel-1) ... *78*
3.2. AUXILIARY DATA ... 82
3.2.1. Graphic parcel register ... *82*
3.2.2. Google Earth ... *83*
3.3. FIELD RESEARCH ... 84
3.3.1. Observation and validation of vegetation in the city of Brest ... *84*
3.3.2. Observation and validation of LULC on the Crozon Peninsula ... *85*
3.3.3. Croplands and winter crops planting situation observation in northern Finistère ... *86*

CHAPTER 4. ANALYSIS AND IMAGE PROCESSING ... 87

4.1. METHODOLOGY OF IMAGE PRE-CLASSIFICATION ... 89
4.1.1. Calculation of vegetation indices ... *89*
4.1.1.1. Definition of the vegetation index ... 89
4.1.1.2. Choice of VI and calculation ... 94
4.1.2. Methodology of segmentation ... *97*
4.1.2.1. OBC vs PBC ... 98
4.1.2.2. Definition of image segmentation ... 100
4.1.2.3. Multiresolution segmentation ... 103
4.1.2.4. Simple Linear Iterative Clustering Superpixels segmentation ... 106
4.2. METHODOLOGY OF IMAGE CLASSIFICATION ... 108
4.2.1. Definition of image classification ... *108*
4.2.2. Shallow machine learning methods ... *112*
4.2.2.1. Definition of machine learning ... 113
4.2.2.2. Support vector machine classification ... 118
4.2.2.3. Random forest classification ... 123
4.2.3. Deep learning methods ... *127*
4.2.3.1. Definition of deep learning ... 127
4.2.3.2. MLP deep architecture ... 133
4.2.3.3. Convolutional NNs deep architecture ... 138
4.3. SAR BACKSCATTERING COEFFICIENT PROCESSING ON GOOGLE EARTH ENGINE (GEE) ... 143
4.3.1. SAR backscattering coefficient (σ°) ... *144*
4.3.2. Google Earth Engine platform ... *147*
4.4. POST-CLASSIFICATION METHODOLOGY ... 150
4.4.1. Accuracy assessment ... *151*
4.4.2. Post-classification comparison ... *154*

CHAPTER 5. MACHINE LEARNING METHODS AND CLASSIFICATION OF VEGETATION IN BREST, FRANCE ... 159

5.1. INTRODUCTION 159
5.2. STUDY AREA AND MATERIALS 163
5.2.1. Study area 163
5.2.2. Data 165
5.3. METHODOLOGY 166
5.3.1. SLIC Segmentation 166
5.3.2. MLP model training and classification 167
5.4. RESULTS AND DISCUSSION 168
5.4.1. Classification accuracy of MLP algorithm 168
5.4.2. Comparison with RF classification results 172
5.5. CONCLUSION 175

CHAPTER 6. MAPPING AND MONITORING OF LAND USE/LAND COVER CHANGES IN THE CROZON PENINSULA (BRITTANY, FRANCE) FROM 2007 TO 2018 BY MACHINE LEARNING ALGORITHMS (SUPPORT VECTOR MACHINE, RANDOM FOREST, AND CONVOLUTIONAL NEURAL NETWORK) AND BY POST-CLASSIFICATION COMPARISON 177

6.1. INTRODUCTION: 177
6.2. STUDY AREA AND MATERIALS 181
6.2.1. Study area 181
6.2.2. Data 183
6.3. METHODOLOGY 184
6.3.1. Image preprocessing 184
6.3.2. Image processing 185
6.4. IMAGE POST-PROCESSING 188
6.4.1. Accuracy assessment 188
6.4.2. Post-Classification Comparison (PCC) 188
6.5. RESULTS AND DISCUSSION 189
6.5.1. Comparison of classifiers 189
6.5.2. LULC Changes Detection (2007-2018) 195
6.6. CONCLUSION 199

CHAPTER 7. MAPPING CROP TYPES USING SENTINEL-2 DATA MACHINE LEARNING AND MONITORING CROP PHENOLOGY WITH SENTINEL-1 BACKSCATTER TIME SERIES IN PAYS DE BREST, BRITTANY, FRANCE 201

7.1. INTRODUCTION 201
7.2. STUDY AREA AND MATERIALS 206
7.2.1. Study area 206
7.2.2. Data 208
7.3. METHODOLOGY 209

7.3.1. Winter crops types mapping methods 210
7.3.2. Crops phenology monitoring methods 213
7.4. Results and discussion 213
7.4.1. Winter Crop Types Classification Methods Comparison 213
7.4.2. Crops phenology monitoring 221
7.5. Conclusion and perspectives 226

GENERAL CONCLUSION 228

Synthesis 228
Limitations of this study 229
Further research 230

APPENDICES 231

Appendix 1 Questionnaire for farmers 232
Appendix 2 : 《Machine Learning Methods and Classification of Vegetation in Brest, France》 233
Appendix 3 : 《Mapping and monitoring of land cover / land use (LCLU) changes in the Crozon Peninsula (Britanny, France) from 2007 to 2018 by Machine Learning algorithms (Support Vector Machine, Random Forest, Convolutional NN) and by Post-classification comparison (PCC)》 245
Appendix 4 : 《Mapping crop types using Sentinel-2 data Machine Learning and monitoring crop phenology with Sentinel-1 backscatter time series in Pays de Brest, Brittany, France》 269

REFERENCES 297

List of figures

Figure 1 Land use changes of the world from 1600 to 2016 (Source: History Database of the Global Environment (HYDE)) 29

Figure 2 Total coastlines of the world (Source: World Bank, 2020) 42

Figure 3 Marine ecoregions of the world (data source: Spalding et al., 2007 and The Nature Conservancy) 43

Figure 4 Localization of study areas. A: localization of Pays de Brest in France; B: localization of study areas, (1) Sentinel-2 satellite image of northern Finistère in 2019, (2) Pléiades image of city of Brest in 2018, (3) Sentinel-2 satellite image of the Crozon Peninsula in 2018 46

Figure 5 Pays de Brest with the seven intercommunalites: Pays d'Iroise, Pays des Abers, Lesneven-Cote des Legendes, Brest Metropole, Pays de Landerneau-Daoulas, Presqu'ile de Crozon-Aulne Maritime and Pleyben-Chateaulin-Porzay (source: Brest Metropole) 47

Figure 6 Distribution of the population by community in Pays de Brest 48

Figure 7 Umbrothermal diagram of the monthly mean temperatures and monthly mean total precipitations from 1991 to 2021 of Brest 49

Figure 8 Topography maps of Pays de Brest with principal landform and summit 50

Figure 9 CLC 2018 in Pays de Brest 51

Figure 10 Distribution of main economic activities in Pays de Brest 53

Figure 11 Protected natural areas in Pays de Brest 54

Figure 12 Artificial area rate in the department of Finistère in 2005, and its evolution between 1984 and 2005 55

Figure 13 Evolution of the population (a) and density of population (b) in Pays de Brest between 1990 and 2019 56

Figure 14 Evolution of population between (a) 1999 and 2008, (b) 2011 and 2016 59

Figure 15 Evolution of land use between natural area, agricultural land and artificial area in Pays de Brest and its coastal area between 1990 and 2018 (Source: CORINE Land Cover 1990, 2018) 62

Figure 16 City of Brest with urban green spaces 64

Figure 17 Location of the Crozon Peninsula and two bordering regions, located in Pays de Brest, Finistère, Brittany, France, with the RGB band combination for Sentinel 2 (2018) 65

Figure 18 Location of the study area in Northern Finistère, as per the RGB band combination of a Sentinel-2 satellite image on April 20, 2019 and the distribution of agricultural land in 2019. 66

Figure 19 Illustration of optical remote sensing (Source: Kumar et al., 2018) 70

Figure 20 The electromagnetic spectrum by wavelength (Source: Topaz, 2018) 70

Figure 21 SPOT-5 image of the Crozon Peninsula 72

Figure 22 Pléiades image of city of Brest 74

Figure 23 Sentinel-2 image of the Crozon Peninsula 76

Figure 24 Sentinel-2 image of northern Finistère 76

Figure 25 SAR system (Source: Lauknes, 2011) 78

Figure 26 SAR bands in electromagnetic spectrum 79

Figure 27 Four observation modes of Sentinel-1 80

Figure 28 RPG 2019 (Source: Geoportail.gouv.fr) 82
Figure 29 Pays de Brest on Google Earth 83
Figure 30 Vegetation in small scale on Google Earth 83
Figure 31 Sentinel-2 image of the Crozon Peninsula with GNSS points for ground truth field research 85
Figure 32 Croplands in northern Finistère 86
Figure 33 General flow path of image processing 87
Figure 34 Spectrum view of vegetation, crop, bare soil and artificial surface 90
Figure 35 Comparison of the original image and salt-and-pepper-noised image (Kelly et al., 2011) 99
Figure 36 Example of MRS applied on Sentinel-2 image 103
Figure 37 Example of SLIC applied on Pléiades image 106
Figure 38 Theoretical SVM model 119
Figure 39 SVM non-linear model 120
Figure 40 Four most frequently used kernel functions of SVM 121
Figure 41 Bagging theory model 124
Figure 42 RF model 125
Figure 43 Machine learning and deep learning in visual data analysis 128
Figure 44 Example of an MLP model with two hidden layers 133
Figure 45 Example of CNN model 138
Figure 46 Backscattered intensity depends on different targets (city, vegetation, and calm water) 144
Figure 47 SAR satellite imagery preprocessing procedure (Xie and Niculescu, 2022) 145
Figure 48 Example of GEE processing interface 148
Figure 49 Confusion matrix 152
Figure 50 Example of several accuracy index calculations (OA, Kappa coefficient, User's accuracy (also called "precision), Producer's accuracy (also called "recall), and F-Score) 153
Figure 51 Example of change detection technique 156
Figure 52 Localization of the city of Brest 163
Figure 53 Vegetated areas in the city of Brest: (a) urban forest (b) meadow (c) public park in the city center (d) croplands (e) street trees (f) private gardens in the residential area 164
Figure 54 Scheme of the proposed methodology in the study 166
Figure 55 MLP model used for classification in the study 168
Figure 56 Classification results of vegetation in the city of Brest on 2016, 2017, and 2018 by using MLP deep structure 170
Figure 57 Example of a transition from vegetated area to non-vegetated area in Brest between 2016 and 2018 171
Figure 58 Example of transition from vegetation to artificial surface 172
Figure 59 Classification results of vegetation in the city of Brest in 2016, 2017, and 2018 using RF machine learning classifier 173
Figure 60 Comparison of MLP and RF classifiers 173
Figure 61 Differences between MLP and RF classification results 174

Figure 62 Location of the study area, including the Crozon Peninsula and two bordering regions, located in Pays de Brest, Finistère, Brittany, France, with the RGB band combination for Sentinel 2 (2018) and the location of the ground truth field Research. 182
Figure 63 Global methodology proposed..... 184
Figure 64 Detailed CNN methodology 187
Figure 65 CNN model proposed and used for the classification of images from 2018 in the study 187
Figure 66 Classification results with SVM, RF and CNN..... 189
Figure 67 LULC change maps with the classification of SVM (a), RF (b), and CNN (c). 196
Figure 68 Details of the three main land cover change types of the CNN classification with comparisons between 2007 and 2018..... 197
Figure 69 Location of study area, the north of the Finistère department, Brittany, France, as per the RGB band combination of a Sentinel-2 satellite image on 20 April 2019 and the distribution of agricultural land in 2019. 207
Figure 70 Hierarchical classification methodology used in the study for crop mapping..... 210
Figure 71 Proposed detail image processing methodology chart..... 211
Figure 72 Sentinel-1 image process in the GEE platform..... 213
Figure 73 Level 1: PBC vegetation (including cropland) extraction results. 214
Figure 74 Level 2: PBC and OBC croplands extraction results..... 215
Figure 75 Level 3: PBC and OBC winter crops extraction results 216
Figure 76 Classification results with hierarchical classification and classical direct extraction 218
Figure 77 Sentinel-1 temporal backscattering coefficient profiles of different land covers (Vegetation, water, urban area, bare soil, winter wheat, and winter barley) in the study area at VV and VH polarizations from 1 October 2018 to 1 September 2019. 221
Figure 78 Winter wheat and winter barley Sentinel-1 temporal backscattering coefficient profiles at VV, VH, and VH/VV polarizations of the north Finistère region for the 2018-2019 growing season, with the daily precipitation data and three main phenological stage 222

List of tables

TABLE 1 SPATIAL RESOLUTION AND WAVELENGTH OF SPOT-5 PRODUCT 73

TABLE 2 REVISITING TIME OF PLÉIADES (SOURCE: EOPORTAL) 74

TABLE 3 SPATIAL RESOLUTION AND WAVELENGTH OF PLÉIADES PRODUCT 75

TABLE 4 SPATIAL RESOLUTION AND WAVELENGTH OF SENTINEL-2 OPERATED BANDS (SOURCE: XIE AND NICULESCU, 2022) 77

TABLE 5 THE MOST COMMON BANDS USED IN SAR IMAGING SYSTEMS 79

TABLE 6 CHARACTERISTICS OF FOUR ACQUISITION MODES OF SENTINEL-1 81

TABLE 7 VHR PLÉIADES SATELLITE IMAGES USED IN THE STUDY 165

TABLE 8 OA OF VEGETATION CLASSIFICATION 169

TABLE 9 CONFUSION MATRIX AND GLOBAL KAPPA COEFFICIENT OF VEGETATION CLASSIFICATION 169

TABLE 10 KAPPA COEFFICIENTS AND OA INDICATORS OF RF CLASSIFICATION RESULTS FROM 2016 TO 2018 172

TABLE 11 SATELLITE IMAGES USED IN THE STUDY 183

TABLE 12 TRAINING SAMPLES SURFACE AREA FOR SVM AND RF MODEL TRAINING IN 2007(2A) AND 2018(2B). 186

TABLE 13 TRAINING OA (%) 190

TABLE 14 VALIDATION OA (%) 190

TABLE 15 TRAINING PRODUCER'S ACCURACY AND USER'S ACCURACY BY CLASS 192

TABLE 16 VALIDATION PRODUCER'S ACCURACY AND USER'S ACCURACY BY CLASS 192

TABLE 17 LAND COVER CHANGE AREA AND PROPORTION OF THE CHANGE TYPE WITH THE THREE METHODS OF CLASSIFICATION. 197

TABLE 18 SENTINEL-2 IMAGE USED IN THE STUDY 208

TABLE 19 SENTINEL-2 SPECTRAL BANDS USED IN THE STUDY 209

TABLE 20 ACCURACY ASSESSMENT OF PBC VEGETATION (INCLUDING CROPLAND) EXTRACTION. 214

TABLE 21 ACCURACY ASSESSMENT OF OBC CROPLANDS EXTRACTION 216

TABLE 22 ACCURACY ASSESSMENT OF PBC CROPLANDS EXTRACTION 216

TABLE 23 ACCURACY ASSESSMENT OF OBC WINTER CROPS EXTRACTION 217

TABLE 24 ACCURACY ASSESSMENT OF PBC WINTER CROPS EXTRACTION 217

TABLE 25 ACCURACY ASSESSMENT OF HIERARCHICAL CLASSIFICATION 218

TABLE 26 ACCURACY ASSESSMENT OF CLASSICAL DIRECT EXTRACTION 219

TABLE 27 THE BEST POLARIZATION OBSERVED FOR EACH PHENOLOGICAL STAGE OF WINTER WHEAT IN THE STUDY 224

TABLE 28 THE BEST POLARIZATION OBSERVED FOR EACH PHENOLOGICAL STAGE OF WINTER BARLEY IN THE STUDY 224

List of equations

$NDVI = (NIR - Red)/(NIR + Red)$ (1) 94
$NDWI = (NIR - SWIR)/(NIR + SWIR)$ (2) 94
$GNDVI = (NIR - Green)/(NIR + Green)$ (3) 95
$EVI = (G * (NIR - Red))/(NIR + C1 * Red - C2 * Blue + L)$ (4) 95
$EVI2 = 2.5((NIR - Red)/(NIR + 2.4Red + 1))$ (5) 96
$SAVI = (NIR - Red/NIR + Red + L)(1 + L)$ (6) 96
$MSAVI = (2 * NIR + 1 - \sqrt{(2 * NIR + 1)2 - 8 * (NIR - Red)}\ )/2$ (7) 97

List of abbreviations

Abbreviation	Definition
5D	Five-Dimension
AE	AutoEncoder
AGB	Forest AboveGround Biomass
ALOMLP	Ant Lion Optimizer MultiLayer Perceptron
ANN	Artificial NN
API	Application Programming Interface
ASAR	Advance Synthetic-Aperture RaDAR
ASCAT	Advanced SCATterometer
ASTER	Advanced Spaceborne Thermal Emission and Reflection
ATR	Automatic Target Recognition
AVHRR	Advanced Very High Resolution Radiometer
BOA	Bottom-Of-Atmosphere
BRDF	Bi-Directional Reflectance Distribution Function
BT	Bagging Trees
CA-MC	Cellular Automata-Markov Chain
CART	Classification And Regression Trees
CCF	Canonical Correlation Forests
CD	Change Detection
CHM	Canopy Height Model
CLC	CORINE Land Cover
CNES	French National Center for Space Studies; French: *Centre National d'Etudes Spatial*
CNN	Convolutional NN
dB	Decibels
DBN	Deep Belief Network
DCNN	Deep Convolutional NN
DEM	Digital Elevation Model
DF	Data Fusion
DL	Deep learning
DpRVI	Dual-Pol RaDAR Vegetation Index

DT	Decision Tree
DTM	Digital Terrain Model
DVI	Difference Vegetation Index
EC	European Commission
ECHO	Extraction and Classification of Homogeneous objects
ED2	Euclidean Distance 2
ELM	Extreme Learning Machine
EMR	Electromagnetic radiation
ENDVI	Enhanced Normalized Difference Vegetation Index
ENVISAT	Environmental Satellite
EO	Earth's Observation
ERS	European Remote Sensing
ESA	European Space Agency
EVI	Enhanced Vegetation Index
EVI2	Enhanced Vegetation Index2
EW	Extra Wide
FAO	Food and Agriculture Organization
FCN	Fully Convolutional Network
F-net	Fixed-scale net
GA	Genetic Algorithm
GAN	Generative Adversarial Network
GB	Gradient Boosting Trees
GBRCN	Gradient Boosting Random Convolutional Network
GEE	Google Earth Engine
GEOBIA	GEographic Object-Based Image Analysis
GI	Greenness Index
GIS	Geographic Information System
GNDVI	Green Normalized Difference Vegetation Index
GNSS	Global Navigation Satellite System
GRD	Ground Range Detected
GRVI	Green Red Vegetation Index
HR	High spatial Resolution
HRNet	High-Resolution deep NN

HRS	High-Resolution Stereoscopic
HRV	High-Resolution Visible
HYDE	History Database of the Global Environment
IGN	French National Institute of Geographic and Forest Information
ISODAT	Iterative Self-Organizing Data Analysis Techniques
IW	Interferometric Wide
IW	Interferometric Wide
KNN	*K*-Nearest Neighbor
LAI	Leaf Area Index
LIDAR	Light Detection and Ranging
LSP	Land Surface Phenology
LSWI	Land Surface Water Index
LSVRC	Large-Scale Visual Recognition Challenge
LULC	Land Use/Land Cover
LULCC	Land Use/ Land Cover Change
MCNN	Multiscale Convolutional NN
MCS	Multiple Classifier System
MIR	Middle InfraRed
ML	Machine Learning
MLC	Maximum-Likelihood Classifier
MLP	Multilayer Perceptron
MLP-MC	Multilayer Perceptron -Markov Chain
MODIS	Moderate Resolution Imaging Spectroradiometer
MRF	Markov Random Field
MRS	MultiResolution Segmentation
MS	MultiSpectral
MSAVI	Modified Soil-Adjusted Vegetation Index
MSCNN	Multiscale Convolutional NN
MSCP	Multilayer Stacked Covariance Pooling
MSS	Multispectral Scanner
NBNDVI	Narrow-Band Normalized Difference Vegetation Index
NDGI	Normalized Different Greenness Index

NDPI	Normalized Difference Phenology Index
NDVI	Normalized Difference Vegetation Index
NDWI	Normalized Difference Water Index
NIR	Near-InfraRed
NLI	Non-Linear Vegetation Index
NN	Neural Network
NN ge	Non-Nested Generalized Exemplars
NNR	Nation Natural Reserves; French: *Réserve naturelle nationale*
NOAA	National Oceanic and Atmospheric Administration
NSR	Number-of-Segments Ratio
OA	Overall Accuracy
OBC	Object-Based Classification
OBIA	Object-Based Image Analysis
OTOP	Offline Training and Online Prediction
PA	Producer's Accuracy
PAI	Plant Area Index
PBC	Pixel-Based Classification
PCA	Principal Component Analysis
PCC	Post-Classification Comparison
PDE	Partial Differential Equation
PRI	Photochemical Reflectance Index
PSE	Potential Segmentation Error
PT-DTW	Phenology-Time-Weighted Dynamic Time Warping
PVI	Perpendicular Vegetation Index
RF	Random Forest
RNN	Recurrent NN
RNR	Regional Natural Reserves; French: *Réserve naturelle régionale*
RoF	Rotation Forests
RPG	Graphic parcel register
RPG	Graphic Parcel Register ; French: *Registre parcellaire graphique*

RVI	Ratio Vegetation Index
RVSI	Red-Edge Vegetation Stress Index
SAE	Stacked Autoencoder
SAR	Synthetic-Aperture RaDAR
SARVI	Soil Adjusted Ratio Vegetation Index
SAVI	Soil Adjusted Vegetation Index
SCAE	Stacked Convolutional Auto Encoder
SCCov	Skip-Connected Covariance
SDA	Stepwise Discriminant Analysis
SIFT	Scale-Invariant Feature Transform
SLC	Single Look Complex
SLIC	Simple Linear Iterative Clustering
SLIC-CNN	Multiscale Simple Linear Iterative Clustering-Convolutional NN
SM	StripMap
SMOS	Soil Moisture and Ocean Salinity
SPC	SuperPixel Contour
SPOT	Earth Observation Satellite; French: *Satellite pour l'Observation de la Terre*
SR	Simple Ratio
SRM	Super-Resolution Mapping
SSAS	Scale Self-Adapting Segmentation
SVM	Support Vector Machine
SWIR	Short Wave InfraRed
TCI	Temperature Condition Index
TD	Transformed divergence
TIR	Thermal InfraRed
TL	Transfer Learning
TM	Thematic Mapper
TSAVI	Transformed Soil Adjusted Vegetation Index
UA	User's Accuracy
UAV	Unmanned Aerial Vehicles
UGS	Urban Green Space

VARI	Visual Atmospheric Resistance Index
VCI	Vegetation Condition Index
VGG	Visual Geometry Group
VHR	Very High Resolution
VI	Vegetation index
VIN	Vegetation Index Number
V-net	Varied-scale net
WV	WorldView
WV	Wave
ZPS	Special Protection Zones; French: *Zone de Protection Spéciale*
ZSC	Special Conservation Zones; French: *Zone Spéciale de Conservation*

General introduction

General context

"Land cover" and "land use" refer to the physical ground cover information of the land (Meyer & Turner, 1994) and the socio-economic and cultural utility of the land occupied by humans (Turner, 1997), respectively. Land use and land cover (LULC) information have long been considered the key element to understanding the Earth's surface and the purpose the land serves. Moreover, land use and land cover change (LULCC) driven by various factors (e.g., economic, biophysical, political, social) (Verburg et al., 2006) has emerged as a fundamental component of global environmental change and sustainability research (Turner et al., 2007). In recent years, LULCC has attracted significant attention from the scientific community, government, and decision-makers because LULCC reflects the pattern of human use in a region (Y. Chang et al., 2018), which significantly affects the function of the Earth's system (Lambin et al., 2001).

Coastal areas—due to the interactions between land, water, and atmosphere that are constantly being altered by natural and human forces (Beatley et al., 2002)—have always played an essential role in LULC studies for their high concentration of functions, socio-economic activities and population, and natural resources (Mossinger et al., 2013). Global economic, social, and environmental changes have been observed on different scales since the late 1990s; coastal LULC issues have become of increasing scientific interest nowadays, considering that more than half of the world's population lives in coastal regions (Neumann et al., 2015), of which only 15% remain in their natural state. In particular, urbanization, the development of infrastructure and associated facilities at high speed, growing intense agriculture production, and the increasing exploitation of natural resources are the main driving factors of dramatically rising LULCC in coastal areas in recent decades.

In the meantime, remote sensing technologies have brought a significant breakthrough in this new scientific discipline known as "land change science" (Turner et al., 2007) with automatic classification algorithms and high spatial, spectral, and temporal resolution, and radiometric satellite imagery. It has become possible to map LULC accurately and monitor the changes that cannot be observed in ground research. In

addition, remote sensing has become an essential tool for LULC studies because it facilitates global, recurrent, and long-term observation. Moreover, the latest generation of satellite imagery from Europe's Copernicus Programme—which provides free access, high-quality multispectral sensors—as well as the development of different digital data, have brought LULC classification and LULCC detection into a new era.

Our study area, Pays de Brest, located on the west coast of France, is the most important metropolitan and agglomeration in the northwestern Finistère department in Brittany region, where around 80% of the population live in coastal areas (i.e., within 30 km of a coastline). The LULC of the Pays de Brest coastline, however, appears to be relatively fragmented due to its particular geographical configuration (e.g., fragmented peninsula, uneven topography) and a long history of land reclamation.

Like the majority of coastland worldwide, Pays de Brest has experienced considerable LULCC since the 1990s and today faces increasing and varied types of pressure, including natural, demographic, residential, economic, and environmental (Adeupa, 2009). The coastline changes in Pays de Brest are driven mostly by rising population, development of tourism, urban expansion, and intense agricultural activities (Adeupa, 2009; Sparfel, 2011). Those factors have led to environmental degradation and conflicts of interest among the private sector, public services, housing, local planning, tourist sectors, and public authorities seeking protection for the natural landscape (*ADEUPa Brest*, n.d.; Sparfel, 2011). For example, the conflict between permanent or vacation housing construction on coastlines with aquaculture and croplands and natural landscape, which are often encroached upon by urban expansion and the artificialization of coastland.

Thus, the use of high spatial and temporal resolution satellite data could offer fresh perspectives for LULC studies in Pays de Brest. In particular, near-real-time remote sensing data (e.g., Sentinel data) appear to be perfectly complementary to large-scale vector data (e.g., BDTopo IGN, CORINE Land Cover, digital cadastral plan) of infrastructure, construction, vegetation cover, and their evolution. Moreover, the vector data are usually annual; satellite observation data, in contrast, are able to provide data at a higher frequency (nearly daily).

However, although remote sensing has become the principal source of LULC information, the European Copernicus Programme and national facilities (e.g., Equipex GEOSUD, THEIA) provide access to a particularly large amount of satellite data for local communities, scientist communities, and industries. LULC information in coastal Pays de Brest is insufficient, and very few previous studies have focused on vegetation cover.

Therefore, local governments and communities seek an efficient way to gain an understanding of LULC in the region and follow the changes that occurred over time to manage urban development and the evolution of LULC, also protecting the natural landscape. In this context, local public sectors are interested in the potential contribution of the new technologies to environmental data processing. In particular, multi-source remote sensing data are available and access is free.

In this thesis, three specific LULC studies were conducted in three different studies areas located within Pays de Brest according to the immediate need of local communities (especially ADEUPa Brest, Parc Naturel Régional d'Armorique, Brest Métropole).

Problematic

The general problematic of the thesis is how remote sensing technologies contribute to fundamental local issues such as coastal LULCC in the context of population growth, urban sprawl and climate change, as well as how remote sensing technologies—especially the latest generation of satellite imagery and advanced classification—bring important breakthroughs to LULC studies of Pays de Brest.

Moreover, some detailed problematics must also be found out:

1) How can the application of the latest generation of high spatial and spectral resolution satellite imagery be strengthened to better respond to environmental management and urban planning issues?

2) What are the significant past and current changes in the coastal Pays de Brest that have not yet been observed by ground research and vector data? In addition, what are their driving factors, as well as short or long-term environmental and socio-economic influences?

3) What are the most suitable tools and methodologies for better detecting, identifying, and monitoring LULCC over time at different spatial scales?

4) Is it possible to generate change models in order to develop forward-looking scenarios?

Apart from the general problematic, local communities are also interested in three specific LULC questions:

1) How can machine learning (ML) classification methods contribute to vegetation cover mapping in Brest?

2) What were the major LULCCs on the Crozon Peninsula (Pays de Brest) from 2007 to 2018, and what are the most commonly adopted classification methods for LULCC detection?

3) How to map winter crops in Pays de Brest and monitor their phenology using open-access, high spectral and spatial resolution Sentinel-1 and -2 data.

Objective

In order to address this issue, this thesis focuses on the different ways to explore the potential of European satellite data (e.g., Vénµs, Pleiades, SPOT, and Sentinel) to propose a robust ML methodology for LULCC analysis and mapping. This methodology has been partially transferred to some local authorities of the Pays de Brest to use them in their territorial governance mission. The main objective can be decomposed into several steps. First, LULC classification was performed to provide accurate thematic maps using different ML and deep learning (DL) algorithms. The observation and monitoring of LULCC were then carried out, mainly using post-classification processing methods. Moreover, we sought to identify and understand the socio-economic factors behind these changes, eventually modeling the changes and impacts, and forecasting the potential changes in a context of global change.

The following specific objectives were also formulated for local government and communities:

1) To propose specific and reproductive image-processing methodology to enable better analysis, modeling and definition of LULC, as well as improved monitoring of LULCC in Pays de Brest. The methodology proposed should effectively improve the accuracy of LULC and vegetation cover maps.

2) Evaluate and validate the classification results and compare different methodologies to select the most suitable methodology for coastal LULC classification in Pays de Brest.

3) To transfer high-resolution remote sensing data to managers for operational purposes, and to propose a three-dimensional (i.e., natural areas, agricultural areas, and built-up areas) LULC model at different scales (e.g., city, municipality, or region).

Moreover, three specific aims have been formulated according to the needs of local communities:

1) To detect, identify, and classify urban green land in three years (2016–2018) in the city of Brest and eventually to study the changes.

2) To map different LULCs and then monitor LULCC from 2007 to 2018, eventually look for abandoned agricultural land on the Crozon Peninsula.

3) To study the feasibility of mapping winter crops with Sentinel-2 data in a fragmented area dominated by small-size fields.

4) To study the correlation between winter crop phenology and Sentinel-1 C-band Synthetic-Aperture RaDAR (SAR) backscattering time-series data.

Outline of thesis

This thesis consists of three parts comprising seven chapters. The first part presents the context of the work; part two discusses the general methodologies, including data and image-processing methodologies. The third part presents the three specific case studies (and publications) carried out during the thesis. The seven chapters are summarized below:

1) Chapter 1 presents the definition of LULC, LULCC and its impacts, as well as the importance of LULC monitoring and management. This is followed by an extensive literature review of previous studies of LULC classification and LULCC detection using remote sensing technologies, especially LULC studies in coastal areas.

2) Chapter 2 analyzes geographical characteristic of the study area essential for our study, such as the localization and geographical condition. In addition, the major LULC in Pays de Brest, including salient issues and conflicts of interest, are presented. This chapter concludes with the detailed research objectives of each case study.

3) Chapter 3 deals with the data employed in our works, including various optical images and SAR time series, auxiliary data, and field studies.

4) Chapter 4 outlines the methodologies of image processing applied in our case studies, namely image pre-classification processing, image classification by using different shallow machine learning or deep architectures, and methods of post-classification processing.

5) Chapter 5 presents the first case study, “Machine Learning Methods and Classification of Vegetation in Brest, France.”

6) Chapter 6 presents the second case study, “Mapping and monitoring of land cover / land use (LULC) changes on the Crozon Peninsula (Brittany, France) from 2007 to 2018 by Machine Learning algorithms (Support Vector Machine, Random Forest, Convolutional NN) and by Post-classification comparison (PCC).”

7) Chapter 7 presents the third case study, “Mapping crop types using Sentinel-2 data Machine Learning and monitoring crop phenology with Sentinel-1 backscatter time series in Pays de Brest, Brittany, France.”

The thesis concludes with a synthesis of the results, a discussion of the success and limitations of the works, and, ultimately, the proposition for further research.

PART I CONTEXT OF THE STUDY

Chapter 1. Detection of land use/land cover changes in coastal area with remote sensing

1.1. Definition of land use/land cover

Land cover and *Land use* have often been confused in daily practice (Giri, 2012) and are often used interchangeably. However, these are two distinct concepts.

1.1.1. Land cover and land use

Land cover has been defined as the observed biotic and abiotic assemblage of the Earth's surface and immediate subsurface (Meyer & Turner, 1994), which refers to the physical ground cover information of the land. Land cover refers to the quantity and type of certain surfaces on the ground in a geographical area, such as vegetation cover, croplands, urban areas, water bodies, and glaciers (Meyer & Turner, 1994).

As the most important descriptor of the Earth's terrestrial surface, land cover allows for studying the operational relationship between terrain, climate, and soil, the characteristics of anthropogenic activity, and biogeographical and eco-climatic diversity (Loveland et al., 2000; Turner et al., 2007; Wulder et al., 2018). Therefore, land cover information monitoring is critical to foreground a range of natural resource management decisions at local, national, and global levels (Wulder et al., 2018).

Land use, on the other hand, refers to the purpose the land serves and describes the social, economic, and cultural utility of the land occupied by humans (Turner, 1997). Therefore, compared to land cover (which is most often pertinent to the natural sciences), land use is more likely related to social sciences such as economy, sociology, anthropology, and social geography (Meyer & Turner, 1994).

The same land use can relate to several different lands covers reciprocally. For example, a vegetated area can be used as grassland, forest, or public green space, and an artificial surface can be a commercial area, residence for inhabitants, or industrial zone. By contrast, urban parks and residential areas generally comprise built-up area and vegetation cover.

According to World Bank (*World Bank Group*, n.d.) statistics and FAO (*FAO*, n.d.), the most important land uses worldwide are livestock grazing land and cropland, forested area, built-up area, shrubland, barren land, glacier, and fresh air and water resources. However, most land uses nowadays—mainly built-up areas—have various important impacts on ecosystem service, including biodiversity degradation, greenhouse effect, and deforestation. For example, agriculture—the most critical land use worldwide, which occupies half of the Earth's habitable land—is threatening biodiversity due to the ceaseless expansion of croplands and intensive agricultural activities.

Thus, knowledge of land use is crucial for understanding the conflict between different land uses and developing strategies to balance the conflict for sustainable development.

1.1.2. LULC changes and the importance of management

Land cover change and *Land use change* can also be interpreted separately. Land cover change refers to the complete modification from one class of land cover to another or to the anthropologic or natural change within the same land cover class (Meyer & Turner, 1994). One example would be conversion from cropland to urban area or forest degradation due to natural disaster (e.g., forest fire and storm damage). Nonetheless, the principal land cover change nowadays is converting the natural environment for human use or changing practices on human-occupied lands (Foley et al., 2005).

Land use change, in comparison, refers either to a shift toward a different employment of land occupied by humans or to an intensification of the current land use. In addition, land use change is human-induced; it can be conducted without land cover change. For example, a primary forest can be occupied by humans and used to produce wood, without ceasing to be forest. Overall, land use and land cover change (LULCC) reflects the pattern of human land use in a region (Y. Chang et al., 2018) and significantly affects the function of the Earth's system (Lambin et al., 2001).

Although various factors are driving LULCC, including biophysical, economic, social, cultural, political, or institutional factors (Verburg et al., 2006), human-induced LULCCs are far more common than natural changes in recent decades (Giri, 2012). Humanity's growing impact on the environment is responsible for most of the recent changes in the biosphere and modification of the Earth (Meyer & Turner, 1994). As shown

in Figure 1, human activities are changing the Earth's surface in pervasive and unprecedented ways, especially after the industrial revolution (1760s–1840s)(R. S. DeFries et al., 2004; Foley et al., 2005).

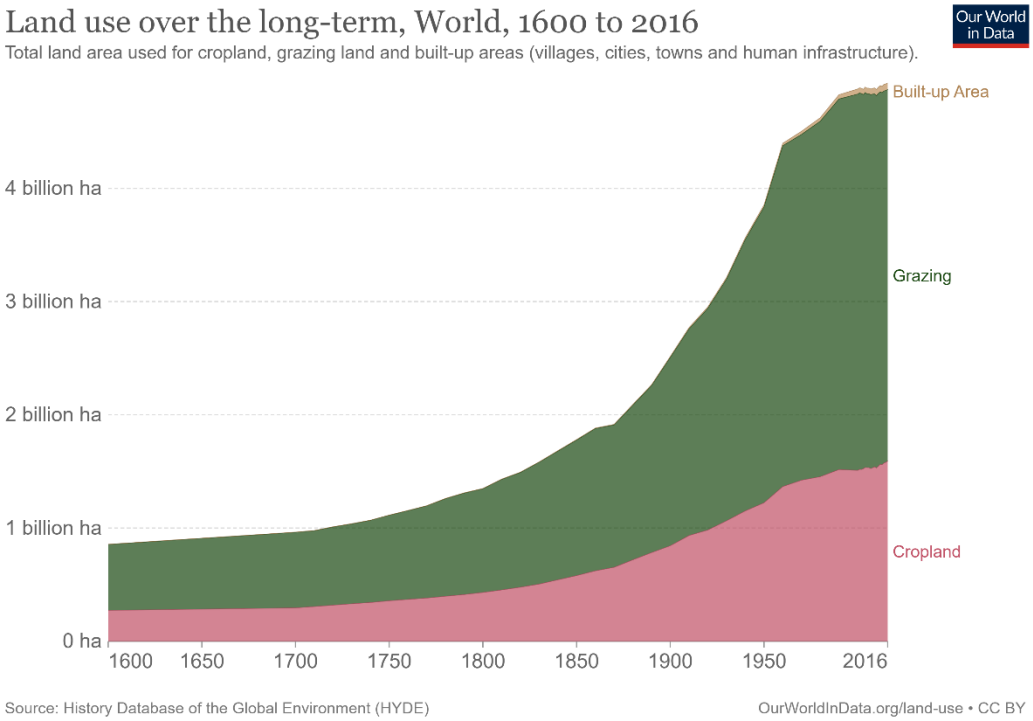

Figure 1Land use changes of the world from 1600 to 2016 (Source: History Database of the Global Environment (HYDE))

Moreover, LULCC is usually related to population growth and poverty and mostly drove by people's immediate needs for natural resources (Foley et al., 2005) as well as their responses to economic opportunities (Lambin et al., 2001). Consequently, rapid LULCC is mainly due to economic globalization, which can directly determine the LULC of a region or indirectly affect LULC through information and technological development (Lambin et al., 2001).

Furthermore, LULCC is not unidirectional; the environmental changes induced by human activities or natural changes generally impact LULC (Y. Chang et al., 2018). Lambin et al. (2001) have summarized that the most essential current LULCC representation on Earth is tropical deforestation (forest shifting to cultivation), rangeland modification and degradation, agricultural intensification, and urbanization in the form of built-up or paved-over areas. In addition, LULCC has direct effects on biodiversity (Sala et al., 2000; Falcucci et al., 2007; Cousins et al., 2015), global carbon cycle change (Houghton et al., 1999; J. Olofsson & Hickler, 2008), and the global climate warming effect (Houghton et al.,

1999; Fearnside, 2000; J. Li et al., 2021), as well as regional or local climate change such as the urban island heat effect (X.-L. Chen et al., 2006; X. Deng et al., 2013), soil degradation (X. Wang et al., 2016; Borrelli et al., 2017), degradation of sustainable natural resources—especially forest resources (Vitousek et al., 1997; Lira et al., 2012)—water and air pollution (S. T. Y. Tong & Chen, 2002; Ren et al., 2003; S. Wu et al., 2012), and increases in infectious disease due to the increased proximity of people and livestock brought on by urbanization (M. X. Tong et al., 2015; Hassell et al., 2017).

Even though LULCC has some positive effects on human society—for instance, the conversion from forests to croplands allows it to feed the rapidly growing population worldwide—it also entails a variety of adverse effects that lead to the significant degradation of the Earth's ecosystem (Giri, 2012). Therefore, monitoring and understanding the distribution and dynamics of LULC (Giri, 2012) as well as modeling, predicting, and managing LULCC at the local or/and global level (Meyer & Turner, 1994) have become crucial and have led to the demand for maintaining a balance between immediate human needs and the sustainable capacity of the ecosystem, in addition to ensuring resources and services in the future (Foley et al., 2005). Moreover, as a critical element in current strategies for natural resource management and environmental changes following up (Turner et al., 1995; Attri et al., 2015), LULC monitoring can provide valuable information—first of all, to governments (from national to local) for implanting sustainable development policies—as well as to nongovernmental organizations and scientists for studying the Earth's ecosystem and human societies (Giri, 2012).

Considering the indispensability of, and increasing need for, understanding LULC and LULCC mechanisms (Petit et al., 2001; Foley et al., 2005), the link between LULC and human activities has been intensively studied in recent decades. The connection has been analyzed on the American and African continents since the 1930s; however, the studies were highly focused on planning and managing land use (Y. Chang et al., 2018). Sixty years on, LULC researches were beginning to attract considerable attention and interact with other disciplines; the LULCC mechanism has since been studied at a regional or global scale (Y. Chang et al., 2018). Also in the 1990s, remote sensing technologies were introduced and developed in the LULC research field for mapping LULC and simulating the major socio-economic and biophysical driving factors and consequences of LULCC

(Verburg et al., 2006). Afterward, remote sensing technologies soon improved to meet research needs, leading to a massive breakthrough in LULC and LULCC studies.

1.2. LULC mapping and detecting changes with remote sensing techniques

Remote sensing technologies can directly detect land cover, and infer land uses, generally with the help of prior knowledge and auxiliary data. As a revolutionary breakthrough, remote sensing provides near-real-time, spatially continuous, and highly consistent information at a variety of spatial and temporal scales in order to accurately detect LULC on diverse scales and help to identify the different characteristics of LULCC that occur over time and cannot be observed by ground research (Foody, 2002; Verburg et al., 2006; Weih & Riggan, 2010), including the types, spatial distribution, and quantity of changes.

Overall, remote sensing technologies facilitate dynamic monitoring and quantitative analysis (Y. Chang et al., 2018) and have become the major sources for LULC mapping and LULCC detection for their rich spectral information of ground objects, a wide selection of spatial and spectral resolutions, high temporal frequency, and low computational complexity (Lunetta et al., 2004; Coops et al., 2006; G. Chen et al., 2012).

Meanwhile, LULC research has reciprocally always been in a key position and has made significant contributions in the remote sensing field, especially in environmental science (Kalnay & Cai, 2003; Aplin, 2004; Y. Chang et al., 2018). In the beginning, LULC information was collected using visual photo interpretation; however, this method was hindered by increasing labor costs, long processing times for outputs, and human subjectivity (because photo interpretation is highly dependent on a priori knowledge) (Wulder et al., 2018).

The breakthrough occurred in 1972 when the first Earth's Observation (EO) satellite, Landsat (originally named Earth Resources Technology Satellite), was launched. This first-generation EO satellite was efficient in providing stable, global, and multispectral satellite data, which officially started the satellite era of LULC research. As one of the earliest representative works of LULC classification, Townshend (1992)

summarized a wide range of applications of land cover information with the first generation of remote sensing data of coarse spatial resolution (Loveland, 2012) and highlighted the necessity to focus on the activities of land cover monitoring over time, and eventually expand the study area by including land use.

The first works were derived from coarse-resolution USA sensor systems, namely the four-spectral-band Landsat MultiSpectral Scanner (MSS), which collected in 79 m (re-sampled to 60 m in processing). For instance, among the most-cited work, Todd et al. (1977) explored the use of four-band Landsat MSS digital images to identify six diverse LULC categories and therefore detect LULCCs between 1972 and 1974 in the urban area of the city of Atlanta. In this study, two satellite images were digitally overlaid, after which LULCCs were extracted by directly comparing two images on a pixel-to-pixel basis. The final decision was made by the ratio of the intensity of reflected electromagnetic radiation (EMR) between two images; the ratio of an unchanged area was around 1.0, yet, whereas the ratio was significantly different where LULC had changed between 1972 and 1974.

Afterward, Byrne et al. (1980) conducted a study of land cover change monitoring by performing the principal component analysis (PCA) of an eight-dimensional data array composed of two four-band Landsat MSS images. PCA effectively identifie areas in which changes have occurred between two dates. Moreover, numerous features were detected in the study, including vegetation growth, deforestation activity, intensive management in forest areas, and urban development.

In the same year, Gordon (1980) applied two Landsat images to monitor land use change in Franklin County, Ohio, USA, induced by an extensive regional project. The results showed that some major errors remained in the image processing and classification (such as misalignment and misclassification) especially in an urban environment. In contrast to the complex and heterogeneous landscape of urban categories, agriculture and open spaces were the most accurately classified categories. However, the author indicated that remote sensing techniques were not yet mature. The direct application of satellite images must await advancements in classification to improve accuracy.

In the 1980s, the spatial resolution of Landsat images was improved from 69 m to 30 m; in addition, three more spectral bands were appended (Loveland, 2012), thus facilitating better classification of LULC.

Several papers in the 1980s and 1990s are well-recognized for their contribution to LULC classification with medium spatial resolution satellite data. Toll (1985) and Haack et al. (1987) both assessed Landsat Thematic mapper (TM) and MSS through the classification performance of urban/suburban land cover by using the maximum-likelihood classifier (MLC) and transformed divergence (TD) calculations, respectively. Both authors indicated that TM data could significantly improve accuracy in the homogenous suburban land cover because the TM data possessed finer spatial and spectral resolution in comparison to MSS. Especially in Toll's study, TM provided considerable improvements in accuracy (from 74.8% to 83.2%). However, both studies also mentioned that the TM data might cause a reduced classification accuracy in heterogeneous complex urban land covers.

Fuller et al. (1994) presented the land cover map of Great Britain that records 25 land cover types, including 18 semi-natural vegetation types. The map was produced using a supervised MLC in Landsat TM multitemporal data acquired in summer and winter. The proposed method effectively classified land cover in Great Britain with high accuracy (around 80% to 85%) and separated a wide range of vegetation cover types. At the same time, the European satellite system arose in the late 1980s with the first launch of the SPOT mission, which was equipped with high-resolution visible instrument (HRV) (20 m); with this advance, urban LULC mapping emerged.

Some research are well-established and presentative for LULC mapping in the urban area, (Gong & Howarth, 1992) developed a cover-frequency method for extracting land use in a rural–urban fringe environment in the town of Markham, Toronto, Canada, which was a typical rural–urban with much agricultural and natural land converted into an urban area for commercial, industrial, and residential uses. A classification with 12 land cover categories was first performed on a single SPOT HRV multispectral data point using MLC, and then cover frequencies were extracted from the classified map for another classification of 14 land use classes using a supervised minimum-city-block classifier. The cover-frequency method proved more efficient than the traditional MLC (with a higher

kappa coefficient of 0.2); moreover, SPOT HRV data proved helpful for LULC mapping in the urban environment.

In another study of rural–urban fringe LULC mapping in Toronto, Treitz et al. (1992) employed both SPOT HRV multispectral and panchromatic data for LULC classification at the rural–urban fringe. First, multispectral and panchromatic data were combined, resampled, and corrected to preserve the spectral and spatial resolution. Second, the LULC classification was performed by using the convolutional supervised MLC. The classification of eight rural–urban fringe LULC classes achieved a high kappa coefficient of 82.2% for training data and 70.3% for test data.

Later on, Alves & Skole (1996) analyzed land cover dynamics in the western Brazilian Amazon from 1986 to 1992, using a time series composed of five SPOT HRV images and MLC, to delimit the total deforested area and characterize areas of secondary vegetation growth. The results indicated that land cover change classification accuracy was significantly increased by using SPOT HRV Multitemporal satellite data.

Since the 1990s, large-area land cover mapping has become possible with the emergence of National Oceanic and Atmospheric Administration (NOAA) Advanced Very High Resolution Radiometer (AVHRR) sensors. The new series of sensors provided global remote sensing data (Loveland, 2012), which are widely used for LULC mapping at regional, national, or even global scales.

Some earliest presentative works have successfully demonstrated the excellent performance of this large-scale sensor using different processing methods for different purposes. The paper by (Ehrlich et al., 1994) is one of the first studies that discussed the general applications of NOAA-AVHRR 1 km data for environmental monitoring and LULC characterizing. Cihlar et al. (1996) demonstrated the efficiency of multispectral and Multitemporal AVHRR data for providing land cover information in the northern environment. DeFries et al. (1995) improved discrimination between 12 land cover types on a global scale from metrics derived from AVHRR data. Lambin & Ehrlich (1997) mapped land cover changes at broad spatial scales in sub-Saharan Africa between 1982 and 1991, identifying seasonal patterns of change using AVHRR data and vegetation index. Laporte et al. (1998) presented a new land cover map of the central African region, which provided a synoptic view of the extent of dense humid forests. The map was derived from

multi-resolution, Multitemporal NOAA AVHRR data by merging Local Area Coverage (1 km) and Global Area Coverage (8 km).

In this period, various land cover mapping projects were operated by governments or organizations. For example, The European Union COoRdination of INformation on the Environment (CORINE) land cover program (*CORINE Land Cover — Copernicus Land Monitoring Service*, n.d.) started to provide ongoing land cover information in Europe using Landsat and SPOT data. Moreover, the UN Food and Agriculture Organization (*FAO*, n.d.) launched a land cover mapping project, Africover, to map the land cover of the African continent (Loveland, 2012). Furthermore, LULC classification accuracy was highly improved during the 1990s. Certain errors (e.g., sub-pixel mixing) were also corrected due to the progress of classification methods, such as the first generation of Artificial NN (ANN) (Kanellopoulos et al., 1992; Foody, 1996; Atkinson et al., 1997), regression and decision trees (Moody & Woodcock, 1995; M. Hansen et al., 1996; Friedl & Brodley, 1997; De Fries et al., 1998).

However, some limitations persisted, mainly induced by the narrow availability and lack of accessibility of data, limited types of sensors, processing complexity, and relatively poor accuracy of classification results. Therefore, some studies began to discuss the possibility of use of multitemporal data or SAR sensors (ERS-1) to break through the limitation of meteor impacts, derive phenological variation, and improve land cover discrimination (Townshend, 1992). However, the Radio Detection And Ranging (RaDAR) data remained complex to interpret in that time.

Since the development of remote sensing sensors in the late 1990s, LULC maps have been increasingly generated from fine-resolution data because higher spatial resolution can significantly improve discrimination among different types of land cover as well as cloud detection, reduce misclassification errors, and facilitate short-term change detection. In addition, more and more studies were carried out to answer defined user needs and solve related social and environmental issues instead of simply classifying the study area.

Among the most-cited works, Wardlow et al. (2007) improved and updated LULC datasets from regional to global scales in the U.S. Central Great Plains by using time-series MODIS 250 m vegetation index datasets for performing large-area crop monitoring in an

agriculturally intensive region. Lu et al. (2007) mapped and monitored LULC types in rural settlements under human-induced stresses in the western Brazilian Amazon to evaluate and map potential land degradation risks associated with deforestation and soil erosion. Feyisa et al. (2016) accurately quantified LULC mapping and landscape change patterns in the urban environment of Addis Ababa, Ethiopia, using eight Landsat images acquired from 1985 to 2012 to understand the relationship among rapid urbanization, increased surface thermal intensity, and urban biophysical composition.

Overall, LULC research has rapidly developed, and LULC classification has been significantly more efficient and accurate in recent decades for the reasons presented below.

1) The arrival of the new generation of near real-time, analysis-ready, high-quality (high spatial, spectral, radiometric and temporal resolution), standardized, easy-access EO satellite data improves spatial information extraction efficiency and results in highly accurate LULC classification.

   For instance, van der Sande et al. (2003) used IKONOS-2 to classify land cover categories in the southern Netherlands. Afterward, the highly accurate classified maps (74% overall accuracy (OA)) were utilized as input to simulate flood hazards, derive an inundated areas map, and eventually assess damage to residential properties, infrastructure, and agricultural area.

   A decade later, Forkuor et al. (2018) evaluated the use of Landsat-8 and Sentinel-2 data in LULC mapping in rural Burkina Faso; they examined the contribution of the red-edge band of Sentinel-2 in improving classification accuracy by using three ML algorithms: Random Forest (RF), Support Vector Machine (SVM), and stochastic gradient boosting. The results indicated that Sentinel-2 outperformed Landsat-8 in LULC mapping, and the red-edge band of Sentinel-2 can effectively provide added value by deriving a more accurate LULC classification than Landsat-8 and Sentinel-2.

   Furthermore, LULC classification was frequently performed using very high-resolution (VHR) remote sensing data, such as WorldView-1 and -2 (WV-1 and WV-2), Pléiades-1, and QuickBird. Compared to HR images, VHR images are generally applied for LULC mapping in a highly heterogeneous complex landscape that requires finer spatial resolution, such as an urban area.

For example, in order to overcome the spectral variation within the same LULC class, the spectral confusion among LULC classes, and shadow impacts, Lu et al. (2010) examined the uses of VHR QuickBird-2 data, segmentation-based classification approach and spatial information to improve urban LULC classification in Lucas do Rio Verde in Mato Grosso State, Brazil. The research showed that suitable combinations of imagery, classification method, and information could significantly improve LULC classification in complex urban areas.

Jawak & Luis (2013) explored the potential of multi-angle HR WV-2 panchromatic and multispectral data for urban LULC information extraction by generating the traditional pan-sharpening for data fusion and multiple spectral index ratios for spectral distortion reduction.

Hashim et al. (2019) used Pléiades-1A VHR remote sensing image for urban vegetation mapping in the city of Kuala Lumpur by employing the Normalized Difference Vegetation Index (NDVI) and MLC.

2) Development of advanced automated processing algorithm, great computational capacity, classification approach, and classifiers. For example, the introduction of Object-Based Classification (OBC) improves land cover types extraction and reduces misclassification errors efficiently. Meanwhile, various reliable non-parametric supervised classification methods, such as ML algorithms (Talukdar et al., 2020; Pandey et al., 2021) and the emergence of DL classifier (L. Ma et al., 2019; Vali et al., 2020), have opened a new era of LULC classification.

Although parametric methods (e.g., MLC) were widely used in the 1970s and 1980s, they had a severely limited capacity for dealing with heterogeneous complex land covers; moreover, land cover distributions cannot be defined based on data distributions due to a great deal of uncertainty (D. Lu & Weng, 2007; Phiri & Morgenroth, 2017). In contrast, non-parametric algorithms, including SVM (C. Huang et al., 2002; M. Pal, 2008; S. K. Singh et al., 2014), Decision Tree (DT) (Friedl & Brodley, 1997; De Fries et al., 1998; M. Pal & Mather, 2003), a variety of DL classifiers (e.g., ANN, Convolutional NN (CNN), and Recurrent NN (RNN) (Foody, 1995; Srivastava et al., 2012; Ienco et al., 2017; C. Zhang et al., 2019a; X.-Y. Tong et al., 2020), make no assumption before classification and are more efficient and accurate (Wulder et al., 2018; Talukdar et al., 2020).

ML classifiers (whether shallow or deep learning) achieved consistently higher accuracy compared to parametric methods in LULC classification in a number of previous studies (X.-H. Liu et al., 2002; D. Lu, Mausel, Batistella, et al., 2004; Otukei & Blaschke, 2010; Szuster et al., 2011; Talukdar et al., 2020).

3) Advancement of cloud detection algorithms (Goodman & Henderson-Sellers, 1988; Foga et al., 2017; Jeppesen et al., 2019) and the emergence of well-functioning cloud masks (Baetens et al., 2019), such as MAJA (Lonjou et al., 2016), Sen2Cor (Main-Knorn et al., 2017) and FMask (Z. Zhu & Woodcock, 2012; Z. Zhu et al., 2015).

4) For real-value, continuous, or discrete series of data, time-series analysis was widely utilized as a powerful tool to reveal land surface dynamics and to analyze the magnitude of these dynamics (e.g., socio-economic transformation, urbanization, deforestation) (Lasaponara & Lanorte, 2012; Kuenzer et al., 2015). Additionally, the time-series employed in LULC classification, especially in LULCC detection, are usually annual and may be composed of different satellite sensors.

   Among the works which made a significant contribution of time-series analysis in remote sensing, Yang & Lo (2002) extracted LULCC of Atlanta, Georgia, USA, over 25 years for modeling the impacts on temperature and air quality in Atlanta by using a time-series of Landsat MSS and TM images.

   Pouliot et al. (2014) studied annual land cover changes covering Canada from 2000 to 2011 using MODIS 250 m coarse-resolution data to identify dominant change transitions in the country.

   Fu & Weng (2016) used the Continuous Change Detection and Classification algorithm on 507 Landsat TM/ETM+ images acquired from 1984 to 2011 to examine human-induced LULCCs and their impacts on the urban thermal environment in Atlanta, Georgia, USA.

   In an investigation by Yan et al. (2019), MODIS time-series data were also applied to detect LULCC in Wuhan, China, from 2000 to 2018. The research achieved very high accuracy (over 90%) by using the Prophet algorithm to detect the change point, as well as the Dynamic Time Warping algorithm to improve the accuracy of time-series classification.

5) Data fusion approaches are also commonly performed in LULC classification to investigate the potential and characteristics of different satellite sensors. The data can be acquired within the same sensors (e.g., data fusion of panchromatic and multispectral bands) or from different sensors of the same types (e.g., by merging data from different SAR satellites or optical satellites).

Among the most-recognized works, Bruzzone et al. (1999) proposed using a data fusion approach to classify multi-source remote sensing data, based on applying the Bayes rule of minimum error to the "compound classification" of multi-source and Multitemporal image pairs. The proposed technique was performed on Landsat TM and ERS-1 SAR data and was shown to outperform classification using a single sensor.

Phiri et al. (2018) conducted land cover classification in a heterogeneous landscape in Zambia using Landsat-8 data. Meanwhile, the importance of pre-processing methods (e.g., pan-sharpening) was also exanimated in the study; the results indicated that classification accuracy was improved to 93% when using pan-sharpened data, compared to 86% with standard data.

Chen et al. (2017) proposed improving land cover classification accuracy by fusing remote sensing data from different sources, including Landsat-8, MODIS, China Environment 1A series (HJ-1A), and Advanced Spaceborne Thermal Emission and Reflection (ASTER) digital elevation model (DEM) data. The results showed that the fusion of various temporal, spectral angular, and topographic characteristics could significantly increase the overall classification accuracy and successfully discriminate vegetation types. Such fusion of different types of sensors (e.g., combined satellite data from optical and SAR satellite sensors) has been applied in LULC classification since the late 1990s (Hall & Llinas, 1997; Solberg et al., 1994) and is still commonly used today.

Clerici et al. (2017) took advantage of the fusion of Sentinel-1 and Sentinel-2 imagery to increase LULC mapping of Colombia's Lower Magdalena region by combining the all-weather capability of the SAR sensor and the spectral information of the optical sensor. The combination of Sentinel-1 and the near-infrared (NIR) band in Sentinel-2 produced the most accurate classification.

Furthermore, satellite images can also fuse with other suitable remote sensing data, including aerial images (Gianinetto & Scaioni, 2003; Persson et al., 2008), Geographic Information System (GIS) data (Weis et al., 2005; Aydöner & Maktav, 2009), and Light Detection And Ranging (LiDAR) data (Zabuawala et al., 2009; X. Huang et al., 2011; K. K. Singh et al., 2012) in order to achieve greater LULC classification accuracy.

6) Ancillary data from distant sources other than remote sensing data are typically utilized to assist image processing and analysis, and the most commonly used ancillary data are DEM (Sanyal & Lu, 2004; Dar et al., 2010), maps and prior knowledge (Combal et al., 2002; Wright & Gallant, 2007), geospatial data (Maselli et al., 2009; Stevens et al., 2015).

7) Ultimately, post-classification processing has become further developed and is more common in LULC classification. Various post-classification processes (e.g., post-classification comparison, accuracy assessment) are effective for error correction (e.g., salt-and-pepper effect reduction) to improve final classified maps.

Methods of LULC classification may vary according to the user's need and the research objective. First, LULC classification at a given time, with either a single image or multiple images acquired in the short term, was widely carried out to understand the LULC and environment of the study area, generating thematic maps for further studies or policy-making. LULC classification is mostly multiclass classification and target class extraction. Moreover, the most important studies of LULC classification nowadays focus on the composition of the main LULC of the study area (Manandhar et al., 2009; Z. Qi et al., 2012; A. Ghosh et al., 2014; Rwanga & Ndambuki, 2017), the development and the impacts of urbanization (Georganos et al., 2018; Cai et al., 2019; Jozdani et al., 2019), agricultural land- and crop-type mapping (Wardlow et al., 2007; Hütt et al., 2016; Gibril et al., 2017), and spatial distribution of natural area and vegetated cover (e.g., forest) (Moskal et al., 2011; Sinha et al., 2015; Hurskainen et al., 2019).

Second, with rapid population growth and urbanization, LULCC has attracted significant attention in the remote sensing field. "LULCC detection" refers to the comparison of more than one remote-sensing dataset acquired at different times in the

same area (Aplin, 2004). Due to its multidisciplinary character, LULCC detection plays a crucial role in environment and resource management; it is thus generally employed to provide valuable information on social and environmental issues, such as changes in the composition of LULC in the area of interest (Alphan, 2003; F. Fan et al., 2007; Srivastava et al., 2012; Kindu et al., 2013), urban expansion and the monitoring of its impact (Lo & Quattrochi, 2003; Pauleit et al., 2005; Araya & Cabral, 2010), human- or nature-induced environment degradation (e.g., deforestation) (Eva & Lambin, 2000; Walker, 2004; Symeonakis et al., 2007), or LULC conversion (Roy & Inamdar, 2019; Mardian et al., 2021; Moisa et al., 2022).

In addition, LULCC detection usually involves changed areas and their change rate, as well as the spatial distribution, changed types and trajectories, and the precision of the change detection (Attri et al., 2015).

As early as the 2000s, Lepers et al. (2005) summarized the most important rapid changes in LULC at the regional to global scale from 1981 to 2000 based on existing datasets, revealing the global geographic patterns of land cover changes. One such finding was that the most significant rapid land cover changes were concentrated in Asia—especially dryland degradation and rapid cropland increase in Southeast Asia. Other findings included significant forest degradation in the Amazon basin and Siberia, as well as rapid cropland decrease in the southeastern USA and eastern China.

Killeen et al. (2007) documented LULCCs in Bolivia over 30 years (1975–2005). The landscapes of eastern lowland Bolivia, known for its rich ecosystem, were primarily composed of different tropical forest types (e.g., humid forest, inundated forest, seasonally dry forest, and cloud forest). The results showed that eastern Bolivia experienced significant deforestation; 9% of the original forest cover had been removed, and 17% of the total original land cover had been changed over the 30-year period of study.

Kindu et al.,(2013) studied LULCC mapping in the landscape of the Munessa-Shashemene area of the Ethiopian highlands from 1973 to 2012 using Landsat and RapidEye data. The classification results revealed the change of dominant LULC types (from grasslands to croplands); a rapid reduction in woodland cover, natural forest cover,

and grassland; and a significant increase in cropland. In addition, 60% of the land cover had been changed over the 39-year period of study.

Accurate LULC mapping and LULCC detection are widely applied in diverse study areas; in particular, the LULC of the *coastal area* is one of the current topics in the remote sensing LULC classification field. The coastal area, where the land and ocean are separated by the coastline (Figure 2), has be defined as "the dynamic interface zones where land, water, and atmosphere interact in a fragile balance that is constantly being altered by natural and human influence" (Beatley et al., 2002).

As the transition point between the sea and the land, offering rich and diverse resources (Crossland et al., 2005), the coastal area is known as the most essential food production source, a center of transport and industrial development, a significant source of minerals and geological production, a repository of biodiversity and ecosystems that are critical for the Earth, and the most developed tourism location (Crossland et al., 2005). Approximately half of the world's population, as well as most of its socio-economic activities and global interactions, are concentrated in coastal areas.

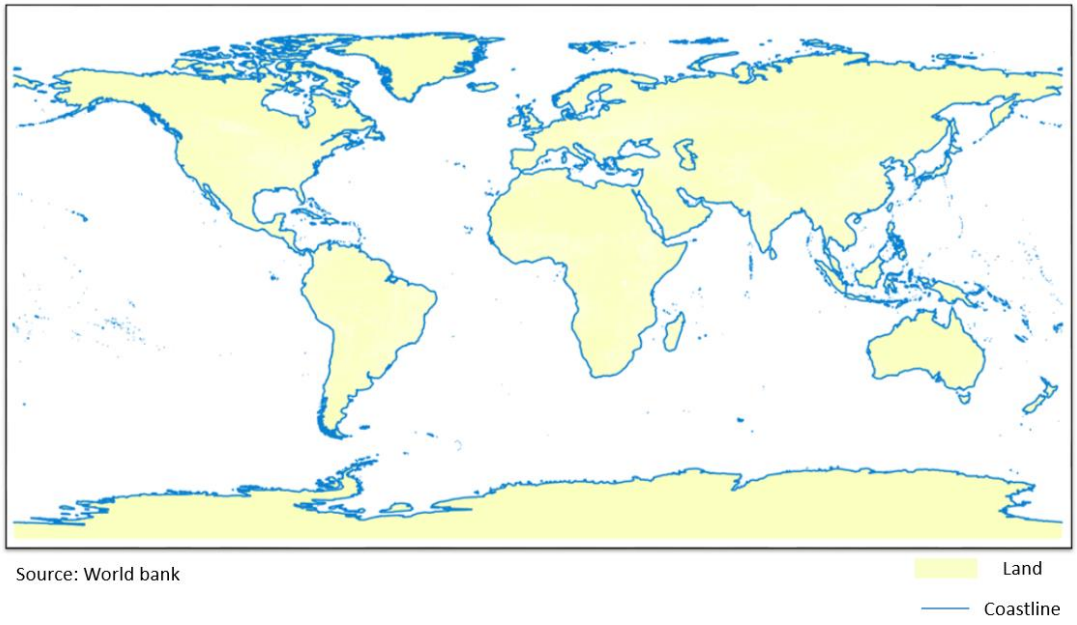

Figure 2 Total coastlines of the world (Source: World Bank, 2020)

Naturally, the coastal zone is recognized as an important place of diverse natural systems and resources (Figure 3) (Crossland et al., 2005); however, coastlands also experience many natural hazards (primarily cyclones and powerful coastal storms), which have inflicted incalculable losses (Beatley et al., 2002).

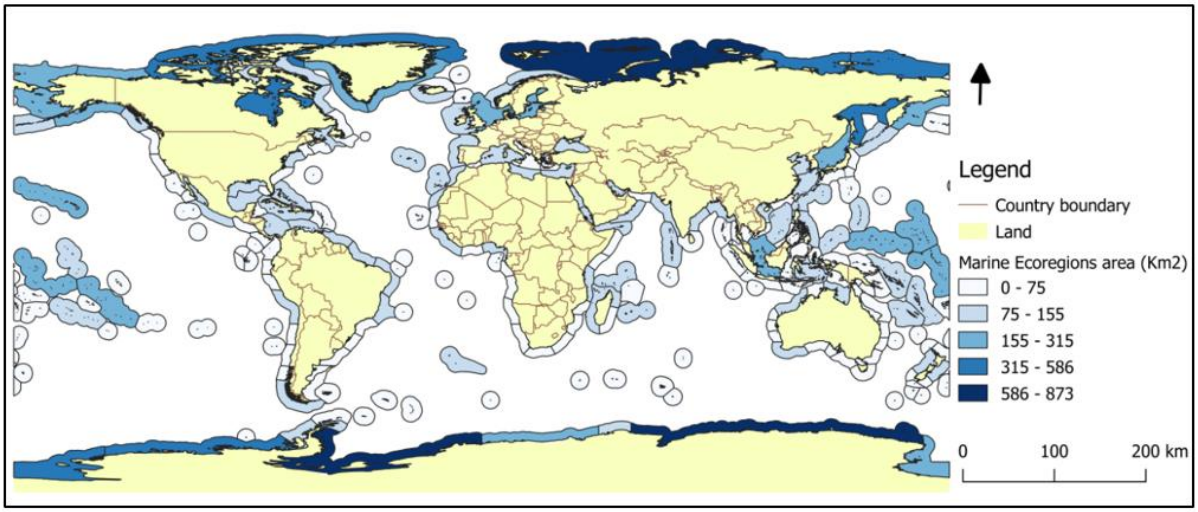

Figure 3 Marine ecoregions of the world (data source: Spalding et al. (2007) and The Nature Conservancy, *n.d.)*

Besides the environmental vulnerability, most coastal regions are under the pressure of human activities. The main driving factors of most of the environmental problems in the coastal zone are population growth, intense socio-economic activities, and conflict over how the use of limited resources (Beatley et al., 2002; Hadley, 2009). These main factors are often manifested as pollution from different sources (R. W. Howarth, 2008; Tiquio et al., 2017), such as industrialization (S.-L. Wang et al., 2013; Patnaik, 2018), artificialization (Ferreira et al., 2009; Freire et al., 2009), intense agricultural production (e.g., aquaculture) (Primavera, 2006; Moreno-González et al., 2013), overfishing (Jackson et al., 2001; Scheffer et al., 2005), sand mining (Mensah, 1997; Masalu, 2002), and waste disposal (Bascom, 1982; Masalu, 2002; Clark, 2018). Thus, most coastland development patterns are not sustainable. It is therefore crucial and urgent to change human activity patterns in coastal zones, find a balance between the immediate needs of humans and the needs of future generations, and develop a solid understanding of coastal geography. To achieve these goals, accurate LULC mapping is needed for complex and dynamic coastal zone management (Beatley et al., 2002).

Many studies on LULC classification in coastal areas have been carried out in recent years due to the advancement of classification methods and the arrival of HR and VHR remote sensing data. First, coastal land cover mapping is applied in physical geography studies, such as shoreline extraction (Dellepiane et al., 2004; Maglione et al., 2014; Bengoufa et al., 2021; Boussetta et al., 2022), dune extraction (Breed & Grow, 1979; Hugenholtz et al., 2012); wetland mapping (Ozesmi & Bauer, 2002; Rebelo et al., 2009),

climate and morphological processes analysis (Seker et al., 2003; Mason et al., 2010), and coastal ecosystem research (Klemas, 2009; Klemas, 2010).

Moreover, remote sensing scientist communities are most interested in LULC mapping and LULCC detection for multidisciplinary studies—for example, reducing coast degradation, improving management for population growth and, ultimately, preparing for the coming impacts of sea-level rise caused by climate change (Hadley, 2009).

Since the launch of the first-generation EO satellite, coastal zones have always been among the most researched areas. For instance, Ruiz-Luna & Berlanga-Robles (2003) focused on coastal LULCC and coastal lagoon surface reduction in northwest Mexico. In their study, supervised classification was performed on Landsat time-series data acquired between 1973 and 1997. Every image was classified into six classes (i.e., urban area, mangrove, agriculture, natural vegetation cover, aquatic system, and aquaculture). In addition, pixel-by-pixel change detection was carried out on the classification results. The LULCC results indicated that the urban area were dramatically increased and had become the dominant land cover by degrading natural vegetation and cropland. Moreover, two lagoons in the study area were found to have been significantly reduced.

Shalaby & Tateishi (2007) studied mapping and monitoring LULCCs over 14 years in the northwestern coastal zone of Egypt using Landsat images acquired in 1987 and 2001. The results revealed that the intense development of agricultural and tourist activities had caused vegetation degradation and waterlogging.

Abdullah et al. (2019) conducted a detailed analysis of the spatiotemporal pattern of LULCC in the coastal region of Bangladesh, which was dominated by a highly heterogeneous landscape using a coarse spatial resolution image, object-based image analysis (OBIA) approach, and RF classification algorithm. Despite lacking quality remote sensing data, the authors successfully revealed increased cropland, built-up area, and water bodies. At the same time, vegetation cover had decreased over 28 years.

Furthermore, like many other coastal regions around the world, Pays de Brest has been analyzed and identified as an important coastal area in France, particularly in vegetation detection. For instance, Talab Ou Ali et al. (2017) proposed a methodology for establishing an interferogram of the main vegetation types in Pays de Brest and monitoring vegetation using the backscattering coefficient based on Multitemporal and

multi-polarized Sentinel-1 SAR time-series data. In addition, vegetation changes between 2015 and 2016 have been assessed using interferometric coherence.

Niculescu et al. (2018) aimed to classify the major vegetation types in the Pays de Brest into six classes—forests, moors and lawns, summer crops, winter crops, grasslands and water, and no vegetation—by fusing data from Sentinel-1, Sentinel-2, SPOT-6 time-series and different vegetation indices using a supervised RF classification algorithm.

Niculescu et al. (2020) deals with the development of a shallow structure ML methodology for the identification and mapping of the vegetation of the Pays de Brest (France) from a time series of Sentinel-1 and Sentinel-2 data. The main objective of this work was to identify and map the vegetation in the Pays de Brest region using a multisensor stack of S1 and S2 satellite data via random forests, rotation forests (RoF) and canonical correlation forests (CCF). The methodological originality of this work consists in the optimization of the RoF model and the CCFs which create diverse learning bases using the transformation of the data and the characteristics of the subsets.

Nonetheless, the previous studies remain inadequate; in particular, the lack of LULC and LULCC information may impede sustainable development policies. Therefore, this thesis is indispensable to generating LULC maps, detecting LULCC in Pays de Brest according to the specific needs of local government and communities, and filling out the gaps in LULC information for the region.

Chapter 2. Geographic localization and major land use / land cover in Pays de Brest

2.1. Geographical localization

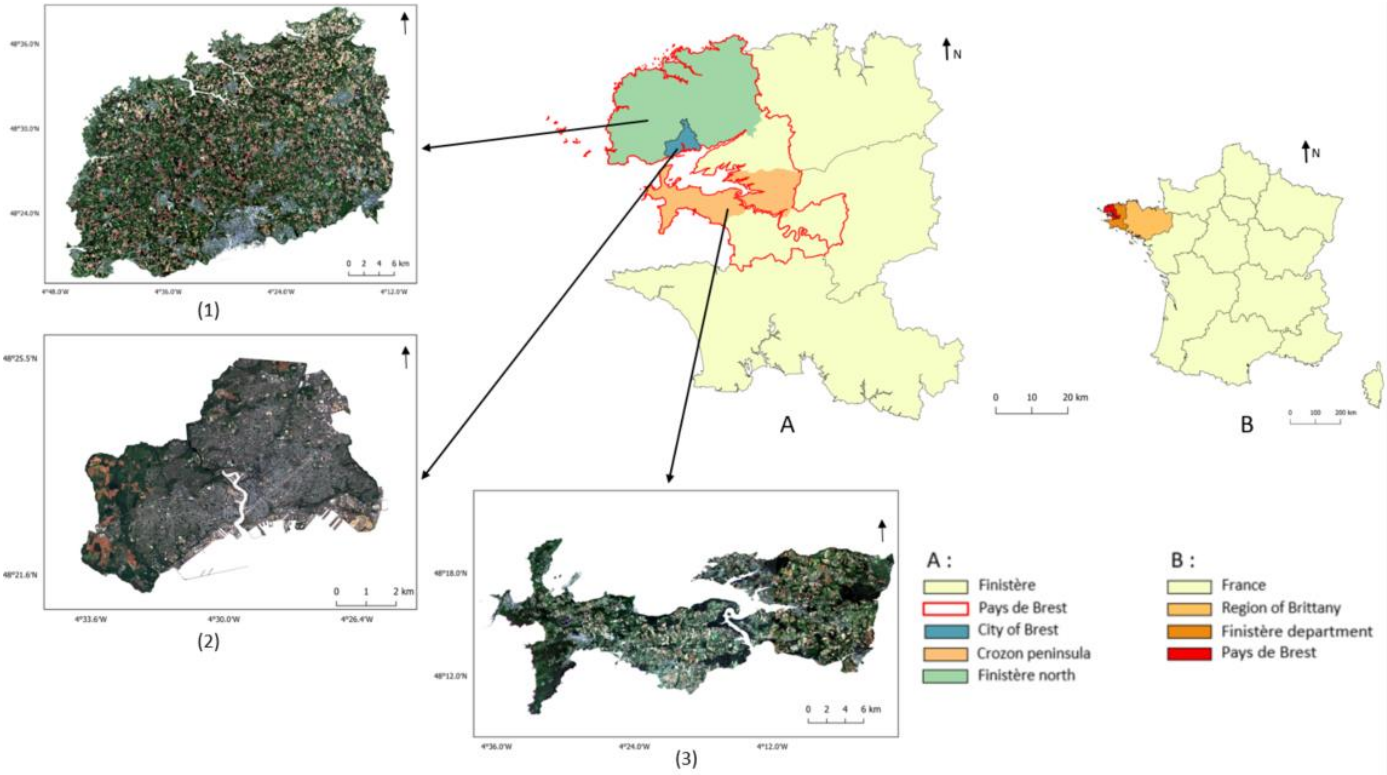

Figure 4 Localization of study areas. A: localization of Pays de Brest in France; B: Localization of study areas, (1) Sentinel-2 satellite image of northern Finistère in 2019, (2) Pléiades image of city of Brest in 2018, (3) Sentinel-2 satellite image of the Crozon Peninsula in 2018.

Our study area, Pays de Brest (Figure 4), located on the west coast of France, is an urban cluster in the northwestern part of the Finistère department and the region of Brittany. Pays de Brest was created in 2002 and covers a land area of 2,101 km^2 that extends between latitudes 48°05′39″ N and 48°40′39″ N, longitudes 3°52′34″ W and 4°47′42″ W. Pays de Brest also occupies 599 linear km of coastline. The area's population of 420,000 yields a population density of approximately 200 inhabitants per km^2.

Besides the vital concentration of population and its flourishing local socio-economic system, Pays de Brest has a wealth of natural and environmental resources. Despite highly developed economic activities, the city of Brest has preserved a large surface of natural area (urban forest, watercourse, valleys). Meanwhile, many urban green spaces have been constructed for citizens' physical and mental health, biodiversity,

and environmental protection. Outside the city, the region is occupied by an essential part of the natural landscape with high geographical research value, such as coastal wetlands, coastlines with dunes and cliffs, mountain ranges, and the regional natural park of Armorique. The natural landscape will be discussed in detail in section 2.2, "Geographical condition of the study area."

Figure 5 Pays de Brest with the seven intercommunalités: Pays d'Iroise, Pays des Abers, Lesneven-Côte des Légendes, Brest Métropole, Pays de Landerneau-Daoulas, Presqu'île de Crozon-Aulne Maritime and Pleyben-Châteaulin-Porzay (source: Brest Métropole)

The agglomeration is composed of 103 communes; more than half of them are coastal, representing a quarter of the coastline in the French territory. The 103 communes are grouped into seven *intercommunalités* for a joint project and different forms of cooperation between them (Figure 5). Most of the urban areas and socio-economic activities are clustered together in the coastal zone and near to Brest Métropole, which is the most crucial agglomeration with the largest population and economy in the department of Finistère. In this chapter, *intercommunalité* will be used as the smallest administrative region in our study area.

Historically, the region's population has always preferred to settle near the ocean; the inland, by contrast, is sparsely populated and less developed (Ollivro, 2015). First, the

region of Brittany is traditionally dominated by various agricultural activities. Thus, farmers and fishermen have settled near the water to gain greater access to natural resources. After the first military harbor was built in the city of Brest in the 17th century, diverse socio-economic activities arose near the harbor, and the harbor clusters were quickly formed with substantial employment opportunities. Furthermore, with the diverse landscape and rapid development, more and more tourists and retirees searched for a second residence at the seaside, intensifying population growth in the coastal communes.

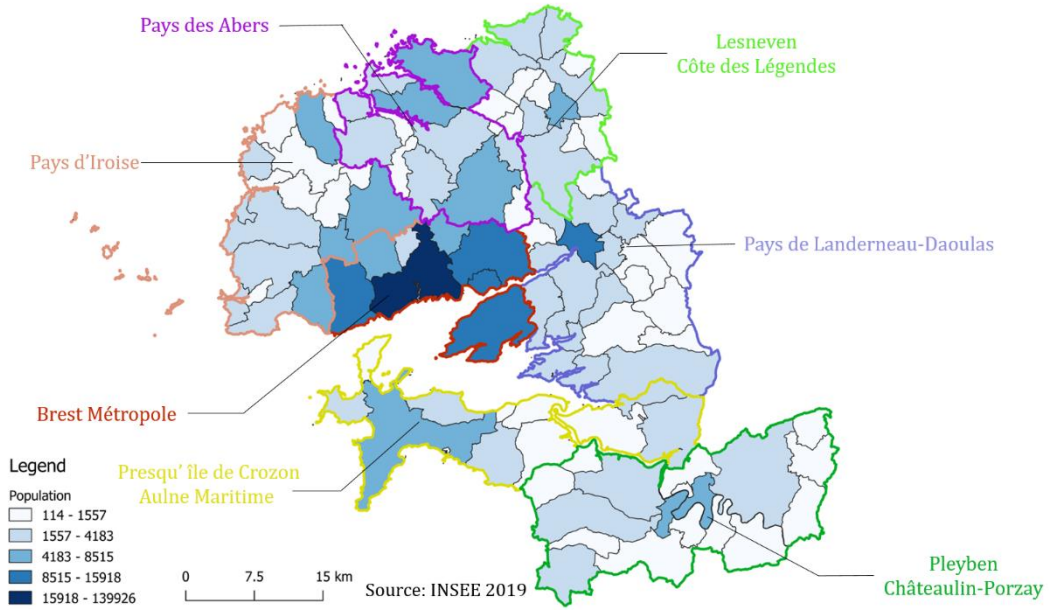

Figure 6 Distribution of the population by community in Pays de Brest

According to Figure 6, the population is highly concentrated in the northern coastal *intercommunalités*, among which Brest Métropole is the most inhabited area with 211,156 inhabitants in 2019, representing half of the population in Pays de Brest. In addition, the neighboring *intercommunalités* (Pays d'Iroise, Pays des Abers) act as satellite cities hosting much of the rest of the population. Therefore, a significant contrast can be observed between the populated *intercommunalités* and the *intercommunalités* not adjacent to, or more distant from, Brest Métropole (Pays de Landerneau-Daoulas, Pleyben-Châteaulin-Porzay and Lesneven-Côte des Légendes); the latter communes host fewer than 4,000 inhabitants on average, except at the center of each *intercommunalité*. Thus, a significant imbalance in terms of population has emerged between the coastal area, which is also close to the metropolis, and the other relatively isolated communes.

2.2. Geographical condition

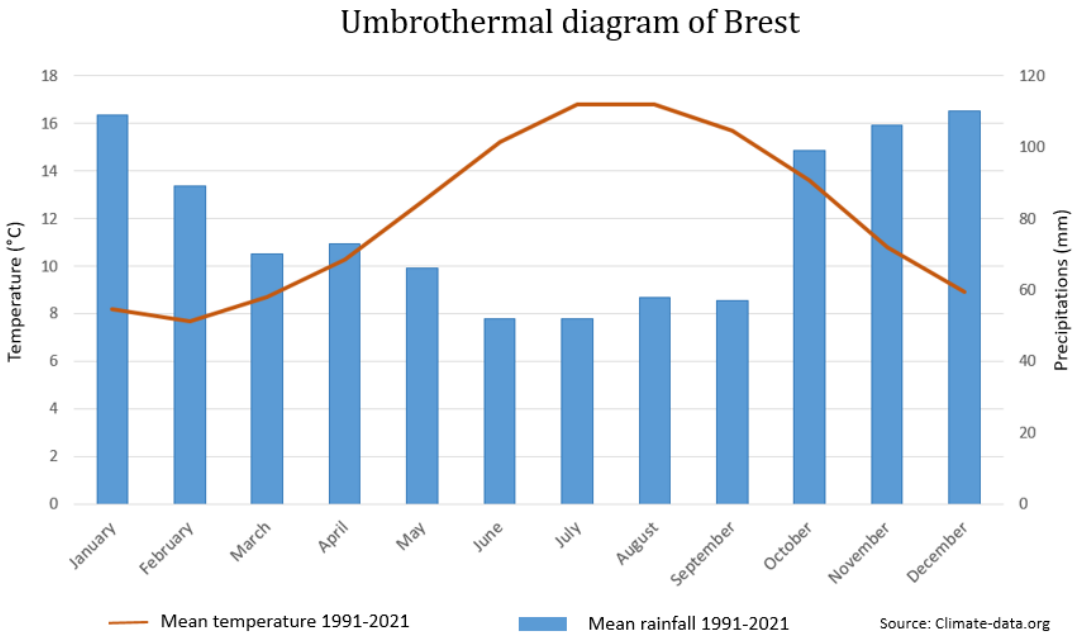

Figure 7 Umbrothermal diagram of the monthly mean temperatures and monthly mean total precipitations from 1991 to 2021 of Brest

Climatically, according to the Köppen–Geiger climate classification, Pays de Brest is classified as type Cfb (temperate oceanic climate) (Köppen, 2011). As demonstrated in Figure 7, on average, the total annual precipitation of the area is 941 mm; the wetter season lasts five months, from October to February, and the highest monthly rainfall of 110 mm is received in December. Conversely, June and July are the driest months, with only 52 mm of rainfall. As a temperate area, the annual average temperature is 12.2 °C. In contrast to the wet season, the hottest season lasts from July to August, with an average temperature of 16.8 °C; an average minimum temperature of 7.7 °C is observed in February. The region's mild weather and ample rainfall provide an ideal habitat for rich biodiversity with landscape heterogeneity as well as optimal conditions for numerous agricultural activities, such as crop planting.

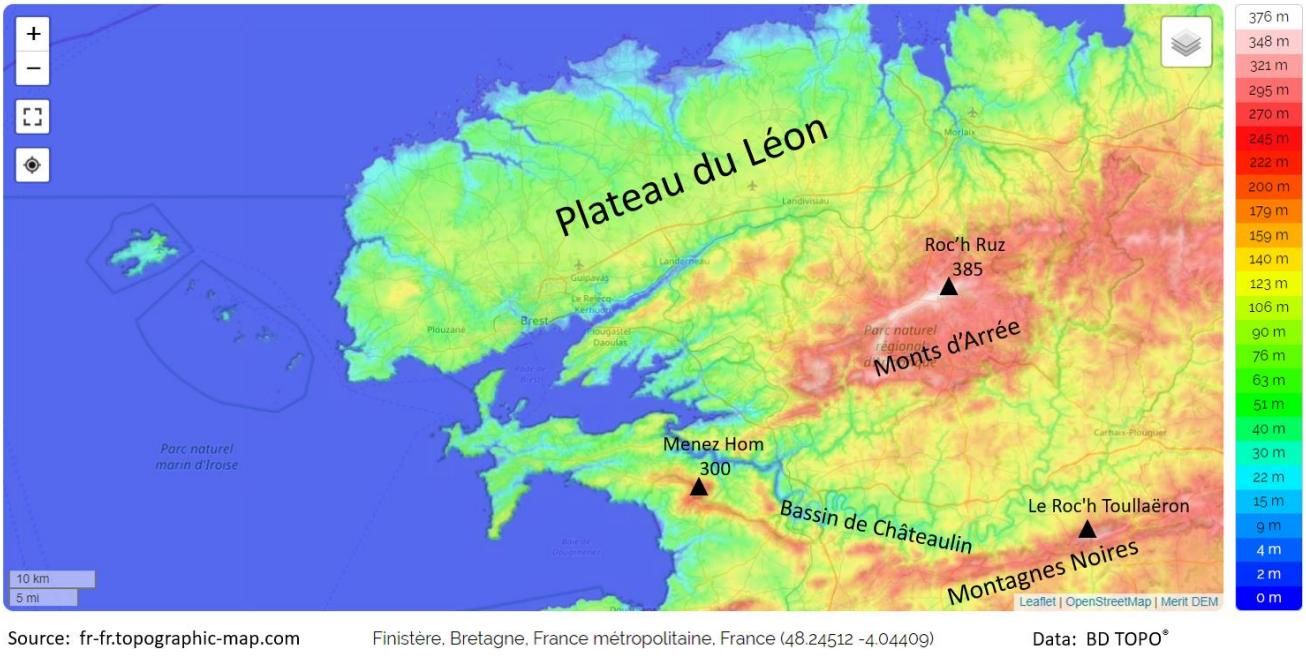

Figure 8 Topography maps of Pays de Brest with principal landform and summit

Three types of resistant rock—sandstone, quartzite, and granite—gave rise to the prominent landform of Pays de Brest; thus, the topography of Pays de Brest consists mostly of plains, which means the low altitude (Figure 8). The elevation of the area ranges from 0 m to 385 m. The natural landscape is a mosaic of cliffs, dunes, moors, peat bogs, and coastal wetlands. However, a few essential landforms are worth noting in Pays de Brest. A vast plateau, Plateau de Leon, occupies a large area in the north, and a local mountain range, Mont d'Arrée, with a series of the highest summits of around 385 m, can be found in the region's center.

Moreover, Montagnes Noires, another essential local mountain range, crosses over the south from Menez Hom, a summit on the Crozon Peninsula, to the central department. Besides the principal summits, Bassin de Châteaulin, a vast hollow with a mean altitude lower than 100 m, lies between two mountain ranges in the south of the study area. The basin, originally constituted by soft carboniferous shales, was created by the Aulne River and its affluent, which take their source from Mont d'Arrée and Montagnes Noires.

Because its landform is relatively plains, especially in the coastal area—and with a basin in the center of the region that secures water resources from the Aulne River and its affluent—Pays de Brest is naturally endowed with excellent geographical features to develop all kinds of socio-economic activities.

2.3. Land use / land cover in Pays de Brest

2.3.1. *CORINE* Land Cover (CLC)

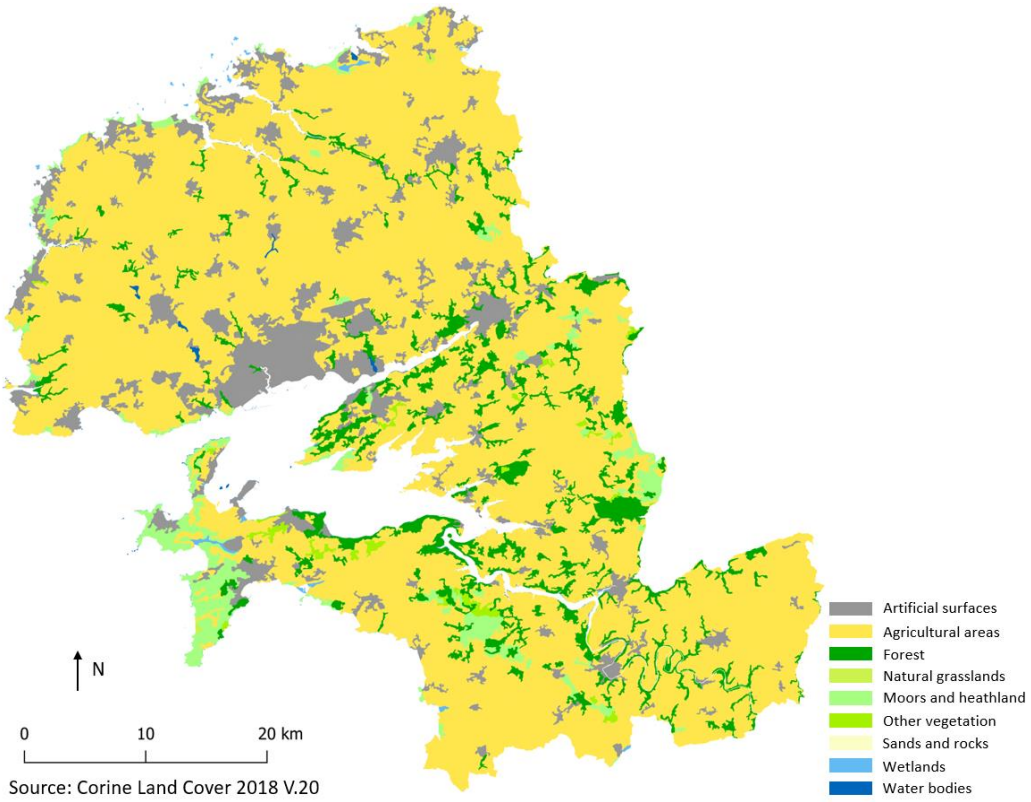

Figure 9 CLC 2018 in Pays de Brest

The CLC geographical database is a biophysics and land use inventory produced in the framework of Copernicus, the European Earth observation program (CORINE Land Cover). According to Figure 9, cultivated lands are the leading land use in Pays de Brest. They are uniformly distributed over the study area, especially in Plateau du Léon, except on the western Crozon Peninsula (Presqu'île de Crozon-Aulne Maritime), which is occupied by natural coastal moorlands. The presence of arborous, fruticose, and herbaceous vegetation is easily identified. Forest can usually be found near water areas, either around the coast (such as in the center of Pays de Brest and around the coast of the Crozon Peninsula) or near the inner water body—for example, the Bassin de Chateaulin. Moors and heathland are found mainly near the coast in the region's north and the west coast in the middle of the Crozon Peninsula. Other vegetation is dispersed throughout the region; wetlands are mainly present on the seaside and are easily identified on the Crozon

Peninsula and the north coast of the area; lakes on the Plateau du Léon comprise most of the water bodies.

The location of artificial surfaces, known as "urban areas," is very similar to the population distribution described in the previous section. Both are highly concentrated in the Brest Métropole and its suburbanization trend, with much of the remainder in some small cities located in central *intercommunalités*. It is worth noting that although Pays de Brest was created with the principle of cohesive development between *intercommunalités*, the distribution of population and the urbanization level is highly imbalanced; more than half of the population of Pays de Brest is concentrated within the Brest Métropole. The presence of artificial areas is essential, even though agricultural land remains the most important land use in the region.

2.3.2. Main activities and protected natural areas

Even though agriculture has always been the region's primary activity, it is clear that for several decades, many other socio-economic activities have been increasing sharply and taking over more and more space in Pays de Brest, accompanied by urbanization trends. Figure 10 clearly illustrates the significant economic activity in the area.

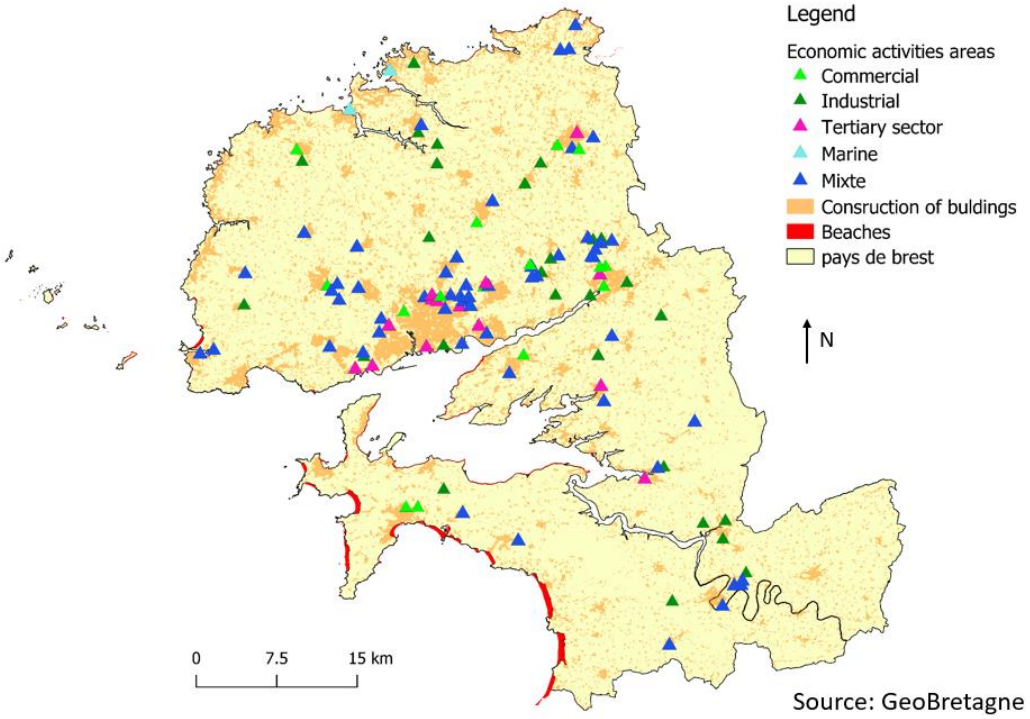

Figure 10 Distribution of main economic activities in Pays de Brest

The two dominant economic activities in Pays de Brest are commerce and industry, followed by the "tertiary," or service sector (which includes transportation, restaurants/hospitality, and sales), or some combination thereof. Reflecting the concentration of artificial areas and population, construction is generally located in the urban areas, mainly on the seaside and in the Brest Métropole. In consequence, the majority of economic activities are concentrated near the cluster of construction—in particular, commercial activities, tertiary sector activities, and marine activities on the northern coast. In addition, some listed activities can also be found near the beaches due to the tourism sector's current rapid development, which—as mentioned previously—is one of the principal factors driving the urbanization and artificialization of coastal areas.

Whereas the tertiary sector and commercial activities can be found only near the principal agglomerations, various other activities are located near the small cities and countryside or along the coasts. Most industrial activities tend to avoid the big cities, where space to build and expand is scarce and more expensive.

Natural area preservation is also a key to development in Pays de Brest; some 99 communes in the department of Finistère cover at least one sensitive natural area and pre-emption zones.

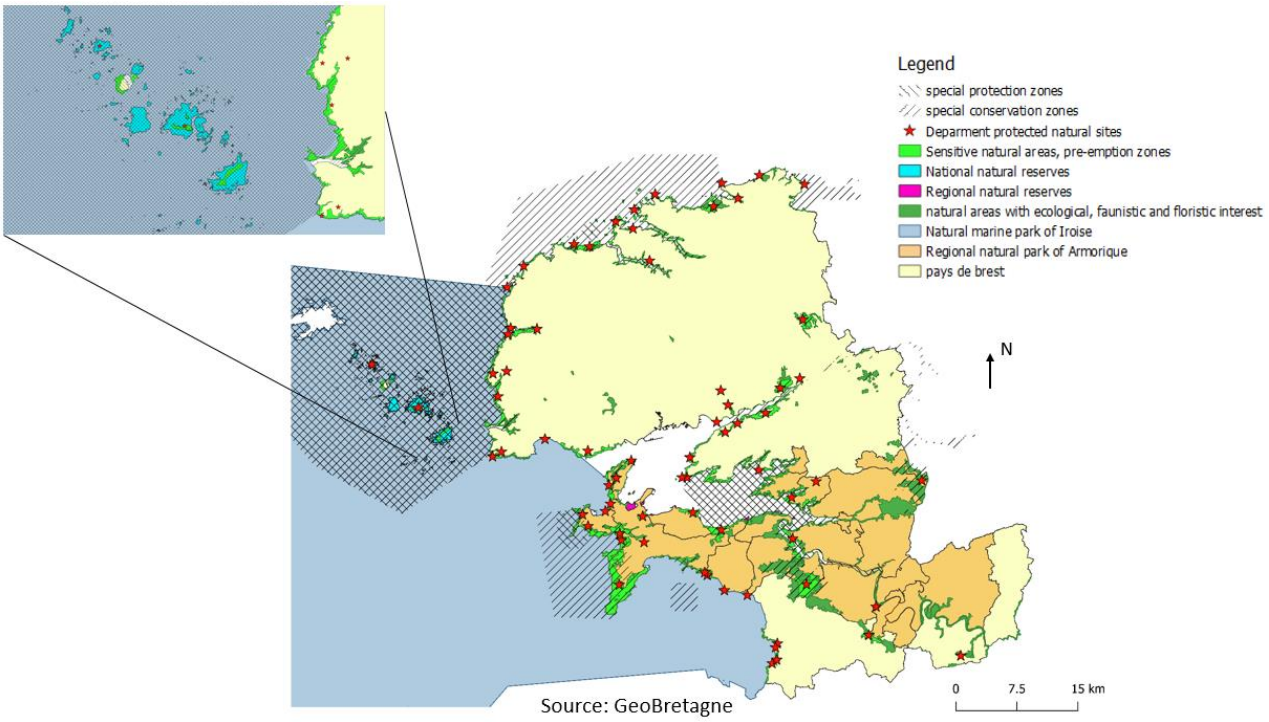

Figure 11 Protected natural areas in Pays de Brest

Due to its rich biodiversity reserve and diverse landscape, nature has always been highly valued in the region of Brittany and the Finistère department (Figure 11). The first National Natural Reserves (NNRs) and Regional Natural Reserves (RNRs) were created in the region in 1913; these two types of reserves mainly cover the islands in the west of the continent and some areas located in the north of the Crozon Peninsula. Since 1979, Special Protection Zones (ZPS) have been created to conserve wild birds, and Special Conservation Zones (ZSC) were created in 1992 to ensure biodiversity by conserving natural habitats as well as wild fauna and flora. ZPSs and ZSCs mainly cover the coasts, a part of the coterminous sea area, and the principal vegetated area, such as the moorlands of the Crozon Peninsula and the forest in the center of the study area. In addition, natural areas with ecological, faunistic, and floristic interest were created in 1982. Sensitive natural areas, pre-emption zones, and department-protected natural sites cover both the coasts, the forests, and the drainage basin of the river of Aulne. Eventually, two essential natural parks were created: in 1969, the regional natural park of Armorique (located on the Crozon Peninsula, Bassin de Châteaulin, and extended to the center of Pays de Brest), and in 2007, the natural marine park of Iroise, which covers a vast area of water surface in the west. Parks play an essential role in the conservation of biodiversity and the environment.

2.4. Major LULCC issues

Despite the fact that the most significant LULCs (artificial area, agricultural land, vegetation) remain the same in Pays de Brest, the region has been undergoing a sharp transition between these three essential LULCs for several decades, and some problems of development—especially the imbalance between *intercommunalités*—are gradually emerging.

Urban sprawl is the most significant of the major LULCCs. During the rapid development and rapid expansion of urban areas between 1984 and 2005 in Pays de Brest, some areas experienced a more remarkable change than others (Figure 12).

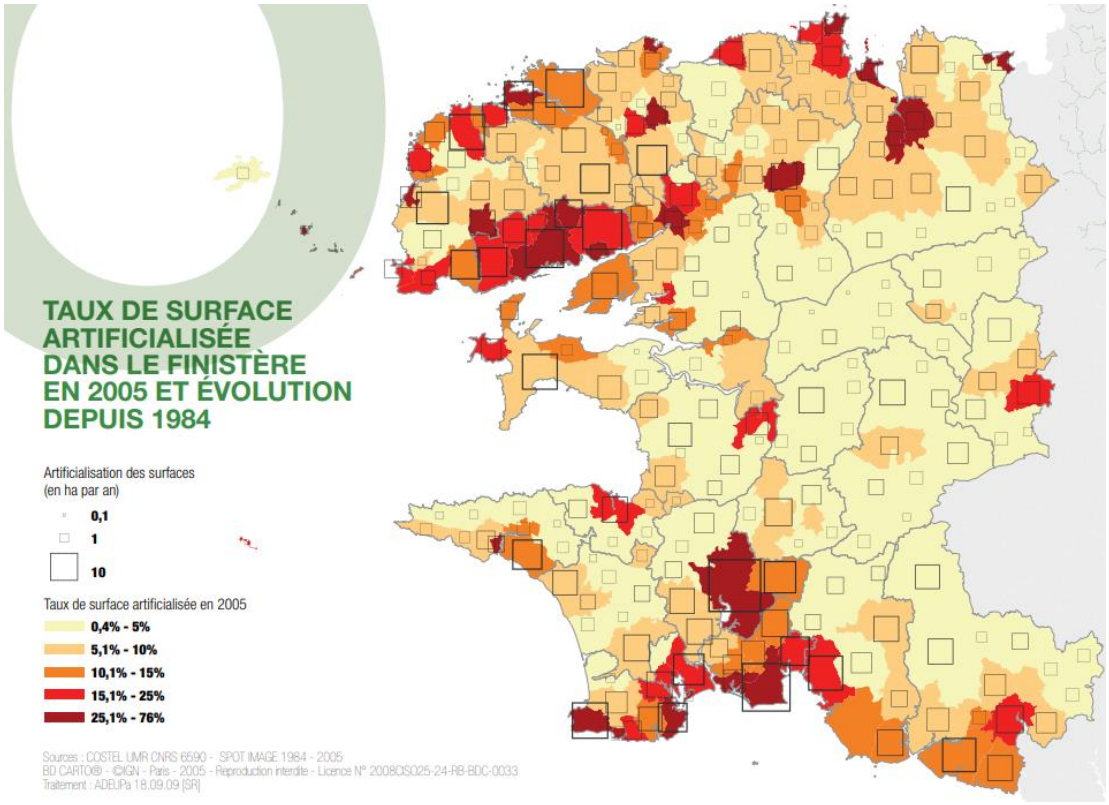

Figure 12 Artificial area rate in the department of Finistère in 2005, and its evolution between 1984 and 2005

Pays de Brest has always been a population and economic center in the Finistère department; 44% of the department's population are concentrated within 25% of its surface. In particular, the metropolis of Brest provides essential socio-economic activities and employment opportunities; 44% of department employment is found in the Brest Métropole (Sparfel, 2011). Even though the foundation of Pays de Brest aimed to strengthen *intercommunalités* and develop joint strategies and policies, the communes of Brest Métropole—which occupy less than 8% of the departmental surface area—

generated more than 13% of the urban sprawl between 1984 and 2005 (Adeupa, 2009). Furthermore, artificialization is more significant on the coastline; coastal communes experienced approximately 46% of urban sprawl, despite representing less than 29% of the departmental surface (Adeupa, 2009). Therefore, the coastal area and the Brest Métropole have a high artificial area rate ranging from 10% to 76%. Otherwise, the surface is highly occupied by construction in the surrounding area of Brest Métropole. By contrast, the Crozon Peninsula and some areas far from the coastlines, located in the center of the region, experienced a more minor change in the artificial surface rate ranging from 0.4% to 10%, because of their isolation and remoteness from socio-economic activities relative to the coastal areas.

The fundamental cause of this significant artificialization is the rising population in Pays de Brest due to immigrants who can be placed into one of three categories: (1) young workers attracted to the jobs created by rapid economic development in the region; (2) vacationers or seasonal residents attracted to the well-protected environment and diverse landscape of the region, which has seen a boom in the construction of second residences or vacation homes, especially on the coast; and (3) retirees—many of them relatively young—are choosing to settle in the region, mainly in the coastal area, owing to the reasons enumerated in item (2).

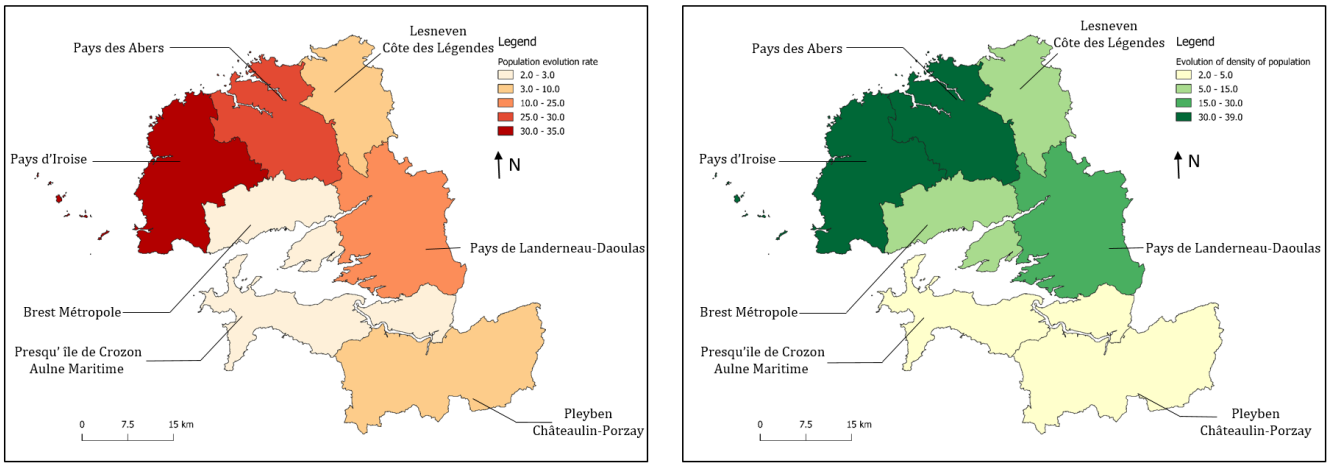

Figure 13 Evolution of the population (a) and density of population (b) in Pays de Brest between 1990 and 2019

According to Figure 13, the population has, on average, increased in all *intercommunalités* between 1990 and 2019 at a rate between 2% and 35%. In the beginning, it can be easily noticed that the population increases are very poor in Presqu'île de Crozon-Aulne Maritime and Brest Métropole. Just as all metropolis, Brest Métropole,

went through urbanization very early, most of the population and socio-economic activities are highly concentrated in these *intercommunalités*. However, the extension of the metropolis is limited by the presence of the sea in the south. Thus, there is a tendency to be overloaded for several decades, and the weak population evolution rate can be explained.

On the other hand, as the essential part of the regional natural park of Armorique, considering the construction restrictions for environmental protection and biodiversity preservation, Presqu'île de Crozon-Aulne Maritime has attracted mainly tourists instead of inhabitants. After that, two *intercommunalités* far from Brest Métropole, Pleyben-Châteaulin-Porzay, and Lesneven-Côte des Légendes have experimented with slow population growth in 29 years in consideration of their isolated geographical location (9% of population growth rate for Pleyben-Châteaulin-Porzay and 10% for Lesneven-Côte des Légendes). Eventually, the three coastal *intercommunalités* near Brest Métropole—Pays des Abers, Pays d'Iroise, and Pays de Landerneau-Daoula—went through the most significant population growth due to the phenomenon of suburbanization. In particular, settling in Pays des Abers (29%) and Pays d'Iroise (35%) appear to be the first choice for young workers or young retirees, who can have a house with a larger surface area while also remaining close to Brest Métropole. However, Pays de Landerneau-Daoulas is relatively sparsely populated due to its less convenient location and greater distance from Brest Métropole.

The population density growth rate from 1990 to 2019 is very similar to the population growth rate. Excepting Presqu'île de Crozon-Aulne Maritime is protected by the regional natural park of Armorique since 1969, the density of the population stay weak in the *intercommunalités* far from the metropolis (Lesneven-Côte des Légendes and Pleyben-Châteaulin-Porzay) due to the lack of socio-economic activities. Considering that Brest Métropole was already inhabited in the early 1990s, the growth of its population density increased relatively slowly (13% in 29 years) compared with its neighboring *intercommunalités*. Mirroring the increase in population, the population density has also increased dramatically in the three adjacent *intercommunalités* of Brest Métropole because they are not traditionally densely inhabited areas. More and more people, either new arrivals in the area or former urban residents, are choosing to settle in these *intercommunalités*, seeking improved quality of life.

Population growth and urban sprawl are currently the most important phenomena in Pays de Brest, and they have led to the gradual emergence of certain concerns and conflicts in recent years. In summary, two imbalance problems are worthy of note in the study area: (1) the imbalanced development in space and the expanded gaps between the coastal area near the metropolis and (2) the other distant areas. Moreover, the balance of different land uses has already been upset. Therefore, conflict and competition between different land uses are increasing, accompanied by worsening undesirable consequences.

2.4.1. Imbalance of development between *intercommunalités*

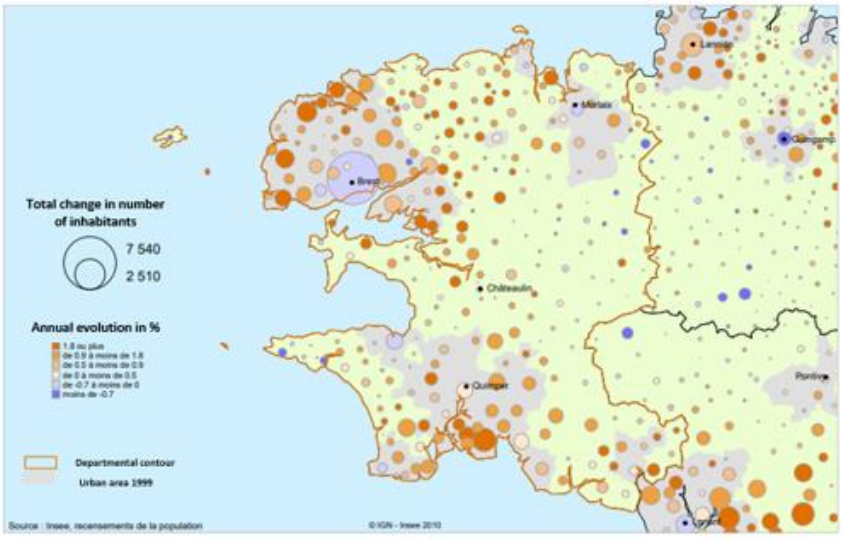

(a)

(b)

Figure 14 Evolution of population between (a) 1999 and 2008, (b) 2011 and 2016 (source: Insee)

Other than the Figure 13, the Figure 14 depicts two maps of the evolution of the urban area and population from 1999 to 2008 and 2011 to 2016, which makes it easier to recognize the tendency of these evolutions over these years and determine the causes of socio-economic inequalities in Pays de Brest. At first, the urban area of Brest Métropole and its periphery remain unchanged in the two maps, and a new urban area was constructed between 1999 and 2010 in Presqu'île de Crozon-Aulne Maritime due to the development of tourism in recent years. Otherwise, the extension of urban areas or the emergence of new agglomerations can hardly be found in other communes. Then, by

comparing two maps of the evolution, it can be concluded that Brest Métropole always had the most significant change in the number of inhabitants. However, its annual evolution remained at approximately 0%, which means the critical flow of population but neither increase nor decrease of population can be observed. This phenomenon is most significant between 1999 and 2008.

Meanwhile, the population growth near Brest Métropole is remarkable. However, the demographic growth was concentrated on the coastline in Pays d'Iroise and Pays de Landerneau-Daoulas from 1999 to 2008. However, the population grew enormously in the adjacent communes of Brest Métropole, with an essential change in the number of inhabitants between 2011 and 2016, which brings out the phenomenon of suburbanization and decentralization, which is strongly developed in Pays de Brest. It is mainly represented by the young workers and retirees seeking improved quality of life. Therefore, they usually look for an isolated house with a private garden far from the city center but still close to the metropolis (Rieu, 2011).

Moreover, less population evolution can be seen on the coastline; Lesneven-Côte des Légendes has even experienced population decrease on the coast. Besides the population evolution near Brest Métropole, the imbalance between inland communes and the coast is another significant development issue. In maps, mostly the coastal communes had a significant change in the number of inhabitants, which indicates the significant inflow of population and a positive annual growth compared with the inland communes, which lost population. Even though the population flow was still very weak in inland communes, the phenomenon of urbanization was slowly emerging. In 2011–2016, except for a few coastal communes (Brest Métropole, Pays d'Iroise, and Pays de Landerneau-Daoulas), which kept gaining inhabitants, the great majority of communes encountered negative population growth of around -1.6%, which means an important number of inhabitants has left the inner communes for the more significant agglomerations. The process of urbanization and suburbanization between these years created—and then aggravated—the socio-economic imbalance between Brest Métropole with its periphery, the coast, and the inland communes in Pays de Brest.

The regional disparity brings a series of consequences. For example, the cities (especially Brest Métropole) are highly saturated in term of population, and rapid urbanization and suburbanization place different stresses on public city infrastructure,

principally traffic congestion (particularly during weekday rush periods), lack of housing in the city and its periphery despite urban sprawl, and tension in public facilities (such as public transport, schools, hospitals, libraries, and sports facilities). At the same times, the high concentration of population and socio-economic activities cause the problems of pollution, sanitation, environmental degradation, etc. In contrast to the populated coastal and urban areas, the small inland communes far from the coast encounter a serious population decrease due to the aging problem. These small cities or villages are slowly but steadily emptying due to the loss of young laborers and the lack of immigrants. The gaps between the coastal urban area and the isolated inner communes are gradually expanding, and the development imbalance is carried to the extreme.

2.4.2. Imbalance between different land uses

The previous section about LULC explained that the cultivated areas are always the leading land use in Pays de Brest, followed by the vegetated and urban areas. However, urbanization and suburbanization not only increase regional inequalities but also cause competition for land uses. Urbanization is a transitory process to decrease the importance of agriculture with artificialization and industrialization. First, the process switches the sectoral composition; the secondary and tertiary sectors outpace agriculture to become the economic lifeblood of the region. Second, the urbanization process turns agricultural land into an artificial surface. Third, the traditional rural agricultural population leaves for the urban area, seeking more employment opportunities. (Moomaw & Shatter, 1996; Henderson, 2003). In most places, urbanization is usually accompanied by rapid economic growth; thus, it is generally considered an indicator of the economic development level (S. Li & Ma, 2014). In consequence, the urban area is most often the privileged land use. Nevertheless, urbanization has created conflicts between different land uses, especially the artificial surfaces, which are slowly occupying not only available unused land, but also many agricultural lands or even natural areas.

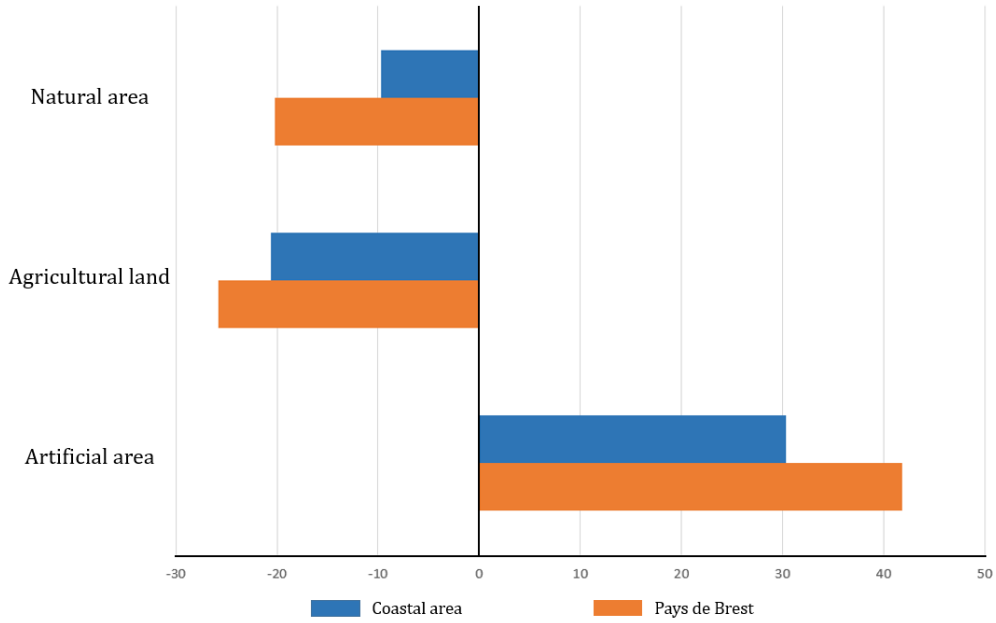

Figure 15 Evolution of land use between natural area, agricultural land and artificial area in Communes in Pays de Brest and its coastal area between 1990 and 2018 (Source: CORINE Land Cover 1990, 2018)

The figure 15 illustrates the evolution of three main types of land use (natural, agricultural, and artificial areas) in Pays de Brest between 1990 and 2018. It can be seen that the artificial area was the only land use that had a significant growth during 28 years, with more than 40 km^2 increase in surface area. In contrast, agricultural land lost 25 km^2 in surface area, and the natural area surface declined precipitously as well. It is also worth noting that the land use changes were usually found in the coastal area; 80% of the decrease in agricultural land and 73% of the artificial area growth were on the coast, although the degradation of the natural area was more evenly distributed in Pays de Brest, with 48% of the decrease on the coast. The evolution indicates the process of urbanization, coastalization, and competition for land uses; the result is natural landscape degradation.

Research has long focused on the delicate balance between urbanization and environmental protection (Ahmed et al., 2020; Seto et al., 2010); some studies show that urbanization rate and changes in regional environmental quality are closely related (S. Li & Ma, 2014; L. Liang et al., 2019). The regional environment is significantly impacted by economic development. Typically, the environment is improved when the degree of economic development rises. Nonetheless, rapid and extensive economic growth can negatively impact the environment and increase social tension (DATAR, 2004; S. Li & Ma, 2014). The negative impacts include not only the problem of pollution and over-

exploitation of natural resources but also the transition from agricultural or natural land use to artificial areas.

Several local studies have mentioned that the preservation of agricultural and natural areas is essential, not just for landscape harmony and the well-being of the population, but also to prevent excessive urbanization and over-development of tourism that contribute can ultimately lead to the formation of a mono-economic activity in the region (Lebahy & Le Délézir, 2006). Even though the coast is an essential reservoir for marine and coastal biodiversity and many natural protected areas were also created in order to preserve the environment. However, many natural areas have been eroded due to urban sprawl, in particular, the undeniable detriments of the coastline due to urbanization and artificialization were observed (Région Bretagne, 2013). For example, 65% of coastal wetlands have been destroyed by reclamation, diking, or filling in the region, and the increasing pollution threatens many natural habitats and species.

2.5. Research objectives and study sites

As analyzed in the section above, Pays de Brest has experienced significant LULCCs over several decades, especially urbanization and artificialization, which have provoked various environmental and social issues, such as the conflict between different land uses and natural environment degradation due to urbanization and uneven development within communes. For this reason, it is crucial to study LULCCs and their consequences in Pays de Brest, particularly for decision-makers in the community and local government, which has long been aware of the population overload and the natural environmental crisis. However, even though the local government is seeking sustainable development, no effective solution has been found, and very few recent studies have investigated LULC or LULCC monitoring in Pays de Brest.

In response to that knowledge gap, this thesis focuses on LULC in Pays de Brest. Its objective is to detect, monitor, and ultimately follow LULCCs, especially the transition between three principal land uses—agricultural lands, vegetated areas, and urban areas—as well as the consequences of that transition. This thesis has chosen to discuss three essential subjects, using three different study sites in Pays de Brest:

- *Machine Learning Methods and Classification of Vegetation in Brest, France*

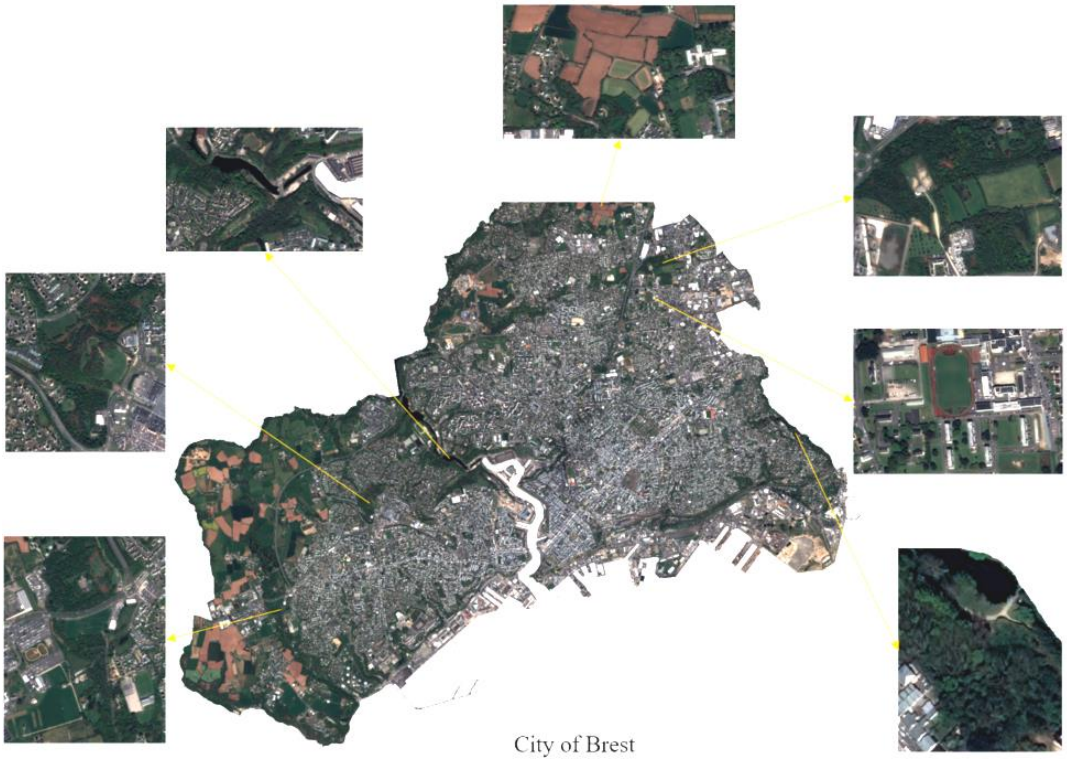

Figure 16 City of Brest with urban green spaces

As the largest agglomeration in Pays de Brest, the city of Brest is the most impacted by urbanization and artificialization. Nonetheless, by the will of local government and citizens, a remarkable number of urban green spaces have been preserved (Figure 16); such preservation is considered to be an essential pre-requisite for the economic development and population growth (Région Bretagne, 2013). Therefore, it is essential to study the urban green spaces changes in the city of Brest and prevent their environmental degradation (G. Xie et al., 2019).

- *Mapping and Monitoring of Land use/land cover (LULC) Change in the Crozon Peninsula (Brittany, France) from 2007 to 2018 by Machine Learning Algorithms (Support Vector Machine, Random Forest, and Convolutional NN) and by Post-classification Comparison (PCC)*.

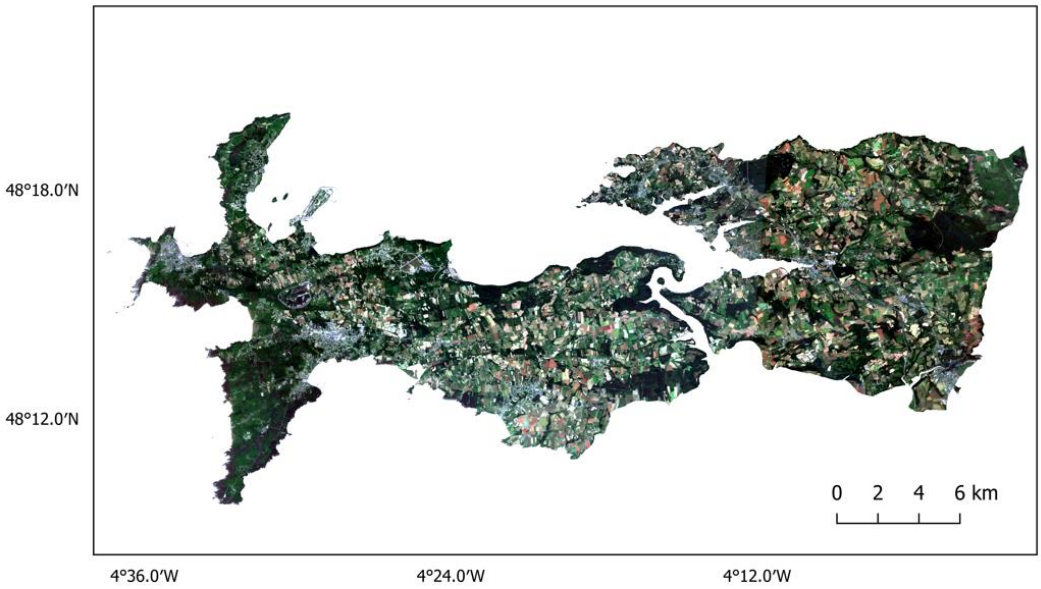

Figure 17 Location of the Crozon Peninsula and two bordering regions, located in Pays de Brest, Finistère, Brittany, France, with the RGB band combination for Sentinel 2 (2018)

A highly fragmented coastal area protected by the regional natural park of Armorique since 1969, the Crozon Peninsula is a unique but rarely studied area (Figure 17). Due to the restriction of construction and the relatively isolated location, the peninsula is sparsely populated. However, with the sharply developed tourism sector in recent years, the problem of artificialization and coastalization of this protected area has become severe. Thus, it is essential to learn about the LULCCs and the driving factors of the changes (G. Xie & Niculescu, 2021).

- *Mapping Crop Types Using Sentinel-2 Data Machine Learning and Monitoring Crop Phenology with Sentinel-1 Backscatter Time Series in Pays de Brest, Brittany, France*.

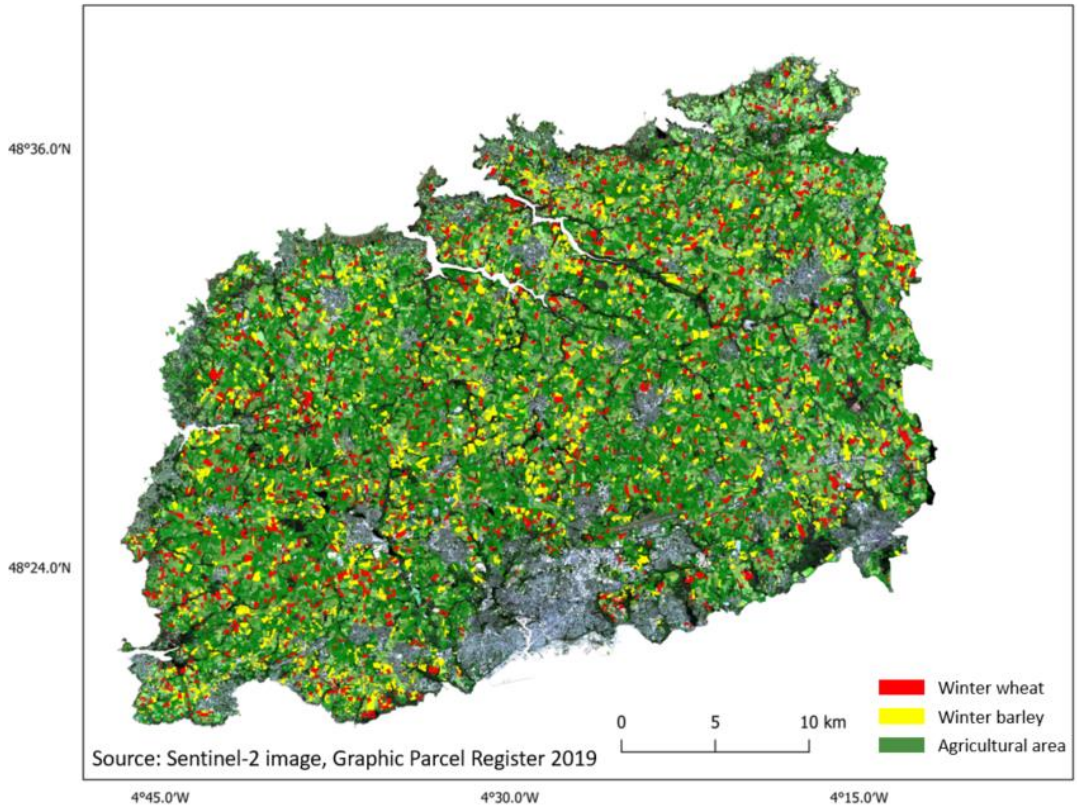

Figure 18 Location of the study area in Northern Finistère, as per the RGB band combination of a Sentinel-2 satellite image on April 20, 2019 and the distribution of agricultural land in 2019.

In the context of rising urbanization and artificialization in Pays de Brest, more and more agricultural lands are being turned into artificial surfaces for secondary or tertiary sector use, especially in northern Finistère, which is near Brest Métropole and thus strongly impacted by the process of suburbanization (Figure 18). Artificialization and urbanization negatively impact biodiversity and the environment, thereby diminishing agricultural production and food security. Therefore, to ensure agricultural supply and facilitate crop management in the region, this study has mapped the croplands, identified the main crop types, studied their spatial distribution in Pays de Brest, and ultimately monitored their growth pattern(G. Xie & Niculescu, 2022).

PART II GENERAL METHODOLOGY

Chapter 3. Data structure and field research

This chapter discusses the data structure used in the three case studies of the thesis. All data applied will be detailed below.

To detect LULCCs and study the trend of LULC evolution and its consequences, it is necessary to have real-time, ultra-high-precision, and easily accessible data. However, traditional ground data are usually quite rare, and involve high labor and time costs. In addition, by using coarse spatial resolution data, global or national land cover maps generally result in poor local accuracy, especially in a highly fragmented area like Pays de Brest. Therefore, high-quality, primarily open-access optical and SAR satellite images, which facilitate easy detection of LULCCs, were applied in our studies because such satellite data are widely used in the field of LULCC detection.

Considering that this thesis is based on several projects of collaboration with local government and communities, their needs usually dictated the period chosen for each study. The first study following the recent changes in vegetation in the city of Brest was requested by the local government of Brest Métropole. Thus, the recent data of very high resolution were applied. The local engineering office then took an interest in LULCCs on the Crozon Peninsula between 2005 and 2020 (due to limited free accessible data and the frequent presence of heavy cloud cover in the region, two images from 2007 and 2018 were finally acquired in this study). At last, the study of winter crop mapping was performed with an image from 2019, which corresponds to our auxiliary data, the latest version of the graphic parcel register (RPG; French: Registre Parcellaire Graphique) published by the French National Institute of Geographic and Forest Information (IGN).

Apart from the optical and SAR satellite data, some auxiliary data were applied, such as RPG in the agricultural field and Google Earth. Several field studies were performed to validate the results, including a survey with local farmers (see questionnaire in Appendix1).

3.1. Satellite imagery

Pays de Brest is known for its picturesque, highly fragmented landscape. The area has been vigorously attacked by artificialization and coastalization in recent years, and its small-scale fields have been most severely impacted. However, it is difficult to observe these "micro-changes" with coarse-resolution data (Sparfel, 2011). Thus, a new generation of high-precision satellite images was acquired in the studies, from the high-spatial-resolution (HR) image used in crop spatial distribution studying and LULCCs detecting to very-high-spatial-resolution (VHR) image for detecting small-scale vegetation in the city of Brest.

Due to the oceanic climate in Pays de Brest, high-quality, cloud-free operational satellite images are difficult to obtain due to the high-intensity annual rainfall and substantial attendant cloud cover. Despite these limitations, a few optical images were acquired from SPOT, Sentinel, and Pléiades platforms during the growing season of vegetation or crops.

Otherwise, compared to a single optical image, the time series is much more difficult to access due to frequent rainfall in the area. Thus, the previous study applied the SAR backscatter time series to follow the phenology of winter crops during their growing season.

3.1.1. Optical image

Since the 1972 launch of Landsat—the first EO satellite—began an era of remote sensing, optical images have become the most widely used type of satellite data. The passive imaging system depends entirely on solar light as the only illumination source. The optical sensors produce images of the Earth's surface by detecting the solar radiation reflected by the target on the ground (Kumar et al., 2018) (Figure 19). The principle of this system is that each object has a unique spectral signature that measures the different ratios between the radiation reflected, absorbed and transmitted at different wavelengths. A sufficient spectral resolution of the sensing system allows the identification of an object from an image with its spectral reflectance profile.

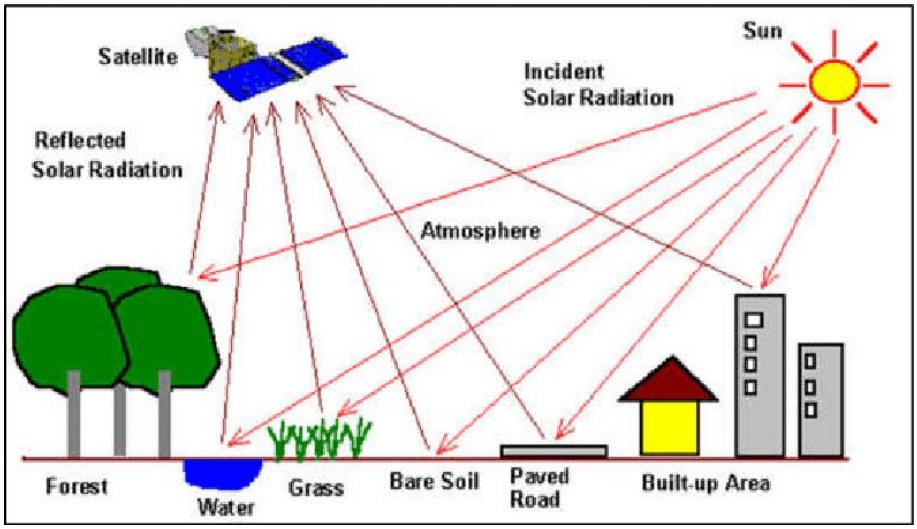

Figure 19 Illustration of optical remote sensing (Source: Kumar et al. (2018))

The optical imaging system uses the light portion of the electromagnetic spectrum (Figure 20), with the wavelength from the visible spectrum to the near-infrared (NIR), the middle infrared (MIR), or even thermal infrared (TIR) to gather the radiation reflected from the target surfaces. This system facilitates the frequent and wide-ranging observation of the Earth's surface at various electromagnetic radiation wavelengths (IREA, n.d.).

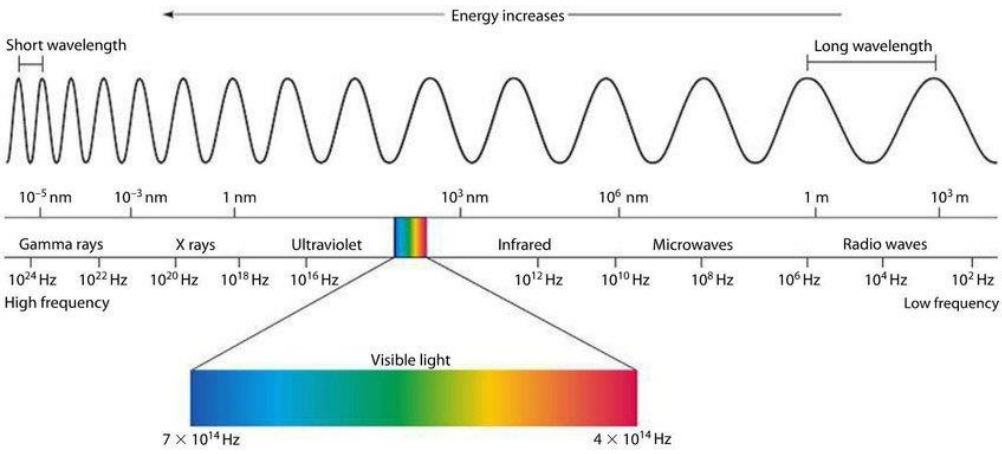

Figure 20 The electromagnetic spectrum by wavelength (Source: Topac (2018))

An optical image is composed of pixels, the most fundamental element and the smallest individual unit of the image, and the criterion to define the quality of an image (Fisher, 1997). A pixel is generally square and depicts a certain region on an image; the number of pixels utilized in the construction of the image determines the spatial resolution, which refers to the size of the finest possible detail in the object being imaged

that a system is capable of detecting. For example, 10 m of spatial resolution indicates that each pixel on the image represents a 10 m x 10 m area on the ground.

Furthermore, depending on the number of spectral bands employed for the imaging process, optical remote sensing can be categorized into various groups, among which panchromatic imaging and multispectral (MS) imaging systems are the most known and used. In the panchromatic scheme, the sensor is a single-channel detector sensitive to radiation over a wide wavelength range. The resulting image is known as a "panchromatic image" when the wavelength range matches the visual range. In contrast, the MS scheme is a multi-channel detector with a limited number of spectral bands, and each channel is sensitive to radiation within a narrow wavelength band (Kumar et al., 2018).

However, each system has its advantages and disadvantages. Panchromatic imaging can produce higher spatial resolution images, but it loses spectral information and produces black-and-white images. On the other hand, the MS imaging system generally has numerous spectral bands (e.g., up to 13 bands for Sentinel-2) but a lower spatial resolution. These two imaging systems are usually merged in image processing (pan-sharpening) to acquire a high-quality image with multiple spectral bands.

In recent years, two key problems have received significant attention in the optical remote sensing area: object detection and change detection. First, object detection refers to identifying and locating an object of interest in images. Object detection has always been a fundamental challenge in optical remote sensing, giving rise to numerous studies methods (Cheng & Han, 2016). In addition, since the beginning of the application of remote sensing data, satellite images have been digitally processed by comparing pixel intensities for detecting changes in a variety of applications, including urban sprawl and LULCCs, vegetation monitoring (Maktav et al., 2005; Jones & Vaughan, 2010; Abd El-Kawy et al., 2011; Tewkesbury et al., 2015). In this thesis, object detection was applied to detect urban green spaces in Brest and locate winter crops in northern Finistère with optical imaging.

In recent years, numerous VHR or HR sensors have been developed with different spatial, spectral, radiometric, and temporal resolutions. Optical satellite images from different platforms were applied in all three case studies featured in this thesis. VHR

images of Pléiades-1 were applied to monitor the vegetation changes in the city of Brest (i.e., urban green spaces on a small scale). LULCCs on the Crozon Peninsula were detected using SPOT-5 VHR images and Sentinel-2 HR images due to the limited open-source data and climate conditions. Finally, a single cloud-free Sentinel-2 image acquired during the growing season of winter crops was employed for winter crop mapping.

3.1.1.1. Very high spatial resolution image (Pléiades-1, SPOT-5)

- SPOT-5

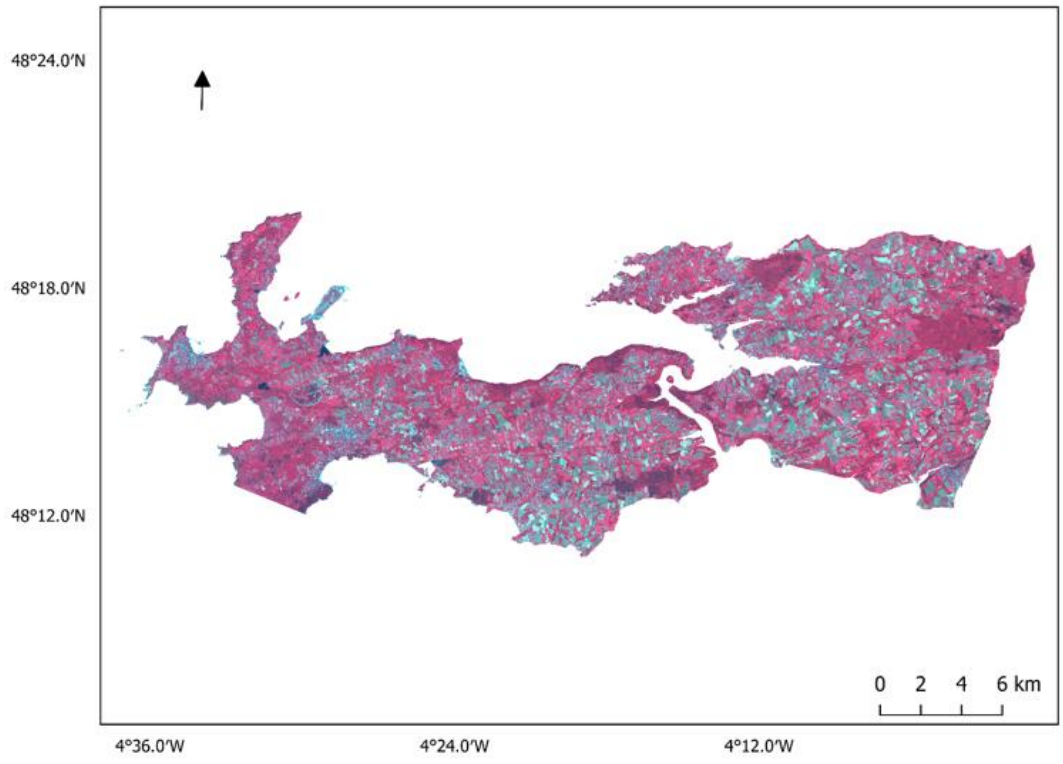

Figure 21 SPOT-5 image of the Crozon Peninsula

SPOT-5 (Figure 21) (Earth Observation Satellite; French: *Satellite pour l'Observation de la Terre*) is a commercial Earth-imaging system from the French National Center for Space Studies (CNES; French: *Centre national d'études spatiales*). As the fifth generation of SPOT mission satellites, SPOT-5 was launched in May 2002 (ceased service in March 2015) to ensure the continuity of service of the SPOT system and improve the quality of data. Thus, the objective was to supply high-resolution, wide-area optical imagery to observe the Earth's surface, monitor human activities, help decision-making

for resource management, follow natural phenomena, and identify and predict climatology and oceanography-related phenomena (European Space Agency (ESA), n.d.-c).

Table 1 Spatial resolution and wavelength of SPOT-5 product

Band	Resolution	Wavelength
Panchromatic	2.5m	480 – 710 nm
	5m	480 – 710 nm
Band 1 - Green	10m	500 – 590 nm
Band 2 - Red	10m	610 – 680 nm
Band 3 - NIR	10m	780 – 890 nm
Band 4 - SWIR	20m	1580 – 1750 nm

As the continuity of the SPOT missions, SPOT-5 provided a better quality image with a higher spatial resolution other than the previous SPOT missions by significantly improving the spatial resolution. SPOT-5 operated in both panchromatic and multispectral modes; the spatial resolution was 2.5 m in panchromatic mode and 10 m in multispectral mode (Table 1). Furthermore, the stereo pair acquisition capabilities were enhanced through a dedicated instrument, the High-Resolution Stereoscopic (HRS) operated in panchromatic mode. In addition, SPOT-5 was equipped with a wide swath of 60 km in both modes and a high frequent revisit capacity of 2 or 3 days (depending on latitude).

The SPOT-5 image of the study was acquired from ESA (earth.eas.int).

- Pléiades-1

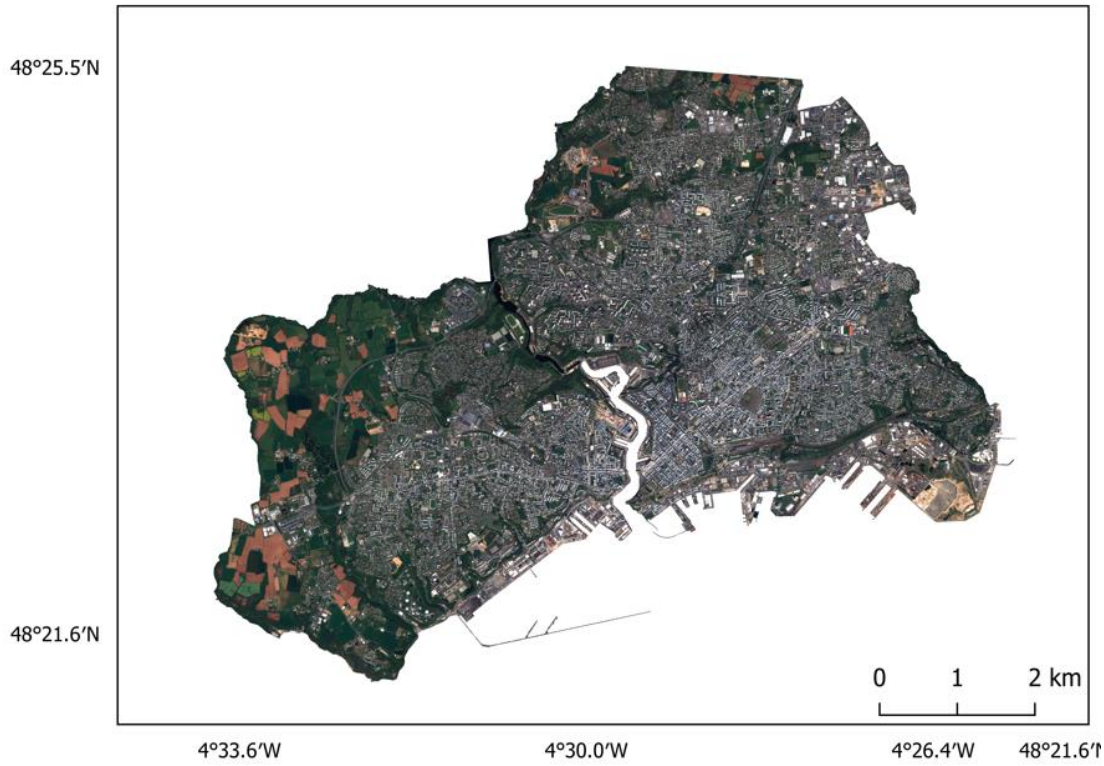

Figure 22 Pléiades image of city of Brest

The successor of the SPOT program before the arrival of SPOT-6 and SPOT-7, Pléiades-1 (Figure 22) is composed of two Earth-observation spacecraft, Pléiades-1A and Pléiades-1B, launched by CNES in December 2011 and 2012, respectively. These two identical satellites are placed at 180° on the same sun-synchronous phased obit, which is the same orbital plane as the SPOT-6 and SPOT-7. A constellation with the aim of EO is therefore forming with these four satellites operated on a single interface. According to Table 2, the nominal repeat cycle is 26 days (with a viewing angle of 5°). Nonetheless, the revisiting time of Pléiades-1 for global access is as long as 5 days with one single satellite, whereas the two satellites of the system can achieve that in 4 days when the viewing angle is 30°.

Table 2 Revisiting time of Pléiades-1 (Source: eoPortal)

Viewing angle	single satellite	Both satellites
5°	26 days	13 days
20°	7 days	5 days
30°	5 days	4 days

Pléiades-1 satellites are well known for their distinctive characteristics, such as the broad swath of approximately 120 km x 110 km, their outstanding capacity to provide VHR MS imagery with highly accurate geo-location for dual civil/military use, and global coverage of Earth's surface with daily observation accessibility from every location on Earth in a variety of modes of operation (eoPortal, 2012c).

Pléiades-1 is operated in both panchromatic or MS modes; for each image, the panchromatic and MS modes are acquired simultaneously. As a VHR image, the resolution of Pléiades reaches 70 cm in the panchromatic band, while the four MS bands—blue, green, red, and NIR (Table 3)—have a spatial resolution of 2.8 m. Later, the images are resampled to the ground at 50 cm in panchromatic mode and 2 m in MS to obtain a robust product for further image processing. Eventually, by combining information from the panchromatic and MS products, MS data sampled at 50 cm can be acquired (IGN, n.d.-a).

The Pléiades-1 images are usually applied in studies of such fields as vegetation cover, landscape topography, LULC, and ice sheet topography (eoPortal, 2012c).

Table 3 Spatial resolution and wavelength of Pléiades product

Band	Resolution	Wavelength
Panchromatic	50cm	480 – 820 nm
Band 1 - Blue	2m	450 – 530 nm
Band 2 - Green	2m	510 – 590 nm
Band 3 - Red	2m	620 – 700 nm
Band 4 - NIR	2m	775 – 915 nm

In this thesis, three Pléiades-1 Level-2 orthorectified MS images from 2018 to 2021 with 50 cm of spatial resolution used in the study of vegetation in the city of Brest were acquired on the DINAMIS platform (https://dinamis.teledetection.fr). The detail of the images will be discussed in Part 3, Chapter 5: Machine Learning Methods and Classification of Vegetation in Brest, France.

3.1.1.2. High-spatial-resolution open-source image (Sentinel-2)

Even though HR optical imaging systems have rapidly improved in recent years, several Sentinel-2 images acquired in different locations and at different times were applied in two studies: (1) Mapping and monitoring of LULCCs on the Crozon Peninsula (Figure 23) and (2) Mapping crop types in Pays de Brest (Figure 24).

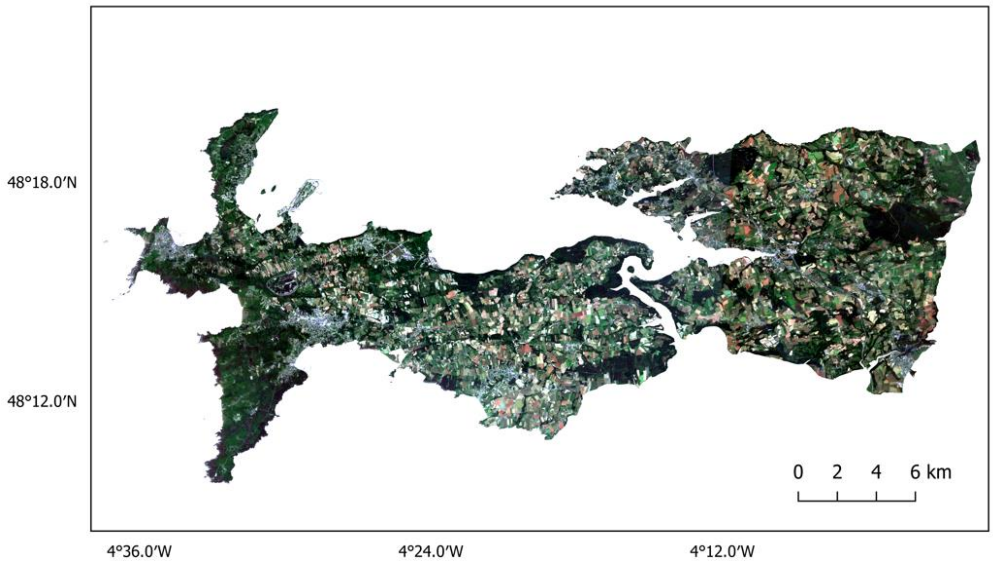

Figure 23 Sentinel-2 image of the Crozon Peninsula

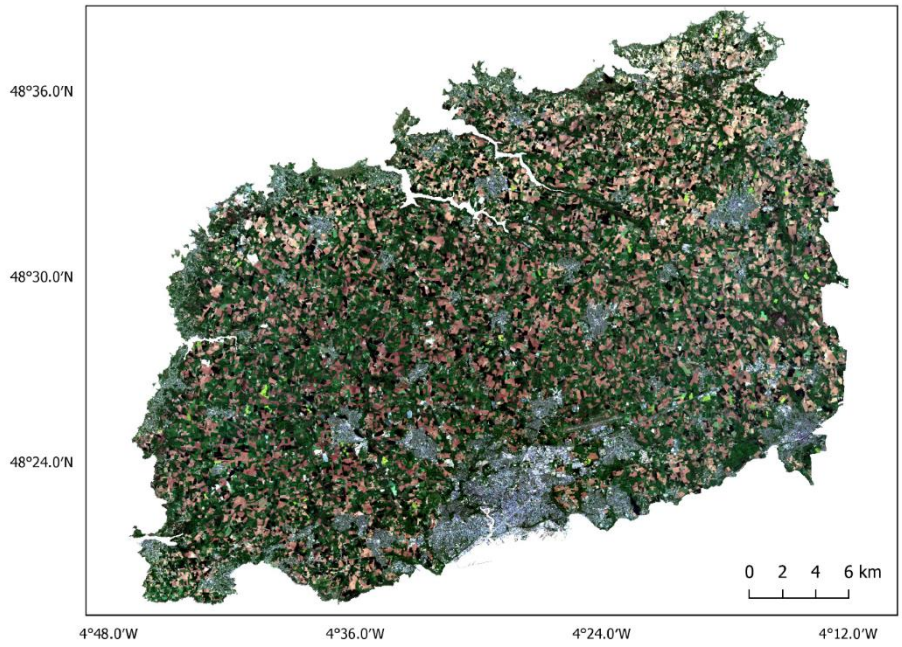

Figure 24 Sentinel-2 image of northern Finistère

Sentinel-2 is a constellation of two identical MS optical imaging satellites located on the same sun-synchronous orbit, including Sentinel-2A and Sentinel-2B, launched in June 2015 and March 2017, respectively (eoPortal, 2012b). The ESA operates the land monitoring satellites and participate in the Copernicus Programme, the European Union's Earth observation program.

The main objectives are to ensure continuity of high-resolution, free-accessed satellite images for multiple purposes (e.g., monitoring inland and coastal areas, managing crops and forests), complete the current Landsat and SPOT projects, and to provide full and systematic coverage of Earth's land surface with a wide swath of 290 km and a significant revisit capability of 5 days with two operational satellites (eoPortal, 2012b). Sentinel-2 data are also used to support the production and update of high-level geographical products, such as LULCC detection maps, geophysical maps, and CLC maps.

Table 4 Spatial resolution and wavelength of Sentinel-2 operated bands (Source : Satellite Imageing Corporation)

Sentinel-2 Bands	Central Wavelength (µm)	Resolution (m)
Band 1 - Coastal aerosol	0.443	60
Band 2 - Blue	0.490	10
Band 3 - Green	0.560	10
Band 4 - Red	0.665	10
Band 5 - Vegetation Red Edge	0.705	20
Band 6 - Vegetation Red Edge	0.740	20
Band 7 - Vegetation Red Edge	0.783	20
Band 8 - NIR	0.842	10
Band 8A - Vegetation Red Edge	0.865	20
Band 9 - Water vapour	0.945	60
Band 10 - SWIR - Cirrus	1.375	60
Band 11 - SWIR	1.610	20
Band 12 - SWIR	2.190	20

The Sentinel-2 satellite provides 13 HR spectral bands (Table 4): three visible bands (blue, green, and red) and a NIR band with 10 m of spatial resolution for primary land-cover classification, three NIR vegetation red-edge bands (B5, B6, B7) with a resolution of 20 m for advanced land-cover classification and vegetation state detection, and finally six short-wave infrared (SWIR) bands with a resolution of 60 m dedicated mainly to atmospheric corrections and cirrus-cloud screening.

All products can be obtained in several processing levels, of which only two—Levels 1C and 2A—are released to users. Level-1C results from radiometric and geometric

corrections with orthorectification and spatial registration on a global reference system with sub-pixel accuracy (ESA, Sentinel-2); cloud and water masks are also generated at this level. On the other hand, Level-2A is generated with the Sen2Cor atmospheric correction processor, which is capable of detecting three different forms of clouds, snow, and cloud shadows, thereby creating a corresponding mask. It also outputs an orthoimage bottom-of-atmosphere (BOA) corrected reflectance product, which is resampled and generated with an equal spatial resolution for all bands (10 m, 20 m, 60 m) (eoPortal, 2012b).

Moreover, THEIA platform (theia.cnes.fr) provides Sentinel Level-3A images, an utterly cloud-free product created during a synthesis period of 45 days. For each pixel in each band of a Sentinel Level-3A image, the average cloud- and shadow-free surface reflectance collected during 45 days is calculated to avoid cloudy or shadowed pixels. Thus, the Sentinel Level-3A image is a mosaic of the pixels acquired on different dates in different view angles. However, to achieve this result, the cloud-free image sacrifices its temporal resolution; it is rarely used to detect the evolution of the surface in a short time. Thus, it can be applied only in studies that do not require high data accuracy (CESBIO, 2018)

3.1.2. Synthetic-aperture RaDAR image (Sentinel-1)

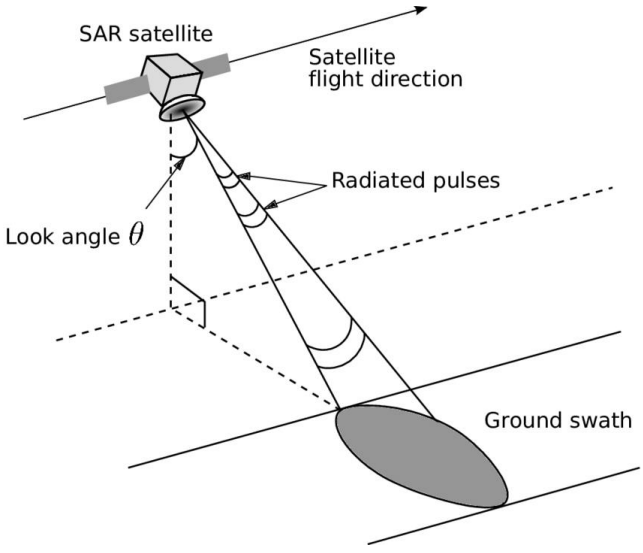

Figure 25 SAR system (Source: Lauknes (2011))

SAR is an active system for data collection. To generate a SAR image, sensors illuminate the target area with its energy source: a series of radio wave pulses. The sensors can record how much of that energy is reflected after interacting with the Earth's surface (Figure 25) (Earth Science Data Systems, n.d.); the spatial resolution of SAR data is directly affected by the ratio of the sensor wavelength to the sensor's antenna length.

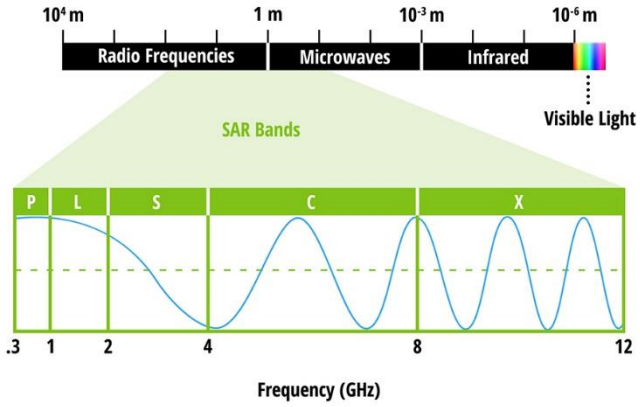

Figure 26 SAR bands in electromagnetic spectrum

Table 5 The most common bands used in SAR imaging systems

Band	Frequency (GHz)	Wavelength (cm)
X	8.0 - 12.5	2.4 – 3.75
C	4.0 - 8.0	3.75 – 7.5
L	1.0 - 2.0	15 - 30

Besides optical imaging systems collecting data in the visible, NIR, and SWIR areas of the electromagnetic spectrum, RaDAR sensors exploit longer wavelengths at the centimeter-to-meter scale (Figure 26). The most frequently used bands in the SAR system are L, C, and X (Table 5). The bands with different frequencies and wavelengths are determined by how the RaDAR signal interacts with the surface and penetrates objects in the target area (Earth Science Data Systems, n.d.). Due to this penetration capacity, SAR images are usually used to detect forest, soil, and ice without limitation of cloud cover and meteor conditions. In general, longer wavelengths achieve greater penetration (Earth Science Data Systems, n.d.).

Besides the bands, the SAR system can emit and collect signals in different types of polarization, which refers to the plane's orientation in which the transmitted

electromagnetic wave oscillates. However, the polarization of SAR sensors is generally linear—i.e., horizontal or vertical (Earth Science Data Systems, n.d.). In addition, the polarization can be different in emission and reception. For example, a signal emitted in horizontal (H) and received in vertical (V) is indicated as "HV." Different structures of surfaces are sensitive to different polarizations.

In this thesis, a Sentinel-1 SAR C-band time series was applied for winter crop phenology monitoring. Sentinel-1 consists of two satellites, Sentinel-1A and Sentinel-1B, launched in 2014 and 2016, respectively; they are operated on the same orbit and each possesses a RaDAR instrument to provide a high-quality image of Earth's surface in day-and-night, all-weather conditions. Just like Sentinel-2, the Sentinel-1 SAR system was developed within the Copernicus Programme by the European Commission (EC) and the ESA to perform day-and-night, all-weather C-band SAR imaging in two polarizations with the capability of brief revisiting time (6 days of repeat cycle with two satellites), rapid product delivery and high global surface coverage. Its outstanding open-access system has been developed to provide reliable wide-area monitoring for environmental and security purposes (ESA, n.d.-b).

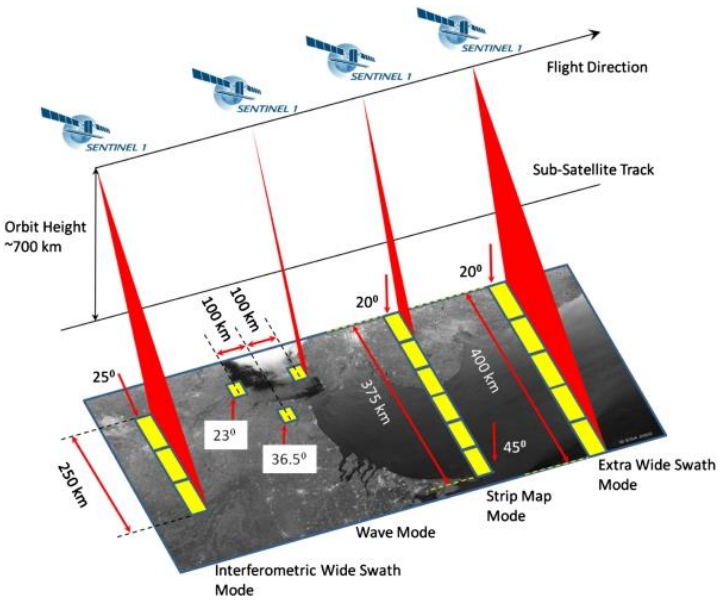

Figure 27 Four observation modes of Sentinel-1 (source: ESA)

Table 6 Characteristics of four acquisition modes of Sentinel-1

Acquisition mode	Polarization	Swath (km)	Resolution (m)	Principal use
SM	HH,VV, HH+HV, VV+VH	80	5	Support ERS* and Envisat missions
IW		250	5x20	Land observation
EW		400	25x100	Maritime, ice, polar zones observation
WV	HH, VV	20	5x20	Open ocean observation

Four observation modes of the Sentinel-1 SAR system for different purposes are displayed in the Figure 27 and Table 6, each with a different swath and spatial resolution: StripMap (SM), Interferometric Wide swath (IW), Extra Wide swath (EW), and WaVe (WV) mode. Among the acquisition modes, SM, IW, and EW equip dual polarization capacity, whereas WV acquires an image in single polarization (HH or VV). Following a different mode, the swath width is also different. EW has the largest swath of 400 km, so it is usually used for maritime, ice, and polar zone observation. IW is performed with a narrower swath of 250 km but higher spatial resolution, and is generally employed for land monitoring. By contrast, WV and SM were equipped with relatively narrow swaths (20 km and 80 km, respectively) and are suited for diverse specific uses, such as open ocean observation as well as European remote sensing (ERS) and Envisat missions supporting (eoPortal, 2012a).

Like Sentinel-2, Sentinel-1 data are available and freely accessible to the public in different types at different processing levels. Level 1, the most common and widely used, has already been through pre-processing (raw data analysis, internal calibration), Doppler centroid estimation, and focusing. Eventually, output as Single Look Complex (SLC) and Ground Range Detected (GRD), two formats of data types are produced. SLC has been georeferenced, contains preserved phase information. GRD, on the other hand, preserves the amplitude information and multi-looks to minimize the effect of speckle (ESA, n.d.-d).

3.2. Auxiliary data

Auxiliary data, also known as reference data structure external to the survey data collected, provide supplementary information to the study. In this thesis, apart from optical and SAR HR images collected. An auxiliary structure composed principally of Google Earth and RPG is used as additional information to produce training data and test data for image classification.

3.2.1. Graphic parcel register

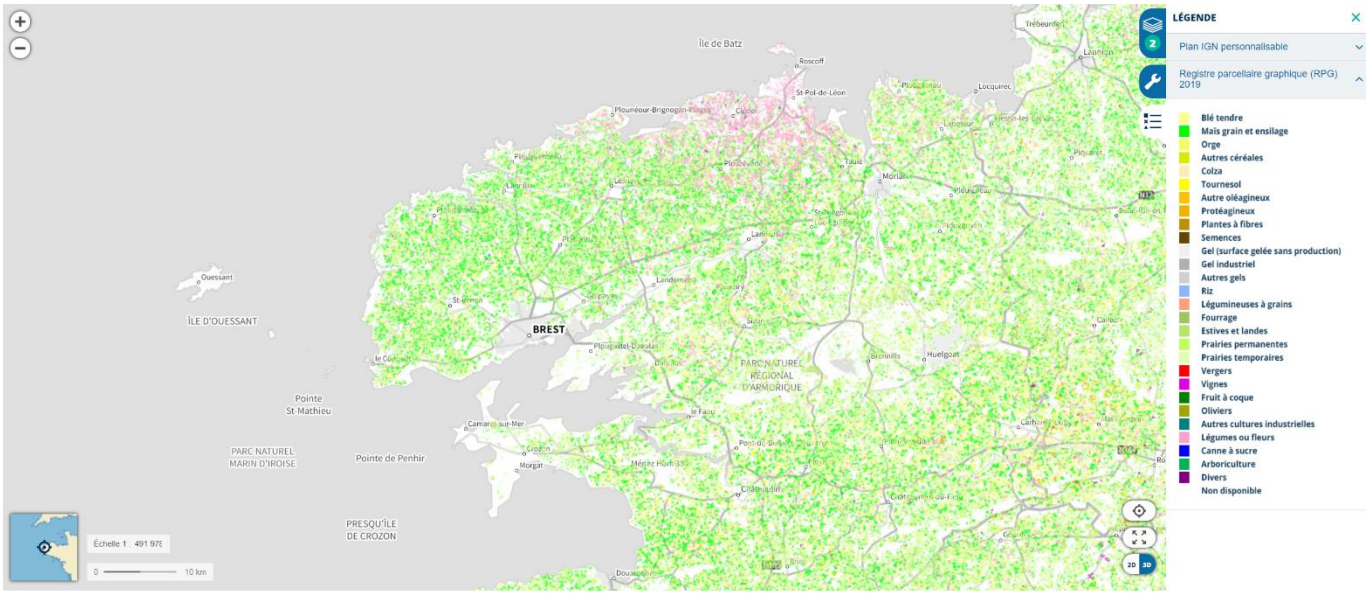

Figure 28 RPG 2019 (Source: Géoportail.gouv.fr)

RPG is the highly accurate georeferenced agricultural land database produced by IGN (Figure 28). The database records the specific crop types (such as wheat, corn, barley, and vegetables) or grassland for the livestock sector each year throughout all French territory (except Mayotte). RPG 2019, the most recent edition of RPG (at the time of data collection for this thesis) was applied in the studies as the ground truth data to be used for creating training data and test data, especially for the winter crops monitoring study (IGN, n.d.-b).

3.2.2. Google Earth

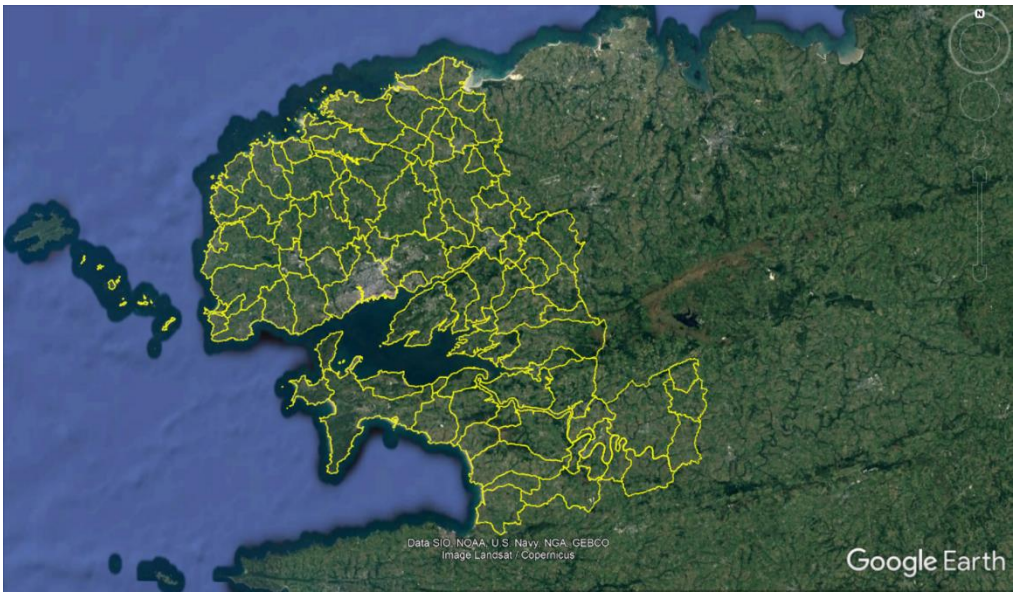

Figure 29 Pays de Brest on Google Earth

Figure 30 Vegetation in small scale on Google Earth

Google Earth, one of the most well-known and widely used computer programs, visualizes the planet Earth by superimposing highly accurate satellite, aerial photography, and GIS data (Figure 29). This allows the public to see cities and landscapes from different angles, including 3D imagery and Street View. Additional satellite images were provided by the Landsat and Copernicus programs. Thus, because Google Earth is a reliable source

of ground truth data—particularly data on a small scale in an urban environment—it was used to study vegetation detection in the city of Brest (Figure 30).

3.3. Field research

Field research, which is essential for most scientific studies, refers to a method of collecting qualitative data by observing the study area's geographical conditions and interacting with groups of people who live in the area to be deeply involved in the research subject. In remote sensing, field research generally refers to direct observation of the ground by visiting the area and collecting data with recording devices (e.g., Global Nativation Satellite System (GNSS) device and camera) or questioning the people on site.

3.3.1. Observation and validation of vegetation in the city of Brest

Figure 31 Urban green spaces in the city of Brest

Field research was carried out to study the evolution of vegetation in the city of Brest. During the image processing, we visited several areas that were not clearly visible from the satellite image to determine the precise vegetation type and structure. After the classification, we also visited some areas where vegetation changes were found to verify the type of change (i.e., permanent or temporary).

3.3.2. Observation and validation of LULC on the Crozon Peninsula

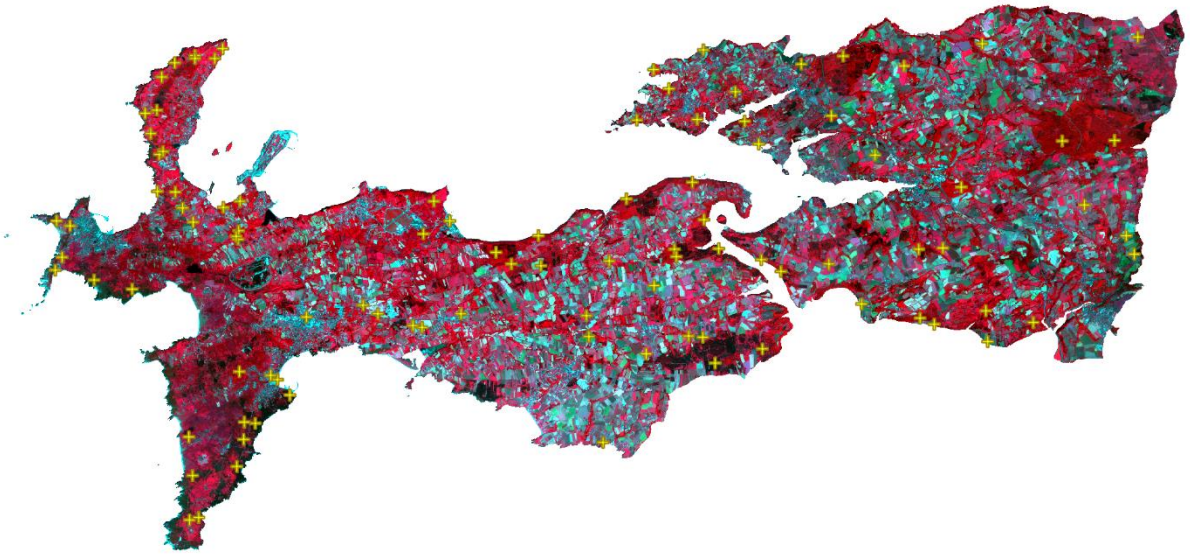

Figure 32 Sentinel-2 image of the Crozon Peninsula with GNSS points for ground truth field research

The Crozon Peninsula is marked by a highly fragmented landscape on a small scale. Thus, direct observation and the validation of the LULCCs detected were indispensable for this study. Before image processing, a field study was performed with a GNSS device to compare the actual landscape and that seen in the satellite image and collect data to be used in the creation of the training dataset (Figure 31).

3.3.3. Croplands and winter crops planting situation observation in northern Finistère

Figure 33 Croplands in northern Finistère

Field research was performed before the image processing step to observe and understand the study area, especially the croplands (Figure 32). However, due to the crop rotation system, planted crops change frequently in the study area, making it impossible to confirm the information on RPG 19 (our reference data in the study) and thereby collect ground truth. For this reason, we conducted additional fieldwork to interact with local farmers using the same questionnaire as that found in Appendix 1.

Chapter 4. Analysis and image processing

In this chapter, different methodologies used in the different topics will be discussed in detail.

Remote sensing refers to the gathering of information in digital or analog form using space-based equipment or sensors without direct contact. Remote sensing data with various spectral, spatial, radiometric, and temporal resolutions are collected from spaceborne or airborne platforms such as satellites, aircraft and drones. Hence, most products must be processed before being applied in studies of different thematic (Khorram et al., 2013).

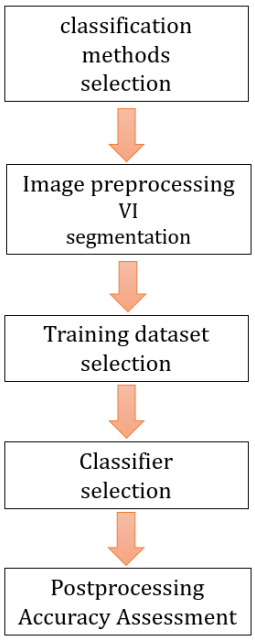

Figure 34 General flow path of image processing

The complete methodology of image processing consists of pre-classification, classification, and post-classification (Figure 33); each step is indispensable in the study of remote sensing. The chain of satellite image processing transforms raw, unprocessed spectral data or radio signals into comprehensible, meaningful and georeferenced data that can be used for further analysis and application in different thematics.

- **Pre-classification processing:** As the preliminary data processing, this step consists of preparing the raw data for further processing or analysis. In general, remote sensing

data suffer different kinds of distortion, such as atmospheric distortion caused by clouds, suspended particles, or other materials present in the atmosphere during imaging acquisition (Khorram et al., 2013). Geometric distortions, including systematic distortions, result from image motion caused by a forward movement of the spacecraft, variations in the mirror scanning rate, panoramic distortions, variations in platform velocity, and distortions due to the curvature of the Earth, as well as nonsystematic distortions due to variations in satellite altitude and attitude acquisition (Khorram et al., 2013) and a variety of radiometric distortions.

Thus, *pre-classification image processing* refers to image restoration and rectification. It consists of a series of procedures by which imagery is georeferenced and orthorectified, as well as atmospherically, geometrically, and radiometrically corrected in order to reduce noise caused by irregularities or errors in the sensor response, data recording and transmission before further processing and analysis such as classification (Government of Canada, 2008). In general, the most commonly used preprocessing techniques include converting, calibrating, resampling, merging, and reducing and fusing data. For instance, data subsetting allows us to save only the information of interest and remove the unrelated information from the image; this technique can effectively reduce image size and computation complexity while economizing computation time and computer storage. However, each preprocessing step depends on different sensors and platforms; specific preprocessing is required for each sensor and platform. Furthermore, other procedures—such as vegetation index, which is performed by ratio calculating between different spectral bands, and segmentation in case of object-based classification—can be carried out according to need.

- **Image classification:** Image processing principally refers to the classification of image by employing different methods, from unsupervised pixel-based to non-parametric supervised object-based methods. Numerous algorithms have also been developed for image classification, such as the K-Nearest Neighbor (KNN), MLC, ML including rapidly advancing DL methods. In our studies, satellite optical images from different sensors were processed with different classifiers (e.g., SVM, RF, CNN,

multilayer perceptron (MLP)); moreover, SAR backscattering time series were processed using the Google Earth Engine (GEE) platform.

- **Post-classification processing:** Finally, the image is ready to be analyzed, and valuable information can be extracted for thematic study. With this aim, several tools can be applied in this step according to the research objectives, such as statistical analysis (e.g., accuracy assessment) for validation of the results and PCC for detecting land cover transition and studying the spatial distribution of changed types and change trajectories between different LULC types.

4.1. Methodology of image pre-classification

Image pre-classification processing was performed after the study area selection and satellite image acquisition.

Satellite data used in the studies were already preprocessed through atmospheric, geometric, and radiometric corrections already applied by the distribution data platform. Otherwise, a series of preprocessing procedures have been performed in our studies—for instance, area of interest extraction by subsetting the raw images with the boundary, data merging, and the two most important techniques: vegetation indices calculation and image segmentation. The performance of the two last techniques will be discussed in the following subchapter.

4.1.1. Calculation of vegetation indices

4.1.1.1. Definition of the vegetation index

As an essential part of remote sensing data interpretation—especially in image pre-classification processing—vegetation indices (VIs) are widely discussed and implanted in the remote sensing field.

The VI is the qualitative and quantitative evolution of the vigor of vegetation as assessed by spectral measurements (Campbell, 1987; Bannari et al., 1995), which can be

defined as the combination of certain bands to obtain differences and ratios between spectral bands by division, addition, subtraction, or multiplication. The indices yielded by the calculation can effectively lead to enhanced information for vegetation detection (Khorram et al., 2013). These relationships between radiometric response and vegetative covers have been a highly active research area. The first research studies of VIs revealed that the red and NIR spectral bands were well suited for vegetation detection. Moreover, as the spectral response of vegetated areas, these indices can be affected by many factors. Various recent studies have sought to maximize the radiant response of vegetative covers—including the vegetation mixture and composition—and to minimize environmental factors such as soil characteristics (e.g., color, brightness, and humidity), and the spatial–temporal atmospheric variations (Bannari et al., 1995).

As mentioned in Chapter 3, each vegetation type has its specific spectral signature, which suggest that each vegetation specy has its unique behavior concerning radiant energy (Figure 34). Hence, calculations between different spectral bands reveal different results, and more than 100 VIs have been developed over two decades to enhance detection of vegetation cover (type and composition).

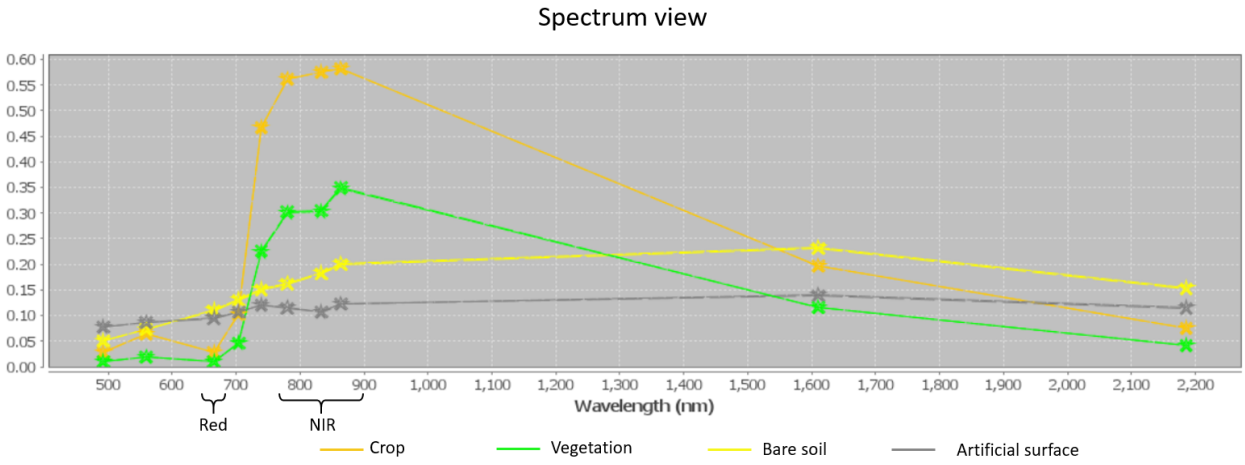

Figure 35 Spectrum view of vegetation, crop, bare soil and artificial surface

The earliest VIs focused on calculating red and NIR channels because most light in red channels is absorbed by chlorophyll; those in NIR channels are strongly reflected by leaf cellular structures. Thus, vegetation in the histogram is usually indicated by the decreasing and increasing wavelengths in the red and NIR channels, respectively (Figure

34). Thus, it is easy to distinguish green vegetation from other elements on the surface by using the combination of red and NIR channels (Major et al., 1990; Bannari et al., 1995).

The first generation of VIs (i.e., the Ratio Vegetation Index (RVI) and the Vegetation Index Number (VIN)), was developed by Pearson & Miller (1972) by simply calculating the ratio of red and NIR bands. After that, the RVI and VIN indices were enhanced by various studies; the best-known version is the Normalized Difference Vegetation Index (NDVI), which was first proposed by Rouse et al. (1974). This VI, which is still widely used in the remote sensing field, can not only capture the presence of green vegetation but can also monitor crops and precipitation (Sellers, 1985; Nicholson et al., 1990; Bullock, 1992). Another well-known index, the Non-Linear Vegetation Index (NLI), also uses NIR and red channels, with straightforward modification by adding the square value of the NIR band; this slight optimization develops a significant sensitivity for detecting Leaf Area Index (LAI) changes by reducing the reflection contrast and saturation (Goel & Qin, 1994; W. Feng et al., 2019).

In addition to chlorophyll and leaf cellular structure—the essential elements of vegetation detection—other vegetative factors also have considerable impacts on VI calculation, such as water content, leaf form, age, and vegetation diseases. These factors are usually more sensitive to radiation in wavelengths outside of the red and NIR channels. Thus, many indices have been developed to detect different vegetative factors. Since 2000, radiation in other wavelengths, such as green bands or MIR bands, have been exploited for VI; such indices help distinguish vegetation from other elements and eliminate disturbance factors mentioned earlier.

For instance, the Normalized Different Greenness Index (NDGI) has been shown to help map various active vegetation formations in flooded areas (Chamard et al., 1991). In the Normalized Difference Water Index (NDWI), Gao (1996) applies the ratio between NIR and SWIR to explore water content at the leaf level. The Green Red Vegetation Index (GRVI), which replaces the NIR channel with the green channel, can determine the vegetation cover and recognize phenological crop changes, detect heterogeneity in field irrigation, and track plant photosynthesis (Tucker, 1979; A. Chen et al., 2019; G. Yin et al., 2022). The Enhanced Normalized Difference Vegetation Index (ENDVI), developed with additional visible blue and green channels compared to traditional NDVI, has been shown

to be more efficient for isolating plant health indicators and detecting plant disease. Thus it can be applied as a reliable marker of plant health (PrecisionHawk, n.d.). The Visual Atmospheric Resistance Index (VARI) (Gitelson et al., 2002) is an index designed to minimize atmospheric effects by using blue channels to better detect Earth's surface and provide more accurate vegetation detection.

VIs are widely used in the remote sensing area, most commonly in vegetation cover mapping; various VIs have been developed and applied for this purpose (Bannari et al., 2002; Y. Xie et al., 2008; Sadeghi et al., 2018). For example, Xavier & Vettorazzi (2004) conducted a study in the subtropical rural watershed of Piracicaba in the State of Sao Paulo, Brazil, using various spectral ratio as Simple Ratio (SR), NDVI, and Soil Adjusted Vegetation Index (SAVI) calculated from Landsat-7 data to generate a LAI map for the watershed, which is closely associated with vegetation productivity. NDVI achieved the best fit among all three VIs, with a correlation of 0.72.

Change detection is also a widespread application of VIs, which have been shown to have a remarkable ability to detect changes in both forest and urban environments (P. J. Howarth & Boasson, 1983; Mouat et al., 1993; Nordberg & Evertson, 2005; Asokan & Anitha, 2019). Lyon et al. (1998) showed that VIs were well adapted for monitoring temporal changes associated with vegetation. In their study, a variety of vegetation indices—Difference Vegetation Index (DVI), Perpendicular Vegetation Index (PVI), RVI, Soil Adjusted Ratio Vegetation Index (SARVI), NDVI, SAVI, and Transformed Soil Adjusted Vegetation Index (TSAVI)—were applied in order to detect vegetation and land cover change between 1975 and 1986 in the State of Chiapas, Mexico, a region plagued by deforestation. Even though each index was developed to better detect vegetation, and despite their ability to identify changes, most were affected (to varying degrees) by topographic factors. Eventually, NDVI was found to be the best vegetation change evaluator in this study.

Various VIs are widely applied to detect and evaluate plant disease (Shafri & Anuar, 2008; Devadas et al., 2009; W. Feng et al., 2016; Isip et al., 2020). Ashourloo et al. (2014) successfully evaluated the effect of various plant diseases and detected wheat leaf rust disease. This prevalent disease had different symptoms, using various spectral vegetation ratios on hyperspectral images. The authors found that all VIs consistently increased with

disease severity; in particular, the narrow-band normalized difference VI (NBNDVI), NDVI, Photochemical Reflectance Index (PRI), Greenness Index (GI), and Red-edge Vegetation Stress Index (RVSI) showed excellent capacity for plant disease detection.

VIs provide valuable and helpful information for crop mapping, forecasting (Wiegand et al., 1991; Thenkabail et al., 2000; Panda et al., 2010; Sharifi, 2020), and crop phenology monitoring (Peña-Barragán et al., 2011; X. Huang et al., 2019). Bolton & Friedl (2013) used the MOderate Resolution Imaging Spectroradiometer (MODIS) to develop empirical models for maize and soybean prediction in the central US by using MODIS two-band Enhanced Vegetation Index2 (EVI2) and NDVI. The results indicated that maize yields in non-semi-arid countries were better predicted by EVI2. Nonetheless, NDWI was more sensitive to irrigation and thus performed better in semi-arid areas with low-density agriculture. However, NDVI and EVI2 both successfully detected soybean yield in the research.

Moreover, crop irrigation is one of the crucial elements that affect agricultural production (Duchemin et al., 2006; B. Yu & Shang, 2017; Coelho et al., 2018; F. Zhang & Zhou, 2019). (González-Dugo & Mateos, 2008) conducted a study about irrigation performance and water productivity benchmarking in southern Spain. Their study developed a method for estimating crop evapotranspiration on sugar beet and cotton fields in irrigated areas by appropriating crop coefficients with two vegetation indices (SAVI, NDVI). Both indices successfully described the crop growth situation and obtained accurate crop coefficients; evapotranspired water productivity was also successfully predicted.

VIs can be an indicator of drought as well; the strong connection between VIs and drought was revealed by previous studies. In particular, NDVI and Vegetation Condition Index (VCI) are widely applied in the drought detection field (Peters et al., 2002; Rahimzadeh Bajgiran et al., 2008; Bushra et al., 2019; Rousta et al., 2020). NDVI was first used to evaluate vegetation conditions in a study by Kogan, (1995). Furthermore, the AVHRR-based VCI built on NDVI has successfully detected large- and small-scale droughts in the USA and provided accurate drought information, such as intensity, duration, and impact on vegetation. In addition, the Temperature Condition Index (TCI), which provides

additional information by indirectly determining stress caused by excessive wetness, was also implanted in Kogan's study.

4.1.1.2. Choice of VI and calculation

Among more than 100 VIs developed for various applications, seven of these were utilized in this thesis to detect LULCCs and map winter crop types. Some of them were implemented in both studies.

- **NDVI**, proposed in 1973 by Rouse et al. is the most well-known and frequently used index in studies on monitoring vegetation. NDVI is defined as the normalized difference between the visible red and NIR spectral reflectance of vegetation. The expression is as follows:

$$NDVI = \frac{NIR-Red}{NIR+Red} \quad (1)$$

Even though some limitations remain in this, one of the earliest developed VIs—such as sensitivity to the impacts of soil characteristics and some atmospheric factors (Xue & Su, 2017)—it is nevertheless the most commonly employed VI in regional or global vegetation monitoring and agriculture-related fields. Thus, NDVI was applied in the studies of LULCCs detection and winter crop mapping.

- **NDWI**, proposed by Gao in 1996 for remote sensing of vegetation liquid water from space. The index is well known for its ability to measure liquid water molecules in vegetation canopies with weak atmospheric aerosol scattering compared to NDVI. However, NDWI does not eliminate the background soil reflectance effects. The equation is as follows (B. Gao, 1996):

$$NDWI = \frac{NIR-SWIR}{NIR+SWIR} \quad (2)$$

NDWI was used for winter crops mapping in the thesis because several studies demonstrated its excellent ability for irrigation and drought detection, as well as for

mapping specific crop types, especially winter crops (Mulianga et al., 2015; Hao et al., 2015; C. Zhang, Pattey, et al., 2018; Valero et al., 2021).

- **Green Normalized Difference Vegetation Index** (GNDVI), proposed by Gitelson et al. in 1996, is documented to be very similar to NDVI. The index was developed to evaluate the photosynthetic activity of vegetation. However, GNDVI uses visible green light that resists atmospheric effects instead of visible red light. In addition, the new index has a wider dynamic range and is much more sensitive than NDVI to chlorophyll-a concentration. The expression of GNDVI is displayed below (Gitelson et al., 1996):

$$GNDVI = \frac{NIR-Green}{NIR+Green} \quad (3)$$

For its numerous advantages and outstanding performance, GNDVI is widely applied in vegetation and agriculture research, especially in vegetation cover, agricultural estimation, and crop type classification (Shanahan et al., 2001; Barati et al., 2011; Ustuner et al., 2014; Rahman & Robson, 2016; Marcial-Pablo et al., 2019). Therefore, GNDVI was implemented in LULCCs and winter crop mapping studies.

- **Enhanced Vegetation Index** (EVI), proposed by the MODIS Land Discipline Group, sought to augment the vegetation signal and correct the imprecision of NDVI with improved sensitivity in high-biomass areas by adding several extra spectral bands. The expression is displayed as follows (A. Huete et al., 2002; Matsushita et al., 2007):

$$EVI = \frac{G*(NIR-Red)}{(NIR+C1*Red-C2*Blue+L)} \quad (4)$$

(L value can be adjusted for canopy background)

EVI was initially derived from MODIS satellite data; nevertheless, it has been shown to be effective and compatible with other satellite data. Due to its sensitivity in discriminating vegetation differences and its improved linearity with vegetation in highly vegetated areas while minimizing soil and atmosphere influences (A. Huete et al., 2002; Z. Wang et al., 2003; Z. Jiang et al., 2008), the index is usually applied for crop type mapping and crop phenology detecting (Y. Pan et al., 2012; L. Li et al., 2014; Cao et al., 2015).

- **EVI2** is a two-band VI developed by Jiang et al. in 2008 as a replacement for EVI. Although EVI is highly sensitive to vegetation variations in high-biomass regions, however, the index was designed with a blue band, which means that it cannot be used in a sensor system without a blue channel, such as SPOT-5, AVHRR, and the ASTER instruments. Thus, EVI2 was invented to break through the limit of the sensor system, with three optimal parameters (L, β, and G) appending in the equation of EVI2 to reduce noise and reach the best similarity between EVI and EVI2 (Z. Jiang et al., 2008):

$$EVI2 = 2.5 * \frac{NIR-Red}{NIR+2.4Red+1} \quad (5)$$

The similarity between EVI and EVI2 was validated; EVI2 can produce the same index as EVI without a blue band. It is able to retain the soil–noise adjustment function and maintain improved sensitivity and linearity in high-biomass regions (Z. Jiang et al., 2008). EVI2 has been extensively applied in a variety of research since its invention (J. Liu et al., 2012; Qiu et al., 2015; Zou & Mõttus, 2017). In this thesis, EVI2 was used in LULCCs, knowing that the study was performed with an image of SPOT-5, which was limited by the lack of a blue band (Z. Jiang et al., 2008).

- **SAVI** was developed by Huete in 1988. Although various VIs were developed with the aim of vegetation detection, soil backgrounds continue to be a considerable influence factor on VIs, especially soil brightness. Therefore, SAVI can be considered a transformation of NDVI to minimize soil brightness influences from VIs calculated with visible red and NIR channels by refining or calibrating spectral indices to normalize soil substrate variations. With an adjustment factor (L from 0.5 to 1) that varies depending on vegetation density, the index was found to be effective in eliminating most of the soil-induced variation in vegetation indices (A. R. Huete, 1988):

$$SAVI = \frac{(NIR-Red)}{(NIR+Red+L)}(1+L) \quad (6)$$

As an important step to establish a model that is capable of describing dynamic soil-vegetation systems from remote sensing data (A. R. Huete, 1988), SAVI was commonly used in the agricultural field for specific crop types monitoring, crop growth monitoring, and crop yield forecasting (Gontia & Tiwari, 2011; Z. Li & Chen, 2011; Messina et al., 2020; Nagy et al., 2021). SAVI was also found helpful in

monitoring winter wheat (Yuping et al., 2008; F. Xu et al., 2020) and distinguishing winter crops from spring crops (Palchowdhuri et al., 2018). SAVI was implanted in the study of winter crop mapping.

- **The Modified Soil-Adjusted Vegetation Index** (MSAVI) was proposed by Qi et al. in 1994. MSAVI improved SAVI with a higher vegetation signal-to-soil noise ratio by modifying the *L* factor; it replaces the constant *L* in the SAVI equation with a self-adjustable functional *L* factor, although the *L* factor is not visible in the equation of MSAVI. Thus, MSAVI can increase the dynamic response of the vegetation signal while minimizing the soil background, improving vegetation sensitivity regardless of vegetation amounts. MSAVI is calculated by the following equation:

$$MSAVI = \frac{\left(2*NIR+1-\sqrt{(2*NIR+1)^2-8*(NIR-Red)}\right)}{2} \quad (7)$$

With the lower sensitivity to soil background and temporal variations, MSAVI can be used in the agricultural fields (H. Wang et al., 2006; Samasse et al., 2020; Wyawahare et al., 2020) or even more effectively for winter wheat mapping (Z. Li & Chen, 2011). MSAVI was therefore applied in the study of winter crop mapping.

4.1.2. Methodology of segmentation

This section will introduce two principal processing methods, OBC and pixel-based classification (PBC), to explain the necessity of image segmentation. Then the theory of segmentation and two methods of segmentation performed in our studies (MultiResolution Segmentation (MRS) and Simple Linear Iterative Clustering (SLIC)) will be presented.

4.1.2.1. OBC vs PBC

PBC and OBC are the most common processing methods for image classification; the two methods have always been analyzed and compared between them, especially in LULC studies.

The traditional PBC has always been the most used classification method in remote sensing, particularly for LULC classification (Weih & Riggan, 2010). Just as its name (pixel-based classification) suggests, PBC is the traditional and natural way to classify a single pixel, considering that remote sensing data are composed of a limited number of pixels, which is also the smallest unit of an image. Moreover, only the spectral information of each pixel was considered in the classification (G. Xie & Niculescu, 2022). Therefore, the operation of PBC relies strongly on spectral heterogeneity between pixels, every individual pixel in the area of interest is assigned to one of the predefined classes by the chosen classification algorithm (Weih & Riggan, 2010; G. Xie & Niculescu, 2022).

PBC is widely carried out for LULC studies. Sekertekin et al. (2017) claimed to acquire satisfactory classification results with pixel-based MLC in Zonguldak, Turkey. Van de Voorde et al. (2007) developed three post-classification techniques to improve pixel-based land cover classification using VHR images. Otukei & Blaschke (2010) performed a land cover changes assessment using three PBC methods: DT, MLC, and SVM; the general accuracy achieved exceeded 85% in all cases. Srivastava et al. (2012) investigated LULCCs in the Walnut Creek area in Iowa, USA, by applying three PBC classifiers: ANN, SVM, and MLC on Landsat ETM+ and researched with over 90% accuracy.

Even though many studies show the results of PBC and OBC are not significantly different (Dingle Robertson & King, 2011; Van de Voorde et al., 2004). However, the traditional PBC methods are limited for the pixel topology and it has the defect of not taking into account the spatial, contextual information (e.g., texture, context, geometry, and shape), which usually improves classification accuracy (de Jong et al., 2001). Consequently, PBC methods produce relatively fragmented feature classes (Weih & Riggan, 2010). Furthermore, the speckle effect, also known as “salt-and-pepper noise” (Figure 35), which refers to a common form of image degradation caused by high local spatial heterogeneity between neighboring pixels, may be derived when PBC is performed

on HR images (Van de Voorde et al., 2004; Weih & Riggan, 2010; Kelly et al., 2011). For these reasons, PBC is often less accurate for most thematic studies.

Figure 36 Comparison of the original image and salt-and-pepper-noised image (Kelly et al., 2011)

Consequently, OBC, another classification approach, was introduced in the 1970s as an alternative to the traditional PBC, especially for the classification of medium- to high-spatial resolution data (Y. Gao & Mas, 2008; Whiteside et al., 2011). After that, OBC became highly developed starting in the 1990s, when HR remote sensing data began to rapidly increase, and the existing PBC methods were limited owing to the "salt-and-pepper noise" effect.

Roughly speaking, the OBC approach was developed with the aim of overcoming the limitations of PBC. In OBC methods, the individual to be classified is no longer pixel but an object, which refers to a group of pixels. Pixels are regrouped into homogeneous, continuous, and contiguous objects based on some criterion of homogeneity (spectral and contextual) (Y. Gao & Mas, 2008; Whiteside et al., 2011). In contrast with PBC, OBC considers not only spectral characteristic features but also spatial and contextual characteristic features (e.g., shape, texture, topology, and color), which are the important factors for an accurate classification because the contextual features allow for distinguishing objects of different forms of land cover that share similar spectral information. For example, the crop reaches its mature stage in the cropland, and the shrubs nearby are much easier to be distinguished by their shape feature than by their

spectral properties (Aggarwal et al., 2016). Thus, OBC was first applied in agriculture to identify croplands with clear predefined boundaries.

Compared to PBC—which performs classification directly on the individual pixel—to perform OBC, the image must be divided into regions of similar pixels before classification. This procedure is known as "image segmentation." Once the regions (also known as "segments") are created by adjacent grouping pixels with similar spectral and contextual properties, they are ready to be assigned to a predefined class by the chosen classifier (Van de Voorde et al., 2004).

Previous publications confirm a variety of advantages of OBC; for instance, OBC is able to produce classification with more uniform and meaningful LULC objects (Dingle Robertson & King, 2011), produce more accurate results (Oruc et al., 2004; Whiteside et al., 2011), detect LULCCs with HR satellite images (Niemeyer & Canty, 2003), facilitate meaningful statistic and texture calculation (Benz et al., 2004), and derive better comprehension of a landscape (Thenkabail, 2015).

OBC and PBC were carried out in our studies for different purposes, and the results of these two approaches were also used for comparison. In addition, considering that OBC was used extensively in our studies, image segmentation and the two most commonly used segmentation algorithms must be introduced and presented in the following section.

4.1.2.2. Definition of image segmentation

After calculating VIs, segmentation can be performed in the case of applying OBC methods. Segmentation is one of the essential steps of remote sensing image processing. According to Schiewe (2002), segmentation can be defined as the process of completely partitioning a scene into non-overlapping regions or segments in scene space.

The process of image segmentation has been present in remote sensing for at least two decades (Benz et al., 2004) following the launch of the first EO satellite, Landsat-1. One of the first applications of image segmentation in the remote sensing field was the Extraction and Classification of Homogeneous Objects (ECHO), successfully operated by Kettig and Landgrebe in 1976 (Dey et al., 2010). Afterward, the first success was rapidly

followed by several extensive fundamental studies of image segmentation applied in remote sensing—for example, Haralick & Shapiro (1985), N. R. Pal & Pal (1993), and Spirkovska (1993). In addition, recognition is one of the first generations of operational software production in the 2000s and the most used OBC software today.

In the remote sensing field, segmentation can be considered the preliminary step in OBC, which plays a crucial and fundamental role in the classification results (Schiewe, 2002; Dey et al., 2010; Kotaridis & Lazaridou, 2021). Even though a large variety of image segmentation techniques have been developed over two decades, the objectives and principal processes of all segmentation techniques are relatively similar. The objective of segmentation is to produce homogeneous objects and effectively enhance the accuracy of classification. The segmentation process generally starts with objects that are one pixel in size. Then the adjacent pixels are merged in order to form bigger objects with respect to spatial continuity, certain similarities based on spectral and contextual information, and the scale parameter, which can be defined by the user (Y. Gao et al., 2011). The principle of the process is to minimize the heterogeneities inside the object while maximizing the homogeneities among objects with a clear, spatially accurate, and non-ragged boundary (Haralick & Shapiro, 1985). After all of the pixels in the image have been clustered into regions of a number predefined, the regions or segments are ready to be labeled and transformed into a meaningful objects by classification algorithms (Kotaridis & Lazaridou, 2021).

Various algorithms and methods have been developed to solve the image segmentation problem and improve segmentation performance. Those methods can be categorized into many different classes. The most commonly used methods are threshold, region-based, edge-based, cluster, and others such as Watershed, ANN, and Partial Differential Equation (PDE).

- **Threshold:** This method may require prior knowledge of the study area to select the threshold before processing. In this method, the image is directly divided into regions based on intensity value relative to the threshold given by the user.

- **Region-based:** The method is based on the similarities in the image. It usually begins by seeking similarity in each element in the area of interest. The segments are then created by grouping and merging adjacent elements (e.g., pixels) that share certain homogeneities. Region-based segmentation method has two approaches: region growing (starting with one individual) and region splitting (starting with the entire scene) (Schiewe, 2002). MRS is the most common region-growing-based segmentation method.

- **Edge-based:** This segmentation approach generates the segments through edge detection, which operates with contrast, texture, color, and saturation variations. The process is then pursued by a contour-generating algorithm that is able to produce outlines of segments. Eventually, contour-filling methods produce the segments by transitioning from the outlines to the interior regions (Schiewe, 2002).

- **Cluster:** As with the region-based method, in this method the image is divided into a number of clusters with common characteristics (e.g., color, intensity). Each pixel can find more similarities with other pixels in the same segment than those in distinct segments. The most widely used cluster segmentation method is K-means.

Broadly speaking, segmentation techniques are powerful tools in image processing, and these techniques considerably improve image classification accuracy. Nevertheless, several defects persist in the segmentation process. The main reasons for inadequate performance are over- or under-segmentation, which refer to too many (small) regions and too few (large) segments, respectively. The two problems can occur in the same image at the same time. Over-segmentation can be solved by the following classification step, although it will cause insignificant boundaries and unnecessary computing time costs. On the other hand, under-segmentation might cause the mixed-pixel problem in classification, which means that elements belonging to more than one class are found in the same segment and will be assigned to the same class in the following processing step. Eventually, misclassification, or even a less accurate classification result, may be induced by the under-segmentation problem.

4.1.2.3. Multiresolution segmentation

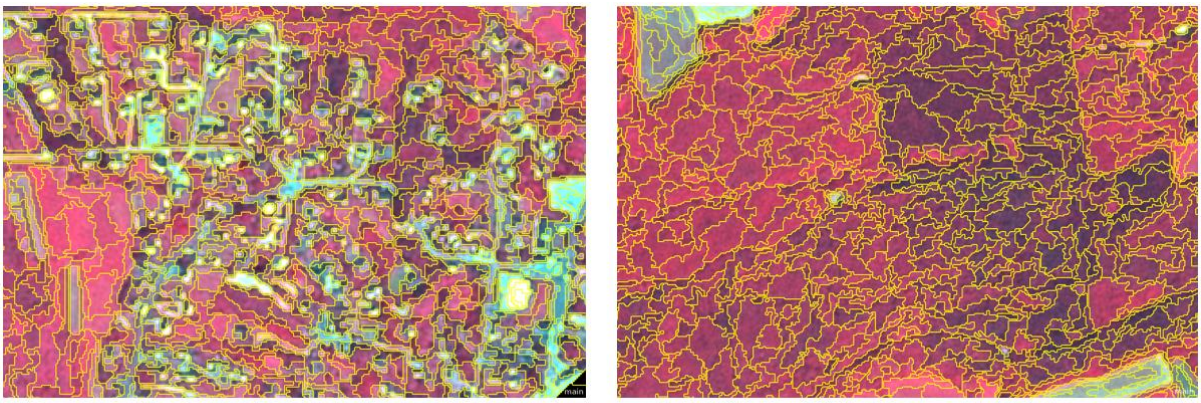

Figure 37 Example of MRS applied on Sentinel-2 image

"Multiresolution" means that the segments can appear simultaneously on different scales in an image to produce highly homogeneous multi-scale image objects (Baatz & Schäpe, 2000). In parallel, MRS (Figure 36) is a relatively complex and user-dependent algorithm; it was proposed by Baatz & Schäpe in 2000 with the purpose of creating universal high-quality object primitives as the first step of the OBC process in the software eCognition for further processing procedures (Baatz & Schäpe, 2000). MRS is also the most commonly used algorithm of region-growing-based segmentation and one of the most efficient segmentation algorithms in the OBC framework (Witharana & Civco, 2014).

Being a classical region growing-based segmentation algorithm, the process of MRS starts with an individual pixel; each pixel is considered an individual segment (so-called "seeds"). After that, each segment seeks to merge their adjacent segments with those possessing similar properties, and pairs of image objects with the smallest increase in the predefined local homogeneity criterion are merged to become more extensive segments (Darwish et al., 2003). Moreover, the merge decision is based on attributes of homogeneous structures of the image objects recently merged in previous steps (Baatz & Schäpe, 2000). Decision heuristics are applied to determine the image objects that will merge at each step. Eventually, the MRS process is complete when the smallest increase of homogeneity exceeds a threshold defined by the user (Darwish et al., 2003).

As a user-dependent algorithm, adjusting parameters is crucial for the MRS process. The merging decision is determined by three principal parameters: scale, shape, and compactness, which are entirely predefined by the user. Additionally, a trial-and-error process usually takes place to reach the optimal parameter. The three main parameters of MRS techniques are:

- **Scale:** This parameter is set to specify the maximum standard deviation of the heterogeneity to manage the amount of spectral fluctuation within objects and the size of their results (G. Xie & Niculescu, 2022). It is usually considered the most critical factor among the three parameters because it is able to control the segment size. A higher-scale parameter value authorizes more merging, thus creating larger segments (Darwish et al., 2003). Additionally, the scale parameter directly affects the following classification step (Smith, 2010; Witharana & Civco, 2014).

- **Shape:** As one of the homogeneity criteria, the shape parameter allows us to define the weight between the object's shape and its spectral color. A higher value gives more weight to the shape and decreases the influence of color homogeneity on object generation (Landmap, n.d.; Rejaur Rahman & Saha, 2008).

- **Compactness:** Another component of the homogeneity criteria defines the weight for representing the compactness of the objects during the segmentation (Landmap, n.d.).

Due to the fact that the parameters are entirely user-defined, a trial-and-error process is usually applied with different combinations of the parameter values so that the user is able to create a hierarchical network of image objects (Rejaur Rahman & Saha, 2008). However, the traditional trial-and-error method can be relatively time-consuming and tedious. Thus, as one of the most used methods of image segmentation, a variety of studies and applications were performed to find the optimal parameters, especially the scale parameter (Drăguț et al., 2010; Nikfar et al., 2012; Cánovas-García & Alonso-Sarría, 2015; Aguilar et al., 2016; Saba et al., 2016), and better performance in LULC classification (Aksoy & Akcay, 2005; Rejaur Rahman & Saha, 2008).

Cánovas-García & Alonso-Sarría (2015) developed a method to optimize the scale parameter in MRS in order to perform land cover mapping in a large and heterogeneous agricultural area, in which intra-object and inter-object measurements are used to evaluate segmentation. The authors discovered that the spectral contrast between objects is larger with the local approach by using uniform spatial units than with the global approach.

Aguilar et al. (2016) focused on finding the optimal parameters (particularly the scale parameter) of the MRS to extract plastic greenhouses from WV-2 multispectral orthoimages. The initial success of plastic greenhouse extraction was achieved with an optimum scale parameter calculated on the local variance of object heterogeneity within a scene. The parameter value was evaluated with Potential Segmentation Error (PSE), Number-of-Segments Ratio (NSR), and Euclidean Distance 2 (ED2).

In another study, Nikfar et al. (2012) also found optimal parameters of the MRS approach by using an efficient genetic algorithm (GA) to replace the traditional trial-and-error methods, which can be very time-consuming.

Rejaur Rahman & Saha (2008) demonstrated the advantage of MRS in LULC classification and compared the results with those of traditional PBC. The results indicated that the OBC with MRS achieved 92% OA (6% higher than PBC) and 90% Kappa (7% higher than PBC). Therefore, MRS appeared to be a suitable image segmentation method for LULC classification.

Kavzoglu & Tonbul (2018) evaluated three segmentation approaches (MRS, SLIC, K-means) by using them on four LULC classes, including artificial surface and vegetation. Overall, MRS achieves the best accuracy not only in segmentation quality but also in classification accuracy.

Because MRS was shown to be well adapted for LULC studies, it was used in the study of LULCC detection on the Crozon Peninsula. The image segmentation was generated on eCognition 9.0 and 10.0.

4.1.2.4. Simple Linear Iterative Clustering Superpixels segmentation

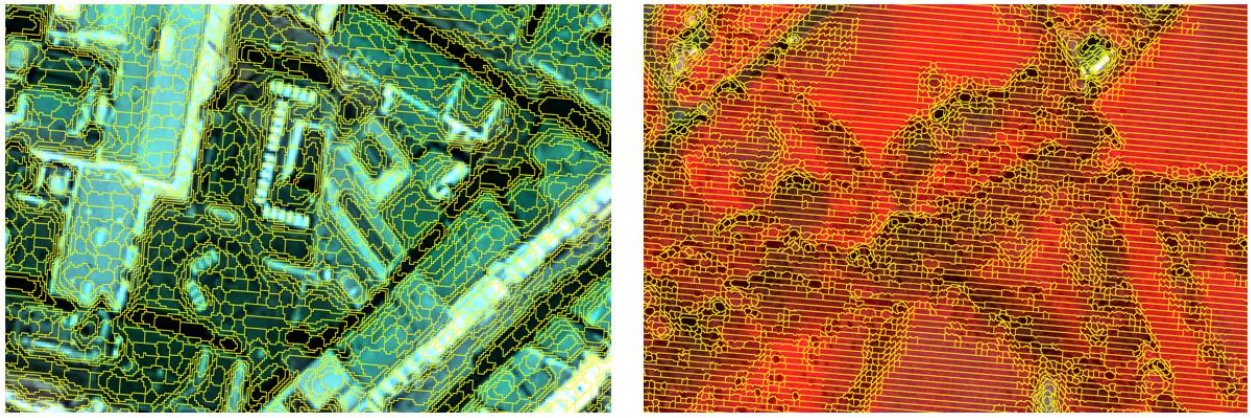

Figure 38 Example of SLIC applied on Pléiades-1 image

The concept of the superpixel was first introduced by Ren & Malik (2003). Superpixels (Figure 37) are the results of clustering pixels carrying common characteristics, which are defined by classical Gestalt theory, including proximity, similarity (e.g., contour, texture, and brightness), and good continuation (Nixon & Aguado, 2020; Ren & Malik, 2003).

Superpixel algorithms refer to segmentation algorithms that can produce the desired number of regular, compact, and meaningful superpixels with low computational overhead (Achanta et al., 2010). For its numerous advantages—such as possessing the perceptual meaning, excellent ability to carry more information than a simple pixel, and providing a convenient image representation—superpixel algorithms have attracted considerable public attention in the computer sciences area in recent years. The main task of superpixel segmentation methods is to reduce the number of pixels, thereby reducing image processing complexity, computing time cost, and capture redundancy.

SLIC, developed by Achanta et al. in 2010, is the most popular superpixel method today (Nixon & Aguado, 2020). SLIC was first introduced as an adaptation of the K-means segmentation technique to generate superpixels. However, in comparison with K-means, SLIC can (1) significantly optimize the distance of calculations by limiting the search space of each cluster center and (2) combine color and spatial proximity to control the size and compactness of the superpixels (Achanta et al., 2012). It is well known for its capability to generate meaningful, nearly uniform sizes that are compact and adhere well to region

boundaries' superpixels by clustering pixels based on their homogeneities and spatial proximity in the image scene.

In SLIC segmentation, local clustering of the pixel is performed in a five-dimension (5D) color and image plane space. Among them, *L*, *a*, and *b* are the pixel color vector generated with the CIELAB color space, which gives a suitable similarity measure for color perception (Nixon & Aguado, 2020), and *x* and *y* are the pixel coordinates (Achanta et al., 2010). Compactness and regularity in the superpixel shapes are enforced using an original distance metric. Moreover, the algorithm can also be flawlessly operated in grayscale images (Achanta et al., 2010).

The process of the SLIC segmentation algorithm starts with a single user-defined parameter that indicates the desired number of superpixels. Then the initial cluster centers are evenly sampled on a regular grid to produce nearly equally sized superpixels. Once the primitive superpixels are formed, the cluster centers are moved to locations corresponding to the lowest gradient position in a 3 x 3 neighborhood to prevent the cluster center from being located on the edge. After that, each pixel is assigned by the nearest cluster center whose search region overlaps its location, which is limited. Afterward, the cluster centers are adjusted to be the mean vector of all pixels in the 5D space, and a residual error between the new and previous cluster center locations is calculated. The last two steps can be repeated iteratively until the error converges (Achanta et al., 2012).

SLIC algorithm is effective in image segmentation processing, simple and practical to manipulate, capable of adhering to image boundaries and of producing superpixels with lower computational cost and memory efficiency, as well as possessing only a single parameter to be determine the desired number of superpixels, SLIC has therefore quickly surpassed the existing superpixel methods (Achanta et al., 2010, 2012).

Furthermore, the superior performance of SLIC has been proved by various studies in different research fields. For example, Crommelinck et al. (2017) investigated the applicability of SLIC to HR unmanned aerial vehicle (UAV) orthoimages; furthermore, its ability to delineate object outlines and showed that SLIC was the most accurate and complete method compared to other segmentation methods. In a study by J. Yin et al. (2022), the SLIC clustering function was modified to adapt the characteristics of

polarimetric statistical measures. The proposed method was validated and shown to significantly improve the segmentation results with the capability to produce better boundary adherence as well as compact, uniform superpixels. In addition, the SLIC segmentation technique is widely applied in vegetation cover classification (G. Xie et al., 2019; Zimudzi et al., 2019; Correa Martins et al., 2021). For instance, Kawamura et al. (2021) demonstrated that SLIC was well suited and useful for different kinds of vegetation and forest segmentation. SLIC can demarcate similar image objects, such as vegetation species, even though they share nearly identical color and texture information. The vegetation classification achieved a very high accuracy by combining SLIC with machine learning (e.g., RF) and deep learning (e.g., CNN) classification algorithms, especially in the urban environment.

For all the above reasons, SLIC was selected to detect vegetation in the city of Brest. The SLIC algorithm was operated in the python language with the scikit library.

4.2. Methodology of image classification

This section presents two crucial image classification approaches—the shallow machine learning classification methods and the recently developed deep learning classification methods—along with their most popular and representative algorithms.

4.2.1. Definition of image classification

Pre-classification processing is the fundamental function of image processing. The classification process is the most critical step in the process and the most complex process that can be affected by various factors (D. Lu & Weng, 2007).

Image classification is a computer science technique that aims to classify and label all elements (e.g., individual pixels, or segments in the case of OBC) within an image into a pre-defined number of classes. During the processing, the classifier chosen by the user automatically assigns a suitable class for each element and turns image objects or meaningless pixels into an interpretable thematic map. Studies of image classification

started in the late 1950s and early 1960s with aircraft data (Cormack, 1971). The interpretation of the first generation of remote sensing data was performed in printed images, and most classification methods were initially developed in the 1970s and 1980s. However, specific classifiers and algorithms have made significant advancements and led to wider applications in more recent decades (Phiri & Morgenroth, 2017), owing to the development of computer software and hardware (Steiner, 1970). In addition, land cover classification has been revolutionized with the introduction of numerical-based pattern recognition algorithms (Steiner, 1970; Thompson & Mikhail, 1976).

Despite making important advances over the decades, accurate classification has always been a challenge in the computer science field because the classification result is easily affected by the complexity of the landscape, the similarity between different categories, the scale of the object to be categorized, and the selection of remote sensing data, training sample and classification system; each decision could be crucial for the result. Thus, studying the user's needs before classification processing is essential. The complete classification process—which involves several steps, including identifying a suitable classification system—selecting training samples, choosing an appropriate classification method, and evaluating accuracy (D. Lu & Weng, 2007), is briefly presented below.

As mentioned in the previous chapter, "remote sensing" refers to gathering information about Earth's surface objects by systems located some distance away; thus, selecting remote sensing systems and data is critical for classification. Selection of the remote sensing data (e.g., airborne vs. spaceborne, RaDAR vs. optical, active vs. passive, different spectral and spatial resolutions) is generally the fundamental and the first encountered difficulty in image classification. Over three decades, various studies have explored the relation of the nature and properties of digital remotely sensed data (e.g., their reaction to the physical, chemical, and biological properties of the Earth's surface) acquired from different instruments and platforms with a data processing algorithm in order to fundamentally enhance classification. Furthermore, the studies demonstrated the importance of the selection of remotely sensed data according to the user's needs, such as the research objectives and the characteristics of the study area, so that the data can be used to produce accurate classification results with maximum effectiveness and

minimum cost (Trotter, 1991; Richards, 1993; Barnsley, 1999; Estes & Loveland, 1999). Selecting a suitable classification system for the user's purpose determines the classification structure; a classification system includes remote sensing data, a classification algorithm, as well as preprocessing and postprocessing methods (D. Lu & Weng, 2007).

Training data selection is necessary for supervised classification methods. The training data is usually presented and collected in three different forms: individual pixels, seeds, and polygons. In addition, the training strategies are affected by the size of the training group, the resolution of the images, and the autocorrelation within each class (D. Chen & Stow, 2002). The selection of training data directly impacts the classification result, especially for HR data and in a highly heterogeneous area. Consequently, the training data should be representative of each class and have a reasonable ratio between different classes (D. Lu & Weng, 2007).

The classification algorithm (also called "the classifier") is the most crucial part of the classification process. Many algorithms have been developed for different uses in recent decades, especially advanced classification algorithms for image classification. In order to choose the optimal classification method, the merits of each method must be considered.

In particular, LULC classification is one of the earliest applications of image classification in the remote sensing field. Early on, a variety of studies have contributed towards developing efficient and effective classification methods for LULC: classification methods for either coarse or fine spatial resolution were developed and summarized for large-scale land cover mapping by Cihlar (2000). Franklin & Wulder (2002) reviewed and assessed large-area land cover classification with general medium spatial resolution and identified the outstanding issues. Phiri & Morgenroth (2017) reviewed the development of land cover classification methods since the launches of a new series of Landsat sensors and advancements in computer science.

Overall, the first generation PBC methods for LULC mapping began to emerge in the 1970s, right after the launch of Landsat-1, with the development of diverse classifiers, such as MLC, K-means, and Iterative Self-Organizing Data Analysis Technique (ISODAT) classifiers (Phiri & Morgenroth, 2017). Afterward, many classification approaches were

proposed after the 1980s, such as the sub-pixel method, knowledge-based method, contextual-based method, OBC, and hybrid approaches in land cover classification (D. Lu & Weng, 2007; Phiri & Morgenroth, 2017). The most commonly applied classification methods can be categorized as follows:

- **PBC:** PBC, which was discussed in the previous section, refers to a direct assignment of a suitable class to each pixel in the image (D. Liu & Xia, 2010). The most commonly used algorithms in PBC are NNs (NN), SVM, and RF.

- **OBC:** Pixels are first regrouped into homogenous image objects using a segmentation algorithm, after which each image object is assigned to one of the predefined classes (D. Liu & Xia, 2010).

- **Sub-pixel classification:** This method evaluates each pixel spectrum as a linear combination of a set of endmember spectra, after which it outputs fraction images with one image for each endmember spectrum (D. Lu & Weng, 2007). The most known sub-pixel classification algorithm is the Fuzzy Classifier.

- **Contextual-based classification:** This method exploits spatial information among neighboring pixels in order to improve the quality of classification results.

- **Knowledge-based classification:** In this method, a priori knowledge and ancillary data are necessary and incorporated into the classification procedure.

- **Hybrid classification:** Also known as the Multiple Classifier System (MCS), hybrid classification refers to a merging of the classification results from more than one classifier to provide the complementary information of the pattern classifiers (Du et al., 2012).

However, there is usually more than one characterization of the classification methods. Classifiers can also be categorized as “supervised” and “unsupervised” methods: *Supervised classification* refers to the classification process with a priori knowledge. The

supervised classification model must be trained in advance with a series of data selected and assigned by the user. *Unsupervised classification*, by contrast, is based solely on the information contained in the input data. Alternatively, as in parametric and non-parametric methods, the parametric classification model is built using a fixed number of parameters; however, the number of parameters is flexible in non-parametric methods. In addition, parametric methods are used to test the means of groups, whereas non-parametric methods test the medians. The most widely used parametric algorithms are MLC, basic linear SVM, and non-parametric algorithms (most notably including NN algorithms such as MLP, or ANN).

Furthermore, numerous studies have shown several classification algorithms from different approaches to be efficient in LULC classification. These include MLC (Hung & Ridd, 2002; Dean & Smith, 2003; Shivakumar & Rajashekararadhya, 2018), RF (Gislason et al., 2006; Rodriguez-Galiano, Chica-Olmo, et al., 2012; Kulkarni & Lowe, 2016), SVM (C. Huang et al., 2002; Kavzoglu & Colkesen, 2009), and ANN (Kavzoglu & Mather, 2003; Kadavi & Lee, 2018). Each algorithm has its limitations and advantages in accordance with the study area or objective. Thus, the choice of classifier is critical for classification results, and diverse classifiers are usually performed simultaneously in a study to make a comparison (M. Pal & Mather, 2003; Otukei & Blaschke, 2010; Talukdar et al., 2020).

The final part of the classification process is post-classification processing, which is able to effectively reduce the noise in the map being classified. For example, the speckle (also called the "salt-and-pepper-effect") induced in PBC methods eliminates spectral confusion, modifies and completes the classification results with auxiliary data, and evaluates the classification results (Section 4.4: Methodology of post-classification).

4.2.2. Shallow machine learning methods

This section will introduce the concept of ML with various related works. Then, two ML methods used in our studies—SVM and RF—will be presented in detail.

4.2.2.1. Definition of machine learning

ML is a subdivision of artificial intelligence and computer science based on the biological learning process; it uses data and algorithms to imitate how humans learn. It optimizes their performance iteratively over time by learning from data (Waske et al., 2009; Lary et al., 2016; IBM, 2022).

For nearly two decades, ML has undergone extensive development as new EO satellites are launched with increasing spatial and temporal resolution and revisiting frequency. Today, ML has become an important topic and one of the hottest research areas in remote sensing data analysis (Waske et al., 2009; Maxwell et al., 2018). Even though ML has an excellent capability to deal with multivariate, non-linear, non-parametric regression or classification problems (Lary et al., 2016), ML techniques are used mainly in image classification tasks to predict a specific phenomenon, create a thematic map of an area of interest, and monitor nature- or human-induced environmental changes and their impacts. Moreover, ML techniques are applied as a supervised classification method. Thus, a training dataset should be generated, and the ML algorithms can make a prediction and improve classification accuracy by learning from training data.

In comparison with traditional classification methods, ML methods provide more effective and efficient classification. The strengths of ML can be attributed to its capability to generate a variety of data with a high degree of dimension and predict highly complex classes. Numerous studies have shown ML to be very effective at classification in different domains. For instance, Waske et al. (2009) discussed the general concept of ML techniques, their critical role in remote sensing data analysis, and the use of their recent advanced developments in supervised classification techniques. Lary et al. (2016) highlighted the capacity of ML for solving problems in geosciences and remote sensing by presenting its ability in multivariate non-linear nonparametric regression solving as well as in multivariate non-linear non-parametric classification dealing. Maxwell et al. (2018) reviewed six relatively mature ML methods—SVM, DTs, boosted DTs, RF, ANN, and *k*-NN—and illustrated their performances in image processing. Meanwhile, another study by Schulz et al. (2018) aimed to explore the potential applications of ML techniques in the remote sensing area, their excellent capacity to solve complex classification problems, and their perspectives. Moreover, many papers have sought to describe ML classification

techniques and their principal algorithms, as well as their recent attempt to improve classification accuracy (Kotsiantis et al., 2006; Akinsola, 2017; Soofi & Awan, 2017; Sen et al., 2020).

ML techniques have been widely used in remote sensing image analysis in recent decades; main applications and related works are summarized below:

Vegetation study is one of the most important application fields of ML classification techniques; ML methods provide highly accurate classification and valuable information for vegetation cover detection, vegetation health monitoring, and mapping of vegetation types or species (Hengl et al., 2018; Tichý et al., 2019; L. Gao et al., 2020; X. Li et al., 2021). Y. Xie et al., (2008) presented an overview of the application of remote sensing imagery and different classification methods, especially the advanced classifiers such as ANN and DT, to perform vegetation cover classification. Mishra & Crews (2014) examined the suitability of integrating hierarchical Object-Based Image Analysis (OBIA) with RF—one of the most widely used ML methods—with a stack of Landsat TM imagery by mapping vegetation morphology types. Moreover, the results indicated a high overall classification accuracy and validated the effectiveness of the ML method applied in mapping vegetation types. Nay et al. (2018) have successfully produced short-term forecasts of vegetation health at high spatial resolution by using global data and an ML approach.

Agriculture is also one of the most important fields where ML techniques are applied; after all, food is a basic need of all human beings. Previous studies have shown that progress in the area of ML helped improve agricultural production by providing essential insights into crops (Liakos et al., 2018; Benos et al., 2021; Meshram et al., 2021). Meshram et al. (2021) demonstrated the efficiency of recent ML techniques by performing ML classification for monitoring agricultural activities in three main agricultural stages: pre-harvest, harvest, and post-harvest. Moreover, they demonstrated the remarkable capability of ML methods to handle non-linear tasks and process highly complex input data. Chlingaryan et al. (2018) indicated that the development of ML techniques application in accurate crop yield prediction and nitrogen status estimation could effectively improve crop forecast, environment state estimation, and decision-making. Savla et al. (2015) implemented several classification algorithms, including ML algorithms (SVM and NN), for studying precision agriculture, such as soybean crop yield.

Urban area classification is one of the most critical and challenging research areas of ML techniques, due to the complex and heterogeneous characteristics of urban areas and of the objects to be classified (e.g., construction, green space, street), which are generally relatively small in scale compared to cropland and forest. Consequently, powerful ML techniques and HR data are critical for urban environmental studies. Examples include urban area mapping, urban green spaces detection, gentrification, or artificialization monitoring (Chan et al., 2001; Donnay et al., 2014; X. X. Yang, 2021). Weng (2012) conducted a study of extracting and mapping impervious surfaces in urban areas by using and evaluating various remote sensing classification approaches, including ML algorithms such as ANN. The author showed that the ANN model outperformed other classification methods in urban area mapping and impervious surface estimation by using HR imagery. Soergel (2010) revealed the excellent performance of ML algorithms (ANN, SVM, DT) in urban environment classification using SAR data. Puissant et al. (2014) proposed a methodology to map and monitor the changes in urban tree spaces using an object-based RF classifier with VHR optical image in Strasbourg, France. The authors found that the RF classifier achieved good accuracy and high robustness of classification results in terms of user's and producer's accuracy.

Biomass estimation and monitoring are also among the typical application fields of ML classification methods. Mapping and quantifying vegetation biomass is crucial for optimizing ecosystem services and effective management. Biomass is usually studied in forest ecosystems—especially in tropical ecosystems (Jachowski et al., 2013; L. Chen et al., 2018; S. M. Ghosh & Behera, 2018). For example, Pham & Brabyn (2017) conducted research on biomass in a mangrove forest. The purpose of their study was to model, map, and analyze the biomass changes in the mangrove forests in the Cangio region of Vietnam between 2000 and 2011 by using SPOT4 and SPOT5 images with OBC ML methods, applying the RF algorithm for modeling and mapping biomass. Their results indicated that the ML classifiers had great potential in biomass modeling with a satisfactory classification accuracy (77.1% for 2000 and 82.9% for 2011). Dang et al. (2019) conducted a study to predict forest aboveground biomass (AGB) in Yok Don National Park in Vietnam using a combination of spectral and texture variables extracted from Sentinel-2 images and the RF algorithm. The authors reported that the RF-based regression algorithm had accurately predicted the forest AGB distribution.

In addition to these common application fields, the application of ML techniques in LULC classifications and change detection has also attracted considerable attention in recent years. Due to increasing social as well as natural pressures—such as rising population, accelerated industrialization and urbanization, climate change, deforestation, and natural disasters—LULC study has become essential to the effective planning and management of natural and man-made resources (Karpatne et al., 2016; Camargo et al., 2019; Talukdar et al., 2020). Moreover, the increasing availability of remote sensing data and improving ML techniques allow real-time accurate LULC mapping and change detection worldwide (Gómez et al., 2016; Karpatne et al., 2016). Therefore, many prior studies have summarized the progress and challenges of ML methods and examined their accuracy in land cover classification; the difficulties encountered have attracted particular attention.

LULC classification for change detection and verification remains challenging for several reasons, such as the heterogeneity in the characteristics of LULCCs. Each classification model must be built and adjusted according to the study area and research object. In addition, LULCCs are often negligible and brief. Otherwise, there are natural phenomenon that take a long time to detect. For detection purposes, the ML model must be trained with available data acquired before and after changes, and must be adjusted in case of dealing with multi-source data when the availability of data is limited (J. S. Deng et al., 2008; Karpatne et al., 2016). Furthermore, previous studies show that the accuracy of the classification can be affected spectrally and spatially by coarse-resolution data (Manandhar et al., 2009; C. Yang et al., 2017). The training data dataset may be challenging to generate due to the difficulty of accessing the ground truth before changes occur or due to the lack of auxiliary data (Karpatne et al., 2016).

Nevertheless, ML is well known for its capability to produce satisfactory classification results even on complex problems. As a result of the emergence and development of ML techniques, and in combination with HR remote sensing datasets, today it is easier to address the computational difficulties associated with LULC classification on a global scale (Gómez et al., 2016; Talukdar et al., 2020). Additionally, the great capability of ML techniques—such as multi-task dealing capacity, multi-instance,

and multi-view learning—provides accurate, cost-effective, and time-saving classification (Karpatne et al., 2016).

Therefore, despite all the limitations of ML application in LULC classification, a number of LULC studies demonstrate the efficiency and effectiveness of ML methods. For example, in order to monitor LULC in a complex mix-used boreal landscape in south-central Sweden, Abdi (2019) utilized four advanced ML non-parametric algorithms—SVM, RF, extreme gradient boosting (Xgboost), and DL—in combination with multitemporal multispectral HR Sentinel-2 data. The results showed that both ML algorithms achieved high accuracy, around 75%, in an extremely complex LULC classification. Due to the complex, heterogeneous mixed landscape, the highly accurate classification of urban land cover remains a challenge. Lu et al., (2010) explored the possibility of improving urban land-cover classification in a highly complex urban–rural landscape with a large surface of impervious area by using MLC algorithms combined with the OBC classification methods and QuickBird imagery. The authors found that such a combination significantly improved urban land cover classification performance. In another study, Rodriguez-Galiano et al. (2012) applied an ML RF classifier on multiseasonal textural features extracted from Landsat TM imagery to perform land cover classification over a complex Mediterranean landscape with numerous different types of LULC, obtaining highly reliable classification results.

Overall, ML classification methods have definitively been shown to provide more accurate classification results particularly with complex multi-resource data in a heterogeneous landscape compared to traditional classification methods (e.g., MLC, distance measure, clustering, logistic regression) (M. Hansen et al., 1996; Carranza-García et al., 2019; Talukdar et al., 2020). Some studies have compared different ML techniques in an effort to determine the best technique for LULC classification, considering that the most suitable classifier may vary depending on the research area and objectives (D. Lu, Mausel, Brondízio, et al., 2004). Thanh Noi & Kappas (2018) examined and evaluated the performance of three ML non-parametric classifiers—RF, *k*-NN and SVM—in LULC classification In Vietnam's Red River Delta using Sentinel-2 images. Their results showed that both classifiers achieved high overall accuracies ranging from 90% to 95%; however, SVM outperformed RF and *k*-NN because it was able to generate fine classification results

with a relatively small volume of training data. Jamali (2019) conducted a study to evaluate eight ML algorithms—RF, DT, MLP, Non-Nested Generalized Exemplars (NN ge), Simple Logistic, DTNB, J48, and Lazy IBK—in LULC classification on Iran's northern coast. The classification results obtained were evaluated based on several accuracy indicators; NN ge achieved the highest accuracy score in both accuracy indicators, followed by Lazy IBK, RF and MLP, which also showed excellent potential for LULC classification. Keshtkar et al. (2017) aimed to compare three ML algorithms—RF, DT and SVM—in land cover classification in Thuringia in Germany, a highly heterogeneous area. Afterward, land cover changes detected from 1990 to 2010 were generated using Landsat data. The study showed that the SVM OBC algorithm obtained the most accurate classification results with 93.54% of OA; the PBC RF and SVM classifiers had also similar accuracy indices (90%).

Even though numerous ML algorithms have been rapidly developed for different purposes in recent years, some well-known, well-developed, and frequently used ML algorithms are still worth noting, such as MLC, SVM, RF, ANN, *k*-NN, and DT. Among these, SVM, RF were applied in our studies; thus, these ML classifications methods will be presented in the following section. Moreover, the DL networks and their related algorithms will be presented in section 4.2.3.

4.2.2.2. Support vector machine classification

SVM, is one of the most popular and robust non-parametric statistical ML techniques due to its ability to generate good classification results from a small training dataset.

The promising development was first proposed by Cortes & Vapnik in 1995. This theoretically superior ML algorithm based on statistical learning theory (C. Huang et al., 2002) have been applied to the remote sensing classification problem since the early 2000s (M. Pal & Mather, 2005).

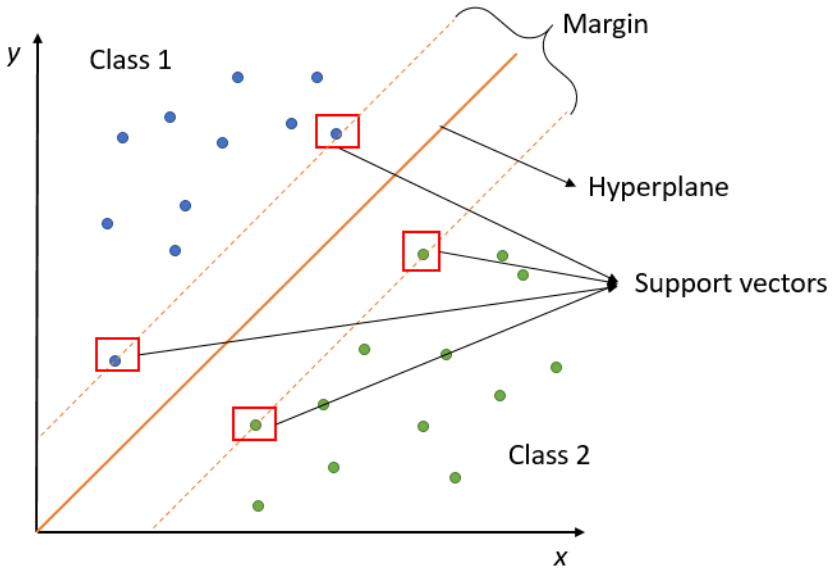

Figure 39 Theoretical SVM model

Initially, the SVM model was designed for solving the linear binary problem with two principal factors: support vector and hyperplane (Figure 38). The technique is focused on the training dataset; support vectors are the closest samples to the optimal boundary (also called the "hyperplane"), which is a single boundary that separates the samples from two different classes of datasets in a multi-dimensional space (C. Huang et al., 2002).

Thus, the algorithm aims to generate the optimal hyperplanes that will separate the classes with the fewest possible errors, thereby significantly minimizing the confusion between classes and maximizing the margin between support vectors of two classes from the samples closest to the hyperplane (C. Huang et al., 2002). However, the theoretical margin can only be applied in the separable dataset, and the soft margin is usually required for non-separable samples, which means relaxing the requirement that all training vectors must lie on the same side of the optimal hyperplane in a given class (Gualtieri & Cromp, 1999). Moreover, a user-defined *c*-parameter, the penalty value of misclassification errors, can highly impact the selection of a support vector in the case of a soft margin applied. In general, a low *c* value allows more misclassification. In contrast, higher *c* values mean more complex decision boundary and less generalization, and an overweight *c* value might cause overfitting problems and generalization errors (Cortes & Vapnik, 1995; Foody & Mathur, 2004; C. Huang et al., 2002; Maxwell et al., 2018).

In addition, another critical parameter in the SVM algorithm is γ, which is used to determine the extent to which the influence of a single training example reaches. Hence, a low value of γ will consider samples at great distances for finding the optimal hyperplane. Therefore, more samples will be considered.

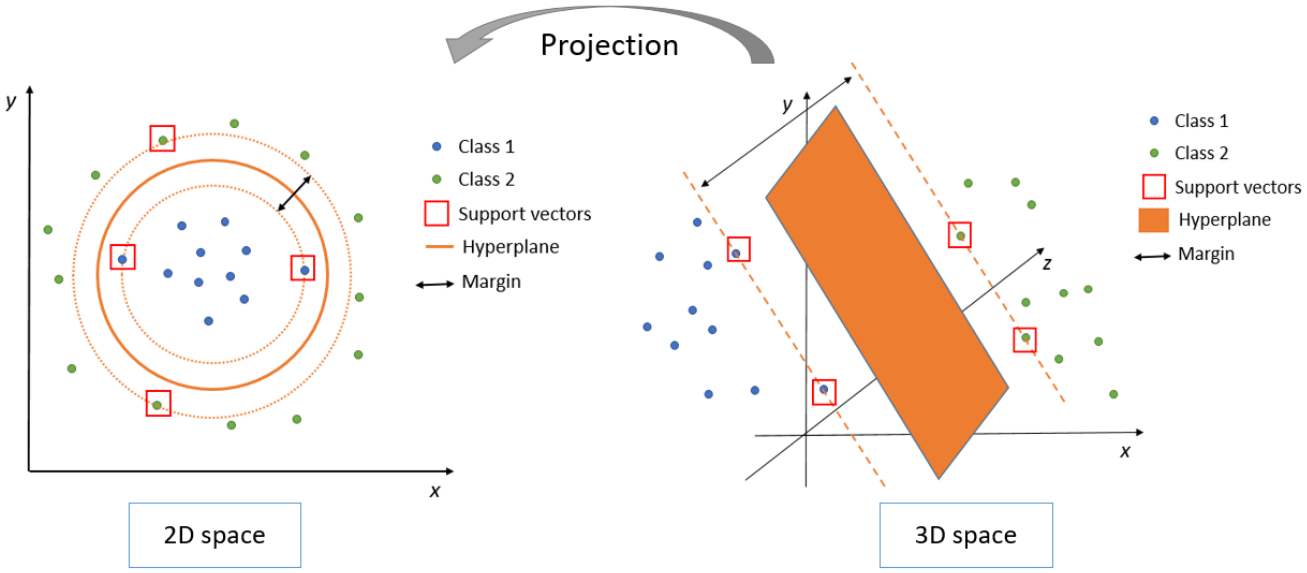

Figure 40 SVM non-linear model

The traditional SVM model was originally developed to solve the linear problem. Thus, in the theoretical model, samples belonging to the same class usually lie on the same sides of the hyperplane (Gualtieri & Cromp, 1999). However, the ideal case occurs rarely, the samples are frequently non-separable, and a misclassification problem might result. Consequently, a non-linear surface is built for solving a non-linear problem, assuming that a higher dimension might exist. As shown in Figure 39, the input is first projected into higher dimensional feature space, and then an optimal hyperplane is generated in the same space afterward; this projection to the higher dimensionality is known as kernel function K. The choice of the kernel has a critical impact on the applicability of SVMs (Mountrakis et al., 2011). Many user-defined kernels are developed since, for example, polynomial and radial kernel functions are tested for land cover classification in Kavzoglu & Colkesen (2009).

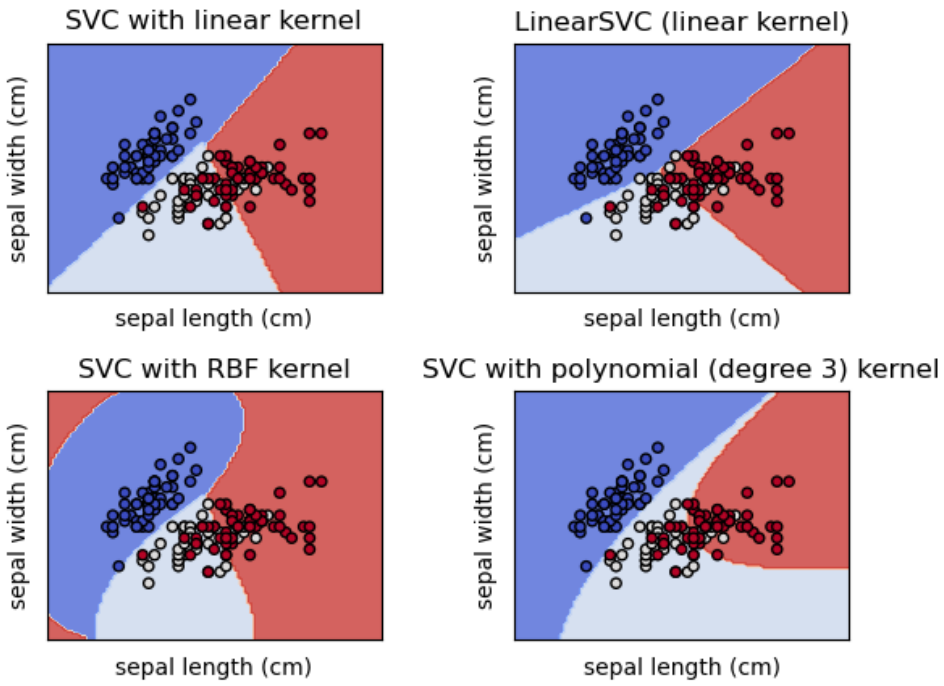

Figure 41 Four most frequently used kernel functions of Support Vector Classification (SVC)

The most used kernel functions are polynomial, sigmoid, linear, and Gaussian kernel Radial Basis Function (RBF) (Figure 40) (Maxwell et al., 2018), which are described below:

- **Sigmoid:** Usually used in the perceptron model of the NN as an activation function for artificial neurons.

- **RBF:** The kernel can be applied when no prior knowledge provides; alternatively, in addition, the radial basis function is developed to improve the kernel.

- **Linear:** This kernel is only considered when the data is linearly separable, which is helpful for dealing with a large number of features.

- **Polynomial:** Fundamentally, this kernel represents the linear kernel in a more generalized way.

The SVM algorithm was initially developed as a binary classifier; in other words, it was designed only to separate two groups, but not to handle multi-class classification. However, because multiclass problems frequently appear in real-case applications, Gualtieri & Cromp (1999) proposed two strategies for converting a binary classifier into *N* classes classifiers:

- **One-against-all:** *N* binary classifiers are created, and each classifier is trained to identify the samples of a class from the rest. The pixel is categorized as the class for which the largest decision value was determined (Foody & Mathur, 2004).

- **One-against-one:** The complex multiclass classification problem is broken down into the binary problem: *N* (*N*-1)/2 binary classifiers are applied to each pair of classes, and each pixel is labeled as the most commonly computed class (Foody & Mathur, 2004).

However, previous studies have also indicated that multi-class classification may be computationally exhaustive, and that the processing time increases with the number of classes (Cortes & Vapnik, 1995).

Various studies report that the SVM classifier has great stability and can usually achieve higher accuracy and training speed than other classification methods (C. Huang et al., 2002; M. Pal & Mather, 2005; Thanh Noi & Kappas, 2018). Additionally, it can generate highly accurate results with high-dimensional data and limited training datasets.

Especially for the LULC classification problem, SVM has been shown to be a suitable and efficient classifier in various study areas with different types of data (Lizarazo, 2008; M. Pal, 2008; Gong et al., 2013; Rodriguez-Galiano & Chica-Rivas, 2014; Thanh Noi & Kappas, 2018). For example, Deilmai et al. (2014) demonstrated that SVM outperformed MLC in a mixed-use landscape including forest, oil palm, rubber, and urban area and indicated the effectiveness of SVM for land cover classification. Shao & Lunetta (2012) used the SVM classification method in MODIS time-series data for land-cover characterization of the Albemarle-Pamlico Estuary System in the USA. The results indicated that SVM provided good classification accuracy while having better behavior in generalization capability than two other classifiers, namely MLP and classification and

regression trees (CART), especially with a small training dataset. He et al. (2005) used a multi-class SVM classifier for land cover classification with multi-source data, including Landsat TM images and auxiliary data. The experiment showed that SVM was capable of generating accurate land cover classification and had the potential to achieve higher accuracy with multi-source data.

Traditionally, SVM is considered and applied as a typical PBC in previously cited research. However, we have found that the SVM algorithm also has excellent performance for producing satisfactory results as an object-based classifier (Tzotsos & Argialas, 2008; H. Li et al., 2010; Devadas et al., 2012; X. Niu & Ban, 2013; Q. Wu et al., 2017).

4.2.2.3. Random forest classification

RF was first proposed by Ho in 1995 to overcome the DT classifier limitation, which is the loss of classification accuracy when processing complex data. Afterward, the idea of RF was extended by Breiman (2001), who combined it with bootstrap aggregating (bagging) theory.

RF is a non-parametric classification method that is one of the most widely known and used classifiers in the remote sensing field over the past two decades due to its efficiency, effectiveness, high processing speed, and ability to handle data of high dimensionality and multi-collinearity. In addition, it can generate accurate classifications or regression results and survival analyses in both supervised and unsupervised learning (Rodriguez-Galiano, Ghimire et al., 2012, p. 201; Belgiu & Drăguţ, 2016).

Although previous simple classifiers (e.g., SVM, MLC, and CART) are capable of generating excellent results, they reach their limits when they encounter the complex interplay between factors such as the complexity of study area, scale, and aggregation (Marceau et al., 1994). Thus, ensemble learning algorithms based on a number of individual identical classifiers—or different classifiers trained with bagging or boosting techniques—have been developed to enhance classification accuracy (Gislason et al., 2006; Belgiu & Drăguţ, 2016).

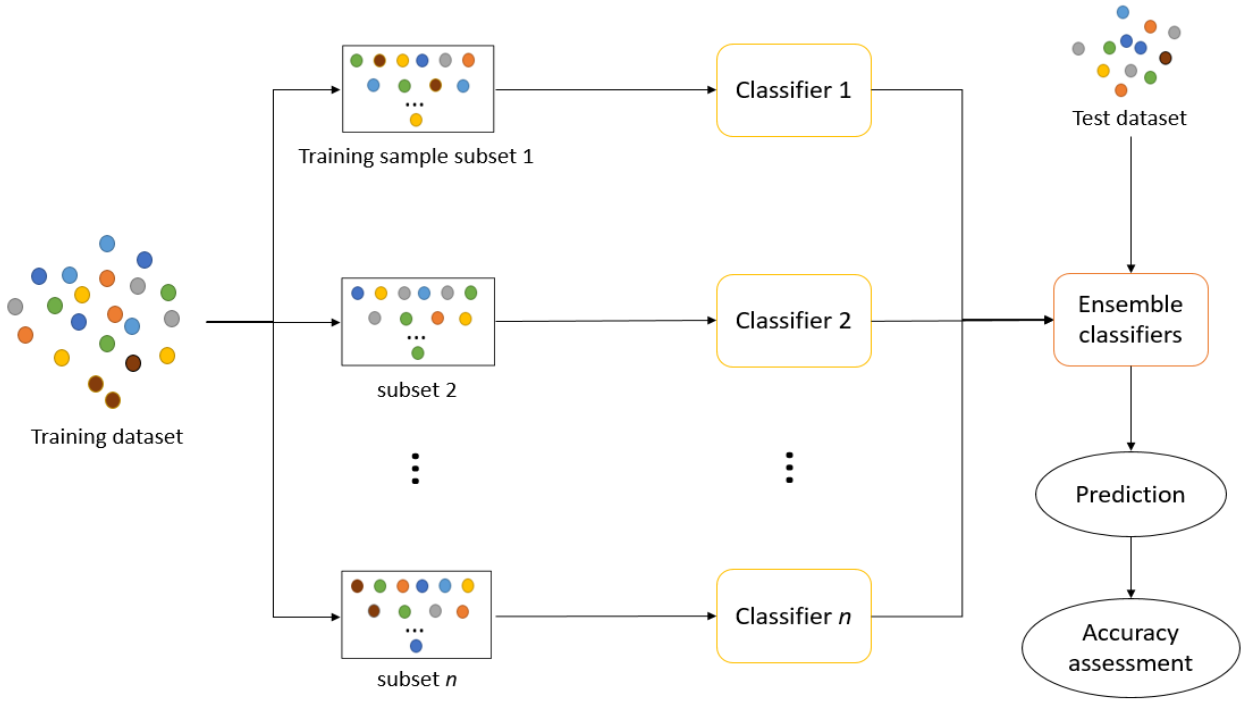

Figure 42 Bagging theory model

Among the various ensemble learning algorithms, the RF classification algorithm employs the technique of bootstrap aggregating, also known as "bagging" (Figure 41). The principle of the bagging technique is to decrease the variance of the model without increasing bias. First, an ensemble of *n* classifiers (ordinarily identical to the number of features in the training dataset) is created. Then, each classifier is trained on a random subset of the complete training datasets. Thus, some of the training datasets can be selected and used several times (so-called "in-bag" samples), whereas some others have never been used ("out-of-bag" samples). The out-of-bag data can be used as test data for evaluating the bagging model (Gislason et al., 2006).

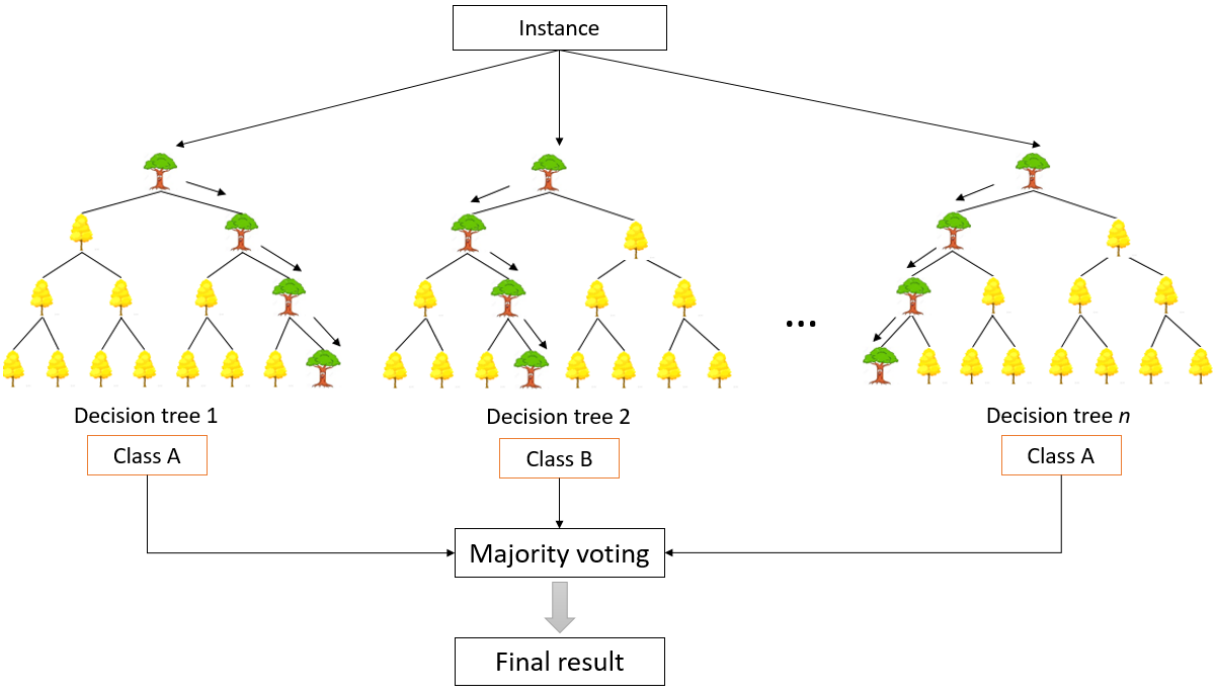

Figure 43 RF model

As shown in Figure 42, the RF algorithm produces an ensemble of *n* tree-like predictors with high variance and low bias to generate a single final prediction (Breiman, 2001). By using a randomly selected subset of the training dataset and variables, for each instance or sample in the subset, each tree in the forest casts a vote independently for the most popular class. The final prediction is then determined by the majority of the vote of all decision trees in the forest (Breiman, 2001; Belgiu & Drăguţ, 2016). This technique can effectively protect the classifiers from variants by minimizing the correlation between the classifiers in an ensemble (Gislason et al., 2006).

In addition, two user-defined parameters are set to train the model: the number of decision trees in the forest (*Ntree*) and the number of variables to be randomly selected at each split when growing the tree (*Mtry*) (Díaz-Uriarte & Alvarez de Andrés, 2006; Genuer et al., 2010; Stumpf & Kerle, 2011; Millard & Richardson, 2015). The *Ntree* value can often be extensive, considering that RF algorithms do not have an overfitting problem. However, some studies suggest that the tree's number *N* has no influence on classification results (Du et al., 2015). On the other hand, *Mtry* is generally set to the square root of the number of input samples (Gislason et al., 2006).

The superiorities of the RF classification algorithm have been enumerated in previous literature. For instance, RF is able to combine high classification accuracy with

great efficiency and can process high dimensional data with low computational cost, low sensitivity to noise, small training sample sizes (Rodriguez-Galiano et al., 2012), and few overtraining or overfitting issues (Gislason et al., 2006). Therefore, RF, which is considered an essential classifier for multi-source classification, has been shown to make significant progress in land cover classification by significantly improving prediction accuracy (Cutler et al., 2012; Ghimire et al., 2012; Rodriguez-Galiano, Ghimire et al., 2012; Kulkarni & Lowe, 2016).

In the early years, RF was usually applied in classification as a PBC method (Evans & Cushman, 2009; Ghimire et al., 2010; Senf et al., 2012; Grinand et al., 2013; Vanselow & Samimi, 2014). However, its applications in OBC have become more and more common, and the technique was demonstrated to be effective and useful for improving accuracy by combining contextual factors (Schroff et al., 2008; Duro et al., 2012; Stefanski et al., 2013; Vogels et al., 2017; Dornik et al., 2018).

Consequently, the RF technique has been successfully used in various research fields with a different types of data, such as LULC and crop mapping. For example, Evans & Cushman (2009) performed a prediction of conifer species with Landsat ETM+7 data. Loosvelt et al. (2012) presented a methodology based on RF to estimate uncertainty with SAR images. C. Deng & Wu (2013) generated an estimation of urban impervious surfaces by using a single-date MODIS image. Räsänen et al. (2013) mapped boreal forest habitat with WV-2 satellite imagery, a LiDAR DEM, and a canopy height model (CHM). Belgiu & Dr Guţ (2014) extracted buildings from VHR imagery of QuickBird and WV-2 with the RF technique. Tatsumi et al. (2015) accomplished crop classification with Landsat 7 ETM+ time series. H. Wang et al. (2015) detected forest health conditions with IKONOS imagery. Vogels et al. (2017) mapped agriculture cropland using black-and-white aerial photography. Dornik et al. (2018) classified soil types using the SPOT DEM and a Landsat-8 satellite image with an ML RF classifier.

Moreover, the RF classifier is widely used in LULC classification for its capability to make accurate mapping of complex LULC categories (Senf et al., 2012; Colditz, 2015; Tsutsumida & Comber, 2015; Kulkarni & Lowe, 2016; Phiri et al., 2018). For instance,

Ghimire et al. (2012) proposed a study of land cover classification in a complex landscape in Cape Cod, Massachusetts, USA using ensemble learning algorithms and a

classification tree. The ensemble learning algorithms (e.g., RF) were shown to provide the highest classification accuracy, especially for heterogeneous areas on a small scale accompanied by seasonal variation.

Rodriguez-Galiano & Chica-Rivas (2014) operated a land cover classification of a heterogeneous area with 14 categories by incorporating a suite of multitemporal Landsat images and digital terrain model (DTM) variables and RF algorithm. Results showed the superiority of RF over traditional single classifiers such as DT. In addition, RF not only provided a very high classification accuracy (0.92 in kappa), successfully generated and classified the most heterogeneous categories (e.g., shrublands) with 30% better accuracy, but it also ran efficiently on high-dimensional data and was able to more clearly differentiate between the different categories.

By contrast, traditional classification trees suffered from data overfitting. Stefanski et al. (2013) developed a strategy for a semi-automatic optimization of OBC of Multitemporal data using the RF technique and the SupePrpixel Contour (SPC) segmentation algorithm. To find the best parameter combination of SPC, various combinations were tested on land cover classification using multitemporal RapidEye and SPOT-5 data. Eventually, the best parameter was found based on the cross-validation-like *out-of-bag* error provided by RF.

4.2.3. Deep learning methods

4.2.3.1. Definition of deep learning

As part of a broader family of ML, deep structured learning, known as "deep learning" (DL) or "hierarchical learning," first emerged in 2006 with the study of NNs by Hinton & Salakhutdinov (2006). Thereafter, between 2006 and 2012, the first generation of simple DL models was developed, including AutoEncoder (AE) (Hinton & Salakhutdinov, 2006), deep belief networks (DBNs) (Hinton, 2009), and Stacked Autoencoder (SAE) (Vincent et al., 2010). Until recent years, DL has been developed at a surprising speed, and has already become a powerful tool in many application fields,

although it remains a highly active research area for science and industry (X. X. Zhu et al., 2017).

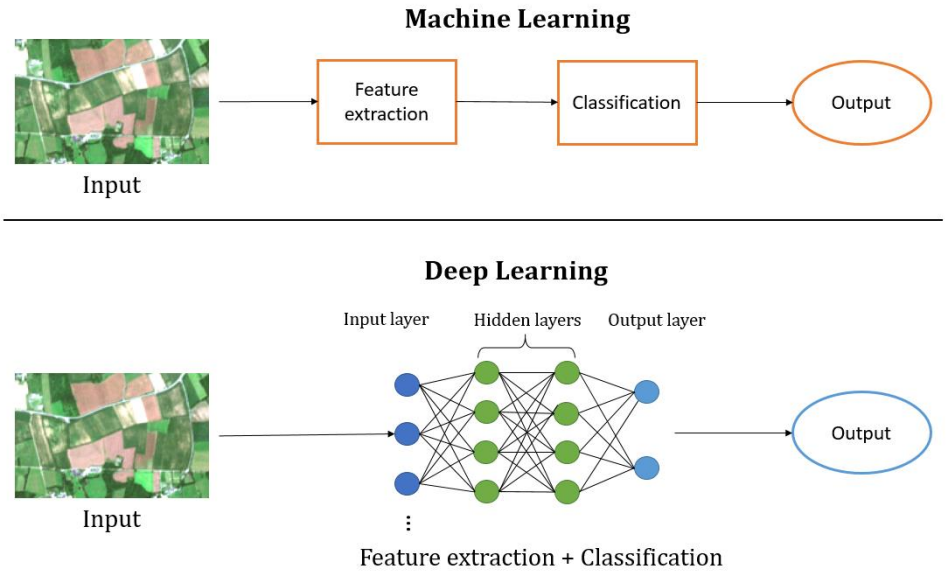

Figure 44 Machine learning and deep learning in visual data analysis

ML algorithms (Figure 43), also known as "shallow-structured architectures," are generally composed one or two of non-linear feature transformation, such as SVM and RF presented in previous sections. ML methods are widely recognized for their capability and effectiveness of solving simple or well-constrained problems; however, they are usually limited by the modeling and representational power, which is their main barrier to accomplishing more difficult tasks (L. Deng & Yu, 2014). Meanwhile, the development of technologies, including equipment such as Graphics Processing Unit (GPU), encourages the birth of a more advanced technique that is able to exploit complex, non-linear compositional functions (L. Deng & Yu, 2014).

Consequently, DL was born in the ANN research, which refers to the use of deep architecture, a multiple-layer network for signal and information processing (Figure 43). Inspired by neuron systems and functions of the human brain, the deep structure is composed of numerous artificial neurons, each of which can receive and process information, and then send it to the next neuron—just as a biological neuron deals with electrical impulse.

Although DL has many definitions, roughly speaking, it can be defined as "a class of machine learning techniques that exploit multiple layers (usually but not necessarily with

more than two hidden layers) of non-linear information processing for supervised or unsupervised complex feature extraction and transformation, and for pattern analysis and classification." (L. Deng & Yu, 2014; X. X. Zhu et al., 2017). Moreover, Deng & Yu also categorized most of the related researches into three major classes by application of the architectures: deep networks for unsupervised or generative learning, deep networks for supervised learning, and hybrid deep networks. Given its basis of imitating human information processing mechanism, visual data processing is one of the most important DL research areas.

DL methods, capable of learning complex representations from data and significantly enhancing classification accuracy, have recently gained ground in the ML community (Karpatne et al., 2016). Furthermore, as a subset of ML, the introduction of DL has become a growing trend that is considered a breakthrough and a robust solution in the remote sensing field (Carranza-García et al., 2019), where DL has experienced an exponential increase, particularly since 2014 (X. X. Zhu et al., 2017).

Meanwhile, remotely sensed image processing also represents a new challenge for DL (Zhu et al., 2017) for several reasons: (1) the data are usually multi-source and multi-modal, and the fusion of different types of data is commonly applied in the classification problem; (2) the data are geolocated and geodetic measurements; (3) satellite revisiting times are considerably shortened, which yields an increased production rate of remote sensing data and indicates that time-series processing is now practicable; and (4) large data volumes are typical on a global scale.

Consequently, various DL algorithms are designed and/or employed to overcome these difficulties and improve the processing procedure and/or result. The algorithms can be categorized according to their applications. For example, two main categories are widely applied for visual data processing:

- **AE models** (e.g., AE (Cheng et al., 2020), sparse autoencoder (Ng, 2011), restricted Boltzmann machine (Fischer & Igel, 2012) and DBNs (Hinton, 2009)) constitute a type of feedforward ANN for unsupervised learning. These models were specifically

designed for representation learning and trained to ignore unnecessary noise to perform dimensionality reduction.

- **Convolutional NNs** (CNNs) (e.g., AlexNet (Krizhevsky et al., 2012), Visual Geometry Group (VGG) Networks (Sengupta et al., 2019), ReST-Net (B. Li et al., 2018), Fully Convolutional Network (FCN) (J. Long et al., 2015)), constitute supervised deep NNs with the filters involved to perform convolutions in the image domain. CNNs have demonstrated their ability to extract mid- and high-level abstract features from raw images by combining convolutional and pooling layers, and have shown efficiency in large-scale recognition, object detection, and semantic segmentation (X. X. Zhu et al., 2017).

With such advanced deep architectures, DL is widely applied in remote sensing with various remotely sensed data types. For instance, hyperspectral imagery—a specific type of optical imagery characterized by hundreds of narrow spectral bands—allows us to identify a better characterization and exploitation of the Earth's surface. However, the difficulty of processing is accordingly increased, and hyperspectral image analysis has always been an active research area in image processing and classification. As a practical feature extraction approach, DL techniques have brought revolutionary advancement in this field (S. Li et al., 2019).

The most familiar deep architectures used for hyperspectral image processing are SAEs (Zabalza et al., 2016), DBNs, supervised CNNs (Goodfellow et al., 2016; Lee & Kwon, 2016), RNNs (Mou et al., 2017; Y. Liu et al., 2018), and Generative Adversarial Networks (GANs) (Goodfellow et al., 2020; Zhong et al., 2020). As presented in Chapter 3, SAR data has become increasingly popular, particularly after the launch of the Sentinel-1 C-band SAR satellite of the ESA's Copernicus Programme. Moreover, the advent of DL methods has revealed increased potential for SAR data application. Examples include Automatic Target Recognition (ATR) with mostly CNN architectures (S. Chen & Wang, 2014; Wilmanski et al., 2016; Pei et al., 2018), terrain surface classification using polarimetric SAR (PolSAR) with AE models (H. Xie et al., 2014; Hou et al., 2016; L. Zhang, Ma, et al., 2016), CNNs (Y. Zhou et al., 2016; Y. Wang et al., 2018; L. Wang et al., 2018), and parameter inversion and de-speckling with CNN models as well (Chierchia et al., 2017; P. Wang et al.,

2017; T. Song et al., 2018; S. Niu et al., 2020). Ultimately, one of the most significant contributions of DL is to bring significantly enhanced LULC classification and object detection with optical imagery, especially with the new generation of VHR optical images. Even though a great number of ML algorithms were already developed for this purpose, and they have achieved excellent performance before the arrival of DL, some limitations yet remain. Therefore, it is increasingly common to use DL methods by combining them with HR images for LULC classification (L. Ma et al., 2019).

First, deep structures show great achievements in image representation, considering that hierarchical structures can provide high-level spatial information (H. Liang & Li, 2016; P. Li et al., 2018). Thus, the earliest studies of LULC classification revolve around simple feature representation rather than the final classification (Karalas et al., 2015; Romero et al., 2016; L. Ma et al., 2019). Then, CNNs have attracted remarkable attention and have become the most commonly used DL algorithms in land cover classification. Furthermore, CNN models are most often used with HR images in order to achieve significant breakthroughs (L. Ma et al., 2019).

Classical CNNs were first widely applied (Al-Najjar et al., 2019; Y. Chen et al., 2019; Mazzia et al., 2020; Memon et al., 2021). For instance, Castelluccio et al. (2015) have generated LULC classification tasks by using two pretrained architectures, CaffeNet and GoogleNet, adapted by two distinct datasets. Kussul et al. (2017) first attempted to apply two different CNN architectures (1-D with spectral convolution and 2-D with spatial convolution) to the fusion data of multitemporal and multisensor satellites (Landsat-8 and Sentinel-1A) for large-scale classification of land cover and crop types. The ensemble of 1-D and 2-D CNNs outperformed the other classifiers used to compare with CNNs (e.g., RF, MLP) with better accuracy and better discrimination of summer crops. In the research of Carranza-García et al. (2019), a general 2-D CNN model was applied to LULC classification with a fixed architecture and standard parametrization trained by a patch-based approach and using multi-source satellite data (SAR and hyperspectral). The results showed that the CNN models considerably improved LULC classification in both accuracy indicators.

Furthermore, CNN models have been improved and performed for specific conditions (C. Zhang et al., 2019b; K. Zhou et al., 2019; R. Fan et al., 2020; Seydi et al., 2020).

For instance, Luus et al. (2015) proposed a multi-scale input strategy for multi-view DL applied in supervised multispectral land use classification. The results indicated that a single deep CNN, trained simultaneously with multi-scale views, could significantly outperform multiple single-scale views. Gaetano et al. (2018) introduced MultiResoLCC, a new two-branch CNN architecture, to jointly use panchromatic and multispectral imagery for a direct classification without any pre-processing procedure. This novel end-to-end network extracted features from panchromatic and multispectral images at their original spatial resolution. The features from different sources are combined to perform direct land cover classification at the finest resolution. CNNs are also developed to overcome the usual limitations encountered in LULC classification, such as the large and complex volumes of training data required for DL model training. Thus, some enhancements are developed to accelerate the training dataset creation (Shin et al., 2016; Lyu et al., 2018) or to use small training datasets to achieve high classification accuracy (B. Pan et al., 2017).

Overall, CNNs are the most commonly used DL algorithms in LULC classification, although other deep architectures are occasionally used as well. For example, Y. Chen et al. (2015) introduced a new feature extraction and image classification framework based on DBN for hyperspectral image analysis. Their proposed framework—which combines PCA, hierarchical learning-based feature extraction, and logistic regression—obtained satisfactory classification results, even when compared to other well-known methods. B. Liu et al. (2018) performed spectral–spatial classification of land cover with a novel RNN model using hyperspectral data. To correctly label each pixel, an RNN model with five layers was constructed and fed with the information of the center pixel and the neighborhood pixels. The authors demonstrated that RNN has effectively improved the accuracy of hyperspectral image classification by modeling the spatial neighborhood relation. Jozdani et al. (2019) compared different classifiers of shallow or deep architecture for urban LULC classification using GEOBIA approach with two VHR satellite images. The classification methods used in this work included five DL methods (i.e., MLP, regular AE, SAE, AE, CNN) and five classical shallow ML methods (i.e., RF, Bagging Trees (BT), GB, Extreme GB and SVM). The authors found that the deep structure MLP algorithm obtained the most accurate classification result. However, neither unsupervised

pretrained AE models nor the integration of CNN and GEOBIA produced any improvement in classification accuracy.

Two standard DL models—MLP and CNNs—were applied in the studies on detecting vegetation in the city of Brest and mapping LULCCs in the Crozon Peninsula, respectively.

4.2.3.2. MLP deep architecture

The first concept of perceptron was developed by Rosenblatt in the late 1950s, becoming the first model of a NN. The original simple perceptron consists of a superficial layer and a simple node that receives weighted input and therefore addressed binary linear separable data (Atkinson & Tatnall, 1997). Due to the multiple layers, MLP is a more sophisticated version of the perceptron that can resolve the non-linear problem of regression and supervised classification with inseparable datasets (Murtagh, 1991).

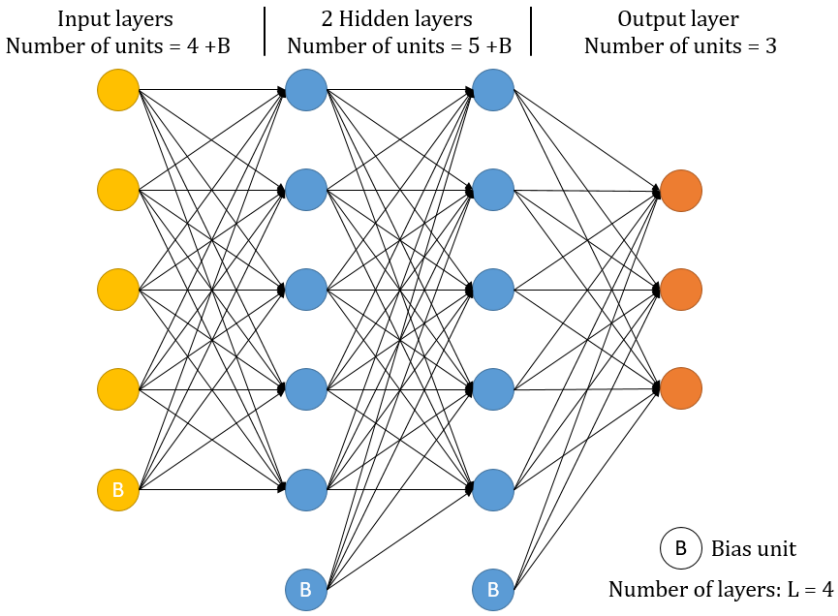

Figure 45 Example of an MLP model with two hidden layers

A MLP model is characterized by its architecture, such as the number of layers and the number of neurons in each layer, as well as the activation methods used at various neurons (Murtagh, 1991). The most common network is a feedforward network with 3

(or >3) layers, as shown in Figure 44. The first layer is always the input layer, which receives training data in the form of a vector; it is followed by at least one hidden layer. Ultimately, the model is completed with an output layer that presents the output data (Atkinson & Tatnall, 1997). As a fully connected algorithm, all nodes at one level have links to all nodes at another level (called "interconnected nodes"), and each node is designed to process the weight it receives from other nodes of the previous layer (Atkinson & Tatnall, 1997). In addition, the arrangement of the number of hidden layers and the number of nodes (also called "units") can vary according to the user's needs. Although more nodes generally mean better sensitivity too many can also cause an overfitting problem (Murtagh, 1991).

Since the late 1980s, many studies have attested to the performance of MLP (Hecht-Nielsen et al., 1987; Lippmann, 1987; Hornik et al., 1989; Lapedes & Farber, 1989; Chester, 1990), although its performance relies highly on training method, suitable representative training dataset, and optimal network parameter adjustment to reduce overall error.

The training method plays a crucial role in MLPs' deep structure, as MLPs have the ability to learn through training (Gardner & Dorling, 1998), which is the process of determining the value of individual weights in order to accurately resolve the relationship that the network is modeling (Gardner & Dorling, 1998). The most commonly used training method is backpropagation.

The backpropagation algorithm, introduced in 1986 by Rumelhart et al. is considered the most computationally straightforward algorithm for training the MLP (Gardner & Dorling, 1998). The backpropagation algorithm is about to use the gradient descent technique to locate the minimum error. Initially, the weights in the network are set to random values, and the first sample (in the form of a vector) from the training dataset is fed to the network as input to obtain the output. Afterward, an error signal is calculated based on the deviation between the desired result and the actual output; this is then propagated back through the network to adjust weights to minimize overall errors. Finally, each training vector is fed to the network individually and repeats all the steps of error calculation until the overall error is acceptable (Bishop, 1995; Gardner & Dorling, 1998). The backpropagation algorithm can be adjusted by two user-defined parameters—

learning rate and momentum term—the former to control the step size while updating the weights, and the latter to help accelerate gradient descent (Gardner & Dorling, 1998).

Optimizing the MLP structure has always been challenging, and many studies have sought to establish optimal parameters. For example, in response to the poor convergence times of the backpropagation algorithm, Swanston et al. (1994) presented a simple adaptive momentum training algorithm that was much more efficient in convergence and significantly improved the computational cost compared to the classical backpropagation. Thimm & Fiesler (1997) aimed to determine the optimal variance for the random weight initialization for MLP using different weight distribution and activation functions. Nearly a decade later, Thomas & Suhner (2015) introduced a new pruning approach for finding the optimal parameters based on variance sensitivity analysis by pruning the different types of units sequentially. Soon afterward, Tang et al. (2016) proposed the Extreme Learning Machine (ELM)-based hierarchical learning framework with a single hidden layer to randomly generate hidden nodes for MLP. Most recently, Heidari et al., (2020) proposed an efficient hybrid training technique, Ant Lion Optimizer MLP (ALOMLP), by combining Ant Lion Optimizer—a swarm-based meta-heuristic—with MLP, in order to find the optimal weights and biases of MLP parameters for achieving a minimum error with the highest possible classification accuracy.

Beginning in the late 1980s, various NNs have come into public view (Lippmann, 1987); for many years, the networks most widely used for remote sensing image processing were MLPs—until the emergence of CNNs (Paola & Schowengerdt, 1995; Atkinson & Tatnall, 1997; C. Huang et al., 2002). MLP is well regarded for its ability to solve regression and classification problems. It is, therefore, one of the typical supervised DL methods used for image recognition.

In order to learn the weights in the learning phase, the MLP model is trained by a training dataset composed of positive and negative samples. Afterward, the input image should be reshaped into a vector for image classification. A final feature representation generated by the fully connected layers is sent to the classification layer to label the input image. The number of nodes in the output layer should match the number of classes in the classification (Atkinson & Tatnall, 1997; L. Zhang et al., 2016).

This innovative methodological approach of DL algorithms is usually used simultaneously with HR images (L. Ma et al., 2017). For instance, Del Frate et al. (2007) investigated the capabilities of MLP as a tool for the fully automatic classification of VHR or HR satellite image collections. C. Zhanget al. (2018) successfully mapped a strongly heterogeneous urban area with an anthropogenic urban surface mixture using a hybrid method based on MLP and CNN algorithms and aerial imagery of 50 cm spatial resolution. Vafaei et al. (2018) improved the accuracy of AGB measurement by combining MLP and other DL methods with Sentinel-2 and Advanced Land Observing Satellite-2 Phased Array type L-band Synthetic Aperture RaDAR-2 (ALOS-2 PALSAR-2). Hoa et al. (2019) conducted a study of soil salinity mapping using Sneinel-1 HR data with the MLP method. A. Zhang et al. (2019) used a gravitational-optimized MLP model and Sentinel-2 imagery to identify coastal wetlands. W. Zhang et al. (2020) identified rice paddies with Sentinel-2 data and various ML and DL methods, including CNN, MLP, and SVM. Debella-Gilo & Gjertsen (2021) detected seasonal agriculture land use types by applying DL methods (MLP and CNN) on Sentinel-2 time series. Safari et al. (2021) proposed a DL strategy for HR hyperspectral imagery classification based on different deep architectures, including MLP. Adagbasa et al. (2022) applied MLP to discriminate grass species in mountainous regions using Sentinel-2 HR images.

Although MLP is no longer the most commonly used DL method, it remains a powerful tool for image classification due to its remarkable ability to achieve high accuracy with minimum error. Thus, MLP is widely applied for many applications, such as vegetation cover detection, LULC classification and change detection, and mapping urban areas. For urban area studies, Fiset et al. (1998) conducted a study of road network mapping using a MLP model trained by two template-machining methods to identify road segments and intersections in the SPOT-HRV panchromatic image and thereby match a rasterized road map to a georeferenced SPOT image. The authors showed that using a deep NN (MLP) considerably improved classification over the previous methods. Moreover, it was shown that reliable results could be obtained by combining several classification approaches.

Ozturk (2015) determined the urban growth dynamics of the Atakum District in Samsun, Turkey, with two hybrid models: Cellular Automata-Markov Chain (CA-MC) and

MLP-Markov Chain (MLP-MC). In order to examine and compare the ability of the two models to accurately determine future urban growth, the authors simulated the urban growth of 2013 based on two Landsat TM/ETM+/OLI images from 1989 and 2000. The simulation results were compared with the 2013 LULC data for validation. The study results indicated that the models could effectively predict future urban growth, especially the MLP-MC method devoted to the most accurate simulation. In a similar study conducted by Losiri et al. (2016), CA-MC and MLP-MC were also applied to model LULC and urban expansions in Thailand's Bangkok Metropolitan Region. The use of these models has indeed improved prediction accuracy (exceeding 90% Overall Accuracy (OA)), especially in the MLP-MC model.

W. Jiang et al. (2018) attempted to extract surface water bodies in specific regions for natural resource management by performing the MLP algorithm on Landsat-8 OLI images. In addition, the results were compared with those of a water index and SVM. The results demonstrated the excellent performance of MLP for precisely extracting different types of surface water bodies and suppressing noise in comparison with the water index and SVM. Additionally, the accuracy assessment showed that MLP could provide the most accurate classification results.

In a recent study, Redowan et al. (2022) analyzed the historical tendency and LULC transitions from 1995 until 2015 at a 10-year interval at Raghunandan Hills Reserve, which had suffered severe forest degradation. Afterward, the future trend of forest LULC transitions for 2025 and 2035 was predicted by using the MLP-MC model. The authors found that the model effectively predicted the trend of increasing forest cover due to afforestation activities by 2025 and 2035 as well as the possibilities of forest expansions, which was valuable and useful to local forest resource management and deforestation monitoring.

Ultimately, as one of the most critical factors and indicators of environmental changes, LULC has always been a focus of studies. V. N. Mishra & Rai (2016) revealed LULCCs in India's Patna district between 1988 and 2013 with the ML MLC method, after which an integrated MLP-MC model was trained to predict LULCCs for 2013 and subsequently validated by the 2013 LULC data. Eventually, the future LULC predictions of 2038 and 2050 were performed with the well-trained and validated MLP-MC model. The results

provided accurate and reliable predictions about the amount and location of potential changes, revealing the trend of decreasing agricultural land and rapidly increasing artificial area.

Silva et al. (2020) sought to model land degradation in Brazil's Taperoá River Basin. Three classifications—1990, 1999, and 2002—were performed on Landsat–5 and Landsat-7 medium spatial resolution images using MLP algorithms (the main land cover change was detected with images from 1990 and 2002). After obtaining very satisfactory results with the MLP model (around 90% OA and 0.61 kappa coefficient), a predicted scenario for 2035 showed a significant increase in the herbaceous class but a decrease in the tree-shrub class.

4.2.3.3. Convolutional NNs deep architecture

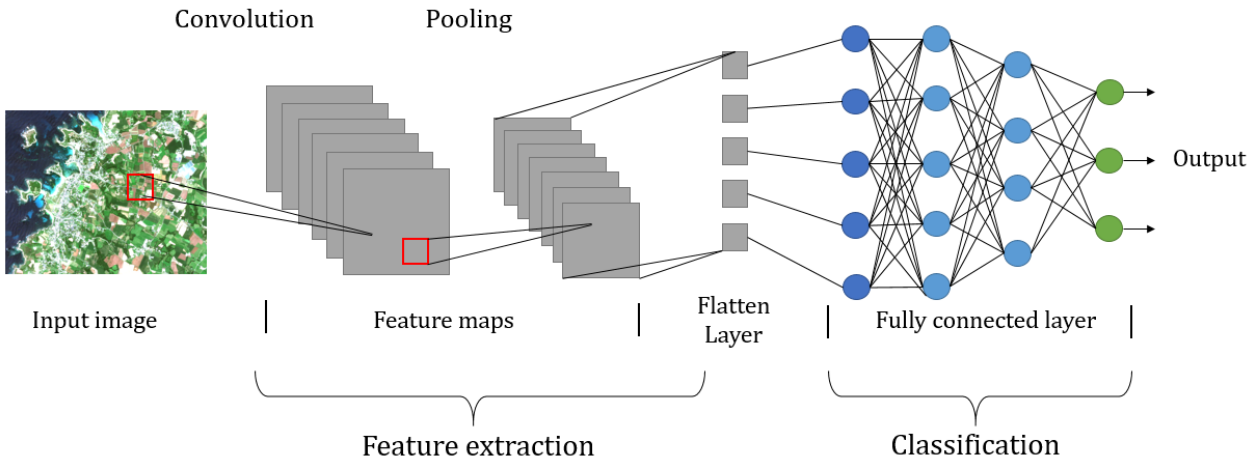

Figure 46 Example of CNN model

As shown in Figure 45, a typical CNN model inspired by a human visual system is a multilayer architecture composed of at least one feature extraction stage and a classification stage; the former stage refers to one or more fully connected layers and the latter to a final classifier. The model takes image patches as input and outputs a final prediction of each object in the image. The feature extraction stage can be decomposed into two principal layers (i.e., a convolutional layer and a pooling layer), and non-linearity, flatten and fully connected layers (L. Zhang et al., 2016). These layers are described below:

- **Convolutional:** The essential layers of the CNN model refer to the filters, which perform convolution operations on feature maps (also called "activation maps") or raw image received, generating a block of feature maps as output. In addition, a non-linear activation function is usually performed after the convolutions. Within the feature maps of a convolutional layer, each unit is connected to local patches, which are located in the feature maps of the previous layer by a set of weights known as a "filter bank" or "kernel." The filter bank can be differentiated according to feature maps. Overall, the convolutional layer aims to detect local conjunctions of features (e.g., lines, structure and shapes) from the previous layers (LeCun et al., 2015; Cheng et al., 2020).

- **Non-linearity:** In this layer, a pointwise non-linearity function is applied to each component of a feature map (L. Zhang et al., 2016).

- **Max-pooling:** The max-pooling layer aims to merge semantically similar features into a single feature; decrease redundant information in images; and reduce the spatial size of the feature maps, the number of parameters, and network computational cost. This layer is applied after the convolutional function for generating the pooling operation. In other words, the maximum value of the current view is selected with a predefined window in the max-pooling layer (LeCun et al., 2015; S. Li et al., 2019).

- **Flatten:** This layer refers to the transition function from the feature extraction stage to the classification of fully connected layers; it consists of converting the multi-dimensional-pooled feature map into a one-dimensional array.

- **Fully connected:** The fully connected layer is the fundamental component of the classification stage, based on the flattened input created by the previous flatten layer. As a traditional fully connected model, each input in this layer is connected to all neurons; each neuron is then connected to every neuron in the next layer until reaching the end of CNN architectures. In order to generate the probability of each class for the classification task, the last fully connected layer is generally followed by a softmax classifier as a normalization function (Cheng et al., 2020).

Finally, the output results that include one unit for each class predicted can be acquired at the end of the classification stage. Furthermore, the backpropagation gradients are used for the learning procedure. Initially, the process data are in the form of multiple arrays (LeCun et al., 2015; L. Ma et al., 2019); thus, they are well adapted for processing multispectral remotely sensed data in which the pixels are generally arranged (L. Ma et al., 2019). Depending on the data modalities, CNNs may be constructed differently. In primitive 1-D CNNs (Kiranyaz et al., 2021), the kernel moves in one dimension in the form of signals and sequences used for speech recognition and document reading. In 2-D CNNs, the kernel moves in two dimensions (x, y), the model recognizes spatial features of image for images or audio spectrograms processing. When the kernel moves in three dimensions, the 3-D CNNs are usually performed in spatial and spectral dimension, for video or volumetric image processing (LeCun et al., 2015; S. Li et al., 2019).

Advanced deep CNNs began their ascendance when AlexNet (Krizhevsky et al., 2012) emerged victorious from the Large-Scale Visual Recognition Challenge (LSVRC) in 2012; since then, they have steadily become the leading DL model (X. X. Zhu et al., 2017; Cheng et al., 2020). CNNs are principally designed for image classification with the advantage of end-to-end feature learning; they have been shown to be effective for solving complex classification problems by many studies (T. Fu et al., 2018; Timilsina et al., 2019; Cheng et al., 2020). Moreover, considering various characteristics of CNNs—such as high effectiveness in large-scale recognition, efficiency in object detection, and semantic segmentation areas—the deep architectures are well recognized for their achievement in advanced classification accuracy as well as mid- and high-level feature abstraction (X. X. Zhu et al., 2017). In other words, the CNN deep structures can learn highly abstract feature detectors and map the input features into representations that significantly impact the performance of subsequent classifiers (L. Zhang et al., 2016).

The applications of CNN models can be categorized into different types according to the deep networks utilized (X. X. Zhu et al., 2017).

Initially, the pre-trained networks were often used as feature extractors on an image dataset (X. X. Zhu et al., 2017) when CNNs were newly introduced into remote sensing scene classification scenarios (Penatti et al., 2015). Penatti et al. (2015) evaluated the general performance of ConvNets' in-depth features by performing image

classification with aerial imagery and satellite datasets. Hu et al. (2015) investigated the use of features extracted from successful pretrained CNNs in HR remote sensing imagery scene classification. Marmanis et al. (2016) proposed a new method by extracting representations of the pre-trained ImageNet, then transferring the representations into a supervised CNN classifier in order to address the limited dataset problem of the traditional CNN model. E. Li et al. (2017) presented a fusion strategy based on integrating multilayer features in a pre-trained CNN model used as an in-depth feature extractor for scene classification. N. He et al. (2018) proposed a new scene classification method, Multilayer Stacked Covariance Pooling (MSCP), which combines multilayer feature maps acquired from pre-trained CNN models.

Afterward, the fine-tuning pretrained CNNS was developed. The principle of this type of CNN is to make a pretrained model adaptive to the specific conditions of the user's needs, and the research aims to fine-tune a pretrained model on a target dataset or optimize the structures—for example, fine-tuning an existing CNN model on a public satellite image dataset to make it more adaptive to satellite images (X. X. Zhu et al., 2017; Cheng et al., 2020). Castelluccio et al. (2015) explored the potential of two well-trained CNN architectures, CaffeNet and GoogleNet, for the semantic classification of LULC by only fine-tuning the target data.

Nogueira et al. (2017) evaluated existing CNN structures in three different scenarios: using CNNs as feature extractors, fine-tuning, and training a new NN. They found that fine-tuning was the best-performing strategy, especially when combined with linear SVM.

Y. Liu et al. (2018) developed a multiscale CNN (MCNN) framework for solving the scale variation problem of scene classification by developing a new structure with two branches of a fixed-scale net (F-net) and a varied-scale net (V-net) for training multiscale images with the same network weights. The excellent capability of fine-tuning pre-trained CNNs is confirmed by previous litteratures. However, CNNs generally need to be trained with massive training data, but the training dataset size is generally limited. Thus, it is difficult to fine-tune a CNN model (X. X. Zhu et al., 2017; Cheng et al., 2020).

Consequently, more recent studies have chosen to use newly trained networks, although it is more challenging than previous applications. When the existing CNNs are

not suitable for the characteristics of target datasets or the study's aims—or when it is impossible to modify the pre-trained models—researchers prefer to build a smaller structure and train it with selected satellite image datasets.

In Luus et al. (2015), a multiscale input strategy for multiview DL is introduced for supervised LULC classification problems. F. Zhang, Du, et al. (2016) proposed a Gradient Boosting Random Convolutional Network (GBRCN) framework, the first deep ensemble framework used for scene classification. Combining a number of deep NNs, GBRCN outperformed the traditional single-CNN approach in the evaluation. Volpi & Tuia (2017) developed a CNN-based system based on a downsample-then-upsample architecture. The system learned how to densely classify each pixel at the original image resolution to improve prediction accuracy. G. Chen et al. (2018) introduced a knowledge distillation training method for scene classification; their proposed framework focused on the effectiveness and efficiency of more minor and shallower network models by matching the output of a small and shallow "student" model with a larger and deeper "teacher" model. N. He et al. (2020) presented another method for remote sensing scene classification: the skip-connected covariance (SCCov) network, which could skip connection and covariance pooling so that the multi-resolution CNN feature maps were merged, and the second-order information in some feature maps could be intensely exploited. The most significant shortcomings of the newly trained CNN models are their decreased generalization ability and the overfitting problem (X. X. Zhu et al., 2017).

As the leading DL algorithm today, CNNs are widely applied in different research areas in the remote sensing field, such as vegetation cover (Nijhawan et al., 2017; Langford et al., 2019; Ayhan et al., 2020; Collin et al., 2021; Kattenborn et al., 2021), agriculture (Kamilaris & Prenafeta-Boldú, 2018; Milioto et al., 2018; N. Zhu et al., 2018; J. Lu et al., 2021), urban area mapping (Yoo et al., 2019; C. Zhang et al., 2019b; W. Zhou et al., 2020), and noise (e.g., cloud and shadow) detection (Shendryk et al., 2019; J. Yang et al., 2019; Y. Chen et al., 2020; J. Guo et al., 2021). Thus, as one of the most studied areas in remote sensing, CNNs occupy an essential position in LULC classification (Bhosle & Musande, 2019; Carranza-García et al., 2019; S. Zhang et al., 2020; Q.-T. Bui et al., 2021). Scott et al. (2017) trained a deep CNN (DCNN) for land cover classification in HR remote sensing images by applying two techniques: (1) use of fine-tuning in the feature extraction

stage for Transfer Learning (TL), which could bootstrap a DCNN while preserving deep visual feature extraction from a different domain of images; and (2) data augmentation customized for remote sensing data for expanding training image datasets. With these two techniques, DCNN was shown to be more robust for remote sensing imagery as well as a vital improvement of classification accuracies by evaluating three DCNNs derived from CaffeNet, GoogleNet, and ResNet50 (ranging from 79.1% to 98.5%).

Mahdianpari et al. (2018) aimed to map the complex land cover of wetlands in Canada's Avalon Peninsula using fully-trained or fine-tuned existing DCNNs—such as DenseNet121, InceptionV3, VGG16, VGG19, Xception, ResNet50 and InceptionResNetV2 on multispectral RapidEye data—evaluating the performance of each one. The results indicated that the deep hierarchical frameworks were effective at improving the classification accuracy of the complex land cover of wetlands—especially the full-training InceptionResNetV2 model using five spectral bands, which achieved the best accuracy among all (about 96%). Therefore, the extra multispectral bands and integration of the Inception and ResNet architectures may be recommendable to improve complex land cover classification.

Helber et al. (2019) challenged the LULC classification problem by applying different patch-based ML methods (SVM, Scale-invariant feature transform (SIFT)) and pre-trained DL methods (a two-layer CNN model, GoogleNet, and ResNet-50) on a new HR multispectral Sentinel-2 dataset containing ten different classes, 27,000 georeferenced samples, and covering 13 spectral bands. The results indicated that DL outperformed both ML methods (GoogleNet > ResNet-50 > two-layer CNN). Moreover, a large-scale, high-quality training dataset enabled every method (particularly the DL methods) to achieve better accuracy (around 20% increase with a more extensive training dataset).

4.3. SAR backscattering coefficient processing on Google Earth Engine (GEE)

This section presents GEE, an image-processing platform, following a brief introduction of the SAR time series used in the studies.

4.3.1. SAR backscattering coefficient (σ°)

Backscatter can be defined as the RaDAR signal received by the RaDAR antenna that has been reflected by the target on Earth's surface. It is a measure of the reflective strength of a RaDAR target on the ground (ESA, n.d.-a). Moreover, the measure of the signal reflected can be quantified and normalized as the SAR backscattering coefficient. Similar to the spectral signature, each object reacts differently with the energy emitted and then reflects a different quantity of signal toward the RaDAR antenna. The backscattered intensity of each target depends on various factors, such as types, sizes, textures, shapes, frequency, polarization of RaDAR pulse, and incidence angle. Therefore, the SAR backscattering coefficient is an essential index for identifying different targets on the ground, even different stages of development of the same targets (e.g., different stages of development of crops). For example, a flat and smooth target surface yields a low backscattering coefficient (represented by darker areas in SAR images) due to the specular reflection effect, whereas a rough surface yields a high backscattering coefficient (represented by brighter areas in SAR images) due to the diffused reflection effect. As shown in Figure 46, calm water appears darker than other areas because most of the RaDAR pulses are specularly reflected by the smooth water surface; the city surface is generally the brightest area in a SAR image due to the corner reflector effect caused by the buildings; the vegetation surface is moderately bright in the image because vegetation surfaces tend to be moderately rough.

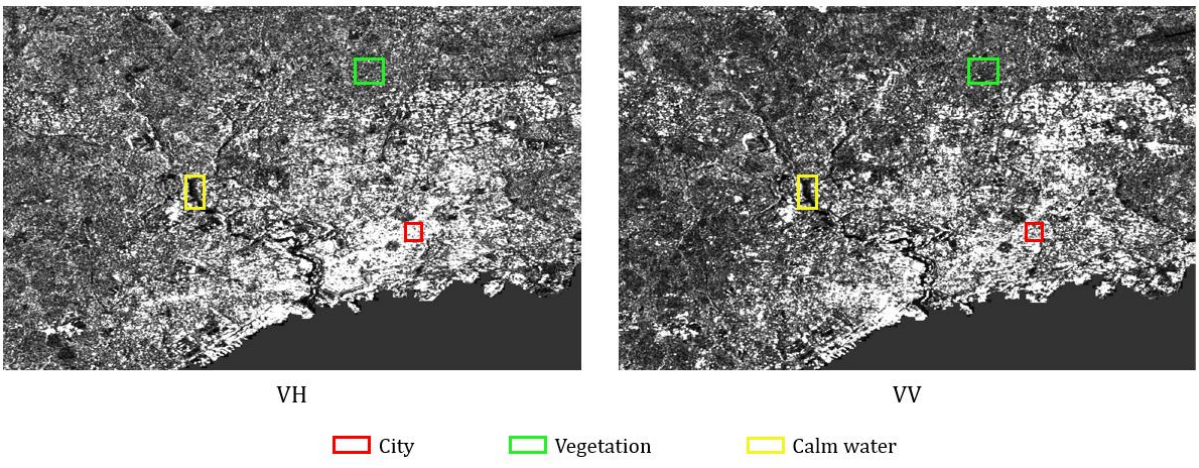

Figure 47 Backscattered intensity depends on different targets (city, vegetation, and calm water)

Generally, the raw SAR image needs to be pre-processed to extract the backscatter information, which can be used for further analysis. In order to quantify and compare the backscattering behavior, the backscattering coefficient is usually converted to decibels (dB) by five pre-processing techniques displayed in the Figure 47; the details of each step are listed below (GEE, 2022).

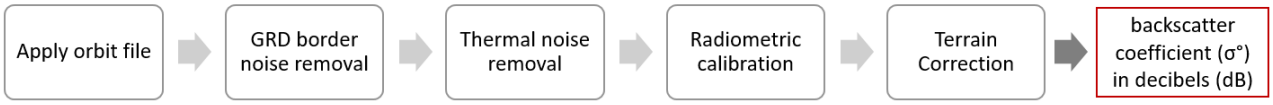

Figure 48 SAR satellite imagery preprocessing procedure (Xie and Niculescu, 2022)

- **Apply orbit file:** The first step is to update the orbit metadata, which contains the satellite's precise orbit state vectors (if the precise orbit is available to download). The orbit file allows the acquisition of accurate satellite positions and velocity information (Filipponi, 2019; GEE, 2022).

- **GRD border noise removal:** This algorithm aims to remove radiometric artifacts caused by the azimuth and range compression on the image edges. The artifacts represent low-intensity noise and invalid data (Filipponi, 2019).

- **Thermal noise removal:** The thermal noise removal operator aims mainly to reduce noise effects in the sub-swath and normalize the backscatter signal within the entire image. For scenes in multi-swath acquisition mode, it can also reduce discontinuities between sub-swaths (Filipponi, 2019; GEE, 2022).

- **Radiometric calibration:** Calibration is one of the principal pre-processing procedures to convert digital pixel values to radiometrically calibrated SAR backscatter. In this step, image intensity values are changed into sigma-naught values while keeping the nominally horizontal plane (Filipponi, 2019).

- **Range Doppler terrain correction:** Also known as "orthorectification," this is a correction procedure that reduces geometric distortions caused by topography and takes into account real terrain information by using a DEM, since most SAR images are captured with some distortions related to side-looking geometry (Filipponi, 2019; GEE, 2022).

- **Conversion to dB**: In this final pre-processing procedure, a logarithmic transformation is used to convert non-dimensional backscatter coefficients to dB (Filipponi, 2019).

The backscattering coefficient is widely used in diverse disciplines. For example, vegetation cover is one of the earliest application areas of the SAR backscattering coefficient. Mougin et al. (1999) investigated the correlation between structural mangrove forest parameters (e.g., tree height, tree diameter at breast height, tree density, and basal area) and total AGB and AIRSAR P-, L- and C-band multitemporal backscattered RaDAR signal. More recently, Frison et al. (2018) revealed the potential of dual-polarization (VV, VH) Sentinel-1 backscattering plot to monitor the phenological behavior of temperate forests and the relationship between RaDAR backscattering coefficient and environmental variables, such as precipitation and temperature.

In biomass estimation, Ferrazzoli et al. (1992) evaluated the performance of active and passive microwave sensors in vegetation biomass estimation. They reported that backscattering coefficients retrieved from both sensors offered good possibilities for vegetation biomass retrieving. Pulliainen et al. (1996) used C-band multitemporal ERS-1 backscattering coefficient to analyze the seasonal dynamics in the boreal forest by estimating forest stem volume (biomass).

In soils characteristics analysis, especially soil moisture is one of the crucial variables in hydrological processes (L. Wang & Qu, 2009), Aly et al. (2007) analyzed the backscattering behavior of salt-affected soils on RaDARSAT-1 SAR images and eventually explored the potential of the backscattering coefficient for salt content monitoring. In addition, Rodríguez-Fernández et al. (2015) retrieved soil moisture from Soil Moisture and Ocean Salinity (SMOS) data by using L-band SMOS brightness temperatures

complemented with C-band Advanced SCATterometer (ASCAT) backscattering coefficient and MODIS NDVI.

In agricultural land mapping, (D. Wang et al., 2010) used dual-polarizations (VV, HH), Multitemporal, multi-polarization ENVIronmental SATellite (ENVISAT) Advance-SAR (ASAR) backscattering data for mapping seven main types of agricultural lands in the Pearl River Delta in China. Lopez-Sanchez et al. (2012) proposed a simple approach for retrieving rice field phenology by employing backscattering coefficients and ratios of the dual-polarization (HH, VV) TerraSAR-X sensors.

In ocean and water resource management, Solberg (2012) detected oil-spill pollution on the ocean surface using the backscattering coefficient of several SAR sensors (e.g., ERS, ENVISAT ASAR, RADARSAT-1 and -2, TerraSAR-X and COSMO SkyMed). Kim et al. (2014) measured the water level with L-band SAR backscatter coefficients in the freshwater marsh.

In our study of winter crop phenology monitoring in Northern Finistère, Sentinel-1 SAR data were generated on the GEE(GEE) platform.

4.3.2. Google Earth Engine platform

Since the rapid development of multiple free-access remote sensing archives in recent years (e.g., Landsat, Sentinel, and NOAA), various tools have also been developed for large-scale processing of geospatial data (Gorelick et al., 2017), such as TerraLib (Câmara et al., 2000), Hadoop (Whitman et al., 2014), and GeoSpark (J. Yu et al., 2015). Yet, the lack of a powerful, easy, free-access, highly popular tool remains an issue for satellite image processing, which is still limited by fundamental information technology problems, data acquisition and storage, computer configuration (GPUs, CPUs), and network (Gorelick et al., 2017).

Under such circumstances, GEE arrived in 2010 as an open-source, planetary-scale cloud-computing platform for a single or a collection of analysis-ready image processing based on Google's massive computational capabilities (Gorelick et al., 2017). GEE is a platform that provides international collaboration, data-intensive analysis, substantial

computing resources, and high-end visualization (Goodchild et al., 2012; Clinton, 2016). Moreover, unlike the majority of coding platforms, the GEE platform is in an interactive mode that allows good visualization of data, analysis results preview, overlapping different data for comparison or detecting the evolution over time.

As displayed in the Figure 48, the platform is composed mainly of (1) an application programming interface (API) for performing processing, analysis, and visualization of the data in JavaScript language; (2) an extensive data catalog (50 Petabytes) that allows access to a variety of Earth observation data, such as optical and SAR satellite imagery (e.g., Sentinel, Landsat, MODIS) with only one or two days of interval between image acquisition and when it is added in the GEE data catalog, geospatial vectors, terrain, and atmosphere data; and (3) a visualization window with an exportation option (Clinton, 2016).

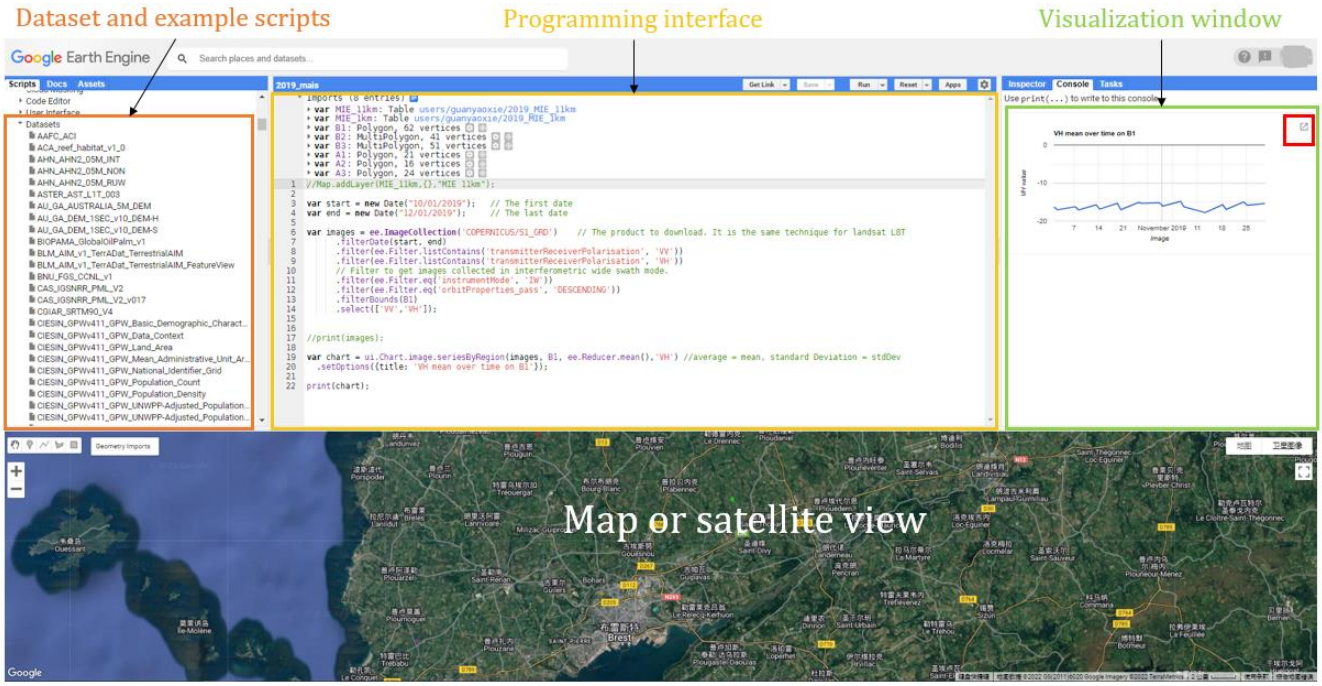

Figure 49 Example of GEE processing interface

The satellite images in the data catalog are generally preprocessed for access and calculation. In addition, various geospatial-processing functions are integrated into the platform, which can perform raster and vector data processing, ML algorithms, kernel application, projection transformation, dataset combination, bandmath calculation, etc.

Overall, GEE has significantly contributed to traditional remote sensing data processing by combining an extensive catalog of different types of data, excellent calculation capabilities, and comprehensive manipulation. For that reason, many studies of crucial natural or social issues use the GEE platform. Examples include forest cover (M. C. Hansen et al., 2013; B. Chen et al., 2017; Oliphant et al., 2019), disaster, including drought (Sazib et al., 2018; Zhao et al., 2021), flood (Uddin et al., 2019), wildfire (T. Long et al., 2019; Sarricolea et al., 2020), food security or agriculture (Jin et al., 2019; Rembold et al., 2019), land cover (Ge et al., 2019; X. Wang et al., 2020), water management (C. Wang et al., 2018; Y. Wang et al., 2020), atmosphere and climate monitoring (H. Zeng et al., 2019; Fuentes et al., 2020), and urban sprawl (Gong et al., 2020; D. Liu et al., 2020).

For instance, Dong et al. (2016) analyzed the spatial expansion information of paddy rice in northeastern Asia, characterized by less cloud coverage, long growing seasons, and more side lap observations of Landsat. For this purpose, the classification was performed on the GEE platform with around 3,290 scenes of 143 path/rows by using the improved phenology completed with pixel-based paddy rice mapping algorithm based on VIs (NDVI, EVI, and land surface water index (LSWI) (Chandrasekar et al., 2010)). The results indicated that the collaboration of an efficient mapping algorithm, high-quality satellite image, and GEE platform with excellent computational capabilities could effectively provide highly accurate classification results and model the spatial distribution and landscape pattern of paddy rice in northeastern Asia for the first time.

B. Chen et al. (2017) developed a new method for accurately monitoring mangrove ecosystem changes in China due to the rapid deforestation of mangrove forests. The new classification method was developed based on the greenness, canopy coverage, tidal inundation calculated with Landsat time series, and auxiliary data such as elevation, slope, and intersection with sea criterion of mangrove forest. The methodology proposed was run on the GEE computing platform. Additionally, the classification was performed on the available open-source data catalog of GEE, including 1,941 Landsat scenes of 25 path/rows and 586 Sentinel-1 images. The authors reported that China's distribution of mangrove forests was adequately identified with very high accuracy indices (User Accuracy (UA), Producer Accuracy (PA), and OA greater than 95%).

GEE is usually limited by the processing algorithms for classification and regression problems (Amani et al., 2020). However, Y. Wang et al. (2020) took advantage of a large data catalog, the outstanding computing capabilities of GEE, and a powerful DL multi-scale CNN (MSCNN) algorithm to perform an "offline training and online prediction" (OTOP) technique for accurate and efficient extraction of urban water from Landsat images. OTOP recommended that the MSCNN model be trained entirely offline. Subsequently, the urban water process extraction was performed on the GEE platform with the trained parameters of MSCNN. The classification results outperformed the RF classifier, thereby showing the efficiency of combining GEE and DL algorithms and the OTOP trick.

4.4. Post-classification methodology

Post-classification processing is considered the final objective of the project and the showcase of the data process, which allows the results to be presented to the general public in a comprehensible way.

In general, post-classification processing is generated in the form of statistical analysis and map, which allows for showing classification accuracy, evaluating the efficiency and effectiveness of the proposed method, and facilitating the comparative analysis of independently produced classifications from different methods (D. T. Bui et al., 2020, p. 202; DeLancey et al., 2020; G. Xie & Niculescu, 2021), and/or from different dates, so as to visualize specific natural or societal issues or evolutions, such as urban expansion (Weng, 2001; X. Liu et al., 2020), deforestation (Saatchi et al., 1997; Margono et al., 2012) and LULCCs (Abd El-Kawy et al., 2011; Dingle Robertson & King, 2011).

This section will present two main post-classification processes: accuracy assessment and PCC. Accuracy assessment is the application of a series of statistical analyses of the classification results to validate the results and compare two or more classifiers performed on the same or similar data. Accuracy assessment can also be used to evaluate remote sensing data from different sensors. Otherwise, PCC refers to the comparative analysis of independently produced classifications from different dates in

the form of a map (Serra et al., 2003). Thus, PCC techniques are also known as a "map-to-map comparison."

4.4.1. Accuracy assessment

Accuracy assessment is the quality evaluation system for the measure of classification accuracy, determined by the degree of "correctness" of a map or classification (Foody, 2002); in other words, accuracy assessment refers to the level of agreement between the ground truth and the classification results.

As one of the key components of remote sensing studies, the accuracy assessment refers to the overall measure of the quality of a classified map. The principle objective is to not only verify and validate the reliability and accuracy of the output results in order to make effective and proper decisions, but also refine the classification and identify the errors, especially for interclass confusion. Consequently, the sophisticated statistical analysis of error matrices—the most widely used procedure of accuracy assessment—are developed with the aims of acquiring unbiased classification results and, therefore, of producing reliable thematic maps, especially for LULC mapping (van Genderen & Lock, 1977). Furthermore, the most critical part of the accuracy assessment is to choose suitable validation samples in the forms of polygons or pixels. Sample design can use random, stratified random, systematic, double, and cluster sampling (D. Lu & Weng, 2007); stratified random techniques have been accepted as the most suitable sampling method for LULC studies (van Genderen & Lock, 1977).

Error matrix (also called "confusion matrix") is considered to be the core of accuracy assessment in addition to being the most widely used and recommended method of accuracy assessment (Foody, 2002; D. Lu & Weng, 2007). The matrix describes the pattern of the class allocation made relative to the reference data (Foody, 2002) by building a table contrasting ground truth and predicted results, one on either side. In addition, the table comprises four categories of values: true positive, false positive, false negative, and true negative. A non-bias matrix is generated by comparing all the data in classification results and the reference data issue of the field survey (Story & Congalton, 1986).

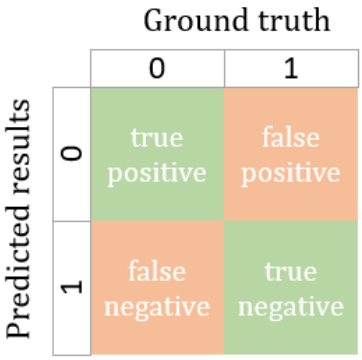

Figure 50 Confusion matrix

In Figure 49, the central diagonal (true positive and true negative), which indicates the portion of correctly classified units, is divided by the total number of classified units of each class (category); higher values indicate higher accuracy. However, there is a diversity of sources of errors that explain the low value of accuracy, such as the nature of the classification problem (e.g., the complexity of the landscape and the number of classes), the generation and adequacy of the training samples, and the dimensionality of the data and the classification method applied (Raudys & Pikelis, 1980; M. Pal & Mather, 2003).

Once the error matrix is generated, other detailed statistical statements of accuracy assessment can be easily derived to express classification accuracy (Foody, 2002; D. Lu & Weng, 2007); some accuracy indices used in our studies are displayed below (Figure 50):

Reference data

Classified data	1	2	3	4	5	Row total
1	85	3	2	1	2	93
2	2	76	4	3	15	100
3	5	9	90	2	3	109
4	4	2	12	84	1	103
5	2	1	6	10	80	99
Colum Total	98	91	114	100	101	504

Overall accuracy:
$(85+76+90+84+80)/504 \approx 0.823$

Kappa coefficient:
$p_o = (85+76+90+84+80)/504 \approx 0.823$
$p_e = (93/504)*(98/504)... (99/504)*(101/504)$
$K = p_o - p_e \ / \ 1 - p_e \approx 0.779$

User's accuracy (Precision):
1: 85/93 ≈ 0.914
2: 76/100 =0.760
3: 90/109 ≈ 0.826
4: 84/103 ≈ 0.816
5: 80/99 ≈ 0.808

Producer's accuracy (Recall):
1: 85/98≈ 0.867
2: 76/91 ≈ 0.835
3: 90/114 ≈ 0.789
4: 84/100 = 0.840
5: 80/101 ≈ 0.792

F-Score:
$F=2*\frac{Precision*Recall}{Precision+Recall}$

Figure 51 Example of several accuracy index calculations (OA, Kappa coefficient, User's accuracy (also called "precision), Producer's accuracy (also called "recall), and F-Score)

➢ Global accuracy indicators:

- **OA**, one of the traditional classification accuracy measures, indicates the probability that an individual unit (pixel) will be correctly classified by the trained classification model. The number of correctly classified pixels is divided by the total number of pixels in the images.

- **Kappa coefficient**, a powerful method for classification results evaluation, refers to a measure of the overall statistical agreement of an error matrix by considering all elements in the errors table (D. Lu & Weng, 2007). It can accommodate the deficiencies of OA, such as some elements being correctly classified only by chance. Additionally, Kappa is a better measurement of interclass agreement than OA.

➢ Local accuracy indices:

- **Producer's accuracy (PA)**, also called "recall" or "positive predictive value," is a measure of errors of omission, which refer to a pixel abnormally excluded from the class to which it belongs— in other words, when samples have been omitted from

the correct class (Story & Congalton, 1986). PA is usually applied to measure the probability that an area of interest can be correctly mapped for the producer.

- **User's accuracy (UA)**, also called "precision" or "sensibility," is a measure of errors of commission, which refer to pixels abnormally included in a class when they should belong to another class. In other words, it indicates the probability that an element assigned to a class by the classifier actually represents that class in reality and how accurate the maps are for users (Story & Congalton, 1986).

- **F-score**, generated from the precision and recall values, is able to provide harmonic mean of the two values.

As a major topic of debates and research in remote sensing for several decades, accuracy assessment remains a highly active research area, especially as it pertains to uncertainty and confidence analysis developed in recent years. For example, an algorithm based on research by P. Olofsson et al. (2014) designed for evaluating the accuracy of a change map and area estimation is essential to quantify uncertainty by reporting confidence intervals for accuracy and estimated area changes. In accuracy assessment, each indicator is represented by an uncertainty rate. Higher uncertainty refers to a greater accuracy interval, and lower uncertainty indicates greater accuracy. The objective of the confidence analysis is to provide continuous improvements and reduce uncertainties (P. Olofsson et al., 2014).

There is no standard method of accuracy assessment; an increasing number of recent studies provide more than one measure of classification accuracy.

4.4.2. Post-classification comparison

Change detection is the comparative analysis of the individual classification of the rectified images from two different dates in order to identify changes that occurred and to provide valuable information about area changes and change rate, the spatial distribution of changed types, change trajectories between different LULC types, and

accuracy assessment of change detection (D. Lu et al., 2004; El-Hattab, 2016). Additionally, change detection can be used to estimate and project the potential changed area. In change detection, multi-temporal data are involved in the evolution of a phenomenon over time.

Various methods are employed for change detection, such as visual analysis, image differencing, principal component analysis, change-vector analysis, and PCC (D. Lu et al., 2004). Of these, PCC change detection is the most commonly used method due to its robustness and superb capacity to detect land cover transition (Castellana et al., 2007). In addition, compared to visual analysis, PCC compares two classified maps from two data that are processed and classified independently. Thus, this change detection technique requires rectifying and classifying each remote sensing image. Moreover, considered the second step of post-classification processing, the PCC process strongly relies on accurate individual classification results that have undergone the evaluation of the accuracy assessment techniques described in the previous section. The classification should be the most accurate possible.

Based on the complete classification of each data, a change map is created that contains X^2 categories (assume that the classification results contain X classes). The analysis is performed at the pixel level, providing detailed "from-to" information; each change from one category to another is highlighted in the change map. Users can also extract the desired changes between two specific categories exclusively. The comparison is performed on a "pixel-by-pixel" basis, as demonstrated in Figure 51.

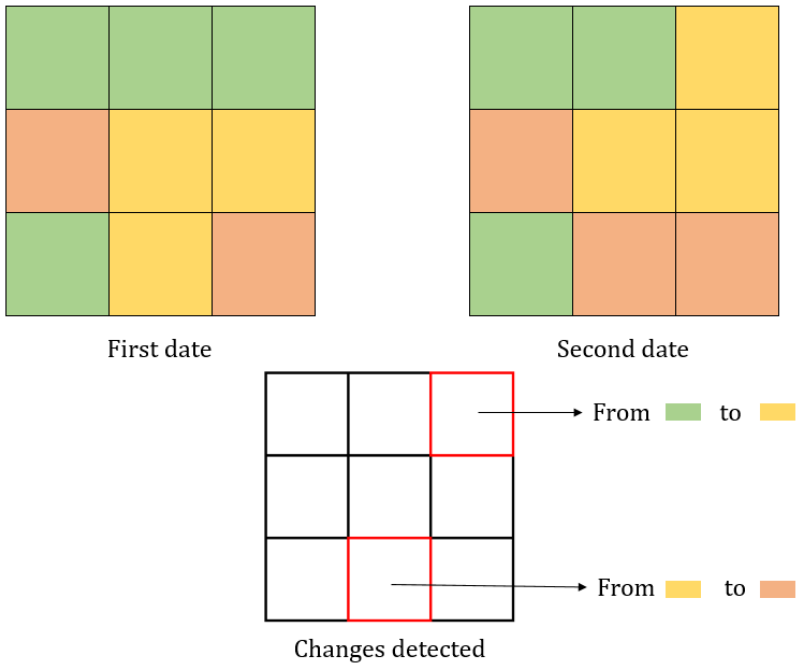

Figure 52 Example of change detection technique

Sources of errors in PCC analysis can be various. For instance, the temporal, spatial, radiometric, and spectral characteristics of sensors may considerably affect the change detection results. In particular, each error in the input classification map will result in an error on the PCC change detection map. Thus, the comparison between images of two seasons is usually challenging. It is, therefore, preferable to choose images of the same season with similar states, especially for vegetation change detection (D. Lu et al., 2004). Differences in pixel size can also affect the comparison results; usually, the finer spatial resolution provides more details in classification and change detection. Furthermore, the thresholds used to differentiate change from no change are also crucial for comparison (Serra et al., 2003).

Accordingly, avoiding using images from different sensors is essential for an accurate PCC analysis, especially images with different spatial resolutions and grid origins that might produce extra problems due to geometric corrections and different pixel sizes (Serra et al., 2003). However, using multi-source data in applications is often unavoidable due to a lack of available data. For example, some sensors may not have existed prior to a certain time, or others may have suspended service for change detection over several decades (Serra et al., 2003). For instance, G. Xie & Niculescu (2021) revealed LULCCs on the Crozon Peninsula, Brittany, France, from 2007 to 2018 by using SPOT-5 and Sentinel-

2 images; PCC was performed on images from two different sensors, because Sentinel-2 started collecting data only after 2013.

PCC change detection is commonly applied in various areas, including LULC conversion due to human activities (e.g., forest to artificial land cover) (Abd El-Kawy et al., 2011; Huiping et al., 2011; Thonfeld et al., 2020); human- or nature-induced change in cover condition (e.g., clearcutting, drought) (Virk & King, 2006; F. Wang & Xu, 2010; Fadhil, 2011); cover transition (e.g., vegetation succession, soil erosion) (W. Q. Guo et al., 2008; Phinzi & Ngetar, 2019); and change in cover properties (e.g., biomass accumulation) (Coppin et al., 2001; V. Klemas, 2013).

Part III LULC CHANGES IN PAYS DE BREST: CASE STUDIES

Chapter 5. Machine learning methods and classification of vegetation in Brest, France

Conference proceeding (invited paper): Guanyao Xie, Simona Niculescu, Chinguyen Lam, Elise Seveno, "Machine learning methods and classification of vegetation in Brest, France," Proc. SPIE 11157, Remote Sensing Technologies and Applications in Urban Environments IV, 111570J (2 October 2019); doi: 10.1117/12.2533436

Event: SPIE Remote Sensing, 2019, Strasbourg, France

Published date: 2 October, 2019

5.1. Introduction

The urban area is the most important land use in the world nowadays. According to the studies, 70% of the world's population will reside in urban areas by 2050 due to rapidly increasing urbanization worldwide (Q. Chang et al., 2015). With such an urbanization rate, urban green space (UGS) has become a vital component of the urban environment (Neyns & Canters, 2022). UGS has various definitions; it can be defined as all kinds of predominantly unsealed, permeable and soft surfaces such as soil, grass, shrubs, trees, and water (James et al., 2009) in different forms, or all-natural, semi-natural, and artificial systems within, around and between urban areas of all spatial scales (Q. Chang et al., 2015).

Therefore, UGSs play a critical role in people's daily lives in different aspects; they not only address environmental issues—such as reducing pollution, noise, and climate perturbations (e.g., urban heat island effect), maintaining microclimate, preserving biodiversity, improving city water and air quality, and carbon sequestration—but also provide physical and psychological wellbeing to urban dwellers (Ossola & Hopton, 2018). Moreover, UGSs are crucial for urban geography and planning (Shahtahmassebi et al., 2021). However, UGSs are threatened by the currently rising population and increasing urbanization. Thus, adequate management and planning with the detection and monitoring of UGS have become crucial for urban development.

Consequently, various approaches have been developed and employed for collecting information about UGS. First, an extensive field survey examined the largest cities. After that, visual interpretation or manual digitizing from maps or aerial photographs became the primary source of USG mapping from the 1970s to the 1990s (Nowak et al., 1996; Morgan & Gergel, 2013; Shojanoori & Shafri, 2016; Shahtahmassebi et al., 2021). However, these two methods are costly, labor-intensive, subjective, and difficult to replicate. In addition, they is usually limited to the major cities, and only public green areas can be mapped.

Subsequently, remote sensing was introduced in UGS studies at the beginning of the 21st century, quickly becoming the most common and significant technique due to its efficiency and effectiveness. Remote sensing techniques have been proven able to provide valuable information on complete coverage of UGS in highly heterogeneous and complex urban areas in different spatial scales (large or medium scale such as parks or urban forests, and small scales such as private gardens and street trees) and for different seasons compared to the previous approaches (Pu & Landry, 2012). Furthermore, they can effectively generate different characteristics of UGSs, such as spatial distribution and species compositions (Shahtahmassebi et al., 2021). For example, Mathieu et al. (2007) developed a methodology to produce vegetation community maps in Dunedin, New Zealand, by combining orthorectified HR multispectral IKONOS images and a hierarchical OBC approach. The authors extracted all vegetated units in the satellite data and then classified fifteen vegetation classes by performing MRS and nearest-neighbor classification algorithms. Their results demonstrated that the methodology proposed in the paper was sufficiently effective to generate accurate and detailed vegetation communities maps (with 77% OA).

Pu & Landry (2012) focused on mapping seven tree species in the urban forest of the city of Tampa, Florida, USA, by employing OBC in IKONOS imagery (4 m of spatial resolution) with four spectral bands and WV2 imagery (2 m of spatial resolution) with four traditional bands. Both images were segmented with the MRS algorithm, after which the different tree species were extracted using two advanced classifiers, Stepwise Discriminant Analysis (SDA) and CART. The results showed that trees were successfully extracted from both images. Furthermore, WV2 imagery (with both bands) significantly

increased the accuracy of identifying most of the tree species compared to IKONOS imagery, likely due to the finer spatial resolution.

Meanwhile, Tigges et al. (2013) discussed the benefits of multitemporal RapidEye satellite data (5 m of spatial resolution) in urban vegetation classification. The authors investigated the potential of different spectral and temporal band combinations of five RapidEye images and an SVM classifier to perform high-precision classification of eight frequently occurring tree genera in Berlin, Germany. The results confirmed the possibilities of classifying tree genera in a heterogeneous urban structure with a high density of trees with Multitemporal and multispectral HR RapidEye images.

Even though the accuracy and efficiency of UGS mapping were considerably increased due to remote sensing techniques, UGSs remain challenging to monitor for several reasons: (1) urban environments are commonly characterized by the complex and spatially and spectrally heterogeneous landscape; (2) UGSs are generally on a smaller scale than forests (from small patches of vegetation to scattered trees), which frequently change due to urbanization policies and increasing artificialization; and (3) urban land cover classification is highly affected by the problem of shadow resulting from the complex dimensional structure of urban areas (Adeline et al., 2013).

Moreover, the traditional classification methods and medium- or high-spatial-resolution remote sensing data allow only brief mapping of the spatial distribution of UGSs and identifying the main categories of vegetation (trees, shrubs, or grassland). Therefore, UGS classification remains a significant challenge that continues to attract interest from remote sensing communities and decision-makers.

In recent years, the already significant number of UGS studies has rapidly increased even further. Fine-scale UGS mapping has become possible due to the arrival of the new generation of free-access high-quality optical and SAR satellite data with very high temporal spectral and spatial resolution, the emergence of available LIDAR and hyperspectral data (Voss & Sugumaran, 2008; Alonzo et al., 2014; X. Tong et al., 2014; L. Liu et al., 2017), advance classification algorithms, and the increase in available computational power (Neyns & Canters, 2022).

In particular, VHR imagery (< 1 m of spatial resolution) and advanced ML algorithms are widely applied in a variety of thematic areas of applications of remote sensing in USGs studies, including change detection (Rafiee et al., 2009; X. Zhou & Wang, 2011; Qian et al., 2015), biomass and carbon estimation (C. Liu & Li, 2012; Raciti et al., 2014), and urban vegetation mapping and characterizing (Höfle et al., 2012; T. Liu & Yang, 2013; Q. Feng et al., 2015), especially urban garden (Baker et al., 2018; Haase et al., 2019) and street tree mapping (Puissant et al., 2014; Parmehr et al., 2016). Ardila et al. (2011) proposed a method for the detection of tree crowns in complex urban areas by using a Markov random field (MRF)-based Super-Resolution Mapping (SRM) approach, which took account of the spatial smoothness prior and the conditional probability of multispectral and panchromatic bands of VRH QuickBird satellite images (spatial resolution ranged from 450–900 nm). The method was found operational and effectively improved tree crown detection over other ML methods, such as MLC and SVM.

Hashim et al. (2019) evaluated the use of VHR remote sensing data (i.e., Pléiades) for urban vegetation mapping in Kuala Lumpur, Malaysia. The authors employed NDVI as the VI and supervised MLC as a classification algorithm for extracting the UGSs. The method proved effective and accurate with a relatively high accuracy indicator (70.74% OA).

Furthermore, the arrival of DL classification methods has significantly improved the accuracy of UGSs mapping. Z. Xu et al. (2020) proposed a new DL classification method for performing real-time, accurate and refined monitoring of UGS status by using phenological feature constraints provided by VHR images (GaoFen-2). The study employed a high-resolution deep NN (HRNet) as a classification model and the Focal Tversky Loss function to minimize the difference between the predicted value and actual value of the model. The results showed that the combination of the DL method, VHR images, and loss function significantly improved the accuracy of urban vegetation classification (with 93.24% OA).

In another study by Abbas et al. (2021), the authors performed another DL method, MLP, on terrestrial hyperspectral data provided by SPECIM-IQ sensor for identifying and characterizing 19 urban tree species in the city of Hong Kong, one of the most urbanized areas in the world. The MLP model used in the study contained three hidden layers, and

the SoftMax function was applied at the output layer. The results showed that the MLP DL model achieved high accuracy (ranging from 85% to 96%) and proved its efficiency in an intensely urban environment.

5.2. Study area and materials

5.2.1. Study area

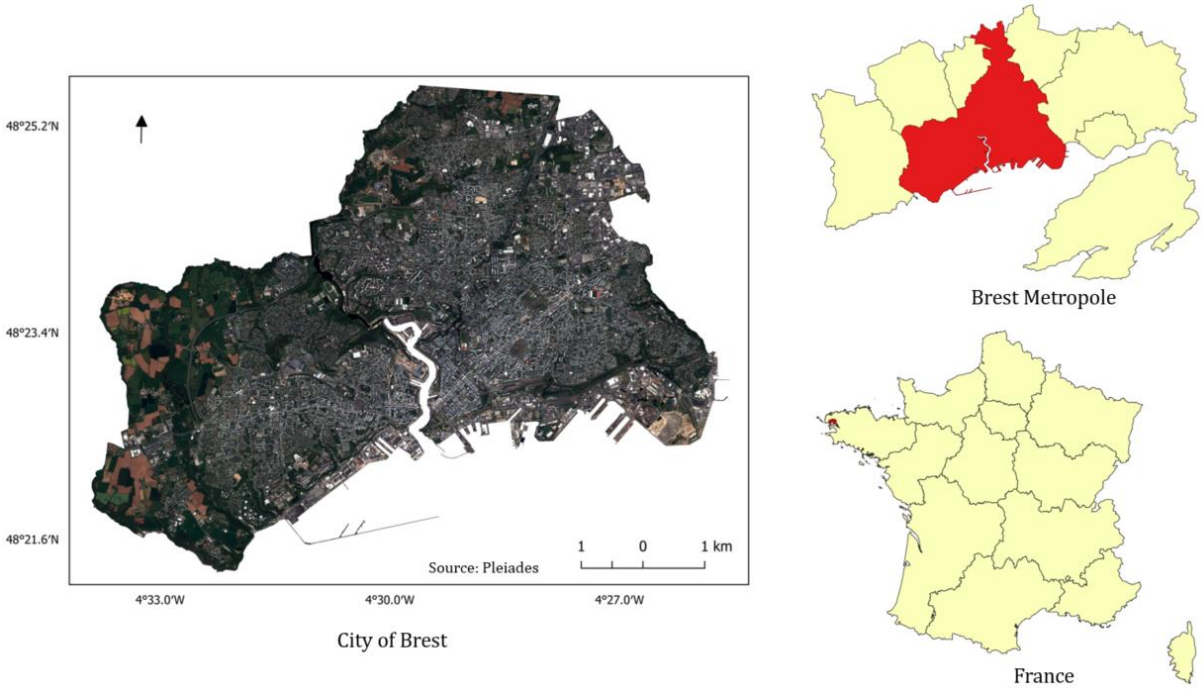

Figure 53 Localization of the city of Brest

The study area, Brest (Figure 52), is a coastal city and the most important urban area of the department of Finistère (48° 23′ 27″, 4° 29′ 08″), which is located on the west coast of the region of Brittany, France. The city of Brest covers a land surface of 49.51 km^2, and the population was 319,947 in 2016.

Brest is mainly occupied by artificial areas, including various types of construction and sealed surfaces located mainly in the city's center; military areas and harbors can be found in the south near the ocean. Moreover, a variety of UGSs are present, which are enumerated below (Figure 53):

Figure 54 Vegetated areas in the city of Brest: (a) urban forest (b) meadow (c) public park in the city center (d) croplands (e) street trees (f) private gardens in the residential area

Although the city of Brest occupies a large urban surface area, vegetation plays a significant role in city planning. The vegetated areas in Brest can be categorized as natural and semi-natural areas and artificial vegetation. The first category includes principally: (1) urban forest (dry and mesophilic or wet), mainly located in the west, east, and center near the Penfeld River; (2) thicket, a specific landscape dominated by a very dense stand of trees or tall shrubs concentrated in the south, close to the harbors; and (3) meadow and lawn, which are evenly distributed in the city, especially in the periphery. The artificial vegetated areas include: (1) croplands located in the western and northern Brest; (2) street trees and public parks in the city center, intended to provide physical and

psychological benefits for urban inhabitants; and (3) private gardens in the residential areas.

5.2.2. Data

In this study, three VHR Pléiades satellite images used are displayed as follows (Table 7):

Table 7 VHR Pléiades satellite images used in the study

Imagery	Date	Spatial resolution(m)	Number of bands
Pléiades 1B	04-05-2016	0.5	4
Pléiades 1B	27-08-2017	0.5	4
Pléiades 1B	28-06-2018	0.5	4

Pléiades is a twin optical satellite launched in 2011 (Pléiades 1A) and 2012 (Pléiades 1B) for Earth monitoring. Two satellites operated on the same orbit can provide a 50 cm spatial resolution panchromatic image and a 2 m spatial resolution multispectral band (red, blue, green, NIR) image with a 20 km swath width and daily revisit time.

In our research, three ready-to-use pan-shaped multispectral images were downloaded from the DINAMIS platform (https://dinamis.teledetection.fr/home) through l'EQUIPEX GEOSUD. Furthermore, different scenes were merged to create a whole image covering our entire area of interest. Then the images were clipped by the contour of the city of Brest to extract the study area and remove the undesired area. Eventually, a new band of NDVI was calculated with the visible red and NIR spectral channels and added to the original spectral bands to improve vegetation classification accuracy.

5.3. Methodology

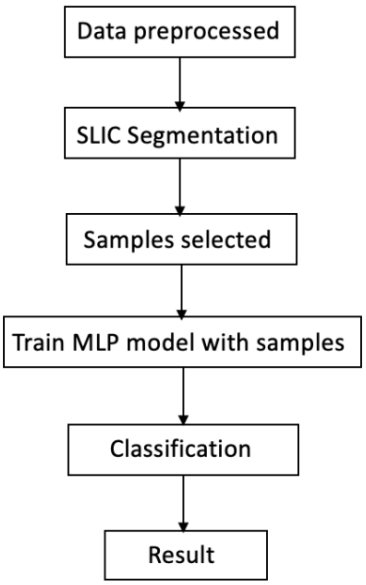

Figure 55 Scheme of the proposed methodology in the study

In this research, the OBC approach was performed on the preprocessed VHR Pléiades satellite data using the SLIC superpixel segmentation algorithm and an MLP DL classification model, detailed in Chapter 4 ("Analysis and image processing") (Figure 54). At first, the SLIC superpixel algorithm was used for segmentation before classification, after which training samples were selected manually from the segmentation results to train the MLP model, and a trial-and-error method was used to find the optimal parameters. Finally, the well-trained MLP model was applied to the entire scene for image classification.

5.3.1. SLIC Segmentation

As described previously, superpixel algorithms have recently become widely used in computer vision; they can effectively cluster pixels into regions to reduce the size of the image and the complexity of image processing tasks, thereby providing better performance and results. SLIC, recently developed, is a fast and memory-efficient algorithm of superpixel developed by Achanta et al. (2010) It adapts the traditional k-means segmentation methods to superpixel generation, adheres well to the boundaries,

and has a better performance on segmentation by grouping pixels into *N* regions based on their color similarity and spatial proximity (Achanta et al., 2012).

The SLIC algorithm was applied to both images using scikit-image, an image-processing library of python. In this function, three parameters were generated by the user:

- N_segments, which is the approximate number of clusters in the segmented output image (value = 1,600,000)
- Compactness the balance between color proximity and space proximity (value = 1)
- Sigma, the width of the Gaussian smoothing kernel for pre-processing for each dimension of the image (value = 2)

Training samples of each class were selected manually from the image segmented; 80% of the samples selected were assigned to training data, and 20% were assigned to validation data. Once samples were selected, tables containing the mean value of each spectral band of all pixels belonging to the same segments were created for MLP model training.

5.3.2. MLP model training and classification

MLP is one of the most well-known supervised ANN classification methods, which refers to a multilayer feedforward NN that includes at least three layers: an input layer to receive signals, an output layer to provide the prediction of result, and at least one hidden layer constituted by neurons with a non-linear activation function. The number of hidden layers and the number of neurons above can be varied according to the user's need. In general, more neurons gave greater sensitivity to the problem, but this also may lead to an overfitting problem (Murtagh, 1991).

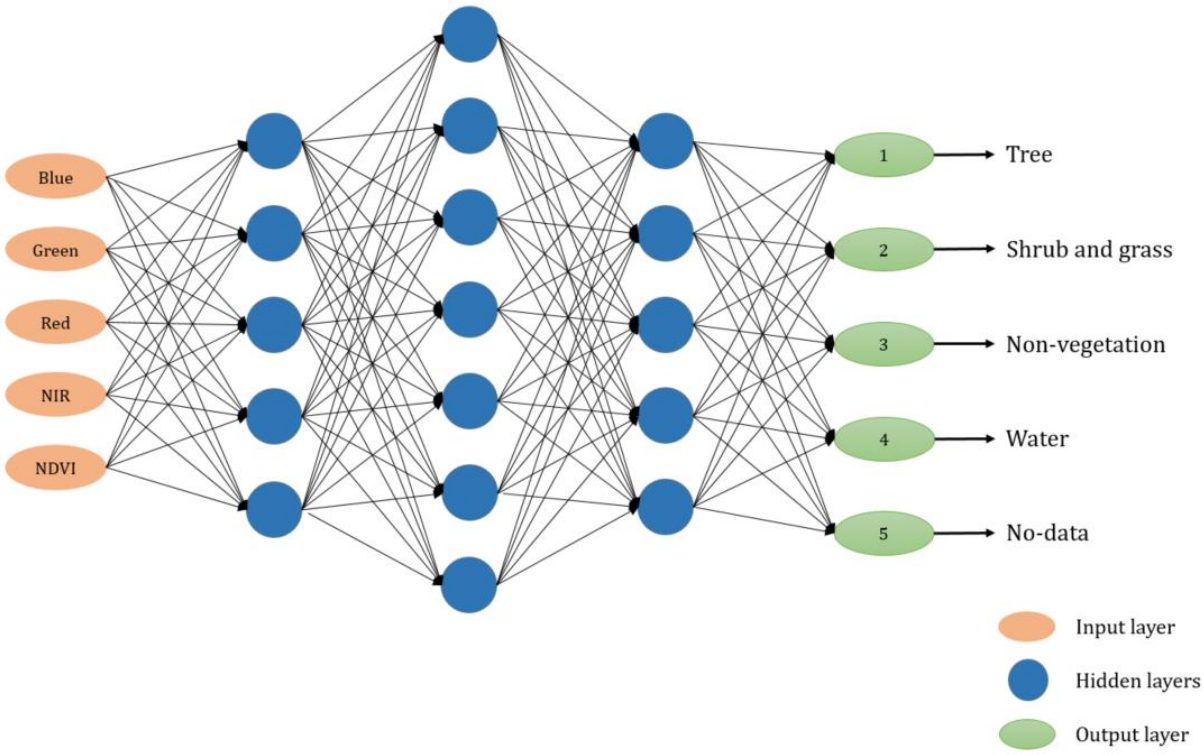

Figure 56 MLP model used for classification in the study

As displayed in the figure 55, the MLP model used for classification was composed of one input layer with five nodes referring to five spectral bands (green, blue, red, NIR, and NDVI), three hidden layers with *tanh* activation function, and one output layer with five nodes referring to five output classes (tree, shrub and grass, non-vegetation, water, and no data). A softmax activation function was applied, and the model was also compiled by RMSprop as an optimizer, categorical_crossentropy as a loss function. The batch size and the epoch value were set to 500 and 200, respectively.

5.4. Results and discussion

5.4.1. Classification accuracy of MLP algorithm

The processing chain presented in the previous section was used on three VHR satellite images acquired in the same scene: the city of Brest. Various accuracy indicators of the MLP model are presented in Table 8 and 9. The evaluation of classification accuracy was performed only on the image of 2016 due to the similarity of the three images. It is worth noting that minor errors may exist between classification results and terrain truth;

precise spatial information is not available for some areas in Brest for reasons of military security.

Table 8 OA of vegetation classification

Class	Overall Accuracy
Tree	0.92
Shrub and grass	0.99
Water	0.91
No vegetation	0.99
No data	0.99
Total accuracy	0.99

Table 9 Confusion matrix and global kappa coefficient of vegetation classification

	Tree	Shrub and grass	Water	No vegetation	No data
Tree	5389	482	0	10	0
Shrub and grass	273	24873	0	20	0
Water	12	1	987	87	0
No vegetation	52	42	73	100270	0
No data	3	1	0	2	5963

Kappa = 0.982552495

As shown in Table 8, the MLP algorithm generally achieved very high accuracy in vegetation classification, especially in low- and non-vegetation categories. Several errors occurred in the tree and water categories, although the result was still acceptable.

According to Table 9, the primary error was the misclassification between different vegetation heights. For example, many trees were misclassified as shrubs or grasses. Meanwhile, the misclassification between water and non-vegetation may be attributable to the similarity of their spectral behaviors. Considering that most of the non-vegetation was found in the urban area, artificial surfaces and construction could cause mirror reflection as the water surface. In addition, the global kappa was also very high, which indicates high agreement between the classification and ground truth.

To sum up, the DL MLP algorithm extracted vegetation in a highly heterogenous and complex area with high construction density. VHR remote sensing data was well adapted for urban area classification due to the small scale of objects.

Additionally, three classified maps are demonstrated in Figure 57.

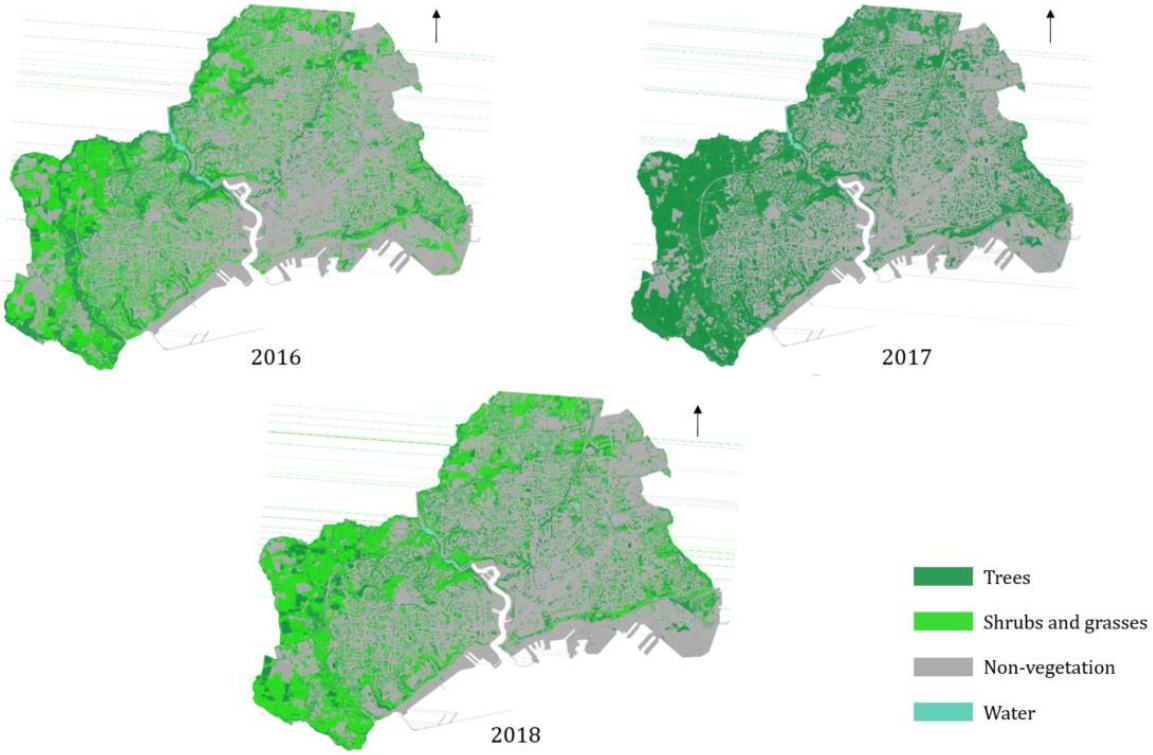

Figure 57 Classification results of vegetation in the city of Brest on 2016, 2017, and 2018 by using MLP deep structure

According to the classification results, the classification results for 2017 found more trees than for other years due to the lack of available images in the same period (the 2017 image was acquired in late August, whereas the 2016 and 2018 images were acquired in late May or early June), as well as and meteorological conditions. The vegetation may differ between early and late summer, especially because the crops generally achieved their maximum height just before harvesting in late August or September and are thus easily confusable with high vegetation.

Some changes between high and low vegetation were also common in the results. For example, some high vegetation in 2016 turned to low vegetation in 2018 in the urban forest near the Penfeld River in the center, and in southwestern Brest, these changes were likely due to pruning, or to misclassification errors. However, most of the vegetation in

the city of Brest remained unchanged during these three years. The croplands were located mainly in the north and the west of the city, and vegetation in the form of grass and trees was evenly distributed in the city as street trees and public gardens. In addition, urban forests were located in the northeast, southeast (botanical garden), and in the Penfeld River near the city center.

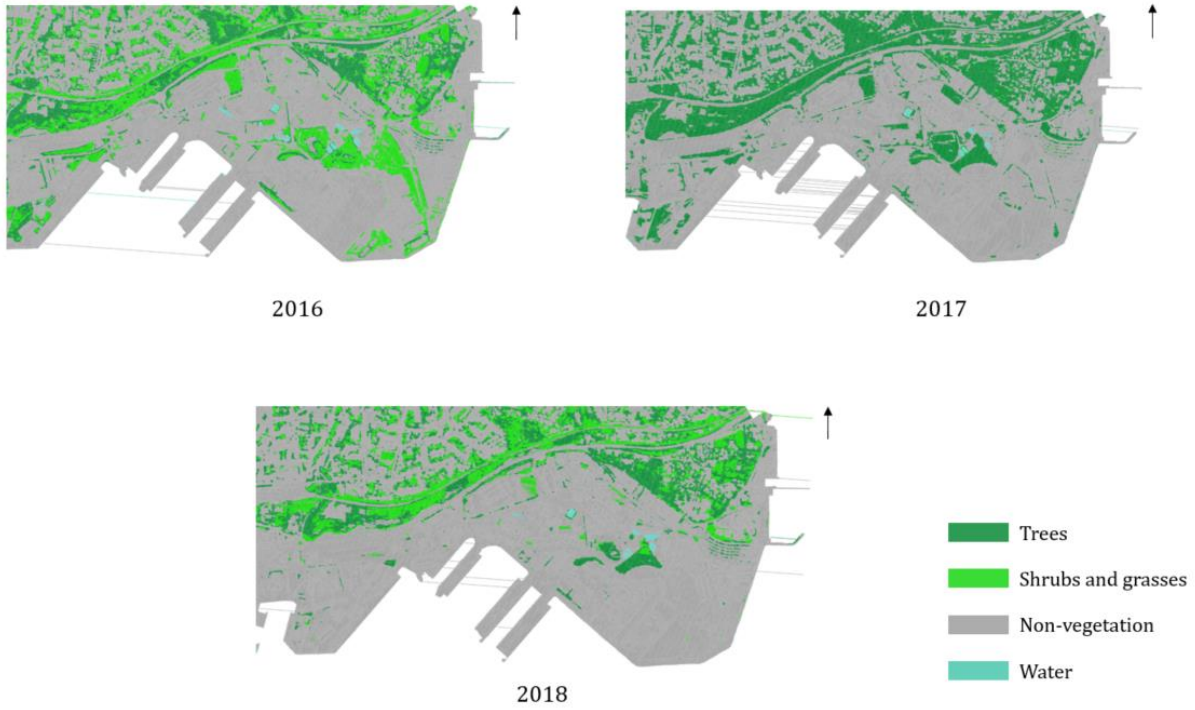

Figure 58 Example of a transition from vegetated area to non-vegetated area in Brest between 2016 and 2018

Besides the transition between high and low vegetation, the changes between vegetation and non-vegetation were also well detected. For example, in Figure 58, aside from the vegetation types of the site, three classified maps of 2016, 2017, and 2018 demonstrated a gradual depletion of vegetation in an industrial area in southeastern Brest. Therefore, this site was likely under construction, and the vegetation was removed for this purpose. The hypotheses were further confirmed by the satellite images of 2016 and 2018 (Figure 59).

Figure 59 Example of transition from vegetation to artificial surface

Overall, the combination of the DL algorithm and VHR images can effectively detect the transition of different LULCs in the urban area, particularly the LULCCs between vegetation and non-vegetation, regardless of the types and scales of the changes.

5.4.2. Comparison with RF classification results

Furthermore, one of the most widely used and efficient ML classifiers, RF, was also used in this study to compare the two classification methods (MLP and RF). This method applied supervised classification to the same VHR Pléiades image with manually selected training samples.

The accuracy assessment of the RF classification is demonstrated in the table 10, and the three classified maps are displayed in the figure 60.

Table 10 Kappa coefficients and OA indicators of RF classification results from 2016 to 2018

	2016	2017	2018
kappa	0.97	0.88	0.85
Overall accuracy	0.98	0.92	0.90

As shown in Table 10, the RF classifier accuracy indicators of all three years are generally high; the kappa coefficient ranged from 0.85 to 0.97, and the OA ranged from 0.90 to .098. The most accurate result was obtained from the 2016 image (0.98 of OA and 0.97 of kappa). However, the classification results obtained from the 2018 Sentinel-2 image were less accurate, with 0.85 in kappa and 0.90 in OA. The difference in kappa was

more important than the OA difference between the most and the least accurate results. Additionally, the OA was globally higher than kappa, which may indicate that the global classification accuracy was better than interclass accuracy.

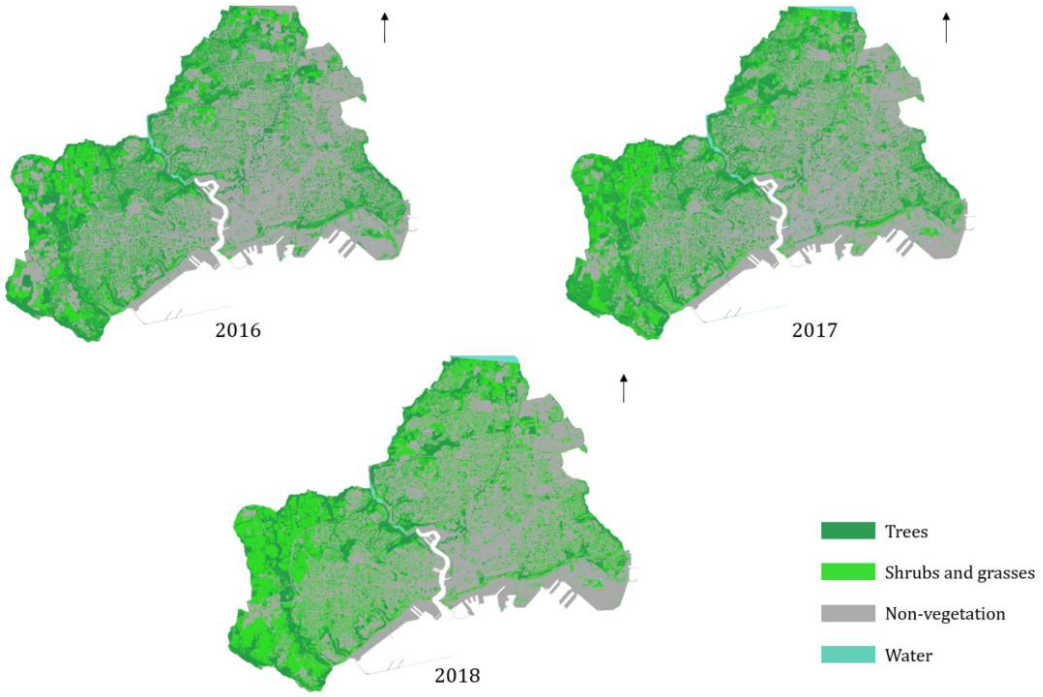

Figure 60 Classification results of vegetation in the city of Brest in 2016, 2017, and 2018 using RF machine learning classifier

Figure 61 Comparison of MLP and RF classifiers

The classification results of the RF classification algorithm (Figure 60) showed a substantial similarity with those of the MLP classifier, particularly the spatial distribution of the vegetation in Brest (Figure 61). Thus, apart from the changes in croplands due to

the acquisition date of three images, most LULC in the city of Brest remained unchanged for three years, regardless of class, according to the RF method.

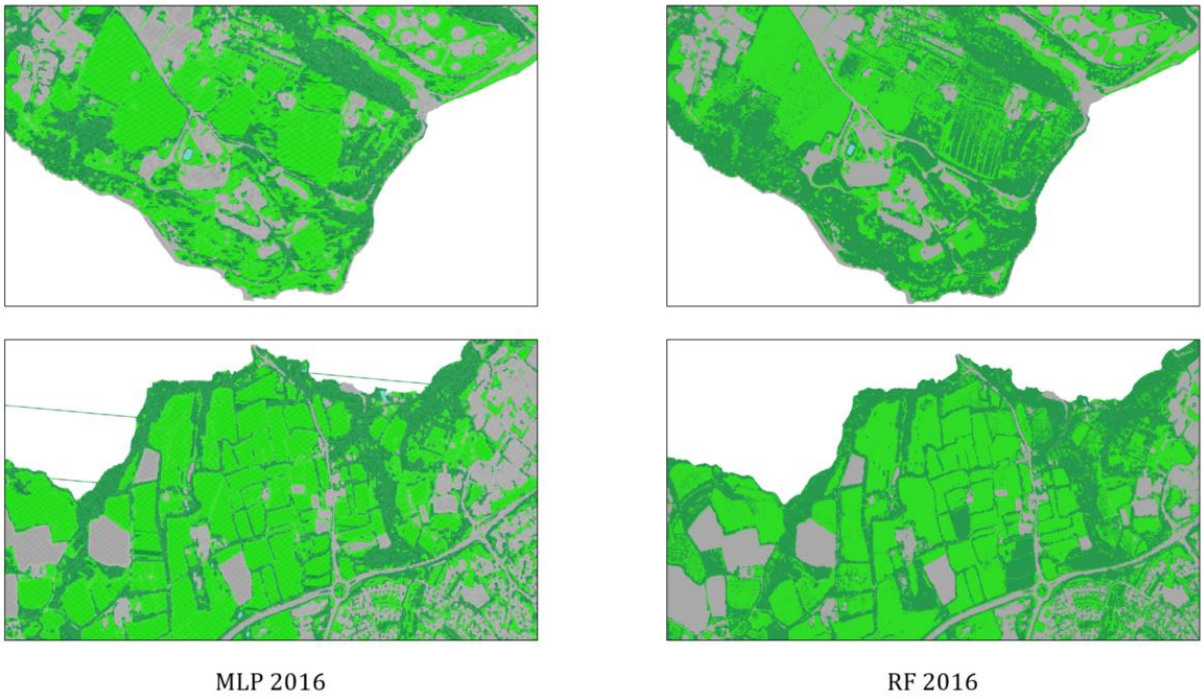

Figure 62 Differences between MLP and RF classification results

Nevertheless, some differences could still be noticed between the classification results of the two classifiers. Regardless of the classification method, the boundary between vegetation and non-vegetation was clear, but the disagreement between high and low vegetation classes was more critical. For instance, according to Figure 62, although the two algorithms were used on the same satellite image, RF detected more trees or high vegetation. At the same time, MLP found more shrubs and grass or low vegetation, even in some croplands. Thus, the RF algorithm resulted in greater confusion between high and low vegetation in this case, which led to the misclassification of low vegetation.

Overall, MLP and RF obtained identical and satisfactory results (close to 1) of simple vegetation extraction in a complex and heterogonous urban environment by using the new generation of VHR remote sensing data. The vegetated area was especially well extracted, and the changes between vegetation and artificial surface were also successfully detected by both classifiers. However, RF may misclassify some low vegetation as high vegetation, which leads to lower accuracy. Furthermore, the evaluation

of two classification methods indicated that MLP outperformed RF, given that MLP successfully resulted in more accurate results in vegetation classification, although RF is recognized as a powerful machine learning classification tool as well.

5.5. Conclusion

In this study, MLP, a DL method, was applied to Pléiades VHR resolution satellite images from three years (2016–2018) in the city of Brest to study the spatial distribution and changes of UGSs in Brest, a highly heterogeneous urban area. Moreover, the performance of MLP was evaluated and compared to RF.

In Brest, the UGSs are not only segmented and on a small scale (e.g., street trees); they are also highly varied, including urban forests, public parks, private gardens, and croplands. It is, therefore, challenging to obtain accurate classifications.

In response to the challenge, this study proposed an OBC-based DL classification method. The processing chain began with SLIC superpixel segmentation to create objects. The training dataset was then selected manually based on segmentation results with the aim of MLP deep architecture training. Finally, three satellite images were fed into the well-trained model to generate the classification result.

According to the accuracy assessment, the classification results of the MLP deep structure model were highly accurate (0.99% OA and 0.98 kappa coefficient), and both classes were also well classified, despite slight confusion between trees and shrubs and grass. Moreover, the changes in vegetation and the transition between vegetation and non-vegetation were also adequately detected. Therefore, combining the SLIC segmentation algorithm, MLP, and VHR remote sensing data was suitable for UGS mapping and change detection in the urban area.

Furthermore, the RF classification method showed highly similar results to those of MLP, although they were less accurate and involved more misclassification between high and low vegetation.

Therefore, vegetation extraction with simple categories (high and low vegetation) is easy to perform and achieves high accuracy. Various classes should be considered for further studies, such as different tree species and crop types.

Chapter 6. Mapping and Monitoring of Land use/Land cover Changes in the Crozon Peninsula (Brittany, France) from 2007 to 2018 by Machine Learning Algorithms (Support Vector Machine, Random Forest, and Convolutional Neural Network) and by Post-classification Comparison

Journal article: Xie, G.; Niculescu, S. Mapping and Monitoring of Land Cover/Land Use (LULC) Changes in the Crozon Peninsula (Brittany, France) from 2007 to 2018 by Machine Learning Algorithms (Support Vector Machine, Random Forest, and Convolutional NN) and by Post-classification Comparison (PCC). Remote Sens. 2021, 13, 3899. https://doi.org/10.3390/rs13193899

Review: Remote sensing

Published date: 29 September 2021

6.1. Introduction:

Coastal zones are the shores of seas or oceans. Today, nearly half of the world's population lives in coastal regions where multiple activities are developed (Crowell et al., 2007). Over the last century, coastal zones throughout the world have undergone major changes related to a significant influx of the population. Coveted, densely populated, and exploited by human societies, coastal zones are therefore subject to significant pressures that generate territorial dynamics and changes in LULC. LULC is always influenced by human actions and environmental features and processes, and it mediates the interactions of these two factors. This means that land use changes are primarily due to human actions, which are associated with economic development, techneology, environmental change, and especially, population growth, which usually has parallel rates to land use change (Waldhoff et al., 2017; Briassoulis, 2020). However, traditional methods require direct observations in the field; usually, they are not only ineffective, expensive, time-consuming, and labor intensive but are also limited on the local scale.

Hence, remote sensing with analysis techniques is highly recommended, and there has been an in-creasing demand for LULC studies since the first launch of Earth observation satellites in 1972 with Landsat-1. Since that time, the monitoring and mapping of LULCs over large areas and in a consistent manner has been made possible with EO data, and detection of these changes by EO data is necessary for the better management of territory and resources. Moreover, each new generation of satellite equipment increases the resolution of sensors that collect high spatial resolution data for LULC mapping and monitoring (Giri et al., 2013). Since high-resolution satellite images are now available, land cover change mapping and monitoring at the landscape or local scale have been developed at a high rate of speed (Y. Xie et al., 2008; L. Ma et al., 2019; Chughtai et al., 2021).

Several national and international organizations have produced regional land change maps that represent a location on a single date (e.g., CLC 2000 in Europe), with Landsat observations acquired in a target year interval (e.g., ±1–3 years). Some programs repeat land cover mapping periodically (e.g., NLCD 2001/2006/2011 in the USA and CESBIO in France) to allow the observation of the changes. The local accuracy of these global or national land cover maps generated from coarse spatial resolution data is low, especially in regions with fragmented land covers (T. Zeng et al., 2019).

At the same time, for studies at larger scales, satellite data have been used to monitor LULC changes worldwide in various fields of research, such as mapping cropland conversions (L. Zhu et al., 2019), monitoring urbanization and its impacts (H. Xu et al., 2000; Dewan & Yamaguchi, 2009; Xiong et al., 2012), monitoring deforestation (Frohn et al., 1996; J. Gao & Liu, 2010; Brink et al., 2014; Weng et al., 2018; de Bem et al., 2020) ,evaluating the environment (Wilson et al., 2003; C. He et al., 2017; J. Li et al., 2020) and biodiversity losses, and examining the influence of LULC on climate change (Mahmood et al., 2010). Nonetheless, all types of land use might lead to detrimental impacts and effects in many fields: for example, the abandonment of agricultural land without restoration is linked to a specific set of problems, including landscape degradation and an increased risk of erosion (Giri et al., 2013). These irreversible impacts of LULC change have significantly increased in recent decades, and so the mapping and

monitoring LULC is very important as the first step in the study and management of this phenomenon.

In recent years, given the importance of LULC changes and the increasing availability of open-access archived multi-temporal datasets, many methods for analyzing and mapping LULC changes have been developed. The diversity of algorithms for studying LULC changes was also determined by the diversity of remote sensing sensor types (e.g., multispectral, hyperspectral, and SAR). Among the most commonly used satellite images in change detection (CD) studies are multispectral images due to the diversity of the types of sensors used to collect the data and the high temporal resolution of datasets for this type of study. For example, Z. Wang et al. (2018) conducted a study in a coastal area of Dongguan City, China, using SPOT-5 images acquired in 2005 and 2010. In this study, a scale self-adapting segmentation (SSAS) approach based on the exponential sampling of a scale parameter and the location of the local maximum of a weighted local variance was proposed to determine the scale selection problem when segmenting images constrained by LULC for detecting changes. Tran et al. (2015) conducted a study in coastal areas of the Mekong Delta on changes in LULC between 1973 and 2011 from Landsat and SPOT images. The supervised maximum likelihood classification algorithm was demonstrated to provide the best results from remotely sensed data when each class had a Gaussian distribution. Guan et al. (2020) studied a CD and classification algorithm for urban expansion processes in Tianjin (a coastal city in China) based on a Landsat time series from 1985 to 2018. They applied the c-factor approach with the Ross Thick-LiSparse-R model to correct the bi-directional reflectance distribution function (BRDF) effect for each Landsat image and calculated a spatial line density feature for improving the CD and the classification. Dou & Chen (2017) proposed a study in Shenzhen, a coastal city in China, from Landsat images using C4.5-based AdaBoost, and a hierarchical classification method was developed to extract specific classes with high accuracy by combining a specific number of base-classifier decisions. According to this study, the landscape of Shenzhen city has been profoundly changed by prominent urban expansion.

In addition, in recent decades, remote sensing techniques have progressed, and many methods, such as machine learning, have been developed for LULC change studies, such as SVMs, RFs, and CNNs. Nonparametric machine learning algorithms such as SVM

and RF are well-known for their optimal classification accuracies in land cover classification applications (Shi & Yang, 2015; Zafari et al., 2019; Sheykhmousa et al., 2020). These algorithms have significant advantages and similar abilities in classifying multitemporal and multisensor data, including high-dimensional datasets and improved overall accuracy (M. Pal, 2006; X. Song et al., 2012). The accurate and timely detection of changes is the most important aspect of this process. Moreover, CNN, a more recently developed but well-represented deep learning method, allows the rapid and effective analysis and classification of LULCs and has proven a suitable and reliable method for accurate CD in complex scenes. Although it is more recent, many studies have made use of this method. M. Wang et al. (2020) proposed a new coarse-to-fine deep learning-based land-use CD method. In this study, several models of CNN well-trained with a new scene classification dataset were able to provide ac-curate pixel-level range CD results with a high detection accuracy and reflect the changes in LULC in detail. In another study of Han et al. (2020), a weighted Demptster-Shafer theory fusion method was proposed. This method achieved reliable CD results with high accuracy using only two very high-resolution multitemporal images by generating object-based CD through combining multiple pixel-based CDs.

At the same time, in the Pays de Brest, which the Crozon Peninsula is part of, a category of LULC has been studied through shallow machine learning algorithms. Niculescu et al. (2018) and Niculescu et al. (2020)applied the algorithms of rotation forest, canonical correlation forests and RF with satisfactory results for the classification of the different categories of land cover (vegetation) of the peninsula, as well as the summer and winter crops from the synergy of optical and RaDAR data from the Sentinel satellite. LULC changes in coastal areas have been studied with machine learning algorithms in different environments. Muñoz et al. (2021) analyzed the coastal wetland dynamics associated with urbanization, the sea level rise and hurricane impacts in the Mobile Bay watershed since 1984. They developed a land cover classification model with CNNs and a data fusion (DF) framework. The classification model achieved the highest overall accuracy (0.93) and f1-scores in the woody (0.90) and emergent wetland classes (0.99) when those datasets were fused into the framework.

More methodological work on the application of CNNs for CD was conducted by Jing et al. (2020). In this study, a CD method was proposed that combines a multiscale simple linear iterative clustering-convolutional NN (SLIC-CNN) with stacked convolutional auto encoder (SCAE) features to improve the CD capabilities with HR satellite images. This method uses the self-learning SCAE architecture as the feature extractor to integrate multiscale, spectral, geometric, textural and deep structural features to enhance the characteristics of ground objects in images.

Machine learning methods were combined with OBIA techniques by Jozdani et al. (2019) for urban LULC classification. The multilayer perceptron model led to the most accurate classification results in this study. However, it is also important to note that GB/XGB and SVM produced highly accurate classification results, demonstrating the versatility of these ML algorithms.

In this work, we aimed to study multiannual changes of LULC in the Crozon Peninsula, an area that has mainly been marked by conversion between three types of LULC: cropland, urban, and vegetation, in recent years, especially from 2007 to 2018. The challenge of this research was to deal with multiannual changes of a coastal area with different shapes and patterns by combining ML methods with PCC. To improve the CD capabilities using high-resolution satellite images, we implemented three remote sensing machine learning algorithms: SVM, RF combined with GEOBIA techniques, and CNN with SPOT 5 and Sentinel 2 data from 2007 and 2018, all effective and valid data sources. An evaluation of these three advanced machine-learning algorithms for image classification in terms of the OA, PA, UA, and confidence interval was conducted to more precisely detect the type of multiannual change.

6.2. Study area and materials

6.2.1. Study area

The study area, the Crozon Peninsula canton south of the Landerneau-Daoulas canton, is located on the west coast of France in the Pays de Brest, Department of Finistère and the region of Brittany (Figure 63).

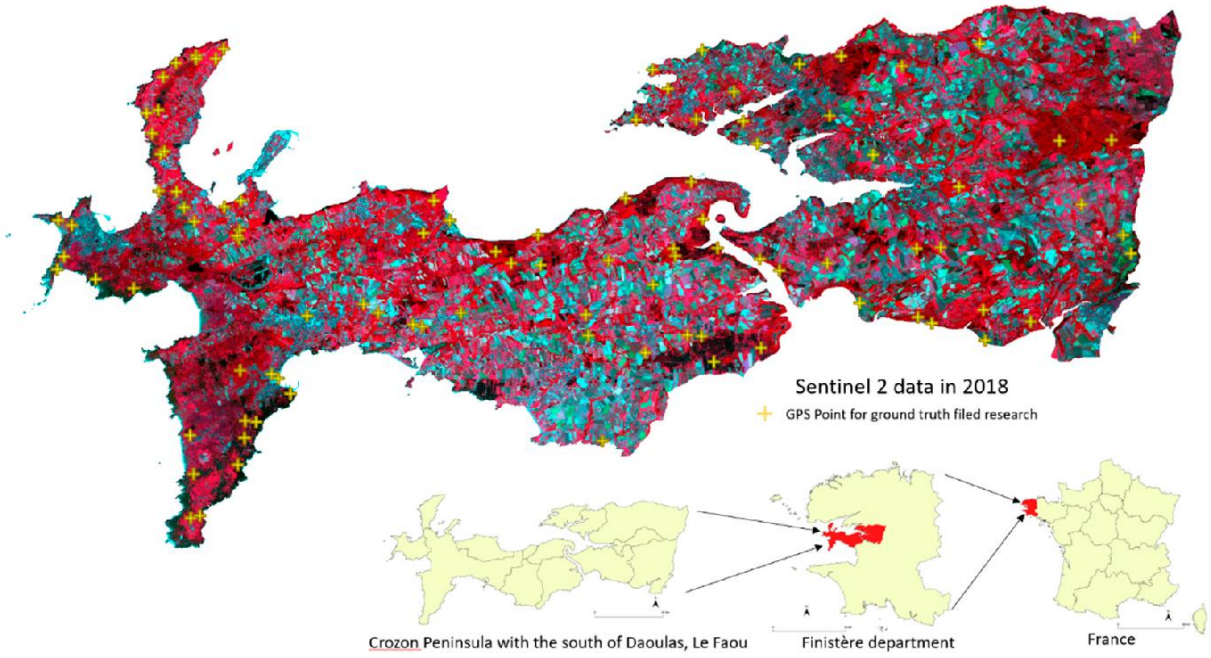

Figure 63 Location of the study area, including the Crozon Peninsula and two bordering regions, located in Pays de Brest, Finistère, Brittany, France, with the RGB band combination for Sentinel 2 (2018) and the location of the ground truth field Research.

It covers a land area of 365.4 km^2 that extends between latitudes 48° 10′04″ N and 48°21′28″ N, longitudes 4°02′44″ W and 4°38′37″ W. The Crozon Peninsula is a sedimentary site with contrasting topography and contours that separate the Bay of Brest and the Bay of Douarnenez. The region is a mosaic of cliffs, dunes, moors, peat bogs, and coastal wetlands. The peninsula thus presents phytocenetic, faunistic, and landscape interests. The population of the study area is 29, 893; this makes the population density approximately 81.6 per km^2. The topography of the Crozon Peninsula is mostly dominated by plains, except for hills in the east and northeast, and the elevation of the area ranges between 0 m and 300 m. The land cover is characterized by forest, shrubs, and grasslands, which are mostly in the west, urban areas, cropland (including mainly corn and wheat) and meadow.

Traditionally, the majority of local people practice agricultural or related activities in the Finistère Department, in which 57% of the department's surface is devoted to agricultural use. However, the French National Defense provides more than half of the employment in the Crozon Peninsula; hence, other activity sectors (e.g., agriculture, industry, construction and commerce) are proportionally less important.

Nevertheless, the land cover was actually in sharp transition in our study area between 2008 and 2018, with the peninsula especially marked by an increasing service and commerce sectors. Therefore, the study area was chosen as a typical ideal case to study land cover changes.

6.2.2. Data

Operable high-quality cloud-free satellite images in this area are extremely rare due to the annual high-intensity rainfall and, hence, heavy cloud cover. Despite these limitations, three cloud-free images from two dates in 2007 and 2018 with the same scene area were acquired from either the SPOT or Sentinel platforms to study land cover changes in the study area during the summer, which is the growing season for crops (Table 11).

Table 11 Satellite images used in the study

Date	Satellite	Spectral Bands	Spatial Resolution
2 July 2007	SPOT-5	Green, Red, Near-infrared	10 m resampled to 2.5 m
24 June 2018	Sentinel-2B	1, 2 (Blue), 3 (Green), 4 (Red), 5, 6, 7, 8 (Near-infrared), 8A, 9, 10, 11, 12	10 m
24 June2018	Sentinel-2B	1, 2 (Blue), 3 (Green), 4 (Red), 5, 6, 7, 8 (Near-infrared), 8A, 9, 10, 11, 12	10 m

First, a SPOT-5 satellite image was obtained from the early summer of 2007. The multispectral SPOT-5 image downloaded from the ESA was obtained by merging the 2.5 m panchromatic band and the 10 m multispectral band, resulting in the spatial information of the image being identical to the information observed with the panchromatic sensor (earth.eas.int).

Second, two level 2A atmospheric effect-corrected Sentinel-2 images of the same date in the middle of the summer in 2018 were acquired from Theia (catalog.theia-land.fr); a mosaic was then created by combining two images to cover the whole study area, and four spectral bands at a 10 m resolution (red, green, blue, and near-infrared) were extracted for further use.

For the purpose of land cover identification at the sample selection step, we also used Google Earth and RPG maps and a French database with agricultural parcel identification as the reference data, complemented by observation and survey in the field when necessary.

6.3. Methodology

The methodology of this paper is detailed in three main parts as follows: preprocessing, image processing, and postprocessing. Three satellite images of two dates were processed in QGIS (SAGA, Grass, OrfeoToolbox7.3.0), eCognition 9.5 and 10.0. A flow chart of the proposed global methodology is displayed below (Figure 64).

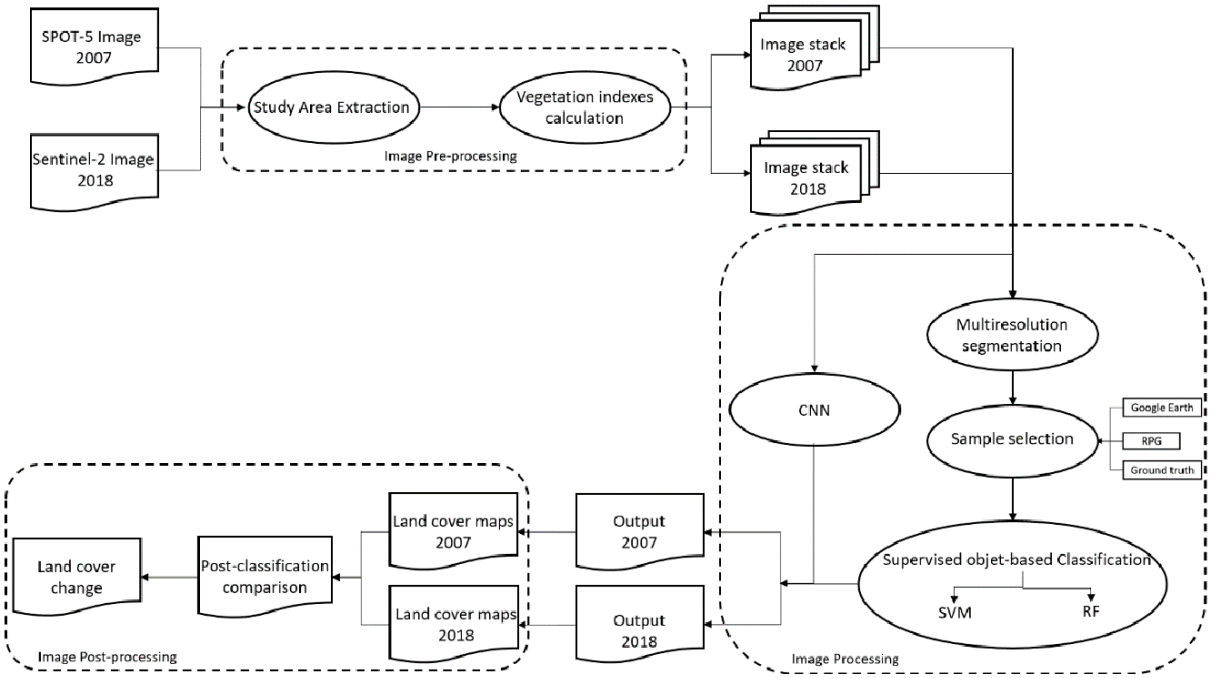

Figure 64 Global methodology proposed

6.3.1. Image preprocessing

After satellite image acquisition, a mosaic of the two images of the same date in 2018 was created to cover the whole study area. Then, the boundary of the Crozon Peninsula and south of Landerneau-Daoulas were used to extract our area of interest by

applying subsets to raw images to reduce the image size, processing time and storage space.

Thereafter, three vegetation indices were calculated and utilized in our study:

- **NDVI**, a normalized ratio between the red and the NIR spectral bands.
- **GNDVI**, which considers the green spectral band instead of red.
- **EVI2** developed as an adaptation of the EVI without the blue band to break through the limit of sensor systems.

After calculating the three vegetation indices, we created an image stack with the original spectral bands and all of the indices for image processing.

6.3.2. Image processing

In this study, supervised object-based classification was performed on two image stacks of two different years. Segmentation was applied first, followed by two nonparametric machine learning algorithms. SVM and RF were trained and applied in this step.

MRS was performed as the first processing step of object-oriented image analysis. In this study, the scale, compactness, and shape parameters used were assigned as follows: 10, 0.1, and 0.3, respectively. The selection of the parameters was completed on a trial-and-error basis.

Afterwards, since Supervised methods were performed in our research, all of the samples presented in Table 12 were selected manually with Google Earth, an RPG map, and ground truth as the reference data, and the ground truth values were taken during a field survey with a GNSS device in August. The samples were then used to train two classifiers in the next step.

Table 12 Training samples surface area for SVM and RF model training in 2007(2a) and 2018(2b).

Class	Area surface of training samples (km^2)
Cropland	13.68
Cropland with bare soils	18.18
Water	00.39
Vegetation	35.61
Non-vegetation	03.86
Total	71.72

2a

Class	Area surface of training samples (km^2)
Cropland	11.76
Cropland with bare soils	17.75
Water	00.14
Vegetation	41.08
Non-vegetation	07.69
Total	78.42

2b

Next, SVM and RF were performed separately on the segmented images as an object-based classifier. The training and classification of the SVM module are applied using ECognition software with a RBF kernel. Furthermore, the module was executed with 10 as its capacity constant, also called the c-parameter, with the aim of minimizing error function and avoiding misclassification problems. Meanwhile, as mentioned in the last chapter, RF classification requires two important user-defined parameters to train the model: Two parameters are set on a trial-and-error basis: the number of decision trees grown in the forest, this parameter was set to 300 and 200 for 2007 and 2018, respectively. In addition, the maximum tree depth, which means the length of each tree in the forest, this parameter was defined as 20 for both years.

Thereafter, CNN deep structure was also applied in the study in order to solve complex problems and recognize image objects with revolutionary accuracy levels that none of the other machine learning approaches have yet achieved. The CNN implemented in eCognition is based on the Google TensorFlow library, and the detailed CNN methodology is demonstrated as follow (Figure 65):

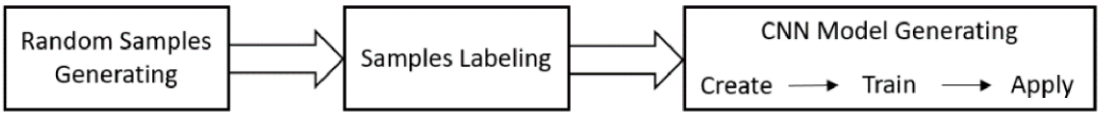

Figure 65 Detailed CNN methodology

Firstly, a well-trained CNN model requires a large number of samples to achieve high accuracy level. All of the training data in this study were thus prepared manually to obtain better accuracy. The samples in the form of points were automatically and evenly selected in QGIS by random selection for the purpose of avoiding bias. We then categorized all of the points manually into five distinct classes and created sample patches by including all of the pixels that surround each point for the model training. The algorithm then shuffled the labeled sample patches and created a random sample order for training.

Secondly, two models were created separately for 2007 and 2018. Each model had two hidden layers, a kernel size for the convolution, a number of feature maps, and a max-pooling step (Figure 66).

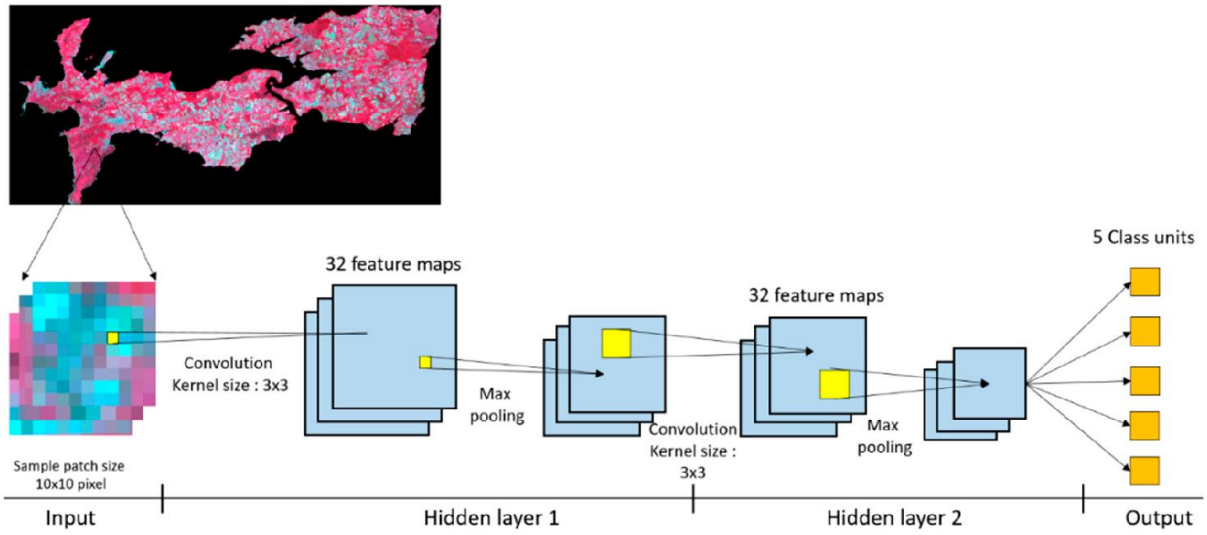

Figure 66 CNN model proposed and used for the classification of images from 2018 in the study

For the processing of the 2007 images, the batch size, the number of training examples utilized in one iteration, was set to 32, the kernel size was assigned to be 3×3

with 64 feature maps in the first hidden layer, and the second hidden layer had a kernel size and feature map of 4×4 and 64, respectively. For the 2018 images, the batch size was set to 10, and both hidden layers were assigned 3×3 and 32 for the kernel size and number of feature maps, respectively. Both hidden layers of the two models contained a max-pooling stage using a 2×2 filter. Then the two models were trained based on the trial-and-error method, with a learning rate of 0.001. After obtaining a satisfactory CNN accuracy, the two models were validated and used to produce the classification of two satellite images, from 2007 and 2018 separately.

6.4. Image post-processing

6.4.1. Accuracy assessment

The accuracy assessment statistics of the classifiers (SVM, RF and CNN), based on confidence intervals (P. Olofsson et al., 2014), were calculated for each method and each class to check the model training and classification quality by comparing the classification with the reference values. The accuracy assessment used in this study included three indices: OA, PA, and UA —which are among the best-known and most highly promoted quantitative accuracy assessment metrics for the evaluation of classification quality or for comparisons among different classifications.

Moreover, the indices of the accuracy assessment were generated with an algorithm from Olofsson based on the confidence interval. Therefore, all indicators presented in the tables are followed by an uncertainty rate. A higher uncertainty signifies that a larger accuracy rate can vary; in contrast, a small uncertainty represents a relationship with a certain accuracy.

6.4.2. Post-Classification Comparison (PCC)

To analyze the land cover changes between 2007 and 2018, a PCC was performed with the semi-automatic classification plugin on QGIS. The open-source plugin allows two classified images to be taken as the input (a new map and a reference map), then creating

an overlap of these images to cross the data at the pixel level and differentiating the land cover changes according to the differences between the two maps. As the output, a change layer is created, and there is also a table that shows how the pixels move between the classes.

6.5. Results and discussion

6.5.1. Comparison of classifiers

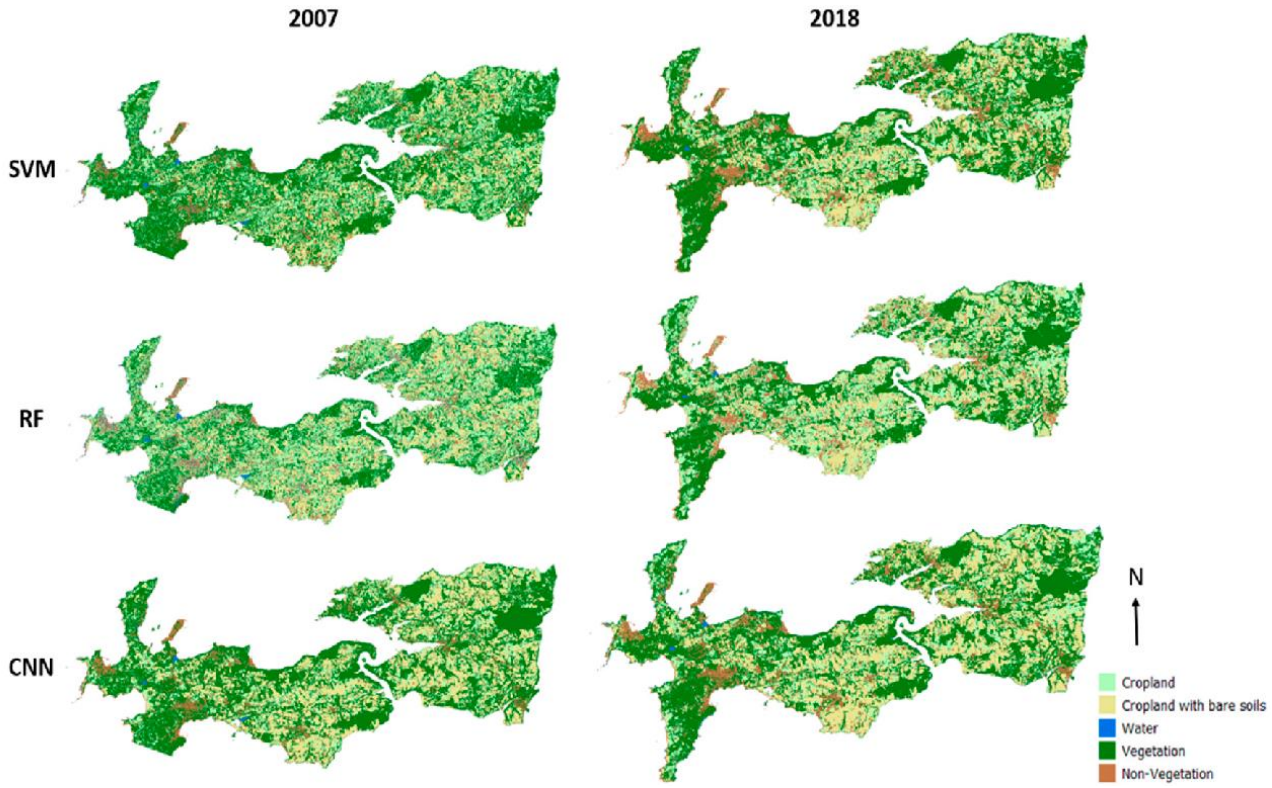

Figure 67 Classification results with SVM, RF and CNN

The classification results of the three methods for the two years are presented in Figure 67. The five classes detected in the classification process were cropland; cropland with bare soil; water; vegetated area; and non-vegetation, including urban area, sand, and rocks. Although some differences might exist, generally, the vegetation, non-vegetation, and cropland could be well-identified from different maps, which are globally identical. The vegetation is located in the south and east, with some vegetation near the coastlines,

similar to the most important urban areas. In contrast, all of the cropland is in the interior of the peninsula.

To make better comparisons possible, each accuracy assessment in this paper is split into two tables, which are the training accuracy and validation accuracy, allowing for cross-validation to avoid the problem of overfitting or underfitting. The training accuracy was computed and used to improve the model performance and classification quality during the classification processing based on the training dataset; otherwise, the validation accuracy was used with the validation data to evaluate each model's final prediction.

Table 13 Training OA (%)

Methods	2007	2018
RF	82.72 ± 01.79	76.78 ± 03.40
SVM	77.17 ± 02.20	81.14 ± 03.18
CNN	89.15 ± 01.36	83.16 ± 01.64

Table 14 Validation OA (%)

Methods	2007	2018
RF	80.23 ± 03.87	70.51 ± 08.38
SVM	77.03 ± 04.36	78.14 ± 06.40
CNN	83.11 ± 03.27	79.85 ± 03.58

According to Table 13 and 14, all of the accuracy indices range from 70% to 90%, and the two tables are very similar. Although the training accuracy is slightly higher and more certain (approximately 2–6%), it suggests a good performance and good training of all three models, a strong level of agreement, and a high level of reliability. Beyond that, it is worthwhile to note that the CNN demonstrated better potential (approximately 1–12% higher in accuracy) for the classification of land cover monitoring than RF and SVM in both years, and it is the most stable and certain method, given its low uncertainty of approximately 1.50 for training accuracy and 3.50 for validation accuracy in comparison with the other methods. In general, the 2007 images have better accuracy indicators and lower uncertainty rates than the 2018 images, and RF achieved better accuracy and lower uncertainty in the 2007 images than in the 2018 (e.g., 80.23 ± 03.87% and 70.51 ± 08.38% for 2007 and 2018, respectively, in the validation accuracy assessment), which is the

opposite of SVM (e.g., 77.03 $\pm$ 04.36% and 78.14 $\pm$ 06.40% for 2007 and 2018, respectively, in the validation accuracy assessment). The most reasonable explanation is that the 2018 images have a rougher resolution than the 2007 images, and so fewer pixels are present in each segment, and since the SVM needs fewer samples and pixels to train the model, it achieved a better performance with the 2018 images.

The PA and UA of each class with the three methods in both years are listed in Table 15 and 16. Table 15 presents the satisfactory training accuracy of both models (approximately 70–90%, with a few acceptable exceptions, such as cropland, which has PA and UA values of approximately 40–50%), which indicates that the three models used in the classification: SVM, RF, and CNN, were generally well-trained. Even though the training accuracy and the validation accuracy are constantly approximate, as shown in Table 16 the training accuracy is very slightly more accurate and certain than the validation accuracy (approximately 1–10% higher). This suggests a slight overfitting problem in the models. Nevertheless, the presence of the overfitting problem is not an important obstacle in our study because the differences between the training and validation accuracies are acceptable (between 1% and 10%). Additionally, the validation accuracy always has a higher uncertainty, which indicates that the real accuracy rate may vary to a large extent.

Table 15 Training producer's accuracy and user's accuracy by class

Land Cover Types		2007			2018	
Cropland	RF	PA	66.45 ± 08.68	RF	PA	78.89 ± 04.48
		UA	40.92 ± 03.90		UA	43.71 ± 04.21
	SVM	PA	46.06 ± 06.58	SVM	PA	69.91 ± 04.74
		UA	51.31 ± 04.79		UA	59.83 ± 05.09
	CNN	PA	79.88 ± 04.53	CNN	PA	71.78 ± 04.62
		UA	75.25 ± 04.86		UA	71.34 ± 05.06
Cropland (with Bare Soil)	RF	PA	46.34 ± 04.75	RF	PA	35.77 ± 05.33
		UA	98.79 ± 01.06		UA	91.89 ± 02.65
	SVM	PA	36.15 ± 03.54	SVM	PA	52.23 ± 07.21
		UA	96.73 ± 01.75		UA	94.78 ± 02.08
	CNN	PA	92.24 ± 02.15	CNN	PA	86.54 ± 02.51
		UA	92.99 ± 02.09		UA	84.72 ± 02.97
Water area	RF	PA	100	RF	PA	100
		UA	41.18 ± 16.54		UA	100
	SVM	PA	58.75 ± 48.12	SVM	PA	100
		UA	72.22 ± 20.69		UA	100
	CNN	PA	100	CNN	PA	100
		UA	100		UA	71.43 ± 33.47
Vegetation (except crop)	RF	PA	91.50 ± 00.73	RF	PA	63.40 ± 06.00
		UA	89.59 ± 02.24		UA	88.56 ± 02.22
	SVM	PA	94.93 ± 00.61	SVM	PA	65.04 ± 06.45
		UA	78.32 ± 02.61		UA	85.26 ± 02.30
	CNN	PA	92.45 ± 01.39	CNN	PA	87.58 ± 01.87
		UA	90.54 ± 01.90		UA	85.81 ± 02.03
Non-vegetation	RF	PA	81.79 ± 06.72	RF	PA	98.22 ± 00.52
		UA	82.14 ± 05.36		UA	77.87 ± 05.21
	SVM	PA	38.73 ± 08.16	SVM	PA	98.99 ± 00.39
		UA	81.71 ± 05.73		UA	80.38 ± 04.83
	CNN	PA	70.71 ± 06.62	CNN	PA	68.08 ± 05.64
		UA	92.99 ± 04.06		UA	84.29 ± 04.92

Table 16 Validation producer's accuracy and user's accuracy by class

Land Cover Types		2007			2018	
Cropland	RF	PA	49.63 ± 14.63	RF	PA	88.71 ± 06.54
		UA	38.27 ± 07.48		UA	54.01 ± 08.35
	SVM	PA	43.21 ± 12.41	SVM	PA	63.20 ± 09.69
		UA	49.58 ± 08.98		UA	66.67 ± 09.29
	CNN	PA	61.86 ± 09.38	CNN	PA	61.34 ± 08.55
		UA	65.79 ± 10.67		UA	72.60 ± 10.23
Cropland (with Bare Soil)	RF	PA	47.04 ± 09.65	RF	PA	25.69 ± 07.37
		UA	94.68 ± 04.54		UA	93.48 ± 05.05
	SVM	PA	35.19 ± 06.81	SVM	PA	47.18 ± 08.56
		UA	96.39 ± 04.02		UA	98.06 ± 02.66
	CNN	PA	89.96 ± 04.85	CNN	PA	90.09 ± 04.81
		UA	86.76 ± 05.07		UA	82.55 ± 06.09
Water area	RF	PA	100	RF	PA	100
		UA	60.00 ± 30.36		UA	50.00 ± 69.30
	SVM	PA	100	SVM	PA	100
		UA	85.71 ± 25.92		UA	62.07 ± 30.54
	CNN	PA	100	CNN	PA	100
		UA	100		UA	70 ± 25.05
Vegetation (except crop)	RF	PA	90.66 ± 01.48	RF	PA	67.21 ± 13.96
		UA	87.22 ± 04.88		UA	91.28 ± 03.96
	SVM	PA	94.91 ± 01.15	SVM	PA	65.08 ± 05.30
		UA	78.42 ± 05.19		UA	86.94 ± 04.43
	CNN	PA	88.36 ± 03.31	CNN	PA	83.79 ± 04.14
		UA	85.00 ± 04.52		UA	81.86 ± 05.15
Non-vegetation	RF	PA	84.10 ± 10.16	RF	PA	97.87 ± 01.28
		UA	77.78 ± 12.15		UA	65.38 ± 12.93
	SVM	PA	45.59 ± 19.51	SVM	PA	99.08 ± 01.31
		UA	78.05 ± 12.67		UA	74.07 ± 11.69
	CNN	PA	66.06 ± 12.64	CNN	PA	63.29 ± 11.88
		UA	90.91 ± 09.81		UA	73.68 ± 14.00

Among the three methods, the CNN remains the most stable and accurate method, and all of the values range between 70% and 100%. Among the classes, water areas were very well predicted but also very extensive (usually with an accuracy between 50% and 70% with a large uncertainty and 100%) by means of their distinctive spectral signature. Cropland had training accuracy indicators between 50% and 70%, with CNN having the best performance in this class (approximately 70–80% in training accuracy and approximately 60–70% in validation accuracy). Of the other two methods, RF was mostly more accurate than SVM (approximately 5–20% higher). In addition, they performed better on the images from 2018 than those from 2007, with a stable uncertainty (approximately 10–20%); the validation accuracies were still approximate and slightly lower. Crops are easily confused with vegetation, which might explain the low accuracy of this classification. Croplands with bare soil are more correctly classified than croplands with plants (with a 20–50% higher rate), and all UA are significantly higher than PA, with a 50% to 70% difference, which suggests that fewer errors of commissions were made during the classification. Except for the CNN, both the UA and PA ranged from 82% to 92%, with less uncertainty at approximately 2.50 in the training accuracy and approximately 5 in the validation accuracy. Even though vegetation has the potential to be confused with crops, it was still the best-predicted class besides water, and the accuracy indicators achieved approximately 80–95%, except for the PA of RF and SVM in 2018, which were approximately 65%. It can be assumed that some errors of omission were made during this classification. The non-vegetation class includes all types of urban land use, sand, and rock; hence, it is globally well-classified due to its particular spectral signature, especially with the 2018 images. The accuracies in general ranged from approximately 70% to 98% in the training accuracy and from approximately 63% to 97% in the validation accuracy. In this class, the fact that the PA is considerably greater than the UA reveals the error of omission, except for the classification of SVM in 2007 and both CNN classifications, which suggests an error of commission instead. In all cases, the CNN was always the most stable and reliable method.

Overall, three different algorithms were applied to two high spatial resolution satellite images from 2007 and 2018, and all of them achieved a good accuracy level, with the OA ranging from 70% to 90% despite the complex landscape and small field size.

The RF and SVM models both performed well for the LULC classification; nonetheless, the CNN obviously is better suited to performing classification in our study area since it generally performs best regardless of the type of dataset and accuracy index. Therefore, the CNN has proven to be a feasible, reliable method with remarkable performance for precisely mapping LULC and analyzing the changes. However, some important considerations regarding its effectiveness are worth discussing. Previous applications of CNN models have tended to emphasize the complexity of these models compared to RF models and SVMs. In this case, parameter tuning and optimization are often performed by cross-validation for CNN algorithms. However, in some cases, CNN models can have millions of weights to optimize at each iteration (LeCun et al., 2015). In such situations, training these models can be tedious. Manual tuning or rules of thumb for cross-validation should be implemented in this case. This manual manipulation could have repercussions on the accuracy of the model. A well-known solution is transfer learning (J. Ma et al., 2019). In this case, instead of a model being trained from scratch, pretrained models are retrained on the user's classes of interest. Pretrained models allow for better accuracy (Hendrycks et al., 2019). In our study, the deep model was very useful for generalization.

Furthermore, according to the accuracy assessment, the lower accuracy occurred for 2018, and we deduced that the spatial resolution of the image is a crucial part of classification that can explain the differences between the SVM and RF's overall accuracy in the different years. The RF performed better on the 2007 data with a 2 m spatial resolution SPOT 5 image; in contrast, SVM achieved a better accuracy in 2018 with a 10 m spatial resolution Sentinel 2 image. Among all of the classes, except for the water areas, which have a very different spectral signature than the other classes, vegetation was the best-detected class, most likely because it occurred on the greatest part of the study area; therefore, it also had the largest sample dataset, since all of the samples were randomly and evenly selected in the images. Non-vegetation areas that are mostly urban land, rocks, and sand were relatively simple to discriminate. Cropland with bail soil was better-classified than planted cropland. Misclassification largely occurred between the vegetation and crops due to their spectral signature similarities, especially during the

growing season, and they were spatially approximate; some croplands were small and intermixed with trees or shrubs.

The results also indicated that the choice of a suitable classifier was critical, and the OBC approach clearly influenced the final classification at the same time.

6.5.2. LULC Changes Detection (2007-2018)

Beyond the problems of the uncertainty and error values caused by classification, multiple LULC changes between two different classes and between two years (2007 and 2018) were detected, the LULC maps resulting from the PCC is shown in Figure 68.

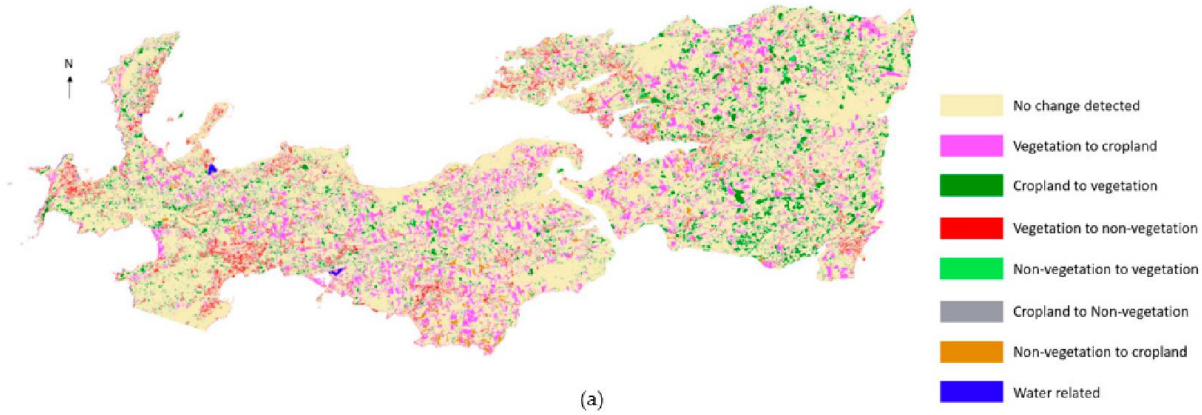

(a)

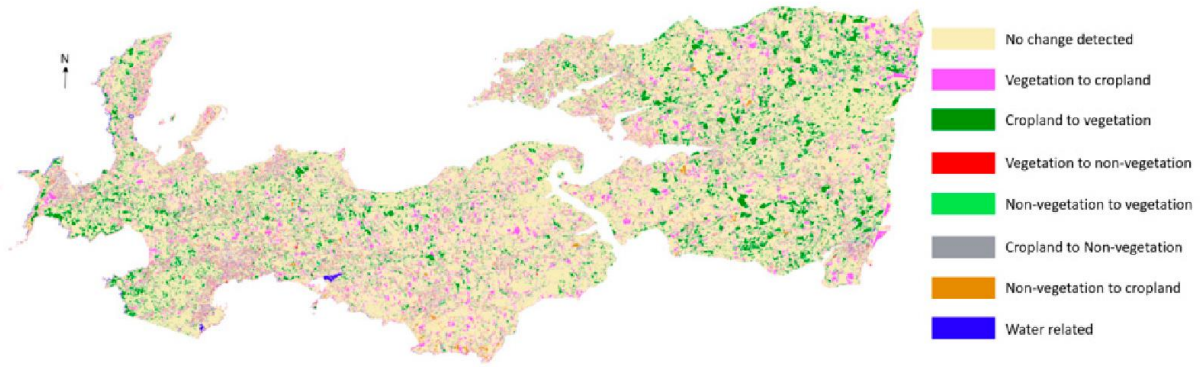

(b)

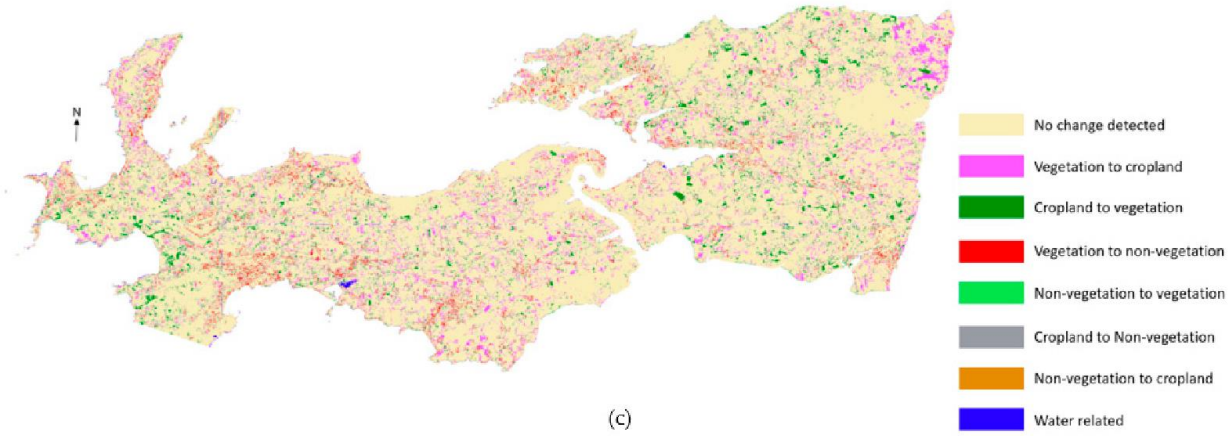

Figure 68 LULC change maps with the classification of SVM (a), RF (b), and CNN (c).

Figure 68 revealed the status of each pixel, which stayed in the same class, meaning no change, or changes to another class, or another LULC. Some changes can be seen among the three land cover change maps with different classifications; for example, many croplands were transformed into vegetation, and vegetation was changed to cropland according to the maps of RF. The SVM maps indicate numerous transformations from vegetation to cropland and vegetation to non-vegetation. However, generally, the cropland surface has slightly increased in the peninsula, and many vegetation areas have turn into cropland, according to the LULC change map. At the same time, many cropland areas have become vegetation areas. However, there may be confusion between vegetation and crops due to the different acquired dates of the two images. Therefore, many of the new vegetation areas are most likely growing crops. The third most important land cover change is vegetation to non-vegetation, which mainly took place near urban areas on the coast, especially in the south, where tourism is the most developed. Some details of the three main land cover change types based on the classification results of the CNN, which is the most stable of the three methods, are shown in Figure 69, with comparisons between 2007 and 2018.

Meanwhile, the evolution of the surface of each class between 2007 and 2018 is presented in Table 17 with their proportion in the total surface area of the peninsula, the surface area of each type of land use change and the proportion of each type in the total surface area.

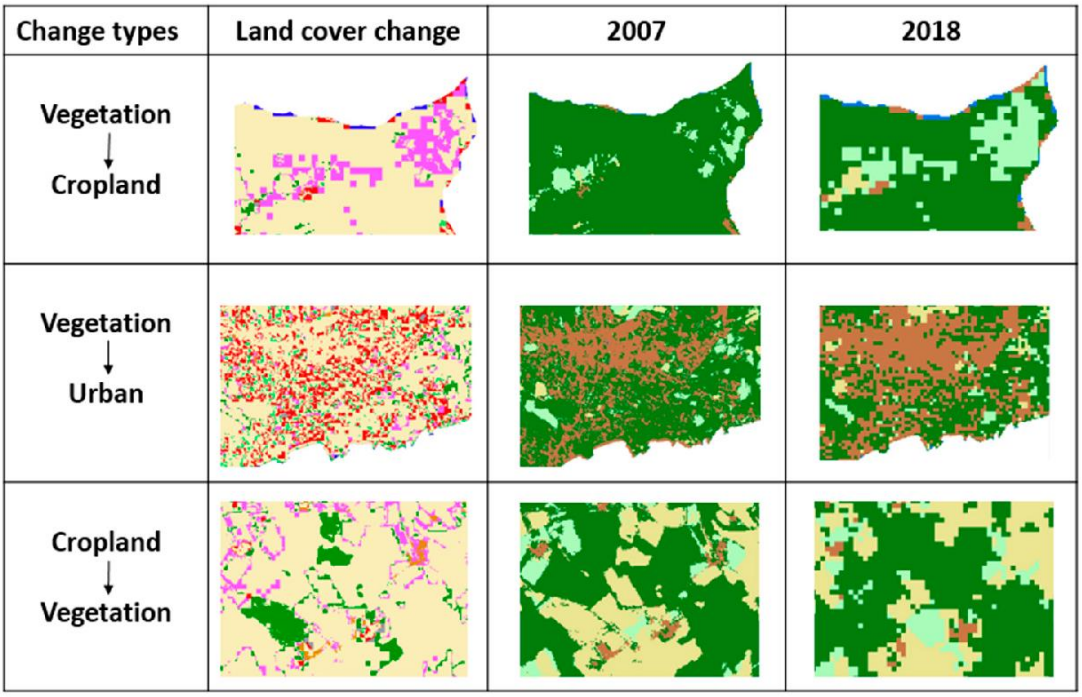

Figure 69 Details of the three main land cover change types of the CNN classification with comparisons between 2007 and 2018.

Table 17 Land cover change area and proportion of the change type with the three methods of classification.

Land Cover Change	SVM		RF		CNN	
	Area (km^2)	Proportion (%)	Area (km^2)	Proportion (%)	Area (km^2)	Proportion (%)
No change	238.74	65.33%	243.40	66.77%	282.51	77.37%
Vegetation to Cropland	45.55	12.47%	31.90	8.73%	35.71	9.78%
Cropland to vegetation	43.55	12.03%	49.94	13.67%	23.96	6.55%
Vegetation to non-vegetation	20.68	5.66%	5.14	1.41%	12.43	3.40%
Non-vegetation to vegetation	1.42	0.39%	3.13	0.86%	3.15	0.86%
Cropland to non-vegetation	9.11	2.49%	15.12	4.14%	2.63	0.72%
Non-vegetation to cropland	4.61	1.26%	12.17	3.33%	2.63	0.72%
Water related	1.34	0.37%	4.04	1.11%	2.14	0.59%
Total	365.42	100%	365.42	100%	365.42	100%

Beside the confusion between growing crops and vegetation, our previous results can be confirmed by Table 17. The table ranges from the most important class with the greatest proportion of land cover change to the least changed class, with the two types of cropland assembled into one class to facilitate the comparisons. The majority of the land in the peninsula retained the same LULC between 2007 and 2018, and at least 65% to 66% of the area remained unchanged according to the SVM and RF classifications. However,

the CNN indicated that approximately 77% of the surface of the Crozon Peninsula did not change between the two years, which is more important. Cropland is clearly increasing: 12.45% of the vegetated area has been converted into cropland, according to SVM classification; however, this transformation is less important according to the RF and CNN classifications, which show approximately 8% and 9%. In contrast, much cropland was identified as vegetation in 2018, more with the SVM and RF classifications (12–13%) than with the CNN (6.55%), which could confuse vegetation and crops due to the different acquired dates of the two images. Undoubtedly, non-vegetation, which includes urban areas, has certainly gained surface area from vegetated areas over the 11-year period by agreement of the three classifications, even though RF presents a lower land cover change value (1.41%) than SVM and CNN (5.66% and 3.40%, respectively). For the RF and SVM classifications, non-vegetation was developed from cropland as well (2.49% and 4.14% in SVM and RF, respectively). A small part of the non-vegetated area was classified as cropland in 2018 in all three models (1.26% in SVM, 3.33% in RF, and 0.72% in CNN); however, it might have been confused with bare soil and non-vegetated areas such as concrete. Finally, the last two classes (non-vegetation to vegetation and all water-related areas) have very low proportions, approximately 0.30–1% in land cover change, which is likely due to the rising tides and increasing water storage in the mid-summer and to planting of small areas, such as in the city.

To conclude, our classification results showed that it is possible to map land use with different algorithms and analyze land use changes between two years. First, increasing cropland surface indicates that agricultural activities remained an important economic sector in the peninsula, and there were essentially no signs of abandoned agricultural land during the study period. Second, non-vegetation areas have sharply grown in the 11-year period due to the dramatically increasing urbanization of the peninsula, especially some coastal cities that are highly frequented by tourists, since tourism is rapidly developed in the peninsula. The very dense population corresponds to a high level of artificialization of the territory, which is growing faster than the national average, fueled by a construction of housing and nonresidential premises. This human concentration also implies the progression of urbanization toward the hinterlands, where the construction of housing and the arrival of new residents increased significantly.

Artificialization is the main change that has affected the coastal zone of the peninsula, with preferential locations around the major urban centers and on certain coastal sectors. Despite the regulatory protection established by the Littoral Law, the changes are also important in the 100 m band nearest to the sea and then decrease as one moves away from it. In 1986, the Littoral Law provided an initial regulatory response to the need to control the anarchic development of construction on the coast. One of the most significant consequences of development has been the drastic reduction of the vegetation surface. Vegetation has been removed for two main reasons: increasing agricultural activities and urban land growth. Therefore, economic development can have negative social and economic implications on the peninsula; in addition, environmental conservation and protection are required.

6.6. Conclusion

CD methods involve analyzing the state of a specific geographic area to identify variations from images taken at different times. With satellite remote sensing, high spatial and spectral resolution images are recorded and used to analyze the scales of changes. In this study, in order to detect multiannual change classes between the series of multitemporal images using a pixel-by-pixel PCC technique, three different well-known and frequently used algorithms, including two machine learning algorithms (i.e., SVM and RF) and one deep learning algorithm (i.e., CNN), were tested on two high spatial resolution satellite images. RF and SVM were applied with an object-based approach, which requires a segmentation step to create subpixel-level objects to avoid the error of mixed pixels since the study area was mainly covered by small fields. The inclusion of the CNN significantly improved the classification performance (5–10% increase in the overall accuracy) compared to the SVM and RF classifiers applied in our study.

Our results showed that the use of remote sensing for complex multiannual small-scale LULC change studies was completely reliable. The study resulted in two maps that showed five different land uses (cropland, cropland with bare soil, water, vegetation and non-vegetation) in 2007 and 2018 with high accuracy. In particular, the CNN had an

overall accuracy that ranged from 80 to 90%, making it the most suitable algorithm in our case, even though RF and SVM also achieved good accuracy levels.

The results may also lead to the conclusion that economic development is rapidly occurring in the peninsula, manifested as urban land and tourism growth, increasing the agricultural activities and grossly decreasing the vegetative areas. Hence, environmental protection measures are demanded for the future. In this context of change, the coastal zones of the peninsula tend to specialize socially and economically, and the maintenance of the agricultural areas, as well as the preservation of the natural areas, are both more sensitive and more complex. Moreover, it appears that the change in land use must be understood in the context of climate change, which is a factor in the aggravation of risks (e.g., flooding and, coastal risks), especially in the sectors that are most subjected to urbanization pressures.

Although we observed relatively high classification accuracies, several uncertainties and limitations persisted. The first is the misclassification between vegetation and planted croplands: the very similar spectral characteristics that they share and their geographical localization lead to this confusion. Second, the two classifications were based on two images with different spatial resolutions; thus, some errors of the land use change analysis could have been induced. Third, useful cloud-free satellite images of the growing season were not easy to obtain in our study area; therefore, a series of annual mappings with more precision was not performed in the study. Hence, some recommendations can be made for further studies, such as applying more vegetation indices or using hyperspectral images to differentiate between vegetation and planted croplands or exploring the potential of synthetic-aperture RaDAR images as a supplement to the traditional optical images on cloudy days.

Chapter 7. Mapping Crop Types Using Sentinel-2 Data Machine Learning and Monitoring Crop Phenology with Sentinel-1 Backscatter Time Series in Pays de Brest, Brittany, France

Journal article: Xie, G.; Niculescu, S. Mapping Crop Types Using Sentinel-2 Data Machine Learning and Monitoring Crop Phenology with Sentinel-1 Backscatter Time Series in Pays de Brest, Brittany, France. Remote Sens. 2022, 14, 4437. https://doi.org/10.3390/rs14184437

Review: Remote sensing

Published date: 6 September 2022

7.1. Introduction

Crop supply is a global issue, particularly in the context of global climate change, rising population, and urbanization. With increasing food demand worldwide, agriculture production and food security should be guaranteed by ensuring biodiversity and limiting the environmental impacts (Schlund & Erasmi, 2020). This makes reliable information about crop spatial distribution and growing patterns crucial for studying regional agriculture production and supply, making political decisions, and facilitating crop management (X.-P. Song et al., 2017; H. Yin et al., 2018).

The classification of crop spatial distributions are valuable for agricultural monitoring and for the implementation and evaluation of crop management strategies (Birrell et al., 1996; Sun et al., 2019). Hence, crop type mapping is in high demand. Field research and remote sensing have always been the most important sources for obtaining agricultural information (Y. Song & Wang, 2019), and since the first launch of Earth observation satellites in 1972, continuous agriculture mapping and monitoring over large areas became possible with EO data. Moreover, the new generation of EO data, nowadays, has increased the resolution of sensors for agriculture uses, therefore since the last few

decades, the science of agriculture mapping and monitoring has developed quickly, with diverse types of high spatial and temporal resolution EO data. For example, Sun et al. in 2019 conducted a study of the crop types that were located at the lower reaches of the Yangzi River in China. They performed a classification of crop-type dynamics during the growing season by using three advanced machine learning algorithms (SVM, ANN, and RF) with a combination of three advanced sensors (Sentinel-1 backscatter, optical Sentinel-2, and Landsat-8). Arvor et al. (2011) in 2011provided a methodology for mapping the main crops and agricultural practices in the Mato Grosso state in Brazil; this study was performed by two successive, supervised classifications with the EVI time series from the MODIS sensor to create an agricultural mask and a crop classification of three main crops in the state. In another study by Forkuor et al. in 2014, they found that an integration of Multitemporal optical RapidEye and dual-polarized SAR TerraSAR-X data can efficiently improve the classification accuracy of crops and crop group mapping in West Africa, in spite of excessive cloud cover, small sized fields, and a heterogeneous landscape. Furthermore, in the Finistère department, G. Xie & Niculescu (2021) evaluated the multiannual change detections of different LULC regions, including agricultural land with accuracy indices between 70% and 90%, by using HR satellite imagery (SPOT-5 and Sentinel-2) and three algorithms that were implemented: RF, SVM, and CNN.

More importantly, many studies of crop mapping focuses on winter crop mapping. Q. Dong et al. in 2020 proposed a method called phenology-time-weighted dynamic time warping (PT-DTW) for mapping winter wheat using Sentinel-2 time series data, and this new method may exploit phenological features in two periods, with a Normalized Difference Phenology Index (NDPI) providing more robust vegetation information and reducing the adverse impacts of soil and snow cover during the overwintering period. T. Zhou et al. in 2017 studied the feasibility of winter wheat mapping in an urban agricultural region with a complex planting structure using three machine learning classification methods (SVM, RF, and NN), and the possibility of improving classification accuracy by combining SAR and optical data.

Besides the contributions of the new generation of EO data, the diversity of the classification approaches and methods have provided more resources for agriculture mapping and monitoring. The classical, direct extraction approach is the traditional and

most used classification approach that is used to extract single or multiple crop types directly from satellite images (Del Frate et al., 2004; Wardlow & Egbert, 2008; Y. Jiang et al., 2020). Moreover, we also propose the hierarchical classification approach for crops mapping in this study. Hierarchical classification is well known for its capacity to solve a complex classification problem by separating the problem into a set of smaller progressive classifications; it produces a series of thematic maps to progressively classify the image into detailed classes. Wardlow & Egbert (2008) investigated the applicability of time-series MODIS 250 m NDVI data for large-scale crop mapping in the Central Great Plains of the USA. The hierarchical classification scheme was applied in this study with high classification accuracy, and instead of directly solving a complex irrigated crop mapping problem, a four-level hierarchical classification framework was implemented to produce a series of crop-related thematic maps that progressively classified cropland areas into detailed classes. Ibrahim et al. in 2021 have also employed the hierarchical classification scheme to map crop types and cropping systems in Nigeria, using the RF classifier and Sentinel-2 imagery. Firstly, they produced a land cover map with five classes in order to eliminate other land cover types, then the next classification was performed only on cropland, where the specific crop types and cropping systems were mapped. The results indicated that the crop types were well classified with high accuracy, despite the study area being heterogeneous and smallholder-dominated.

In recent years, most studies in the agricultural field have explored the performance of different classification algorithms. RF is one of the most well-known and widely used algorithms in the field for its optimal classification accuracy, effectiveness on large data bases, and its capability of estimating the importance of the variables in the classification (Ok et al., 2012; Rodriguez-Galiano, Ghimire, et al., 2012; Forkuor et al., 2014; Tatsumi et al., 2015; Son et al., 2018). The RF classification algorithm is traditionally run as a PBC, which has proven efficient and accurate in agriculture fields by many studies (Ok et al., 2012; Hao et al., 2015; Saini & Ghosh, 2018; H. Li et al., 2020). On the other hand, the advantage of OBC is well documented and many recent studies have the conclusion that OBC usually outperforms PBC for its higher classification accuracy, better potential for extracting land cover information in a heterogeneous area with small size field, and the capacity to produce a more homogenous class (Weih & Riggan, 2010; Whiteside et al.,

2011). However, even though OBC is better developed and considered as more accurate than PBC, both classification methods are able to achieve a great degree of accuracy.

Aside from mapping and analyzing the crop spatial distribution, understanding agricultural growing patterns is also a key element for crop management. Crop phenology monitoring and the identification of the main phenological stages are highly necessary for agricultural production predicting, efficient interventions of farmers and decision-makers during the phenological phases such as fertilization, pesticide application, and irrigation (Nasrallah et al., 2019). In particular, germination is the most critical phase to be understood, and it is the starting point of the growing season. Based on the germination information, the farmer and decision-makers are able to make a future projection of the season, estimate the whole seasonal phenology for crop growth, and predict its production (Nasrallah et al., 2019). Furthermore, phenology is highly related to the seasonal dynamics of a growth environment, therefore, in the context of global warming, the phenology of many plants, especially crops, may have changed (Y. Song & Wang, 2019).

Crop phenology is usually monitored with optical satellite images using vegetation indices. For example, Z. Pan et al. in 2015 analyzed the phenology of winter wheat and summer corn in the Guanzhong Plain in the Shanxi Province, China by using NDVI time series data and extracted seasonality information from the NDVI time series for measuring phenology parameters. The potential of another less-known index, the NDPI, is exploited by Gan et al. in 2020 in order to detect winter wheat green-up dates. During the evaluation with three other indices (NDVI, EVI, and EVI2), the results indicate that NDPI outperforms the other indices with the highest consistency with the ground truth.

Compared to the optical data, SAR data is less used in agricultural areas. Nevertheless, lately, with the emergence of a new generation of high-resolution SAR data, in particular since the Copernicus program Sentinel-1 C-band high spatial–temporal resolution images became available, SAR data has begun to draw interest, especially for its advantage of having its own source of energy, making it nearly independent of weather conditions (Forkuor et al., 2014). Thus, SAR backscattering coefficient time series data is now more frequently used for crop phenology monitoring. While optical data strongly depends on the chlorophyll content in the plants, SAR data can reveal the main changes in the canopy structure, identify significant phenological stages, and determine the main

growing period with the signal that is received after interacting with the canopy of the plants. Therefore, studies of crop phenology monitoring using SAR data have increased considerably in recent years. Meroni et al. in 2020 conducted a study of retrieving the crop-specific land surface phenology (LSP) of eight major European crops from Sentinel-1 SAR and Sentinel-2 optical data, where crop phenology was detected on the temporal profiles of the ratio of the backscattering coefficient VH/VV from Sentinel-1 and NDVI from Sentinel-2. They revealed that the crop phenology that was detected by Sentinel-1 and 2 could be complementary. Wali et al. in 2020 introduced rice phenology monitoring in the Miyazaki prefecture of Japan by using Sentinel-1 dual polarization (VV and VH) time series data, and attempted to clarify the relationship between rice growth parameters and the backscattering coefficient using the combination of two linear-regression lines. Canisius et al. in 2018 exploited SAR polarimetric parameters that were derived from fully polarimetric RADARSAT-2 SAR time series data to predict the growth pattern and phenological stages of canola and spring wheat in the Nipissing agricultural district of Northern Ontario, Canada. Mandal et al. in 2020 proposed a dual-pol RaDAR vegetation index (DpRVI) from Sentinel-1 difference data (VV-VH) to characterize the vegetation growth of three crop types (canola, soybean, and wheat) from sowing to full canopy development, with the accumulation of the Plant Area Index (PAI) and biomass.

The feasibility and effectiveness of winter crop type mapping and phenology monitoring with optical or SAR satellite data has been proven by many studies in agricultural field, however, some limitations remain. For example, the potential of a vegetation index other than NDVI and EVI has rarely been explored, and the studies have never been performed in a coastal area with fragmented and small-scale fields. More importantly, almost all the research perform and evaluate a single classification approach or method, instead of comparing different approaches and methods for crop type mapping.

In this study, we introduce a methodology to map two winter crop types (winter wheat and winter barley) with Sentinel-2 optical data that was acquired during the growing season of the winter crops. Two different classification approaches (hierarchical classification and classical direct extraction) were performed using RF-supervised classification algorithms, and two classification methods (PBC and OBC) were operated

and evaluated within the hierarchical classification framework. With the classification results of the winter crops, we are able to monitor their phenology with Sentinel-1 C-band SAR backscatter time series and precipitation data in order to understand their temporal behavior from sowing to harvesting, identify the three main phenological stages (germination, heading, and ripening, including harvesting), and study how crop phenology responds to weather conditions.

The main objectives of this study are listed as follows:

(1) Study the feasibility of mapping winter crops with Sentinel-2 10 m spatial resolution data in a fragmented area that is dominated by small-size fields;

(2) Perform hierarchical classification and classical direct extraction and evaluate the performance of both classification approaches;

(3) Perform PBC and OBC and compare the performance in each level of the hierarchical classification structure;

(4) Study the correlation between crop phenology and Sentinel-1 C-band SAR backscatter time series data and identify three phenological stages and the main growth period of the winter crops.

7.2. Study area and materials

7.2.1. Study area

The study area is located on the west coast of France in the north of the Finistère department and the region of Brittany (Figure 70).

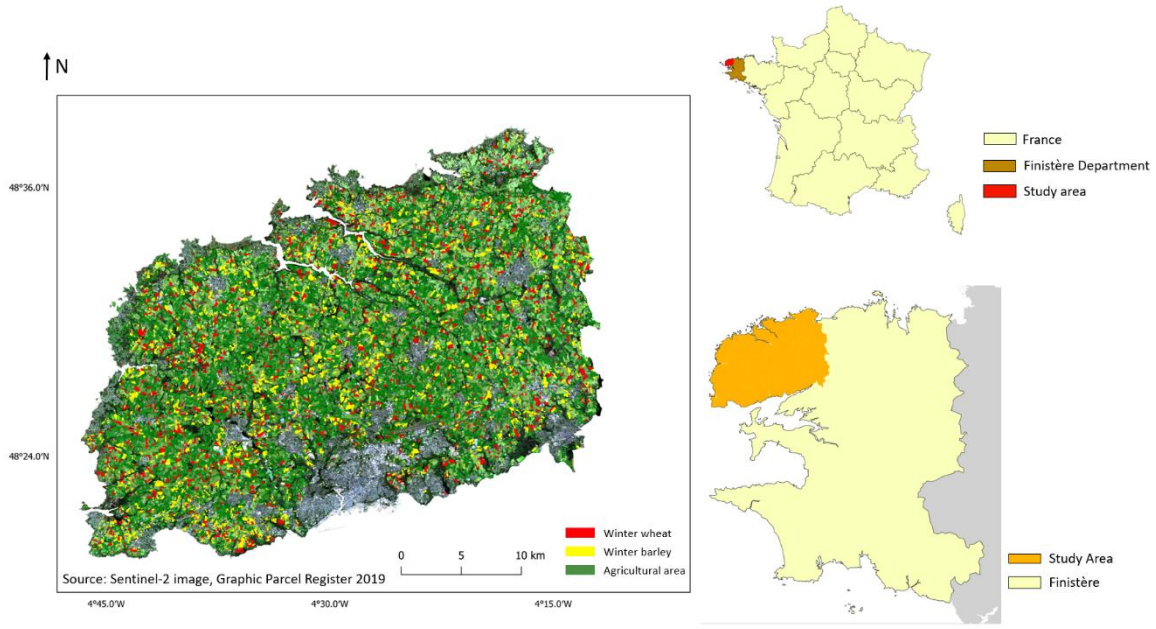

Figure 70 Location of study area, the north of the Finistère department, Brittany, France, as per the RGB band combination of a Sentinel-2 satellite image on 20 April 2019 and the distribution of agricultural land in 2019.

The study area covers a land surface of 1, 034.41 km^2, and extends between the latitudes of 48°19′39″N and 48°40′41″N, and the longitudes of 4°12′50″W and 4°47′13″W. According to IGN, the northern part of Finistère is mostly dominated by plains, and the elevation of the area ranges between 0 m and 100 m (*Géoportail*, n.d.). The study area is mostly occupied by cropland, temporal or permanent grasslands, small area of forests and shrubs, urban agglomeration in the south, and a wetland area in the north (Rouault, 2019). On average, the northern region of Finistère receives 941 mm of total precipitation per year, with the annual average temperature being 12.1 °C (7.7 °C and 16.8 °C are the monthly average temperatures for the coldest and warmest months, respectively), and therefore the warm temperate climate with frequent rainfall provides very favorable conditions for agriculture activities.

With such climate and topography conditions, agriculture is an important economic sector in the study area, and a considerable number of locals work in an agricultural or related sector in the department. There are 384, 408 ha of useful agricultural area in the department, so 57% of the department's surface is devoted to agricultural use (*ADEUPa Brest*, n.d.). One of main agricultural productions are crops, including corn, winter wheat, and winter barley, and vegetables (*Chambres d'Agriculture de Bretagne*, n.d.).

Hence, it is important to develop a methodology to map one or several specific crop types and monitor their growth stages by using free access, high quality satellite images for crop production management. The north of the Finistère department was chosen as our first study area because of its favorable natural conditions, highly active agricultural activities, and its proximity, which facilitate the field research and interaction with farmers.

7.2.2. Data

The study was executed in the Finistère department in France during 2019, using open-access high-quality satellite data from the Sentinel platform. It is worth noting that the latest version of the graphic parcel register was published in 2019 by IGN, and this information was relevant to our study.

Due to the annual high-intensity precipitation there is frequent heavy cloud cover in the region, therefore, operable optical satellite images are very rare in the study area. Nevertheless, one cloud-free level 2A atmospheric effect-corrected Sentinel-2 image from 20 April 2019 was acquired from the Theia platform (catalog.theia-land.fr) (ESA, n.d.-e) (Table 18). Ten spectral bands (Table 19) were extracted for further processing and analysis.

Table 18 Sentinel-2 image used in the study

Date	Satellite	Platform	Processing Level	Tiles
20 April 2019	Sentinel-2	2B	Level 2A	T30UUU

Table 19 Sentinel-2 spectral bands used in the study

Sentinel-2 Bands	Spatial Resolution (m)	Wavelength Range (nm)
Band 2-Blue	10	458-523
Band 3-Green	10	543-578
Band 4-Red	10	650-680
Band 5-Vegetation red edge	20	698-713
Band 6-Vegetation red edge	20	733-748
Band 7-Vegetation red edge	20	773-793
Band 8-Near Infrared	10	785-899
Band 8A-Vegetation red edge	20	855-875
Band 11-Short-Wave Infrared	20	1565-1655
Band 12-Short-Wave Infrared	20	2100-2280

Moreover, in order to create a cloud-free time series of the study, the phenological phrases of winter crops from the SAR data were applied to the phenology monitoring process. In this study, interferometric Wide (IW) Swath mode level-1 Ground Range Detected (GRD) Sentinel-1 data with an incidence angle ranging from 30 to 46 were acquired to create the time series of the growing period of the winter crops (winter wheat and winter barley) in 2019, from 1 October 2018 to 1 September 2019. Both polarizations (VV + VH) were used, but only the descending orbit was retained for the processing. In total, 109 Sentinel-1 C-band SAR images with descending orbit were acquired for this study.

In addition, RPG was applied as the ground truth data in our study, used for creating training data and test data. RPG 2019 is the latest version of the very precise, georeferenced agricultural land database that covers the entire France territory (except Mayotte) that was published by IGN. The databases show the precise crop types (e.g., wheat, corn, vegetables, sunflower) or temporary and permanent grasslands in that are in the recorded agricultural lands in each year (*RPG*, n.d.).

7.3. Methodology

The methodology of this paper is detailed in two parts, which relate to the two research subjects: mapping winter crop types using Sentinel-2 data, and monitoring crop

phenology with Sentinel-1 backscatter time series. The data were processed in QGIS with Orfeo Toolbox, eCognition 10.0, and GEE.

7.3.1. Winter crops types mapping methods

A flow chart of the proposed global methodology is displayed below (Figure 71).

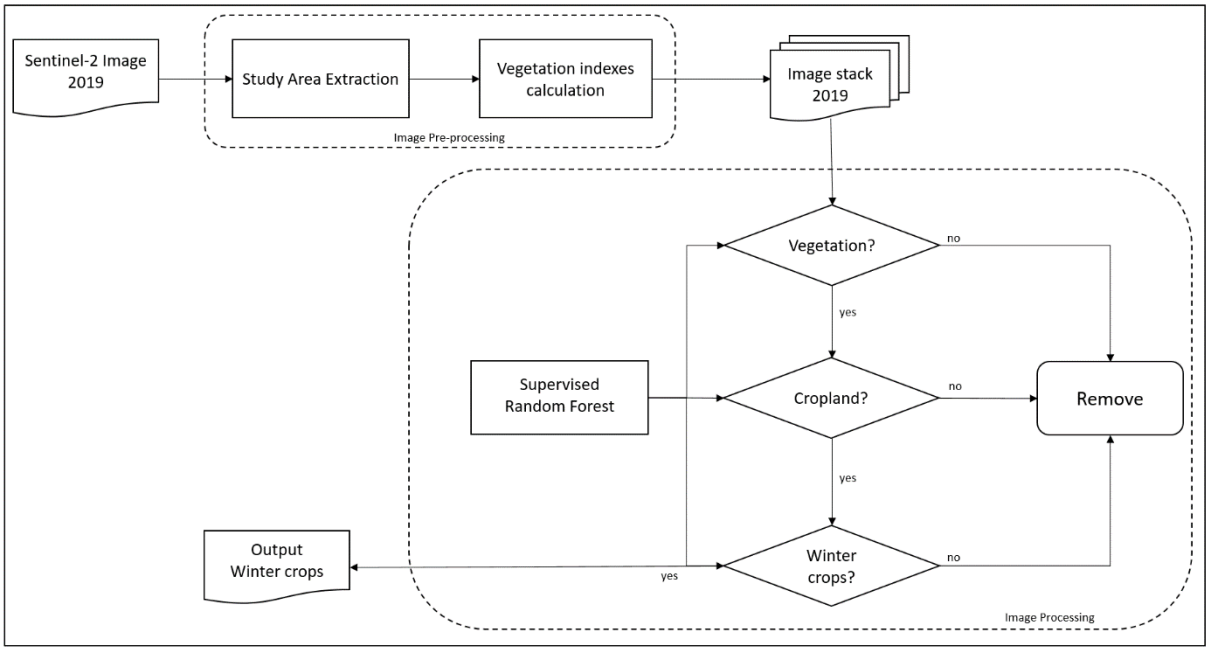

Figure 71 Hierarchical classification methodology used in the study for crop mapping

Firstly, after the study area selection and satellite image acquisition, the boundary of the northern region of Finistère area was applied in order to extract our area of interest by sub setting the raw images for the purpose of reducing the image size and shortening the processing time.

Afterwards, six VIs are used with the aim of mapping winter crop types using Sentinel-2 data in this study.

- NDVI
- NDWI
- GNDVI
- EVI
- SAVI

- MSAVI

After calculating the vegetation indices, an image stack with the ten original spectral bands and all of the indices was created for further image processing.

Secondly, supervised image processing using different approaches was performed in order to make comparisons and attempt to reach the most adapted classification in this study (Figure 72).

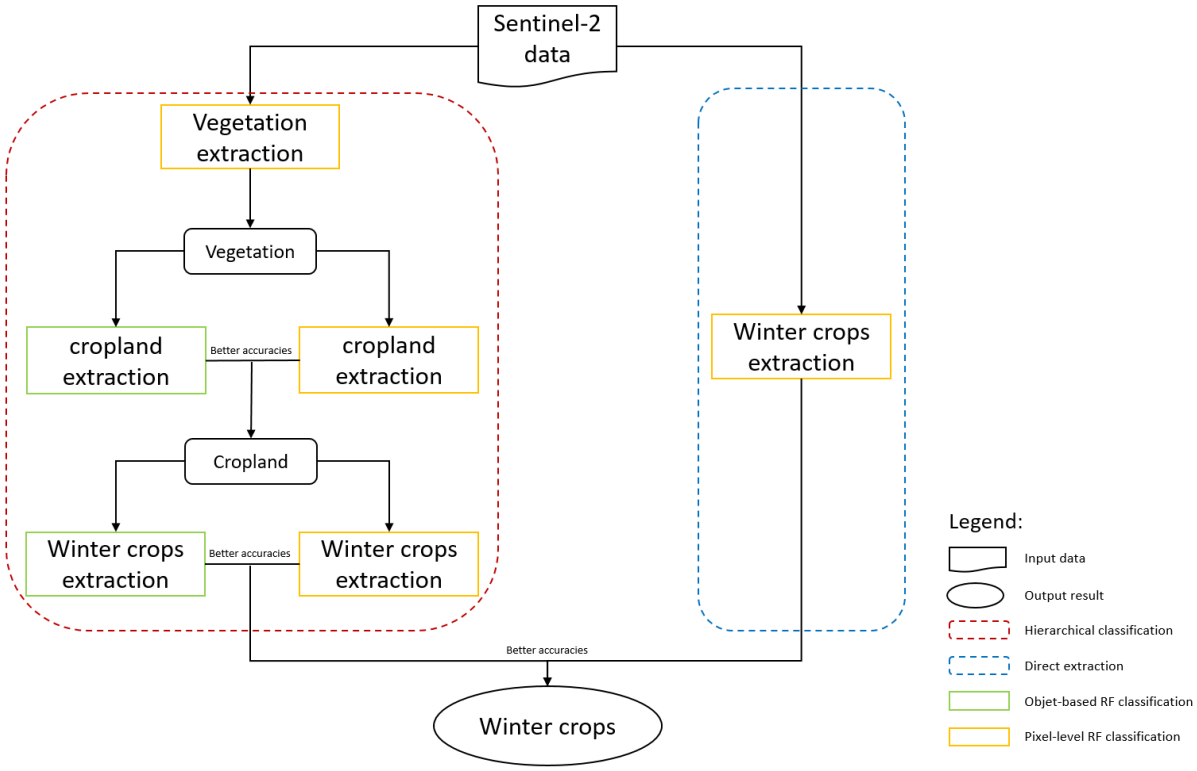

Figure 72 Proposed detail image processing methodology chart

Compared to the direct extraction of winter crops with pixel-based RF algorithms, hierarchical classification methods are effectuated in three progressive levels, each with different objectives. The objectives from the first level of the hierarchy to the last one are extracting vegetation (including croplands) from raw images, extracting croplands from vegetated areas (trees, shrubs, and grassland), and finally, obtaining exclusively winter wheat and winter barley from all crop types detected in previous stages, respectively. Finally, the results of the two classification approaches were evaluated with accuracy indices, in order to distinguish which one had better agreement with the ground truth data.

In addition, inside the hierarchical classification structure, except for during the first step, separating vegetation and non-vegetation exclusively used the pixel-based RF algorithm and this reached a very close agreement with ground truth data. Each step has been performed using the two methods, pixel-based and object-based RF classification, in order to determine the result with better accuracies for further processing and analysis.

In OBC methods, MRS algorithm was applied as the first step, and several combinations of parameters were used, and the optimal ones were found on a trial-and-error basis. The scale, compactness, and shape parameters were assigned as follows: 15, 0.5, and 0.3, respectively, for cropland extraction, and 20, 0.5, and 0.1, respectively, for winter crops extraction.

Moreover, the training data and test data in RF classification were selected manually using the RPG 2019 map. For the purpose of comparing different methods of classification, training data that were selected for PBC and OBC were as similar as possible, such as using the same area and very approximate surfaces, in order to improve the global comparability of the two methods. The training and classification of the RF module were applied using the Orfeo toolbox with two user-defined parameters that were set on a trial-and-error basis: the number of decision trees grown in the forest and the maximum tree depth, which is the length of each tree in the forest. The two parameters that were used in this study were defined as 100 and 25, respectively.

Thirdly, the accuracy assessment was performed with test data after the classification in order to evaluate the classification's degree of agreement with the reality and therefore assess the reliability of the classified results. In this study, in order to evaluate the classification quality and compare it amongst the different classification methods, five well-known and highly promoted accuracy indices were calculated for each classification method and each class. Among them, OA and kappa were employed for the global accuracy assessment, otherwise, precision, recall, and F-score were computed to assess the classification results of each class.

Moreover, in the hierarchical classification process, test data that were used for evaluating the classification of each step were generated as random points from the image that were used to perform classification, which is the result of the previous steps.

Afterwards, the random points were labelled manually with the Graphic Parcel Register map as ground truth. However, with the aim of evaluating the performance of the proposed hierarchical classification approach by comparing with traditional direct extraction, a completely new test dataset was produced from the original Sentinel-2 image that was not classified.

7.3.2. Crops phenology monitoring methods

This second part of the study was performed, based on the mapped winter crops from the previous step. Due to limited climate conditions in the study area, winter crop phenology monitoring was performed with Sentinel-1 C-band SAR data using the GEE platform.

In this study, the backscatter coefficient (σ°) in dB of both polarizations (VV and VH) and their ratios of a Sentinel-1 image time series during a complete growing period of winter crops (from October to September) on a few chosen croplands was automatically generated in a line chart on the GEE platform. In order to study the scattering behavior of our target croplands, each image was preprocessed, and the backscatter coefficient was converted to dB by GEE using the Sentinel-1 Toolbox. A flow chart of the Sentinel-1 image time series process in GEE is displayed as follow (Figure 73):

Figure 73 Sentinel-1 image process in the GEE platform

7.4. Results and discussion

7.4.1. Winter Crop Types Classification Methods Comparison

At first, the results of PBC and OBC of each step in the hierarchical classification are demonstrated and evaluated through accuracy assessment, the more accurate results were retained for further processing and comparison with classical direct extractions.

For vegetation extraction (including cropland) (Level 1), only PBC was performed since it achieved a great accuracy, approximately close to 1. From Figure 74, we see that the distribution of vegetation and cropland is coherent in the study area, apart from some urban environments, which are marked by intense non-vegetation pixels, in particular these areas are in the south and the northeast of the study area. According to Table 20, both global and interclass accuracy indices are very close to 1, this indicates a high probability of a correct classification of each individual pixel, and a great overall agreement level with the ground truth. Besides a good performance and good training of the PBC method, the distinction between the vegetated area and non-vegetation is very significant, and therefore, it is easy to classify.

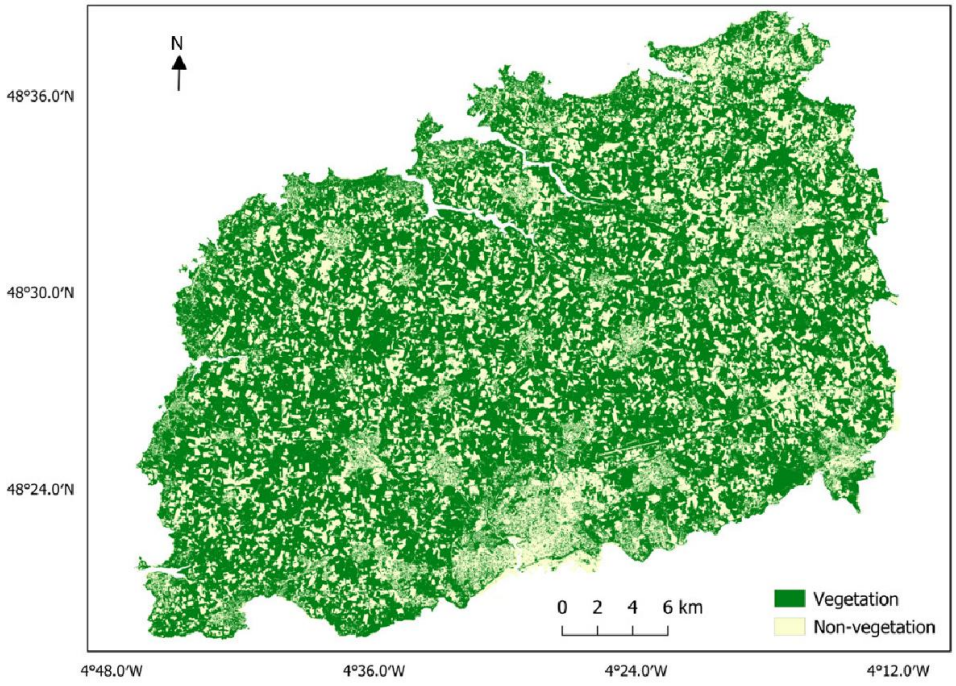

Figure 74 Level 1: PBC vegetation (including cropland) extraction results.

Table 20 Accuracy assessment of PBC vegetation (including cropland) extraction.

	Precision	Recall	F-Score
Vegetation	0.992	0.997	0.995
Non-vegetation	0.994	0.984	0.989
Kappa:	0.984		
Overall accuracy (OA):	0.993		

Subsequently, based on the vegetated area that was extracted from the previous step, we aimed to distinguish and preserve only the croplands from all arboreal

vegetation, shrub, and grasslands, including pasture. In level 2, OBC and PBC were both performed and evaluated. Figure 75 demonstrates that the results of the two methods are almost identical, although more individual pixels were classified as cropland in PBC considering that PBC was operated on pixel-level.

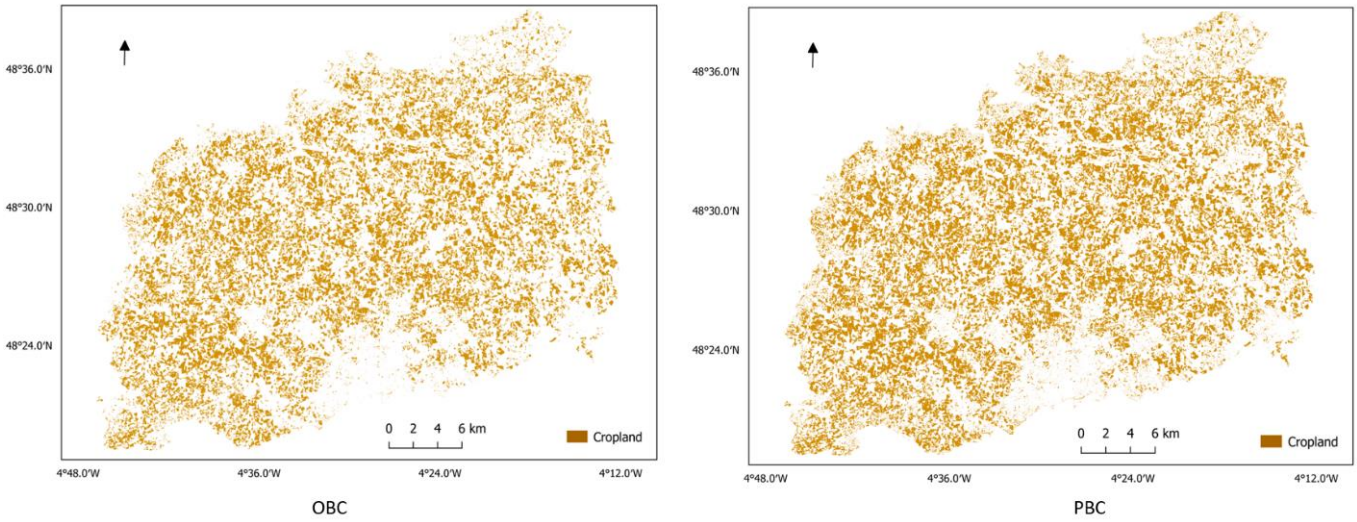

Figure 75 Level 2: PBC and OBC croplands extraction results

Pursuant to Table 21 and Table 22, even though the global accuracy indices of the results of OBC are slightly better than PBC with a difference of 0.024 in kappa and 0.004 in OA, the indices of the two results are still comparable. The tables below show that a large proportion of pixels are correctly predicted in general and that the level of agreement with the ground truth data is somewhat lower but still acceptable. Furthermore, for the interclass accuracy evaluation, cropland generally has the highest precision, recall, and F-score, which are all around 0.90. The models were well trained to make a good prediction of the cropland class, especially for the OBC model, and most of the individual pixels belonging to the cropland class were correctly detected. This can be explained by the OBC taking into account the geometry, form, and texture, which are the key elements used to distinguish the croplands from other vegetation. The classification of the vegetation has slightly lower accuracy of approximately 0.2 in comparison with croplands because of the mix of different kinds of vegetation and the uncertain form of the vegetated area, though OBC remains more precise compared to PBC. Finally, the classes of the other pixels in our study area, which are mainly some isolated pixels left from the previous step due to some errors, were better classified with PBC since the non-

vegetated area has highly different spectral behavior as compared to vegetation. Considering the better accuracy assessments of OBC, its classification result was preserved to perform the next step of classification.

Table 21 Accuracy assessment of OBC croplands extraction

	Precision	Recall	F-score
Vegetation	0.786	0.746	0.765
Cropland	0.912	0.905	0.908
Others	0.700	0.875	0.778
Kappa: 0.716 **Overall accuracy(OA)**: 0.861			

Table 22 Accuracy assessment of PBC croplands extraction

	Precision	Recall	F-score
Vegetation	0.769	0.678	0.721
Cropland	0.879	0.932	0.905
Others	0.929	0.813	0.867
Kappa: 0.692 **Overall accuracy(OA)**: 0.857			

In level 3, two winter crop types were extracted based on the results of the previous step, the classification result of the cropland extraction by using OBC. The results of the two classification methods (Figure 76) are very close to identical in this level, differences between the two maps can hardly be noticed.

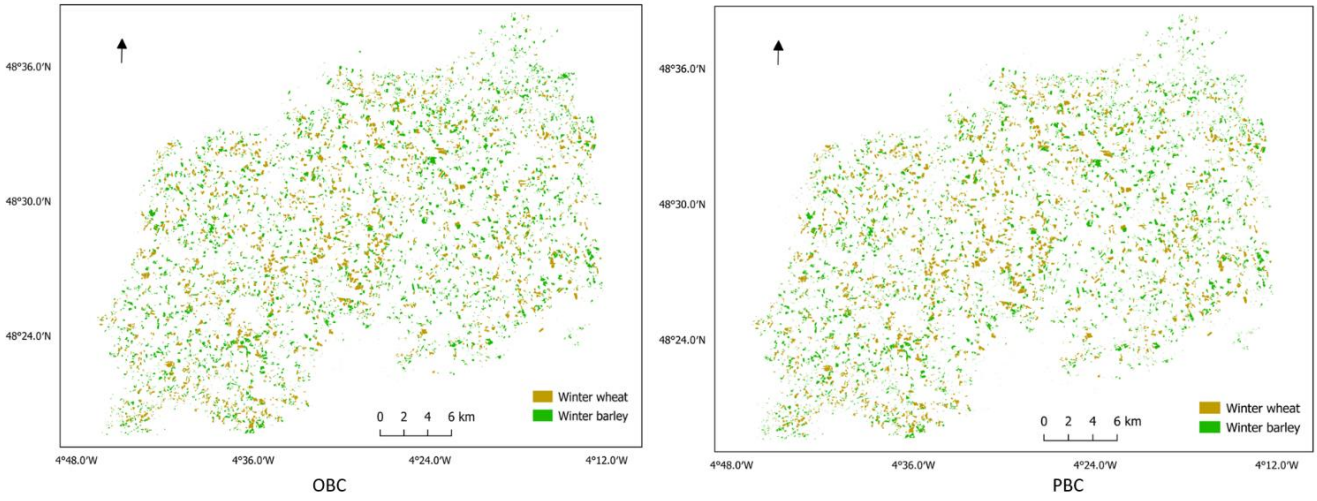

Figure 76 Level 3: PBC and OBC winter crops extraction results

With the lack of possibility of visual comparison of the two methods, they were evaluated and compared by using accuracy assessments (Table 23 and 24). In regards to the global accuracy indices, all classes were accurate using the two methods, which signifies a good performance of both methods with a high accuracy and a strong level of agreement for the classification. Beyond that, it is worth noticing that PBC shows a better potential with about 0.03 higher in OA and 0.04 in kappa, moreover, PBC basically achieves a better accuracy indicator of three classes in comparison with OBC. The results illustrate that the difference in spectral behavior was exploited to distinguish winter crops from other crops, since all the croplands share similar geometry, form, and texture characteristics. Nonetheless, among different crop types presented in our area of study, winter wheat has the most distinctive spectral signature, thus it was found to be the class with the best accuracy indices in both results, with very strong reliability in terms of prediction and a high rate of precisely identifying winter wheat. In contrast, the classification of winter barley and other crops are somewhat less accurate with approximately 0.1-0.5, and the advantage of PBC is more significant, with higher accuracy indicators around 0.04, which might be caused by the confusion of winter barley and other crops due to the similarity of their spectral behavior. In addition, the difference between these two classes were better detected by PBC with spectral information.

Table 23 Accuracy assessment of OBC winter crops extraction

	Precision	Recall	F-score
Winter wheat	0.998	0.978	0.988
Winter barley	0.833	0.871	0.852
Other crops	0.870	0.848	0.859
Kappa: 0.848			
Overall accuracy(OA): 0.899			

Table 24 Accuracy assessment of PBC winter crops extraction

	Precision	Recall	F-score
Winter wheat	0.994	0.976	0.985
Winter barley	0.876	0.913	0.894
Other crops	0.917	0.895	0.906
Kappa: 0.892			
Overall accuracy(OA): 0.928			

In the second step, the final results of the hierarchical classification and classical direct extraction are displayed and compared with accuracy assessments as well, the two classified maps are presented in Figure 77.

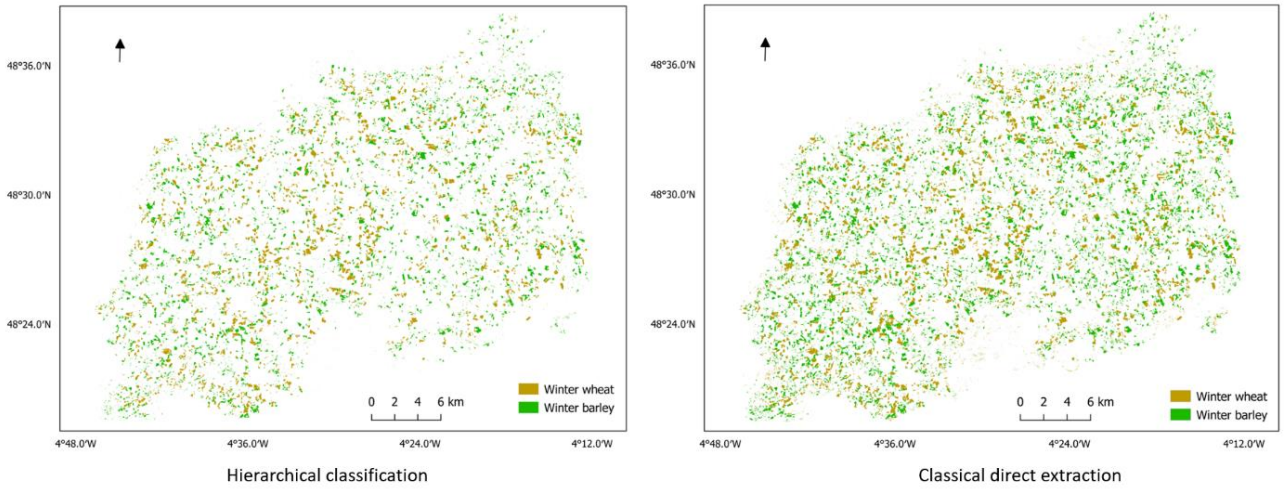

Figure 77 Classification results with hierarchical classification and classical direct extraction

Generally, winter wheat and winter barley were well detected and extracted from the Sentinel-2 image as shown in Figure 76; the results of two classification approaches are globally identical, particularly the homogeneous distribution of the winter crops over the area of interest. Nevertheless, the classical direct extraction approach identified more winter croplands, especially winter barley, and the winter croplands detected are much more fragmented; many small pixels were classified as croplands. This could be explained by the fact that winter crops are directly extracted from the preprocessed image; in addition, there might be some confusion between winter barley, grasslands, and some different crops considering the resemblance of their spectral behavior.

Table 25 Accuracy assessment of hierarchical classification

	Precision	Recall	F-score
Winter wheat	0.991	0.904	0.946
Winter barley	0.886	0.900	0.893
Others crops	0.929	0.959	0.944
Kappa: 0.888			
Overall accuracy(OA): 0.932			

Table 26 Accuracy assessment of classical direct extraction

	Precision	Recall	F-score
Winter wheat	0.959	0.928	0.943
Winter barley	0.683	0.960	0.799
Others	0.955	0.797	0.869
Kappa: 0.789			
Overall accuracy(OA): 0.866			

To make a better comparison, the accuracy assessments of the two approaches are displayed in Table 25 and 26. According to the tables, both classification results are very satisfactory as mostly all of the accuracy indicators range from 0.8 to 1, specifically with the hierarchical classification almost all indices are superior to 0.9. This suggests a good performance and training of the models and also a strong agreement with ground truth of all classification approaches in the study. Still, it is worth noticing that the hierarchical classification shows a better potential for specific crop types mapping as compared to classical direct extraction (approximately 0.1 higher in kappa and 0.07 in OA). Additionally, nearly every class achieves a higher accuracy in hierarchical classification, which indicates that the model is solid and able to make a good prediction. Among three classes, winter wheat is the most correctly classified class in both classification approaches, the indicators range from 0.90 to 0.99 with the F-score highly similar. Hierarchical classification reaches a better precision index, that means the model is more exact, yet classical direction extraction achieved a finer recall, which means the models returned more relevant results, it can correctly and efficiently identify winter wheat. Besides, winter barley and the other classes were evaluated and less accurately classified, especially with the classical direct extraction approach. According to Table 8, the winter barley class obtained a high recall (0.960) and a relatively lower precision (0.683), which suggests a high false positive rate, many individuals predicted as winter barley that the model returns were found misclassified when compared to the test data. On the contrary, the others class received a high precision index (0.955) and a comparatively low recall (0.797), the indicators demonstrate that the pixels were correctly detected and labelled despite less results returned by the model. The comparably low accuracy of the two classes and the imbalance between precision and recall indices might be explained by (1) the similarity of the spectral behavior between winter barley and other crops and even

grassland in the case of the classical direct extraction approach. (2) Since two winter crops are extracted directly from the Sentinel-2 image, the class others included not only non-vegetated urban areas, but also vegetation and other croplands which occupies a large area of our study site. Therefore an imbalance between classes was caused, thus, more training datasets of the class others were acquired in consideration of its weak intraclass correlation.

To conclude, both classification approaches achieved a good accuracy level despite the complex occupation and small cropland size in the region. In addition, the accuracy assessment indicates that the hierarchical classification has proven to be reliable and more accurate with outstanding performance in classification of both winter crops classes, particularly the winter wheat by turning a complex multi-class classification problem into series of smaller classifications. Additionally, PBC and OBC were implemented in two steps of the classification process within the hierarchical classification structure (croplands extraction from all vegetated area, and winter croplands extraction from all croplands). Although numerous studies in the remote sensing field demonstrate that OBC usually achieves a better classification with different data and in different landscapes over PBC by bringing complementary information other than the spectral signal and turning classification units from pixels to image objects (D. Liu & Xia, 2010; Estoque et al., 2015; B. Fu et al., 2017). However, the results illustrate that each method has its advantage in the classification process in this work. OBC slightly outperformed PBC in cropland extraction as the complementary texture, geometry, and shape information are helpful for cropland detecting. On the other hand, PBC reaches a higher accuracy in winter crops extraction, since all croplands have a similar shape but winter crops can be easily distinguished from other crops with direct spectral information. Additionally, the statistical difference between the results of PBC and OBC is not particularly significant. Therefore, small differences induced by several factors between two methods can be noticed, yet both methods are equally useful for our classification.

7.4.2. Crops phenology monitoring

The Sentinel-1 temporal backscattering coefficient profiles of diverse land cover types at VV and VH dual-polarizations from the study area during the growing season of the winter crops (from 1 October 2018 to 1 September 2019) are shown in Figure 78. The temporal profiles of mean σvv and σvh values of urban, vegetation (including other crops), water, bare soil, winter wheat, and winter barley land cover are displayed.

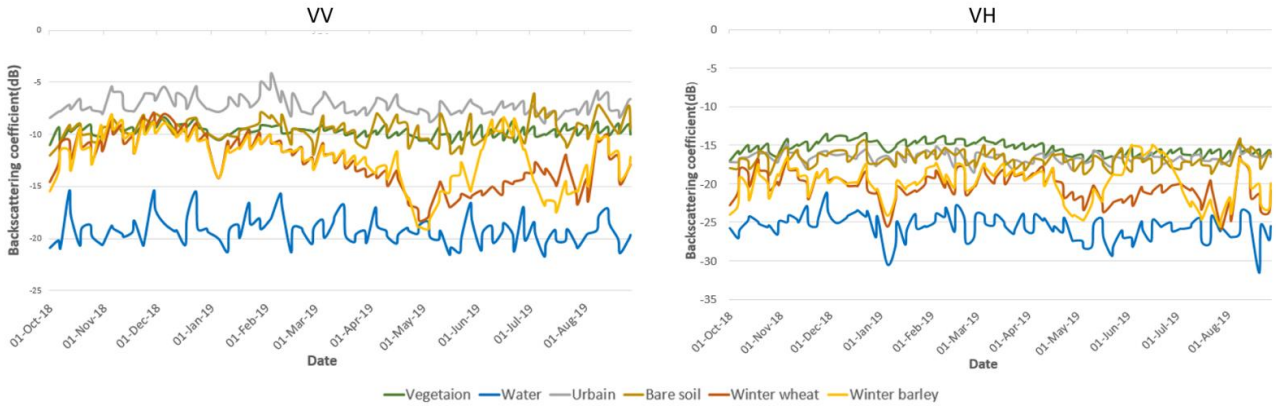

Figure 78 Sentinel-1 temporal backscattering coefficient profiles of different land covers (Vegetation, water, urban area, bare soil, winter wheat, and winter barley) in the study area at VV and VH polarizations from 1 October 2018 to 1 September 2019.

As shown in Figure 78, besides the profiles of the water area, which fluctuate significantly due to the weather conditions, the temporal profiles of vegetation, urban, and bare soil are much more stable than the profiles of winter crops, which have a significant fluctuation according to their different growth stages. Especially in the σvh profile, the vegetation, urban, and bare soil profiles are generally close to their mean value regardless of the season. Nonetheless, the variation of the backscattering coefficients of the two winter crops are clearly evident, for example a peak is seen in early December, followed by a minimum value in early summer and a maximum value in midsummer. Thus, the results indicate that it is feasible to distinguish winter crops from other types of land cover, particularly vegetation and other crops, and furthermore we are able to identify and study the main phenological stages from germination to ripening (harvesting) by using Sentinel-1 temporal profiles.

Based on prior knowledge and field research with local farmers, winter wheat and winter barley are both cereal crop types that are planted from October to November.

Generally, winter barley is sowed earlier than winter wheat in the Finistère department. Germination, which is the first growth stage of the crops, takes place three to four weeks after sowing, hence early December for winter wheat and mid-November for winter barley. The crops remain in their vegetative stage during winter, and stem elongation begins in spring and lasts until the plants reach their maximum height, usually in early summer. Lastly, ripening, the final growth stage, and harvesting occur in summer (early summer for winter barley and mid-summer for winter wheat).

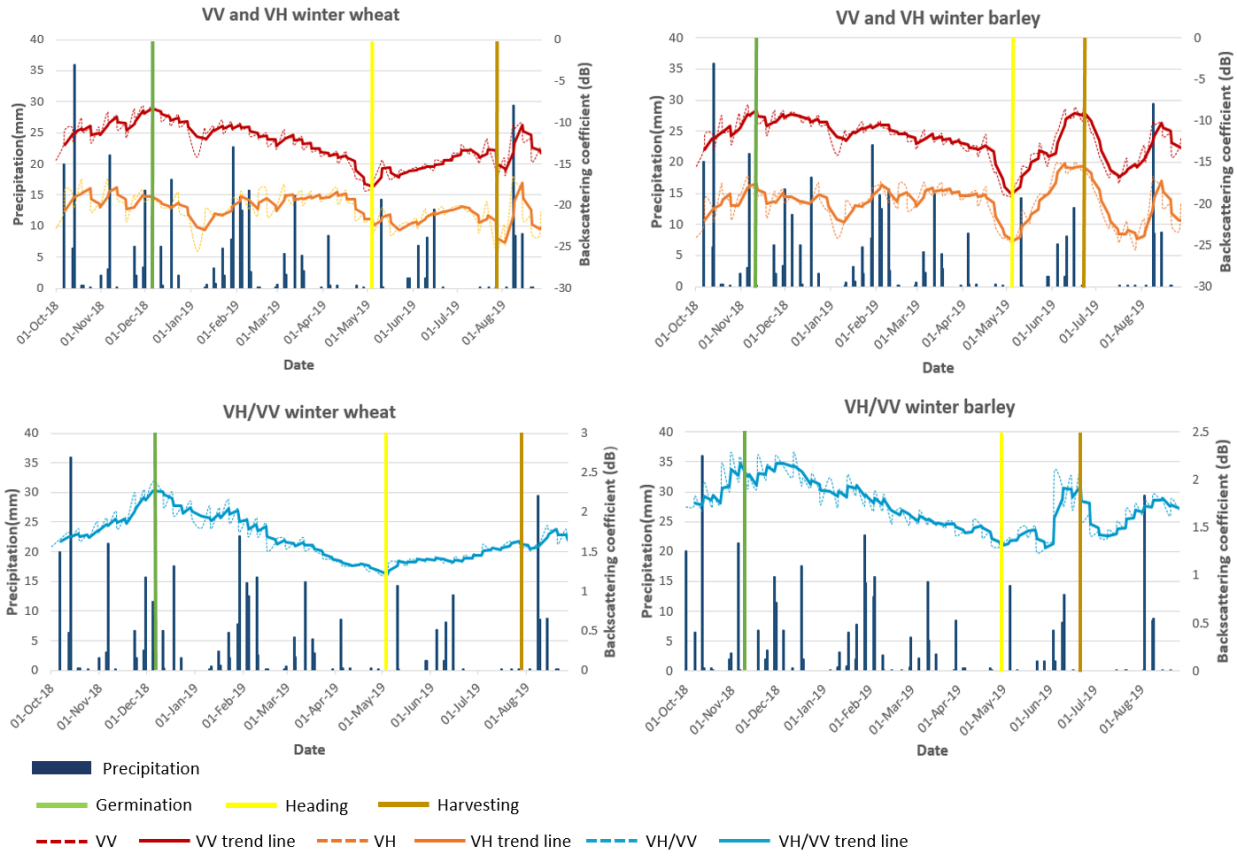

Figure 79 Winter wheat and winter barley Sentinel-1 temporal backscattering coefficient profiles at VV, VH, and VH/VV polarizations of the north Finistère region for the 2018-2019 growing season, with the daily precipitation data and three main phenological stage

In Figure 79, both the raw signal and smoothed trend line of temporal backscattering coefficient profiles of VV, VH, and the VH/VV ratio for the 2018-2019 growing season are displayed. Looking at the charts, it is shown that large variations occur before the germination due to the interaction between bare soil and vegetation caused by stem-ground double scattering (Picard et al., 2003; Y. Song & Wang, 2019), while previous researches suggest that the fluctuation in the backscattering profiles are mostly induced

by changes in soil water content and roughness (Y. Song & Wang, 2019). Pursuant to previous research, germination as the first stage of emergence of the plant can be recognized as the first maximum value of the profiles before decreasing (Nasrallah et al., 2019), therefore the germination stage is observed around 1 December for winter wheat, and in early November for winter barley. Moreover, for winter wheat this phase is best observed with VV and the VH/VV polarizations as the first peak of the curves; however, the peak is better illustrated at VV and VH polarizations for winter barley. Afterwards the overwintering stage occurs, and the crops remain in their vegetative stage during winter (generally around 1 January); a gentle decreasing and a slight flattening can be observed in VV polarization during this stage for both two crops. Furthermore, a fluctuation of the VV and VH curves of the two crops around 1 January 2019 is driven by a short pause of rainfall, as the signals are highly affected by the soil water content. The stem elongation stage starts in spring, where the vertical development of stems and leaves of the plants cause soil scattering attenuation, represented as a continuous and steadily decreasing line until they reach the heading stage, where the plants achieve their maximum height. After a long decreasing phase, σ° reaches the minimum value of the temporal profiles at the heading stage around 1 May 2019 for both winter crops, this stage can be better observed in σvv and σvh/vv for winter wheat phenology, and in σvh and σvh for winter barley. However, the sharp decrease in σvv and σvh at the heading stage, specifically in the profiles of winter barley might be the results of the relative lack of rainfall since early April. After heading, the inflorescence emergence, anthesis, grain development, and dough development stages occur. As seen on the graphs the curves start to increase during the flowering and grain development stages. These stages are illustrated by a sharp increase in winter barley regardless of the polarization, while by contrast the σvv and σvh/vv of winter wheat shows a smooth increase. At last, the ripening, which is the maturation stage, occurs and the crops are ready to be harvested. This phase is shown as the last peak of the profiles during the growing season, followed by a sharp decrease caused by the absence of volume and multiple scattering after the harvesting (Nasrallah et al., 2019). As the results show, harvesting, which took place around 1 August 2019, is better demonstrated by σvv and σvh for winter wheat, while the harvesting was in late June for winter barley, and is clearly shown by all polarizations, particularly in VV and VH.

Table 27 The best polarization observed for each phenological stage of winter wheat in the study

Stage	Polarization	Date	Determination
Germination	VH/VV, VV	Early December	First peak of the temporal series
Heading	VV, VH/VV	Early May	The minimum value after emergence
Ripening (Harvesting)	VV, VH	Around August 1	Last maximum of the profiles, following by a sharp decrease

Table 28 The best polarization observed for each phenological stage of winter barley in the study

Stage	Polarization	Date	Determination
Germination	VV, VH	Early November	First maximum of the temporal series
Heading	VV, VH	Around May 1	The minimum after emergence
Ripening (Harvesting)	VV, VH, VH/VV	Around July 1	Last maximum of the profiles, following by a sharp decrease

The best polarization for each phenological stage (Germination, Heading, Ripening (Harvesting)) are detailed in Table 27 and 28. The phenology monitoring of winter wheat highly relies on VV polarization, while the VH/VV ratio is also very helpful in identifying the germination and heading stages. Otherwise, VH polarization was used to detect the ripening stage and the harvesting event.

Meanwhile, phenology monitoring of the winter barley depends more on VV and VH polarizations, which are able to easily identify the three phenological statuses. In addition, VH/VV polarization is also effective for detecting the ripening and the harvesting.

Overall, this study proved that Sentinel-1 C-band SAR polarized backscatter time series has great potential to monitor winter crop phenology in a coastal area marked by frequent precipitation, and some important considerations of the behavior of different polarizations in regards to different phenological stages are worth discussing.

Firstly, despite the σ° of both polarizations and the ratio being relatively similar, the curves of the VH and VV polarizations are sharper compared to those of the ratio, due to the fact that the ratio is less sensitive to varying conditions like moisture and incidence angle variations. This can be explained by such effects having certain impacts in both polarizations, where the impacts would be reduced in the ratio (Schlund & Erasmi, 2020). As seen in Figure 78, the curves of the ratio VH/VV of winter wheat and winter barley are

smoother in comparison with the single polarization and less impacted by continuous rainfalls or drought due to absence of precipitation.

Secondly, the timing of phenological stages or growing periods of the crops based on the field knowledge are in agreement with the observations of the results. Based on prior knowledge, the sowing takes place between October and November, winter barley is usually planted earlier than winter wheat, and the germination occurs 3-4 weeks after sowing. This period can be confirmed by noting the large variations of the curves in the beginning induced by the interaction between bare soil and vegetation caused by stem-ground double scattering (Y. Song & Wang, 2019), afterwards the germination is represented by the first peak of the curves, especially well demonstrated in the polarization ratio for winter wheat and in the single polarizations for winter barley. After the overwintering period, the stem elongation, which begins in spring, can be recognized on the curves as a decreasing period caused by the attenuation of the signal when the vegetation cover occurs. Thereafter, the heading stage, where the crops attain their maximum height, occurs in early summer. This stage was confirmed with a minimum value on the curves around 1 May, which can be well observed in the polarization ratio for winter wheat and in single polarization for winter barley. After heading, the volume backscattering increased due to the increase of plant biomass ratio (Schlund & Erasmi, 2020), and the winter barley is harvested in early summer and winter wheat in mid summer. This is illustrated by the curves in all polarizations decreasing as expected with large variations post-harvesting depending on the in soil conditions.

This leads to the conclusion that it is feasible to map crop phenology with high accuracy by using SAR data, which is highly sensitive to the phenology of agriculture crops. In addition, unlike many methods which exclusively use the single polarization or the ratio (McNairn & Shang, 2016; Mandal et al., 2020; Son et al., 2021), our study shows that the combination of both is able to provide a better observation of agriculture phenology. Further studies can investigate the feasibility and performance of combining SAR and optical data for crop phenology monitoring.

7.5. Conclusion and perspectives

Three issues surrounding winter crops have been studied and discussed in this paper. Firstly, two types of winter crops (winter wheat, winter barley) were mapped by using a Sentinel-2 high-resolution image, and two different classification approaches were performed. Both the hierarchical classification, which turns a complex classification problem into a series of smaller classifications and the classical direct extraction, which extracts the winter crops directly from the original satellite image, were carried out. The hierarchical classification was composed of three smaller classifications: vegetation extraction from the original image, cropland extraction from vegetation, and finally winter crop extraction from other crops. Additionally, PBC and OBC were both performed in the last two steps and evaluated in order to keep the most accurate classification for further processing and analysis. Subsequently, crop phenology monitoring was performed based on the results of the previous step by using Sentinel-1 C-band SAR time series data, and the three important phenological stages (germination, heading, and ripening (harvesting)) and main growing periods were identified as well.

To respond to the objectives of the study and as the contribution of this paper, our results showed that winter crops in a fragmented landscape with heterogeneous land cover were successfully detected with high accuracy by using a Sentinel-2 image and the classification approaches proposed. In particular, the hierarchical classification framework significantly improved the classification accuracy (0.1 and 0.06 increase in the kappa and OA, respectively, against classical direct extraction), moreover the classification of winter barley is also enhanced by reducing confusion between winter barley and grassland with hierarchical classification framework (0.094 increase in F-score). Within the hierarchical classification, each classification method has its advantage, OBC slightly outperformed PBC in cropland extraction, yet PBC achieved higher accuracy in winter crops mapping. Although some small differences can be noticed, however there is no significant statistical divergence between the two classification methods.

The results also lead to the conclusion that Sentinel-1 C-band SAR polarized backscatter time series has great potential to monitor winter agriculture phenology in a coastal area with frequent rainfalls. Three phenological stages and main growing periods

could be easily identified from the time series in single polarization or the ratio, and furthermore the timing of the stages and growing periods of the crops observed on the results highly conform to the field knowledge.

Although very satisfactory results were acquired in this study, some limitations were revealed during the process of result analyzing. Despite the fact that the hierarchical classification approach acquired a better accuracy (0.099 in kappa and 0.066 in OA), this classification approach required more complicated processing steps and was more costly when one is comparing it to the direct extraction, for a slight enhancement in the results. Moreover, the confusion between winter barley and grassland was no negligible. For increasing classification accuracy, extra data such as SAR or Sentinel- 2 time series data can be applied for crop mapping. Additionally, even though the three main phenological statuses were successfully extracted from Sentinel-1 backscatter time series, more field research and expert knowledge, moreover, the combination of SAR and optical data could be required for identifying some others important phenological stages (e.g., tillering, flowering, soft dough and hard dough) and growth periods from the time series.

General conclusion

Synthesis

To conclude, this work has adequately achieved the initial objective, which is to propose robust, specific, and reproductive ML methodologies adapted to coastal areas for the cost-effective mapping LULC and the assessment of changes in Pays de Brest using the latest European satellite data (Pléiades, SPOT, and Sentinel). Specifically, LULC mapping was first accurately performed using diverse ML and DL classification algorithms. Then the major LULCC were successfully detected with post-classification methods based on the LULC classification results, the socio-economic driving factors of the changes were also well identified and analyzed, and eventually, the changes and their impacts were modeled for future studies. Therefore, the study contributes to the current LULC studies of Pays de Brest, a highly fragmented coastal area with small-scale fields, and provides valuable LULC information on Pays de Brest for local government and communities.

In this work, the latest generation of high spatial, spectral, and temporal resolution satellite imagery is shown to be well suited for LULC classification in fragmented coastal areas. In addition, the complex LULCC pattern was successfully revealed in various spatial and temporal dimensions. The satellite data, therefore, are able to provide helpful information to respond to environmental and urban management issues and to solve specific conflicts of interest.

In addition, remote sensing technologies were also shown to be a powerful tool for mapping coastal Pays de Brest, particularly with the contribution of the latest generation of European satellite systems and advanced classification methods. However, the most suitable methodologies depend greatly on other factors, such as the geographical characteristic of the study area, the spatial and spectral resolution of the satellite data, and—most of all—the specific objective of the study. Generally speaking, both DL algorithms (MLP, CNN) achieved the highest accuracy, although ML classifiers (RF, SVM) also obtained adequate results. Moreover, the winter crop classification revealed that hierarchical classification is more appropriate for the extraction of specific crops or vegetation types. However, OBC and PBC have their advantages in crop-type classification.

In addition, the SAR time-series backscattering coefficient was shown to have great potential to monitor winter crop phenology in coastal areas with frequent rainfalls.

Urbanization remains the most significant change in coastal Pays de Brest; the conversion from vegetated areas to urban areas is particularly significant on the coastland. Accordingly, the vegetation cover was significantly decreased. However, most of the croplands remained surprisingly unchanged. As in the most coastal areas, the main driving factors of LULCC in Pays de Brest are urban expansion, artificialization, and coastal tourism development, which are especially important near the coastlines. Overall, economic development is rapidly occurring in Pays de Brest, manifested as urban sprawl, tourism growth, increasing agricultural activities, and environmental degradation.

Furthermore, three study cases with specific objectives were performed in different test areas within Pays de Brest, in which adequate results were obtained as well: 1) Vegetation cover in the city of Brest, a highly heterogeneous urban area, was accurately extracted by using a combination of OBC methods, VHR satellite data and deep structure MLP algorithms. RF algorithms showed similar results; however, misclassification between high and low vegetation could be observed. 2) Compared to RF and SVM classification methods, DL CNN was found to be the most suitable classifier for LULC classification in a highly fragmented coastal area with a small-scale field. Additionally, the coastline of Pays de Brest has encroached on economic development since the 2000s. 3) The accurate mapping and extraction of specific crop types are feasible with the HR Sentinel-2 image, and hierarchical classification was well adapted in this case.

Limitations of this study

The objectives and adequate results are achieved through the three successfully performed study cases. The results of this work can be helpful for the local government, communities, and urban planners to formulate policies for sustainable development in Pays de Brest. Nevertheless, some uncertainties and limitations persisted:

1) Due to the meteorological conditions and annual high-intensity precipitations, it is very rare to obtain cloud-free optical images of the study area. For example, two

different sources and spatial resolution images were used in the study of LULC classification due to the lack of processable optical data.

2) Misclassification of different types of vegetation and planted crops (e.g., confusion between grassland and winter barley) is caused by very similar spectral characteristics.

3) It is difficult to validate cropland classification results in the past years owing to the crop rotation system.

Further research

Some suggestions can be proposed for completing the unfinished task of the study, improving the LULC studies to achieve better results, and further meaningful research on LULC in Pays de Brest.

1) To achieve the final unmet objective of generating LULCC models to develop forward-looking scenarios with classification results.

2) To use hyperspectral data for LULC classification, especially for better discrimination between different types of vegetation and croplands.

3) To explore more potential contributions of SAR images, because the meteorological conditions limits the optical sensors, and eventually LiDAR morphometry.

4) To conduct the three study cases throughout the entire territory of Pays de Brest.

5) To study the natural landscapes in Pays de Brest (e.g., wetland and intertidal areas), which provide essential resource but are increasingly degraded by human activities.

Appendices

Appendix 1 Questionnaire for farmers

We are interested in two winter crops (winter wheat (purple), and winter barley (blue)) in 2019.

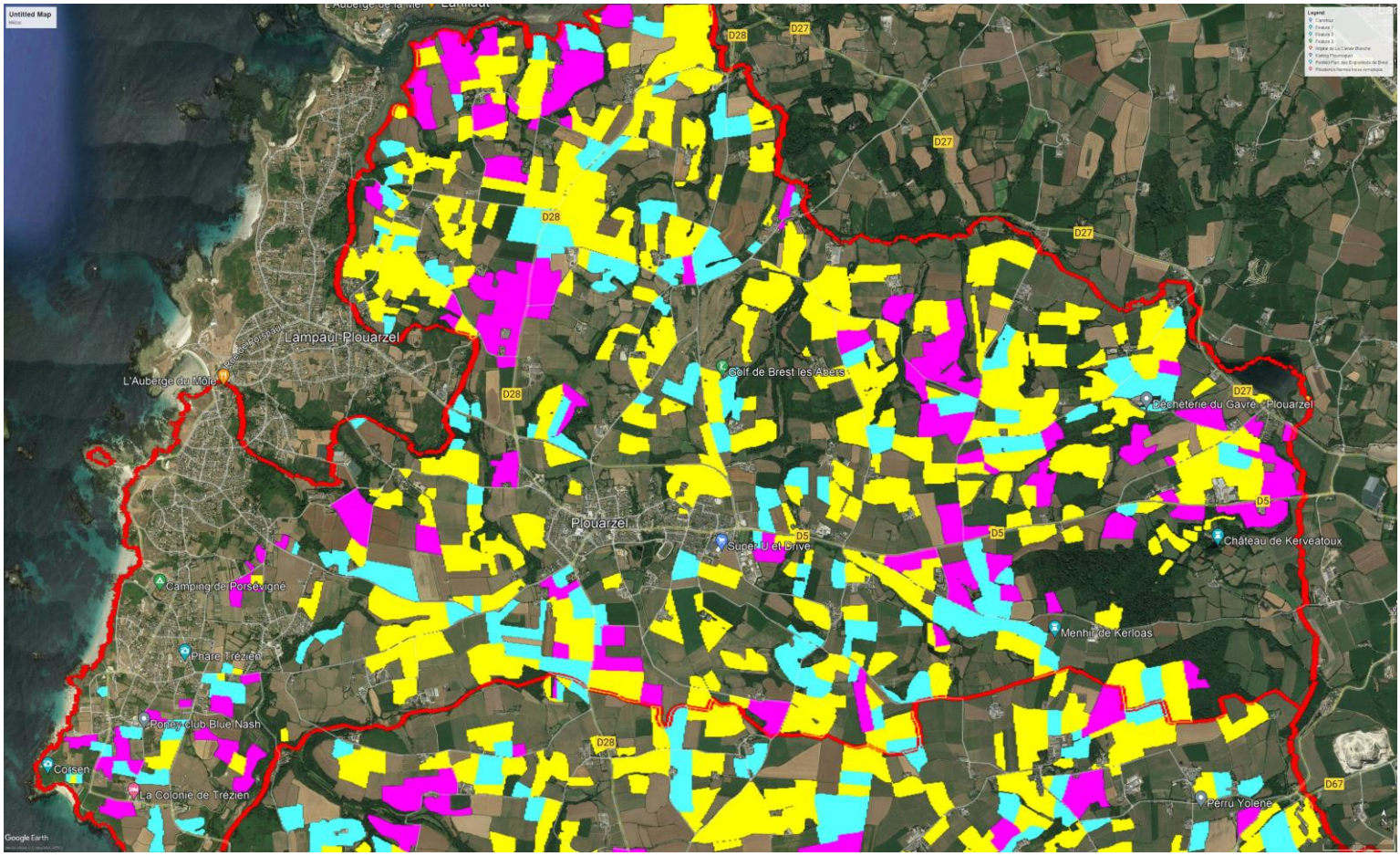

1. Could you locate your croplands on this map?

2. If positif, does the map faithful to reality? (Did you really have this crop (wheat, maize, barley) in your field in 2019?

3. If negatif, what was the crop?

4. Could you please indicate the growing cycle of this crops (e.g. month of sowing, emergence, bolting, heading, maturation and approximate harvest date)?

5. Do you recall any natural event that could disrupt the growth cycle in 2019, e.g. very important climate change (such as anomalous warming, increased rainfall etc.)?

Appendix 2

《Machine Learning Methods and Classification of Vegetation in Brest, France》

(Conference proceeding 2019)

Machine learning methods and classification of vegetation in Brest, France

Guanyao Xie, Simona Niculescu, Chinguyen Lam, Elise Seveno

Guanyao Xie, Simona Niculescu, Chinguyen Lam, Elise Seveno, "Machine learning methods and classification of vegetation in Brest, France," Proc. SPIE 11157, Remote Sensing Technologies and Applications in Urban Environments IV, 111570J (2 October 2019); doi: 10.1117/12.2533436

SPIE.

Event: SPIE Remote Sensing, 2019, Strasbourg, France

Invited Paper

Machine learning methods and classification of vegetation in Brest (France)

Guanyao XIE, Dr. Simona NICULESCU, Chinguyen LAM, Elise SEVENO

Laboratory LETG-Brest, Géomer, UMR 6554 CNRS, IUEM·UBO

ABSTRACT

Urban green land plays a special significant role in our life. Many previous studies have already proven the feasibility of satellite imagery processing for urban green land detection, and many classification techniques were tested for this purpose. In this paper, two methods of Machine learning, such as Artificial Neural Networks (ANN) and Random Forest (RF) were tested on a series of very high spatial resolution satellite imagery to classify, highlight urban green lands and eventually study their change in three years. Firstly, we present Multilayer Perceptron (MLP), a simple feed-forward neural network which consists of two steps, SLIC superpixel segmentation and image classification through MLP trained model. Secondly, RF technique was applied and compared to the previous classification. Then the classification results were interpreted at the final stage. These methods are performed on satellite images Pléiades of the city of Brest (3 images acquired in 2016, 2017 and 2018), these multispectral images are already preprocessed and all pan-sharpened to 50 cm spatial resolution.

1. INTRODUCTION

Due to rising population, urbanization, green land area is sharply shrinking on the planet and therefore more and more difficult for urban residents to get close to nature. And so, urban green land plays a special significant role in our life in several aspects, such as physical and mental health, microclimate, reduce pollution, heat island effect, preserve biodiversity, improve city water and air quality, create connection in neighborhood. Urban green land can be defined as "predominantly unsealed, permeable and soft surfaces such as soil, grass, shrubs, trees and water" (James et al. 2009) and in different forms, such as parks, garden and infrastructures like stadium.

Therefore, urban green land is an important space that need to be detected, monitored, analyzed, mapped, and the most common technique is remote sensing which is also the most significant technology because it consumes less time and labors, and it has already been proven by many previous studies in several cities (Xiuying Zhang and Xuezhi Feng 2005), (Nichol and Lee 2005), (Tunay et al. 2007), (Yang et al. 2009), (Ye Lizao et al. 2013), (Qian et al. 2015), (Trisakti 2017), (Kopecká, Szatmári, and Rosina 2017), (Haas and Ban 2017), (Wang et al. 2018), etc.

However, urban green area, other than forest, is usually in smaller scale, such as parks, gardens, square, stadium, therefore, high resolution imagery and high precision classification method are very necessary for monitoring as like in numerous works (Burbridge and Yun Zhang 2003), (Bonora et al. 2008), (Pena-Salmon and Rojas-Caldelas 2009), (Mustafa et al. 2015), (Zhang et al. 2018), (Huang, Zhao, and Song 2018).

Since the last decades, machine learning methods have been widely used in numerous various fields of geoscience for classification, regression, segmentation problems, such as in land use cover (Buscombe and Ritchie 2018), atmosphere (Zamani Joharestani et al. 2019), oceanology (Bolton and Zanna 2019), crop field (Gonzalez-Sanchez, Frausto-Solis, and Ojeda-Bustamante 2014) and forest monitoring (Liu et al. 2008). Also, several algorithms are adopted for remote sensing

Remote Sensing Technologies and Applications in Urban Environments IV, edited by Thilo Erbertseder, Nektarios Chrysoulakis, Ying Zhang, Proc. of SPIE Vol. 11157, 111570J · © 2019 SPIE
CCC code: 0277-786X/19/$21 · doi: 10.1117/12.2533436

uses, such as support vector machine, decision tree, and today, deep learning, a concept of machine learning has become popular, which uses computational models composed of multiple processing layers to learning representations of data with multiple levels of abstraction (LeCun, Bengio, and Hinton 2015). A variety of algorithms are developed, the most common are: Artificial Neural Network (ANN), Convolutional Neural Network (CNN), Recurrent Neural Network (RNN), etc.

More recently, ANN, a well-established method for solving non-linear problem becomes popular in the field of machine learning applied in remote sensing and achieves a remarkable improvement, for diverse purposes such as classification and regression. In this study, the most widely known and used ANN method, Multilayer Perceptron, also known as multilayer feedforward neural network is explored and applied to Pléiades very high spatial resolution satellite images of 3 years (2016-2018) in the city of Brest in order to study the change of urban green areas in the city. Also, random forest, a supervised ensemble method and a powerful algorithm which is used in large scale, especially in purpose of land cover detection and it is recognized for its good performance on classification and the capacity of providing high precision result is tested in the same study area. In the end, results of 2 methods are compared to evaluate their performance.

This paper is organized as follows, firstly study area and dataset, including data preprocessing are presented, secondly the MLP processing chain, finally results and comparison between the 2 methods.

2. STUDY AREA

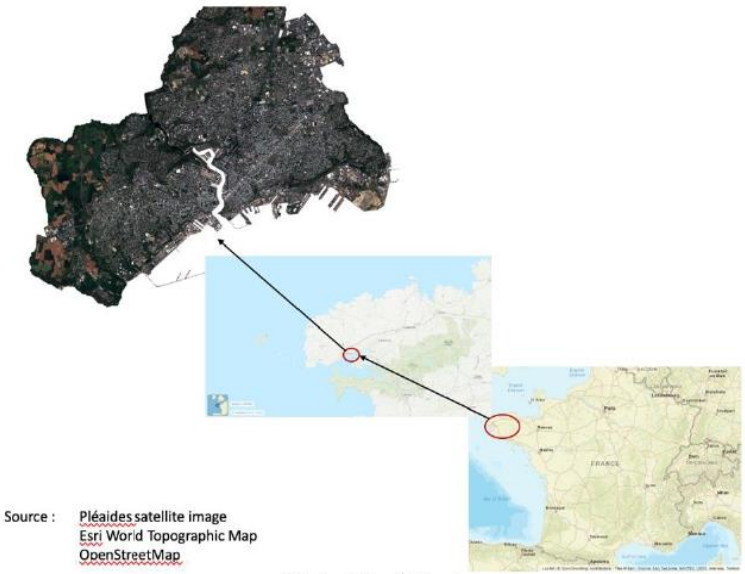

Fig.1. City of Brest

Brest is a coastal and main city and second military city of France located in the west of the region of Brittany, in northwest of France (48° 23′ 27″, 4° 29′ 08”). The surface of the city in 49.51 km2 and the population is 319 947 in 2016.

Brest is composed mostly by large parts of urban area, including building and sealed surface in the center of the city, military area and harbor in the south, the variety of urban green areas such as botanical garden located in the east and some urban forest on the left bank, and agriculture area in the north and west of the city.

3. DATASET AND DATA PREPROCESSING

In this study, three very high-resolution satellite images used are as follows:

Imagery	Date	Spatial resolution(m)	Number of bands
Pléiades 1B	04-05-2016	0.5	4
Pléiades 1B	27-08-2017	0.5	4
Pléiades 1B	28-06-2018	0.5	4

Table.1. Dataset used of the study

Pléiades is a twin optical satellite launched in 2011 (Pléiades 1A) and 2012 (Pléiades 1B) for the purpose of earth monitoring, two satellites operate on the same orbit and provide 50cm spatial resolution panchromatic image and 2m spatial resolution multiband (Red, Blue, Green, Near-Infrared) image with 20km swath width and daily revisit time. Pléiades images are applied in numerous areas like defense, mapping, geophysical risks, hydrology applications, renewable resources, marine environment and civil security ('Pleiades' n.d.).

3 pan-shaped multiband images were downloaded from the platform of DINAMIS (https://dinamis.teledetection.fr/home) throw l'EQUIPEX GEOSUD, then
we merged different parts of the image to create a mosaic, and the images were clipped by the contour of Brest. In the end, a new band of Normalized Difference Vegetation Index (NDVI) is added
in order to get better results in vegetation monitoring.

4. METHODOLOGY

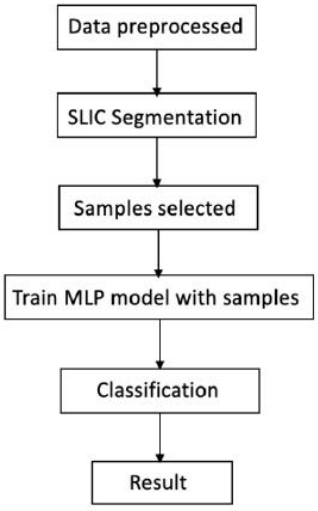

Fig.2. Scheme of the proposed methodology

4.1. Simple Linear Iterative Clustering (SLIC) Segmentation:

Recently, superpixel has become important and well-used in computer vision area, superpixel algorithms are able to cluster pixels into regions in order to reduce the size of image and the complexity of image processing tasks, therefore provide a better performance and result.

SLIC is a recent but fast and memory efficient algorithm of superpixel proposed by Achanta R., it adapts the traditional k-means segmentation methods to superpixel generation, adheres well to the boundaries and has a better performance on segmentation by grouping pixels into N regions based on their color similarity and spatial proximity(Achanta et al. 2012).

As a powerful algorithm, SLIC is also easy to understand and use, it starts by choosing a desirable number of cluster, centers of cluster were distributed on image on the basis of the number of cluster chosen in order to produce roughly equally sized superpixels, then these centers are moved to the lowest gradient position in a 3x3 neighborhood for avoiding centering pixels on the edge or a noisy pixel, next, each pixel is assigned to the closest cluster center and the pixel must be located in the search region of this cluster center as well, once every pixel is assigned to the closest cluster center, then the cluster center is adjusted to mean vector of all the pixels belonging to this cluster and the assignment and update steps are repeated until the residual error between the new and the previous cluster center converges. In the end, re-assigning disjoint pixel to the nearby cluster center can enforce connectivity (Achanta et al. 2012).

In this step, the image was segmented with scikit-image, an image processing library of python. In this function, three parameters are set, n_segments (the approximate number of clusters in the segmented output image) = 1,600,000, compactness (balances color proximity and space proximity, higher values give more weight to space proximity) = 1 and sigma (width of Gaussian smoothing kernel for pre-processing for each dimension of the image) = 2 ('Module: Segmentation — Skimage v0.16.Dev0 Docs' n.d.).

4.2. Samples selected:

Samples of each class are selected manually based on the image segmented, and 80% of samples selected are assigned to training data, 20% are validation data. Once samples are selected, we created tables which contain the mean value of each spectral band of all pixels belonging to the same area.

4.3. Train MLP model with samples and classification:

MLP is the most widely known and used supervised classification method of ANN, it is a multilayer feedforward neural network, which has at least three layers(Fig.3): an input layer which receives signals, an output layer which provides the prediction of result, and numerous hidden layers constituted by neurons with a nonlinear activation function, the number of hidden layers and the number of neurons on it can be vary according to the problem, more neurons given, greater sensitivity to the problem in general case, but also the risk of overfitting (Murtagh 1991).

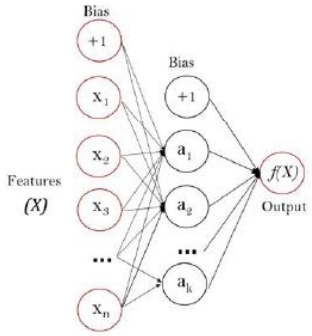

Fig.3. MLP model with one hidden layer

In this step, MLP model is trained with samples selected in the previous step by using backpropagation technique, and the parameters of the model are adjusted several times for better prediction and less error rate of classification. After that, a table which contains mean values of each spectral band of each segment of the entire image was put into the model in order to obtain the classification result.

Therefore, our MLP model has one input layer with 5 nodes corresponding to 5 spectral bands (Green, Blue, Red, Near-infrared (NIR) and NDVI), four hidden layers with tanh activation function, and one output layer with 5 nodes corresponding to 5 classes (tree, shrub and grass, non-vegetation, water and no data) and softmax activation function. The model is also compiled by RMSprop as an optimizer, categorical_crossentropy as loss function, 500 as batch size and 200 epochs (Fig.4).

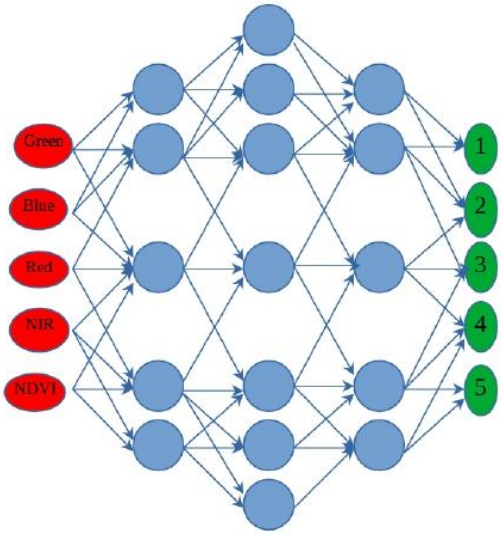

Fig.4. Multilayer Perceptron model proposed in the study

5 RESULT

5.1 MLP classification result:

The processing chain presented in this paper is applied on three satellite images of the same study area, city of Brest. Results are shown in Fig. 5, and accuracy indexes of MLP model training are presented in Table 2 and 3. It is worth nothing that small error may exist between classification result and terrain truth, very high spatial resolution pixel of some areas in Brest is not provided by Pléiades because of military reason.

Class	Overall Accuracy
Tree	0.92
Shrub and grass	0.99
Water	0.91
No vegetation	0.99
No data	0.99
Total accuracy	0.99

Table.2. Overall accuracy of MLP model

	Tree	Shrub and grass	Water	No vegetation	No data
Tree	5389	482	0	10	0
Shrub and grass	273	24873	0	20	0
Water	12	1	987	87	0
No vegetation	52	42	73	100270	0
No data	3	1	0	2	5963

Kappa = 0.982552495

Table.3. Confusion matrix and kappa of MLP model

According theses tables, it is noticeable that overall accuracy and kappa indexes of all the classes are good and approach to 1, although the tree and water classes are less accurate from Table 2 and the small confusion between 2 vegetation classes from the Table 3 as expected. It reveals that the MLP model has well training by using selected samples, and it is capable to produce fine classification results. So, urban green areas in the city of Brest are accurately extracted for further analysis.

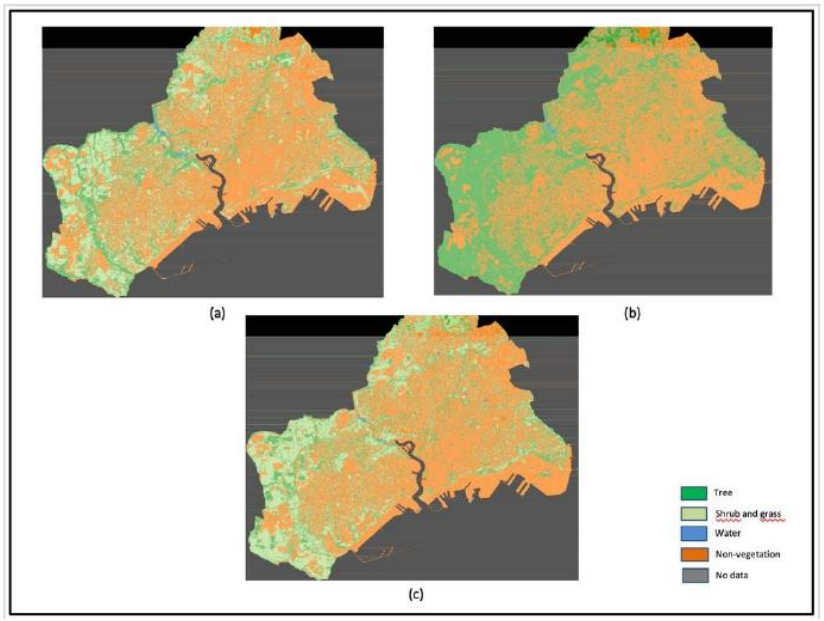

Fig.5. Classification results of city of Brest on 2016(a), 2017(b), 2018(c) bases on pléiades very high spatial resolution satellite image by using MLP model

From visual inspection of classification result, globally urban green areas and non-vegetation areas in the city are almost unchanged expect agricultural area variation which located on the west and the north of the city, and so vegetation cover stays the same in three years (2016-2018). Classification result of 2017 shows more trees, it can be explained by the satellite image was produced in August other than May and June in 2016 and 2018. Then some changes can be noticed that some vegetation areas turned to non-vegetation areas in the southeast in 2017 and 2018, and there were generally more trees in the city in 2016, 2017 than in 2018.

5.2 Comparison with random forest classification result:

Random forest is an efficient, fast method for classification and regression, and it made a significant improvement in classification accuracy. This method is an ensemble of decision trees, each tree depends on the values of a random vector sampled independently and with the same distribution of all trees in the forest, the ensemble of trees votes for the most popular class (Breiman 2001). In this method, classification supervised is applied to the satellite image by selecting a training set manually and training decision trees then making the final prediction.

Accuracy indexes table is presented in Table 4, also comparison between result of the MLP classification and random forest in 2016 is demonstrated in Fig.6.

	2016	2017	2018
kappa	0.97	0.88	0.85
Overall accuracy	0.98	0.92	0.90

Table.4. Accuracy indexes of random forest classification of 3 years (2016-2018)

From Table 4. It is worth noticing that indexes are generally good, although 2 indexes of the first year are higher, indexes of 2017 and 2018 are around 0.90. Therefore, to sum up classification results of 3 years with random forest are relatively satisfactory such that urban green areas are well extracted. By contrast, the deep learning method which has results around 1 has a better performance on classification accuracy.

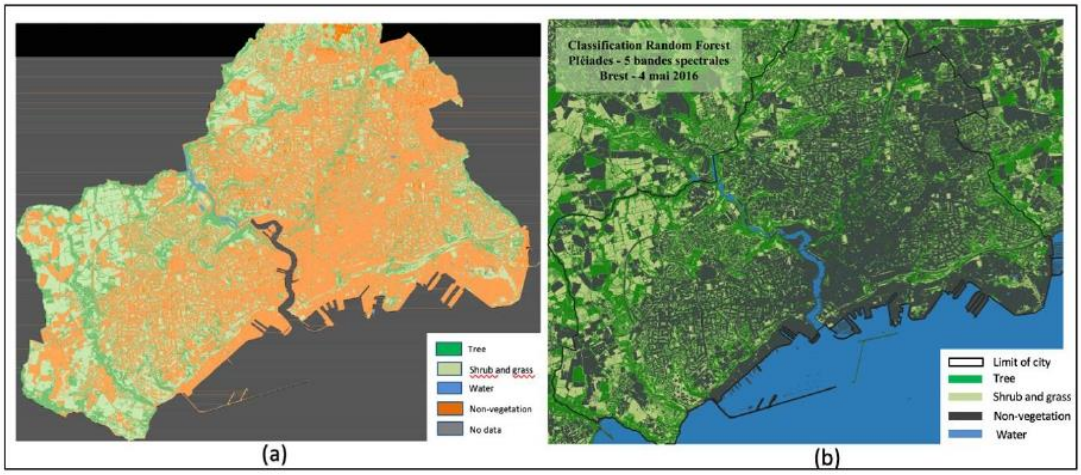

Fig.6. Comparison of MLP classification result (a) and Random Forest classification result (b)

Due to good classification accuracy of 2 methods, 2 maps form Fig.6. shows extremely high similarity, except there are some confusions between water and shadow of building in the random forest classification result.

Therefore, even though these 2 methods have different processing chain, there are both effective and powerful methods for classification problem which is able to provide very fine classification accuracy. Then, deep learning method shows a better performance by comparing accuracy indexes.

6 CONCLUSION

In this study, Multilayer Perceptron, a deep learning method is applied to Pléiades very high spatial resolution satellite images of 3 years (2016-2018) in the city of Brest in order to study the change of urban green areas in the city, also

performance of this method is evaluated by comparing with random forest, a well-known and widely used machine learning method.

We proposed a processing chain starting with SLIC superpixel segmentation, a fast and memory efficient segmentation method which groups pixels into N regions based on their color similarity and spatial proximity(Achanta et al. 2012). Then the training dataset is selected manually based on segmentation result for the purpose of MLP model training. Finally, 3 satellite images were put into the well-trained model to obtain the classification result.

Classification results are satisfactory according to accuracy indexes which are around 1, it proves that MLP method and Pléiades very high spatial resolution image are suitable for urban green lands mapping and monitoring. Random Forest method shows very similar result, although has relatively lower accuracy than MLP.

REFERENCES

Achanta, R., A. Shaji, K. Smith, A. Lucchi, P. Fua, and Sabine Süsstrunk. 2012. 'SLIC Superpixels Compared to State-of-the-Art Superpixel Methods'. *IEEE Transactions on Pattern Analysis and Machine Intelligence* 34 (11): 2274–82. https://doi.org/10.1109/TPAMI.2012.120.

Bolton, Thomas, and Laure Zanna. 2019. 'Applications of Deep Learning to Ocean Data Inference and Subgrid Parameterization'. *Journal of Advances in Modeling Earth Systems* 11 (1): 376–99. https://doi.org/10.1029/2018MS001472.

Bonora, Nico, Valter Sambucini, Ines Marinosci, Federico Azzolini, Fabio Baiocco, Roberto Visentin, and Marcello Marinelli. 2008. 'Remote sensinig survey of italian urban green areas'. *Italian Journal of Remote Sensing*, October, 17–25. https://doi.org/10.5721/ItJRS20084032.

Breiman, L. Random forests. Mach. Learn. 2001, 45, 5–32.

Burbridge, S., and Yun Zhang. 2003. 'A Neural Network Based Approach to Detecting Urban Land Cover Changes Using Landsat TM and IKONOS Imagery'. In *22nd Digital Avionics Systems Conference. Proceedings (Cat. No.03CH37449)*, 157–61. Berlin, Germany: IEEE. https://doi.org/10.1109/DFUA.2003.1219978.

Buscombe, Daniel, and Andrew Ritchie. 2018. 'Landscape Classification with Deep Neural Networks'. *Geosciences* 8 (7): 244. https://doi.org/10.3390/geosciences8070244.

Gonzalez-Sanchez, Alberto, Juan Frausto-Solis, and Waldo Ojeda-Bustamante. 2014. 'Predictive Ability of Machine Learning Methods for Massive Crop Yield Prediction'. *Spanish Journal of Agricultural Research* 12 (2): 313. https://doi.org/10.5424/sjar/2014122-4439.

Haas, Jan, and Yifang Ban. 2017. 'Mapping and Monitoring Urban Ecosystem Services Using Multitemporal High-Resolution Satellite Data'. *IEEE Journal of Selected Topics in Applied Earth Observations and Remote Sensing* 10 (2): 669–80. https://doi.org/10.1109/JSTARS.2016.2586582.

Huang, Bo, Bei Zhao, and Yimeng Song. 2018. 'Urban Land-Use Mapping Using a Deep Convolutional Neural Network with High Spatial Resolution Multispectral Remote Sensing Imagery'. *Remote Sensing of Environment* 214 (September): 73–86. https://doi.org/10.1016/j.rse.2018.04.050.

James, P., K. Tzoulas, M.D. Adams, A. Barber, J. Box, J. Breuste, T. Elmqvist, et al. 2009. 'Towards an Integrated Understanding of Green Space in the European Built Environment'. *Urban Forestry & Urban Greening* 8 (2): 65–75. https://doi.org/10.1016/j.ufug.2009.02.001.

Kopecká, Monika, Daniel Szatmári, and Konštantín Rosina. 2017. 'Analysis of Urban Green Spaces Based on Sentinel-2A: Case Studies from Slovakia'. *Land* 6 (2): 25. https://doi.org/10.3390/land6020025.

LeCun, Yann, Yoshua Bengio, and Geoffrey Hinton. 2015. 'Deep Learning'. *Nature* 521 (7553): 436–44. https://doi.org/10.1038/nature14539.

Liu, Kai, Xia Li, Xun Shi, and Shugong Wang. 2008. 'Monitoring Mangrove Forest Changes Using Remote Sensing and GIS Data with Decision-Tree Learning'. *Wetlands* 28 (2): 336–46. https://doi.org/10.1672/06-91.1.

Murtagh, Fionn. 1991. 'Multilayer Perceptrons for Classification and Regression'. *Neurocomputing* 2 (5–6): 183–97. https://doi.org/10.1016/0925-2312(91)90023-5.

Mustafa, Y. T., H. N. Habeeb, A. Stein, and F. Y. Sulaiman. 2015. 'IDENTIFICATION AND MAPPING OF TREE SPECIES IN URBAN AREAS USING WORLDVIEW-2 IMAGERY'. *ISPRS Annals of Photogrammetry, Remote Sensing and Spatial Information Sciences* II-2/W2 (October): 175–81. https://doi.org/10.5194/isprsannals-II-2-W2-175-2015.

Nichol, J., and C. M. Lee. 2005. 'Urban Vegetation Monitoring in Hong Kong Using High Resolution Multispectral Images'. *International Journal of Remote Sensing* 26 (5): 903–18. https://doi.org/10.1080/01431160412331291198.

Pena-Salmon, C. A., and R. Rojas-Caldelas. 2009. 'Methodology for Planning Urban Green Areas: The Case of Mexicali, Baja California, Mexico'. In , 33–41. Cyprus. https://doi.org/10.2495/SDP090041.

Qian, Yuguo, Weiqi Zhou, Weifeng Li, and Lijian Han. 2015. 'Understanding the Dynamic of Greenspace in the Urbanized Area of Beijing Based on High Resolution Satellite Images'. *Urban Forestry & Urban Greening* 14 (1): 39–47. https://doi.org/10.1016/j.ufug.2014.11.006.

Trisakti, Bambang. 2017. 'Vegetation Type Classification and Vegetation Cover Percentage Estimation in Urban Green Zone Using Pleiades Imagery'. *IOP Conference Series: Earth and Environmental Science* 54 (January): 012003. https://doi.org/10.1088/1755-1315/54/1/012003.

Tunay, M., M. A. Marangoz, S Karakis, and A. Atesoglu. 2007. 'Detecting Urban Vegetation from Different Images Using an Object-Based Approach in Bartin, Turkey'. In *2007 3rd International Conference on Recent Advances in Space Technologies*, 636–40. Istanbul, Turkey: IEEE. https://doi.org/10.1109/RAST.2007.4284070.

Wang, Jing, Weiqi Zhou, Yuguo Qian, Weifeng Li, and Lijian Han. 2018. 'Quantifying and Characterizing the Dynamics of Urban Greenspace at the Patch Level: A New Approach Using Object-Based Image Analysis'. *Remote Sensing of Environment* 204 (January): 94–108. https://doi.org/10.1016/j.rse.2017.10.039.

Xiuying Zhang, and Xuezhi Feng. 2005. 'Detecting Urban Vegetation from IKONOS Data Using an Object-Oriented Approach'. In *Proceedings. 2005 IEEE International Geoscience and Remote Sensing Symposium, 2005. IGARSS '05.*, 2:1475–78. Seoul, Korea: IEEE. https://doi.org/10.1109/IGARSS.2005.1525404.

Yang, Cunjian, He Huang, Yang Zhang, and Jin-an Cheng. 2009. 'Comparison of Extracting the Urban Green Land from Satellite Images with Multi-Resolutions'. In *2009 Joint Urban Remote Sensing Event*, 1–5. Shanghai, China: IEEE. https://doi.org/10.1109/URS.2009.5137678.

Ye Lizao, Li Hu, He Guangjun, Niu Ting, and Chen Donghua. 2013. 'Study on Urban Green Landscape Pattern Based on High Resolution Remote Sensing Image'. In *Proceedings 2013 International Conference on Mechatronic Sciences, Electric Engineering and Computer (MEC)*, 703–6. Shengyang, China: IEEE. https://doi.org/10.1109/MEC.2013.6885152.

Zamani Joharestani, Mehdi, Chunxiang Cao, Xiliang Ni, Barjeece Bashir, and Somayeh Talebiesfandarani. 2019. 'PM2.5 Prediction Based on Random Forest, XGBoost, and Deep Learning Using Multisource Remote Sensing Data'. *Atmosphere* 10 (7): 373. https://doi.org/10.3390/atmos10070373.

Zhang, Ce, Isabel Sargent, Xin Pan, Huapeng Li, Andy Gardiner, Jonathon Hare, and Peter M. Atkinson. 2018. 'An Object-Based Convolutional Neural Network (OCNN) for Urban Land Use Classification'. *Remote Sensing of Environment* 216 (October): 57–70. https://doi.org/10.1016/j.rse.2018.06.034.

'Pleiades'. n.d. Pleiades. Accessed 17 August 2019. https://pleiades.cnes.fr/en/PLEIADES/index.htm.

'Module: Segmentation — Skimage v0.16.Dev0 Docs'. n.d. Accessed 21 August 2019. https://scikit-image.org/docs/dev/api/skimage.segmentation.html#skimage.segmentation.slic.

Appendix 3

《Mapping and monitoring of land cover / land use (LCLU) changes in the Crozon Peninsula (Britanny, France) from 2007 to 2018 by Machine Learning algorithms (Support Vector Machine, Random Forest, Convolutional NN) and by Post-classification comparison (PCC)》 (Journal article 2021)

remote sensing

MDPI

Article

Mapping and Monitoring of Land Cover/Land Use (LCLU) Changes in the Crozon Peninsula (Brittany, France) from 2007 to 2018 by Machine Learning Algorithms (Support Vector Machine, Random Forest, and Convolutional Neural Network) and by Post-classification Comparison (PCC)

Guanyao Xie [1,*] and Simona Niculescu [1,2]

[1] Laboratory LETG-Brest, Géomer, UMR 6554 CNRS, IUEM UBO, 29200 Brest, France; Simona.Niculescu@univ-brest.fr
[2] Department of Geography, University of Western Brittany, 3 Rue des Archives, 29238 Brest, France
* Correspondence: Guanyao.Xie@univ-brest.fr

Abstract: Land cover/land use (LCLU) is currently a very important topic, especially for coastal areas that connect the land and the coast and tend to change frequently. LCLU plays a crucial role in land and territory planning and management tasks. This study aims to complement information on the types and rates of LCLU multiannual changes with the distributions, rates, and consequences of these changes in the Crozon Peninsula, a highly fragmented coastal area. To evaluate the multiannual change detection (CD) capabilities using high-resolution (HR) satellite imagery, we implemented three remote sensing algorithms: a support vector machine (SVM), a random forest (RF) combined with geographic object-based image analysis techniques (GEOBIA), and a convolutional neural network (CNN), with SPOT 5 and Sentinel 2 data from 2007 and 2018. Accurate and timely CD is the most important aspect of this process. Although all algorithms were indicated as efficient in our study, with accuracy indices between 70% and 90%, the CNN had significantly higher accuracy than the SVM and RF, up to 90%. The inclusion of the CNN significantly improved the classification performance (5–10% increase in the overall accuracy) compared with the SVM and RF classifiers applied in our study. The CNN eliminated some of the confusion that characterizes a coastal area. Through the study of CD results by post-classification comparison (PCC), multiple changes in LCLU could be observed between 2007 and 2018: both the cultivated and non-vegetated areas increased, accompanied by high deforestation, which could be explained by the high rate of urbanization in the peninsula.

Keywords: remote sensing; machine learning; GEOBIA; CNN; land cover/land use; SPOT 5; Sentinel 2; change detection

Citation: Xie, G.; Niculescu, S. Mapping and Monitoring of Land Cover/Land Use (LCLU) Changes in the Crozon Peninsula (Brittany, France) from 2007 to 2018 by Machine Learning Algorithms (Support Vector Machine, Random Forest, and Convolutional Neural Network) and by Post-classification Comparison (PCC). *Remote Sens.* **2021**, *13*, 3899. https://doi.org/10.3390/rs13193899

Academic Editor: Magaly Koch

Received: 13 July 2021
Accepted: 25 September 2021
Published: 29 September 2021

1. Introduction

Coastal zones are the shores of seas or oceans. Today, nearly half of the world's population lives in coastal regions where multiple activities are developed [1]. Over the last century, coastal zones throughout the world have undergone major changes related to a significant influx of the population. Coveted, densely populated, and exploited by human societies, coastal zones are therefore subject to significant pressures that generate territorial dynamics and changes in land cover/land use (LCLU). LCLU is al-ways influenced by human actions and environmental features and processes, and it mediates the interactions of these two factors. This means that land use changes are primarily due to human actions, which are associated with economic development, tech-neology, environmental change, and especially, population growth, which usually has parallel rates to land use change [2,3]. However, traditional methods require direct observations in the field; usually, they are not

only ineffective, expensive, time-consuming, and labor intensive but are also limited on the local scale. Hence, remote sensing with analysis techniques is highly recommended, and there has been an in-creasing demand for LCLU studies since the first launch of Earth observation satellites in 1972 with Landsat-1. Since that time, the monitoring and mapping of LCLUs over large areas and in a consistent manner has been made possible with Earth observation (EO) data, and detection of these changes by EO data is necessary for the better management of territory and resources. Moreover, each new generation of satellite equipment increases the resolution of sensors that collect high spatial resolution data for LCLU mapping and monitoring [4]. Since high-resolution satellite images are now available, land cover change mapping and monitoring at the landscape or local scale have been developed at a high rate of speed [5–7].

Several national and international organizations have produced regional land change maps that represent a location on a single date (e.g., CORINE Land Cover 2000 in Europe), with Landsat observations acquired in a target year interval (e.g., ±1–3 years). Some programs repeat land cover mapping periodically (e.g., NLCD 2001/2006/2011 in the United States and CSBIO in France) to allow the observation of the changes. The local accuracy of these global or national land cover maps generated from coarse spatial resolution data is low, especially in regions with fragmented land covers [8].

At the same time, for studies at larger scales, satellite data have been used to monitor LCLU changes worldwide in various fields of research, such as mapping cropland conversions [9], monitoring urbanization and its impacts [10–12], monitoring deforestation [13–17], evaluating the environment [18–20] and biodiversity losses, and examining the influence of LCLU on climate change [21]. Nonetheless, all types of land use might lead to detrimental impacts and effects in many fields: for example, the abandonment of agricultural land without restoration is linked to a specific set of problems, including landscape degradation and an increased risk of erosion [4]. These irreversible impacts of LCLU change have significantly increased in recent decades, and so the mapping and monitoring LCLU is very important as the first step in the study and management of this phenomenon.

In recent years, given the importance of LCLU changes and the increasing availability of open-access archived multitemporal datasets, many methods for analyzing and mapping LCLU changes have been developed. The diversity of algorithms for studying LCLU changes was also determined by the diversity of remote sensing sensor types (e.g., multispectral, hyperspectral, and SAR). Among the most commonly used satellite images in change detection (CD) studies are multispectral images due to the diversity of the types of sensors used to collect the data and the high temporal resolution of datasets for this type of study. For example, Wang et al. 2018 [22] conducted a study in a coastal area of Dongguan City, China, using SPOT-5 images acquired in 2005 and 2010. In this study, a scale self-adapting segmentation (SSAS) approach based on the exponential sampling of a scale parameter and the location of the local maximum of a weighted local variance was proposed to determine the scale selection problem when segmenting images constrained by LCLU for detecting changes. Tran et al. 2015 [23] conducted a study in coastal areas of the Mekong Delta on changes in LCLU between 1973 and 2011 from Landsat and SPOT images. The supervised maximum likelihood classification algorithm was demonstrated to provide the best results from remotely sensed data when each class had a Gaussian distribution. Guan et al. 2020 [24] studied a CD and classification algorithm for urban expansion processes in Tianjin (a coastal city in China) based on a Landsat time series from 1985 to 2018. They applied the c-factor approach with the Ross Thick-LiSparse-R model to correct the bi-directional reflectance distribution function (BRDF) effect for each Landsat image and calculated a spatial line density feature for improving the CD and the classification. Dou and Chen 2017 [25] proposed a study in Shenzhen, a coastal city in China, from Landsat images using C4.5-based AdaBoost, and a hierarchical classification method was developed to extract specific classes with high accuracy by combining a specific number of

base-classifier decisions. According to this study, the landscape of Shenzhen city has been profoundly changed by prominent urban expansion.

In addition, in recent decades, remote sensing techniques have progressed, and many methods, such as machine learning, have been developed for LCLU change studies, such as support vector machines (SVMs), random forests (RFs), and convolutional neural networks (CNNs). Nonparametric machine learning algorithms such as SVM and RF are well-known for their optimal classification accuracies in land cover classification applications [26–28]. These algorithms have significant advantages and similar abilities in classifying multitemporal and multisensor data, including high-dimensional datasets and improved overall accuracy [29,30]. The accurate and timely detection of changes is the most important aspect of this process. Moreover, CNN, a more recently developed but well-represented deep learning method, allows the rapid and effective analysis and classification of LCLUs and has proven a suitable and reliable method for accurate CD in complex scenes. Although it is more recent, many studies have made use of this method. Wang et al., 2020 [31] proposed a new coarse-to-fine deep learning-based land-use CD method. In this study, several models of CNN well-trained with a new scene classification dataset were able to provide ac-curate pixel-level range CD results with a high detection accuracy and reflect the changes in LCLU in detail. In another study of Han et al., 2020 [32], a weighted Demptster-Shafer theory fusion method was proposed. This method achieved reliable CD results with high accuracy using only two very high-resolution multitemporal images by generating object-based CD through combining multiple pixel-based CDs.

At the same time, in the Pays de Brest, which the Crozon Peninsula is part of, a category of LCLU has been studied through shallow machine learning algorithms. Niculescu et al. 2018 [33] and Niculescu et al. 2020 [34] applied the algorithms of rotation forest, canonical correlation forests and random forest (RF) with satisfactory results for the classification of the different categories of land cover (vegetation) of the peninsula, as well as the summer and winter crops from the synergy of optical and radar data from the Sentinel satellite.

LCLU changes in coastal areas have been studied with machine learning algorithms in different environments. Munoz et al 2021 [35] analyzed the coastal wetland dynamics associated with urbanization, the sea level rise and hurricane impacts in the Mobile Bay watershed since 1984. They developed a land cover classification model with CNNs and a data fusion (DF) framework. The classification model achieved the highest overall accuracy (0.93) and f1-scores in the woody (0.90) and emergent wetland classes (0.99) when those datasets were fused into the framework.

More methodological work on the application of CNNs for CD was conducted by Jing et al. 2020 [36]. In this study, a CD method was proposed that combines a multiscale simple linear iterative clustering-convolutional neural network (SLIC-CNN) with stacked convolutional auto encoder (SCAE) features to improve the CD capabilities with HR satellite images. This method uses the self-learning SCAE architecture as the feature extractor to integrate multiscale, spectral, geometric, textural and deep structural features to enhance the characteristics of ground objects in images.

Machine learning methods were combined with Object-based Image Analysis (OBIA) techniques by Jozdani et al., 2019 [37] for urban LCLU classification. The multi-layer perceptron model led to the most accurate classification results in this study. However, it is also important to note that GB/XGB and SVM produced highly accurate classification results, demonstrating the versatility of these ML algorithms.

In this work, we aimed to study multiannual changes of LCLU in the Crozon Peninsula, an area that has mainly been marked by conversion between three types of LCLU: cropland, urban, and vegetation, in recent years, especially from 2007 to 2018. The challenge of this research was to deal with multiannual changes of a coastal area with different shapes and patterns by combining machine learning methods with PCC. To improve the CD capabilities using high-resolution satellite images, we implemented three remote sensing machine learning algorithms: SVM, RF combined with GEOBIA techniques, and CNN with SPOT 5 and Sentinel 2 data from 2007 and 2018, all effective and valid data sources. An

evaluation of these three advanced machine-learning algorithms for image classification in terms of the overall accuracy (OA), producer's accuracy (PA), user's accuracy (UA), and confidence interval was conducted to more precisely detect the type of multiannual change.

2. Study Area

The study area, the Crozon Peninsula canton south of the Landerneau-Daoulas canton, is located on the west coast of France in the Pays de Brest, Department of Finistère and the region of Brittany (Figure 1).

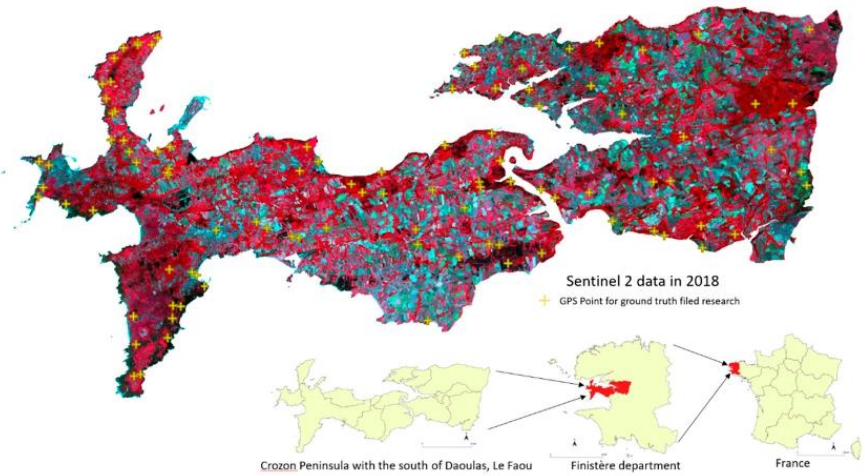

Figure 1. Location of the study area, including the Crozon Peninsula and two bordering regions, located in Pays de Brest, Finistère, Brittany, France, with the RGB band combination for Sentinel 2 (2018) and the location of the ground truth field research.

It covers a land area of 365.4 km^2 that extends between latitudes 48° 10′04″ N and 48° 21′28″ N, longitudes 4°02′44″ W and 4°38′37″ W. The Crozon Peninsula is a sedimentary site with contrasting topography and contours that separate the Bay of Brest and the Bay of Douarnenez. The region is a mosaic of cliffs, dunes, moors, peat bogs, and coastal wetlands. The peninsula thus presents phytocenetic, faunistic, and landscape interests. The population of the study area is 29,893; this makes the population density approximately 81.6 per km^2. The topography of the Crozon Peninsula is mostly dominated by plains, except for hills in the east and northeast, and the elevation of the area ranges between 0 m and 300 m. Climatically, the study area is classified as type Cfb (temperate oceanic climate) according to the Köppen climate classification. On average, the Crozon Peninsula reaches 1208 mm of precipitation per year, and the annual average temperature is 12.2 °C. The land cover is characterized by forest, shrubs, and grasslands, which are mostly in the west, urban areas, cropland (including mainly corn and wheat) and meadow.

Traditionally, the majority of local people practice agricultural or related activities in the Finistère Department, in which 57% of the department's surface is devoted to agricultural use. However, the French National Defense provides more than half of the employment in the Crozon Peninsula; hence, other activity sectors (e.g., agriculture, industry, construction and commerce) are proportionally less important.

Nevertheless, the land cover was actually in sharp transition in our study area between 2008 and 2018, with the peninsula especially marked by an increasing service and commerce sectors. Therefore, the study area was chosen as a typical ideal case to study land cover changes.

3. Data

Operable high-quality cloud-free satellite images in this area are extremely rare due to the annual high-intensity rainfall and, hence, heavy cloud cover. Despite these limitations, three cloud-free images from two dates in 2007 and 2018 with the same scene area were acquired from either the SPOT or Sentinel platforms to study land cover changes in the study area during the summer, which is the growing season for crops (Table 1).

Table 1. Satellite images used in the study.

Date	Satellite	Spectral Bands	Spatial Resolution
2 July 2007	SPOT-5	Green, Red, Near-infrared	10 m resampled to 2.5 m
24 June 2018	Sentinel-2B	1, 2 (Blue), 3 (Green), 4 (Red), 5, 6, 7, 8 (Near-infrared), 8A, 9, 10, 11, 12	10 m
24 June2018	Sentinel-2B	1, 2 (Blue), 3 (Green), 4 (Red), 5, 6, 7, 8 (Near-infrared), 8A, 9, 10, 11, 12	10 m

First, a SPOT-5 satellite image was obtained from the early summer of 2007. SPOT-5 was the fifth satellite in the SPOT series of CNES (Space Agency of France). It was launched in 2002 and completed its mission by the end of 2012. It provided very high spatial resolution (2.5 m in the panchromatic band and 10 m in the multispectral band) and wide-area coverage satellite images with a revisit frequency of 2 to 3 days [38]. The multispectral SPOT-5 image downloaded from the ESA was obtained by merging the 2.5 m panchromatic band and the 10 m multispectral band, resulting in the spatial information of the image being identical to the information observed with the panchromatic sensor (earth.eas.int).

Second, Sentinel-2 is an imaging mission that operates in the frame of the Copernicus (ex-GMES Global Monitoring for Environment and Security) program, which is implemented by the European Commission (EC) and the European Space Agency (ESA). The twin Sentinel-2 satellites (2A and 2B) deliver continually polar-orbiting; multispectral; high-resolution (10 m spatial resolution for B2, B3, B4, and B8; 20 m for B5, B6, B7, B8a, B11, and B12; and 60 m for B1, B9, and B10); high revisit frequency (10 days of revisit frequency for each satellite and a combined revisit frequency of five days); wide-swath; and open-access satellite imagery [39]. Two level 2A atmospheric effect-corrected Sentinel-2 images of the same date in the middle of the summer in 2018 were acquired from Theia (catalog.theia-land.fr); a mosaic was then created by combining two images to cover the whole study area, and four spectral bands at a 10 m resolution (red, green, blue, and near-infrared) were extracted for further use.

For the purpose of land cover identification at the sample selection step, we also used Google Earth and RPG (Graphic parcel register) maps and a French database with agricultural parcel identification as the reference data, complemented by observation and survey in the field when necessary.

4. Methods

The methodology of this paper is detailed in three main parts as follows: preprocessing, image processing, and postprocessing. Three satellite images of two dates were processed in QGIS (SAGA, Grass, OrfeoToolbox7.3.0), eCognition 9.5 and 10.0. A flow chart of the proposed global methodology and details of the CNN are displayed below (Figures 2 and 3).

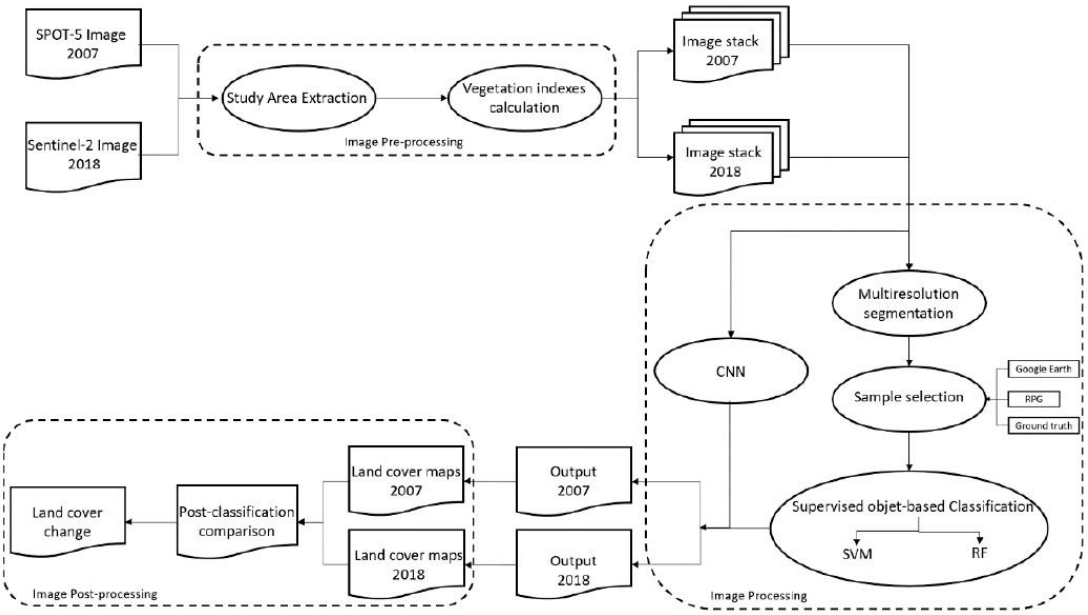

Figure 2. Global methodology proposed.

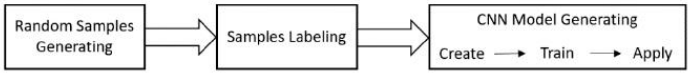

Figure 3. Detailed CNN methodology.

4.1. Image Preprocessing

4.1.1. Study Area Extraction

After satellite image acquisition, a mosaic of the two images of the same date in 2018 was created to cover the whole study area. Then, the boundary of the Crozon Peninsula and south of Landerneau-Daoulas were used to extract our area of interest by applying subsets to raw images to reduce the image size, processing time and storage space.

4.1.2. Vegetation Indices Calculation

The vegetation index is a qualitative and quantitative evaluation of vegetative cover and growth dynamics using spectral band measurements, which have been proven to have better sensitivity than individual spectral bands in identifying vegetated areas or different vegetation types and evaluating the vegetative cover density [40,41].

Due to the different spectral bands used and their ratios, the results are also different, not only because the reflectance of vegetation to the electromagnetic spectrum is determined by the chemical and morphological characteristics of the surfaces of the organs or leaves of the plants [42,43] but also because the values are heavily influenced by the atmosphere, sensor calibration, sensor viewing conditions, soil moisture, soil color, and brightness [41].

For this reason, different indices highlight different specific properties of vegetation features, and thus, more than 100 vegetation indices have been developed by scientists for various purposes and specific applications. Three of these were utilized in our study.

- The normalized difference vegetation index (NDVI), the most known and widely used vegetation index, was proposed in 1973 by Rousse et al. [44]. This index is a normalized ratio between the red and near-infrared spectral bands, as follows:

$$\mathrm{NDVI} = \frac{\mathrm{NIR} - \mathrm{RED}}{\mathrm{NIR} + \mathrm{RED}} \quad (1)$$

Although the NDVI is widely used in research related to regional or global vegetation monitoring, some limitations remain, such as a sensitivity to the effects of soil brightness, soil color and a series of atmospheric effects [43].

- The green normalized difference vegetation index (GNDVI), the index proposed in 1996 by Gitelson et al. [45], is very similar to the NDVI; nonetheless, it considers the green spectral band an instance of red, and the expression is as follows:

$$\mathrm{GNDVI} = \frac{\mathrm{NIR} - \mathrm{Green}}{\mathrm{NIR} + \mathrm{Green}} \quad (2)$$

The GNDVI is proven to be more sensitive to chlorophyll than the original "red" band and enabled a precise estimation of the pigment concentration [45].

- The Enhanced Vegetation Index 2 (EVI2), the two-band index, was developed by Jiang et al. in 2007 [46] as an adaptation of the enhanced vegetation index (EVI) that was designed to improve on its sensitivity in high biomass regions while minimizing the soil background signals and atmospheric influences. However, since the role of the blue band in the EVI only reduces noise, the EVI2 was developed without the blue band to maintain the soil-adjustment and linearization functions in the EVI but to break through its limit to sensor systems [46]. The index is expressed as follows:

$$\mathrm{EVI2} = 2.5\frac{\mathrm{N} - \mathrm{R}}{\mathrm{N} + 2.4\mathrm{R} + 1} \quad (3)$$

After calculating the three vegetation indices, we created an image stack with the original spectral bands and all of the indices for image processing.

4.2. Image Processing

4.2.1. Shallow Machine Learning Methods (SVM and RF)

In this study, supervised object-based classification was performed on two image stacks of two different years. Segmentation was applied first, followed by two nonparametric machine learning algorithms. SVM and RF were trained and applied in this step.

Multiresolution Segmentation (MRS)

Segmentation is the first processing step of object-oriented image analysis. MRS is one of the most successful region-based segmentation algorithms [47] and is based on homogeneity by extracting meaningful image objects with a reasonable processing speed. At the same time, the texture, color, form, spectra, and sizes of objects are accounted for [48]. The process starts by considering each pixel as an individual object; afterwards, pairs of adjacent image objects are merged to form larger segments [49]. The scale, compactness, and shape are the main parameters of the merging decision of the algorithm. Among the three parameters, the scale parameter allows users to define the maximum standard deviation of the heterogeneity used for image segmentation controlling the amount of spectral variation within objects and the size of their results [47,50]. There are two compositions of homogeneity criteria, which are the weight of the shape criterion and the compactness criterion [51]. The shape parameter is a weighting between the shape and the spectral information of the objects. When the parameter is 0, only color is considered. Then, the higher the value, the more important the shape is. The compactness parameter defines the weight of the compactness criterion, which represents the compactness of the objects formed during segmentation. The higher the value, the more compact objects are [51].

In this study, the scale, compactness, and shape parameters used were assigned as follows: 10, 0.1, and 0.3, respectively. The selection of the parameters was completed on a trial-and-error basis.

Sample Selection

Supervised methods were performed in our research, of which the goal was to build a concise model of the distribution of class labels in terms of the predictor features [52]. In contrast to the unsupervised methods, users are able to provide knowledge and experience to the process with these methods. Sample selection is an indispensable step in training machine-learning models using supervised methods. In this study, all of the samples presented in Table 2 were selected manually with Google Earth, an RPG (Graphic parcel register) map, and ground truth as the reference data, and the ground truth values were taken during a field survey with a Global Positioning System (GPS) in August. The samples were then used to train two classifiers in the next step.

Table 2. Training samples surface area for SVM and RF model training in 2007(2a) and 2018(2b).

Class	Area surface of training samples (km^2)
Cropland	13.68
Cropland with bare soils	18.18
Water	00.39
Vegetation	35.61
Non-vegetation	03.86
Total	71.72

2a

Class	Area surface of training samples (km^2)
Cropland	11.76
Cropland with bare soils	17.75
Water	00.14
Vegetation	41.08
Non-vegetation	07.69
Total	78.42

2b

SVM Classification

SVM, also called the Support Vector Network, is one of the most robust and frequently used supervised nonparametric statistical machine-learning methods. It is capable of generating good classification results with a simple training dataset in comparison to many supervised learning methods [53]. Originally, SVM was a learning machine with the aim of solving a binary classification problem [54]. SVM is capable of handling two different cases: when the classes are linearly separable, the machine seeks a linear decision boundary called a hyperplane that minimizes the generalization error and leaves the greatest margin between the two classes [55]. In contrast, in the case of nonlinearly separable classes, a method of projecting the input data onto a high-dimensional feature space with kernel functions was proposed, which worked in such a way that the problem is transformed into a linear classification problem in that space [54,55].

Some multiclass classification methods were developed for cases in which this initially two-group classification learning machine faces a multiclass problem. The most commonly used strategies are described as "one against one" and "one against all." Traditionally, SVM has always been considered to be a pixel-based classification method, and it always obtains great classification results in this way [56–60]. However, some studies have proven that SVMs can also produce very satisfactory results as object-based classifiers [61–63], which involves spectra, texture, form and shape information [64]. Therefore, the SVM is tested and evaluated as an object-based classifier in this paper. In this method, segmentation was previously completed [64].

The training and classification of the SVM module are applied using ECognition software with a radial basis function (RBF) kernel. The SVM kernel is a set of mathematic functions for taking sequence data as the input and then transforming them into the required form of processing data. This function can transform a non-linear problem into a

linear equation in a higher-dimensional feature space. RBF, a very effective and accurate kernel type, is capable of performing the transformation with the radial basis method in the case of lack of prior knowledge about the data [65,66]. Furthermore, the module was executed with 10 as its capacity constant, also called the c-parameter, with the aim of minimizing error function and avoiding a misclassification problems. The higher the c-parameter value, the smaller-margin hyperplane the optimizer looks for [51].

RF Classification

Other than the SVM and most classifiers, RF is a combination of multiple tree-based classifiers to produce a single classification, an ensemble of decision trees, where each single tree contributes a vote for the assignment of the most popular class to the input data [55,67–69].

This type of ensemble method has been highly developed and used for two decades and has been proven to make significant progress in the classification accuracy for land cover classification. In particular, RF can address thousands of input data without variable deletion and estimates the importance of the variables in the classification [55,68,70–72].

The RF classification requires two important user-defined parameters to train the model: Two parameters are set on a trial-and-error basis: the number of decision trees grown in the forest; decision trees are capable of contributing a prediction then voting for the final model's prediction; this parameter was set to 300 and 200 for 2007 and 2018, respectively. In addition, the maximum tree depth, which means the length of each tree in the forest; generally, a larger tree can capture more information about the data with the more splits it has; this parameter was defined as 20 for both years.

4.2.2. Deep Learning Method (CNN)

As a subset of machine learning, the CNN was inspired by the functioning of the nervous system of the human brain; it utilizes artificial neural networks (ANNs) but has multiple layers. CNNs are mainly designed for image classification [73,74]. They are well-suited for solving complex problems and recognizing image objects with revolutionary accuracy levels that none of the other machine learning approaches have yet achieved [51]. The CNN implemented in eCognition is based on the Google TensorFlow library.

It has an input layer that consists of an image patch, at least one hidden layer, and an output layer where the classified output has a unit for each class that the network predicts. Images as input layers must go through multiple hidden layers for the output to be obtained (Figure 4).

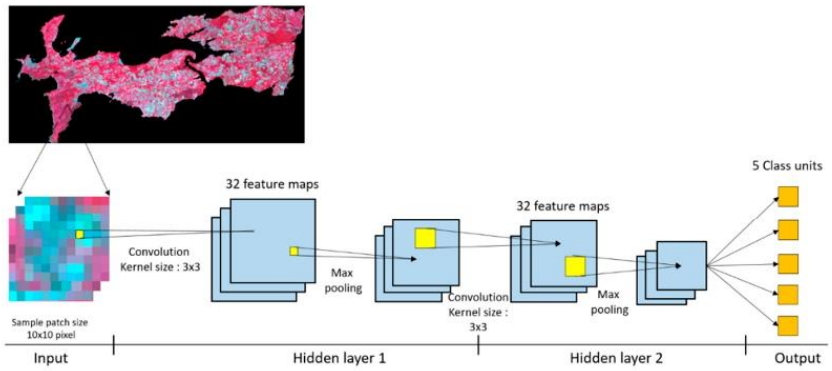

Figure 4. CNN model proposed and used for the classification of images from 2018 in the study.

Generating Labeled Samples

The training of a CNN model requires a large number of samples because with a larger training sample, a better model is trained, and a higher accuracy level can be achieved [73,74]. All of the training data in this study were prepared manually to obtain better accuracy. For years between 1960 and 1980, the samples in the form of points were automatically and evenly selected in QGIS by random selection for the purpose of avoiding bias. We then categorized all of the points manually into five distinct classes and created sample patches by including all of the pixels that surround each point for the model training. The algorithm then shuffled the labeled sample patches and created a random sample order for training [51].

Model Generation

Two models were created separately for 2007 and 2018. Each model had two hidden layers, a kernel size for the convolution, which is a matrix used to extract the features from the image, a number of feature maps, defined as the output activations for one filter applied to the previous layer, and a max-pooling step that can significantly reduce the number of units by keeping only the maximum response of several units from the first stage [51]. For the processing of the 2007 images, the batch size, the number of training examples utilized in one iteration, was set to 32, the kernel size was assigned to be 3×3 with 64 feature maps in the first hidden layer, and the second hidden layer had a kernel size and feature map of 4×4 and 64, respectively. For the 2018 images, the batch size was set to 10, and both hidden layers were assigned 3×3 and 32 for the kernel size and number of feature maps, respectively. Both hidden layers of the two models contained a max-pooling stage using a 2×2 filter. Then the two models were trained based on the trial-and-error method, with a learning rate of 0.001. After obtaining a satisfactory CNN accuracy, the two models were validated and used to produce the classification of two satellite images, from 2007 and 2018 separately.

4.3. Image Postprocessing

4.3.1. Accuracy Assessment

The accuracy assessment, a principal component of land cover classification, is used to express the classification's degree of agreement with reality [75–77]. The accuracy assessment statistics of the classifiers (SVM, RF and CNN), based on confidence intervals [78], were calculated for each method and each class to check the model training and classification quality by comparing the classification with the reference values. The accuracy assessment used in this study included three indices: the overall accuracy (OA), the producer's accuracy (PA) and the user's accuracy (UA) —which are among the best-known and most highly promoted quantitative accuracy assessment metrics for the evaluation of classification quality or for comparisons among different classifications.

The OA is the probability that something will be correctly classified by a classifier. It is computed by dividing the total number of correct pixels by the total number of pixels in the error matrix [76–79]. The PA is a measure of errors of omission; it refers to instances in which something is erroneously excluded from consideration when it should have been included. On the other hand, the UA measures the error of commission, which refers to something that is erroneously included for consideration when it should have been excluded [80–82].

The indices of the accuracy assessment were generated with an algorithm from Olofsson based on the confidence interval. Therefore, all indicators presented in the tables are followed by an uncertainty rate. A higher uncertainty signifies that a larger accuracy rate can vary; in contrast, a small uncertainty represents a relationship with a certain accuracy.

4.3.2. Post-classification Comparison

To analyze the land cover changes between 2007 and 2018, a PCC was performed with the semi-automatic classification plugin on QGIS. The open-source plugin allows two

classified images to be taken as the input (a new map and a reference map), then creating an overlap of these images to cross the data at the pixel level and differentiating the land cover changes according to the differences between the two maps. As the output, a change layer is created, and there is also a table that shows how the pixels move between the classes.

5. Results

5.1. Comparison of Classifiers

The classification results of the three methods for the two years are presented in Figure 5. The five classes detected in the classification process were cropland; cropland with bare soil; water; vegetated area; and non-vegetation, including urban area, sand, and rocks. Although some differences might exist, generally, the vegetation, non-vegetation, and cropland could be well-identified from different maps, which are globally identical. The vegetation is located in the south and east, with some vegetation near the coastlines, similar to the most important urban areas. In contrast, all of the cropland is in the interior of the peninsula.

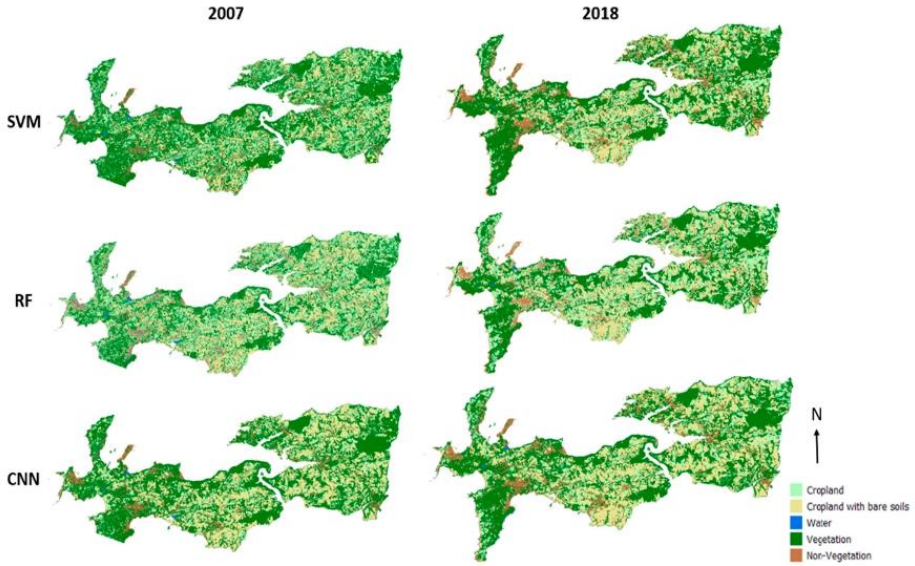

Figure 5. Classification results with SVM, RF, and CNN.

To make better comparisons possible, each accuracy assessment in this paper is split into two tables, which are the training accuracy and validation accuracy, allowing for cross-validation to avoid the problem of overfitting or underfitting. The training accuracy was computed and used to improve the model performance and classification quality during the classification processing based on the training dataset; otherwise, the validation accuracy was used with the validation data to evaluate each model's final prediction.

According to Tables 3 and 4, all of the accuracy indices range from 70% to 90%, and the two tables are very similar. Although the training accuracy is slightly higher and more certain (approximately 2–6%), it suggests a good performance and good training of all three models, a strong level of agreement, and a high level of reliability. Beyond that, it is worthwhile to note that the CNN demonstrated better potential (approximately 1–12% higher in accuracy) for the classification of land cover monitoring than RF and SVM in both years, and it is the most stable and certain method, given its low uncertainty of approximately 1.50 for training accuracy and 3.50 for validation accuracy in comparison

with the other methods. In general, the 2007 images have better accuracy indicators and lower uncertainty rates than the 2018 images, and RF achieved better accuracy and lower uncertainty in the 2007 images than in the 2018 (e.g., 80.23 ± 03.87% and 70.51 ± 08.38% for 2007 and 2018, respectively, in the validation accuracy assessment), which is the opposite of SVM (e.g., 77.03 ± 04.36% and 78.14 ± 06.40% for 2007 and 2018, respectively, in the validation accuracy assessment). The most reasonable explanation is that the 2018 images have a rougher resolution than the 2007 images, and so fewer pixels are present in each segment, and since the SVM needs fewer samples and pixels to train the model, it achieved a better performance with the 2018 images.

Table 3. Training overall accuracy (%).

Methods	2007	2018
RF	82.72 ± 01.79	76.78 ± 03.40
SVM	77.17 ± 02.20	81.14 ± 03.18
CNN	89.15 ± 01.36	83.16 ± 01.64

Table 4. Validation overall accuracy (%).

Methods	2007	2018
RF	80.23 ± 03.87	70.51 ± 08.38
SVM	77.03 ± 04.36	78.14 ± 06.40
CNN	83.11 ± 03.27	79.85 ± 03.58

The PA and UA of each class with the three methods in both years are listed in Tables 5 and 6. Table 5 presents the satisfactory training accuracy of both models (approximately 70–90%, with a few acceptable exceptions, such as cropland, which has PA and UA values of approximately 40–50%), which indicates that the three models used in the classification: SVM, RF, and CNN, were generally well-trained. Even though the training accuracy and the validation accuracy are constantly approximate, as shown in Tables 3 and 4, the training accuracy is very slightly more accurate and certain than the validation accuracy (approximately 1–10% higher). This suggests a slight overfitting problem in the models. Overfitting, which can be revealed when the training accuracy is significantly greater than the validation accuracy, occurs when the model for the classification is too close and too well-adapted to the training data, in such a way that it is not capable of processing and fitting additional data or making a proper prediction for global images. Nevertheless, the presence of the overfitting problem is not an important obstacle in our study because the differences between the training and validation accuracies are acceptable (between 1% and 10%). Additionally, the validation accuracy always has a higher uncertainty, which indicates that the real accuracy rate may vary to a large extent.

Table 5. Training producer's accuracy and user's accuracy by class.

Land Cover Types		2007			2018	
Cropland	RF	PA	66.45 ± 08.68	RF	PA	78.89 ± 04.48
		UA	40.92 ± 03.90		UA	43.71 ± 04.21
	SVM	PA	46.06 ± 06.58	SVM	PA	69.91 ± 04.74
		UA	51.31 ± 04.79		UA	59.83 ± 05.09
	CNN	PA	79.88 ± 04.53	CNN	PA	71.78 ± 04.62
		UA	75.25 ± 04.86		UA	71.34 ± 05.06
Cropland (with Bare Soil)	RF	PA	46.34 ± 04.75	RF	PA	35.77 ± 05.33
		UA	98.79 ± 01.06		UA	91.89 ± 02.65
	SVM	PA	36.15 ± 03.54	SVM	PA	52.23 ± 07.21
		UA	96.73 ± 01.75		UA	94.78 ± 02.08
	CNN	PA	92.24 ± 02.15	CNN	PA	86.54 ± 02.51
		UA	92.99 ± 02.09		UA	84.72 ± 02.97
Water area	RF	PA	100	RF	PA	100
		UA	41.18 ± 16.54		UA	100
	SVM	PA	58.75 ± 48.12	SVM	PA	100
		UA	72.22 ± 20.69		UA	100
	CNN	PA	100	CNN	PA	100
		UA	100		UA	71.43 ± 33.47
Vegetation (except crop)	RF	PA	91.50 ± 00.73	RF	PA	63.40 ± 06.00
		UA	89.59 ± 02.24		UA	88.56 ± 02.22
	SVM	PA	94.93 ± 00.61	SVM	PA	65.04 ± 06.45
		UA	78.32 ± 02.61		UA	85.26 ± 02.30
	CNN	PA	92.45 ± 01.39	CNN	PA	87.58 ± 01.87
		UA	90.54 ± 01.90		UA	85.81 ± 02.03
Non-vegetation	RF	PA	81.79 ± 06.72	RF	PA	98.22 ± 00.52
		UA	82.14 ± 05.36		UA	77.87 ± 05.21
	SVM	PA	38.73 ± 08.16	SVM	PA	98.99 ± 00.39
		UA	81.71 ± 05.73		UA	80.38 ± 04.83
	CNN	PA	70.71 ± 06.62	CNN	PA	68.08 ± 05.64
		UA	92.99 ± 04.06		UA	84.29 ± 04.92

Table 6. Validation producer's accuracy and user's accuracy by class.

Land Cover Types		2007			2018	
Cropland	RF	PA	49.63 ± 14.63	RF	PA	88.71 ± 06.54
		UA	38.27 ± 07.48		UA	54.01 ± 08.35
	SVM	PA	43.21 ± 12.41	SVM	PA	63.20 ± 09.69
		UA	49.58 ± 08.98		UA	66.67 ± 09.29
	CNN	PA	61.86 ± 09.38	CNN	PA	61.34 ± 08.55
		UA	65.79 ± 10.67		UA	72.60 ± 10.23
Cropland (with Bare Soil)	RF	PA	47.04 ± 09.65	RF	PA	25.69 ± 07.37
		UA	94.68 ± 04.54		UA	93.48 ± 05.05
	SVM	PA	35.19 ± 06.81	SVM	PA	47.18 ± 08.56
		UA	96.39 ± 04.02		UA	98.06 ± 02.66
	CNN	PA	89.96 ± 04.85	CNN	PA	90.09 ± 04.81
		UA	86.76 ± 05.07		UA	82.55 ± 06.09
Water area	RF	PA	100	RF	PA	100
		UA	60.00 ± 30.36		UA	50.00 ± 69.30
	SVM	PA	100	SVM	PA	100
		UA	85.71 ± 25.92		UA	62.07 ± 30.54
	CNN	PA	100	CNN	PA	100
		UA	100		UA	70 ± 25.05
Vegetation (except crop)	RF	PA	90.66 ± 01.48	RF	PA	67.21 ± 13.96
		UA	87.22 ± 04.88		UA	91.28 ± 03.96
	SVM	PA	94.91 ± 01.15	SVM	PA	65.08 ± 05.30
		UA	78.42 ± 05.19		UA	86.94 ± 04.43
	CNN	PA	88.36 ± 03.31	CNN	PA	83.79 ± 04.14
		UA	85.00 ± 04.52		UA	81.86 ± 05.15
Non-vegetation	RF	PA	84.10 ± 10.16	RF	PA	97.87 ± 01.28
		UA	77.78 ± 12.15		UA	65.38 ± 12.93
	SVM	PA	45.59 ± 19.51	SVM	PA	99.08 ± 01.31
		UA	78.05 ± 12.67		UA	74.07 ± 11.69
	CNN	PA	66.06 ± 12.64	CNN	PA	63.29 ± 11.88
		UA	90.91 ± 09.81		UA	73.68 ± 14.00

Among the three methods, the CNN remains the most stable and accurate method, and all of the values range between 70% and 100%. Among the classes, water areas were very well predicted but also very extensive (usually with an accuracy between 50% and 70% with a large uncertainty and 100%) by means of their distinctive spectral signature. Cropland had training accuracy indicators between 50% and 70%, with CNN having the best

performance in this class (approximately 70–80% in training accuracy and approximately 60–70% in validation accuracy). Of the other two methods, RF was mostly more accurate than SVM (approximately 5–20% higher). In addition, they performed better on the images from 2018 than those from 2007, with a stable uncertainty (approximately 10–20%); the validation accuracies were still approximate and slightly lower. Crops are easily confused with vegetation, which might explain the low accuracy of this classification. Croplands with bare soil are more correctly classified than croplands with plants (with a 20–50% higher rate), and all UA are significantly higher than PA, with a 50% to 70% difference, which suggests that fewer errors of commissions were made during the classification. Except for the CNN, both the UA and PA ranged from 82% to 92%, with less uncertainty at approximately 2.50 in the training accuracy and approximately 5 in the validation accuracy. Even though vegetation has the potential to be confused with crops, it was still the best-predicted class besides water, and the accuracy indicators achieved approximately 80–95%, except for the PA of RF and SVM in 2018, which were approximately 65%. It can be assumed that some errors of omission were made during this classification. The non-vegetation class includes all types of urban land use, sand, and rock; hence, it is globally well-classified due to its particular spectral signature, especially with the 2018 images. The accuracies in general ranged from approximately 70% to 98% in the training accuracy and from approximately 63% to 97% in the validation accuracy. In this class, the fact that the PA is considerably greater than the UA reveals the error of omission, except for the classification of SVM in 2007 and both CNN classifications, which suggests an error of commission instead. In all cases, the CNN was always the most stable and reliable method.

5.2. LCLU Detection Changes (2007–2018)

The land use change map resulting from the PCC is shown in Figure 6.

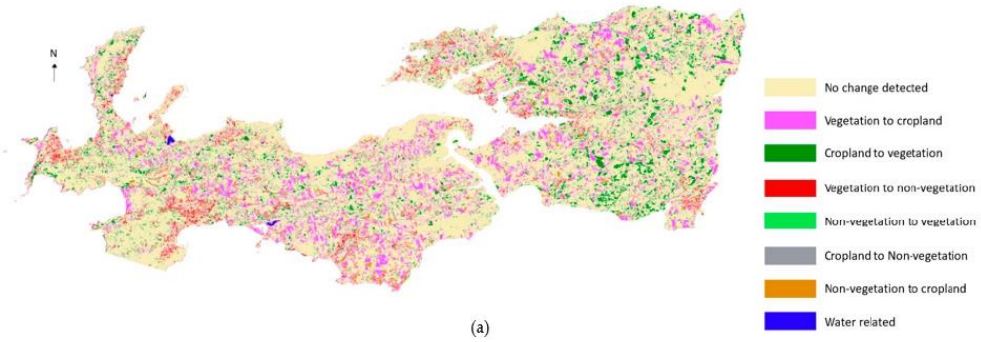

(a)

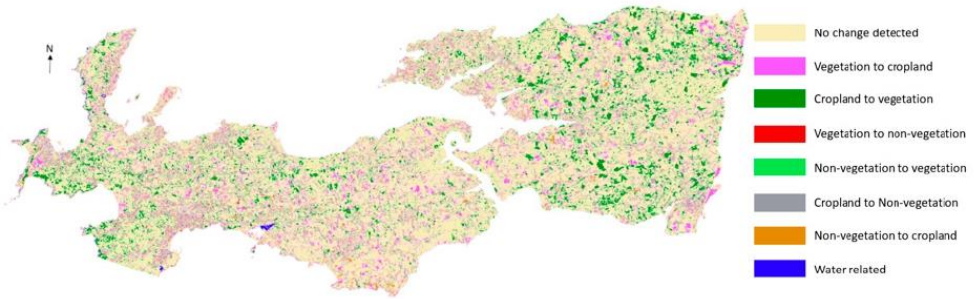

(b)

Figure 6. *Cont.*

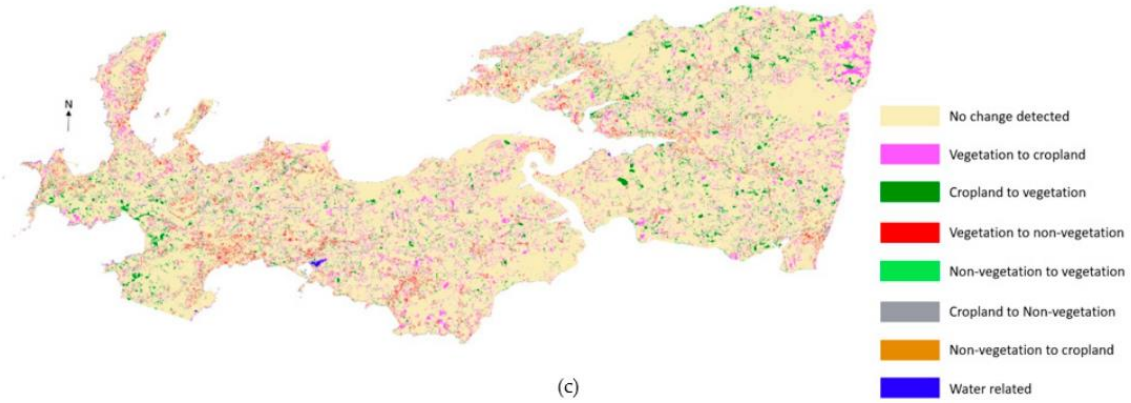

Figure 6. Land cover change maps with the classification of SVM (**a**), RF (**b**), and CNN (**c**).

In addition to the problems of the uncertainty and error values caused by classification and spatial resolution differences between two satellite images, multiple changes between the two classes and between the two years (2007 and 2018) were detected. Land cover change maps revealed the status of each pixel, which stayed in the same class, meaning no change, or changes to another class, or another LCLU. Some changes can be seen among the three land cover change maps with different classifications; for example, many croplands were transformed into vegetation, and vegetation was changed to cropland according to the maps of RF. The SVM maps indicate numerous transformations from vegetation to cropland and vegetation to non-vegetation. However, generally, the cropland surface has slightly increased in the peninsula, and many vegetation areas have trun into cropland, according to the land cover change map. At the same time, many cropland areas have become vegetation areas. However, there may be confusion between vegetation and crops due to the different acquired dates of the two images. Therefore, many of the new vegetation areas are most likely growing crops. The third most important land cover change is vegetation to non-vegetation, which mainly took place near urban areas on the coast, especially in the south, where tourism is the most developed. Some details of the three main land cover change types based on the classification results of the CNN, which is the most stable of the three methods, are shown in Figure 7, with comparisons between 2007 and 2018.

Table 7 presents the evolution of the surface of each class between 2007 and 2018 with their proportion in the total surface area of the peninsula, the surface area of each type of land use change and the proportion of each type in the total surface area.

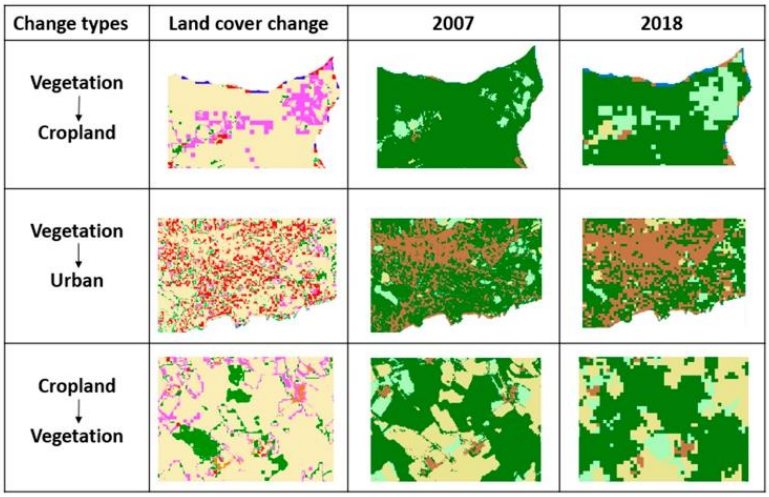

Figure 7. Details of the three main land cover change types of the CNN classification with comparisons between 2007 and 2018.

Table 7. Land cover change area and proportion of the change type with the three methods of classification.

Land Cover Change	SVM		RF		CNN	
	Area (km^2)	Proportion (%)	Area (km^2)	Proportion (%)	Area (km^2)	Proportion (%)
No change	238.74	65.33%	243.40	66.77%	282.51	77.37%
Vegetation to Cropland	45.55	12.47%	31.90	8.73%	35.71	9.78%
Cropland to vegetation	43.55	12.03%	49.94	13.67%	23.96	6.55%
Vegetation to non-vegetation	20.68	5.66%	5.14	1.41%	12.43	3.40%
Non-vegetation to vegetation	1.42	0.39%	3.13	0.86%	3.15	0.86%
Cropland to non-vegetation	9.11	2.49%	15.12	4.14%	2.63	0.72%
Non-vegetation to cropland	4.61	1.26%	12.17	3.33%	2.63	0.72%
Water related	1.34	0.37%	4.04	1.11%	2.14	0.59%
Total	365.42	100%	365.42	100%	365.42	100%

In addition to the confusion between growing crops and vegetation, our previous results can be confirmed by Table 7. The table ranges from the most important class with the greatest proportion of land cover change to the least changed class, with the two types of cropland assembled into one class to facilitate the comparisons. The majority of the land in the peninsula retained the same LCLU between 2007 and 2018, and at least 65% to 66% of the area remained unchanged according to the SVM and RF classifications. However, the CNN indicated that approximately 77% of the surface of the Crozon Peninsula did not change between the two years, which is more important. Cropland is clearly increasing: 12.45% of the vegetated area has been converted into cropland, according to SVM classification; however, this transformation is less important according to the RF and CNN classifications, which show approximately 8% and 9%. In contrast, much cropland was identified as vegetation in 2018, more with the SVM and RF classifications (12–13%) than with the CNN (6.55%), which could confuse vegetation and crops due to the different acquired dates of the two images. Undoubtedly, non-vegetation, which includes urban areas, has certainly

gained surface area from vegetated areas over the 11-year period by agreement of the three classifications, even though RF presents a lower land cover change value (1.41%) than SVM and CNN (5.66% and 3.40%, respectively). For the RF and SVM classifications, non-vegetation was developed from cropland as well (2.49% and 4.14% in SVM and RF, respectively). A small part of the non-vegetated area was classified as cropland in 2018 in all three models (1.26% in SVM, 3.33% in RF, and 0.72% in CNN); however, it might have been confused with bare soil and non-vegetated areas such as concrete. Finally, the last two classes (non-vegetation to vegetation and all water-related areas) have very low proportions, approximately 0.30–1% in land cover change, which is likely due to the rising tides and increasing water storage in the mid-summer and to planting of small areas, such as in the city.

To conclude, according to the models, the cropland surface has slightly increased, and non-vegetation areas have sharply grown in the 11-year period. The dramatically increasing urbanization of the peninsula, requiring more cropland to address the population growth and tourism development, has resulted in a rapid decrease in vegetation surface area.

6. Discussion

6.1. LCLU Classification

In this study, three different algorithms were applied to two high spatial resolution satellite images from 2007 and 2018, which were both acquired in the growing season, to map LCLU changes in the Crozon Peninsula, a highly fragmented region. Our objective was to map different LCLUs (cropland, water, vegetation and non-vegetation, including urban land use) and then map and monitor LCLU changes between two years. Another important aspect in the application of the machine learning methods was to recognize the specific type of change when collecting samples for training.

Three classification algorithms (SVM, RF, and CNN) were used, and all of them achieved a good accuracy level, with the overall accuracy ranging from 70% to 90%, despite the complex landscape and small field size. Two machine learning methods, RF and SVM, are object-based approaches, and features other than spectral values play an important role in the classification.

The RF and SVM models both performed well for the LCLU classification; nonetheless, the CNN obviously is better suited to performing classification in our study area, as indicated by the accuracy assessments. According to the results presented in Figure 5 and the statistical evaluations of accuracy provided in Tables 3–6, the proposed method (CNN) generally performs best regardless of the type of dataset and accuracy index. Therefore, the CNN has proven to be a feasible, reliable method with remarkable performance for precisely mapping LCLU and analyzing the changes. Our experiments have shown the superiority of the CNN over other state-of-the-art machine learning classifiers in terms of classification accuracy. However, some important considerations regarding its effectiveness are worth discussing. Previous applications of CNN models have tended to emphasize the complexity of these models compared to RF models and SVMs. In this case, parameter tuning and optimization are often performed by cross-validation for CNN algorithms. However, in some cases, CNN models can have millions of weights to optimize at each iteration [83]. In such situations, training these models can be tedious. Manual tuning or rules of thumb for cross-validation should be implemented in this case. This manual manipulation could have repercussions on the accuracy of the model. A well-known solution is transfer learning [84]. In this case, instead of a model being trained from scratch, pretrained models are retrained on the user's classes of interest. Pretrained models allow for better accuracy [85]. In our study, the deep model was very useful for generalization.

6.2. Accuracy Assessment

In accordance with Table 4, the highest OA was obtained by applying the CNN algorithm to 2007 (83.11 $\pm$ 03.27). The RF gives the lowest OA, 70.51 $\pm$ 08.38. The SVM showed intermediate values between 77.03 $\pm$ 04.36 (2007) and 78.14 $\pm$ 06.40 (2018).

Regarding the PU and UA (validated results) by class, the best results were obtained with SVM for the PA in 2018 for the non-vegetation class (99.08 ± 01.31; except for the water class). The worst results were always obtained with the SVM for the PA of the cropland class (with bare soil), which was 35.19 ± 06.81.

However, the lower accuracy occurred for 2018, and we deduced that the spatial resolution of the image is a crucial part of classification that can explain the differences between the SVM and RF's overall accuracy in the different years. The RF performed better on the 2007 data with a 2 m spatial resolution SPOT 5 image; in contrast, SVM achieved a better accuracy in 2018 with a 10 m spatial resolution Sentinel 2 image. Among all of the classes, except for the water areas, which have a very different spectral signature than the other classes, vegetation was the best-detected class, most likely because it occurred on the greatest part of the study area; therefore, it also had the largest sample dataset, since all of the samples were randomly and evenly selected in the images. Non-vegetation areas that are mostly urban land, rocks, and sand were relatively simple to discriminate. Cropland with bail soil was better-classified than planted cropland. Misclassification largely occurred between the vegetation and crops due to their spectral signature similarities, especially during the growing season, and they were spatially approximate; some croplands were small and intermixed with trees or shrubs.

The choice of a good classifier is very important, but at the same time, the features extracted from the image are also important. GEOBIA techniques allow the use of hand-created features in the classification phase. The number and choice of features clearly influence the final classification. At the same time, the features of an RF and SVM are learned automatically from the input data during training. The features automatically learned by RF and SVM based on the spectral, contextual and spatial property classes increased the generalization capabilities of the models.

6.3. LCLU Changes Detection (2007–2018)

CD techniques can be grouped into two types of objectives: change enhancement and change "from-to" information extraction. In this study, the detection and direction of the changes were processed by applying PCC on a pixel-by-pixel basis through SVM, RF, and CNN classification, with the best performances of the change classes detection between the series of multitemporal images. The multitemporal images were stacked together and then classified directly to detect land cover changes. This work presents a CD protocol that allows reliable PCC to account for the classification accuracies, landscape heterogeneity, and pixel sizes. However, the accuracy of the final change map depends on the quality of each individual classification [86–88]. Errors in the individual maps are additive in the combination (change mapping). In connection with this error question, Liu and Zhou, 2004 [89] proposed a set of rules for the probability of changes from one class to another based on field knowledge. They used these rules to separate "real changes" from possible classification errors. Thus, they determined the accuracy of trajectory changes by arguing the rationality of the changes through a PCC.

Our classification results showed that it is possible to map land use with different algorithms and analyze land use changes between two years. First, increasing the cropland surface indicates that agricultural activities remained an important economic sector in the peninsula, and there were essentially no signs of abandoned agricultural land during the study period. Second, non-vegetation areas increased dramatically due to urbanization, especially some coastal cities that are highly frequented by tourists, since tourism is highly developed in the peninsula. The very dense population corresponds to a high level of artificialization of the territory, which is growing faster than the national average, fueled by a construction of housing and nonresidential premises. This human concentration also implies the progression of urbanization toward the hinterlands, where the construction of housing and the arrival of new residents increased significantly. Artificialization is the main change that has affected the coastal zone of the peninsula, with preferential locations around the major urban centers and on certain coastal sectors. Despite the

regulatory protection established by the Littoral Law, the changes are also important in the 100 m band nearest to the sea and then decrease as one moves away from it. In 1986, the Littoral Law provided an initial regulatory response to the need to control the anarchic development of construction on the coast. One of the most significant consequences of development has been the drastic reduction of the vegetation surface. Vegetation has been removed for two main reasons: increasing agricultural activities and urban land growth. Therefore, economic development can have negative social and economic implications on the peninsula; in addition, environmental conservation and protection are required.

7. Conclusions

CD methods involve analyzing the state of a specific geographic area to identify variations from images taken at different times. With satellite remote sensing, high spatial and spectral resolution images are recorded and used to analyze the scales of changes. In this study, in order to detect multiannual change classes between the series of multitemporal images using a pixel-by-pixel PCC technique, three different well-known and frequently used algorithms, including two machine learning algorithms (SVM and RF) and one deep learning algorithm (CNN), were tested on two high spatial resolution satellite images. RF and SVM were applied with an object-based approach, which requires a segmentation step to create subpixel-level objects to avoid the error of mixed pixels since the study area was mainly covered by small fields. The inclusion of the CNN significantly improved the classification performance (5–10% increase in the overall accuracy) compared to the SVM and RF classifiers applied in our study.

Our results showed that the use of remote sensing for complex multiannual small-scale LCLU change studies was completely reliable. The study resulted in two maps that showed five different land uses (cropland, cropland with bare soil, water, vegetation and non-vegetation) in 2007 and 2018 with high accuracy. In particular, the CNN had an overall accuracy that ranged from 80 to 90%, making it the most suitable algorithm in our case, even though RF and SVM also achieved good accuracy levels.

The results may also lead to the conclusion that economic development is rapidly occurring in the peninsula, manifested as urban land and tourism growth, increasing the agricultural activities and grossly decreasing the vegetative areas. Hence, environmental protection measures are demanded for the future. In this context of change, the coastal zones of the peninsula tend to specialize socially and economically, and the maintenance of the agricultural areas, as well as the preservation of the natural areas, are both more sensitive and more complex. Moreover, it appears that the change in land use must be understood in the context of climate change, which is a factor in the aggravation of risks (e.g., flooding and, coastal risks), especially in the sectors that are most subjected to urbanization pressures.

Although we observed relatively high classification accuracies, several uncertainties and limitations persisted. The first is the misclassification between vegetation and planted croplands: the very similar spectral characteristics that they share and their geographical localization lead to this confusion. Second, the two classifications were based on two images with different spatial resolutions; thus, some errors of the land use change analysis could have been induced. Third, useful cloud-free satellite images of the growing season were not easy to obtain in our study area; therefore, a series of annual mappings with more precision was not performed in the study. Hence, some recommendations can be made for further studies, such as applying more vegetation indices or using hyperspectral images to differentiate between vegetation and planted croplands or exploring the potential of synthetic-aperture radar images as a supplement to the traditional optical images on cloudy days.

Author Contributions: Conceptualization, S.N. and G.X.; methodology, G.X.; software, G.X.; validation, S.N.; formal analysis, S.N.; investigation, G.X.; resources, G.X.; data curation, G.X.; writing—original draft preparation, G.X.; writing—review and editing, S.N.; visualization, S.N.; supervision,

S.N.; project administration, S.N.; funding acquisition, S.N. All authors have read and agreed to the published version of the manuscript.

Funding: This research was funded by Fondation de France.

Conflicts of Interest: The authors declare no conflict of interest.

References

1. Crowell, M.; Edelman, S.; Coulton, K.; McAfee, S. How Many People Live in Coastal Areas? *J. Coast. Res.* **2007**, *23*, iii–vi. [CrossRef]
2. Briassoulis, H. *Analysis of Land Use Change: Theoretical and Modeling Approaches*; Wholbk, Regional Research Institute, West Virginia University: Morgantown, WV, USA, 2000.
3. Waldhoff, G.; Lussem, U.; Bareth, G. Multi-Data Approach for remote sensing-based regional crop rotation mapping: A case study for the Rur catchment, Germany. *Int. J. Appl. Earth Obs. Geoinf.* **2017**, *61*, 55–69. [CrossRef]
4. Giri, C.; Pengra, B.; Long, J.; Loveland, T. Next generation of global land cover characterization, mapping, and monitoring. *Int. J. Appl. Earth Obs. Geoinf.* **2013**, *25*, 30–37. [CrossRef]
5. Xie, Y.; Sha, Z.; Yu, M. Remote sensing imagery in vegetation mapping: A review. *J. Plant Ecol.* **2008**, *1*, 9–23. [CrossRef]
6. Ma, L.; Liu, Y.; Zhang, X.; Ye, Y.; Yin, G.; Johnson, B.A. Deep learning in remote sensing applications: A meta-analysis and review. *ISPRS J. Photogramm. Remote Sens.* **2019**, *152*, 166–177. [CrossRef]
7. Chughtai, A.H.; Abbasi, H.; Karas, I.R. A review on change detection method and accuracy assessment for land use land cover. *Remote Sens. Appl. Soc. Environ.* **2021**, *22*, 100482. [CrossRef]
8. Zeng, T.; Wang, L.; Zhang, Z.; Wen, Q.; Wang, X.; Yu, L. An Integrated Land Cover Mapping Method Suitable for Low-Accuracy Areas in Global Land Cover Maps. *Remote Sens.* **2019**, *11*, 1777. [CrossRef]
9. Zhu, L.; Liu, X.; Wu, L.; Tang, Y.; Meng, Y. Long-Term Monitoring of Cropland Change near Dongting Lake, China, Using the LandTrendr Algorithm with Landsat Imagery. *Remote Sens.* **2019**, *11*, 1234. [CrossRef]
10. Xu, H.; Wang, X.; Xiao, G. A Remote Sensing and GIS Integrated Study on Urbanization with Its Impact on Arable Lands: Fuqing City, Fujian Province, China. *Land Degrad. Dev.* **2000**, *11*, 301–314. [CrossRef]
11. Xiong, Y.; Huang, S.; Chen, F.; Ye, H.; Wang, C.; Zhu, C. The Impacts of Rapid Urbanization on the Thermal Environment: A Remote Sensing Study of Guangzhou, South China. *Remote Sens.* **2012**, *4*, 2033–2056. [CrossRef]
12. Dewan, A.; Yamaguchi, Y. Land use and land cover change in Greater Dhaka, Bangladesh: Using remote sensing to promote sustainable urbanization. *Appl. Geogr.* **2009**, *29*, 390–401. [CrossRef]
13. Frohn, R.C.; McGwire, K.C.; Dale, V.H.; Estes, J.E. Using satellite remote sensing analysis to evaluate a socio-economic and ecological model of deforestation in Rondônia, Brazil. *Int. J. Remote Sens.* **1996**, *17*, 3233–3255. [CrossRef]
14. De Bem, P.P.; de Carvalho, O.A., Jr.; Guimarães, R.F.; Gomes, R.A.T. Change Detection of Deforestation in the Brazilian Amazon Using Landsat Data and Convolutional Neural Networks. *Remote Sens.* **2020**, *12*, 901. [CrossRef]
15. Weng, Q.; Mao, Z.; Lin, J.; Liao, X. Land-use scene classification based on a CNN using a constrained extreme learning machine. *Int. J. Remote Sens.* **2018**, *39*, 6281–6299. [CrossRef]
16. Gao, J.; Liu, Y. Determination of land degradation causes in Tongyu County, Northeast China via land cover change detection. *Int. J. Appl. Earth Obs. Geoinf.* **2010**, *12*, 9–16. [CrossRef]
17. Brink, A.B.; Bodart, C.; Brodsky, L.; Defourney, P.; Ernst, C.; Donney, F.; Lupi, A.; Tuckova, K. Anthropogenic pressure in East Africa—Monitoring 20 years of land cover changes by means of medium resolution satellite data. *Int. J. Appl. Earth Obs. Geoinf.* **2014**, *28*, 60–69. [CrossRef]
18. He, C.; Gao, B.; Huang, Q.; Ma, Q.; Dou, Y. Environmental degradation in the urban areas of China: Evidence from multi-source remote sensing data. *Remote Sens. Environ.* **2017**, *193*, 65–75. [CrossRef]
19. Li, J.; Pei, Y.; Zhao, S.; Xiao, R.; Sang, X.; Zhang, C. A Review of Remote Sensing for Environmental Monitoring in China. *Remote Sens.* **2020**, *12*, 1130. [CrossRef]
20. Wilson, J.S.; Clay, M.; Martin, E.; Stuckey, D.; Vedder-Risch, K. Evaluating environmental influences of zoning in urban ecosystems with remote sensing. *Remote Sens. Environ.* **2003**, *86*, 303–321. [CrossRef]
21. Mahmood, R.; Pielke, R.A.; Hubbard, K.; Niyogi, D.; Bonan, G.; Lawrence, P.; McNider, R.; McAlpine, C.; Etter, A.; Gameda, S.; et al. Impacts of Land Use/Land Cover Change on Climate and Future Research Priorities. *Bull. Am. Meteorol. Soc.* **2010**, *91*, 37–46. [CrossRef]
22. Wang, Z.; Yang, X.; Lu, C.; Yang, F. A scale self-adapting segmentation approach and knowledge transfer for automatically updating land use/cover change databases using high spatial resolution images. *Int. J. Appl. Earth Obs. Geoinf.* **2018**, *69*, 88–98. [CrossRef]
23. Tran, H.; Tran, T.; Kervyn, M. Dynamics of Land Cover/Land Use Changes in the Mekong Delta, 1973–2011: A Remote Sensing Analysis of the Tran Van Thoi District, Ca Mau Province, Vietnam. *Remote Sens.* **2015**, *7*, 2899–2925. [CrossRef]
24. Guan, Y.; Zhou, Y.; He, B.; Liu, X.; Zhang, H.; Feng, S. Improving Land Cover Change Detection and Classification With BRDF Correction and Spatial Feature Extraction Using Landsat Time Series: A Case of Urbanization in Tianjin, China. *IEEE J. Sel. Top. Appl. Earth Obs. Remote Sens.* **2020**, *13*, 4166–4177. [CrossRef]

25. Dou, P.; Chen, Y. Dynamic monitoring of land-use/land-cover change and urban expansion in Shenzhen using Landsat imagery from 1988 to 2015. *Int. J. Remote Sens.* **2017**, *38*, 5388–5407. [CrossRef]
26. Zafari, A.; Zurita-Milla, R.; Izquierdo-Verdiguier, E. Evaluating the Performance of a Random Forest Kernel for Land Cover Classification. *Remote Sens.* **2019**, *11*, 575. [CrossRef]
27. Dee, S.; Yang, X. Support Vector Machines for Land Cover Mapping from Remote Sensor Imagery. In *Monitoring and Modeling of Global Changes: A Geomatics Perspective*; Li, J., Yang, X., Eds.; Springer Remote Sensing/Photogrammetry; Springer: Dordrecht, The Netherlands, 2015; pp. 265–279. [CrossRef]
28. Sheykhmousa, M.; Mahdianpari, M.; Ghanbari, H.; Mohammadimanesh, F.; Ghamisi, P.; Homayouni, S. Support Vector Machine Versus Random Forest for Remote Sensing Image Classification: A Meta-Analysis and Systematic Review. *IEEE J. Sel. Top. Appl. Earth Obs. Remote Sens.* **2020**, *13*, 6308–6325. [CrossRef]
29. Pal, M. Support vector machine-based feature selection for land cover classification: A case study with DAIS hyperspectral data. *Int. J. Remote Sens.* **2006**, *27*, 2877–2894. [CrossRef]
30. Song, X.; Duan, Z.; Jiang, X. Comparison of artificial neural networks and support vector machine classifiers for land cover classification in Northern China using a SPOT-5 HRG image. *Int. J. Remote Sens.* **2012**, *33*, 3301–3320. [CrossRef]
31. Wang, M.; Zhang, H.; Sun, W.; Li, S.; Wang, F.; Yang, G. A Coarse-to-Fine Deep Learning Based Land Use Change Detection Method for High-Resolution Remote Sensing Images. *Remote Sens.* **2020**, *12*, 1933. [CrossRef]
32. Han, Y.; Javed, A.; Jung, S.; Liu, S. Object-Based Change Detection of Very High Resolution Images by Fusing Pixel-Based Change Detection Results Using Weighted Dempster–Shafer Theory. *Remote Sens.* **2020**, *12*, 983. [CrossRef]
33. Niculescu, S.; Ali, H.T.O.; Billey, A. Random forest classification using Sentinel-1 and Sentinel-2 series for vegetation monitoring in the Pays de Brest (France). In *Remote Sensing for Agriculture, Ecosystems, and Hydrology XX.*; International Society for Optics and Photonics: Bellingham, WA, USA, 2018; Volume 10783, p. 1078305. [CrossRef]
34. Niculescu, S.; Xia, J.; Roberts, D.; Billey, A. Rotation Forests and Random Forest classifiers for monitoring of vegetation in Pays de Brest (France). *Int. Arch. Photogramm. Remote Sens. Spat. Inf. Sci.* **2020**, *43*, 727–732. [CrossRef]
35. Munoz, D.F.; Munoz, P.; Alipour, A.; Moftakhari, H.; Moradkhani, H.; Mortazavi, B. Fusing Multisource Data to Estimate the Effects of Urbanization, Sea Level Rise, and Hurricane Impacts on Long-Term Wetland Change Dynamics. *IEEE J. Sel. Top. Appl. Earth Obs. Remote Sens.* **2021**, *14*, 1768–1782. [CrossRef]
36. Jing, R.; Gong, Z.; Guan, H. Land Cover Change Detection With VHR Satellite Imagery Based on Multi-Scale SLIC-CNN and SCAE Features. *IEEE Access* **2020**, *8*, 228070–228087. [CrossRef]
37. Jozdani, S.E.; Johnson, B.A.; Chen, D. Comparing Deep Neural Networks, Ensemble Classifiers, and Support Vector Machine Algorithms for Object-Based Urban Land Use/Land Cover Classification. *Remote Sens.* **2019**, *11*, 1713. [CrossRef]
38. SPOT-5-EoPortal Directory-Satellite Missions. Available online: https://earth.esa.int/web/eoportal/satellite-missions/s/spot-5 (accessed on 31 August 2021).
39. The European Space Agency: Sentinel-2. Available online: Esa.int/Applications/Observing_the_Earth/Copernicus/Sentinel-2 (accessed on 14 August 2021).
40. Asrar, G.; Fuchs, M.; Kanemasu, E.T.; Hatfield, J.L. Estimating Absorbed Photosynthetic Radiation and Leaf Area Index from Spectral Reflectance in Wheat 1. *Agron. J.* **1984**, *76*, 300–306. [CrossRef]
41. Bannari, A.; Morin, D.; Bonn, F.; Huete, A. A review of vegetation indices. *Remote Sens. Rev.* **1995**, *13*, 95–120. [CrossRef]
42. Zhang, C.; Kovacs, J.M. The application of small unmanned aerial systems for precision agriculture: A review. *Precis. Agric.* **2012**, *13*, 693–712. [CrossRef]
43. Xue, J.; Su, B. Significant Remote Sensing Vegetation Indices: A Review of Developments and Applications. *J. Sens.* **2017**, *2017*, 1–17. [CrossRef]
44. Rouse, J.W.; Haas, R.H.; Scheel, J.A.; Deering, D.W. Monitoring Vegetation Systems in the Great Plains with ERTS. In Proceedings of the 3rd Earth Resource Technology Satellite (ERTS) Symposium, Washington, DC, USA, 10–14 December 1974; Volume 1, pp. 48–62.
45. Gitelson, A.A.; Kaufman, Y.J.; Merzlyak, M.N. Use of a green channel in remote sensing of global vegetation from EOS-MODIS. *Remote Sens. Environ.* **1996**, *58*, 289–298. [CrossRef]
46. Jiang, Z.; Huete, A.; Didan, K.; Miura, T. Development of a two-band enhanced vegetation index without a blue band. *Remote Sens. Environ.* **2008**, *112*, 3833–3845. [CrossRef]
47. Witharana, C.; Civco, D.L. Optimizing multi-resolution segmentation scale using empirical methods: Exploring the sensitivity of the supervised discrepancy measure Euclidean distance 2 (ED2). *ISPRS J. Photogramm. Remote Sens.* **2014**, *87*, 108–121. [CrossRef]
48. Baatz, M.; Schape, A. Multiresolution Segmentation: An Optimization Approach for High Quality Multi-Scale Image Segmentation. In *Angewandte Geographische Informations-Verarbeitung, XII*; Strobl, J., Blaschke, T., Griesbner, G., Eds.; Wichmann Verlag: Karlsruhe, Germany, 2000; pp. 12–23.
49. Darwish, A.; Leukert, K.; Reinhardt, W. Image segmentation for the purpose of object-based classification. In *IGARSS 2003. 2003 IEEE International Geoscience and Remote Sensing Symposium. Proceedings (IEEE Cat. No.03CH37477)*; IEEE: Piscataway, NJ, USA, 2004; Volume 3, pp. 2039–2041. [CrossRef]
50. Benz, U.C.; Hofmann, P.; Willhauck, G.; Lingenfelder, I.; Heynen, M. Multi-resolution, object-oriented fuzzy analysis of remote sensing data for GIS-ready information. *ISPRS J. Photogramm. Remote Sens.* **2004**, *58*, 239–258. [CrossRef]

51. ECognition Suite Documentation. Available online: https://docs.ecognition.com/v9.5.0/Page%20collection/eCognition%20Suite%20Documentation.htm?tocpath=Documentation%20eCognition%20Suite%7C_____0 (accessed on 14 April 2021).
52. Kotsiantis, S.B. Supervised Machine Learning: A Review of Classification Techniques. *Emerg. Artif. Intell. Appl. Comput. Eng.* **2007**, *160*, 3–24.
53. Mountrakis, G.; Im, J.; Ogole, C. Support vector machines in remote sensing: A review. *ISPRS J. Photogramm. Remote Sens.* **2011**, *66*, 247–259. [CrossRef]
54. Cortes, C.; Vapnik, V. Support-vector networks. *Mach. Learn.* **1995**, *20*, 273–297. [CrossRef]
55. Pal, M.; Mather, P.M. Support vector machines for classification in remote sensing. *Int. J. Remote Sens.* **2005**, *26*, 1007–1011. [CrossRef]
56. Huang, C.; Davis, L.S.; Townshend, J.R.G. An assessment of support vector machines for land cover classification. *Int. J. Remote Sens.* **2002**, *23*, 725–749. [CrossRef]
57. Noi, P.T.; Kappas, M. Comparison of Random Forest, k-Nearest Neighbor, and Support Vector Machine Classifiers for Land Cover Classification Using Sentinel-2 Imagery. *Sensors* **2017**, *18*, 18. [CrossRef]
58. Otukei, J.; Blaschke, T. Land cover change assessment using decision trees, support vector machines and maximum likelihood classification algorithms. *Int. J. Appl. Earth Obs. Geoinf.* **2010**, *12*, S27–S31. [CrossRef]
59. Srivastava, P.K.; Han, D.; Rico-Ramirez, M.A.; Bray, M.; Islam, T. Selection of classification techniques for land use/land cover change investigation. *Adv. Space Res.* **2012**, *50*, 1250–1265. [CrossRef]
60. Varma, M.K.S.; Rao, N.K.K.; Raju, K.K.; Varma, G.P.S. Pixel-Based Classification Using Support Vector Machine Classifier. In Proceedings of the 2016 IEEE 6th International Conference on Advanced Computing (IACC), Andhra Pradesh, India, 27–28 February 2016; pp. 51–55. [CrossRef]
61. Li, H.; Gu, H.; Han, Y.; Yang, J. Object-oriented classification of high-resolution remote sensing imagery based on an improved colour structure code and a support vector machine. *Int. J. Remote Sens.* **2010**, *31*, 1453–1470. [CrossRef]
62. Devadas, R.; Denham, R.J.; Pringle, M. Support vector machine classification of object-based data for crop mapping, using multi-temporal Landsat imagery. *ISPRS—Int. Arch. Photogramm. Remote Sens. Spat. Inf. Sci.* **2012**, *39*, 185–190. [CrossRef]
63. Niu, X.; Ban, Y. Multi-temporal RADARSAT-2 polarimetric SAR data for urban land-cover classification using an object-based support vector machine and a rule-based approach. *Int. J. Remote Sens.* **2012**, *34*, 1–26. [CrossRef]
64. Tzotsos, A.; Argialas, D. Support Vector Machine Classification for Object-Based Image Analysis. In *Object-Based Image Analysis*; Blaschke, T., Lang, S., Hay, G.J., Eds.; Lecture Notes in Geoinformation and Cartography; Springer: Berlin/Heidelberg, Germany, 2008; pp. 663–677. [CrossRef]
65. Hsu, C.-W.; Lin, C.-J. A comparison of methods for multiclass support vector machines. *IEEE Trans. Neural Netw.* **2002**, *13*, 415–425. [CrossRef]
66. Angelos, T. A support vector machine approach for object based image analysis. In Proceedings of the OBIA, Salzburg, Austria, 4–5 July 2006.
67. Briem, G.; Benediktsson, J.A.; Sveinsson, J.R. Multiple classifiers applied to multisource remote sensing data. *IEEE Trans. Geosci. Remote Sens.* **2002**, *40*, 2291–2299. [CrossRef]
68. Gislason, P.O.; Benediktsson, J.A.; Sveinsson, J.R. Random Forests for land cover classification. *Pattern Recognit. Lett.* **2006**, *27*, 294–300. [CrossRef]
69. Rodriguez-Galiano, V.F.; Ghimire, B.; Rogan, J.; Olmo, M.C.; Rigol-Sanchez, J.P. An assessment of the effectiveness of a random forest classifier for land-cover classification. *ISPRS J. Photogramm. Remote Sens.* **2012**, *67*, 93–104. [CrossRef]
70. Dietterich, T.G. An Experimental Comparison of Three Methods for Constructing Ensembles of Decision Trees: Bagging, Boosting, and Randomization. *Mach. Learn.* **2000**, *40*, 139–157. [CrossRef]
71. Chan, J.C.-W.; Paelinckx, D. Evaluation of Random Forest and Adaboost tree-based ensemble classification and spectral band selection for ecotope mapping using airborne hyperspectral imagery. *Remote Sens. Environ.* **2008**, *112*, 2999–3011. [CrossRef]
72. Rodriguez-Galiano, V.F.; Olmo, M.C.; Abarca-Hernandez, F.; Atkinson, P.; Jeganathan, C. Random Forest classification of Mediterranean land cover using multi-seasonal imagery and multi-seasonal texture. *Remote Sens. Environ.* **2012**, *121*, 93–107. [CrossRef]
73. Fu, T.; Ma, L.; Li, M.; Johnson, B.A. Using convolutional neural network to identify irregular segmentation objects from very high-resolution remote sensing imagery. *J. Appl. Remote Sens.* **2018**, *12*, 025010. [CrossRef]
74. Timilsina, S.; Sharma, S.K.; Aryal, J. Mapping urban trees within cadastral parcels using an object-based convolutional neural network. *ISPRS Ann. Photogramm. Remote Sens. Spat. Inf. Sci.* **2019**, *4*, 111–117. [CrossRef]
75. Cihlar, J. Land cover mapping of large areas from satellites: Status and research priorities. *Int. J. Remote Sens.* **2000**, *21*, 1093–1114. [CrossRef]
76. Congalton, R.G. A review of assessing the accuracy of classifications of remotely sensed data. *Remote Sens. Environ.* **1991**, *37*, 35–46. [CrossRef]
77. Foody, G.M. Status of land cover classification accuracy assessment. *Remote Sens. Environ.* **2001**, *80*, 185–201. [CrossRef]
78. Olofsson, P.; Foody, G.M.; Herold, M.; Stehman, S.V.; Woodcock, C.E.; Wulder, M.A. Good practices for estimating area and assessing accuracy of land change. *Remote Sens. Environ.* **2014**, *148*, 42–57. [CrossRef]
79. Alberg, A.J.; Park, J.W.; Hager, B.W.; Brock, M.V.; Diener-West, M. The use of "overall accuracy" to evaluate the validity of screening or diagnostic tests. *J. Gen. Intern. Med.* **2004**, *19*, 460–465. [CrossRef] [PubMed]

80. Story, M.; Congalton, R.G. Accuracy Assessment: A User's Perspective. *Photogramm. Eng. Remote Sens.* **1986**, *52*, 397–399.
81. Tung, F.; LeDrew, E. The Determination of Optimal Threshold Levels for Change Detection Using Various Accuracy Indices. *Photogramm. Eng. Remote Sens.* **1988**, *54*, 1449–1454.
82. Lavrakas, P.J. *Encyclopedia of Survey Research Methods*; SAGE Publications: Thousand Oaks, CA, USA, 2008; Available online: http://www.credoreference.com/book/sagesurveyr (accessed on 20 April 2021).
83. LeCun, Y.; Bengio, Y.; Hinton, G. Deep learning. *Nature* **2015**, *521*, 436–444. [CrossRef] [PubMed]
84. Ma, J.; Cheng, J.C.; Lin, C.; Tan, Y.; Zhang, J. Improving air quality prediction accuracy at larger temporal resolutions using deep learning and transfer learning techniques. *Atmos. Environ.* **2019**, *214*, 116885. [CrossRef]
85. Hendrycks, D.; Lee, K.; Mazeika, M. Using Pre-Training Can Improve Model Robustness and Uncertainty. *arXiv* **2019**, arXiv:1901.09960.
86. Fuller, R.; Smith, G.; Devereux, B. The characterisation and measurement of land cover change through remote sensing: Problems in operational applications? *Int. J. Appl. Earth Obs. Geoinf.* **2003**, *4*, 243–253. [CrossRef]
87. Tewkesbury, A.P.; Comber, A.J.; Tate, N.J.; Lamb, A.; Fisher, P.F. A Critical Synthesis of Remotely SensedOptical Image Change Detection Techniques. *Remote Sens. Environ.* **2015**, *160*, 1–14. [CrossRef]
88. Lu, D.; Li, G.; Moran, E. Current situation and needs of change detection techniques. *Int. J. Image Data Fusion* **2014**, *5*, 13–38. [CrossRef]
89. Liu, H.; Zhou, Q. Accuracy analysis of remote sensing change detection by rule-based rationality evaluation with post-classification comparison. *Int. J. Remote Sens.* **2004**, *25*, 1037–1050. [CrossRef]

Appendix 4

《Mapping crop types using Sentinel-2 data Machine Learning and monitoring crop phenology with Sentinel-1 backscatter time series in Pays de Brest, Brittany, France》(Journal article 2022)

remote sensing

MDPI

Article

Mapping Crop Types Using Sentinel-2 Data Machine Learning and Monitoring Crop Phenology with Sentinel-1 Backscatter Time Series in Pays de Brest, Brittany, France

Guanyao Xie [1,*] and Simona Niculescu [1,2]

[1] Laboratory LETG-Brest, Géomer, UMR 6554 CNRS, IUEM UBO, 29200 Brest, France
[2] Department of Geography, University of Western Brittany, 3 Rue des Archives, 29238 Brest, France
* Correspondence: guanyao.xie@univ-brest.fr

Abstract: Crop supply and management is a global issue, particularly in the context of global climate change and rising urbanization. Accurate mapping and monitoring of specific crop types are crucial for crop studies. In this study, we proposed: (1) a methodology to map two main winter crops (winter wheat and winter barley) in the northern region of Finistère with high-resolution Sentinel-2 data. Different classification approaches (the hierarchical classification and the classical direct extraction), and classification methods (pixel-based classification (PBC) and object-based classification (OBC)) were performed and evaluated. Subsequently, (2) a further study that involved monitoring the phenology of the winter crops was carried out, based on the previous results. The aim is to understand the temporal behavior from sowing to harvesting, identifying three important phenological statuses (germination, heading, and ripening, including harvesting). Due to the high frequency of precipitation in our study area, crop phenology monitoring was performed using Sentinel-1 C-band SAR backscatter time series data using the Google Earth Engine (GEE) platform. The results of the classification showed that the hierarchical classification achieved a better accuracy when it is compared to the direct extraction, with an overall accuracy of 0.932 and a kappa coefficient of 0.888. Moreover, in the hierarchical classification process, OBC reached a better accuracy in cropland mapping, and PBC was proven more suitable for winter crop extraction. Additionally, in the time series backscatter coefficient of winter wheat, the germination and ripening (harvesting) phases can be identified at VV and VH/VV polarizations, and heading can be identified in both VV and VH polarizations. Secondly, we were able to detect the germination phase of winter barley in VV and VH, ripening with both polarizations and VH/VV, and finally, heading in VV and VH polarizations.

Keywords: winter crops mapping; winter crops phenology; machine learning; hierarchical classification; object-based classification; pixel-based classification; Google Earth Engine (GEE); Sentinel-1; Sentinel-2

Citation: Xie, G.; Niculescu, S. Mapping Crop Types Using Sentinel-2 Data Machine Learning and Monitoring Crop Phenology with Sentinel-1 Backscatter Time Series in Pays de Brest, Brittany, France. *Remote Sens.* **2022**, *14*, 4437. https://doi.org/10.3390/rs14184437

Academic Editor: Jianxi Huang

Received: 1 August 2022
Accepted: 31 August 2022
Published: 6 September 2022

1. Introduction

Crop supply is a global issue, particularly in the context of global climate change, rising population, and urbanization. With increasing food demand worldwide, agriculture production and food security should be guaranteed by ensuring biodiversity and limiting the environmental impacts [1]. This makes reliable information about crop spatial distribution and growing patterns crucial for studying regional agriculture production and supply, making political decisions, and facilitating crop management [2,3].

The classification of crop spatial distributions are valuable for agricultural monitoring and for the implementation and evaluation of crop management strategies [4,5]. Hence, crop type mapping is in high demand. Field research and remote sensing have always been the most important sources for obtaining agricultural information [6], and

since the first launch of Earth observation satellites in 1972, continuous agriculture mapping and monitoring over large areas became possible with the Earth Observation (EO) data. Moreover, the new generation of EO data, nowadays, has increased the resolution of sensors for agriculture uses, therefore since the last few decades, the science of agriculture mapping and monitoring has developed quickly, with diverse types of high spatial and temporal resolution EO data. For example, Sun et al. in 2019 [4] conducted a study of the crop types that were located at the lower reaches of the Yangzi River in China. They performed a classification of crop-type dynamics during the growing season by using three advanced machine learning algorithms (Support Vector Machine (SVM), Artificial Neural Network (ANN), and Random Forest (RF)) with a combination of three advanced sensors (Sentinel-1 backscatter, optical Sentinel-2, and Landsat-8). Arvor et al. in 2010 [7] provided a methodology for mapping the main crops and agricultural practices in the Mato Grosso state in Brazil; this study was performed by two successive, supervised classifications with the Enhanced Vegetation Index (EVI) time series from the MODIS sensor to create an agricultural mask and a crop classification of three main crops in the state. In another study by Forkuor et al. in 2014 [8], they found that an integration of multi-temporal optical RapidEye and dual-polarized Synthetic Aperture Radar (SAR) TerraSAR-X data can efficiently improve the classification accuracy of crops and crop group mapping in West Africa, in spite of excessive cloud cover, small sized fields, and a heterogeneous landscape. Furthermore, in the Finistère department, Xie and Niculescu 2021 [9] evaluated the multiannual change detections of different Land Cover Land Use (LCLU) regions, including agricultural land with accuracy indices between 70% and 90%, by using high-resolution satellite imagery (SPOT 5 and Sentinel-2) and three algorithms that were implemented: RF, SVM, and the Convolutional Neural Network (CNN).

More importantly, many studies of crop mapping focuses on winter crop mapping. Dong et al. in 2020 [10] proposed a method called phenology-time-weighted dynamic time warping (PT-DTW) for mapping winter wheat using Sentinel-2 time series data, and this new method may exploit phenological features in two periods, with a NDPI (Normalized Difference Phenology Index) providing more robust vegetation information and reducing the adverse impacts of soil and snow cover during the overwintering period. Zhou et al. in 2017 [11] studied the feasibility of winter wheat mapping in an urban agricultural region with a complex planting structure using three machine learning classification methods (SVM, RF, and neural network (NN)), and the possibility of improving classification accuracy by combining SAR and optical data.

Besides the contributions of the new generation of EO data, the diversity of the classification approaches and methods have provided more resources for agriculture mapping and monitoring. The classical, direct extraction approach is the traditional and most used classification approach that is used to extract single or multiple crop types directly from satellite images [12–14]. Moreover, we also propose the hierarchical classification approach for crops mapping in this study. Hierarchical classification is well known for its capacity to solve a complex classification problem by separating the problem into a set of smaller progressive classifications; it produces a series of thematic maps to progressively classify the image into detailed classes. Wardlow and Egbert [12] investigated the applicability of time-series Moderate Resolution Imaging Spectro-radiometer (MODIS) 250 m normalized difference vegetation index (NDVI) data for large-scale crop mapping in the Central Great Plains of the U.S. The hierarchical classification scheme was applied in this study with high classification accuracy, and instead of directly solving a complex irrigated crop mapping problem, a four-level hierarchical classification framework was implemented to produce a series of crop-related thematic maps that progressively classified cropland areas into detailed classes. Ibrahim et al. in 2021 [15] have also employed the hierarchical classification scheme to map crop types and cropping systems in Nigeria, using the RF classifier and Sentinel-2 imagery. Firstly, they produced a land cover map with five classes in order to eliminate other land cover types, then the next classification was performed only on cropland, where the specific crop types and cropping systems were

mapped. The results indicated that the crop types were well classified with high accuracy, despite the study area being heterogeneous and smallholder-dominated.

In recent years, most studies in the agricultural field have explored the performance of different classification algorithms. Random Forest (RF) is one of the most well-known and widely used algorithms in the field for its optimal classification accuracy, effectiveness on large data bases, and its capability of estimating the importance of the variables in the classification [8,16–19]. The RF classification algorithm is traditionally run as a Pixel-Based Classification, which has proven efficient and accurate in agriculture fields by many studies [16,20–22]. On the other hand, the advantage of Object-Based Classification (OBC) is well documented and many recent studies have the conclusion that OBC usually outperforms PBC for its higher classification accuracy, better potential for extracting land cover information in a heterogeneous area with small size field, and the capacity to produce a more homogenous class [23,24]. However, even though Object-Based Classification is better developed and considered as more accurate than PBC, both classification methods are able to achieve a great degree of accuracy.

Aside from mapping and analyzing the crop spatial distribution, understanding agricultural growing patterns is also a key element for crop management. Crop phenology monitoring and the identification of the main phenological stages are highly necessary for agricultural production predicting, efficient interventions of farmers and decision-makers during the phenological phases such as fertilization, pesticide application, and irrigation [25]. In particular, germination is the most critical phase to be understood, and it is the starting point of the growing season. Based on the germination information, the farmer and decision-makers are able to make a future projection of the season, estimate the whole seasonal phenology for crop growth, and predict its production [25]. Furthermore, phenology is highly related to the seasonal dynamics of a growth environment, therefore, in the context of global warming, the phenology of many plants, especially crops, may have changed [6].

Crop phenology is usually monitored with optical satellite images using vegetation indices. For example, Pan et al. in 2015 [26] analyzed the phenology of winter wheat and summer corn in the Guanzhong Plain in the Shanxi Province, China by using Normalized Difference Vegetation index (NDVI) time series data and extracted seasonality information from the NDVI time series for measuring phenology parameters. The potential of another less-known index, the Normalized Difference Phenology Index (NDPI), is exploited by Gan et al. in 2020 [27] in order to detect winter wheat green-up dates. During the evaluation with three other indices (NDVI, EVI, and EVI2), the results indicate that NDPI outperforms the other indices with the highest consistency with the ground truth.

Compared to the optical data, SAR data is less used in agricultural areas. Nevertheless, lately, with the emergence of a new generation of high-resolution SAR data, in particular since the Copernicus program Sentinel-1 C-band high spatial–temporal resolution images became available, SAR data has begun to draw interest, especially for its advantage of having its own source of energy, making it nearly independent of weather conditions [8]. Thus, SAR backscattering coefficient time series data is now more frequently used for crop phenology monitoring. While optical data strongly depends on the chlorophyll content in the plants, SAR data can reveal the main changes in the canopy structure, identify significant phenological stages, and determine the main growing period with the signal that is received after interacting with the canopy of the plants. Therefore, studies of crop phenology monitoring using SAR data have increased considerably in recent years. Meroni et al. in 2020 [28] conducted a study of retrieving the crop-specific land surface phenology (LSP) of eight major European crops from Sentinel-1 SAR and Sentinel-2 optical data, where crop phenology was detected on the temporal profiles of the ratio of the backscattering coefficient VH/VV from Sentinel-1 and NDVI from Sentinel-2. They revealed that the crop phenology that was detected by Sentinel-1 and 2 can be complementary. Wali et al. in 2020 [29] introduced rice phenology monitoring in the Miyazaki prefecture of Japan by using Sentinel-1 dual polarization (VV and VH) time series data, and

attempted to clarify the relationship between rice growth parameters and the backscattering coefficient using the combination of two linear-regression lines. Canisius et al. in 2018 [30] exploited SAR polarimetric parameters that were derived from fully polarimetric RADARSAT-2 SAR time series data to predict the growth pattern and phenological stages of canola and spring wheat in the Nipissing agricultural district of Northern Ontario, Canada. Mandal et al. in 2020 [31] proposed a dual-pol radar vegetation index (DpRVI) from Sentinel-1 difference data (VV-VH) to characterize the vegetation growth of three crop types (canola, soybean, and wheat) from sowing to full canopy development, with the accumulation of the Plant Area Index (PAI) and biomass.

The feasibility and effectiveness of winter crop type mapping and phenology monitoring with optical or SAR satellite data has been proven by many studies in agricultural field, however, some limitations remain. For example, the potential of a vegetation index other than NDVI and EVI has rarely been explored, and the studies have never been performed in a coastal area with fragmented and small-scale fields. More importantly, almost all the research perform and evaluate a single classification approach or method, instead of comparing different approaches and methods for crop type mapping.

In this study, we introduce a methodology to map two winter crop types (winter wheat and winter barley) with Sentinel-2 optical data that was acquired during the growing season of the winter crops. Two different classification approaches (hierarchical classification and classical direct extraction) were performed using RF-supervised classification algorithms, and two classification methods (PBC and OBC) were operated and evaluated within the hierarchical classification framework. With the classification results of the winter crops, we are able to monitor their phenology with Sentinel-1 C-band SAR backscatter time series and precipitation data in order to understand their temporal behavior from sowing to harvesting, identify the three main phenological stages (germination, heading, and ripening, including harvesting), and study how crop phenology responds to weather conditions.

The main objectives of this study are listed as follows:

(1) Study the feasibility of mapping winter crops with Sentinel-2 10 m spatial resolution data in a fragmented area that is dominated by small-size fields;
(2) Perform hierarchical classification and classical direct extraction and evaluate the performance of both classification approaches;
(3) Perform PBC and OBC and compare the performance in each level of the hierarchical classification structure;
(4) Study the correlation between crop phenology and Sentinel-1 C-band SAR backscatter time series data and identify three phenological stages and the main growth period of the winter crops.

2. Study Area

The study area is located on the west coast of France in the north of the Finistère department and the region of Brittany (Figure 1).

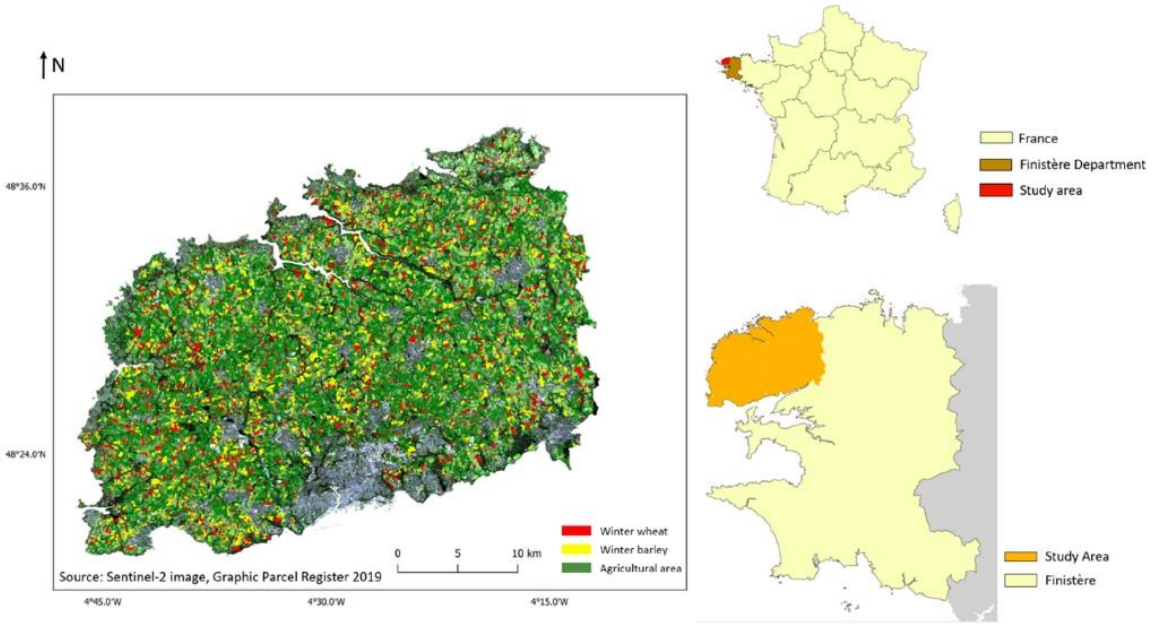

Figure 1. Location of study area, the north of the Finistère department, Brittany, France, as per the RGB band combination of a Sentinel-2 satellite image on 20 April 2019 and the distribution of agricultural land in 2019.

The study area covers a land surface of 1034.41 km^2, and extends between the latitudes of 48°19′39″N and 48°40′41″N, and the longitudes of 4°12′50″W and 4°47′13″W. According to French National Institute of Geographic and Forest Information (IGN), the northern part of Finistère is mostly dominated by plains, and the elevation of the area ranges between 0 m and 100 m [32]. The study area is mostly occupied by cropland, temporal or permanent grasslands, small area of forests and shrubs, urban agglomeration in the south, and a wetland area in the north [33]. Climatically, the north of Finistère is classified as type Cfb (temperate oceanic climate), according to the Köppen climate classification, and it is characterized by warm winters and cool summers. On average, the northern region of Finistère receives 941 mm of total precipitation per year, with the annual average temperature being 12.1 °C (7.7 °C and 16.8 °C are the monthly average temperatures for the coldest and warmest months, respectively), and therefore the warm temperate climate with frequent rainfall provides very favorable conditions for agriculture activities.

With such climate and topography conditions, agriculture is an important economic sector in the study area, and a considerable number of locals work in an agricultural or related sector in the department. There are 384,408 hectares of useful agricultural area in the department, so 57% of the department's surface is devoted to agricultural use [34]. One of main agricultural productions are crops, including corn, winter wheat, and winter barley, and vegetables [35].

Hence, it is important to develop a methodology to map one or several specific crop types and monitor their growth stages by using free access, high quality satellite images for crop production management. The north of the Finistère department was chosen as

our first study area because of its favorable natural conditions, highly active agricultural activities, and its proximity, which facilitate the field research and interaction with farmers.

3. Data

The study was executed in the Finistère department in France during 2019, using open-access high-quality satellite data from the Sentinel platform. It is worth noting that the latest version of the graphic parcel register was published in 2019 by the French National Institute of Geographic and Forest Information, and this information was relevant to our study.

Due to the annual high-intensity precipitation there is frequent heavy cloud cover in the region, therefore, operable optical satellite images are very rare in the study area. Nevertheless, a Sentinel-2 optical satellite image was acquired in the spring, which is the growing season of the winter crops. In order to create a cloud-free time series of the study, the phenological phrases of winter crops from the SAR data were applied to the phenology monitoring process.

3.1. Sentinel-2 Optical Data

Sentinel-2 is an satellite imaging mission that is implemented by the European Commission (EC) and the European Space Agency (ESA) as a part of the Copernicus program [36]. The two identical satellites (Sentinel-2A and Sentinel-2B) provide continually open-access, multispectral, wide swath (290 km), high spatial resolution (four bands at 10 m, six bands at 20 m, and three bands at 60 m), and high revisit frequency (five days with combined satellites) image data [36]. Due to frequent heavy cloud cover in the area, only one cloud-free level 2A atmospheric effect-corrected Sentinel-2 image from 20 April 2019 was acquired from the Theia platform (catalog.theia-land.fr) [37] (Table 1). Ten spectral bands (Table 2) were extracted for further processing and analysis.

Table 1. Sentinel-2 image used in the study.

Date	Satellite	Platform	Processing Level	Tiles
20 April 2019	Sentinel-2	2B	Level 2A	T30UUU

Table 2. Sentinel-2 spectral bands used in the study.

Sentinel-2 Bands	Spatial Resolution (m)	Wavelength Range (nm)
Band 2-Blue	10	458-523
Band 3-Green	10	543-578
Band 4-Red	10	650-680
Band 5-Vegetation red edge	20	698-713
Band 6-Vegetation red edge	20	733-748
Band 7-Vegetation red edge	20	773-793
Band 8-Near Infrared	10	785-899
Band 8A-Vegetation red edge	20	855-875
Band 11-Short-Wave Infrared	20	1565-1655
Band 12-Short-Wave Infrared	20	2100-2280

3.2. Sentinel-1 SAR Data

The Sentinel-1 C-band SAR (Synthetic-aperture radar) is one of the ESA missions under the Copernicus program [38]. Sentinel-1 possesses two polar-orbiting satellites (Sentinel-1A and Sentinel-1B) sharing the same orbital plane, which are able to operate day and night using their own energy source in order to perform high spatial resolution (10 m), wide coverage, high repeat cycle (generally five days with two satellites), C-band SAR imaging in all weather conditions [38].

In this study, interferometric Wide Swath mode level-1 GRD (Ground Range Detected) Sentinel-1 data with an incidence angle ranging from 30 to 46 were acquired to create the time series of the growing period of the winter crops (winter wheat and winter barley) in 2019, from 1 October 2018 to 1 September 2019. Both polarizations (VV + VH) were used, but only the descending orbit was retained for the processing. In total, 109 Sentinel-1 C-band SAR images with descending orbit were acquired for this study.

3.3. Auxiliary Data

RPG (Graphic Parcel Register) was applied as the ground truth data in our study, used for creating training data and test data. RPG 2019 is the latest version of the very precise, geo-referenced agricultural land database that covers the entire France territory (except Mayotte) that was published by IGN. The databases show the precise crop types (e.g., wheat, corn, vegetables, sunflower) or temporary and permanent grasslands in that are in the recorded agricultural lands in each year [39].

4. Methods

The methodology of this paper is detailed in two parts, which relate to the two research subjects: mapping winter crop types using Sentinel-2 data, and monitoring crop phenology with Sentinel-1 backscatter time series. The data were processed in QGIS with Orfeo Toolbox, eCognition 10.0, and GEE (Google Earth Engine).

4.1. Winter Crop Types Mapping

A flow chart of the proposed global methodology is displayed below (Figure 2)

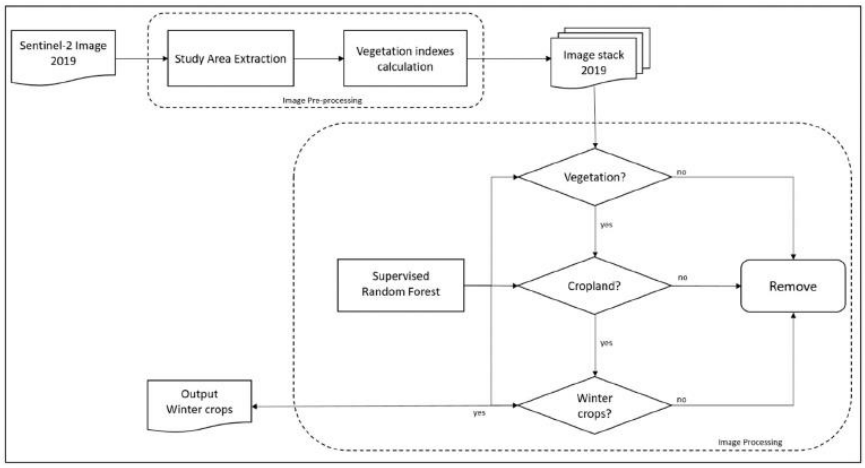

Figure 2. Hierarchical classification methodology used in the study for crop mapping.

4.1.1. Image Preprocessing

After the study area selection and satellite image acquisition, the boundary of the northern region of Finistère area was applied in order to extract our area of interest by subsetting the raw images for the purpose of reducing the image size and shortening the processing time.

In remote sensing fields, vegetation indices (VI) are the qualitative and quantitative evaluation of vegetation covers and their growth dynamics, using different combinations of spectral measurements. The results of the indices are different due to the different chemical and morphological characteristics of the surfaces of the organs or leaves of the

plants [40], however the spectral responses are also affected by other factors, such as environmental effects, soil reflectance and its components, shadows, and atmospheric and topographic effects [41].

For this reason, over a hundred VIs have been developed and enhanced for various applications over the past three decades in order to enhance spectral responses, increase sensitivity for identifying vegetated areas, distinguish different vegetation types, evaluate the vegetation density, and provide data on the health of the vegetation [42], and also to minimize the effects of other factors that are described above [41]. In this study, six VIs are used with the aim of mapping winter crop types using Sentinel-2 data.

- The Normalized Difference Vegetation Index (NDVI), proposed in 1973 by [43], is the most known and widely used index in research related to vegetation monitoring. NDVI is the normalized difference between the visible red and near-infrared spectral reflectance of vegetation, as follows:

$$NDVI = \frac{NIR-RED}{NIR+RED} \quad (1)$$

Even though the index is often affected by atmospheric conditions and soil reflectance and its components, it remains a highly used index in agriculture-related fields to measure the rate of vegetation cover and evaluate the health of the crops.

- The Normalized Difference Water Index (NDWI), proposed by Gao in 1996 [44], is a vegetation index that is used to highlight the changes in the liquid water content of vegetation canopies with weak atmospheric aerosol scattering effects, while remaining independent of the soil background [44]. The index is the normalized ratio between visible red and short-wave infrared spectral bands, and the expression of this is displayed below:

$$NDWI = \frac{NIR-SWIR}{NIR+SWIR} \quad (2)$$

With its high sensitively to water stress, NDWI is frequently used for the agricultural monitoring of drought and irrigation management. As well, some studies reveal the possibility of distinguishing crop types, especially winter crops, with NDWI [20,45–47].

- The Green Normalized Difference Water Index (GNDVI) was proposed in 1996 by Gitelson et al. [48], as NDVI; it is the index for evaluating the photosynthetic activity of the vegetation, except that the visible red band is replaced by the green band, ranging from 0.54 to 0.57 microns, and the expression of it is as follows:

$$GNDVI = \frac{NIR-Green}{NIR+Green} \quad (3)$$

Besides NDVI, the "Green" NDVI is more sensitive for assessing the chlorophyll concentration at the canopy level and it enables a precise estimation of the pigment concentration [48].

- The Enhanced Vegetation Index (EVI), developed by the MODIS Land Discipline Group [49], is aimed at optimizing the vegetation signal and correcting the imprecision of NDVI with improved sensitivity in high biomass regions by appending several additional spectral bands [50], and it is calculated by the following equation:

$$EVI = \frac{G * (NIR - Red)}{(NIR + C1 * Red - C2 * Blue + L)} \quad (4)$$

EVI is able to reduce the atmospheric conditions and canopy background noise with high sensitivity in densely vegetated areas and it is more responsive to canopy structural variations as compared to NDVI [50].

- The Soil-Adjusted Vegetation Index (SAVI), was proposed by Huete in 1988 [51] as an attempt to improve NDVI, which is frequently affected by the soil background conditions. Therefore, the index aims at minimizing the influence of soil brightness

and eliminating the need for the additional calibration for different soils by using a soil-brightness correction factor [51]. It has an adjustment factor (L) in its calculation:

$$SAVI = \frac{(NIR-Red)}{(NIR+Red+L)}(1+L) \quad (5)$$

SAVI was found to be helpful in separating different crop types, especially spring crops from winter ones [52].

- The Modified Soil Adjusted Vegetation Index (MSAVI) was developed by [53] in 1994 as an improved version of SAVI, with the constant soil adjustment factor L being replaced. It is proven to increase the dynamic range of the vegetation signal while further minimizing the soil backgrounds spatial and temporal variations, therefore resulting a greater vegetation sensitivity:

$$MSAVI = \frac{\left(2*NIR+1-\sqrt{(2*NIR+1)^2-8*(NIR-RED)}\right)}{2} \quad (6)$$

Studies have proven that MSAVI can be used in the agriculture field [54,55], and even more in winter crop monitoring [56].

After calculating the vegetation indices, an image stack with the ten original spectral bands and all of the indices was created for further image processing.

4.1.2. Image Processing

In this study, for the better extraction of winter wheat and winter barley in the study area from the satellite image, supervised image processing using different approaches was performed in order to make comparisons and attempt to reach the most adapted classification in this study (Figure 3).

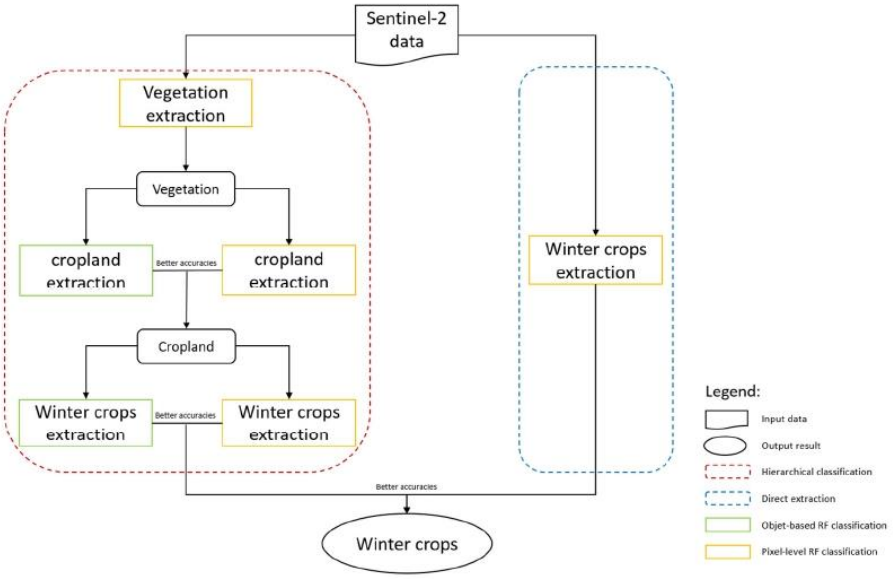

Figure 3. Proposed detail image processing methodology chart.

Compared to the direct extraction of winter crops with pixel-based RF algorithms, hierarchical classification methods are effectuated in three progressive levels, each with different objectives. The objectives from the first level of the hierarchy to the last one are extracting vegetation (including croplands) from raw images, extracting croplands from vegetated areas (trees, shrubs, and grassland), and finally, obtaining exclusively winter

wheat and winter barley from all crop types detected in previous stages, respectively. Finally, the results of the two classification approaches were evaluated with accuracy indices, in order to distinguish which one had better agreement with the ground truth data.

In addition, inside the hierarchical classification structure, except for during the first step, separating vegetation and non-vegetation exclusively used the pixel-based RF algorithm and this reached a very close agreement with ground truth data. Each step has been performed using the two methods, pixel-based and object-based RF classification, in order to determine the result with better accuracies for further processing and analysis.

Pixel-Based Classification (PBC)

The traditional PBC is the most used method in remote sensing, especially for land use classification; therefore, this method was also widely employed in this study. The PBC was done on the pixel level, which is the smallest unit in an image, where only the spectral information of each single pixel was used. During the classification, each pixel was assigned predefined classes by using a model that was well trained with training data and a classification algorithm. In this paper, PBC is performed in both classification approaches.

Object-Based Classification (OBC)

OBC starts with an additional processing step before classification, which involves the segmentation of an image into numerous, non-overlapping, homogeneous objects [23], hence, the OBC was done on the object level instead of the pixel level. At the same time, aside from the simple spectral information, the texture, color, form, and size of the objects are taken into account. Later the individual object that was generated by the segmentation algorithm was used for classification.

A Multiresolution Segmentation (MRS) algorithm was applied as the first step of the object-based image analysis (OBIA) in the current study. This relatively complex and user-dependent algorithm has proven to be one of the most successful image segmentation algorithms in the OBIA area [57]. At the beginning of the process, each pixel is considered as a segment; afterwards, pairs of adjacent image objects are merged to form larger segments [58]. The three main parameters of the algorithm: scale, shape, and compactness, can be adjusted by users. The scale parameter is able to define the maximum standard deviation of the heterogeneity in order to control the amount of spectral variation within objects and the size of their results [57,59]. Thereafter, there are also two homogeneity criteria, the shape criterion that defines the weight between the shape and the spectral information of the objects, and the compactness criterion which represents the compactness of the objects during segmentation [60].

In this study, several combinations of parameters were used, and the optimal ones were found on a trial-and-error basis. The scale, compactness, and shape parameters were assigned as follows: 15, 0.5, and 0.3, respectively, for cropland extraction, and 20, 0.5, and 0.1, respectively, for winter crops extraction.

Supervised RF Classification

Supervised RF classification was performed on the Sentinel-2 data. It is the most common procedure for the quantitative analysis of remote sensing imagery [61], and it involves the use of training data for machine-learning classification. The training data were selected with reference data, knowledge, and experience provided by the user, and the selected samples were considered representative of each class.

Training data and test data in our research were selected in this step, using the RPG 2019 map. For the purpose of comparing different methods of classification, training data that were selected for PBC and OBC were as similar as possible, such as using the same area and very approximate surfaces, in order to improve the global comparability of the two methods.

RF classification has been one of the most known and widely used classification algorithms, especially in the land cover classification field, over the past two decades. This powerful machine learning classifier has numerous key advantages, such as a low sensitivity to noise or overtraining, the ability to handle high-dimensional data, its high classification accuracy and non-parametric-nature, and its capacity to determine variable importance [19].

RF is also one of the ensemble learning algorithms that builds numerous classifiers that have been proven to improve classification accuracy considerably. For classification, RF forms an ensemble method using a tree-like classifier, where each tree in the forest contributes a single vote for the most popular class, and the majority of the vote determines the final prediction of the RF model [62].

The training and classification of the RF module were applied using the Orfeo toolbox with two user-defined parameters that were set on a trial-and-error basis: the number of decision trees grown in the forest and the maximum tree depth, which is the length of each tree in the forest. The two parameters that were used in this study were defined as 100 and 25, respectively.

4.1.3. Image Post Processing

After the classification, the accuracy assessment was performed with test data in order to evaluate the classification's degree of agreement with the reality and therefore assess the reliability of the classified results. In this study, in order to evaluate the classification quality and compare it amongst the different classification methods, five well-known and highly promoted accuracy indices were calculated for each classification method and each class. Among them, overall accuracy (OA) and kappa were employed for the global accuracy assessment, otherwise, precision, recall, and F-score were computed to assess the classification results of each class.

The OA is one of the traditional measures of classification accuracy that is derived from the confusion matrix [63]. It indicates the probability that an individual pixel will be correctly classified by a classifier [64], hence, it is computed by dividing the number of correctly classified pixels by the total number of pixels in the confusion matrix. The popular kappa coefficient was first applied in the remote sensing community to express the classification accuracy in the early 1980s [65], and it is considered to be the assessment of the inter-classifier agreement and the accuracy of two classifiers; it usually gives a statistically more sophisticated measure of interclass agreement, also it gives a better interclass discrimination than OA does [66].

Among the per-class accuracy assessments, precision and recall were computed from the confusion matrix as well. Precision is also called the positive predictive value, which is related to the rate of correct positive predictions among the total predictions that are classified as positive, and the recall or sensibility represents the rate of the actual positive individual pixels that are correctly detected by the classifier. Furthermore, the F-score was generated from the precision and recall; it provides a single harmonic mean of the model's precision and recall.

In the hierarchical classification process, test data that were used for evaluating the classification of each step were generated as random points from the image that were used to perform classification, which is the result of the previous steps. Afterwards, the random points were labelled manually with the Graphic Parcel Register map as ground truth. However, with the aim of evaluating the performance of the proposed hierarchical classification approach by comparing with traditional direct extraction, a completely new test dataset was produced from the original Sentinel-2 image that was not classified.

4.2. Crops Phenology Monitoring

This second part of the study was performed, based on the mapped winter crops from the previous step. Due to limited climate conditions in the study area, winter crop phenology monitoring was performed with Sentinel-1 C-band SAR data using the Google

Earth Engine (GEE) platform. GEE is an open-source, cloud computing platform with a fast, high-performance computation and visualization system and a large data catalog which hosts a large repository of publicly available geospatial datasets, including a variety of satellite imaging systems [67]. The platform is designed for global-scale geospatial big data storage, processing, and analyzing [68]. The utility of GEE has been examined in different fields, for vegetation mapping and monitoring, land cover change mapping, and agriculture applications [68].

The platform proposes a complete data process chain from a single or a collection of analysis-ready images to library functions or user-defined algorithms that are applied to achieve results generation and visualizing. One of its main advantages is allowing long-term monitoring using a user-defined period with free access to preprocessed time series data. Hence, in this study, the backscatter coefficient (σ°) in decibels (dB) of both polarizations (VV and VH) and their ratios of a Sentinel-1 image time series during a complete growing period of winter crops (from October to September) on a few chosen croplands was automatically generated in a line chart on the GEE platform. In order to study the scattering behavior of our target croplands, each image was preprocessed, and the backscatter coefficient was converted to dB by GEE using the Sentinel-1 Toolbox (Figure 4) A flow chart of the Sentinel-1 image time series process in GEE is displayed as follow (Figure 4):

Figure 4. Sentinel-1 image process in the GEE platform.

The first step in applying the orbit file aims at updating the orbit metadata with a restituted orbit file, then Ground Range Detected (GRD) border noise removal attempts were performed to remove the low intensity noise and invalid data on the scene edges. Afterward, a thermal noise removal function aims to remove the additive noise in sub-swaths to reduce the discontinuities between sub-swaths for scenes in different acquisition modes. Thereafter, radiometric calibration is applied to compute the backscatter intensity, and subsequently, a terrain correction, also called an orthorectification, was performed to convert the data from ground range geometry to σ° [69]. Lastly, dB was calculated from σ° with the equation dB = 10*log10σ°. A series of line charts in dB were plotted for each polarization and ratio of each winter crop.

5. Results

5.1. Winter Crop Types Classification Methods Comparison

The classification results of the different approaches and methods of the winter wheat and winter barley and their accuracy analysis are presented in this part. Firstly, the results of PBC and OBC of each step in the hierarchical classification are demonstrated and evaluated through accuracy assessments, the more accurate results were retained for further processing and comparison with classical direct extractions. Then the final results of the hierarchical classification and classical direct extraction are displayed and compared with accuracy assessments as well.

5.1.1. PBC versus OBC

Vegetation Extraction

For vegetation extraction (including cropland), only PBC was performed since it achieved a great accuracy, approximately close to 1. From Figure 5 we see that the distribution of vegetation and cropland is coherent in the study area, apart from some urban

environments, which are marked by intense non-vegetation pixels, in particular these areas are in the south and the northeast of the study area. According to Table 3, both global and interclass accuracy indices are very close to 1, this indicates a high probability of a correct classification of each individual pixel, and a great overall agreement level with the ground truth. Besides a good performance and good training of the PBC method, the distinction between the vegetated area and non-vegetation is very significant, and therefore, it is easy to classify.

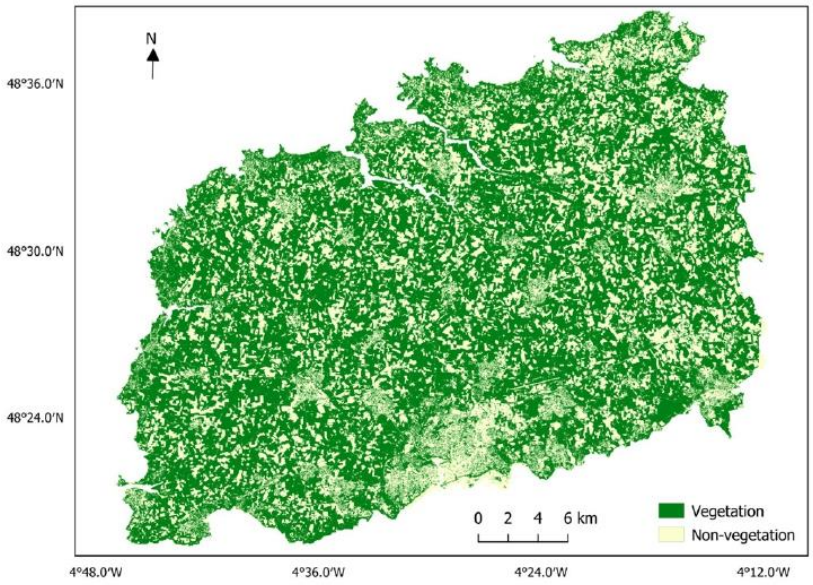

Figure 5. Level 1: PBC vegetation (including cropland) extraction results.

Table 3. Accuracy assessment of PBC vegetation (including cropland) extraction.

	Precision	Recall	F-Score
Vegetation	0.992	0.997	0.995
Non-vegetation	0.994	0.984	0.989
Kappa:	0.984		
Overall accuracy (OA):	0.993		

Croplands Extraction

Subsequently, based on the vegetated area that was extracted from the previous step, we aimed to distinguish and preserve only the croplands from all arboreal vegetation, shrub, and grasslands, including pasture. In this step, OBC and PBC were both performed and evaluated. Figure 6 demonstrates that the results of the two methods are almost identical, although more individual pixels were classified as cropland in PBC considering that PBC was operated on pixel-level.

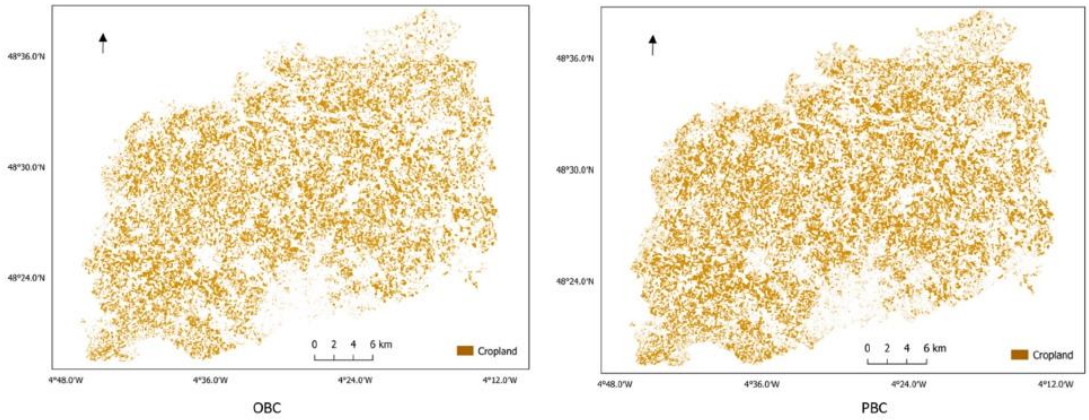

Figure 6. Level 2: PBC and OBC croplands extraction results.

Pursuant to Tables 4 and 5, even though the global accuracy indices of the results of OBC are slightly better than PBC with a difference of 0.024 in kappa and 0.004 in OA, the indices of the two results are still comparable. The tables below show that a large proportion of pixels are correctly predicted, in general, and that the level of agreement with the ground truth data is somewhat lower, but it is still acceptable. Furthermore, for the inter-class accuracy evaluation, cropland generally has the highest precision, recall, and F-score results, which are all around 0.90. The models were well trained to make a good prediction of the cropland class, especially for the OBC model, and most of the individual pixels belonging to the cropland class were correctly detected. This can be explained by the OBC taking into account the geometry, form, and texture elements, which are the key elements that are used to distinguish the croplands from other vegetation. The classification of the vegetation has a slightly lower accuracy of approximately 0.2 in comparison with croplands because of the mix of different kinds of vegetation and the uncertain form of the vegetated area, though OBC remains more precise when it is compared to PBC. Finally, the classes of the other pixels in our study area, which were mainly some isolated pixels that were left from the previous step due to some errors, were better classified with PBC since the non-vegetated area has highly different spectral behavior as compared to that of vegetation. Considering the better accuracy assessments of OBC, its classification result was preserved to perform the next step of classification.

Table 4. Accuracy assessment of OBC croplands extraction.

	Precision	Recall	F-Score
Vegetation	0.786	0.746	0.765
Cropland	0.912	0.905	0.908
Others	0.700	0.875	0.778
Kappa:	0.716		
Overall accuracy (OA):	0.861		

Table 5. Accuracy assessment of PBC croplands extraction.

	Precision	Recall	F-Score
Vegetation	0.769	0.678	0.721
Cropland	0.879	0.932	0.905
Others	0.929	0.813	0.867
Kappa:	0.692		
Overall accuracy (OA):	0.857		

Winter Crops Extraction

In this final step, two winter crop types were extracted, based on the results of the previous step, and the classification result of the cropland extraction was achieved by using OBC. The results of the two classification methods (Figure 7) are very close to identical in this level, wherein the differences between the two maps can hardly be noticed.

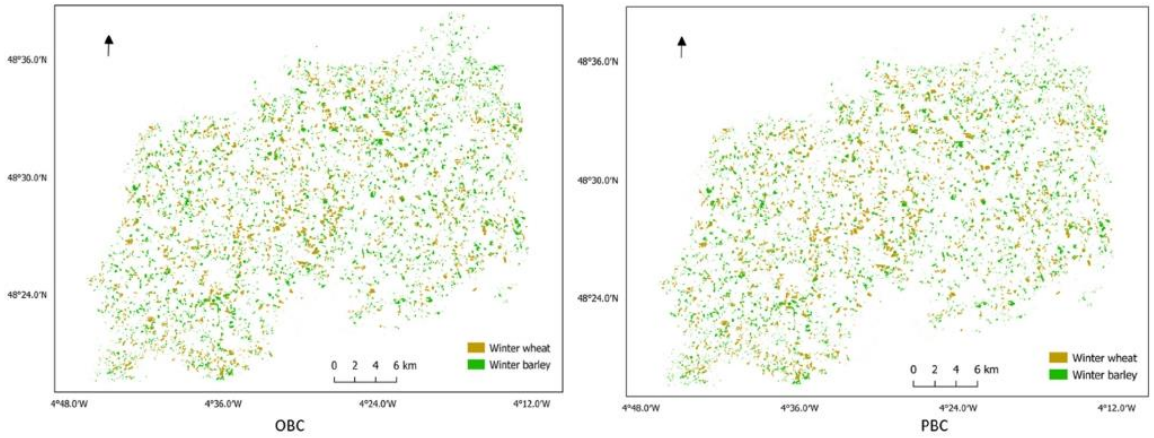

Figure 7. Level 3: PBC and OBC winter crops extraction results.

With the lack of a possibility to visually compare the two methods, they were evaluated and compared by using accuracy assessments (Tables 6 and 7). In regard to the global accuracy indices, all classes were stated as accurate when using the two methods, which signifies a good performance by both methods with a high accuracy and a strong level of agreement for the classification. Beyond that, it is worth noticing that PBC shows a better potential with about 0.03 higher value in the OA and 0.04 in kappa, moreover, PBC basically achieves a better accuracy indicator of three classes in comparison with that of the OBC. The results illustrate that the difference in spectral behavior was exploited to distinguish winter crops from other crops, since all the croplands share similar geometry, form, and texture characteristics. Nonetheless, among the different crop types that were presented in our area of study, winter wheat has the most distinctive spectral signature, thus it was found to be the class with the best accuracy indices in both results, with very strong reliability in terms of prediction and a high rate of precisely identifying winter wheat. In contrast, the classification of winter barley and other crops are somewhat less accurate with approximately 0.1–0.5, and the advantage of PBC is more significant, with higher accuracy indicators of around 0.04, which might be caused by the confusion of winter barley and other crops due to the similarity of their spectral behavior. In addition, the difference between these two classes were better detected by PBC with spectral information.

Table 6. Accuracy assessment of OBC winter crops extraction.

	Precision	Recall	F-Score
Winter wheat	0.998	0.978	0.988
Winter barley	0.833	0.871	0.852
Other crops	0.870	0.848	0.859
Kappa:	0.848		
Overall accuracy (OA):	0.899		

Table 7. Accuracy assessment of PBC winter crops extraction.

	Precision	Recall	F-Score
Winter wheat	0.994	0.976	0.985
Winter barley	0.876	0.913	0.894
Other crops	0.917	0.895	0.906
Kappa:	0.892		
Overall accuracy (OA):	0.928		

5.1.2. Hierarchical Classification versus Classical Direct Extraction

The results of the hierarchical classification, which is the classification approach that was proposed in this study, and the classical direct extraction for the winter crops mapping are presented in Figure 8. Generally, winter wheat and winter barley were well detected and extracted from the Sentinel-2 image; the results of two classification approaches are globally identical, with particular reference to the homogeneous distribution of the winter crops over the area of interest. Nevertheless, the classical direct extraction approach identified more winter croplands, especially winter barley, and the winter croplands that were detected are much more fragmented; many small pixels were classified as croplands. This could be explained by the fact that winter crops are directly extracted from the preprocessed image; in addition, there might be some confusion between winter barley, grasslands, and some different crops considering the resemblance of their spectral behavior.

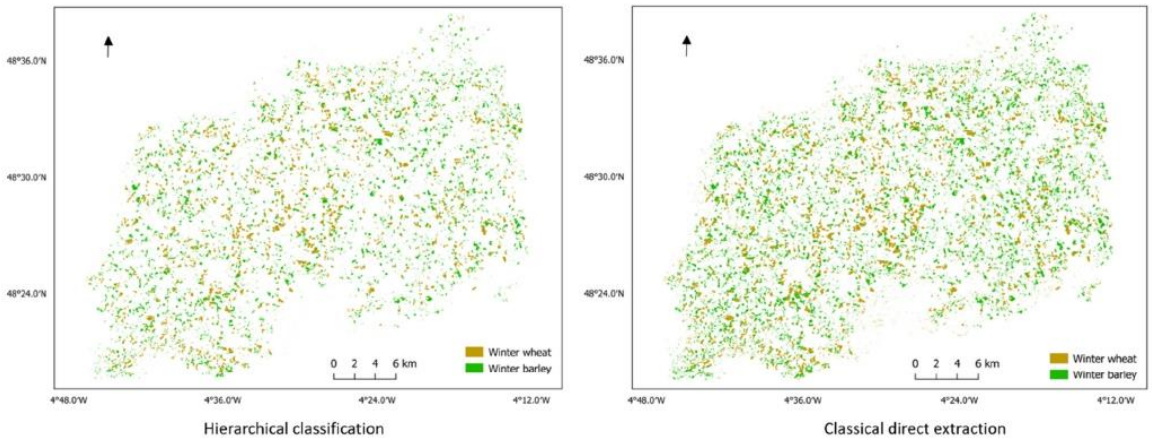

Figure 8. Classification results with hierarchical classification and classical direct extraction.

To make a better comparison, the accuracy assessments of the two approaches are displayed in Tables 8 and 9. According to the tables, both classification results are very satisfactory as mostly all of the accuracy indicators range from 0.8 to 1, specifically, with the hierarchical classification, almost all indices are superior to 0.9. This suggests a good performance and training of the models and also a strong agreement with ground truth of all classification approaches in the study. Still, it is worth noticing that the hierarchical classification shows a better potential for specific crop type mapping as compared to the classical direct extraction (approximately 0.1 higher in kappa and 0.07 in OA). Additionally, nearly every class achieved a higher accuracy in hierarchical classification, which indicates that the model is solid, and it is able to make a good prediction. Among the three classes, winter wheat is the most correctly classified class in both of the classification approaches, the indicators that range from 0.90 to 0.99 and with an F-score that is highly similar. Hierarchical classification reaches a better precision index, that means that the

model is more exact, yet classical direction extraction achieved a finer recall, which means that the model returned more relevant results, and it can correctly and efficiently identify winter wheat. In addition, winter barley and the other classes were evaluated and less accurately classified, especially with the classical direct extraction approach. According to Table 8, the winter barley class obtained a high recall (0.960) and a relatively lower precision (0.683), which suggests a high false-positive rate; many individuals that were predicted as winter barley that the model returned were found misclassified when they were compared to the test data. On the contrary, the other class received a high precision index (0.955) and a comparatively low recall (0.797), and these indicators demonstrate that the pixels were correctly detected and labelled despite there being fewer results returned by the model. The comparably low accuracy of the two classes and the imbalance between the precision and recall indices might be explained by: (1) the similarity of the spectral behavior between winter barley and other crops and even grassland in the case of the classical direct extraction approach. (2) Since two winter crops are extracted directly from the Sentinel-2 image, the other class included not only non-vegetated urban areas, but also vegetation and other croplands which occupy a large area of our study site. Therefore, an imbalance between classes was caused, thus, more training datasets of the other class were acquired in consideration of its weak intraclass correlation.

Table 8. Accuracy assessment of hierarchical classification.

	Precision	Recall	F-Score
Winter wheat	0.991	0.904	0.946
Winter barley	0.886	0.900	0.893
Others	0.929	0.959	0.944
Kappa:	0.888		
Overall accuracy (OA):	0.932		

Table 9. Accuracy assessment of classical direct extraction.

	Precision	Recall	F-Score
Winter wheat	0.959	0.928	0.943
Winter barley	0.683	0.960	0.799
Others	0.955	0.797	0.869
Kappa:	0.789		
Overall accuracy (OA):	0.866		

5.2. Crops Phenology Monitoring

The Sentinel-1 temporal backscattering coefficient profiles of diverse land cover types at VV and VH dual-polarizations from the study area during the growing season of the winter crops (from 1 October 2018 to 1 September 2019) are shown in Figure 9; the temporal profiles of the mean σvv and σvh values of urban, vegetation (including other crops), water, bare soil, winter wheat, and winter barley land cover are displayed. As shown in Figure 9, besides the profiles of the water area, which fluctuate significantly due to the weather conditions, the temporal profiles of the vegetation, urban, and bare soil are much more stable than the profiles of winter crops are, which have a significant fluctuation according to their different growth stages. Especially in the σvh profile, the vegetation, urban, and bare soil profiles are generally close to their mean value, regardless of the season. Nonetheless, the variation of the backscattering coefficients of the two winter crops are clearly evident, for example, a peak is seen in early December, followed by a minimum value in early summer and a maximum value in midsummer. Thus, the results indicate that it is feasible to distinguish winter crops from other types of land cover, particularly vegetation and other crops, and furthermore, we are able to identify and study

the main phenological stages from germination to ripening (harvesting) by using Sentinel-1 temporal profiles.

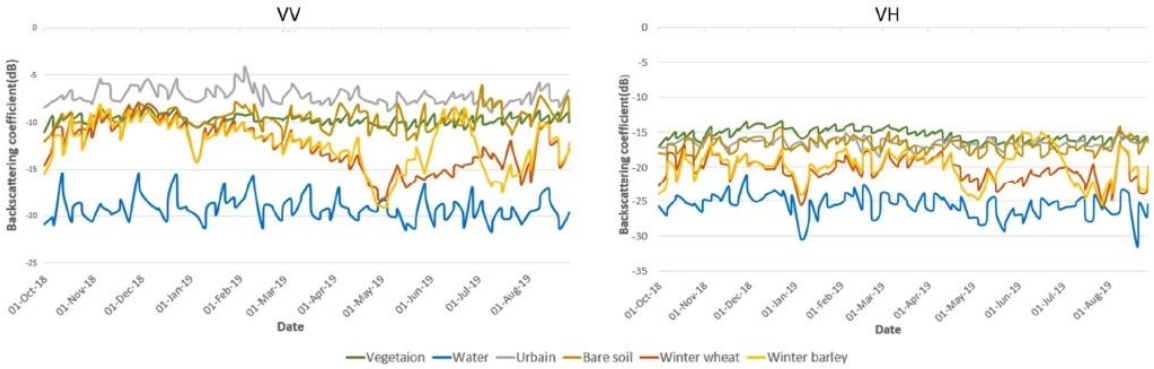

Figure 9. Sentinel-1 temporal backscattering coefficient profiles of different land covers (vegetation, water, urban area, bare soil, winter wheat, and winter barley) in the study area at VV and VH polarizations from 1 October 2018 to 1 September 2019.

Based on prior knowledge and field research with local farmers, winter wheat and winter barley are both cereal crop types that are planted from October to November. Generally, winter barley is sowed earlier than winter wheat in the Finistère department. Germination, which is the first growth stage of the crops, takes place three to four weeks after sowing, hence, this is in early December for winter wheat and in mid-November for winter barley. The crops remain in their vegetative stage during winter, and stem elongation begins in spring, and it lasts until the plants reach their maximum height, usually in early summer. Lastly, ripening, the final growth stage, and harvesting occur in summer (early summer for winter barley and mid-summer for winter wheat).

In Figure 10, both the raw signal and smoothed trend line of the temporal backscattering coefficient profiles of VV, VH, and the VH/VV ratio for the 2018–2019 growing season are displayed. Looking at the charts, it is shown that large variations occur before the germination due to the interaction between the bare soil and vegetation that is caused by stem-ground double scattering [6,70], while previous research suggests that the fluctuation in the backscattering profiles is mostly induced by changes in soil water content and roughness [6]. Pursuant to previous research, germination as the first stage of emergence of the plant can be recognized as the first maximum value of the profiles before they begin decreasing [25], therefore the germination stage is observed at around 1 December for winter wheat, and in early November for winter barley. Moreover, for winter wheat, this phase is best observed with VV and the VH/VV polarizations as they represent the first peak of the curves; however, the peak is better illustrated at VV and VH polarizations for winter barley. Afterwards the overwintering stage occurs, and the crops remain in their vegetative stage during winter (generally around 1 January); a gentle decreasing and a slight flattening can be observed in the VV polarization curves during this stage for both the crops. Furthermore, a fluctuation of the VV and VH curves of the two crops at around 1 January 2019 is driven by a short pause of rainfall, as the signals are highly affected by the soil water content. The stem elongation stage starts in spring, where the vertical development of the stems and leaves of the plants cause soil scattering attenuation, represented as a continuous and steadily decreasing line, until they reach the heading stage, where the plants achieve their maximum height. After a long decreasing phase, σ° reaches the minimum value of the temporal profiles at the heading stage at around 1 May 2019 for both winter crops, and this stage can be better observed in σvv and $\sigma vh/vv$ for winter wheat phenology, and in σvh and σvh for winter barley. However, the sharp decrease in σvv and σvh at the heading stage, specifically in the profiles of the winter barley might be

the result of the relative lack of rainfall that occurred after early April. After heading, the inflorescence emergence, anthesis, grain development, and dough development stages occur. As seen on the graphs the curves start to increase during the flowering and grain development stages. These stages are illustrated by a sharp increase in the winter barley, regardless of the polarization, while by contrast the σvv and σvh/vv of the winter wheat shows a smooth increase. At last, the ripening stage, which is the maturation stage, occurs and the crops are ready to be harvested. This phase is shown as the last peak of the profiles during the growing season, followed by a sharp decrease which is caused by the absence of volume and multiple scattering after the harvesting [25]. As the results show, harvesting, which took place around 1 August 2019, is better demonstrated by σvv and σvh for winter wheat, while the harvesting stage was in late June for winter barley, and it is clearly shown by all polarizations, particularly in VV and VH.

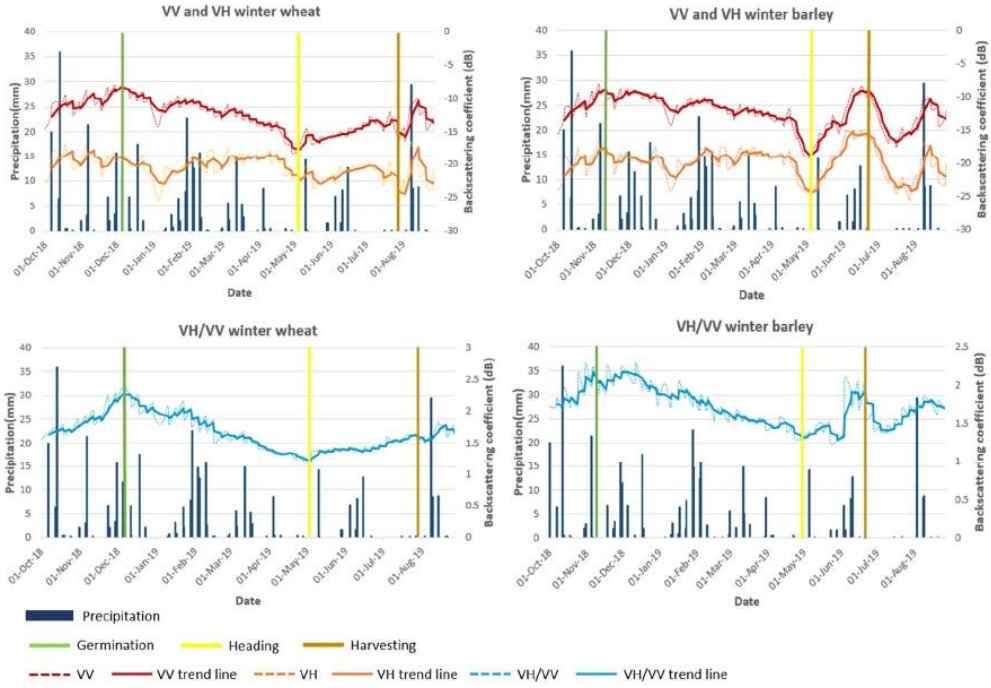

Figure 10. Winter wheat and winter barley Sentinel-1 temporal backscattering coefficient profiles at VV, VH, and VH/VV polarizations of the northern part of the Finistère region for the 2018–2019 growing season, with the daily precipitation data and three main phenological stages, which are presented by a vertical line as well.

The best polarization for each phenological stage (germination, heading, and ripening (harvesting)) are detailed as follows in Tables 10 and 11. The phenology monitoring of the winter wheat highly relies on VV polarization, while the VH/VV ratio is also very helpful in identifying the germination and heading stages. Otherwise, the VH polarization was used to detect the ripening stage and the harvesting event.

Meanwhile, the phenology monitoring of the winter barley depends more on VV and VH polarizations, which are able to easily identify the three phenological statuses. In addition, VH/VV polarization is also effective for detecting the ripening and the harvesting stages.

Table 10. The best polarization observed for each phenological stage of winter wheat in the study.

Stage	Polarization	Date	Determination
Germination	VH/VV, VV	Early December	First peak of the temporal series
Heading	VV, VH/VV	Early May	The minimum value after emergence
Ripening (Harvesting)	VV, VH	Around 1 August	Last maximum of the profiles, following by a sharp decrease

Table 11. The best polarization observed for each phenological stage of winter barley in the study.

Stage	Polarization	Date	Determination
Germination	VV, VH	Early November	First maximum of the temporal series
Heading	VV, VH	Around 1 May	The minimum after emergence
Ripening (Harvesting)	VV, VH, VH/VV	Around 1 July	Last maximum of the profiles, following by a sharp decrease

6. Discussion

6.1. Hierarchical Classification for Winter Crops Mapping

In this study, two different classification approaches using Random Forest machine learning methods were performed on a Sentinel-2 high spatial resolution satellite image that was acquired in April 2019, which is the growing season of the winter crops, in order to detect and map winter wheat and winter barley in a fragmented area that was occupied by different land categories. One of the main objectives of this paper was to successfully extract winter crops data with the hierarchical classification that was proposed in this study, which allows an efficient winter crop type mapping for a study area with a complex landscape, and to easily distinguish winter crops from other land cover types, especially arboreal vegetation, shrubs, grassland, and other crop types. The results of the hierarchical classification were evaluated with different accuracy indicators (global or interclass) and were finally compared with the traditional direct extraction approach.

Both classification approaches achieved a good accuracy level despite the complex occupation and small cropland size in the region, with an overall accuracy of 0.866 and 0.932 and a kappa index of 0.789 and 0.888 for classical direct extraction and hierarchical classification, respectively. Even though the classical extraction method worked well for winter crop mapping, the accuracy assessment indicates that the hierarchical classification is clearly more accurate and better suited to our study by turning a complex multi-class classification problem into a series of smaller classifications. According to the results that are presented in Figure 8 and the accuracy indicators that are displayed in Tables 8 and 9, apart from the global accuracy indicators, the hierarchical classification has proven to be reliable, with outstanding performance in the classification of both winter crops classes, particularly the winter wheat.

The hierarchical classification approach is widely used in many different fields, such as for categorization problems [71], biological predictions [72,73], and music genre classification [74,75], meanwhile the concept of solving a complete classification problem step-by-step using agglomerative algorithms plays also an important role in image classification and its efficacy is well known and it is recognized by previous studies [76–79]. In this study, we proposed a hierarchical classification framework that was constituted by three smaller classifiers for extracting winter crop data, and we have clearly demonstrated the superiority of the hierarchical framework over the classical extraction method.

Additionally, both classifications in this study were performed with supervised RF machine learning methods and highly accurate results were acquired, regardless of the approach or the method. Therefore, RF has proven to be a feasible, well-suited classification algorithm for precisely mapping specific winter crop types from a small-sized field in a complex area.

6.2. Comparison of PBC and OBC

In this work, PBC and OBC were implemented in the two steps of the classification process within the hierarchical classification structure (croplands extraction from all vegetated area, and winter croplands extraction from all croplands). In addition, the two classification models were trained by a similar dataset, and then evaluated using the same test data. The two classification methods are widely known and used, and they are always compared in different fields. OBC provides a method to the satellite image classification, and numerous studies in the remote sensing field it is demonstrated that OBC usually achieves a better classification with different data and in different landscapes over PBC by bringing complementary information other than the spectral signal and turning classification units from pixels to image objects [80–83]. Whiteside et al. in 2011 [23] indicated that OBC has a better potential for extracting land cover information in a spatially heterogeneous land cover area, while Weih and Riggan in 2010 [24] proposed that OBC produced more homogeneous classes, as the classes that were produced by PBC are more fragmented. Furthermore, many studies have also pointed out that OBC regularly outperforms PBC for crop type mapping and they noted that it has a more efficient calculation time [84–86]. However, OBC is limited by segmentation errors, such as over-segmentation and under-segmentation, which bring negative impacts to the classification; consequently, low segmentation accuracy leads to low classification accuracy [79,86,87]. Furthermore, some studies have also revealed that the difference in accuracy values between the two methods decreases or even disappears when the same classification algorithms are applied, or the spatial resolution of the image is increased [88–90].

In this work, the results illustrate that each method has its advantage in the classification process. OBC slightly outperformed PBC in cropland extraction as the complementary texture, geometry, and shape information are helpful for cropland detecting. On the other hand, PBC reaches a higher accuracy in winter crops extraction, since all croplands have a similar shape, but winter crops can be easily distinguished from other crops with direct spectral information. Additionally, the statistical difference between the results of PBC and OBC is not particularly significant. In conclusion, small differences that are induced by several factors between the two methods can be noticed, yet both methods are equally useful for our classification.

6.3. Potential of Sentinel-1 Data in Crops Phenology Monitoring

Optical satellite data are well developed and have traditionally been used for different crop phenology monitoring by using vegetation indices time series [91–93], with NDVI being the most used vegetation index for crop phenology mapping [26,94,95]. However, Sakamoto et al. in 2005 [96] proposed rice phenology detection with time-series EVI data with fewer errors between the estimated phenological dates and the statistical data. Dong et al. in 2020 [10] have exploited the potentialities of a newly developed vegetation index, the Normalized Difference Phenology Index (NDPI), to provide more robust vegetation information and to reduce the adverse impacts of soil and snow cover for winter wheat mapping. In recent years, with the emergence of the new generation of high spatial and temporal resolution SAR data, a particular interest in radar data for crop phenology monitoring was found, especially for its "all weather" capacity, which leads directly to an increased role of SAR data in the field [97–99]. This study proved that Sentinel-1 C-band SAR-polarized backscatter time series data has great potential to monitor winter crop phenology in a coastal area that is marked by frequent precipitation, and some important considerations of the behavior of different polarizations in regard to different phenological stages are worth discussing.

Firstly, despite the σ° of both polarizations and their ratios being relatively similar, the curves of the VH and VV polarizations are sharper when they are compared to those of the ratio, due to the fact that the ratio is less sensitive to varying conditions like moisture

and incidence angle variations. This can be explained by such effects having certain impacts in both polarizations, where the impacts would be reduced in the ratio [1]. As seen in Figure 10, the curves of the ratio VH/VV of winter wheat and winter barley are smoother in comparison with those of the single polarization and they are less impacted by continuous rainfalls or drought due to absence of precipitation.

Secondly, the timing of the phenological stages or growing periods of the crops based on the field knowledge are in agreement with the observations of the results. Based on prior knowledge, the sowing takes place between October and November, and winter barley is usually planted earlier than winter wheat is, and the germination occurs 3–4 weeks after sowing. This period can be confirmed by noting the large variations of the curves in the beginning which are induced by the interaction between the bare soil and the vegetation that is caused by the stem-ground double scattering [6], afterwards the germination is represented by the first peak of the curves, and this is especially well demonstrated in the polarization ratio for winter wheat and in the single polarizations for winter barley. After the overwintering period, the stem elongation, which begins in spring, can be recognized on the curves as a decreasing period that is caused by the attenuation of the signal when the vegetation cover occurs. Thereafter, the heading stage, where the crops attain their maximum height, occurs in early summer. This stage was confirmed with a minimum value on the curves at around 1 May, which can be well observed in the polarization ratio for winter wheat and in single polarization for winter barley. After heading, the volume backscattering was increased due to the increase of the plant biomass [1], and the winter barley is harvested in early summer, and the winter wheat is harvested in midsummer. This is illustrated by the curves in all polarizations decreasing as expected with large variations post-harvesting, depending on the soil conditions.

This leads to the conclusion that it is feasible to map crop phenology with high accuracy by using SAR data, which is highly sensitive to the phenology of agriculture crops. In addition, unlike many methods which exclusively use the single polarization or the ratio [31,100,101], our study shows that the combination of both is able to provide a better observation of agriculture phenology. Further studies can investigate the feasibility and performance of combining SAR and optical data for crop phenology monitoring.

6.4. Limitations and Perspectives

Some limitations were revealed during the process of result analyzing. Despite the fact that the hierarchical classification approach acquired a better accuracy (0.099 in kappa and 0.066 in OA), this classification approach required more complicated processing steps and was more costly when one is comparing it to the direct extraction, for a slight enhancement in the results. Moreover, the confusion between winter barley and grassland was nonnegligible. For increasing classification accuracy, extra data such as SAR or Sentinel-2 time series data can be applied. Additionally, even though the three main phenological statuses were successfully extracted from Sentinel-1 backscatter time series, more field research and expert knowledge is required for identifying some others important phenological stages (e.g., tillering, flowering, soft dough and hard dough).

7. Conclusions

Three issues surrounding winter crops have been studied and discussed in this paper. Firstly, two types of winter crops (winter wheat and winter barley) were mapped by using a Sentinel-2 high-resolution image, and two different classification approaches were performed. Both the hierarchical classification, which turns a complex classification problem into a series of smaller classifications, and the classical direct extraction, which extracts the winter crops directly from the original satellite image, were carried out. The hierarchical classification was composed of three smaller classifications: vegetation extraction from the original image, cropland extraction from the vegetation, and finally the winter crop extraction from other crops. Additionally, PBC and OBC were both performed in

the last two steps and evaluated in order to keep the most accurate classification for further processing and analysis. Subsequently, crop phenology monitoring was performed, based on the results of the previous step by using Sentinel-1 C-band SAR time series data, and the three important phenological stages (germination, heading, and ripening (harvesting)) and the main growing periods were identified as well.

To respond to the objectives of the study and as the contribution of this paper, our results showed that winter crops in a fragmented landscape with heterogeneous land cover were successfully detected with high accuracy by using a Sentinel-2 image and the classification approaches that have been proposed. In particular, the hierarchical classification framework significantly improved the classification accuracy (0.1 and 0.06 increase in the kappa and OA, respectively, against classical direct extraction), moreover the classification of winter barley is also enhanced by reducing the confusion between winter barley and grassland with the hierarchical classification framework (0.094 increase in the F-score). Within the hierarchical classification, each classification method has its advantage; OBC slightly outperformed PBC in cropland extraction, yet PBC achieved higher accuracy in winter crops mapping. Although some small differences can be noticed, however there is no significant statistical divergence between the two classification methods.

The results also lead to the conclusion that Sentinel-1 C-band SAR-polarized backscatter time series has great potential to monitor winter agriculture phenology in a coastal area with frequent rainfall. Three phenological stages and main growing periods could be easily identified from the time series in a single polarization or from the ratio, and furthermore the timing of the stages and the growing periods of the crops that are observed in the results highly conform to the field knowledge.

Although very satisfactory results were acquired in this study, some recommendations can be made for further studies, such as applying Sentinel-2 time series or SAR data for crop mapping in order to increase the classification accuracy, and in particular to reduce the confusion between winter barley and grasslands or other crop types. Exploring the potential of the combination of SAR and optical data for identifying more phenological stages and growth periods from the time series is advocated by us.

Author Contributions: G.X.: Conceptualization, methodology, software, investigation, resources, data curation, writing—original draft preparation; S.N.: Conceptualization, validation, formal analysis, writing—review and editing, visualization, supervision, project administration, funding acquisition. All authors have read and agreed to the published version of the manuscript.

Funding: This research was funded by Fondation de France and the French Space Agency (CNES).

Data Availability Statement: Publicly available datasets were analyzed in this study. The data can be found here: theia.cnes.fr/ (accessed on 31 July 2022) for Sentinel-2 image, earthengine.google.com for Sentinel-1 image, www.geoportail.gouv.fr/ (accessed on 31 July 2022) for RPG 2018 data.

Acknowledgments: We would like to thank the French Space Agency (CNES) and the project CNES/Tosca for funding the publication.

Conflicts of Interest: The authors declare no conflict of interest.

References

1. Schlund, M.; Erasmi, S. Sentinel-1 Time Series Data for Monitoring the Phenology of Winter Wheat. *Remote Sens. Environ.* **2020**, *246*, 111814. https://doi.org/10.1016/j.rse.2020.111814.
2. Yin, H.; Prishchepov, A.V.; Kuemmerle, T.; Bleyhl, B.; Buchner, J.; Radeloff, V.C. Mapping Agricultural Land Abandonment from Spatial and Temporal Segmentation of Landsat Time Series. *Remote Sens. Environ.* **2018**, *210*, 12–24. https://doi.org/10.1016/j.rse.2018.02.050.
3. Song, X.-P.; Potapov, P.V.; Krylov, A.; King, L.; Di Bella, C.M.; Hudson, A.; Khan, A.; Adusei, B.; Stehman, S.V.; Hansen, M.C. National-Scale Soybean Mapping and Area Estimation in the United States Using Medium Resolution Satellite Imagery and Field Survey. *Remote Sens. Environ.* **2017**, *190*, 383–395. https://doi.org/10.1016/j.rse.2017.01.008.
4. Sun, C.; Bian, Y.; Zhou, T.; Pan, J. Using of Multi-Source and Multi-Temporal Remote Sensing Data Improves Crop-Type Mapping in the Subtropical Agriculture Region. *Sensors* **2019**, *19*, 2401. https://doi.org/10.3390/s19102401.

5. Birrell, S.J.; Sudduth, K.A.; Borgelt, S.C. Comparison of Sensors and Techniques for Crop Yield Mapping. *Comput. Electron. Agric.* **1996**, *14*, 215–233. https://doi.org/10.1016/0168-1699(95)00049-6.
6. Song, Y.; Wang, J. Mapping Winter Wheat Planting Area and Monitoring Its Phenology Using Sentinel-1 Backscatter Time Series. *Remote Sens.* **2019**, *11*, 449. https://doi.org/10.3390/rs11040449.
7. Arvor, D.; Jonathan, M.; Meirelles, M.S.P.; Dubreuil, V.; Durieux, L. Classification of MODIS EVI Time Series for Crop Mapping in the State of Mato Grosso, Brazil. *Int. J. Remote Sens.* **2011**, *32*, 7847–7871. https://doi.org/10.1080/01431161.2010.531783.
8. Forkuor, G.; Conrad, C.; Thiel, M.; Ullmann, T.; Zoungrana, E. Integration of Optical and Synthetic Aperture Radar Imagery for Improving Crop Mapping in Northwestern Benin, West Africa. *Remote Sens.* **2014**, *6*, 6472–6499. https://doi.org/10.3390/rs6076472.
9. Xie, G.; Niculescu, S. Remote Sensing Mapping and Monitoring of Land Cover/Land Use (LCLU) Changes in the Crozon Peninsula (Brittany, France) from 2007 to 2018 by Machine Learning Algorithms (Support Vector Machine, Random Forest, and Convolutional Neural Network) and by Post-Classification Comparison (PCC). *Remote Sens.* **2021**, *13*, 3899. https://doi.org/10.3390/rs13193899.
10. Dong, Q.; Chen, X.; Chen, J.; Zhang, C.; Liu, L.; Cao, X.; Zang, Y.; Zhu, X.; Cui, X. Mapping Winter Wheat in North China Using Sentinel 2A/B Data: A Method Based on Phenology-Time Weighted Dynamic Time Warping. *Remote Sens.* **2020**, *12*, 1274. https://doi.org/10.3390/rs12081274.
11. Zhou, T.; Pan, J.; Zhang, P.; Wei, S.; Han, T. Mapping Winter Wheat with Multi-Temporal SAR and Optical Images in an Urban Agricultural Region. *Sensors* **2017**, *17*, 1210. https://doi.org/10.3390/s17061210.
12. Wardlow, B.D.; Egbert, S.L. Large-Area Crop Mapping Using Time-Series MODIS 250 m NDVI Data: An Assessment for the U.S. Central Great Plains. *Remote Sens. Environ.* **2008**, *112*, 1096–1116. https://doi.org/10.1016/j.rse.2007.07.019.
13. Jiang, Y.; Lu, Z.; Li, S.; Lei, Y.; Chu, Q.; Yin, X.; Chen, F. Large-Scale and High-Resolution Crop Mapping in China Using Sentinel-2 Satellite Imagery. *Agriculture* **2020**, *10*, 433. https://doi.org/10.3390/agriculture10100433.
14. Del Frate, F.; Ferrazzoli, P.; Guerriero, L.; Strozzi, T.; Wegmuller, U.; Cookmartin, G.; Quegan, S. Wheat Cycle Monitoring Using Radar Data and a Neural Network Trained by a Model. *IEEE Trans. Geosci. Remote Sens.* **2004**, *42*, 35–44. https://doi.org/10.1109/TGRS.2003.817200.
15. Ibrahim, E.S.; Rufin, P.; Nill, L.; Kamali, B.; Nendel, C.; Hostert, P. Mapping Crop Types and Cropping Systems in Nigeria with Sentinel-2 Imagery. *Remote Sens.* **2021**, *13*, 3523. https://doi.org/10.3390/rs13173523.
16. Ok, A.O.; Akar, O.; Gungor, O. Evaluation of Random Forest Method for Agricultural Crop Classification. *Eur. J. Remote Sens.* **2012**, *45*, 421–432. https://doi.org/10.5721/EuJRS20124535.
17. Tatsumi, K.; Yamashiki, Y.; Canales Torres, M.A.; Taipe, C.L.R. Crop Classification of Upland Fields Using Random Forest of Time-Series Landsat 7 ETM+ Data. *Comput. Electron. Agric.* **2015**, *115*, 171–179. https://doi.org/10.1016/j.compag.2015.05.001.
18. Son, N.-T.; Chen, C.-F.; Chen, C.-R.; Minh, V.-Q. Assessment of Sentinel-1A Data for Rice Crop Classification Using Random Forests and Support Vector Machines. *Geocarto Int.* **2018**, *33*, 587–601. https://doi.org/10.1080/10106049.2017.1289555.
19. Rodriguez-Galiano, V.F.; Ghimire, B.; Rogan, J.; Chica-Olmo, M.; Rigol-Sanchez, J.P. An Assessment of the Effectiveness of a Random Forest Classifier for Land-Cover Classification. *ISPRS J. Photogramm. Remote Sens.* **2012**, *67*, 93–104. https://doi.org/10.1016/j.isprsjprs.2011.11.002.
20. Hao, P.; Zhan, Y.; Wang, L.; Niu, Z.; Shakir, M. Feature Selection of Time Series MODIS Data for Early Crop Classification Using Random Forest: A Case Study in Kansas, USA. *Remote Sens.* **2015**, *7*, 5347–5369. https://doi.org/10.3390/rs70505347.
21. Li, H.; Zhang, C.; Zhang, S.; Atkinson, P.M. Crop Classification from Full-Year Fully-Polarimetric L-Band UAVSAR Time-Series Using the Random Forest Algorithm. *Int. J. Appl. Earth Obs. Geoinf.* **2020**, *87*, 102032. https://doi.org/10.1016/j.jag.2019.102032.
22. Saini, R.; Ghosh, S.K. Crop classification on single date sentinel-2 imagery using random forest and suppor vector machine. *Int. Arch. Photogramm. Remote Sens. Spatial Inf. Sci.* **2018**, *XLII-5*, 683–688. https://doi.org/10.5194/isprs-archives-XLII-5-683-2018.
23. Whiteside, T.G.; Boggs, G.S.; Maier, S.W. Comparing Object-Based and Pixel-Based Classifications for Mapping Savannas. *Int. J. Appl. Earth Obs. Geoinf.* **2011**, *13*, 884–893. https://doi.org/10.1016/j.jag.2011.06.008.
24. Weih, R.; Riggan, N. Object-Based Classification vs. Pixel-Based Classification: Comparitive Importance of Multi-Resolution Imagery. *Int. Arch. Photogramm. Remote Sens. Spat. Inf. Sci. ISPRS Arch.* **2010**, *38*, C7.
25. Nasrallah, A.; Baghdadi, N.; El Hajj, M.; Darwish, T.; Belhouchette, H.; Faour, G.; Darwich, S.; Mhawej, M. Sentinel-1 Data for Winter Wheat Phenology Monitoring and Mapping. *Remote Sens.* **2019**, *11*, 2228. https://doi.org/10.3390/rs11192228.
26. Pan, Z.; Huang, J.; Zhou, Q.; Wang, L.; Cheng, Y.; Zhang, H.; Blackburn, G.A.; Yan, J.; Liu, J. Mapping Crop Phenology Using NDVI Time-Series Derived from HJ-1 A/B Data. *Int. J. Appl. Earth Obs. Geoinf.* **2015**, *34*, 188–197. https://doi.org/10.1016/j.jag.2014.08.011.
27. Gan, L.; Cao, X.; Chen, X.; Dong, Q.; Cui, X.; Chen, J. Comparison of MODIS-Based Vegetation Indices and Methods for Winter Wheat Green-up Date Detection in Huanghuai Region of China. *Agric. For. Meteorol.* **2020**, *288–289*, 108019. https://doi.org/10.1016/j.agrformet.2020.108019.
28. Meroni, M.; d'Andrimont, R.; Vrieling, A.; Fasbender, D.; Lemoine, G.; Rembold, F.; Seguini, L.; Verhegghen, A. Comparing Land Surface Phenology of Major European Crops as Derived from SAR and Multispectral Data of Sentinel-1 and -2. *Remote Sens. Environ.* **2021**, *253*, 112232. https://doi.org/10.1016/j.rse.2020.112232.
29. Wali, E.; Tasumi, M.; Moriyama, M. Combination of Linear Regression Lines to Understand the Response of Sentinel-1 Dual Polarization SAR Data with Crop Phenology—Case Study in Miyazaki, Japan. *Remote Sens.* **2020**, *12*, 189. https://doi.org/10.3390/rs12010189.

30. Canisius, F.; Shang, J.; Liu, J.; Huang, X.; Ma, B.; Jiao, X.; Geng, X.; Kovacs, J.M.; Walters, D. Tracking Crop Phenological Development Using Multi-Temporal Polarimetric Radarsat-2 Data. *Remote Sens. Environ.* **2018**, *210*, 508–518. https://doi.org/10.1016/j.rse.2017.07.031.
31. Mandal, D.; Kumar, V.; Ratha, D.; Dey, S.; Bhattacharya, A.; Lopez-Sanchez, J.M.; McNairn, H.; Rao, Y.S. Dual Polarimetric Radar Vegetation Index for Crop Growth Monitoring Using Sentinel-1 SAR Data. *Remote Sens. Environ.* **2020**, *247*, 111954. https://doi.org/10.1016/j.rse.2020.111954.
32. Géoportail. Available online: https://www.geoportail.gouv.fr/ (accessed on 21 August 2022).
33. Rouault, S. Observer L'occupation des Sols Pour Guider les Politiques D'aménagement (MOS). Available online: https://www.adeupa-brest.fr/nos-publications/observer-loccupation-des-sols-pour-guider-les-politiques-damenagement-mos-0 (accessed on 21 August 2022).
34. Agence d'Urbanisme Brest Bretagne | ADEUPa Brest. Available online: https://adeupa-brest.fr/ (accessed on 21 August 2022).
35. Chambres d'Agriculture de Bretagne. Available online: http://www.chambres-agriculture-bretagne.fr/synagri/accueilRegion (accessed on 22 August 2022).
36. Sentinel-2—Missions—Sentinel Online—Sentinel Online. Available online: https://sentinel.esa.int/web/sentinel/missions/sentinel-2 (accessed on 18 August 2022).
37. Sentinel-1—Missions—Sentinel Online—Sentinel Online. Available online: https://sentinels.copernicus.eu/web/sentinel/missions/sentinel-1 (accessed on 18 August 2022).
38. Registre Parcellaire Graphique (RPG). Available online: https://artificialisation.developpement-durable.gouv.fr/bases-donnees/registre-parcellaire-graphique (accessed on 18 August 2022).
39. Xue, J.; Su, B. Significant Remote Sensing Vegetation Indices: A Review of Developments and Applications. *J. Sens.* **2017**, *2017*, 1–17. https://doi.org/10.1155/2017/1353691.
40. Bannari, A.; Morin, D.; Bonn, F.; Huete, A.R. A Review of Vegetation Indices. *Remote Sens. Rev.* **1995**, *13*, 95–120. https://doi.org/10.1080/02757259509532298.
41. Campbell, J.B.; Wynne, R.H. *Introduction to Remote Sensing, Fifth Edition*; Guilford Press: New York, NY, USA, 2011; ISBN 978-1-60918-177-2.
42. Rouse, J.W.; Haas, R.H.; Scheel, J.A.; Deering, D.W. Monitoring Vegetation Systems in the Great Plains with ERTS. In Proceedings of the 3rd Earth Resource Technology Satellite (ERTS) Symposium, Washington, DC, USA, 10–14 December 1973; Volume 1, pp. 48–62.
43. Gao, B. NDWI—A Normalized Difference Water Index for Remote Sensing of Vegetation Liquid Water from Space. *Remote Sens. Environ.* **1996**, *58*, 257–266. https://doi.org/10.1016/S0034-4257(96)00067-3.
44. Mulianga, B.; Bégué, A.; Clouvel, P.; Todoroff, P. Mapping Cropping Practices of a Sugarcane-Based Cropping System in Kenya Using Remote Sensing. *Remote Sens.* **2015**, *7*, 14428–14444. https://doi.org/10.3390/rs71114428.
45. Valero, S.; Arnaud, L.; Planells, M.; Ceschia, E. Synergy of Sentinel-1 and Sentinel-2 Imagery for Early Seasonal Agricultural Crop Mapping. *Remote Sens.* **2021**, *13*, 4891. https://doi.org/10.3390/rs13234891.
46. Yin, L.; You, N.; Zhang, G.; Huang, J.; Dong, J. Optimizing Feature Selection of Individual Crop Types for Improved Crop Mapping. *Remote Sens.* **2020**, *12*, 162. https://doi.org/10.3390/rs12010162.
47. Gitelson, A.A.; Kaufman, Y.J.; Merzlyak, M.N. Use of a Green Channel in Remote Sensing of Global Vegetation from EOS-MODIS. *Remote Sens. Environ.* **1996**, *58*, 289–298. https://doi.org/10.1016/S0034-4257(96)00072-7.
48. Matsushita, B.; Yang, W.; Chen, J.; Onda, Y.; Qiu, G. Sensitivity of the Enhanced Vegetation Index (EVI) and Normalized Difference Vegetation Index (NDVI) to Topographic Effects: A Case Study in High-Density Cypress Forest. *Sensors* **2007**, *7*, 2636–2651.
49. Huete, A.; Didan, K.; Miura, T.; Rodriguez, E.P.; Gao, X.; Ferreira, L.G. Overview of the Radiometric and Biophysical Performance of the MODIS Vegetation Indices. *Remote Sens. Environ.* **2002**, *83*, 195–213. https://doi.org/10.1016/S0034-4257(02)00096-2.
50. Huete, A.R. A Soil-Adjusted Vegetation Index (SAVI). *Remote Sens. Environ.* **1988**, *25*, 295–309. https://doi.org/10.1016/0034-4257(88)90106-X.
51. Palchoudhuri, Y.; Valcarce-Diñeiro, R.; King, P.; Sanabria-Soto, M. Classification of Multi-Temporal Spectral Indices for Crop Type Mapping: A Case Study in Coalville, UK. *J. Agric. Sci.* **2018**, *156*, 1–13. https://doi.org/10.1017/S0021859617000879.
52. Qi, J.; Chehbouni, A.; Huete, A.R.; Kerr, Y.H.; Sorooshian, S. A Modified Soil Adjusted Vegetation Index. *Remote Sens. Environ.* **1994**, *48*, 119–126. https://doi.org/10.1016/0034-4257(94)90134-1.
53. Samasse, K.; Hanan, N.P.; Anchang, J.Y.; Diallo, Y. A High-Resolution Cropland Map for the West African Sahel Based on High-Density Training Data, Google Earth Engine, and Locally Optimized Machine Learning. *Remote Sens.* **2020**, *12*, 1436. https://doi.org/10.3390/rs12091436.
54. Wyawahare, M.; Kulkarni, P.; Kulkarni, A.; Lad, A.; Majji, J.; Mehta, A. Agricultural Field Analysis Using Satellite Surface Reflectance Data and Machine Learning Technique. In *Proceedings of the Advances in Computing and Data Sciences*; Singh, M., Gupta, P.K., Tyagi, V., Flusser, J., Ören, T., Valentino, G., Eds.; Springer: Singapore, 2020; pp. 439–448.
55. Li, Z.; Chen, Z. Remote Sensing Indicators for Crop Growth Monitoring at Different Scales. In Proceedings of the 2011 IEEE International Geoscience and Remote Sensing Symposium, Vancouver, BC, Canada, 24–29 July 2011; pp. 4062–4065.
56. Witharana, C.; Civco, D.L. Optimizing Multi-Resolution Segmentation Scale Using Empirical Methods: Exploring the Sensitivity of the Supervised Discrepancy Measure Euclidean Distance 2 (ED2). *ISPRS J. Photogramm. Remote Sens.* **2014**, *87*, 108–121. https://doi.org/10.1016/j.isprsjprs.2013.11.006.

57. Darwish, A.; Leukert, K.; Reinhardt, W. Image Segmentation for the Purpose of Object-Based Classification. In Proceedings of the IGARSS 2003. 2003 IEEE International Geoscience and Remote Sensing Symposium. Proceedings (IEEE Cat. No.03CH37477), Toulouse, France, 21–25 July 2003; Volume 3, pp. 2039–2041.
58. Benz, U.C.; Hofmann, P.; Willhauck, G.; Lingenfelder, I.; Heynen, M. Multi-Resolution, Object-Oriented Fuzzy Analysis of Remote Sensing Data for GIS-Ready Information. *ISPRS J. Photogramm. Remote Sens.* **2004**, *58*, 239–258. https://doi.org/10.1016/j.isprsjprs.2003.10.002.
59. ECognition Suite Documentation. Available online: https://docs.ecognition.com/v9.5.0/Page%20collection/eCognition%20Suite%20Documentation.htm?tocpath=Documentation%20eCognition%20Suite%7C_____0 (accessed on 14 April 2021).
60. Richards, J.A.; Jia, X. Supervised Classification Techniques. In *Remote Sensing Digital Image Analysis: An Introduction*; Richards, J.A., Jia, X., Eds.; Springer: Berlin/Heidelberg, Germany, 1999; pp. 181–222, ISBN 978-3-662-03978-6.
61. Gislason, P.O.; Benediktsson, J.A.; Sveinsson, J.R. Random Forests for Land Cover Classification. *Pattern Recognit. Lett.* **2006**, *27*, 294–300. https://doi.org/10.1016/j.patrec.2005.08.011.
62. Foody, G.M. Status of Land Cover Classification Accuracy Assessment. *Remote Sens. Environ.* **2002**, *80*, 185–201. https://doi.org/10.1016/S0034-4257(01)00295-4.
63. Alberg, A.J.; Park, J.W.; Hager, B.W.; Brock, M.V.; Diener-West, M. The Use of "Overall Accuracy" to Evaluate the Validity of Screening or Diagnostic Tests. *J. Gen. Intern. Med.* **2004**, *19*, 460–465. https://doi.org/10.1111/j.1525-1497.2004.30091.x.
64. Foody, G.M. Explaining the Unsuitability of the Kappa Coefficient in the Assessment and Comparison of the Accuracy of Thematic Maps Obtained by Image Classification. *Remote Sens. Environ.* **2020**, *239*, 111630. https://doi.org/10.1016/j.rse.2019.111630.
65. Fitzgerald, R.W.; Lees, B.G. Assessing the Classification Accuracy of Multisource Remote Sensing Data. *Remote Sens. Environ.* **1994**, *47*, 362–368. https://doi.org/10.1016/0034-4257(94)90103-1.
66. Gorelick, N.; Hancher, M.; Dixon, M.; Ilyushchenko, S.; Thau, D.; Moore, R. Google Earth Engine: Planetary-Scale Geospatial Analysis for Everyone. *Remote Sens. Environ.* **2017**, *202*, 18–27. https://doi.org/10.1016/j.rse.2017.06.031.
67. Mutanga, O.; Kumar, L. Google Earth Engine Applications. *Remote Sens.* **2019**, *11*, 591. https://doi.org/10.3390/rs11050591.
68. Sentinel-1 Algorithms|Google Earth Engine. Available online: https://developers.google.com/earth-engine/guides/sentinel1 (accessed on 4 July 2022).
69. Picard, G.; Thuy Le Toan; Mattia, F. Understanding C-Band Radar Backscatter from Wheat Canopy Using a Multiple-Scattering Coherent Model. *IEEE Trans. Geosci. Remote Sens.* **2003**, *41*, 1583–1591. https://doi.org/10.1109/TGRS.2003.813353.
70. Koller, D.; Sahami, M. Hierarchically Classifying Documents Using Very Few Words. In Proceedings of the 14th International Conference on Machine Learning (ICML), San Francisco, CA, USA, 28 June–1 July 2001; Volume 223.
71. Costa, E.P.; Lorena, A.C.; Carvalho, A.C.P.L.F.; Freitas, A.A. A Review of Performance Evaluation Measures for Hierarchical Classifiers. In *Evaluation Methods for Machine Learning II: Papers from the AAAI-2007 Workshop, AAAI Technical Report WS-07-05*; Drummond, C., Elazmeh, W., Japkowicz, N., Macskassy, S.A., Eds.; AAAI Press: Palo Alto, CA, USA, 2007; pp. 1–6, ISBN 978-1-57735-332-4.
72. Costa, E.P.; Lorena, A.C.; Carvalho, A.C.P.L.F.; Freitas, A.A.; Holden, N. Comparing Several Approaches for Hierarchical Classification of Proteins with Decision Trees. In Proceedings of the Advances in Bioinformatics and Computational Biology, Angra dos Reis, Brazil, 29–31 August 2007; Sagot, M.-F., Walter, M.E.M.T., Eds.; Springer: Berlin/Heidelberg, Germany, 2007; pp. 126–137.
73. Silla, C.N.; Freitas, A.A. A Survey of Hierarchical Classification across Different Application Domains. *Data Min. Knowl. Disc.* **2011**, *22*, 31–72. https://doi.org/10.1007/s10618-010-0175-9.
74. Burred, J.J.; Lerch, A. A Hierarchical Approach to Automatic Musical Genre Classification. In Proceedings of the 6th international Conference on Digital Audio Effects, London, UK, 8–11 September 2003; pp. 8–11.
75. Guo, Y.; Liu, Y.; Bakker, E.M.; Guo, Y.; Lew, M.S. CNN-RNN: A Large-Scale Hierarchical Image Classification Framework. *Multimed Tools Appl.* **2018**, *77*, 10251–10271. https://doi.org/10.1007/s11042-017-5443-x.
76. Fan, J.; Gao, Y.; Luo, H. Hierarchical Classification for Automatic Image Annotation. In Proceedings of the 30th Annual International ACM SIGIR Conference on Research and Development in Information Retrieval, Amsterdam, The Netherlands, 23–27 July 2007; Association for Computing Machinery: New York, NY, USA, 2007; pp. 111–118.
77. Uca Avci, Z.D.; Karaman, M.; Ozelkan, E.; Kumral, M.; Budakoglu, M. OBIA Based Hierarchical Image Classification for Industrial Lake Water. *Sci. Total Environ.* **2014**, *487*, 565–573. https://doi.org/10.1016/j.scitotenv.2014.04.048.
78. Gerylo, G.; Hall, R.J.; Franklin, S.E.; Roberts, A.; Milton, E.J. Hierarchical Image Classification and Extraction of Forest Species Composition and Crown Closure from Airborne Multispectral Images. *Can. J. Remote Sens.* **1998**, *24*, 219–232. https://doi.org/10.1080/07038992.1998.10855243.
79. Liu, D.; Xia, F. Assessing Object-Based Classification: Advantages and Limitations. *Remote Sens. Lett.* **2010**, *1*, 187–194. https://doi.org/10.1080/01431161003743173.
80. Estoque, R.C.; Murayama, Y.; Akiyama, C.M. Pixel-Based and Object-Based Classifications Using High- and Medium-Spatial-Resolution Imageries in the Urban and Suburban Landscapes. *Geocarto Int.* **2015**, *30*, 1113–1129. https://doi.org/10.1080/10106049.2015.1027291.
81. Fu, B.; Wang, Y.; Campbell, A.; Li, Y.; Zhang, B.; Yin, S.; Xing, Z.; Jin, X. Comparison of Object-Based and Pixel-Based Random Forest Algorithm for Wetland Vegetation Mapping Using High Spatial Resolution GF-1 and SAR Data. *Ecol. Indic.* **2017**, *73*, 105–117. https://doi.org/10.1016/j.ecolind.2016.09.029.
82. Blaschke, T. Object Based Image Analysis for Remote Sensing. *ISPRS J. Photogramm. Remote Sens.* **2010**, *65*, 2–16. https://doi.org/10.1016/j.isprsjprs.2009.06.004.

83. Castillejo-González, I.L.; López-Granados, F.; García-Ferrer, A.; Peña-Barragán, J.M.; Jurado-Expósito, M.; de la Orden, M.S.; González-Audicana, M. Object- and Pixel-Based Analysis for Mapping Crops and Their Agro-Environmental Associated Measures Using QuickBird Imagery. *Comput. Electron. Agric.* **2009**, *68*, 207–215. https://doi.org/10.1016/j.compag.2009.06.004.
84. Belgiu, M.; Csillik, O. Sentinel-2 Cropland Mapping Using Pixel-Based and Object-Based Time-Weighted Dynamic Time Warping Analysis. *Remote Sens. Environ.* **2018**, *204*, 509–523. https://doi.org/10.1016/j.rse.2017.10.005.
85. Devadas, R.; Denham, R.J.; Pringle, M. Support vector machine classification of object-based data for crop mapping, using multi-temporal landsat imagery. *Int. Arch. Photogramm. Remote Sens. Spat. Inf. Sci.* **2012**, *XXXIX-B7*, 185–190. https://doi.org/10.5194/isprsarchives-XXXIX-B7-185-2012.
86. Möller, M.; Lymburner, L.; Volk, M. The Comparison Index: A Tool for Assessing the Accuracy of Image Segmentation. *Int. J. Appl. Earth Obs. Geoinf.* **2007**, *9*, 311–321. https://doi.org/10.1016/j.jag.2006.10.002.
87. Kampouraki, M.; Wood, G.A.; Brewer, T.R. Opportunities and Limitations of Object Based Image Analysis for Detecting Urban Impervious and Vegetated Surfaces Using True-Colour Aerial Photography. In *Object-Based Image Analysis: Spatial Concepts for Knowledge-Driven Remote Sensing Applications*; Lecture Notes in Geoinformation and Cartography; Blaschke, T., Lang, S., Hay, G.J., Eds.; Springer: Berlin/Heidelberg, Germany, 2008; pp. 555–569, ISBN 978-3-540-77058-9.
88. Duro, D.C.; Franklin, S.E.; Dubé, M.G. A Comparison of Pixel-Based and Object-Based Image Analysis with Selected Machine Learning Algorithms for the Classification of Agricultural Landscapes Using SPOT-5 HRG Imagery. *Remote Sens. Environ.* **2012**, *118*, 259–272. https://doi.org/10.1016/j.rse.2011.11.020.
89. Gao, Y.; Mas, J. A Comparison of the Performance of Pixel Based and Object Based Classifications over Images with Various Spatial Resolutions. *Online J. Earth Sci.* **2008**, *2*, 27–35.
90. Berhane, T.M.; Lane, C.R.; Wu, Q.; Anenkhonov, O.A.; Chepinoga, V.V.; Autrey, B.C.; Liu, H. Comparing Pixel- and Object-Based Approaches in Effectively Classifying Wetland-Dominated Landscapes. *Remote Sens.* **2018**, *10*, 46. https://doi.org/10.3390/rs10010046.
91. Bolton, D.K.; Friedl, M.A. Forecasting Crop Yield Using Remotely Sensed Vegetation Indices and Crop Phenology Metrics. *Agric. For. Meteorol.* **2013**, *173*, 74–84. https://doi.org/10.1016/j.agrformet.2013.01.007.
92. Gao, F.; Zhang, X. Mapping Crop Phenology in Near Real-Time Using Satellite Remote Sensing: Challenges and Opportunities. *J. Remote Sens.* **2021**, *2021*, 1–14. https://doi.org/10.34133/2021/8379391.
93. Boschetti, M.; Stroppiana, D.; Brivio, P.A.; Bocchi, S. Multi-Year Monitoring of Rice Crop Phenology through Time Series Analysis of MODIS Images. *Int. J. Remote Sens.* **2009**, *30*, 4643–4662. https://doi.org/10.1080/01431160802632249.
94. De Castro, A.I.; Six, J.; Plant, R.E.; Peña, J.M. Mapping Crop Calendar Events and Phenology-Related Metrics at the Parcel Level by Object-Based Image Analysis (OBIA) of MODIS-NDVI Time-Series: A Case Study in Central California. *Remote Sens.* **2018**, *10*, 1745. https://doi.org/10.3390/rs10111745.
95. De Bernardis, C.; Vicente-Guijalba, F.; Martinez-Marin, T.; Lopez-Sanchez, J.M. Contribution to Real-Time Estimation of Crop Phenological States in a Dynamical Framework Based on NDVI Time Series: Data Fusion with SAR and Temperature. *IEEE J. Sel. Top. Appl. Earth Obs. Remote Sens.* **2016**, *9*, 3512–3523. https://doi.org/10.1109/JSTARS.2016.2539498.
96. Sakamoto, T.; Yokozawa, M.; Toritani, H.; Shibayama, M.; Ishitsuka, N.; Ohno, H. A Crop Phenology Detection Method Using Time-Series MODIS Data. *Remote Sens. Environ.* **2005**, *96*, 366–374. https://doi.org/10.1016/j.rse.2005.03.008.
97. Bargiel, D. A New Method for Crop Classification Combining Time Series of Radar Images and Crop Phenology Information. *Remote Sens. Environ.* **2017**, *198*, 369–383. https://doi.org/10.1016/j.rse.2017.06.022.
98. Steele-Dunne, S.C.; McNairn, H.; Monsivais-Huertero, A.; Judge, J.; Liu, P.-W.; Papathanassiou, K. Radar Remote Sensing of Agricultural Canopies: A Review. *IEEE J. Sel. Top. Appl. Earth Obs. Remote Sens.* **2017**, *10*, 2249–2273. https://doi.org/10.1109/JSTARS.2016.2639043.
99. McNairn, H.; Shang, J. A Review of Multitemporal Synthetic Aperture Radar (SAR) for Crop Monitoring. In *Multitemporal Remote Sensing: Methods and Applications*; Ban, Y., Ed.; Remote Sensing and Digital Image Processing; Springer International Publishing: Cham, Switzerland, 2016; pp. 317–340, ISBN 978-3-319-47037-5.
100. Son, N.-T.; Chen, C.-F.; Chen, C.-R.; Toscano, P.; Cheng, Y.-S.; Guo, H.-Y.; Syu, C.-H. A Phenological Object-Based Approach for Rice Crop Classification Using Time-Series Sentinel-1 Synthetic Aperture Radar (SAR) Data in Taiwan. *Int. J. Remote Sens.* **2021**, *42*, 2722–2739. https://doi.org/10.1080/01431161.2020.1862440.
101. Van de Voorde, T.; Vlaeminck, J.; Canters, F. Comparing Different Approaches for Mapping Urban Vegetation Cover from Landsat ETM+ Data: A Case Study on Brussels. *Sensors* **2008**, *8*, 3880–3902. https://doi.org/10.3390/s8063880.

References

Abbas, S., Peng, Q., Wong, M. S., Li, Z., Wang, J., Ng, K. T. K., Kwok, C. Y. T., & Hui, K. K. W. (2021). Characterizing and classifying urban tree species using bi-monthly terrestrial hyperspectral images in Hong Kong. *ISPRS Journal of Photogrammetry and Remote Sensing*, *177*, 204–216. https://doi.org/10.1016/j.isprsjprs.2021.05.003

Abd El-Kawy, O. R., Rød, J. K., Ismail, H. A., & Suliman, A. S. (2011). Land use and land cover change detection in the western Nile delta of Egypt using remote sensing data. *Applied Geography*, *31*(2), 483–494. https://doi.org/10.1016/j.apgeog.2010.10.012

Abdi, A. M. (2019). Land cover and land use classification performance of machine learning algorithms in a boreal landscape using Sentinel-2 data. *GIScience & Remote Sensing*, *57*(1), 1–20. https://doi.org/10.1080/15481603.2019.1650447

Abdullah, A. Y. M., Masrur, A., Adnan, M. S. G., Baky, M. A. A., Hassan, Q. K., & Dewan, A. (2019). Spatio-Temporal Patterns of Land Use/Land Cover Change in the Heterogeneous Coastal Region of Bangladesh between 1990 and 2017. *Remote Sensing*, *11*(7), 7. https://doi.org/10.3390/rs11070790

Achanta, R., Shaji, A., Smith, K., Lucchi, A., Fua, P., & Süsstrunk, S. (2010). SLIC superpixels. *Technical Report, EPFL*.

Achanta, R., Shaji, A., Smith, K., Lucchi, A., Fua, P., & Süsstrunk, S. (2012). SLIC Superpixels Compared to State-of-the-Art Superpixel Methods. *IEEE Transactions on Pattern Analysis and Machine Intelligence*, *34*(11), 2274–2282. https://doi.org/10.1109/TPAMI.2012.120

Adagbasa, E. G., Adelabu, S. A., & Okello, T. W. (2022). Application of deep learning with stratified K-fold for vegetation species discrimation in a protected mountainous region using Sentinel-2 image. *Geocarto International*, *37*(1), 142–162. https://doi.org/10.1080/10106049.2019.1704070

Adeline, K. R. M., Chen, M., Briottet, X., Pang, S. K., & Paparoditis, N. (2013). Shadow detection in very high spatial resolution aerial images: A comparative study. *ISPRS Journal of Photogrammetry and Remote Sensing*, *80*, 21–38. https://doi.org/10.1016/j.isprsjprs.2013.02.003

Adeupa. (2009). *La lettre des observatoires de l'ADEUPa-Octobre 2009*. Adeupa de Brest. https://www.adeupa-brest.fr/system/files/publications/obs-foncier-29-n1-conso-fonciere.pdf

ADEUPa Brest. (n.d.). Retrieved December 8, 2022, from https://adeupa-brest.fr/

Aggarwal, N., Srivastava, M., & Dutta, M. (2016). Comparative Analysis of Pixel-Based and Object-Based Classification of High Resolution Remote Sensing Images – A Review. *International Journal of Engineering Trends and Technology*, *38*, 5–11. https://doi.org/10.14445/22315381/IJETT-V38P202

Aguilar, M. A., Aguilar, F. J., García Lorca, A., Guirado, E., Betlej, M., Cichon, P., Nemmaoui, A., Vallario, A., & Parente, C. (2016). Assessment of Multiresolution Segmentation for Extracting Greenhouses from WORLDVIEW-2 Imagery. *ISPRS - International Archives of the Photogrammetry, Remote Sensing and Spatial Information Sciences*, *41B7*, 145–152. https://doi.org/10.5194/isprs-archives-XLI-B7-145-2016

Ahmed, Z., Asghar, M. M., Malik, M. N., & Nawaz, K. (2020). Moving towards a sustainable environment: The dynamic linkage between natural resources, human capital, urbanization, economic growth, and ecological footprint in China. *Resources Policy*, *67*, 101677. https://doi.org/10.1016/j.resourpol.2020.101677

Akinsola, J. E. T. (2017). Supervised Machine Learning Algorithms: Classification and Comparison. *International Journal of Computer Trends and Technology (IJCTT)*, *48*, 128–138. https://doi.org/10.14445/22312803/IJCTT-V48P126

Aksoy, S., & Akcay, H. G. (2005). Multi-resolution segmentation and shape analysis for remote sensing image classification. *Proceedings of 2nd International Conference on Recent Advances in Space Technologies, 2005. RAST 2005.*, 599–604. https://doi.org/10.1109/RAST.2005.1512638

Al-Najjar, H. A. H., Kalantar, B., Pradhan, B., Saeidi, V., Halin, A. A., Ueda, N., & Mansor, S. (2019). Land Cover Classification from fused DSM and UAV Images Using Convolutional NNs. *Remote Sensing*, *11*(12), 12. https://doi.org/10.3390/rs11121461

Alonzo, M., Bookhagen, B., & Roberts, D. A. (2014). Urban tree species mapping using hyperspectral and LiDAR data fusion. *Remote Sensing of Environment*, *148*, 70–83. https://doi.org/10.1016/j.rse.2014.03.018

Alphan, H. (2003). Land-use change and urbanization of Adana, Turkey. *Land Degradation & Development*, *14*(6), 575–586. https://doi.org/10.1002/ldr.581

Alves, D. S., & Skole, D. L. (1996). Characterizing land cover dynamics using Multitemporal imagery. *International Journal of Remote Sensing*, *17*(4), 835–839. https://doi.org/10.1080/01431169608949049

Aly, Z., Bonn, F. J., & Magagi, R. (2007). Analysis of the Backscattering Coefficient of Salt-Affected Soils Using Modeling and RADARSAT-1 SAR Data. *IEEE Transactions on Geoscience and Remote Sensing*, *45*(2), 332–341. https://doi.org/10.1109/TGRS.2006.887163

Amani, M., Ghorbanian, A., Ahmadi, S. A., Kakooei, M., Moghimi, A., Mirmazloumi, S. M., Moghaddam, S. H. A., Mahdavi, S., Ghahremanloo, M., Parsian, S., Wu, Q., & Brisco, B. (2020). Google Earth Engine Cloud Computing Platform for Remote Sensing Big Data Applications: A Comprehensive Review. *IEEE Journal of Selected Topics in Applied Earth Observations and Remote Sensing*, *13*, 5326–5350. https://doi.org/10.1109/JSTARS.2020.3021052

Aplin, P. (2004). Remote sensing: Land cover. *Progress in Physical Geography: Earth and Environment*, *28*(2), 283–293. https://doi.org/10.1191/0309133304pp413pr

Araya, Y. H., & Cabral, P. (2010). Analysis and Modeling of Urban Land Cover Change in Setúbal and Sesimbra, Portugal. *Remote Sensing*, *2*(6), 6. https://doi.org/10.3390/rs2061549

Ardila, J. P., Tolpekin, V. A., Bijker, W., & Stein, A. (2011). Markov-random-field-based super-resolution mapping for identification of urban trees in VHR images. *ISPRS Journal of Photogrammetry and Remote Sensing*, *66*(6), 762–775. https://doi.org/10.1016/j.isprsjprs.2011.08.002

Arvor, D., Jonathan, M., Meirelles, M. S. P., Dubreuil, V., & Durieux, L. (2011). Classification of MODIS EVI time series for crop mapping in the state of Mato Grosso, Brazil. *International Journal of Remote Sensing*, *32*(22), 7847–7871. https://doi.org/10.1080/01431161.2010.531783

Ashourloo, D., Mobasheri, M. R., & Huete, A. (2014). Evaluating the Effect of Different Wheat Rust Disease Symptoms on Vegetation Indices Using Hyperspectral Measurements. *Remote Sensing*, *6*(6), 6. https://doi.org/10.3390/rs6065107

Asokan, A., & Anitha, J. (2019). Change detection techniques for remote sensing applications: A survey. *Earth Science Informatics*, *12*(2), 143–160. https://doi.org/10.1007/s12145-019-00380-5

Atkinson, P. M., Cutler, M. E. J., & Lewis, H. (1997). Mapping sub-pixel proportional land cover with AVHRR imagery. *International Journal of Remote Sensing*, *18*(4), 917–935. https://doi.org/10.1080/014311697218836

Atkinson, P. M., & Tatnall, A. R. L. (1997). Introduction NNs in remote sensing. *International Journal of Remote Sensing*, *18*(4), 699–709. https://doi.org/10.1080/014311697218700

Attri, P., Chaudhry, S., & Sharma, S. (2015). Remote Sensing & GIS based Approaches for LULC Change Detection – A Review. *International Journal of Current Engineering and Technology*, *5*.

Aydöner, C., & Maktav, D. (2009). The role of the integration of remote sensing and GIS in land use/land cover analysis after an earthquake. *International Journal of Remote Sensing*, *30*(7), 1697–1717. https://doi.org/10.1080/01431160802642289

Ayhan, B., Kwan, C., Budavari, B., Kwan, L., Lu, Y., Perez, D., Li, J., Skarlatos, D., & Vlachos, M. (2020). Vegetation Detection Using Deep Learning and Conventional Methods. *Remote Sensing*, *12*(15), 15. https://doi.org/10.3390/rs12152502

Baatz, M., & Schäpe, A. (2000). Multiresolution Segmentation: An optimization approach for high quality multi-scale image segmentation. *Angewandte Geographische Informations-Verarbeitung XII*, 12–23.

Baetens, L., Desjardins, C., & Hagolle, O. (2019). Validation of Copernicus Sentinel-2 Cloud Masks Obtained from MAJA, Sen2Cor, and FMask Processors Using Reference Cloud Masks Generated with a Supervised Active Learning Procedure. *Remote Sensing*, *11*(4), 4. https://doi.org/10.3390/rs11040433

Baker, F., Smith, C. L., & Cavan, G. (2018). A Combined Approach to Classifying Land Surface Cover of Urban Domestic Gardens Using Citizen Science Data and High Resolution Image Analysis. *Remote Sensing*, *10*(4), 4. https://doi.org/10.3390/rs10040537

Bannari, A., Asalhi, H., & Teillet, P. M. (2002). Transformed difference vegetation index (TDVI) for vegetation cover mapping. *IEEE International Geoscience and Remote Sensing Symposium*, *5*, 3053–3055 vol.5. https://doi.org/10.1109/IGARSS.2002.1026867

Bannari, A., Morin, D., Bonn, F., & Huete, A. R. (1995). A review of vegetation indices. *Remote Sensing Reviews*, *13*(1–2), 95–120. https://doi.org/10.1080/02757259509532298

Barati, S., Rayegani, B., Saati, M., Sharifi, A., & Nasri, M. (2011). Comparison the accuracies of different spectral indices for estimation of vegetation cover fraction in sparse vegetated areas. *The Egyptian Journal of Remote Sensing and Space Science*, *14*(1), 49–56. https://doi.org/10.1016/j.ejrs.2011.06.001

Barnsley, M. J. (1999). Digital remotely-sensed data and their characteristics. In *Geographical Information Systems: Principles, techniques, applications, and management* (2nd ed., pp. 451–466). John Wiley and Sons.

Bascom, W. (1982). The effects of waste disposal on the coastal waters of Southern California. *Environmental Science & Technology*, *16*(4), 226A-236A. https://doi.org/10.1021/es00098a001

Beatley, T., Brower, D., & Schwab, A. K. (2002). *An Introduction to Coastal Zone Management: Second Edition*. Island Press.

Belgiu, M., & Dr Guţ, L. (2014). Comparing supervised and unsupervised multiresolution segmentation approaches for extracting buildings from very high resolution imagery. *ISPRS Journal of Photogrammetry and Remote Sensing: Official Publication of the International Society for Photogrammetry and Remote Sensing (ISPRS)*, *96*, 67–75. https://doi.org/10.1016/j.isprsjprs.2014.07.002

Belgiu, M., & Drăguţ, L. (2016). Random forest in remote sensing: A review of applications and future directions. *ISPRS Journal of Photogrammetry and Remote Sensing*, *114*, 24–31. https://doi.org/10.1016/j.isprsjprs.2016.01.011

Bengoufa, S., Niculescu, S., Mihoubi, M. K., Belkessa, R., Rami, A., Rabehi, W., & Abbad, K. (2021). Machine learning and shoreline monitoring using optical satellite images: Case study of the Mostaganem shoreline, Algeria. *Journal of Applied Remote Sensing*, *15*(2), 026509. https://doi.org/10.1117/1.JRS.15.026509

Benos, L., Tagarakis, A. C., Dolias, G., Berruto, R., Kateris, D., & Bochtis, D. (2021). Machine Learning in Agriculture: A Comprehensive Updated Review. *Sensors*, *21*(11), 11. https://doi.org/10.3390/s21113758

Benz, U. C., Hofmann, P., Willhauck, G., Lingenfelder, I., & Heynen, M. (2004). Multi-resolution, object-oriented fuzzy analysis of remote sensing data for GIS-ready information. *ISPRS Journal of Photogrammetry and Remote Sensing*, *58*(3–4), 239–258. https://doi.org/10.1016/j.isprsjprs.2003.10.002

Bhosle, K., & Musande, V. (2019). Evaluation of Deep Learning CNN Model for Land Use Land Cover Classification and Crop Identification Using Hyperspectral Remote Sensing Images. *Journal of the Indian Society of Remote Sensing*, *47*(11), 1949–1958. https://doi.org/10.1007/s12524-019-01041-2

Birrell, S. J., Sudduth, K. A., & Borgelt, S. C. (1996). Comparison of sensors and techniques for crop yield mapping. *Computers and Electronics in Agriculture*, *14*(2), 215–233. https://doi.org/10.1016/0168-1699(95)00049-6

Bishop, C. M. (1995). *NNs for Pattern Recognition*. Clarendon Press.

Bolton, D. K., & Friedl, M. A. (2013). Forecasting crop yield using remotely sensed vegetation indices and crop phenology metrics. *Agricultural and Forest Meteorology*, *173*, 74–84. https://doi.org/10.1016/j.agrformet.2013.01.007

Borrelli, P., Robinson, D. A., Fleischer, L. R., Lugato, E., Ballabio, C., Alewell, C., Meusburger, K., Modugno, S., Schütt, B., Ferro, V., Bagarello, V., Oost, K. V., Montanarella, L., & Panagos, P. (2017). An assessment of the global impact of 21st century land use change on soil erosion. *Nature Communications*, *8*(1), 1. https://doi.org/10.1038/s41467-017-02142-7

Boussetta, A., Niculescu, S., Bengoufa, S., & Zagrarni, M. F. (2022). Spatio-temporal analysis of shoreline changes and erosion risk assessment along Jerba island (Tunisia) based on remote-sensing data and geospatial tools. *Regional Studies in Marine Science*, *55*, 102564. https://doi.org/10.1016/j.rsma.2022.102564

Breed, C. S., & Grow, T. (1979). Morphology and distribution of dunes in sand seas observed by remote sensing. In E. D. McKee (Ed.), *A Study of Global Sand Seas* (p. 429). U.S. Government Printing Office.

Breiman, L. (2001). Random Forests. *Machine Learning*, *45*(1), 5–32. https://doi.org/10.1023/A:1010933404324

Briassoulis, H. (2020). Analysis of Land Use Change: Theoretical and Modeling Approaches. *Web Book of Regional Science*. https://researchrepository.wvu.edu/rri-web-book/3

Brink, A. B., Bodart, C., Brodsky, L., Defourney, P., Ernst, C., Donney, F., Lupi, A., & Tuckova, K. (2014). Anthropogenic pressure in East Africa—Monitoring 20 years of land cover changes by means of medium resolution satellite data. *International Journal of Applied Earth Observation and Geoinformation*, *28*, 60–69. https://doi.org/10.1016/j.jag.2013.11.006

Bruzzone, L., Prieto, D. F., & Serpico, S. B. (1999). A neural-statistical approach to multitemporal and multisource remote-sensing image classification. *IEEE Transactions on Geoscience and Remote Sensing*, *37*(3), 1350–1359. https://doi.org/10.1109/36.763299

Bui, D. T., Tsangaratos, P., Nguyen, V.-T., Liem, N. V., & Trinh, P. T. (2020). Comparing the prediction performance of a Deep Learning NN model with conventional machine learning models in landslide susceptibility assessment. *CATENA*, *188*, 104426. https://doi.org/10.1016/j.catena.2019.104426

Bui, Q.-T., Chou, T.-Y., Hoang, T.-V., Fang, Y.-M., Mu, C.-Y., Huang, P.-H., Pham, V.-D., Nguyen, Q.-H., Anh, D. T. N., Pham, V.-M., & Meadows, M. E. (2021). Gradient Boosting Machine and Object-Based CNN for Land Cover Classification. *Remote Sensing*, *13*(14), 14. https://doi.org/10.3390/rs13142709

Bullock, D. G. (1992). Crop rotation. *Critical Reviews in Plant Sciences*, *11*(4), 309–326. https://doi.org/10.1080/07352689209382349

Bushra, N., Rohli, R. V., Lam, N. S. N., Zou, L., Mostafiz, R. B., & Mihunov, V. (2019). The relationship between the Normalized Difference Vegetation Index and drought indices in the South Central United States. *Natural Hazards*, *96*(2), 791–808. https://doi.org/10.1007/s11069-019-03569-5

Byrne, G. F., Crapper, P. F., & Mayo, K. K. (1980). Monitoring land-cover change by principal component analysis of multitemporal landsat data. *Remote Sensing of Environment*, *10*(3), 175–184. https://doi.org/10.1016/0034-4257(80)90021-8

Cai, G., Ren, H., Yang, L., Zhang, N., Du, M., & Wu, C. (2019). Detailed Urban Land Use Land Cover Classification at the Metropolitan Scale Using a Three-Layer Classification Scheme. *Sensors*, *19*(14), 14. https://doi.org/10.3390/s19143120

Câmara, G., Pedrosa, B. M., Vinhas, L., Monteiro, A. M. V., Paiva, J. A., Carvalho, M. T. D., & Gattass, M. (2000). *TerraLib: Technology in Support of GIS Innovation*. *2*, 1–8.

Camargo, F. F., Sano, E. E., Almeida, C. M., Mura, J. C., & Almeida, T. (2019). A Comparative Assessment of Machine-Learning Techniques for Land Use and Land Cover Classification of the Brazilian Tropical Savanna Using ALOS-2/PALSAR-2 Polarimetric Images. *Remote Sensing*, *11*(13), 13. https://doi.org/10.3390/rs11131600

Campbell, J. B. (1987). *Introduction to Remote Sensing*. The Guilford Press.

Canisius, F., Shang, J., Liu, J., Huang, X., Ma, B., Jiao, X., Geng, X., Kovacs, J. M., & Walters, D. (2018). Tracking crop phenological development using Multitemporal polarimetric RaDARsat-2 data. *Remote Sensing of Environment*, *210*, 508–518. https://doi.org/10.1016/j.rse.2017.07.031

Cánovas-García, F., & Alonso-Sarría, F. (2015). A local approach to optimize the scale parameter in multiresolution segmentation for multispectral imagery. *Geocarto International*, *30*(8), 937–961. https://doi.org/10.1080/10106049.2015.1004131

Cao, R., Chen, J., Shen, M., & Tang, Y. (2015). An improved logistic method for detecting spring vegetation phenology in grasslands from MODIS EVI time-series data. *Agricultural and Forest Meteorology*, *200*, 9–20. https://doi.org/10.1016/j.agrformet.2014.09.009

Carranza-García, M., García-Gutiérrez, J., & Riquelme, J. C. (2019). A Framework for Evaluating Land Use and Land Cover Classification Using Convolutional NNs. *Remote Sensing*, *11*(3), 3. https://doi.org/10.3390/rs11030274

Castellana, L., D'Addabbo, A., & Pasquariello, G. (2007). A composed supervised/unsupervised approach to improve change detection from remote sensing. *Pattern Recognition Letters*, *28*(4), 405–413. https://doi.org/10.1016/j.patrec.2006.08.010

Castelluccio, M., Poggi, G., Sansone, C., & Verdoliva, L. (2015). Land Use Classification in Remote Sensing Images by Convolutional NNs. *ArXiv:1508.00092 [Cs]*. http://arxiv.org/abs/1508.00092

CESBIO. (2018). *Theia's Sentinel-2 L3A monthly cloud free syntheses – Séries Temporelles*. https://labo.obs-mip.fr/multitemp/theias-sentinel-2-l3a-monthly-cloud-free-syntheses/

Chamard, Ph. C., Courel, M. F., Guenegou, M. C., Lerhun, J., Levasseur, J., & Togola, M. (1991). Utilisation des bandes spectrales du vert et du rouge pour une meilleure évaluation des formations végétales actives. In *Télédétection et Cartographie* (pp. 203–209). Éd. AUPELF-UREF. https://hal.archives-ouvertes.fr/hal-00327879

Chambres d'Agriculture de Bretagne. (n.d.). Retrieved August 22, 2022, from http://www.chambres-agriculture-bretagne.fr/synagri/accueilRegion

Chan, J.-W., Chan, K.-P., & Yeh, A.-O. (2001). DETECTING THE NATURE OF CHANGE IN AN URBAN ENVIRONMENT: A COMPARISON OF MACHINE LEARNING ALGORITHMS. *Photogrammetric Engineering and Remote Sensing*, *67*(2). https://trid.trb.org/view/676157

Chandrasekar, K., Sesha Sai, M. V. R., Roy, P. S., & Dwevedi, R. S. (2010). Land Surface Water Index (LSWI) response to rainfall and NDVI using the MODIS Vegetation Index product. *International Journal of Remote Sensing*, *31*(15), 3987–4005. https://doi.org/10.1080/01431160802575653

Chang, Q., Liu, X., Wu, J., & He, P. (2015). MSPA-Based Urban Green Infrastructure Planning and Management Approach for Urban Sustainability: Case Study of Longgang in China. *Journal of Urban Planning and Development*, *141*(3), A5014006. https://doi.org/10.1061/(ASCE)UP.1943-5444.0000247

Chang, Y., Hou, K., Li, X., Zhang, Y., & Chen, P. (2018). Review of Land Use and Land Cover Change research progress. *IOP Conference Series: Earth and Environmental Science*, *113*, 012087. https://doi.org/10.1088/1755-1315/113/1/012087

Chen, A., Orlov-Levin, V., & Meron, M. (2019). Applying high-resolution visible-channel aerial imaging of crop canopy to precision irrigation management. *Agricultural Water Management*, *216*, 196–205. https://doi.org/10.1016/j.agwat.2019.02.017

Chen, B., Huang, B., & Xu, B. (2017). Multi-source remotely sensed data fusion for improving land cover classification. *ISPRS Journal of Photogrammetry and Remote Sensing*, *124*, 27–39. https://doi.org/10.1016/j.isprsjprs.2016.12.008

Chen, B., Xiao, X., Li, X., Pan, L., Doughty, R., Ma, J., Dong, J., Qin, Y., Zhao, B., Wu, Z., Sun, R., Lan, G., Xie, G., Clinton, N., & Giri, C. (2017). A mangrove forest map of China in 2015: Analysis of time series Landsat 7/8 and Sentinel-1A imagery in Google Earth Engine cloud computing platform. *ISPRS Journal of Photogrammetry and Remote Sensing*, *131*, 104–120. https://doi.org/10.1016/j.isprsjprs.2017.07.011

Chen, D., & Stow, D. (2002). THE EFFECT OF TRAINING STRATEGIES ON SUPERVISED CLASSIFICATION AT DIFFERENT SPATIAL RESOLUTIONS. *Photogrammetric Engineering and Remote Sensing*, *68*(11). https://trid.trb.org/view/728155

Chen, G., Hay, G. J., Carvalho, L. M. T., & Wulder, M. A. (2012). Object-based change detection. *International Journal of Remote Sensing*, *33*(14), 4434–4457. https://doi.org/10.1080/01431161.2011.648285

Chen, G., Zhang, X., Tan, X., Cheng, Y., Dai, F., Zhu, K., Gong, Y., & Wang, Q. (2018). Training Small Networks for Scene Classification of Remote Sensing Images via Knowledge Distillation. *Remote Sensing*, *10*(5), 5. https://doi.org/10.3390/rs10050719

Chen, L., Ren, C., Zhang, B., Wang, Z., & Xi, Y. (2018). Estimation of Forest Above-Ground Biomass by Geographically Weighted Regression and Machine Learning with Sentinel Imagery. *Forests*, *9*(10), 10. https://doi.org/10.3390/f9100582

Chen, S., & Wang, H. (2014). SAR target recognition based on deep learning. *2014 International Conference on Data Science and Advanced Analytics (DSAA)*, 541–547. https://doi.org/10.1109/DSAA.2014.7058124

Chen, X.-L., Zhao, H.-M., Li, P.-X., & Yin, Z.-Y. (2006). Remote sensing image-based analysis of the relationship between urban heat island and land use/cover changes. *Remote Sensing of Environment*, *104*(2), 133–146. https://doi.org/10.1016/j.rse.2005.11.016

Chen, Y., Ming, D., & Lv, X. (2019). Superpixel based land cover classification of VHR satellite image combining multi-scale CNN and scale parameter estimation. *Earth Science Informatics*, *12*(3), 341–363. https://doi.org/10.1007/s12145-019-00383-2

Chen, Y., Tang, L., Kan, Z., Latif, A., Yang, X., Bilal, M., & Li, Q. (2020). Cloud and Cloud Shadow Detection Based on Multiscale 3D-CNN for High Resolution Multispectral Imagery. *IEEE Access*, *8*, 16505–16516. https://doi.org/10.1109/ACCESS.2020.2967590

Chen, Y., Zhao, X., & Jia, X. (2015). Spectral–Spatial Classification of Hyperspectral Data Based on Deep Belief Network. *IEEE Journal of Selected Topics in Applied Earth Observations and Remote Sensing*, *8*(6), 2381–2392. https://doi.org/10.1109/JSTARS.2015.2388577

Cheng, G., & Han, J. (2016). A survey on object detection in optical remote sensing images. *ISPRS Journal of Photogrammetry and Remote Sensing*, *117*, 11–28. https://doi.org/10.1016/j.isprsjprs.2016.03.014

Cheng, G., Xie, X., Han, J., Guo, L., & Xia, G.-S. (2020). Remote Sensing Image Scene Classification Meets Deep Learning: Challenges, Methods, Benchmarks, and Opportunities. *IEEE Journal of Selected Topics in Applied Earth Observations and Remote Sensing*, *13*, 3735–3756. https://doi.org/10.1109/JSTARS.2020.3005403

Chester, D. L. (1990). Why two hidden layers are better than one. *Proceedings of the International Joint Conference on NNs*, *1*, 265–268. https://cir.nii.ac.jp/crid/1572824498901538944

Chierchia, G., Cozzolino, D., Poggi, G., & Verdoliva, L. (2017). *SAR image despeckling through convolutional NNs*. 5441. https://doi.org/10.1109/IGARSS.2017.8128234

Chlingaryan, A., Sukkarieh, S., & Whelan, B. (2018). Machine learning approaches for crop yield prediction and nitrogen status estimation in precision agriculture: A review. *Computers and Electronics in Agriculture*, *151*, 61–69. https://doi.org/10.1016/j.compag.2018.05.012

Chughtai, A. H., Abbasi, H., & Karas, I. R. (2021). A review on change detection method and accuracy assessment for land use land cover. *Remote Sensing Applications: Society and Environment*, *22*, 100482. https://doi.org/10.1016/j.rsase.2021.100482

Cihlar, J. (2000). Land cover mapping of large areas from satellites: Status and research priorities. *International Journal of Remote Sensing*, *21*(6–7), 1093–1114. https://doi.org/10.1080/014311600210092

Cihlar, J., Ly, H., & Xiao, Q. (1996). Land cover classification with AVHRR multichannel composites in northern environments. *Remote Sensing of Environment*, *58*(1), 36–51. https://doi.org/10.1016/0034-4257(95)00210-3

Clark, J. R. (2018). *Coastal Zone Management Handbook*. CRC Press.

Clerici, N., Valbuena Calderón, C. A., & Posada, J. M. (2017). Fusion of Sentinel-1A and Sentinel-2A data for land cover mapping: A case study in the lower Magdalena region, Colombia. *Journal of Maps*, *13*(2), 718–726. https://doi.org/10.1080/17445647.2017.1372316

Clinton, N. (2016). *What is Google Earth Engine?* Google Docs. https://docs.google.com/presentation/d/1hT9q6kWigM1MM3p7IEcvNQlpPvkedW-lgCCrIqbNeis/htmlpresent?usp=embed_facebook

Coelho, A. P., Rosalen, D. L., & Faria, R. T. de. (2018). Vegetation indices in the prediction of biomass and grain yield of white oat under irrigation levels. *Pesquisa Agropecuária Tropical*, *48*, 109–117. https://doi.org/10.1590/1983-40632018v4851523

Colditz, R. R. (2015). An Evaluation of Different Training Sample Allocation Schemes for Discrete and Continuous Land Cover Classification Using Decision Tree-Based Algorithms. *Remote Sensing*, *7*(8), 8. https://doi.org/10.3390/rs70809655

Combal, B., Baret, F., & Weiss, M. (2002). Improving canopy variables estimation from remote sensing data by exploiting ancillary information. Case study on sugar beet canopies. *Agronomie*, *22*(2), 205–215. https://doi.org/10.1051/agro:2002008

Coops, N., Wulder, M., & White, J. (2006). Identifying and Describing Forest Disturbance and Spatial Pattern: Data Selection Issues and Methodological Implications. In *Understanding Forest Disturbance and Spatial Pattern: Remote Sensing and GIS Approaches* (pp. 31–61). https://doi.org/10.1201/9781420005189.ch2

Coppin, P., Nackaerts, K., Queen, L., & Brewer, K. (2001). Operational monitoring of green biomass change for forest management. *Photogrammetric Engineering and Remote Sensing*, *67*, 603–611.

CORINE Land Cover—Copernicus Land Monitoring Service. (n.d.). [Land Section]. Retrieved December 27, 2022, from https://land.copernicus.eu/pan-european/corine-land-cover

Cormack, R. M. (1971). A Review of Classification. *Journal of the Royal Statistical Society: Series A (General)*, *134*(3), 321–353. https://doi.org/10.2307/2344237

Correa Martins, J. A., Menezes, G., Gonçalves, W., Sant'Ana, D. A., Osco, L. P., Liesenberg, V., Li, J., Ma, L., Oliveira, P. T., Astolfi, G., Pistori, H., & Junior, J. M. (2021). Machine learning and SLIC for Tree Canopies segmentation in urban areas. *Ecological Informatics*, *66*, 101465. https://doi.org/10.1016/j.ecoinf.2021.101465

Cortes, C., & Vapnik, V. (1995). Support-vector networks. *Machine Learning*, *20*(3), 273–297. https://doi.org/10.1007/BF00994018

Cousins, S. A. O., Auffret, A. G., Lindgren, J., & Tränk, L. (2015). Regional-scale land-cover change during the 20th century and its consequences for biodiversity. *AMBIO*, *44*(1), 17–27. https://doi.org/10.1007/s13280-014-0585-9

Crommelinck, S., Bennett, R., Gerke, M., Koeva, M. N., Yang, M. Y., & Vosselman, G. (2017). Slic Superpixels for Object Delineation from Uav Data. *ISPRS Annals of Photogrammetry, Remote Sensing and Spatial Information Sciences*, *42W3*, 9–16. https://doi.org/10.5194/isprs-annals-IV-2-W3-9-2017

Crossland, C. J., Baird, D., Ducrotoy, J.-P., Lindeboom, H., Buddemeier, R. W., Dennison, W. C., Maxwell, B. A., Smith, S. V., & Swaney, D. P. (2005). The Coastal Zone—A Domain of Global Interactions. In C. J. Crossland, H. H. Kremer, H. J. Lindeboom, J. I. Marshall Crossland, & M. D. A. Le Tissier (Eds.), *Coastal Fluxes in the Anthropocene: The Land-Ocean Interactions in the Coastal Zone Project of the International Geosphere-Biosphere Programme* (pp. 1–37). Springer. https://doi.org/10.1007/3-540-27851-6_1

Crowell, M., Edelman, S., Coulton, K., & McAfee, S. (2007). How Many People Live in Coastal Areas? *Journal of Coastal Research*, *23*, iii–vi. https://doi.org/10.2112/07A-0017.1

Cutler, A., Cutler, D. R., & Stevens, J. R. (2012). Random Forests. In C. Zhang & Y. Ma (Eds.), *Ensemble Machine Learning: Methods and Applications* (pp. 157–175). Springer US. https://doi.org/10.1007/978-1-4419-9326-7_5

Dang, A. T. N., Nandy, S., Srinet, R., Luong, N. V., Ghosh, S., & Senthil Kumar, A. (2019). Forest aboveground biomass estimation using machine learning regression algorithm in Yok Don National Park, Vietnam. *Ecological Informatics*, *50*, 24–32. https://doi.org/10.1016/j.ecoinf.2018.12.010

Dar, I. A., Sankar, K., & Dar, M. A. (2010). Remote sensing technology and geographic information system modeling: An integrated approach towards the mapping of groundwater potential zones in Hardrock terrain, Mamundiyar basin. *Journal of Hydrology*, *394*(3), 285–295. https://doi.org/10.1016/j.jhydrol.2010.08.022

Darwish, A., Leukert, K., & Reinhardt, W. (2003). Image segmentation for the purpose of object-based classification. *IGARSS 2003. 2003 IEEE International Geoscience and Remote Sensing Symposium. Proceedings (IEEE Cat. No.03CH37477)*, *3*, 2039–2041. https://doi.org/10.1109/IGARSS.2003.1294332

DATAR. (2004). *Construire ensemble un développement équilibré du littoral. Collect. Etude Prospective. Rapport de la DATAR* (p. 122).

de Bem, P. P., de Carvalho Junior, O. A., Fontes Guimarães, R., & Trancoso Gomes, R. A. (2020). Change Detection of Deforestation in the Brazilian Amazon Using Landsat Data and Convolutional NNs. *Remote Sensing*, *12*(6), 6. https://doi.org/10.3390/rs12060901

De Fries, R. S., Hansen, M., Townshend, J. R. G., & Sohlberg, R. (1998). Global land cover classifications at 8 km spatial resolution: The use of training data derived from Landsat imagery in decision tree classifiers. *International Journal of Remote Sensing*, *19*(16), 3141–3168. https://doi.org/10.1080/014311698214235

de Jong, S. M., Hornstra, T., & Maas, H.-G. (2001). An integrated spatial and spectral approach to the classification of Mediterranean land cover types: The SSC method. *International Journal of Applied Earth Observation and Geoinformation*, *3*(2), 176–183. https://doi.org/10.1016/S0303-2434(01)85009-1

Dean, A. M., & Smith, G. M. (2003). An evaluation of per-parcel land cover mapping using maximum likelihood class probabilities. *International Journal of Remote Sensing*, *24*(14), 2905–2920. https://doi.org/10.1080/01431160210155910

Debella-Gilo, M., & Gjertsen, A. K. (2021). Mapping Seasonal Agricultural Land Use Types Using Deep Learning on Sentinel-2 Image Time Series. *Remote Sensing*, *13*(2), 2. https://doi.org/10.3390/rs13020289

DeFries, R., Hansen, M., & Townshend, J. (1995). Global discrimination of land cover types from metrics derived from AVHRR pathfinder data. *Remote Sensing of Environment*, *54*(3), 209–222. https://doi.org/10.1016/0034-4257(95)00142-5

DeFries, R. S., Asner, G. P., & Houghton, R. A. (2004). Ecosystems and Land Use Change. *Washington DC American Geophysical Union Geophysical Monograph Series*, *153*. https://doi.org/10.1029/GM153

Deilmai, B. R., Ahmad, B. B., & Zabihi, H. (2014). Comparison of two Classification methods (MLC and SVM) to extract land use and land cover in Johor Malaysia. *IOP Conference Series: Earth and Environmental Science*, *20*(1), 012052. https://doi.org/10.1088/1755-1315/20/1/012052

Del Frate, F., Ferrazzoli, P., Guerriero, L., Strozzi, T., Wegmuller, U., Cookmartin, G., & Quegan, S. (2004). Wheat cycle monitoring using RaDAR data and a NN trained by a model. *IEEE Transactions on Geoscience and Remote Sensing*, *42*(1), 35–44. https://doi.org/10.1109/TGRS.2003.817200

Del Frate, F., Pacifici, F., Schiavon, G., & Solimini, C. (2007). Use of NNs for Automatic Classification From High-Resolution Images. *IEEE Transactions on Geoscience and Remote Sensing*, *45*(4), 800–809. https://doi.org/10.1109/TGRS.2007.892009

DeLancey, E. R., Simms, J. F., Mahdianpari, M., Brisco, B., Mahoney, C., & Kariyeva, J. (2020). Comparing Deep Learning and Shallow Learning for Large-Scale Wetland Classification in Alberta, Canada. *Remote Sensing*, *12*(1), 1. https://doi.org/10.3390/rs12010002

Dellepiane, S., De Laurentiis, R., & Giordano, F. (2004). Coastline extraction from SAR images and a method for the evaluation of the coastline precision. *Pattern Recognition Letters*, *25*(13), 1461–1470. https://doi.org/10.1016/j.patrec.2004.05.022

Deng, C., & Wu, C. (2013). The use of single-date MODIS imagery for estimating large-scale urban impervious surface fraction with spectral mixture analysis and machine learning techniques. *ISPRS Journal of Photogrammetry and Remote Sensing*, *86*, 100–110. https://doi.org/10.1016/j.isprsjprs.2013.09.010

Deng, J. S., Wang, K., Deng, Y. H., & Qi, G. J. (2008). PCA-based land-use change detection and analysis using multitemporal and multisensor satellite data. *International Journal of Remote Sensing*, *29*(16), 4823–4838. https://doi.org/10.1080/01431160801950162

Deng, L., & Yu, D. (2014). Deep Learning: Methods and Applications. *Foundations and Trends® in Signal Processing*, *7*(3–4), 197–387. https://doi.org/10.1561/2000000039

Deng, X., Zhao, C., & Yan, H. (2013). Systematic Modeling of Impacts of Land Use and Land Cover Changes on Regional Climate: A Review. *Advances in Meteorology*, *2013*, e317678. https://doi.org/10.1155/2013/317678

Devadas, R., Denham, R. J., & Pringle, M. (2012). SUPPORT VECTOR MACHINE CLASSIFICATION OF OBJECT-BASED DATA FOR CROP MAPPING, USING MULTITEMPORAL LANDSAT IMAGERY. *ISPRS - International Archives of the Photogrammetry, Remote Sensing and Spatial Information Sciences*, *XXXIX-B7*, 185–190. https://doi.org/10.5194/isprsarchives-XXXIX-B7-185-2012

Devadas, R., Lamb, D. W., Simpfendorfer, S., & Backhouse, D. (2009). Evaluating ten spectral vegetation indices for identifying rust infection in individual wheat leaves. *Precision Agriculture*, *10*(6), 459–470. https://doi.org/10.1007/s11119-008-9100-2

Dewan, A. M., & Yamaguchi, Y. (2009). Land use and land cover change in Greater Dhaka, Bangladesh: Using remote sensing to promote sustainable urbanization. *Applied Geography*, *29*(3), 390–401. https://doi.org/10.1016/j.apgeog.2008.12.005

Dey, V., Zhang, Y., & Zhong, M. (2010). A review on image segmentation techniques with remote sensing perspective. *ISPRS TC VII Symposium - 100 Years ISPRS*, *38*.

Díaz-Uriarte, R., & Alvarez de Andrés, S. (2006). Gene selection and classification of microarray data using random forest. *BMC Bioinformatics*, *7*(1), 3. https://doi.org/10.1186/1471-2105-7-3

Dingle Robertson, L., & King, D. (2011). Comparison of pixel- and object-based classification in land cover change mapping. *International Journal of Remote Sensing*, *32*, 1505–1529. https://doi.org/10.1080/01431160903571791

Dong, J., Xiao, X., Menarguez, M. A., Zhang, G., Qin, Y., Thau, D., BiRaDAR, C., & Moore, B. (2016). Mapping paddy rice planting area in northeastern Asia with Landsat 8 images, phenology-based algorithm and Google Earth Engine. *Remote Sensing of Environment*, *185*, 142–154. https://doi.org/10.1016/j.rse.2016.02.016

Dong, Q., Chen, X., Chen, J., Zhang, C., Liu, L., Cao, X., Zang, Y., Zhu, X., & Cui, X. (2020). Mapping Winter Wheat in North China Using Sentinel 2A/B Data: A Method Based on Phenology-Time Weighted Dynamic Time Warping. *Remote Sensing*, *12*(8), 1274. https://doi.org/10.3390/rs12081274

Donnay, J.-P., Barnsley, M. J., & Longley, P. A. (Eds.). (2014). *Remote Sensing and Urban Analysis: GISDATA 9*. CRC Press. https://doi.org/10.1201/9781482268119

Dornik, A., Drăguț, L., & Urdea, P. (2018). Classification of Soil Types Using Geographic Object-Based Image Analysis and Random Forests. *Pedosphere*, *28*(6), 913–925. https://doi.org/10.1016/S1002-0160(17)60377-1

Dou, P., & Chen, Y. (2017). Dynamic monitoring of land-use/land-cover change and urban expansion in Shenzhen using Landsat imagery from 1988 to 2015. *International Journal of Remote Sensing*, *38*(19), 5388–5407. https://doi.org/10.1080/01431161.2017.1339926

Drăguț, L., Tiede, D., & Levick, S. R. (2010). ESP: A tool to estimate scale parameter for multiresolution image segmentation of remotely sensed data. *International Journal of Geographical Information Science*, *24*(6), 859–871. https://doi.org/10.1080/13658810903174803

Du, P., Samat, A., Waske, B., Liu, S., & Li, Z. (2015). Random Forest and Rotation Forest for fully polarized SAR image classification using polarimetric and spatial features. *ISPRS Journal of Photogrammetry and Remote Sensing*, *105*, 38–53. https://doi.org/10.1016/j.isprsjprs.2015.03.002

Du, P., Xia, J., Zhang, W., Tan, K., Liu, Y., & Liu, S. (2012). Multiple Classifier System for Remote Sensing Image Classification: A Review. *Sensors*, *12*(4), 4. https://doi.org/10.3390/s120404764

Duchemin, B., Hadria, R., Erraki, S., Boulet, G., Maisongrande, P., Chehbouni, A., Escadafal, R., Ezzahar, J., Hoedjes, J. C. B., Kharrou, M. H., Khabba, S., Mougenot, B., Olioso, A., Rodriguez, J.-C., & Simonneaux, V. (2006). Monitoring wheat phenology and irrigation in Central Morocco: On the use of relationships between evapotranspiration, crops coefficients, leaf area index and remotely-sensed vegetation indices. *Agricultural Water Management*, *79*(1), 1–27. https://doi.org/10.1016/j.agwat.2005.02.013

Duro, D. C., Franklin, S. E., & Dubé, M. G. (2012). A comparison of pixel-based and object-based image analysis with selected machine learning algorithms for the classification of agricultural landscapes using SPOT-5 HRG imagery. *Remote Sensing of Environment*, *118*, 259–272. https://doi.org/10.1016/j.rse.2011.11.020

Earth Science Data Systems, N. (n.d.). *Earthdata*. Earthdata; Earth Science Data Systems, NASA. Retrieved October 3, 2022, from http://www.earthdata.nasa.gov/learn/backgrounders/what-is-sar

Ehrlich, D., Estes, J. E., & Singh, A. (1994). Applications of NOAA-AVHRR 1 km data for environmental monitoring. *International Journal of Remote Sensing*, *15*(1), 145–161. https://doi.org/10.1080/01431169408954056

El-Hattab, M. M. (2016). Applying post classification change detection technique to monitor an Egyptian coastal zone (Abu Qir Bay). *The Egyptian Journal of Remote Sensing and Space Science*, *19*(1), 23–36. https://doi.org/10.1016/j.ejrs.2016.02.002

eoPortal. (2012a). *Copernicus: Sentinel-1*. https://www.eoportal.org/satellite-missions/copernicus-sentinel-1

eoPortal. (2012b). *Copernicus: Sentinel-2*. https://www.eoportal.org/satellite-missions/copernicus-sentinel-2

eoPortal. (2012c). *Pleiades eoPortal Directory*. https://www.eoportal.org/satellite-missions/pleiades

ESA. (n.d.-a). *Sentinel-1*. Retrieved October 3, 2022, from https://www.esa.int/Applications/Observing_the_Earth/Copernicus/Sentinel-1

ESA. (n.d.-b). *Sentinel-1—Missions—Sentinel Online*. Retrieved October 3, 2022, from https://sentinels.copernicus.eu/web/sentinel/missions/sentinel-1

ESA. (n.d.-c). *SPOT 5—Earth Online*. Retrieved September 29, 2022, from https://earth.esa.int/eogateway/missions/spot-5

ESA. (n.d.-d). *User Guides—Sentinel-1 SAR - Sentinel Online*. Retrieved October 4, 2022, from https://sentinels.copernicus.eu/web/sentinel/user-guides/sentinel-1-sar

ESA. (n.d.-e). *User Guides—Sentinel-2 MSI - Sentinel Online*. Retrieved October 2, 2022, from https://sentinels.copernicus.eu/web/sentinel/user-guides/sentinel-2-msi/processing-levels/level-1

Estes, J. E., & Loveland, T. R. (1999). Characteristics, sources, and management of remotely-sensed data. In *Geographical Information Systems: Principles, Techniques, Applications, and Management* (2nd ed., pp. 667–675). John Wiley and Sons.

Estoque, R. C., Murayama, Y., & Akiyama, C. M. (2015). Pixel-based and object-based classifications using high- and medium-spatial-resolution imageries in the urban and suburban landscapes. *Geocarto International*, *30*(10), 1113–1129. https://doi.org/10.1080/10106049.2015.1027291

Eva, H., & Lambin, E. F. (2000). Fires and land-cover change in the tropics:a remote sensing analysis at the landscape scale. *Journal of Biogeography*, *27*(3), 765–776. https://doi.org/10.1046/j.1365-2699.2000.00441.x

Evans, J. S., & Cushman, S. A. (2009). Gradient modeling of conifer species using random forests. *Landscape Ecology*, *24*(5), 673–683. https://doi.org/10.1007/s10980-009-9341-0

Fadhil, A. M. (2011). Drought mapping using Geoinformation technology for some sites in the Iraqi Kurdistan region. *International Journal of Digital Earth*, *4*(3), 239–257. https://doi.org/10.1080/17538947.2010.489971

Falcucci, A., Maiorano, L., & Boitani, L. (2007). Changes in land-use/land-cover patterns in Italy and their implications for biodiversity conservation. *Landscape Ecology*, *22*(4), 617–631. https://doi.org/10.1007/s10980-006-9056-4

Fan, F., Weng, Q., & Wang, Y. (2007). Land Use and Land Cover Change in Guangzhou, China, from 1998 to 2003, Based on Landsat TM /ETM+ Imagery. *Sensors*, *7*(7), 7. https://doi.org/10.3390/s7071323

Fan, R., Feng, R., Wang, L., Yan, J., & Zhang, X. (2020). Semi-MCNN: A Semisupervised Multi-CNN Ensemble Learning Method for Urban Land Cover Classification Using Submeter HRRS Images. *IEEE Journal of Selected Topics in Applied Earth Observations and Remote Sensing*, *13*, 4973–4987. https://doi.org/10.1109/JSTARS.2020.3019410

FAO. (n.d.). FAOHome. Retrieved December 27, 2022, from https://www.fao.org/home/en

Fearnside, P. M. (2000). Global Warming and Tropical Land-Use Change: Greenhouse Gas Emissions from Biomass Burning, Decomposition and Soils in Forest Conversion, Shifting Cultivation and Secondary Vegetation. *Climatic Change*, *46*(1), 115–158. https://doi.org/10.1023/A:1005569915357

Feng, Q., Liu, J., & Gong, J. (2015). UAV Remote Sensing for Urban Vegetation Mapping Using Random Forest and Texture Analysis. *Remote Sensing*, *7*(1), 1. https://doi.org/10.3390/rs70101074

Feng, W., Shen, W., He, L., Duan, J., Guo, B., Li, Y., Wang, C., & Guo, T. (2016). Improved remote sensing detection of wheat powdery mildew using dual-green vegetation indices. *Precision Agriculture*, *17*(5), 608–627. https://doi.org/10.1007/s11119-016-9440-2

Feng, W., Wu, Y., He, L., Ren, X., Wang, Y., Hou, G., Wang, Y., Liu, W., & Guo, T. (2019). An optimized non-linear vegetation index for estimating leaf area index in winter wheat. *Precision Agriculture*, *20*(6), 1157–1176. https://doi.org/10.1007/s11119-019-09648-8

Ferrazzoli, P., Paloscia, S., Pampaloni, P., Schiavon, G., Solimini, D., & Coppo, P. (1992). Sensitivity of microwave measurements to vegetation biomass and soil moisture content: A case study. *IEEE Transactions on Geoscience and Remote Sensing*, *30*(4), 750–756. https://doi.org/10.1109/36.158869

Ferreira, J. C., Silva, L., & Polette, M. (2009). The Coastal Artificialization Process. Impacts and Challenges for the Sustainable Management of the Coastal Cities of Santa Catarina (Brazil). *Journal of Coastal Research*, 1209–1213.

Feyisa, G. L., Meilby, H., Darrel Jenerette, G., & Pauliet, S. (2016). Locally optimized separability enhancement indices for urban land cover mapping: Exploring thermal environmental consequences of rapid urbanization in Addis Ababa, Ethiopia. *Remote Sensing of Environment*, *175*, 14–31. https://doi.org/10.1016/j.rse.2015.12.026

Filipponi, F. (2019). Sentinel-1 GRD Preprocessing Workflow. *3rd International Electronic Conference on Remote Sensing*, 11. https://doi.org/10.3390/ECRS-3-06201

Fischer, A., & Igel, C. (2012). An Introduction to Restricted Boltzmann Machines. In L. Alvarez, M. Mejail, L. Gomez, & J. Jacobo (Eds.), *Progress in Pattern Recognition, Image Analysis, Computer Vision, and Applications* (pp. 14–36). Springer. https://doi.org/10.1007/978-3-642-33275-3_2

Fiset, R., Cavayas, F., Mouchot, M.-C., Solaiman, B., & Desjardins, R. (1998). Map-image matching using a multilayer perceptron: The case of the road network. *ISPRS Journal of Photogrammetry and Remote Sensing*, *53*(2), 76–84. https://doi.org/10.1016/S0924-2716(97)00038-5

Fisher, P. (1997). The pixel: A snare and a delusion. *International Journal of Remote Sensing*, *18*. https://doi.org/10.1080/014311697219015

Foga, S., Scaramuzza, P. L., Guo, S., Zhu, Z., Dilley, R. D., Beckmann, T., Schmidt, G. L., Dwyer, J. L., Joseph Hughes, M., & Laue, B. (2017). Cloud detection algorithm comparison and validation for operational Landsat data products. *Remote Sensing of Environment*, *194*, 379–390. https://doi.org/10.1016/j.rse.2017.03.026

Foley, J. A., Defries, R., Asner, G. P., Barford, C., Bonan, G., Carpenter, S. R., Chapin, F. S., Coe, M. T., Daily, G. C., Gibbs, H. K., Helkowski, J. H., Holloway, T., Howard, E. A., Kucharik, C. J., Monfreda, C., Patz, J. A., Prentice, I. C., Ramankutty, N., & Snyder, P. K. (2005). Global consequences of land use. *Science (New York, N.Y.)*, *309*(5734), 570–574. https://doi.org/10.1126/science.1111772

Foody, G. M. (1995). Land cover classification by an artificial NN with ancillary information. *International Journal of Geographical Information Systems*, *9*(5), 527–542. https://doi.org/10.1080/02693799508902054

Foody, G. M. (1996). Relating the land-cover composition of mixed pixels to artificial NN classification output. *Photogrammetric Engineering and Remote Sensing (USA)*. https://scholar.google.com/scholar_lookup?title=Relating+the+land-cover+composition+of+mixed+pixels+to+artificial+neural+network+classification+output&author=Foody%2C+G.M.+%28University+of+Salford%2C+Salford%2C+UK.%29&publication_year=1996

Foody, G. M. (2002). Status of land cover classification accuracy assessment. *Remote Sensing of Environment*, *80*(1), 185–201. https://doi.org/10.1016/S0034-4257(01)00295-4

Foody, G. M., & Mathur, A. (2004). A relative evaluation of multiclass image classification by support vector machines. *IEEE Transactions on Geoscience and Remote Sensing*, *42*(6), 1335–1343. https://doi.org/10.1109/TGRS.2004.827257

Forkuor, G., Conrad, C., Thiel, M., Ullmann, T., & Zoungrana, E. (2014). Integration of Optical and Synthetic Aperture RaDAR Imagery for Improving Crop Mapping in Northwestern Benin, West Africa. *Remote Sensing*, *6*(7), 7. https://doi.org/10.3390/rs6076472

Forkuor, G., Dimobe, K., Serme, I., & Tondoh, J. E. (2018). Landsat-8 vs. Sentinel-2: Examining the added value of sentinel-2's red-edge bands to land-use and land-cover mapping in Burkina Faso. *GIScience & Remote Sensing*, *55*(3), 331–354. https://doi.org/10.1080/15481603.2017.1370169

Franklin, S. E., & Wulder, M. A. (2002). Remote sensing methods in medium spatial resolution satellite data land cover classification of large areas. *Progress in Physical Geography: Earth and Environment*, *26*(2), 173–205. https://doi.org/10.1191/0309133302pp332ra

Freire, S., Santos, T., & Tenedório, J. A. (2009). Recent urbanization and land use/land cover change in Portugal—The influence of coastline and coastal urban centers. *Journal of Coastal Research*, 1499–1503.

Friedl, M. A., & Brodley, C. E. (1997). Decision tree classification of land cover from remotely sensed data. *Remote Sensing of Environment*, *61*(3), 399–409. https://doi.org/10.1016/S0034-4257(97)00049-7

Frison, P.-L., Fruneau, B., Kmiha, S., Soudani, K., Dufrêne, E., Le Toan, T., Koleck, T., Villard, L., Mougin, E., & Rudant, J.-P. (2018). Potential of Sentinel-1 Data for Monitoring Temperate Mixed Forest Phenology. *Remote Sensing*, *10*(12), 12. https://doi.org/10.3390/rs10122049

Frohn, R. C., McGwire, K. C., Dale, V. H., & Estes, J. E. (1996). Using satellite remote sensing analysis to evaluate a socio-economic and ecological model of deforestation in Rondônia, Brazil. *International Journal of Remote Sensing*, *17*(16), 3233–3255. https://doi.org/10.1080/01431169608949141

Fu, B., Wang, Y., Campbell, A., Li, Y., Zhang, B., Yin, S., Xing, Z., & Jin, X. (2017). Comparison of object-based and pixel-based Random Forest algorithm for wetland vegetation mapping using high spatial resolution GF-1 and SAR data. *Ecological Indicators*, *73*, 105–117. https://doi.org/10.1016/j.ecolind.2016.09.029

Fu, P., & Weng, Q. (2016). A time series analysis of urbanization induced land use and land cover change and its impact on land surface temperature with Landsat imagery. *Remote Sensing of Environment*, *175*, 205–214. https://doi.org/10.1016/j.rse.2015.12.040

Fu, T., Ma, L., Li, M., & Johnson, B. A. (2018). Using convolutional NN to identify irregular segmentation objects from very high-resolution remote sensing imagery. *Journal of Applied Remote Sensing*, *12*(2), 025010. https://doi.org/10.1117/1.JRS.12.025010

Fuentes, M., Millard, K., & Laurin, E. (2020). Big geospatial data analysis for Canada's Air Pollutant Emissions Inventory (APEI): Using google earth engine to estimate particulate matter from exposed mine disturbance areas. *GIScience & Remote Sensing*, *57*(2), 245–257. https://doi.org/10.1080/15481603.2019.1695407

Fuller, R. M., Groom, G. B., & Jones, A. R. (1994). Land cover map of Great Britain. An automated classification of Landsat Thematic Mapper data. *Photogrammetric Engineering and Remote Sensing*, *60*(5). https://www.osti.gov/biblio/53458

Gaetano, R., Ienco, D., Ose, K., & Cresson, R. (2018). A Two-Branch CNN Architecture for Land Cover Classification of PAN and MS Imagery. *Remote Sensing*, *10*(11), 11. https://doi.org/10.3390/rs10111746

Gan, L., Cao, X., Chen, X., Dong, Q., Cui, X., & Chen, J. (2020). Comparison of MODIS-based vegetation indices and methods for winter wheat green-up date detection in Huanghuai region of China. *Agricultural and Forest Meteorology*, *288–289*, 108019. https://doi.org/10.1016/j.agrformet.2020.108019

Gao, B. (1996). NDWI—A normalized difference water index for remote sensing of vegetation liquid water from space. *Remote Sensing of Environment*, *58*(3), 257–266. https://doi.org/10.1016/S0034-4257(96)00067-3

Gao, J., & Liu, Y. (2010). Determination of land degradation causes in Tongyu County, Northeast China via land cover change detection. *International Journal of Applied Earth Observation and Geoinformation*, *12*(1), 9–16. https://doi.org/10.1016/j.jag.2009.08.003

Gao, L., Wang, X., Johnson, B. A., Tian, Q., Wang, Y., Verrelst, J., Mu, X., & Gu, X. (2020). Remote sensing algorithms for estimation of fractional vegetation cover using pure vegetation index values: A review. *ISPRS Journal of Photogrammetry and Remote Sensing*, *159*, 364–377. https://doi.org/10.1016/j.isprsjprs.2019.11.018

Gao, Y., & Mas, J. (2008). A comparison of the performance of pixel based and object based classifications over images with various spatial resolutions. *Online Journal of Earth Science*, *2*, 27–35.

Gao, Y., Mas, J. F., Kerle, N., & Navarrete Pacheco, J. A. (2011). Optimal region growing segmentation and its effect on classification accuracy. *International Journal of Remote Sensing*, *32*(13), 3747–3763. https://doi.org/10.1080/01431161003777189

Gardner, M. W., & Dorling, S. R. (1998). Artificial NNs (the multilayer perceptron)—A review of applications in the atmospheric sciences. *Atmospheric Environment*, *32*(14), 2627–2636. https://doi.org/10.1016/S1352-2310(97)00447-0

Ge, Y., Hu, S., Ren, Z., Jia, Y., Wang, J., Liu, M., Zhang, D., Zhao, W., Luo, Y., Fu, Y., Bai, H., & Chen, Y. (2019). Mapping annual land use changes in China's poverty-stricken areas from 2013 to 2018. *Remote Sensing of Environment*, *232*, 111285. https://doi.org/10.1016/j.rse.2019.111285

Genuer, R., Poggi, J.-M., & Tuleau-Malot, C. (2010). Variable selection using Random Forests. *Pattern Recognition Letters*, *31*(14), 2225–2236.

Géoportail. (n.d.). Retrieved August 21, 2022, from https://www.geoportail.gouv.fr/

Georganos, S., Grippa, T., Vanhuysse, S., Lennert, M., Shimoni, M., & Wolff, E. (2018). Very High Resolution Object-Based Land Use–Land Cover Urban Classification Using Extreme Gradient Boosting. *IEEE Geoscience and Remote Sensing Letters*, *15*(4), 607–611. https://doi.org/10.1109/LGRS.2018.2803259

Ghimire, B., Rogan, J., Galiano, V. R., Panday, P., & Neeti, N. (2012). An Evaluation of Bagging, Boosting, and Random Forests for Land-Cover Classification in Cape Cod, Massachusetts, USA. *GIScience & Remote Sensing*, *49*(5), 623–643. https://doi.org/10.2747/1548-1603.49.5.623

Ghimire, B., Rogan, J., & Miller, J. (2010). Contextual land-cover classification: Incorporating spatial dependence in land-cover classification models using random forests and the Getis statistic. *Remote Sensing Letters*, *1*(1), 45–54. https://doi.org/10.1080/01431160903252327

Ghosh, A., Sharma, R., & Joshi, P. K. (2014). Random forest classification of urban landscape using Landsat archive and ancillary data: Combining seasonal maps with decision level fusion. *Applied Geography*, *48*, 31–41. https://doi.org/10.1016/j.apgeog.2014.01.003

Ghosh, S. M., & Behera, M. D. (2018). Aboveground biomass estimation using multisensor data synergy and machine learning algorithms in a dense tropical forest. *Applied Geography*, *96*, 29–40. https://doi.org/10.1016/j.apgeog.2018.05.011

Gianinetto, M., & Scaioni, M. (2003). Fusion of aerial and satellite imagery over the city of Venezia. *2003 2nd GRSS/ISPRS Joint Workshop on Remote Sensing and Data Fusion over Urban Areas*, 216–219. https://doi.org/10.1109/DFUA.2003.1219990

Gibril, M. B. A., Bakar, S. A., Yao, K., Idrees, M. O., & Pradhan, B. (2017). Fusion of RADARSAT-2 and multispectral optical remote sensing data for LULC extraction in a tropical agricultural area. *Geocarto International*, *32*(7), 735–748. https://doi.org/10.1080/10106049.2016.1170893

Giri, C. (2012). Brief Overview of Remote Sensing of Land Cover. In C. Giri (Ed.), *Remote Sensing of Land Use and Land Cover: Principles and Applications* (pp. 3–12). CRC Press. https://doi.org/10.1201/b11964-3

Giri, C., Pengra, B., Long, J., & Loveland, T. R. (2013). Next generation of global land cover characterization, mapping, and monitoring. *International Journal of Applied Earth Observation and Geoinformation*, *25*, 30–37. https://doi.org/10.1016/j.jag.2013.03.005

Gislason, P. O., Benediktsson, J. A., & Sveinsson, J. R. (2006). Random Forests for land cover classification. *Pattern Recognition Letters*, *27*(4), 294–300. https://doi.org/10.1016/j.patrec.2005.08.011

Gitelson, A. A., Kaufman, Y. J., & Merzlyak, M. N. (1996). Use of a green channel in remote sensing of global vegetation from EOS-MODIS. *Remote Sensing of Environment*, *58*(3), 289–298. https://doi.org/10.1016/S0034-4257(96)00072-7

Gitelson, A. A., Stark, R., Grits, U., Rundquist, D., Kaufman, Y., & Derry, D. (2002). Vegetation and soil lines in visible spectral space: A concept and technique for remote estimation of vegetation fraction. *International Journal of Remote Sensing*, *23*(13), 2537–2562. https://doi.org/10.1080/01431160110107806

Goel, N. S., & Qin, W. (1994). Influences of canopy architecture on relationships between various vegetation indices and LAI and Fpar: A computer simulation. *Remote Sensing Reviews*, *10*(4), 309–347. https://doi.org/10.1080/02757259409532252

Gómez, C., White, J. C., & Wulder, M. A. (2016). Optical remotely sensed time series data for land cover classification: A review. *ISPRS Journal of Photogrammetry and Remote Sensing*, *116*, 55–72. https://doi.org/10.1016/j.isprsjprs.2016.03.008

Gong, P., & Howarth, P. J. (1992). Land-use classification of SPOT HRV data using a cover-frequency method. *International Journal of Remote Sensing*, *13*(8), 1459–1471. https://doi.org/10.1080/01431169208904202

Gong, P., Li, X., Wang, J., Bai, Y., Chen, B., Hu, T., Liu, X., Xu, B., Yang, J., Zhang, W., & Zhou, Y. (2020). Annual maps of global artificial impervious area (GAIA) between 1985 and 2018. *Remote Sensing of Environment*, *236*, 111510. https://doi.org/10.1016/j.rse.2019.111510

Gong, P., Wang, J., Yu, L., Zhao, Y., Zhao, Y., Liang, L., Niu, Z., Huang, X., Fu, H., Liu, S., Li, C., Li, X., Fu, W., Liu, C., Xu, Y., Wang, X., Cheng, Q., Hu, L., Yao, W., … Chen, J. (2013). Finer resolution observation and monitoring of global land cover: First mapping results with Landsat TM and ETM+ data. *International Journal of Remote Sensing*, *34*(7), 2607–2654. https://doi.org/10.1080/01431161.2012.748992

Gontia, N. K., & Tiwari, K. N. (2011). Yield Estimation Model and Water Productivity of Wheat Crop (Triticum aestivum) in an Irrigation Command Using Remote Sensing and GIS. *Journal of the Indian Society of Remote Sensing*, *39*(1), 27–37. https://doi.org/10.1007/s12524-011-0065-7

González-Dugo, M. P., & Mateos, L. (2008). Spectral vegetation indices for benchmarking water productivity of irrigated cotton and sugarbeet crops. *Agricultural Water Management*, *95*(1), 48–58. https://doi.org/10.1016/j.agwat.2007.09.001

Goodchild, M. F., Guo, H., Annoni, A., Bian, L., de Bie, K., Campbell, F., Craglia, M., Ehlers, M., van Genderen, J., Jackson, D., Lewis, A. J., Pesaresi, M., Remetey-Fülöpp, G., Simpson, R., Skidmore, A., Wang, C., & Woodgate, P. (2012). Next-generation Digital Earth. *Proceedings of the National Academy of Sciences*, *109*(28), 11088–11094. https://doi.org/10.1073/pnas.1202383109

Goodfellow, I., Bengio, Y., & Courville, A. (2016). *Deep Learning*. MIT Press.

Goodfellow, I., Pouget-Abadie, J., Mirza, M., Xu, B., Warde-Farley, D., Ozair, S., Courville, A., & Bengio, Y. (2020). Generative adversarial networks. *Communications of the ACM*, *63*(11), 139–144. https://doi.org/10.1145/3422622

Goodman, A. H., & Henderson-Sellers, A. (1988). Cloud detection and analysis: A review of recent progress. *Atmospheric Research*, *21*(3), 203–228. https://doi.org/10.1016/0169-8095(88)90027-0

Google Earth Engine. (2022). *Sentinel-1 Algorithms | Google Earth Engine*. Google Developers. https://developers.google.com/earth-engine/guides/sentinel1

Gordon, S. I. (1980). Utilizing LANDSAT imagery to monitor land-use change: A case study in ohio. *Remote Sensing of Environment*, *9*(3), 189–196. https://doi.org/10.1016/0034-4257(80)90028-0

Gorelick, N., Hancher, M., Dixon, M., Ilyushchenko, S., Thau, D., & Moore, R. (2017). Google Earth Engine: Planetary-scale geospatial analysis for everyone. *Remote Sensing of Environment*, *202*, 18–27. https://doi.org/10.1016/j.rse.2017.06.031

Gouvernment of Canada, N. R. (2008, January 29). *Pre-processing*. Natural Resources Canada. https://www.nrcan.gc.ca/maps-tools-and-publications/satellite-imagery-and-air-photos/tutorial-fundamentals-remote-sensing/image-interpretation-analysis/pre-processing/9403

Grinand, C., Rakotomalala, F., Gond, V., Vaudry, R., Bernoux, M., & Vieilledent, G. (2013). Estimating deforestation in tropical humid and dry forests in Madagascar from 2000 to 2010 using multi-date Landsat satellite images and the random forests classifier. *Remote Sensing of Environment*, *139*, 68–80. https://doi.org/10.1016/j.rse.2013.07.008

Gualtieri, J. A., & Cromp, R. F. (1999). Support vector machines for hyperspectral remote sensing classification. *27th AIPR Workshop: Advances in Computer-Assisted Recognition*, *3584*, 221–232. https://doi.org/10.1117/12.339824

Guan, Y., Zhou, Y., He, B., Liu, X., Zhang, H., & Feng, S. (2020). Improving Land Cover Change Detection and Classification With BRDF Correction and Spatial Feature Extraction Using Landsat Time Series: A Case of Urbanization in Tianjin, China. *IEEE Journal of Selected Topics in Applied Earth Observations and Remote Sensing*, *13*, 4166–4177. https://doi.org/10.1109/JSTARS.2020.3007562

Guo, J., Yang, J., Yue, H., Tan, H., Hou, C., & Li, K. (2021). CDnetV2: CNN-Based Cloud Detection for Remote Sensing Imagery With Cloud-Snow Coexistence. *IEEE Transactions on Geoscience and Remote Sensing*, *59*(1), 700–713. https://doi.org/10.1109/TGRS.2020.2991398

Guo, W. Q., Yang, T. B., Dai, J. G., Shi, L., & Lu, Z. Y. (2008). Vegetation cover changes and their relationship to climate variation in the source region of the Yellow River, China, 1990–2000. *International Journal of Remote Sensing*, *29*(7), 2085–2103. https://doi.org/10.1080/01431160701395229

Haack, B., Bryant, N., & Adams, S. (1987). An assessment of landsat MSS and TM data for urban and near-urban land-cover digital classification. *Remote Sensing of Environment*, *21*(2), 201–213. https://doi.org/10.1016/0034-4257(87)90053-8

Haase, D., Jänicke, C., & Wellmann, T. (2019). Front and back yard green analysis with subpixel vegetation fractions from earth observation data in a city. *Landscape and Urban Planning*, *182*, 44–54. https://doi.org/10.1016/j.landurbplan.2018.10.010

Hadley, D. (2009). Land use and the coastal zone. *Land Use Policy*, *26*, S198–S203. https://doi.org/10.1016/j.landusepol.2009.09.014

Hall, D. L., & Llinas, J. (1997). An introduction to multisensor data fusion. *Proceedings of the IEEE*, *85*(1), 6–23. https://doi.org/10.1109/5.554205

Han, Y., Javed, A., Jung, S., & Liu, S. (2020). Object-Based Change Detection of Very High Resolution Images by Fusing Pixel-Based Change Detection Results Using Weighted Dempster–Shafer Theory. *Remote Sensing*, *12*(6), 6. https://doi.org/10.3390/rs12060983

Hansen, M. C., Potapov, P. V., Moore, R., Hancher, M., Turubanova, S. A., Tyukavina, A., Thau, D., Stehman, S. V., Goetz, S. J., Loveland, T. R., Kommareddy, A., Egorov, A., Chini, L., Justice, C. O., & Townshend, J. R. G. (2013). High-Resolution Global Maps of 21st-Century Forest Cover Change. *Science*, *342*(6160), 850–853. https://doi.org/10.1126/science.1244693

Hansen, M., Dubayah, R., & DeFries, R. (1996). Classification trees: An alternative to traditional land cover classifiers. *International Journal of Remote Sensing*, *17*(5), 1075–1081. https://doi.org/10.1080/01431169608949069

Hao, P., Zhan, Y., Wang, L., Niu, Z., & Shakir, M. (2015). Feature Selection of Time Series MODIS Data for Early Crop Classification Using Random Forest: A Case Study in Kansas, USA. *Remote Sensing*, *7*(5), 5. https://doi.org/10.3390/rs70505347

Haralick, R. M., & Shapiro, L. G. (1985). Image segmentation techniques. *Computer Vision, Graphics, and Image Processing*, *29*(1), 100–132. https://doi.org/10.1016/S0734-189X(85)90153-7

Hashim, H., Abd Latif, Z., & Adnan, N. A. (2019). URBAN VEGETATION CLASSIFICATION WITH NDVI THRESHOLD VALUE METHOD WITH VERY HIGH RESOLUTION (VHR) PLEIADES IMAGERY. *The International Archives of the Photogrammetry, Remote Sensing and Spatial Information Sciences*, *XLII-4/W16*, 237–240. https://doi.org/10.5194/isprs-archives-XLII-4-W16-237-2019

Hassell, J. M., Begon, M., Ward, M. J., & Fèvre, E. M. (2017). Urbanization and Disease Emergence: Dynamics at the Wildlife–Livestock–Human Interface. *Trends in Ecology & Evolution*, *32*(1), 55–67. https://doi.org/10.1016/j.tree.2016.09.012

He, C., Gao, B., Huang, Q., Ma, Q., & Dou, Y. (2017). Environmental degradation in the urban areas of China: Evidence from multi-source remote sensing data. *Remote Sensing of Environment*, *193*, 65–75. https://doi.org/10.1016/j.rse.2017.02.027

He, L.-M., Kong, F.-S., & Shen, Z.-Q. (2005). Multiclass SVM based land cover classification with multisource data. *2005 International Conference on Machine Learning and Cybernetics*, *6*, 3541-3545 Vol. 6. https://doi.org/10.1109/ICMLC.2005.1527555

He, N., Fang, L., Li, S., Plaza, A., & Plaza, J. (2018). Remote Sensing Scene Classification Using Multilayer Stacked Covariance Pooling. *IEEE Transactions on Geoscience and Remote Sensing*, *56*(12), 6899–6910. https://doi.org/10.1109/TGRS.2018.2845668

He, N., Fang, L., Li, S., Plaza, J., & Plaza, A. (2020). Skip-Connected Covariance Network for Remote Sensing Scene Classification. *IEEE Transactions on NNs and Learning Systems*, *31*(5), 1461–1474. https://doi.org/10.1109/TNNLS.2019.2920374

Hecht-Nielsen, R., Drive, O., & Diego, S. (1987). Kolmogorov's Mapping NN Existence Theorem. *Proc. IEEE First Internat. Conf. NNs*, 11–14.

Heidari, A. A., Faris, H., Mirjalili, S., Aljarah, I., & Mafarja, M. (2020). Ant Lion Optimizer: Theory, Literature Review, and Application in Multilayer Perceptron NNs. In S. Mirjalili, J. Song Dong, & A. Lewis (Eds.), *Nature-Inspired Optimizers: Theories, Literature Reviews and Applications* (pp. 23–46). Springer International Publishing. https://doi.org/10.1007/978-3-030-12127-3_3

Helber, P., Bischke, B., Dengel, A., & Borth, D. (2019). EuroSAT: A Novel Dataset and Deep Learning Benchmark for Land Use and Land Cover Classification. *IEEE Journal of Selected Topics in Applied Earth Observations and Remote Sensing*, *12*(7), 2217–2226. https://doi.org/10.1109/JSTARS.2019.2918242

Henderson, J. V. (2003). Urbanization and Economic Development. *Annals of Economics and Finance*, *4*(2), 275–341.

Hendrycks, D., Lee, K., & Mazeika, M. (2019). Using Pre-Training Can Improve Model Robustness and Uncertainty. *Proceedings of the 36th International Conference on Machine Learning*, 2712–2721. https://proceedings.mlr.press/v97/hendrycks19a.html

Hengl, T., Walsh, M. G., Sanderman, J., Wheeler, I., Harrison, S. P., & Prentice, I. C. (2018). Global mapping of potential natural vegetation: An assessment of machine learning algorithms for estimating land potential. *PeerJ*, *6*, e5457. https://doi.org/10.7717/peerj.5457

Hinton, G. E. (2009). Deep belief networks. *Scholarpedia*, *4*(5), 5947. https://doi.org/10.4249/scholarpedia.5947

Hinton, G. E., & Salakhutdinov, R. R. (2006). Reducing the Dimensionality of Data with NNs. *Science*, *313*(5786), 504–507. https://doi.org/10.1126/science.1127647

Hoa, P. V., Giang, N. V., Binh, N. A., Hai, L. V. H., Pham, T.-D., Hasanlou, M., & Tien Bui, D. (2019). Soil Salinity Mapping Using SAR Sentinel-1 Data and Advanced Machine Learning Algorithms: A Case Study at Ben Tre Province of the Mekong River Delta (Vietnam). *Remote Sensing*, *11*(2), 2. https://doi.org/10.3390/rs11020128

Höfle, B., Hollaus, M., & Hagenauer, J. (2012). Urban vegetation detection using radiometrically calibrated small-footprint full-waveform airborne LiDAR data. *ISPRS Journal of Photogrammetry and Remote Sensing*, *67*, 134–147. https://doi.org/10.1016/j.isprsjprs.2011.12.003

Hornik, K., Stinchcombe, M., & White, H. (1989). Multilayer feedforward networks are universal approximators. *NNs*, *2*(5), 359–366. https://doi.org/10.1016/0893-6080(89)90020-8

Hou, B., Kou, H., & Jiao, L. (2016). Classification of Polarimetric SAR Images Using Multilayer Autoencoders and Superpixels. *IEEE Journal of Selected Topics in Applied Earth Observations and Remote Sensing*, *9*(7), 3072–3081. https://doi.org/10.1109/JSTARS.2016.2553104

Houghton, R. A., Hackler, J. L., & Lawrence, K. T. (1999). The U.S. Carbon Budget: Contributions from Land-Use Change. *Science*, *285*(5427), 574–578. https://doi.org/10.1126/science.285.5427.574

Howarth, P. J., & Boasson, E. (1983). Landsat digital enhancements for change detection in urban environments. *Remote Sensing of Environment*, *13*(2), 149–160. https://doi.org/10.1016/0034-4257(83)90019-6

Howarth, R. W. (2008). Coastal nitrogen pollution: A review of sources and trends globally and regionally. *Harmful Algae*, *8*(1), 14–20. https://doi.org/10.1016/j.hal.2008.08.015

Hu, F., Xia, G.-S., Hu, J., & Zhang, L. (2015). Transferring Deep Convolutional NNs for the Scene Classification of High-Resolution Remote Sensing Imagery. *Remote Sensing*, *7*(11), 11. https://doi.org/10.3390/rs71114680

Huang, C., Davis, L. S., & Townshend, J. R. G. (2002). An assessment of support vector machines for land cover classification. *International Journal of Remote Sensing*, *23*(4), 725–749. https://doi.org/10.1080/01431160110040323

Huang, X., Liu, J., Zhu, W., Atzberger, C., & Liu, Q. (2019). The Optimal Threshold and Vegetation Index Time Series for Retrieving Crop Phenology Based on a Modified Dynamic Threshold Method. *Remote Sensing*, *11*(23), 23. https://doi.org/10.3390/rs11232725

Huang, X., Zhang, L., & Gong, W. (2011). Information fusion of aerial images and LIDAR data in urban areas: Vector-stacking, re-classification and post-processing approaches. *International Journal of Remote Sensing*, *32*(1), 69–84. https://doi.org/10.1080/01431160903439882

Huete, A., Didan, K., Miura, T., Rodriguez, E. P., Gao, X., & Ferreira, L. G. (2002). Overview of the radiometric and biophysical performance of the MODIS vegetation indices. *Remote Sensing of Environment*, *83*(1), 195–213. https://doi.org/10.1016/S0034-4257(02)00096-2

Huete, A. R. (1988). A soil-adjusted vegetation index (SAVI). *Remote Sensing of Environment*, *25*(3), 295–309. https://doi.org/10.1016/0034-4257(88)90106-X

Hugenholtz, C. H., Levin, N., Barchyn, T. E., & Baddock, M. C. (2012). Remote sensing and spatial analysis of aeolian sand dunes: A review and outlook. *Earth-Science Reviews*, *111*(3), 319–334. https://doi.org/10.1016/j.earscirev.2011.11.006

Huiping, Z., Hong, J., & Qinghua, H. (2011). Landscape and Water Quality Change Detection in Urban Wetland: A Post-classification Comparison Method with IKONOS Data. *Procedia Environmental Sciences*, *10*, 1726–1731. https://doi.org/10.1016/j.proenv.2011.09.271

Hung, M.-C., & Ridd, M. K. (2002). A SUBPIXEL CLASSIFIER FOR URBAN LAND-COVER MAPPING BASED ON A MAXIMUM-LIKELIHOOD APPROACH AND EXPERT SYSTEM RULES. *Photogrammetric Engineering and Remote Sensing*, *68*(11). https://trid.trb.org/view/728156

Hurskainen, P., Adhikari, H., Siljander, M., Pellikka, P. K. E., & Hemp, A. (2019). Auxiliary datasets improve accuracy of object-based land use/land cover classification in heterogeneous savanna landscapes. *Remote Sensing of Environment*, *233*, 111354. https://doi.org/10.1016/j.rse.2019.111354

Hütt, C., Koppe, W., Miao, Y., & Bareth, G. (2016). Best Accuracy Land Use/Land Cover (LULC) Classification to Derive Crop Types Using Multitemporal, Multisensor, and Multi-Polarization SAR Satellite Images. *Remote Sensing*, *8*(8), 8. https://doi.org/10.3390/rs8080684

IBM. (2022, July 6). *What is Machine Learning?* IBM. https://www.ibm.com/cloud/learn/machine-learning

Ibrahim, E. S., Rufin, P., Nill, L., Kamali, B., Nendel, C., & Hostert, P. (2021). Mapping Crop Types and Cropping Systems in Nigeria with Sentinel-2 Imagery. *Remote Sensing*, *13*(17), 17. https://doi.org/10.3390/rs13173523

Ienco, D., Gaetano, R., Dupaquier, C., & Maurel, P. (2017). Land Cover Classification via Multitemporal Spatial Data by Deep Recurrent NNs. *IEEE Geoscience and Remote Sensing Letters*, *14*(10), 1685–1689. https://doi.org/10.1109/LGRS.2017.2728698

IGN. (n.d.-a). *Les satellites PLEIADES-Portail Spatial*. Retrieved September 29, 2022, from https://spatial.ign.fr/infos/pleiades

IGN. (n.d.-b). *RPG | Géoservices*. Retrieved October 4, 2022, from https://geoservices.ign.fr/rpg

IREA. (n.d.). *Optical Remote Sensing*. National Research Council of Italy. Retrieved September 27, 2022, from http://www.irea.cnr.it/en/index.php?option=com_k2&view=itemlist&task=category&id=1&Itemid=61

Isip, M. F., Alberto, R. T., & Biagtan, A. R. (2020). Exploring vegetation indices adequate in detecting twister disease of onion using Sentinel-2 imagery. *Spatial Information Research*, *28*(3), 369–375. https://doi.org/10.1007/s41324-019-00297-7

Jachowski, N. R. A., Quak, M. S. Y., Friess, D. A., Duangnamon, D., Webb, E. L., & Ziegler, A. D. (2013). Mangrove biomass estimation in Southwest Thailand using machine learning. *Applied Geography*, *45*, 311–321. https://doi.org/10.1016/j.apgeog.2013.09.024

Jackson, J. B. C., Kirby, M. X., Berger, W. H., Bjorndal, K. A., Botsford, L. W., Bourque, B. J., Bradbury, R. H., Cooke, R., Erlandson, J., Estes, J. A., Hughes, T. P., Kidwell, S., Lange, C. B., Lenihan, H. S., Pandolfi, J. M., Peterson, C. H., Steneck, R. S., Tegner, M. J., & Warner, R. R. (2001). Historical Overfishing and the Recent Collapse of Coastal Ecosystems. *Science*, *293*(5530), 629–637. https://doi.org/10.1126/science.1059199

Jamali, A. (2019). Evaluation and comparison of eight machine learning models in land use/land cover mapping using Landsat 8 OLI: A case study of the northern region of Iran. *SN Applied Sciences*, *1*(11), 1448. https://doi.org/10.1007/s42452-019-1527-8

James, P., Tzoulas, K., Adams, M. D., Barber, A., Box, J., Breuste, J., Elmqvist, T., Frith, M., Gordon, C., Greening, K. L., Handley, J., Haworth, S., Kazmierczak, A. E., Johnston, M., Korpela, K., Moretti, M., Niemelä, J., Pauleit, S., Roe, M. H., … Ward Thompson, C. (2009). Towards an integrated understanding of green space in

the European built environment. *Urban Forestry & Urban Greening*, *8*(2), 65–75. https://doi.org/10.1016/j.ufug.2009.02.001

Jawak, S. D., & Luis, A. J. (2013). Improved land cover mapping using high resolution multiangle 8-band WorldView-2 satellite remote sensing data. *Journal of Applied Remote Sensing*, *7*(1), 073573. https://doi.org/10.1117/1.JRS.7.073573

Jeppesen, J. H., Jacobsen, R. H., Inceoglu, F., & Toftegaard, T. S. (2019). A cloud detection algorithm for satellite imagery based on deep learning. *Remote Sensing of Environment*, *229*, 247–259. https://doi.org/10.1016/j.rse.2019.03.039

Jiang, W., He, G., Long, T., Ni, Y., Liu, H., Peng, Y., Lv, K., & Wang, G. (2018). Multilayer Perceptron NN for Surface Water Extraction in Landsat 8 OLI Satellite Images. *Remote Sensing*, *10*(5), 5. https://doi.org/10.3390/rs10050755

Jiang, Y., Lu, Z., Li, S., Lei, Y., Chu, Q., Yin, X., & Chen, F. (2020). Large-Scale and High-Resolution Crop Mapping in China Using Sentinel-2 Satellite Imagery. *Agriculture*, *10*(10), 10. https://doi.org/10.3390/agriculture10100433

Jiang, Z., Huete, A., Didan, K., & Miura, T. (2008). Development of a two-band enhanced vegetation index without a blue band. *Remote Sensing of Environment*, *112*(10), 3833–3845. https://doi.org/10.1016/j.rse.2008.06.006

Jin, Z., Azzari, G., You, C., Di Tommaso, S., Aston, S., Burke, M., & Lobell, D. B. (2019). Smallholder maize area and yield mapping at national scales with Google Earth Engine. *Remote Sensing of Environment*, *228*, 115–128. https://doi.org/10.1016/j.rse.2019.04.016

Jing, R., Gong, Z., & Guan, H. (2020). Land Cover Change Detection With VHR Satellite Imagery Based on Multi-Scale SLIC-CNN and SCAE Features. *IEEE Access*, *8*, 228070–228087. https://doi.org/10.1109/ACCESS.2020.3045740

Jones, H. G., & Vaughan, R. A. (2010). *Remote Sensing of Vegetation: Principles, Techniques, and Applications*. OUP Oxford.

Jozdani, S. E., Johnson, B. A., & Chen, D. (2019). Comparing Deep NNs, Ensemble Classifiers, and Support Vector Machine Algorithms for Object-Based Urban Land Use/Land Cover Classification. *Remote Sensing*, *11*(14), 14. https://doi.org/10.3390/rs11141713

Kadavi, P. R., & Lee, C.-W. (2018). Land cover classification analysis of volcanic island in Aleutian Arc using an artificial NN (ANN) and a support vector machine (SVM) from Landsat imagery. *Geosciences Journal*, *22*(4), 653–665. https://doi.org/10.1007/s12303-018-0023-2

Kalnay, E., & Cai, M. (2003). Impact of urbanization and land-use change on climate. *Nature*, *423*(6939), 6939. https://doi.org/10.1038/nature01675

Kamilaris, A., & Prenafeta-Boldú, F. X. (2018). A review of the use of convolutional NNs in agriculture. *The Journal of Agricultural Science*, *156*(3), 312–322. https://doi.org/10.1017/S0021859618000436

Kanellopoulos, I., Varfis, A., Wilkinson, G. G., & Megier, J. (1992). Land-cover discrimination in SPOT HRV imagery using an artificial NN—A 20-class experiment. *International Journal of Remote Sensing*, *13*(5), 917–924. https://doi.org/10.1080/01431169208904164

Karalas, K., Tsagkatakis, G., Zervakis, M., & Tsakalides, P. (2015). Deep learning for multi-label land cover classification. *Image and Signal Processing for Remote Sensing XXI*, *9643*, 244–257. https://doi.org/10.1117/12.2195082

Karpatne, A., Jiang, Z., Vatsavai, R. R., Shekhar, S., & Kumar, V. (2016). Monitoring Land-Cover Changes: A Machine-Learning Perspective. *IEEE Geoscience and Remote Sensing Magazine*, *4*(2), 8–21. https://doi.org/10.1109/MGRS.2016.2528038

Kattenborn, T., Leitloff, J., Schiefer, F., & Hinz, S. (2021). Review on Convolutional NNs (CNN) in vegetation remote sensing. *ISPRS Journal of Photogrammetry and Remote Sensing*, *173*, 24–49. https://doi.org/10.1016/j.isprsjprs.2020.12.010

Kavzoglu, T., & Colkesen, I. (2009). A kernel functions analysis for support vector machines for land cover classification. *International Journal of Applied Earth Observation and Geoinformation*, *11*(5), 352–359. https://doi.org/10.1016/j.jag.2009.06.002

Kavzoglu, T., & Mather, P. M. (2003). The use of backpropagating artificial NNs in land cover classification. *International Journal of Remote Sensing*, *24*(23), 4907–4938. https://doi.org/10.1080/0143116031000114851

Kavzoglu, T., & Tonbul, H. (2018). An experimental comparison of multi-resolution segmentation, SLIC and K-means clustering for object-based classification of VHR imagery. *International Journal of Remote Sensing*, *39*(18), 6020–6036. https://doi.org/10.1080/01431161.2018.1506592

Kawamura, K., Asai, H., Yasuda, T., Soisouvanh, P., & Phongchanmixay, S. (2021). Discriminating crops/weeds in an upland rice field from UAV images with the SLIC-RF algorithm. *Plant Production Science*, *24*(2), 198–215. https://doi.org/10.1080/1343943X.2020.1829490

Kelly, M., Blanchard, S., Kersten, E., & Koy, K. (2011). Terrestrial Remotely Sensed Imagery in Support of Public Health: New Avenues of Research Using Object-Based Image Analysis. *Remote Sensing*, *3*, 2321–2345. https://doi.org/10.3390/rs3112321

Keshtkar, H., Voigt, W., & Alizadeh, E. (2017). Land-cover classification and analysis of change using machine-learning classifiers and Multitemporal remote sensing imagery. *Arabian Journal of Geosciences*, *10*(6), 154. https://doi.org/10.1007/s12517-017-2899-y

Khorram, S., Nelson, S. A. C., Cakir, H., & van der Wiele, C. F. (2013). Digital Image Acquisition: Preprocessing and Data Reduction. In J. N. Pelton, S. Madry, & S. Camacho-Lara (Eds.), *Handbook of Satellite Applications* (pp. 809–837). Springer. https://doi.org/10.1007/978-1-4419-7671-0_46

Killeen, T. J., Calderon, V., Soria, L., Quezada, B., Steininger, M. K., Harper, G., Solórzano, L. A., & Tucker, C. J. (2007). Thirty Years of Land-cover Change in Bolivia. *AMBIO: A Journal of the Human Environment*, *36*(7), 600–606. https://doi.org/10.1579/0044-7447(2007)36[600:TYOLCI]2.0.CO;2

Kim, J.-W., Lu, Z., Jones, J. W., Shum, C. K., Lee, H., & Jia, Y. (2014). Monitoring Everglades freshwater marsh water level using L-band synthetic aperture RaDAR backscatter. *Remote Sensing of Environment*, *150*, 66–81. https://doi.org/10.1016/j.rse.2014.03.031

Kindu, M., Schneider, T., Teketay, D., & Knoke, T. (2013). Land Use/Land Cover Change Analysis Using Object-Based Classification Approach in Munessa-Shashemene Landscape of the Ethiopian Highlands. *Remote Sensing*, *5*(5), 5. https://doi.org/10.3390/rs5052411

Kiranyaz, S., Avci, O., Abdeljaber, O., Ince, T., Gabbouj, M., & Inman, D. J. (2021). 1D convolutional NNs and applications: A survey. *Mechanical Systems and Signal Processing*, *151*, 107398. https://doi.org/10.1016/j.ymssp.2020.107398

Klemas, V. (2010). Remote Sensing Techniques for Studying Coastal Ecosystems: An Overview. *Journal of Coastal Research*, *27*(1), 2–17. https://doi.org/10.2112/JCOASTRES-D-10-00103.1

Klemas, V. (2013). Remote Sensing of Coastal Wetland Biomass: An Overview. *Journal of Coastal Research*, *29*(5), 1016–1028. https://doi.org/10.2112/JCOASTRES-D-12-00237.1

Klemas, V. V. (2009). Sensors and Techniques for Observing Coastal Ecosystems. In X. Yang (Ed.), *Remote Sensing and Geospatial Technologies for Coastal Ecosystem Assessment and Management* (pp. 17–44). Springer. https://doi.org/10.1007/978-3-540-88183-4_2

Kogan, F. N. (1995). Application of vegetation index and brightness temperature for drought detection. *Advances in Space Research*, *15*(11), 91–100. https://doi.org/10.1016/0273-1177(95)00079-T

Köppen, W. (2011). The thermal zones of the Earth according to the duration of hot, moderate and cold periods and to the impact of heat on the organic world. *Meteorologische Zeitschrift*, *20*(3), 351–360. https://doi.org/10.1127/0941-2948/2011/105

Kotaridis, I., & Lazaridou, M. (2021). Remote sensing image segmentation advances: A meta-analysis. *ISPRS Journal of Photogrammetry and Remote Sensing*, *173*, 309–322. https://doi.org/10.1016/j.isprsjprs.2021.01.020

Kotsiantis, S. B., Zaharakis, I. D., & Pintelas, P. E. (2006). Machine learning: A review of classification and combining techniques. *Artificial Intelligence Review*, *26*(3), 159–190. https://doi.org/10.1007/s10462-007-9052-3

Krizhevsky, A., Sutskever, I., & Hinton, G. (2012). ImageNet Classification with Deep Convolutional NNs. *Neural Information Processing Systems*, *25*. https://doi.org/10.1145/3065386

Kuenzer, C., Dech, S., & Wagner, W. (Eds.). (2015). *Remote Sensing Time Series* (Vol. 22). Springer International Publishing. https://doi.org/10.1007/978-3-319-15967-6

Kulkarni, A., & Lowe, B. (2016). Random Forest Algorithm for Land Cover Classification. *Computer Science Faculty Publications and Presentations*. https://scholarworks.uttyler.edu/compsci_fac/1

Kumar, P., Huan, T., Li, X., & Yuan, Y. (2018). Panchromatic and Multispectral Remote Sensing Image Fusion Using Machine Learning for Classifying Bucolic and Farming Region. *International Journal of Computational Science and Engineering*, *15*, 340–370.

Kussul, N., Lavreniuk, M., Skakun, S., & Shelestov, A. (2017). Deep Learning Classification of Land Cover and Crop Types Using Remote Sensing Data. *IEEE Geoscience and Remote Sensing Letters*, *14*(5), 778–782. https://doi.org/10.1109/LGRS.2017.2681128

Lambin, E. F., & Ehrlich, D. (1997). Land-cover changes in sub-saharan Africa (1982–1991): Application of a change index based on remotely sensed surface temperature and vegetation indices at a continental scale. *Remote Sensing of Environment*, *61*(2), 181–200. https://doi.org/10.1016/S0034-4257(97)00001-1

Lambin, E. F., Turner, B. L., Geist, H. J., Agbola, S. B., Angelsen, A., Bruce, J. W., Coomes, O. T., Dirzo, R., Fischer, G., Folke, C., George, P. S., Homewood, K., Imbernon, J., Leemans, R., Li, X., Moran, E. F., Mortimore, M., Ramakrishnan, P. S., Richards, J. F., … Xu, J. (2001). The causes of land-use and land-cover change: Moving beyond the myths. *Global Environmental Change*, *11*(4), 261–269. https://doi.org/10.1016/S0959-3780(01)00007-3

Landmap. (n.d.). *2.5. Multi-Resolution Segmentation | Object-oriented Classification | Learning Materials*. Retrieved October 18, 2022, from http://learningzone.rspsoc.org.uk/index.php/Learning-Materials/Object-oriented-Classification/2.5.-Multi-Resolution-Segmentation

Langford, Z. L., Kumar, J., Hoffman, F. M., Breen, A. L., & Iversen, C. M. (2019). Arctic Vegetation Mapping Using Unsupervised Training Datasets and Convolutional NNs. *Remote Sensing*, *11*(1), 1. https://doi.org/10.3390/rs11010069

Lapedes, A., & Farber, R. (1989). How Neural Nets Work. In *Evolution, Learning and Cognition* (pp. 331–346). WORLD SCIENTIFIC. https://doi.org/10.1142/9789814434102_0012

Laporte, N. T., Goetz, S. J., Justice, C. O., & Heinicke, M. (1998). A new land cover map of central Africa derived from multi-resolution, Multitemporal AVHRR data. *International Journal of Remote Sensing*, *19*(18), 3537–3550. https://doi.org/10.1080/014311698213803

Lary, D. J., Alavi, A. H., Gandomi, A. H., & Walker, A. L. (2016). Machine learning in geosciences and remote sensing. *Geoscience Frontiers*, *7*(1), 3–10. https://doi.org/10.1016/j.gsf.2015.07.003

Lasaponara, R., & Lanorte, A. (2012). Satellite time-series analysis. *International Journal of Remote Sensing*, *33*(15), 4649–4652. https://doi.org/10.1080/01431161.2011.638342

Lauknes, T. R. (2011). *Rockslide Mapping in Norway by Means of Interferometric SAR Time Series Analysis* [Ph.D. Thesis]. The Arctic Universityof Norway UiT.

Lebahy, Y., & Le Délézir, R. (2006). *Le littoral agressé Pour une politique volontariste de l'aménagement en Bretagne*. Editions Apogée. https://bretagne-environnement.fr/littoral-agresse-pour-politique-volontariste-amenagement-bretagne

LeCun, Y., Bengio, Y., & Hinton, G. (2015). Deep learning. *Nature*, *521*(7553), 436–444. https://doi.org/10.1038/nature14539

Lee, H., & Kwon, H. (2016). Contextual deep CNN based hyperspectral classification. *2016 IEEE International Geoscience and Remote Sensing Symposium (IGARSS)*, 3322–3325. https://doi.org/10.1109/IGARSS.2016.7729859

Lepers, E., Lambin, E. F., Janetos, A. C., DeFries, R., Achard, F., Ramankutty, N., & Scholes, R. J. (2005). A Synthesis of Information on Rapid Land-cover Change for the Period 1981–2000. *BioScience*, *55*(2), 115–124. https://doi.org/10.1641/0006-3568(2005)055[0115:ASOIOR]2.0.CO;2

Li, B., Wei, W., Ferreira, A., & Tan, S. (2018). ReST-Net: Diverse Activation Modules and Parallel Subnets-Based CNN for Spatial Image Steganalysis. *IEEE Signal Processing Letters*, *25*(5), 650–654. https://doi.org/10.1109/LSP.2018.2816569

Li, E., Xia, J., Du, P., Lin, C., & Samat, A. (2017). Integrating Multilayer Features of Convolutional NNs for Remote Sensing Scene Classification. *IEEE Transactions on Geoscience and Remote Sensing*, *55*(10), 5653–5665. https://doi.org/10.1109/TGRS.2017.2711275

Li, H., Gu, H., Han, Y., & Yang, J. (2010). Object-oriented classification of high-resolution remote sensing imagery based on an improved colour structure code and a support vector machine. *International Journal of Remote Sensing*, *31*(6), 1453–1470. https://doi.org/10.1080/01431160903475266

Li, H., Zhang, C., Zhang, S., & Atkinson, P. M. (2020). Crop classification from full-year fully-polarimetric L-band UAVSAR time-series using the Random Forest algorithm. *International Journal of Applied Earth Observation and Geoinformation*, *87*, 102032. https://doi.org/10.1016/j.jag.2019.102032

Li, J., Pei, Y., Zhao, S., Xiao, R., Sang, X., & Zhang, C. (2020). A Review of Remote Sensing for Environmental Monitoring in China. *Remote Sensing*, *12*(7), 7. https://doi.org/10.3390/rs12071130

Li, J., Zheng, X., & Zhang, C. (2021). Retrospective research on the interactions between land-cover change and global warming using bibliometrics during 1991–2018. *Environmental Earth Sciences*, *80*(17), 573. https://doi.org/10.1007/s12665-021-09804-2

Li, L., Friedl, M. A., Xin, Q., Gray, J., Pan, Y., & Frolking, S. (2014). Mapping Crop Cycles in China Using MODIS-EVI Time Series. *Remote Sensing*, *6*(3), 3. https://doi.org/10.3390/rs6032473

Li, P., Ren, P., Zhang, X., Wang, Q., Zhu, X., & Wang, L. (2018). Region-Wise Deep Feature Representation for Remote Sensing Images. *Remote Sensing*, *10*(6), 6. https://doi.org/10.3390/rs10060871

Li, S., & Ma, Y. (2014). Urbanization, Economic Development and Environmental Change. *Sustainability*, *6*(8), 8. https://doi.org/10.3390/su6085143

Li, S., Song, W., Fang, L., Chen, Y., Ghamisi, P., & Benediktsson, J. A. (2019). Deep Learning for Hyperspectral Image Classification: An Overview. *IEEE Transactions on Geoscience and Remote Sensing*, *57*(9), 6690–6709. https://doi.org/10.1109/TGRS.2019.2907932

Li, X., Yuan, W., & Dong, W. (2021). A Machine Learning Method for Predicting Vegetation Indices in China. *Remote Sensing*, *13*(6), 6. https://doi.org/10.3390/rs13061147

Li, Z., & Chen, Z. (2011). Remote sensing indicators for crop growth monitoring at different scales. *2011 IEEE International Geoscience and Remote Sensing Symposium*, 4062–4065. https://doi.org/10.1109/IGARSS.2011.6050124

Liakos, K. G., Busato, P., Moshou, D., Pearson, S., & Bochtis, D. (2018). Machine Learning in Agriculture: A Review. *Sensors*, *18*(8), 8. https://doi.org/10.3390/s18082674

Liang, H., & Li, Q. (2016). Hyperspectral Imagery Classification Using Sparse Representations of Convolutional NN Features. *Remote Sensing*, *8*(2), 2. https://doi.org/10.3390/rs8020099

Liang, L., Wang, Z., & Li, J. (2019). The effect of urbanization on environmental pollution in rapidly developing urban agglomerations. *Journal of Cleaner Production*, *237*, 117649. https://doi.org/10.1016/j.jclepro.2019.117649

Lippmann, R. (1987). An introduction to computing with neural nets. *IEEE ASSP Magazine*, *4*(2), 4–22. https://doi.org/10.1109/MASSP.1987.1165576

Lira, P. K., Tambosi, L. R., Ewers, R. M., & Metzger, J. P. (2012). Land-use and land-cover change in Atlantic Forest landscapes. *Forest Ecology and Management*, *278*, 80–89. https://doi.org/10.1016/j.foreco.2012.05.008

Liu, B., Yu, X., Yu, A., Zhang, P., & Wan, G. (2018). Spectral-spatial classification of hyperspectral imagery based on recurrent NNs. *Remote Sensing Letters*, *9*(12), 1118–1127. https://doi.org/10.1080/2150704X.2018.1511933

Liu, C., & Li, X. (2012). Carbon storage and sequestration by urban forests in Shenyang, China. *Urban Forestry & Urban Greening*, *11*(2), 121–128. https://doi.org/10.1016/j.ufug.2011.03.002

Liu, D., Chen, N., Zhang, X., Wang, C., & Du, W. (2020). Annual large-scale urban land mapping based on Landsat time series in Google Earth Engine and OpenStreetMap data: A case study in the middle Yangtze River basin. *ISPRS Journal of Photogrammetry and Remote Sensing*, *159*, 337–351. https://doi.org/10.1016/j.isprsjprs.2019.11.021

Liu, D., & Xia, F. (2010). Assessing object-based classification: Advantages and limitations. *Remote Sensing Letters*, *1*(4), 187–194. https://doi.org/10.1080/01431161003743173

Liu, J., Pattey, E., & Jégo, G. (2012). Assessment of vegetation indices for regional crop green LAI estimation from Landsat images over multiple growing seasons. *Remote Sensing of Environment*, *123*, 347–358. https://doi.org/10.1016/j.rse.2012.04.002

Liu, L., Coops, N. C., Aven, N. W., & Pang, Y. (2017). Mapping urban tree species using integrated airborne hyperspectral and LiDAR remote sensing data. *Remote Sensing of Environment*, *200*, 170–182. https://doi.org/10.1016/j.rse.2017.08.010

Liu, T., & Yang, X. (2013). Mapping vegetation in an urban area with stratified classification and multiple endmember spectral mixture analysis. *Remote Sensing of Environment*, *133*, 251–264. https://doi.org/10.1016/j.rse.2013.02.020

Liu, X., Huang, Y., Xu, X., Li, X., Li, X., Ciais, P., Lin, P., Gong, K., Ziegler, A. D., Chen, A., Gong, P., Chen, J., Hu, G., Chen, Y., Wang, S., Wu, Q., Huang, K., Estes, L., & Zeng, Z. (2020). High-spatiotemporal-resolution mapping of global urban change from 1985 to 2015. *Nature Sustainability*, *3*(7), 7. https://doi.org/10.1038/s41893-020-0521-x

Liu, X.-H., Skidmore, A. K., & Van Oosten, H. (2002). Integration of classification methods for improvement of land-cover map accuracy. *ISPRS Journal of Photogrammetry and Remote Sensing*, *56*(4), 257–268. https://doi.org/10.1016/S0924-2716(02)00061-8

Liu, Y., Zhong, Y., & Qin, Q. (2018). Scene Classification Based on Multiscale Convolutional NN. *IEEE Transactions on Geoscience and Remote Sensing*, *56*(12), 7109–7121. https://doi.org/10.1109/TGRS.2018.2848473

Lizarazo, I. (2008). SVM-based segmentation and classification of remotely sensed data. *International Journal of Remote Sensing*, *29*(24), 7277–7283. https://doi.org/10.1080/01431160802326081

Lo, C. P., & Quattrochi, D. A. (2003). Land-Use and Land-Cover Change, Urban Heat Island Phenomenon, and Health Implications. *Photogrammetric Engineering & Remote Sensing*, *69*(9), 1053–1063. https://doi.org/10.14358/PERS.69.9.1053

Long, J., Shelhamer, E., & Darrell, T. (2015). *Fully Convolutional Networks for Semantic Segmentation*. 3431–3440. https://openaccess.thecvf.com/content_cvpr_2015/html/Long_Fully_Convolutional_Networks_2015_CVPR_paper.html

Long, T., Zhang, Z., He, G., Jiao, W., Tang, C., Wu, B., Zhang, X., Wang, G., & Yin, R. (2019). 30 m Resolution Global Annual Burned Area Mapping Based on Landsat Images and Google Earth Engine. *Remote Sensing*, *11*(5), 5. https://doi.org/10.3390/rs11050489

Lonjou, V., Desjardins, C., Hagolle, O., Petrucci, B., Tremas, T., Dejus, M., Makarau, A., & Auer, S. (2016). MACCS-ATCOR joint algorithm (MAJA). *Remote Sensing of Clouds and the Atmosphere XXI*, *10001*, 25–37. https://doi.org/10.1117/12.2240935

Loosvelt, L., Peters, J., Skriver, H., Lievens, H., Coillie, F. M. B. V., Baets, B. D., & Verhoest, N. E. C. (2012). Random Forests as a tool for estimating uncertainty at pixel-level in SAR image classification. *International Journal of Applied Earth Observation and Geoinformation*, *19*, 173–184. https://doi.org/10.1016/j.jag.2012.05.011

Lopez-Sanchez, J. M., Cloude, S. R., & Ballester-Berman, J. D. (2012). Rice Phenology Monitoring by Means of SAR Polarimetry at X-Band. *IEEE Transactions on Geoscience and Remote Sensing*, *50*(7), 2695–2709. https://doi.org/10.1109/TGRS.2011.2176740

Losiri, C., Nagai, M., Ninsawat, S., & Shrestha, R. P. (2016). Modeling Urban Expansion in Bangkok Metropolitan Region Using Demographic–Economic Data through Cellular Automata-Markov Chain and Multilayer Perceptron-Markov Chain Models. *Sustainability*, *8*(7), 7. https://doi.org/10.3390/su8070686

Loveland, T. R. (2012). History of land cover mapping. In C. P. Giri (Ed.), *Remote sensing of land use and land cover: Principles and applications* (pp. 13–22). CRC Press. https://pubs.er.usgs.gov/publication/70156861

Loveland, T. R., Reed, B. C., Brown, J. F., Ohlen, D. O., Zhu, Z., Yang, L., & Merchant, J. W. (2000). Development of a global land cover characteristics database and IGBP DISCover from 1 km AVHRR data. *International Journal of Remote Sensing*, *21*(6–7), 1303–1330. https://doi.org/10.1080/014311600210191

Lu, D., Batistella, M., Mausel, P., & Moran, E. (2007). Mapping and monitoring land degradation risks in the Western Brazilian Amazon using multitemporal Landsat TM/ETM+ images. *Land Degradation & Development*, *18*(1), 41–54. https://doi.org/10.1002/ldr.762

Lu, D., Hetrick, S., & Moran, E. (2010). Land Cover Classification in a Complex Urban-Rural Landscape with QuickBird Imagery. *Photogrammetric Engineering & Remote Sensing*, *76*(10), 1159–1168. https://doi.org/10.14358/PERS.76.10.1159

Lu, D., Mausel, P., Batistella, M., & Moran, E. (2004). Comparison of Land-Cover Classification Methods in the Brazilian Amazon Basin. *Photogrammetric Engineering & Remote Sensing*, *70*(6), 723–731. https://doi.org/10.14358/PERS.70.6.723

Lu, D., Mausel, P., Brondízio, E., & Moran, E. (2004). Change detection techniques. *International Journal of Remote Sensing*, *25*(12), 2365–2401. https://doi.org/10.1080/0143116031000139863

Lu, D., & Weng, Q. (2007). A survey of image classification methods and techniques for improving classification performance. *International Journal of Remote Sensing*, *28*(5), 823–870. https://doi.org/10.1080/01431160600746456

Lu, J., Tan, L., & Jiang, H. (2021). Review on Convolutional NN (CNN) Applied to Plant Leaf Disease Classification. *Agriculture*, *11*(8), 8. https://doi.org/10.3390/agriculture11080707

Lunetta, R. S., Johnson, D. M., Lyon, J. G., & Crotwell, J. (2004). Impacts of imagery temporal frequency on land-cover change detection monitoring. *Remote Sensing of Environment*, *89*(4), 444–454. https://doi.org/10.1016/j.rse.2003.10.022

Luus, F. P. S., Salmon, B. P., van den Bergh, F., & Maharaj, B. T. J. (2015). Multiview Deep Learning for Land-Use Classification. *IEEE Geoscience and Remote Sensing Letters*, *12*(12), 2448–2452. https://doi.org/10.1109/LGRS.2015.2483680

Lyon, J. G., Yuan, D., Lunetta, R., & Elvidge, C. D. (1998). A change detection experiment using vegetation indices. *Photogrammetric Engineering and Remote Sensing*, *64*(2), 143–150.

Lyu, H., Lu, H., Mou, L., Li, W., Wright, J., Li, X., Li, X., Zhu, X. X., Wang, J., Yu, L., & Gong, P. (2018). Long-Term Annual Mapping of Four Cities on Different Continents by Applying a Deep Information Learning Method to Landsat Data. *Remote Sensing*, *10*(3), 3. https://doi.org/10.3390/rs10030471

Ma, J., Cheng, J. C. P., Lin, C., Tan, Y., & Zhang, J. (2019). Improving air quality prediction accuracy at larger temporal resolutions using deep learning and transfer learning techniques. *Atmospheric Environment*, *214*, 116885. https://doi.org/10.1016/j.atmosenv.2019.116885

Ma, L., Fu, T., Blaschke, T., Li, M., Tiede, D., Zhou, Z., Ma, X., & Chen, D. (2017). Evaluation of Feature Selection Methods for Object-Based Land Cover Mapping of Unmanned Aerial Vehicle Imagery Using Random Forest and Support Vector Machine Classifiers. *ISPRS International Journal of Geo-Information*, *6*(2), 2. https://doi.org/10.3390/ijgi6020051

Ma, L., Liu, Y., Zhang, X., Ye, Y., Yin, G., & Johnson, B. A. (2019). Deep learning in remote sensing applications: A meta-analysis and review. *ISPRS Journal of Photogrammetry and Remote Sensing*, *152*, 166–177. https://doi.org/10.1016/j.isprsjprs.2019.04.015

Maglione, P., Parente, C., & Vallario, A. (2014). Coastline extraction using high resolution WorldView-2 satellite imagery. *European Journal of Remote Sensing*, *47*(1), 685–699. https://doi.org/10.5721/EuJRS20144739

Mahdianpari, M., Salehi, B., Rezaee, M., Mohammadimanesh, F., & Zhang, Y. (2018). Very Deep Convolutional NNs for Complex Land Cover Mapping Using Multispectral Remote Sensing Imagery. *Remote Sensing*, *10*(7), 7. https://doi.org/10.3390/rs10071119

Mahmood, R., Pielke Sr, R., Hubbard, K., yogi, D., Bonan, G., Lawrence, P., McNider, R., Mcalpine, C., Etter, A., Gameda, S., Qian, B., Carleton, A., Beltran-Przekurat, A., Chase, T., Quintanar, A., Adegoke, J., Vezhapparambu, S., Conner, G., Asefi-Najafabady, S., & Syktus, J. (2010). Impacts of Land Use/Land Cover Change on Climate and Future Research Priorities. *Bulletin of the American Meteorological Society*, *91*, 37–46. https://doi.org/10.1175/2009BAMS2769.1

Main-Knorn, M., Pflug, B., Louis, J., Debaecker, V., Müller-Wilm, U., & Gascon, F. (2017, October 4). *Sen2Cor for Sentinel-2*. Image and Signal Processing for Remote Sensing. https://doi.org/10.1117/12.2278218

Major, D. J., Baret, F., & Guyot, G. (1990). A ratio vegetation index adjusted for soil brightness. *International Journal of Remote Sensing*, *11*(5), 727–740. https://doi.org/10.1080/01431169008955053

Maktav, D., Erbek, F. S., & Jürgens, C. (2005). Remote sensing of urban areas. *International Journal of Remote Sensing*, *26*(4), 655–659. https://doi.org/10.1080/01431160512331316469

Manandhar, R., Odeh, I. O. A., & Ancev, T. (2009). Improving the Accuracy of Land Use and Land Cover Classification of Landsat Data Using Post-Classification Enhancement. *Remote Sensing*, *1*(3), 3. https://doi.org/10.3390/rs1030330

Mandal, D., Kumar, V., Ratha, D., Dey, S., Bhattacharya, A., Lopez-Sanchez, J. M., McNairn, H., & Rao, Y. S. (2020). Dual polarimetric RaDAR vegetation index for crop growth monitoring using sentinel-1 SAR data. *Remote Sensing of Environment*, *247*, 111954. https://doi.org/10.1016/j.rse.2020.111954

Marceau, D. J., Gratton, D. J., Fournier, R. A., & Fortin, J.-P. (1994). Remote sensing and the measurement of geographical entities in a forested environment. 2. The optimal spatial resolution. *Remote Sensing of Environment*, *49*(2), 105–117. https://doi.org/10.1016/0034-4257(94)90047-7

Marcial-Pablo, M. de J., Gonzalez-Sanchez, A., Jimenez-Jimenez, S. I., Ontiveros-Capurata, R. E., & Ojeda-Bustamante, W. (2019). Estimation of vegetation fraction using RGB and multispectral images from UAV. *International Journal of Remote Sensing*, *40*(2), 420–438. https://doi.org/10.1080/01431161.2018.1528017

Mardian, J., Berg, A., & Daneshfar, B. (2021). Evaluating the temporal accuracy of grassland to cropland change detection using multitemporal image analysis. *Remote Sensing of Environment*, *255*, 112292. https://doi.org/10.1016/j.rse.2021.112292

Margono, B. A., Turubanova, S., Zhuravleva, I., Potapov, P., Tyukavina, A., Baccini, A., Goetz, S., & Hansen, M. C. (2012). Mapping and monitoring deforestation and forest degradation in Sumatra (Indonesia) using Landsat time series data sets from 1990 to 2010. *Environmental Research Letters*, *7*(3), 034010. https://doi.org/10.1088/1748-9326/7/3/034010

Marmanis, D., Datcu, M., Esch, T., & Stilla, U. (2016). Deep Learning Earth Observation Classification Using ImageNet Pretrained Networks. *IEEE Geoscience and Remote Sensing Letters*, *13*(1), 105–109. https://doi.org/10.1109/LGRS.2015.2499239

Masalu, D. C. P. (2002). Coastal Erosion and Its Social and Environmental Aspects in Tanzania: A Case Study in Illegal Sand Mining. *Coastal Management*, *30*(4), 347–359. https://doi.org/10.1080/089207502900255

Maselli, F., Papale, D., Puletti, N., Chirici, G., & Corona, P. (2009). Combining remote sensing and ancillary data to monitor the gross productivity of water-limited forest ecosystems. *Remote Sensing of Environment*, *113*(3), 657–667. https://doi.org/10.1016/j.rse.2008.11.008

Mason, D. C., Scott, T. R., & Dance, S. L. (2010). Remote sensing of intertidal morphological change in Morecambe Bay, U.K., between 1991 and 2007. *Estuarine, Coastal and Shelf Science*, *87*(3), 487–496. https://doi.org/10.1016/j.ecss.2010.01.015

Mathieu, R., Aryal, J., & Chong, A. K. (2007). Object-Based Classification of Ikonos Imagery for Mapping Large-Scale Vegetation Communities in Urban Areas. *Sensors*, *7*(11), 11. https://doi.org/10.3390/s7112860

Matsushita, B., Yang, W., Chen, J., Onda, Y., & Qiu, G. (2007). Sensitivity of the Enhanced Vegetation Index (EVI) and Normalized Difference Vegetation Index (NDVI) to Topographic Effects: A Case Study in High-Density Cypress Forest. *Sensors (Basel, Switzerland)*, *7*(11), 2636–2651.

Maxwell, A. E., Warner, T. A., & Fang, F. (2018). Implementation of machine-learning classification in remote sensing: An applied review. *International Journal of Remote Sensing*, *39*(9), 2784–2817. https://doi.org/10.1080/01431161.2018.1433343

Mazzia, V., Khaliq, A., & Chiaberge, M. (2020). Improvement in Land Cover and Crop Classification based on Temporal Features Learning from Sentinel-2 Data Using Recurrent-Convolutional NN (R-CNN). *Applied Sciences*, *10*(1), 1. https://doi.org/10.3390/app10010238

McNairn, H., & Shang, J. (2016). A Review of Multitemporal Synthetic Aperture RaDAR (SAR) for Crop Monitoring. In Y. Ban (Ed.), *Multitemporal Remote Sensing: Methods and Applications* (pp. 317–340). Springer International Publishing. https://doi.org/10.1007/978-3-319-47037-5_15

Memon, N., Parikh, H., Patel, S. B., Patel, D., & Patel, V. D. (2021). Automatic land cover classification of multi-resolution dualpol data using convolutional NN (CNN). *Remote Sensing Applications: Society and Environment*, *22*, 100491. https://doi.org/10.1016/j.rsase.2021.100491

Mensah, J. V. (1997). Causes and Effects of Coastal Sand Mining in Ghana. *Singapore Journal of Tropical Geography*, *18*(1), 69–88. https://doi.org/10.1111/1467-9493.00005

Meroni, M., d'Andrimont, R., Vrieling, A., Fasbender, D., Lemoine, G., Rembold, F., Seguini, L., & Verhegghen, A. (2021). Comparing land surface phenology of major European crops as derived from SAR and multispectral data of Sentinel-1 and -2. *Remote Sensing of Environment*, *253*, 112232. https://doi.org/10.1016/j.rse.2020.112232

Meshram, V., Patil, K., Meshram, V., Hanchate, D., & Ramkteke, S. D. (2021). Machine learning in agriculture domain: A state-of-art survey. *Artificial Intelligence in the Life Sciences*, *1*, 100010. https://doi.org/10.1016/j.ailsci.2021.100010

Messina, G., Peña, J. M., Vizzari, M., & Modica, G. (2020). A Comparison of UAV and Satellites Multispectral Imagery in Monitoring Onion Crop. An Application in the 'Cipolla Rossa di Tropea' (Italy). *Remote Sensing*, *12*(20), 20. https://doi.org/10.3390/rs12203424

Meyer, W. B., & Turner, B. L. (1994). *Changes in Land Use and Land Cover: A Global Perspective* (Vol. 4). Cambridge University Press.

Milioto, A., Lottes, P., & Stachniss, C. (2018). Real-Time Semantic Segmentation of Crop and Weed for Precision Agriculture Robots Leveraging Background Knowledge in CNNs. *2018 IEEE International Conference on Robotics and Automation (ICRA)*, 2229–2235. https://doi.org/10.1109/ICRA.2018.8460962

Millard, K., & Richardson, M. (2015). On the Importance of Training Data Sample Selection in Random Forest Image Classification: A Case Study in Peatland Ecosystem Mapping. *Remote Sensing*, *7*(7), 7. https://doi.org/10.3390/rs70708489

Mishra, N. B., & Crews, K. A. (2014). Mapping vegetation morphology types in a dry savanna ecosystem: Integrating hierarchical object-based image analysis with Random Forest. *International Journal of Remote Sensing*, *35*(3), 1175–1198. https://doi.org/10.1080/01431161.2013.876120

Mishra, V. N., & Rai, P. K. (2016). A remote sensing aided multilayer perceptron-Markov chain analysis for land use and land cover change prediction in Patna district (Bihar), India. *Arabian Journal of Geosciences*, *9*(4), 249. https://doi.org/10.1007/s12517-015-2138-3

Moisa, M. B., Dejene, I. N., Merga, B. B., & Gemeda, D. O. (2022). Impacts of land use/land cover dynamics on land surface temperature using geospatial techniques in Anger River Sub-basin, Western Ethiopia. *Environmental Earth Sciences*, *81*(3), 99. https://doi.org/10.1007/s12665-022-10221-2

Moody, A., & Woodcock, C. E. (1995). The influence of scale and the spatial characteristics of landscapes on land-cover mapping using remote sensing. *Landscape Ecology*, *10*(6), 363–379. https://doi.org/10.1007/BF00130213

Moomaw, R. L., & Shatter, A. M. (1996). Urbanization and Economic Development: A Bias toward Large Cities? *Journal of Urban Economics*, *40*(1), 13–37. https://doi.org/10.1006/juec.1996.0021

Moreno-González, R., Campillo, J. A., & León, V. M. (2013). Influence of an intensive agricultural drainage basin on the seasonal distribution of organic pollutants in seawater from a Mediterranean coastal lagoon (Mar Menor, SE Spain). *Marine Pollution Bulletin*, *77*(1), 400–411. https://doi.org/10.1016/j.marpolbul.2013.09.040

Morgan, J. L., & Gergel, S. E. (2013). Automated analysis of aerial photographs and potential for historic forest mapping. *Canadian Journal of Forest Research*, *43*(8), 699–710. https://doi.org/10.1139/cjfr-2012-0492

Moskal, L. M., Styers, D. M., & Halabisky, M. (2011). Monitoring Urban Tree Cover Using Object-Based Image Analysis and Public Domain Remotely Sensed Data. *Remote Sensing*, *3*(10), 10. https://doi.org/10.3390/rs3102243

Mossinger, J., White, M., & Goymer, P. (2013). Coastal regions. *Nature*, *504*(7478), 7478. https://doi.org/10.1038/504035a

Mou, L., Ghamisi, P., & Zhu, X. X. (2017). Deep Recurrent NNs for Hyperspectral Image Classification. *IEEE Transactions on Geoscience and Remote Sensing*, *55*(7), 3639–3655. https://doi.org/10.1109/TGRS.2016.2636241

Mouat, D. A., Mahin, G. G., & Lancaster, J. (1993). Remote sensing techniques in the analysis of change detection. *Geocarto International*, *8*(2), 39–50. https://doi.org/10.1080/10106049309354407

Mougin, E., Proisy, C., Marty, G., Fromard, F., Puig, H., Betoulle, J. L., & Rudant, J. P. (1999). Multifrequency and multipolarization RaDAR backscattering from mangrove forests. *IEEE Transactions on Geoscience and Remote Sensing*, *37*(1), 94–102. https://doi.org/10.1109/36.739128

Mountrakis, G., Im, J., & Ogole, C. (2011). Support vector machines in remote sensing: A review. *ISPRS Journal of Photogrammetry and Remote Sensing*, *66*(3), 247–259. https://doi.org/10.1016/j.isprsjprs.2010.11.001

Mulianga, B., Bégué, A., Clouvel, P., & Todoroff, P. (2015). Mapping Cropping Practices of a Sugarcane-Based Cropping System in Kenya Using Remote Sensing. *Remote Sensing*, *7*(11), 11. https://doi.org/10.3390/rs71114428

Muñoz, D. F., Muñoz, P., Alipour, A., Moftakhari, H., Moradkhani, H., & Mortazavi, B. (2021). Fusing Multisource Data to Estimate the Effects of Urbanization, Sea Level Rise, and Hurricane Impacts on Long-Term Wetland Change Dynamics. *IEEE Journal of Selected Topics in Applied Earth Observations and Remote Sensing*, *14*, 1768–1782. https://doi.org/10.1109/JSTARS.2020.3048724

Murtagh, F. (1991). Multilayer perceptrons for classification and regression. *Neurocomputing*, *2*(5–6), 183–197. https://doi.org/10.1016/0925-2312(91)90023-5

Nagy, A., Szabó, A., Adeniyi, O. D., & Tamás, J. (2021). Wheat Yield Forecasting for the Tisza River Catchment Using Landsat 8 NDVI and SAVI Time Series and Reported Crop Statistics. *Agronomy*, *11*(4), 4. https://doi.org/10.3390/agronomy11040652

Nasrallah, A., Baghdadi, N., El Hajj, M., Darwish, T., Belhouchette, H., Faour, G., Darwich, S., & Mhawej, M. (2019). Sentinel-1 Data for Winter Wheat Phenology Monitoring and Mapping. *Remote Sensing*, *11*(19), 2228. https://doi.org/10.3390/rs11192228

Nay, J., Burchfield, E., & Gilligan, J. (2018). A machine-learning approach to forecasting remotely sensed vegetation health. *International Journal of Remote Sensing*, *39*(6), 1800–1816. https://doi.org/10.1080/01431161.2017.1410296

Neumann, B., Vafeidis, A. T., Zimmermann, J., & Nicholls, R. J. (2015). Future Coastal Population Growth and Exposure to Sea-Level Rise and Coastal Flooding—A Global Assessment. *PLOS ONE*, *10*(3), e0118571. https://doi.org/10.1371/journal.pone.0118571

Neyns, R., & Canters, F. (2022). Mapping of Urban Vegetation with High-Resolution Remote Sensing: A Review. *Remote Sensing*, *14*(4), 4. https://doi.org/10.3390/rs14041031

Ng, A. (2011). *Sparse autoencoder*. CS294A Lecture Notes 72.

Nicholson, S. E., Davenport, M. L., & Malo, A. R. (1990). A comparison of the vegetation response to rainfall in the Sahel and East Africa, using normalized difference vegetation index from NOAA AVHRR. *Climatic Change*, *17*(2–3), 209–241. https://doi.org/10.1007/BF00138369

Niculescu, S., Billey, A., & Jr, H. T.-O.-A. (2018). Random forest classification using Sentinel-1 and Sentinel-2 series for vegetation monitoring in the Pays de Brest (France). *Remote Sensing for Agriculture, Ecosystems, and Hydrology XX*, *10783*, 1078305. https://doi.org/10.1117/12.2325546

Niculescu, S., Xia, J., Roberts, D., & Billey, A. (2020). Rotation Forests and Random Forest Classifiers for Monitoring of Vegetation in Pays de Brest (france). *ISPRS - International Archives of the Photogrammetry, Remote Sensing and Spatial Information Sciences*, *43B3*, 727–732. https://doi.org/10.5194/isprs-archives-XLIII-B3-2020-727-2020

Niemeyer, I., & Canty, M. J. (2003). *Pixel-based and object-oriented change detection analysis using high-resolution imagery* (No. 92-894-5654–X; p. 6).

Nijhawan, R., Sharma, H., Sahni, H., & Batra, A. (2017). A Deep Learning Hybrid CNN Framework Approach for Vegetation Cover Mapping Using Deep Features. *2017 13th International Conference on Signal-Image Technology & Internet-Based Systems (SITIS)*, 192–196. https://doi.org/10.1109/SITIS.2017.41

Nikfar, M., Zoej, M. J. V., Mohammadzadeh, A., Mokhtarzade, M., & Navabi, A. (2012). Optimization of multiresolution segmentation by using a genetic algorithm. *Journal of Applied Remote Sensing*, *6*(1), 063592. https://doi.org/10.1117/1.JRS.6.063592

Niu, S., Qiu, X., Lei, B., Ding, C., & Fu, K. (2020). Parameter Extraction Based on Deep NN for SAR Target Simulation. *IEEE Transactions on Geoscience and Remote Sensing*, *58*(7), 4901–4914. https://doi.org/10.1109/TGRS.2020.2968493

Niu, X., & Ban, Y. (2013). Multitemporal RADARSAT-2 polarimetric SAR data for urban land-cover classification using an object-based support vector machine and a rule-based approach. *International Journal of Remote Sensing*, *34*(1), 1–26. https://doi.org/10.1080/01431161.2012.700133

Nixon, M. S., & Aguado, A. S. (2020). 8—Region-based analysis. In M. S. Nixon & A. S. Aguado (Eds.), *Feature Extraction and Image Processing for Computer Vision (Fourth Edition)* (pp. 399–432). Academic Press. https://doi.org/10.1016/B978-0-12-814976-8.00008-7

Nogueira, K., Penatti, O. A. B., & Santos, J. A. dos. (2017). Towards Better Exploiting Convolutional NNs for Remote Sensing Scene Classification. *Pattern Recognition*, *61*, 539–556. https://doi.org/10.1016/j.patcog.2016.07.001

Nordberg, M.-L., & Evertson, J. (2005). Vegetation index differencing and linear regression for change detection in a Swedish mountain range using Landsat TM® and ETM+® imagery. *Land Degradation & Development*, *16*(2), 139–149. https://doi.org/10.1002/ldr.660

Nowak, D. J., Rowntree, R. A., McPherson, E. G., Sisinni, S. M., Kerkmann, E. R., & Stevens, J. C. (1996). Measuring and analyzing urban tree cover. *Landscape and Urban Planning*, *36*(1), 49–57. https://doi.org/10.1016/S0169-2046(96)00324-6

Ok, A. O., Akar, O., & Gungor, O. (2012). Evaluation of random forest method for agricultural crop classification. *European Journal of Remote Sensing*, *45*(1), 421–432. https://doi.org/10.5721/EuJRS20124535

Oliphant, A. J., Thenkabail, P. S., Teluguntla, P., Xiong, J., Gumma, M. K., Congalton, R. G., & Yadav, K. (2019). Mapping cropland extent of Southeast and Northeast Asia using multi-year time-series Landsat 30-m data using a random forest classifier on the Google Earth Engine Cloud. *International Journal of Applied Earth Observation and Geoinformation*, *81*, 110–124. https://doi.org/10.1016/j.jag.2018.11.014

Ollivro, J. (2015). *Bretagne. 150 ans d'évolution démographique* (fr). PUR. http://eso-rennes.cnrs.fr/fr/publications/collection-espace-et-territoires-p-u-r/bretagne-150-ans-d-evolution-demographique.html

Olofsson, J., & Hickler, T. (2008). Effects of human land-use on the global carbon cycle during the last 6,000 years. *Vegetation History and Archaeobotany*, *17*(5), 605–615. https://doi.org/10.1007/s00334-007-0126-6

Olofsson, P., Foody, G. M., Herold, M., Stehman, S. V., Woodcock, C. E., & Wulder, M. A. (2014). Good practices for estimating area and assessing accuracy of land change. *Remote Sensing of Environment*, *148*, 42–57. https://doi.org/10.1016/j.rse.2014.02.015

Oruc, M., Marangoz, A. M., & Buyuksalih, G. (2004). COMPARISON OF PIXEL-BASED AND OBJECT-ORIENTED CLASSIFICATION APPROACHES USING LANDSAT-7 ETM SPECTRAL BANDS. *Proceedings of ISPRS Conference*, 5.

Ossola, A., & Hopton, M. E. (2018). Measuring urban tree loss dynamics across residential landscapes. *Science of The Total Environment*, *612*, 940–949. https://doi.org/10.1016/j.scitotenv.2017.08.103

Otukei, J. R., & Blaschke, T. (2010). Land cover change assessment using decision trees, support vector machines and maximum likelihood classification algorithms. *International Journal of Applied Earth Observation and Geoinformation*, *12*, S27–S31. https://doi.org/10.1016/j.jag.2009.11.002

Ozesmi, S. L., & Bauer, M. E. (2002). Satellite remote sensing of wetlands. *Wetlands Ecology and Management*, *10*(5), 381–402. https://doi.org/10.1023/A:1020908432489

Ozturk, D. (2015). Urban Growth Simulation of Atakum (Samsun, Turkey) Using Cellular Automata-Markov Chain and Multilayer Perceptron-Markov Chain Models. *Remote Sensing*, *7*(5), 5. https://doi.org/10.3390/rs70505918

Pal, M. (2006). Support vector machine-based feature selection for land cover classification: A case study with DAIS hyperspectral data. *International Journal of Remote Sensing*, *27*(14), 2877–2894. https://doi.org/10.1080/01431160500242515

Pal, M. (2008). Ensemble of support vector machines for land cover classification. *International Journal of Remote Sensing*, *29*(10), 3043–3049. https://doi.org/10.1080/01431160802007624

Pal, M., & Mather, P. (2005). Support vector machines for classification in remote sensing. *International Journal of Remote Sensing*, *26*. https://doi.org/10.1080/01431160512331314083

Pal, M., & Mather, P. M. (2003). An assessment of the effectiveness of decision tree methods for land cover classification. *Remote Sensing of Environment*, *86*(4), 554–565. https://doi.org/10.1016/S0034-4257(03)00132-9

Pal, N. R., & Pal, S. K. (1993). A review on image segmentation techniques. *Pattern Recognition*, *26*(9), 1277–1294. https://doi.org/10.1016/0031-3203(93)90135-J

Palchowdhuri, Y., Valcarce-Diñeiro, R., King, P., & Sanabria-Soto, M. (2018). Classification of Multitemporal spectral indices for crop type mapping: A case study in Coalville, UK. *The Journal of Agricultural Science*, *156*(1), 24–36. https://doi.org/10.1017/S0021859617000879

Pan, B., Shi, Z., & Xu, X. (2017). MugNet: Deep learning for hyperspectral image classification using limited samples. *ISPRS Journal of Photogrammetry and Remote Sensing*, *145*. https://doi.org/10.1016/j.isprsjprs.2017.11.003

Pan, Y., Li, L., Zhang, J., Liang, S., Zhu, X., & Sulla-Menashe, D. (2012). Winter wheat area estimation from MODIS-EVI time series data using the Crop Proportion Phenology Index. *Remote Sensing of Environment*, *119*, 232–242. https://doi.org/10.1016/j.rse.2011.10.011

Pan, Z., Huang, J., Zhou, Q., Wang, L., Cheng, Y., Zhang, H., Blackburn, G. A., Yan, J., & Liu, J. (2015). Mapping crop phenology using NDVI time-series derived from HJ-1 A/B data. *International Journal of Applied Earth Observation and Geoinformation*, *34*, 188–197. https://doi.org/10.1016/j.jag.2014.08.011

Panda, S. S., Ames, D. P., & Panigrahi, S. (2010). Application of Vegetation Indices for Agricultural Crop Yield Prediction Using NN Techniques. *Remote Sensing*, *2*(3), 3. https://doi.org/10.3390/rs2030673

Pandey, P. C., Koutsias, N., Petropoulos, G. P., Srivastava, P. K., & Ben Dor, E. (2021). Land use/land cover in view of earth observation: Data sources, input dimensions, and classifiers—a review of the state of the art. *Geocarto International*, *36*(9), 957–988. https://doi.org/10.1080/10106049.2019.1629647

Paola, J. D., & Schowengerdt, R. A. (1995). A review and analysis of backpropagation NNs for classification of remotely-sensed multispectral imagery. *International Journal of Remote Sensing*, *16*(16), 3033–3058. https://doi.org/10.1080/01431169508954607

Parmehr, E. G., Amati, M., Taylor, E. J., & Livesley, S. J. (2016). Estimation of urban tree canopy cover using random point sampling and remote sensing methods. *Urban Forestry & Urban Greening*, *20*, 160–171. https://doi.org/10.1016/j.ufug.2016.08.011

Patnaik, R. (2018). Impact of Industrialization on Environment and Sustainable Solutions – Reflections from a South Indian Region. *IOP Conference Series: Earth and Environmental Science*, *120*(1), 012016. https://doi.org/10.1088/1755-1315/120/1/012016

Pauleit, S., Ennos, R., & Golding, Y. (2005). Modeling the environmental impacts of urban land use and land cover change—A study in Merseyside, UK. *Landscape and Urban Planning*, *71*(2), 295–310. https://doi.org/10.1016/j.landurbplan.2004.03.009

Pearson, R. L., & Miller, L. D. (1972). Remote mapping of standing crop biomass for estimation of the productivity of the shortgrass prairie, Pawnee National Grasslands, Colorado. *Proceedings of the 8th International Symposium on Remote Sensing of the Environment*, II: 1355-1379.

Pei, J., Huang, Y., Huo, W., Zhang, Y., Yang, J., & Yeo, T.-S. (2018). SAR Automatic Target Recognition Based on Multiview Deep Learning Framework. *IEEE Transactions on Geoscience and Remote Sensing*, *56*(4), 2196–2210. https://doi.org/10.1109/TGRS.2017.2776357

Peña-Barragán, J. M., Ngugi, M. K., Plant, R. E., & Six, J. (2011). Object-based crop identification using multiple vegetation indices, textural features and crop phenology. *Remote Sensing of Environment*, *115*(6), 1301–1316. https://doi.org/10.1016/j.rse.2011.01.009

Penatti, O. A. B., Nogueira, K., & dos Santos, J. A. (2015). Do deep features generalize from everyday objects to remote sensing and aerial scenes domains? *2015 IEEE Conference on Computer Vision and Pattern Recognition Workshops (CVPRW)*, 44–51. https://doi.org/10.1109/CVPRW.2015.7301382

Persson, M., Duckett, T., & Lilienthal, A. J. (2008). Fusion of aerial images and sensor data from a ground vehicle for improved semantic mapping. *Robotics and Autonomous Systems*, *56*(6), 483–492. https://doi.org/10.1016/j.robot.2008.03.002

Peters, A. J., Walter-Shea, E. A., Ji, L., Viña, A., Hayes, M., & Svoboda, M. D. (2002). Drought monitoring with NDVI-based Standardized Vegetation Index. *Photogramm Eng*, *68*(1), 71–75.

Petit, C., Scudder, T., & Lambin, E. (2001). Quantifying processes of land-cover change by remote sensing: Resettlement and rapid land-cover changes in south-eastern Zambia. *International Journal of Remote Sensing*, *22*(17), 3435–3456. https://doi.org/10.1080/01431160010006881

Pham, L. T. H., & Brabyn, L. (2017). Monitoring mangrove biomass change in Vietnam using SPOT images and an object-based approach combined with machine learning algorithms. *ISPRS Journal of Photogrammetry and Remote Sensing*, *128*, 86–97. https://doi.org/10.1016/j.isprsjprs.2017.03.013

Phinzi, K., & Ngetar, N. S. (2019). Land use/land cover dynamics and soil erosion in the Umzintlava catchment (T32E), Eastern Cape, South Africa. *Transactions of the Royal Society of South Africa*, *74*(3), 223–237. https://doi.org/10.1080/0035919X.2019.1634652

Phiri, D., & Morgenroth, J. (2017). Developments in Landsat Land Cover Classification Methods: A Review. *Remote Sensing*, *9*(9), 9. https://doi.org/10.3390/rs9090967

Phiri, D., Morgenroth, J., Xu, C., & Hermosilla, T. (2018). Effects of pre-processing methods on Landsat OLI-8 land cover classification using OBIA and random forests classifier. *International Journal of Applied Earth Observation and Geoinformation*, *73*, 170–178. https://doi.org/10.1016/j.jag.2018.06.014

Picard, G., Thuy Le Toan, & Mattia, F. (2003). Understanding c-band RaDAR backscatter from wheat canopy using a multiple-scattering coherent model. *IEEE Transactions on Geoscience and Remote Sensing*, *41*(7), 1583–1591. https://doi.org/10.1109/TGRS.2003.813353

Pouliot, D., Latifovic, R., Zabcic, N., Guindon, L., & Olthof, I. (2014). Development and assessment of a 250m spatial resolution MODIS annual land cover time series (2000–2011) for the forest region of Canada derived from change-based updating. *Remote Sensing of Environment*, *140*, 731–743. https://doi.org/10.1016/j.rse.2013.10.004

PrecisionHawk. (n.d.). *NDVI, VARI, and Other Vegetation Indices for use with Drones*. Retrieved October 11, 2022, from https://www.precisionhawk.com/agriculture/vegetation-indices

Primavera, J. H. (2006). Overcoming the impacts of aquaculture on the coastal zone. *Ocean & Coastal Management*, *49*(9), 531–545. https://doi.org/10.1016/j.ocecoaman.2006.06.018

Pu, R., & Landry, S. (2012). A comparative analysis of high spatial resolution IKONOS and WorldView-2 imagery for mapping urban tree species. *Remote Sensing of Environment*, *124*, 516–533. https://doi.org/10.1016/j.rse.2012.06.011

Puissant, A., Rougier, S., & Stumpf, A. (2014). Object-oriented mapping of urban trees using Random Forest classifiers. *International Journal of Applied Earth Observation and Geoinformation*, *26*, 235–245. https://doi.org/10.1016/j.jag.2013.07.002

Pulliainen, J. T., Mikhela, P. J., Hallikainen, M. T., & Ikonen, J.-P. (1996). Seasonal dynamics of C-band backscatter of boreal forests with applications to biomass and soil moisture estimation. *IEEE Transactions on Geoscience and Remote Sensing*, *34*(3), 758–770. https://doi.org/10.1109/36.499781

Qi, J., Chehbouni, A., Huete, A. R., Kerr, Y. H., & Sorooshian, S. (1994). A modified soil adjusted vegetation index. *Remote Sensing of Environment*, *48*(2), 119–126. https://doi.org/10.1016/0034-4257(94)90134-1

Qi, Z., Yeh, A. G.-O., Li, X., & Lin, Z. (2012). A novel algorithm for land use and land cover classification using RADARSAT-2 polarimetric SAR data. *Remote Sensing of Environment*, *118*, 21–39. https://doi.org/10.1016/j.rse.2011.11.001

Qian, Y., Zhou, W., Li, W., & Han, L. (2015). Understanding the dynamic of greenspace in the urbanized area of Beijing based on high resolution satellite images. *Urban Forestry & Urban Greening*, *14*(1), 39–47. https://doi.org/10.1016/j.ufug.2014.11.006

Qiu, B., Li, W., Tang, Z., Chen, C., & Qi, W. (2015). Mapping paddy rice areas based on vegetation phenology and surface moisture conditions. *Ecological Indicators*, *56*, 79–86. https://doi.org/10.1016/j.ecolind.2015.03.039

Raciti, S. M., Hutyra, L. R., & Newell, J. D. (2014). Mapping carbon storage in urban trees with multi-source remote sensing data: Relationships between biomass, land use, and demographics in Boston neighborhoods. *Science of The Total Environment*, *500–501*, 72–83. https://doi.org/10.1016/j.scitotenv.2014.08.070

Rafiee, R., Salman Mahiny, A., & Khorasani, N. (2009). Assessment of changes in urban green spaces of Mashad city using satellite data. *International Journal of Applied Earth Observation and Geoinformation*, *11*(6), 431–438. https://doi.org/10.1016/j.jag.2009.08.005

Rahimzadeh Bajgiran, P., Darvishsefat, A. A., Khalili, A., & Makhdoum, M. F. (2008). Using AVHRR-based vegetation indices for drought monitoring in the Northwest of Iran. *Journal of Arid Environments*, *72*(6), 1086–1096. https://doi.org/10.1016/j.jaridenv.2007.12.004

Rahman, M. M., & Robson, A. J. (2016). A Novel Approach for Sugarcane Yield Prediction Using Landsat Time Series Imagery: A Case Study on Bundaberg Region. *Advances in Remote Sensing*, *5*(2), 2. https://doi.org/10.4236/ars.2016.52008

Räsänen, A., Rusanen, A., Kuitunen, M., & Lensu, A. (2013). What makes segmentation good? A case study in boreal forest habitat mapping. *International Journal of Remote Sensing*, *34*(23), 8603–8627. https://doi.org/10.1080/01431161.2013.845318

Raudys, S., & Pikelis, V. (1980). On dimensionality, sample size, classification error, and complexity of classification algorithm in pattern recognition. *IEEE Transactions on Pattern Analysis and Machine Intelligence*, *2*(3), 242–252. https://doi.org/10.1109/tpami.1980.4767011

Rebelo, L.-M., Finlayson, C. M., & Nagabhatla, N. (2009). Remote sensing and GIS for wetland inventory, mapping and change analysis. *Journal of Environmental Management*, *90*(7), 2144–2153. https://doi.org/10.1016/j.jenvman.2007.06.027

Redowan, M., Phinn, S. R., Roelfsema, C. M., & Aziz, A. A. (2022). Modeling forest cover dynamics in Bangladesh using multilayer perceptron NN with Markov chain. *Journal of Applied Remote Sensing*, *16*(3), 034502. https://doi.org/10.1117/1.JRS.16.034502

Région Bretagne. (2013). *La charte des espaces côtiers bretons: Pour un développement durable de la zone côtière bretonne · Région Bretagne*. Région Bretagne. https://www.bretagne.bzh/documents/la-charte-des-espaces-cotiers-bretons-pour-un-developpement-durable-de-la-zone-cotiere-bretonne/

Registre parcellaire graphique (RPG). (n.d.). Portail de l'artificialisation. Retrieved August 18, 2022, from https://artificialisation.developpement-durable.gouv.fr/bases-donnees/registre-parcellaire-graphique

Rejaur Rahman, Md., & Saha, S. K. (2008). Multi-resolution segmentation for object-based classification and accuracy assessment of land use/land cover classification using remotely sensed data. *Journal of the Indian Society of Remote Sensing*, *36*(2), 189–201. https://doi.org/10.1007/s12524-008-0020-4

Rembold, F., Meroni, M., Urbano, F., Csak, G., Kerdiles, H., Perez-Hoyos, A., Lemoine, G., Leo, O., & Negre, T. (2019). ASAP: A new global early warning system to detect anomaly hot spots of agricultural production for food security analysis. *Agricultural Systems*, *168*, 247–257. https://doi.org/10.1016/j.agsy.2018.07.002

Ren, & Malik. (2003). Learning a classification model for segmentation. *Proceedings Ninth IEEE International Conference on Computer Vision*, 10–17 vol.1. https://doi.org/10.1109/ICCV.2003.1238308

Ren, W., Zhong, Y., Meligrana, J., Anderson, B., Watt, W. E., Chen, J., & Leung, H.-L. (2003). Urbanization, land use, and water quality in Shanghai: 1947–1996. *Environment International*, *29*(5), 649–659. https://doi.org/10.1016/S0160-4120(03)00051-5

Richards, J. A. (1993). Sources and Characteristics of Remote Sensing Image Data. In J. A. Richards (Ed.), *Remote Sensing Digital Image Analysis: An Introduction* (pp. 1–37). Springer. https://doi.org/10.1007/978-3-642-88087-2_1

Rieu, C. (2011). *Le renouveau des campagnes bretonnes (Octant Analyse n°13)—Octant Analyse | Insee*. INSEE Bretagne. https://www.insee.fr/fr/statistiques/1292549

Rodríguez-Fernández, N. J., Aires, F., Richaume, P., Kerr, Y. H., Prigent, C., Kolassa, J., Cabot, F., Jiménez, C., Mahmoodi, A., & Drusch, M. (2015). Soil Moisture Retrieval Using NNs: Application to SMOS. *IEEE Transactions on Geoscience and Remote Sensing*, *53*(11), 5991–6007. https://doi.org/10.1109/TGRS.2015.2430845

Rodriguez-Galiano, V. F., Chica-Olmo, M., Abarca-Hernandez, F., Atkinson, P. M., & Jeganathan, C. (2012). Random Forest classification of Mediterranean land cover using multi-seasonal imagery and multi-seasonal texture. *Remote Sensing of Environment*, *121*, 93–107. https://doi.org/10.1016/j.rse.2011.12.003

Rodriguez-Galiano, V. F., & Chica-Rivas, M. (2014). Evaluation of different machine learning methods for land cover mapping of a Mediterranean area using multi-seasonal Landsat images and Digital Terrain Models. *International Journal of Digital Earth*, *7*(6), 492–509. https://doi.org/10.1080/17538947.2012.748848

Rodriguez-Galiano, V. F., Ghimire, B., Rogan, J., Chica-Olmo, M., & Rigol-Sanchez, J. P. (2012). An assessment of the effectiveness of a random forest classifier for land-cover classification. *ISPRS Journal of Photogrammetry and Remote Sensing*, *67*, 93–104. https://doi.org/10.1016/j.isprsjprs.2011.11.002

Romero, A., Gatta, C., & Camps-Valls, G. (2016). Unsupervised Deep Feature Extraction for Remote Sensing Image Classification. *IEEE Transactions on Geoscience and Remote Sensing*, *54*(3), 1349–1362. https://doi.org/10.1109/TGRS.2015.2478379

Rouault, S. (2019). *Observer l'occupation des sols pour guider les politiques d'aménagement (MOS)* (L'Ouest breton, Le Finistère, Le Pays de Brest et ses EPCI). ADEUPa Brest Bretagne. https://www.adeupa-

brest.fr/nos-publications/observer-loccupation-des-sols-pour-guider-les-politiques-damenagement-mos-0

Rouse, J. W., Haas, R. H., Scheel, J. A., & Deering, D. W. (1974). Monitoring Vegetation Systems in the Great Plains with ERTS. *Proceedings of the 3rd Earth Resource Technology Satellite (ERTS) Symposium*, *1*, 48–62.

Rousta, I., Olafsson, H., Moniruzzaman, M., Zhang, H., Liou, Y.-A., Mushore, T. D., & Gupta, A. (2020). Impacts of Drought on Vegetation Assessed by Vegetation Indices and Meteorological Factors in Afghanistan. *Remote Sensing*, *12*(15), 15. https://doi.org/10.3390/rs12152433

Roy, A., & Inamdar, A. B. (2019). Multitemporal Land Use Land Cover (LULC) change analysis of a dry semi-arid river basin in western India following a robust multisensor satellite image calibration strategy. *Heliyon*, *5*(4), e01478. https://doi.org/10.1016/j.heliyon.2019.e01478

Ruiz-Luna, A., & Berlanga-Robles, C. A. (2003). Land use, land cover changes and coastal lagoon surface reduction associated with urban growth in northwest Mexico. *Landscape Ecology*, *18*(2), 159–171. https://doi.org/10.1023/A:1024461215456

Rumelhart, D. E., Hinton, G. E., & Williams, R. J. (1986). Learning internal representations by error propagation. In *Parallel distributed processing: Explorations in the microstructure of cognition, vol. 1: Foundations* (pp. 318–362). MIT Press.

Rwanga, S. S., & Ndambuki, J. M. (2017). Accuracy Assessment of Land Use/Land Cover Classification Using Remote Sensing and GIS. *International Journal of Geosciences*, *08*(04), 04. https://doi.org/10.4236/ijg.2017.84033

Saatchi, S. S., Soares, J. V., & Alves, D. S. (1997). Mapping deforestation and land use in amazon rainforest by using SIR-C imagery. *Remote Sensing of Environment*, *59*(2), 191–202. https://doi.org/10.1016/S0034-4257(96)00153-8

Saba, F., Valadan Zoej, M. J., & Mokhtarzade, M. (2016). Optimization of Multiresolution Segmentation for Object-Oriented Road Detection from High-Resolution Images. *Canadian Journal of Remote Sensing*, *42*(2), 75–84. https://doi.org/10.1080/07038992.2016.1160770

Sadeghi, Y., St-Onge, B., Leblon, B., Prieur, J.-F., & Simard, M. (2018). Mapping boreal forest biomass from a SRTM and TanDEM-X based on canopy height model and Landsat spectral indices. *International Journal of Applied Earth Observation and Geoinformation*, *68*, 202–213. https://doi.org/10.1016/j.jag.2017.12.004

Safari, K., Prasad, S., & Labate, D. (2021). A Multiscale Deep Learning Approach for High-Resolution Hyperspectral Image Classification. *IEEE Geoscience and Remote Sensing Letters*, *18*(1), 167–171. https://doi.org/10.1109/LGRS.2020.2966987

Saini, R., & Ghosh, S. K. (2018). CROP CLASSIFICATION ON SINGLE DATE SENTINEL-2 IMAGERY USING RANDOM FOREST AND SUPPOR VECTOR MACHINE. *The International Archives of the Photogrammetry, Remote Sensing and Spatial Information Sciences*, *XLII–5*, 683–688. https://doi.org/10.5194/isprs-archives-XLII-5-683-2018

Sala, O. E., Chapin, F. S., Armesto, J. J., Berlow, E., Bloomfield, J., Dirzo, R., Huber-Sanwald, E., Huenneke, L. F., Jackson, R. B., Kinzig, A., Leemans, R., Lodge, D. M., Mooney, H. A., Oesterheld, M., Poff, N. L., Sykes, M. T., Walker, B. H., Walker, M., & Wall, D. H. (2000). Global biodiversity scenarios for the year 2100. *Science (New York, N.Y.)*, *287*(5459), 1770–1774. https://doi.org/10.1126/science.287.5459.1770

Samasse, K., Hanan, N. P., Anchang, J. Y., & Diallo, Y. (2020). A High-Resolution Cropland Map for the West African Sahel Based on High-Density Training Data, Google Earth Engine, and Locally Optimized Machine Learning. *Remote Sensing*, *12*(9), 9. https://doi.org/10.3390/rs12091436

Sanyal, J., & Lu, X. X. (2004). Application of Remote Sensing in Flood Management with Special Reference to Monsoon Asia: A Review. *Natural Hazards*, *33*(2), 283–301. https://doi.org/10.1023/B:NHAZ.0000037035.65105.95

Sarricolea, P., Serrano-Notivoli, R., Fuentealba, M., Hernández-Mora, M., de la Barrera, F., Smith, P., & Meseguer-Ruiz, Ó. (2020). Recent wildfires in Central Chile: Detecting links between burned areas and population exposure in the wildland urban interface. *Science of The Total Environment*, *706*, 135894. https://doi.org/10.1016/j.scitotenv.2019.135894

Savla, A., Israni, N., Dhawan, P., Mandholia, A., Bhadada, H., & Bhardwaj, S. (2015). Survey of classification algorithms for formulating yield prediction accuracy in precision agriculture. *2015 International Conference on Innovations in Information, Embedded and Communication Systems (ICIIECS)*, 1–7. https://doi.org/10.1109/ICIIECS.2015.7193120

Sazib, N., Mladenova, I., & Bolten, J. (2018). Leveraging the Google Earth Engine for Drought Assessment Using Global Soil Moisture Data. *Remote Sensing*, *10*(8), 8. https://doi.org/10.3390/rs10081265

Scheffer, M., Carpenter, S., & Young, B. de. (2005). Cascading effects of overfishing marine systems. *Trends in Ecology & Evolution*, *20*(11), 579–581. https://doi.org/10.1016/j.tree.2005.08.018

Schiewe, J. (2002). Segmentation of high-resolution remotely sensed data-concepts, applications and problems. *International Archives of Photogrammetry Remote Sensing and Spatial Information Sciences*, *34*(4), 380–385.

Schlund, M., & Erasmi, S. (2020). Sentinel-1 time series data for monitoring the phenology of winter wheat. *Remote Sensing of Environment*, *246*, 111814. https://doi.org/10.1016/j.rse.2020.111814

Schroff, F., Criminisi, A., & Zisserman, A. (2008, January 1). Object Class Segmentation using Random Forests. *Proceedings of the British Machine Vision Conference*. British Machine Vision Conference, Leeds,. https://doi.org/10.5244/C.22.54

Schulz, K., Hänsch, R., & Sörgel, U. (2018). Machine learning methods for remote sensing applications: An overview. *Earth Resources and Environmental Remote Sensing/GIS Applications IX*, *10790*, 1079002. https://doi.org/10.1117/12.2503653

Scott, G. J., England, M. R., Starms, W. A., Marcum, R. A., & Davis, C. H. (2017). Training Deep Convolutional NNs for Land–Cover Classification of High-Resolution Imagery. *IEEE Geoscience and Remote Sensing Letters*, *14*(4), 549–553. https://doi.org/10.1109/LGRS.2017.2657778

Seker, D. Z., Goksel, C., Kabdasli, S., Musaoglu, N., & Kaya, S. (2003). Investigation of coastal morphological changes due to river basin characteristics by means of remote sensing and GIS techniques. *Water Science and Technology*, *48*(10), 135–142. https://doi.org/10.2166/wst.2003.0558

Sekertekin, A., Marangoz, A. M., & Akcin, H. (2017). PIXEL-BASED CLASSIFICATION ANALYSIS OF LAND USE LAND COVER USING SENTINEL-2 AND LANDSAT-8 DATA. *The International Archives of the Photogrammetry, Remote Sensing and Spatial Information Sciences*, *XLII-4-W6*, 91–93. https://doi.org/10.5194/isprs-archives-XLII-4-W6-91-2017

Sellers, P. J. (1985). Canopy reflectance, photosynthesis and transpiration. *International Journal of Remote Sensing*, *6*(8), 1335–1372. https://doi.org/10.1080/01431168508948283

Sen, P. C., Hajra, M., & Ghosh, M. (2020). Supervised Classification Algorithms in Machine Learning: A Survey and Review. In J. K. Mandal & D. Bhattacharya (Eds.), *Emerging Technology in Modelling and Graphics* (pp. 99–111). Springer. https://doi.org/10.1007/978-981-13-7403-6_11

Senf, C., Hostert, P., & van der Linden, S. (2012). Using MODIS time series and random forests classification for mapping land use in South-East Asia. *2012 IEEE International Geoscience and Remote Sensing Symposium*, 6733–6736. https://doi.org/10.1109/IGARSS.2012.6352560

Sengupta, A., Ye, Y., Wang, R., Liu, C., & Roy, K. (2019). Going Deeper in Spiking NNs: VGG and Residual Architectures. *Frontiers in Neuroscience*, *13*. https://www.frontiersin.org/articles/10.3389/fnins.2019.00095

Serra, P., Pons, X., & Saurí, D. (2003). Post-classification change detection with data from different sensors: Some accuracy considerations. *International Journal of Remote Sensing*, *24*(16), 3311–3340. https://doi.org/10.1080/0143116021000021189

Seto, K. C., Sánchez-Rodríguez, R., & Fragkias, M. (2010). The New Geography of Contemporary Urbanization and the Environment. *Annual Review of Environment and Resources*, *35*(1), 167–194. https://doi.org/10.1146/annurev-environ-100809-125336

Seydi, S. T., Hasanlou, M., & Amani, M. (2020). A New End-to-End Multi-Dimensional CNN Framework for Land Cover/Land Use Change Detection in Multi-Source Remote Sensing Datasets. *Remote Sensing*, *12*(12), 12. https://doi.org/10.3390/rs12122010

Shafri, H. Z. M., & Anuar, M. I. (2008). Hyperspectral Signal Analysis for Detecting Disease Infection in Oil Palms. *2008 International Conference on Computer and Electrical Engineering*, 312–316. https://doi.org/10.1109/ICCEE.2008.196

Shahtahmassebi, A. R., Li, C., Fan, Y., Wu, Y., lin, Y., Gan, M., Wang, K., Malik, A., & Blackburn, G. A. (2021). Remote sensing of urban green spaces: A review. *Urban Forestry & Urban Greening*, *57*, 126946. https://doi.org/10.1016/j.ufug.2020.126946

Shalaby, A., & Tateishi, R. (2007). Remote sensing and GIS for mapping and monitoring land cover and land-use changes in the Northwestern coastal zone of Egypt. *Applied Geography*, *27*(1), 28–41. https://doi.org/10.1016/j.apgeog.2006.09.004

Shanahan, J. F., Schepers, J. S., Francis, D. D., Varvel, G. E., Wilhelm, W. W., Tringe, J. M., Schlemmer, M. R., & Major, D. J. (2001). Use of Remote-Sensing Imagery to Estimate Corn Grain Yield. *Agronomy Journal*, *93*(3), 583–589. https://doi.org/10.2134/agronj2001.933583x

Shao, Y., & Lunetta, R. S. (2012). Comparison of support vector machine, NN, and CART algorithms for the land-cover classification using limited training data points. *ISPRS Journal of Photogrammetry and Remote Sensing*, *70*, 78–87. https://doi.org/10.1016/j.isprsjprs.2012.04.001

Sharifi, A. (2020). Remotely sensed vegetation indices for crop nutrition mapping. *Journal of the Science of Food and Agriculture*, *100*(14), 5191–5196. https://doi.org/10.1002/jsfa.10568

Shendryk, Y., Rist, Y., Ticehurst, C., & Thorburn, P. (2019). Deep learning for multi-modal classification of cloud, shadow and land cover scenes in PlanetScope and Sentinel-2 imagery. *ISPRS Journal of Photogrammetry and Remote Sensing*, *157*, 124–136. https://doi.org/10.1016/j.isprsjprs.2019.08.018

Sheykhmousa, M., Mahdianpari, M., Ghanbari, H., Mohammadimanesh, F., Ghamisi, P., & Homayouni, S. (2020). Support Vector Machine Versus Random Forest for Remote Sensing Image Classification: A Meta-Analysis and Systematic Review. *IEEE Journal of Selected Topics in Applied Earth Observations and Remote Sensing*, *13*, 6308–6325. https://doi.org/10.1109/JSTARS.2020.3026724

Shi, D., & Yang, X. (2015). *Support Vector Machines for Land Cover Mapping from Remote Sensor Imagery* (pp. 265–279). https://doi.org/10.1007/978-94-017-9813-6_13

Shin, H.-C., Roth, H. R., Gao, M., Lu, L., Xu, Z., Nogues, I., Yao, J., Mollura, D., & Summers, R. M. (2016). Deep Convolutional NNs for Computer-Aided Detection: CNN Architectures, Dataset Characteristics and

Transfer Learning. *IEEE Transactions on Medical Imaging*, *35*(5), 1285–1298. https://doi.org/10.1109/TMI.2016.2528162

Shivakumar, B. R., & Rajashekararadhya, S. V. (2018). Investigation on Land Cover Mapping Capability of Maximum Likelihood Classifier: A Case Study on North Canara, India. *Procedia Computer Science*, *143*, 579–586. https://doi.org/10.1016/j.procs.2018.10.434

Shojanoori, R., & Shafri, H. (2016). Review on the Use of Remote Sensing for Urban Forest Monitoring. *Arboriculture & Urban Forestry*, *42*, 400–417. https://doi.org/10.48044/jauf.2016.034

Silva, L. P. e, Xavier, A. P. C., da Silva, R. M., & Santos, C. A. G. (2020). Modeling land cover change based on an artificial NN for a semiarid river basin in northeastern Brazil. *Global Ecology and Conservation*, *21*, e00811. https://doi.org/10.1016/j.gecco.2019.e00811

Singh, K. K., Vogler, J. B., Shoemaker, D. A., & Meentemeyer, R. K. (2012). LiDAR-Landsat data fusion for large-area assessment of urban land cover: Balancing spatial resolution, data volume and mapping accuracy. *ISPRS Journal of Photogrammetry and Remote Sensing*, *74*, 110–121. https://doi.org/10.1016/j.isprsjprs.2012.09.009

Singh, S. K., Srivastava, P. K., Gupta, M., Thakur, J. K., & Mukherjee, S. (2014). Appraisal of land use/land cover of mangrove forest ecosystem using support vector machine. *Environmental Earth Sciences*, *71*(5), 2245–2255. https://doi.org/10.1007/s12665-013-2628-0

Sinha, S., Sharma, L. K., & Nathawat, M. S. (2015). Improved Land-use/Land-cover classification of semi-arid deciduous forest landscape using thermal remote sensing. *The Egyptian Journal of Remote Sensing and Space Science*, *18*(2), 217–233. https://doi.org/10.1016/j.ejrs.2015.09.005

Smith, A. (2010). Image segmentation scale parameter optimization and land cover classification using the Random Forest algorithm. *Journal of Spatial Science*, *55*(1), 69–79. https://doi.org/10.1080/14498596.2010.487851

Soergel, U. (2010). Review of RaDAR Remote Sensing on Urban Areas. In U. Soergel (Ed.), *RaDAR Remote Sensing of Urban Areas* (pp. 1–47). Springer Netherlands. https://doi.org/10.1007/978-90-481-3751-0_1

Solberg, A. H. S. (2012). Remote Sensing of Ocean Oil-Spill Pollution. *Proceedings of the IEEE*, *100*(10), 2931–2945. https://doi.org/10.1109/JPROC.2012.2196250

Solberg, A. H. S., Jain, A. K., & Taxt, T. (1994). Multisource classification of remotely sensed data: Fusion of Landsat TM and SAR images. *IEEE Transactions on Geoscience and Remote Sensing*, *32*(4), 768–778. https://doi.org/10.1109/36.298006

Son, N.-T., Chen, C.-F., Chen, C.-R., & Minh, V.-Q. (2018). Assessment of Sentinel-1A data for rice crop classification using random forests and support vector machines. *Geocarto International*, *33*(6), 587–601. https://doi.org/10.1080/10106049.2017.1289555

Son, N.-T., Chen, C.-F., Chen, C.-R., Toscano, P., Cheng, Y.-S., Guo, H.-Y., & Syu, C.-H. (2021). A phenological object-based approach for rice crop classification using time-series Sentinel-1 Synthetic Aperture RaDAR (SAR) data in Taiwan. *International Journal of Remote Sensing*, *42*(7), 2722–2739. https://doi.org/10.1080/01431161.2020.1862440

Song, T., Kuang, L., Han, L., Wang, Y., & Liu, Q. H. (2018). Inversion of Rough Surface Parameters From SAR Images Using Simulation-Trained Convolutional NNs. *IEEE Geoscience and Remote Sensing Letters*, *15*(7), 1130–1134. https://doi.org/10.1109/LGRS.2018.2822821

Song, X., Duan, Z., & Jiang, X. (2012). Comparison of artificial NNs and support vector machine classifiers for land cover classification in Northern China using a SPOT-5 HRG image. *International Journal of Remote Sensing*, *33*(10), 3301–3320. https://doi.org/10.1080/01431161.2011.568531

Song, X.-P., Potapov, P. V., Krylov, A., King, L., Di Bella, C. M., Hudson, A., Khan, A., Adusei, B., Stehman, S. V., & Hansen, M. C. (2017). National-scale soybean mapping and area estimation in the United States using medium resolution satellite imagery and field survey. *Remote Sensing of Environment*, *190*, 383–395. https://doi.org/10.1016/j.rse.2017.01.008

Song, Y., & Wang, J. (2019). Mapping Winter Wheat Planting Area and Monitoring Its Phenology Using Sentinel-1 Backscatter Time Series. *Remote Sensing*, *11*(4), 449. https://doi.org/10.3390/rs11040449

Soofi, A. A., & Awan, A. (2017). Classification Techniques in Machine Learning: Applications and Issues. *Journal of Basic & Applied Sciences*, *13*, 459–465. https://doi.org/10.6000/1927-5129.2017.13.76

Spalding, M. D., Fox, H. E., Allen, G. R., Davidson, N., Ferdaña, Z. A., Finlayson, M., Halpern, B. S., Jorge, M. A., Lombana, A., Lourie, S. A., Martin, K. D., McManus, E., Molnar, J., Recchia, C. A., & Robertson, J. (2007). Marine Ecoregions of the World: A Bioregionalization of Coastal and Shelf Areas. *BioScience*, *57*(7), 573–583. https://doi.org/10.1641/B570707

Sparfel, L. (2011). Etude des changements d'occupation des sols dans la zone côtière à partir de données hétérogènes: Application au pays de Brest. *Géographie.Université de Bretagne occidentale*, 246.

Spirkovska, L. (1993). *A summary of image segmentation techniques*.

Srivastava, P. K., Han, D., Rico-Ramirez, M. A., Bray, M., & Islam, T. (2012). Selection of classification techniques for land use/land cover change investigation. *Advances in Space Research*, *50*(9), 1250–1265. https://doi.org/10.1016/j.asr.2012.06.032

Stefanski, J., Mack, B., & Waske, B. (2013). Optimization of Object-Based Image Analysis With Random Forests for Land Cover Mapping. *Selected Topics in Applied Earth Observations and Remote Sensing, IEEE Journal Of*, *6*, 2492–2504. https://doi.org/10.1109/JSTARS.2013.2253089

Steiner, D. (1970). Automation in photo interpretation. *Geoforum*, *1*(2), 75–88. https://doi.org/10.1016/0016-7185(70)90030-8

Stevens, F. R., Gaughan, A. E., Linard, C., & Tatem, A. J. (2015). Disaggregating Census Data for Population Mapping Using Random Forests with Remotely-Sensed and Ancillary Data. *PLOS ONE*, *10*(2), e0107042. https://doi.org/10.1371/journal.pone.0107042

Story, M., & Congalton, R. G. (1986). Accuracy Assessment: A User's Perspective. *PHOTOGRAMMETRIC ENGINEERING AND REMOTE SENSING*, *52*(3), 397–399.

Stumpf, A., & Kerle, N. (2011). Object-oriented mapping of landslides using Random Forests. *Remote Sensing of Environment*, *115*(10), 2564–2577. https://doi.org/10.1016/j.rse.2011.05.013

Sun, C., Bian, Y., Zhou, T., & Pan, J. (2019). Using of Multi-Source and Multitemporal Remote Sensing Data Improves Crop-Type Mapping in the Subtropical Agriculture Region. *Sensors*, *19*(10), 10. https://doi.org/10.3390/s19102401

Swanston, D. J., Bishop, J. M., & Mitchell, R. J. (1994). Simple adaptive momentum: New algorithm for training multilayer perceptrons. *Electronics Letters*, *30*(18), 18.

Symeonakis, E., Calvo-Cases, A., & Arnau-Rosalen, E. (2007). Land Use Change and Land Degradation in Southeastern Mediterranean Spain. *Environmental Management*, *40*(1), 80–94. https://doi.org/10.1007/s00267-004-0059-0

Szuster, B. W., Chen, Q., & Borger, M. (2011). A comparison of classification techniques to support land cover and land use analysis in tropical coastal zones. *Applied Geography*, *31*(2), 525–532. https://doi.org/10.1016/j.apgeog.2010.11.007

Talab Ou Ali, H., Niculescu, S., Sellin, V., & Bougault, C. (2017, November). Contribution de la nouvelle série d'images Sentinel-1 pour le suivi de la végétation côtière dans le Pays de Brest. *Spatial Analysis and GEOmatics 2017*. https://hal.archives-ouvertes.fr/hal-01650671

Talukdar, S., Singha, P., Mahato, S., Shahfahad, Pal, S., Liou, Y.-A., & Rahman, A. (2020). Land-Use Land-Cover Classification by Machine Learning Classifiers for Satellite Observations—A Review. *Remote Sensing*, *12*(7), 7. https://doi.org/10.3390/rs12071135

Tang, J., Deng, C., & Huang, G.-B. (2016). Extreme Learning Machine for Multilayer Perceptron. *IEEE Transactions on NNs and Learning Systems*, *27*(4), 809–821. https://doi.org/10.1109/TNNLS.2015.2424995

Tatsumi, K., Yamashiki, Y., Canales Torres, M. A., & Taipe, C. L. R. (2015). Crop classification of upland fields using Random forest of time-series Landsat 7 ETM+ data. *Computers and Electronics in Agriculture*, *115*, 171–179. https://doi.org/10.1016/j.compag.2015.05.001

Tewkesbury, A. P., Comber, A. J., Tate, N. J., Lamb, A., & Fisher, P. F. (2015). A critical synthesis of remotely sensed optical image change detection techniques. *Remote Sensing of Environment*, *160*, 1–14. https://doi.org/10.1016/j.rse.2015.01.006

Thanh Noi, P., & Kappas, M. (2018). Comparison of Random Forest, k-Nearest Neighbor, and Support Vector Machine Classifiers for Land Cover Classification Using Sentinel-2 Imagery. *Sensors*, *18*(1), 1. https://doi.org/10.3390/s18010018

The Nature Conservancy. (n.d.). The Nature Conservancy. Retrieved December 23, 2022, from https://www.nature.org/en-us/

Thenkabail, P. S. (Ed.). (2015). *Remotely Sensed Data Characterization, Classification, and Accuracies*. CRC Press. https://doi.org/10.1201/b19294

Thenkabail, P. S., Smith, R. B., & De Pauw, E. (2000). Hyperspectral Vegetation Indices and Their Relationships with Agricultural Crop Characteristics. *Remote Sensing of Environment*, *71*(2), 158–182. https://doi.org/10.1016/S0034-4257(99)00067-X

Thimm, G., & Fiesler, E. (1997). High-order and multilayer perceptron initialization. *IEEE Transactions on NNs*, *8*(2), 349–359. https://doi.org/10.1109/72.557673

Thomas, P., & Suhner, M.-C. (2015). A New Multilayer Perceptron Pruning Algorithm for Classification and Regression Applications. *Neural Processing Letters*, *42*(2), 437–458. https://doi.org/10.1007/s11063-014-9366-5

Thompson, M. M., & Mikhail, E. M. (1976). Automation in photogrammetry: Recent developments and applications (1972–1976). *Photogrammetria*, *32*(4), 111–145. https://doi.org/10.1016/0031-8663(76)90008-9

Thonfeld, F., Steinbach, S., Muro, J., & Kirimi, F. (2020). Long-Term Land Use/Land Cover Change Assessment of the Kilombero Catchment in Tanzania Using Random Forest Classification and Robust Change Vector Analysis. *Remote Sensing*, *12*(7), 7. https://doi.org/10.3390/rs12071057

Tichý, L., Chytrý, M., & Landucci, F. (2019). GRIMP: A machine-learning method for improving groups of discriminating species in expert systems for vegetation classification. *Journal of Vegetation Science*, *30*(1), 5–17. https://doi.org/10.1111/jvs.12696

Tigges, J., Lakes, T., & Hostert, P. (2013). Urban vegetation classification: Benefits of multitemporal RapidEye satellite data. *Remote Sensing of Environment*, *136*, 66–75. https://doi.org/10.1016/j.rse.2013.05.001

Timilsina, S., Sharma, S., & Aryal, J. (2019). MAPPING URBAN TREES WITHIN CADASTRAL PARCELS USING AN OBJECT-BASED CONVOLUTIONAL NN. *ISPRS Annals of Photogrammetry, Remote Sensing and Spatial Information Sciences*, *IV-5/W2*, 111–117. https://doi.org/10.5194/isprs-annals-IV-5-W2-111-2019

Tiquio, Ma. G. J. P., Marmier, N., & Francour, P. (2017). Management frameworks for coastal and marine pollution in the European and South East Asian regions. *Ocean & Coastal Management*, *135*, 65–78. https://doi.org/10.1016/j.ocecoaman.2016.11.003

Todd, W. J., Falls, S., & Dak, S. (1977). Urban and regional land use change detected by using Landsat data. In *Journal of Research of the U.S. Geological Survey* (Vol. 5, Issue 5, p. 6).

Toll, D. L. (1985). Effect of Landsat thematic mapper sensor parameters on land cover classification. *Remote Sensing of Environment*, *17*(2), 129–140. https://doi.org/10.1016/0034-4257(85)90069-0

Tong, M. X., Hansen, A., Hanson-Easey, S., Cameron, S., Xiang, J., Liu, Q., Sun, Y., Weinstein, P., Han, G.-S., Williams, C., & Bi, P. (2015). Infectious Diseases, Urbanization and Climate Change: Challenges in Future China. *International Journal of Environmental Research and Public Health*, *12*(9), 9. https://doi.org/10.3390/ijerph120911025

Tong, S. T. Y., & Chen, W. (2002). Modeling the relationship between land use and surface water quality. *Journal of Environmental Management*, *66*(4), 377–393. https://doi.org/10.1006/jema.2002.0593

Tong, X., Li, X., Xu, X., Xie, H., Feng, T., Sun, T., Jin, Y., & Liu, X. (2014). A Two-Phase Classification of Urban Vegetation Using Airborne LiDAR Data and Aerial Photography. *IEEE Journal of Selected Topics in Applied Earth Observations and Remote Sensing*, *7*(10), 4153–4166. https://doi.org/10.1109/JSTARS.2014.2312717

Tong, X.-Y., Xia, G.-S., Lu, Q., Shen, H., Li, S., You, S., & Zhang, L. (2020). Land-cover classification with high-resolution remote sensing images using transferable deep models. *Remote Sensing of Environment*, *237*, 111322. https://doi.org/10.1016/j.rse.2019.111322

Topac, E. (2018). *Design of a turbulent flow facility and development of an algorithm for PIV* [Technische Universität Wien]. https://doi.org/10.13140/RG.2.2.11352.75525

Townshend, J. R. G. (1992). Land cover. *International Journal of Remote Sensing*, *13*(6–7), 1319–1328. https://doi.org/10.1080/01431169208904193

Tran, H., Tran, T., & Kervyn, M. (2015). Dynamics of Land Cover/Land Use Changes in the Mekong Delta, 1973–2011: A Remote Sensing Analysis of the Tran Van Thoi District, Ca Mau Province, Vietnam. *Remote Sensing*, *7*(3), 3. https://doi.org/10.3390/rs70302899

Treitz, P. M., Howarth, P. J., & Gong, P. (1992). Application of satellite and GIS technologies for land-cover and land-use mapping at the rural-urban fringe—A case study. *Photogrammetric Engineering and Remote Sensing*, *58*, 439–448.

Trotter, C. M. (1991). Remotely-sensed data as an information source for geographical information systems in natural resource management a review. *International Journal of Geographical Information Systems*, *5*(2), 225–239. https://doi.org/10.1080/02693799108927845

Tsutsumida, N., & Comber, A. J. (2015). Measures of spatio-temporal accuracy for time series land cover data. *International Journal of Applied Earth Observation and Geoinformation*, *41*, 46–55. https://doi.org/10.1016/j.jag.2015.04.018

Tucker, C. J. (1979). Red and photographic infrared linear combinations for monitoring vegetation. *Remote Sensing of Environment*, *8*(2), 127–150. https://doi.org/10.1016/0034-4257(79)90013-0

Turner, B. L. (1997). The Sustainability Principle in Global Agendas: Implications for Understanding Land-Use/Cover Change. *The Geographical Journal*, *163*(2), 133–140. https://doi.org/10.2307/3060176

Turner, B. L., Lambin, E. F., & Reenberg, A. (2007). The emergence of land change science for global environmental change and sustainability. *Proceedings of the National Academy of Sciences*, *104*(52), 20666–20671. https://doi.org/10.1073/pnas.0704119104

Turner, B. L., Skole, D., Sanderson, S., Fischer, G., Fresco, L., & Leemans, R. (1995). Land-Use and Land-Cover Change: Science/research plan. *IGBP*, *35*, 132.

Tzotsos, A., & Argialas, D. (2008). Support Vector Machine Classification for Object-Based Image Analysis. In T. Blaschke, S. Lang, & G. J. Hay (Eds.), *Object-Based Image Analysis* (pp. 663–677). Springer Berlin Heidelberg. https://doi.org/10.1007/978-3-540-77058-9_36

Uddin, K., Matin, M. A., & Meyer, F. J. (2019). Operational Flood Mapping Using Multitemporal Sentinel-1 SAR Images: A Case Study from Bangladesh. *Remote Sensing*, *11*(13), 13. https://doi.org/10.3390/rs11131581

Ustuner, M., Sanli, F. B., Abdikan, S., Esetlili, M. T., & Kurucu, Y. (2014). Crop Type Classification Using Vegetation Indices of RapidEye Imagery. *The International Archives of the Photogrammetry, Remote Sensing and Spatial Information Sciences*, *XL–7*, 195–198. https://doi.org/10.5194/isprsarchives-XL-7-195-2014

Vafaei, S., Soosani, J., Adeli, K., Fadaei, H., Naghavi, H., Pham, T. D., & Tien Bui, D. (2018). Improving Accuracy Estimation of Forest Aboveground Biomass Based on Incorporation of ALOS-2 PALSAR-2 and Sentinel-2A Imagery and Machine Learning: A Case Study of the Hyrcanian Forest Area (Iran). *Remote Sensing*, *10*(2), 2. https://doi.org/10.3390/rs10020172

Valero, S., Arnaud, L., Planells, M., & Ceschia, E. (2021). Synergy of Sentinel-1 and Sentinel-2 Imagery for Early Seasonal Agricultural Crop Mapping. *Remote Sensing*, *13*, 4891. https://doi.org/10.3390/rs13234891

Vali, A., Comai, S., & Matteucci, M. (2020). Deep Learning for Land Use and Land Cover Classification Based on Hyperspectral and Multispectral Earth Observation Data: A Review. *Remote Sensing*, *12*(15), 15. https://doi.org/10.3390/rs12152495

Van de Voorde, T., De Genst, W., & Canters, F. (2007). Improving Pixel-based VHR Land-cover Classifications of Urban Areas with Post-classification Techniques. *Photogrammetric Engineering and Remote Sensing*, *73*(9). https://trid.trb.org/view/836104

Van de Voorde, T., Genst, W., Canters, F., Stephenne, N., Wolff, E., & Binard, M. (2004). Extraction of land use / land cover—Related information from very high resolution data in urban and suburban areas. *Remote Sensing in Transition*.

van der Sande, C. J., de Jong, S. M., & de Roo, A. P. J. (2003). A segmentation and classification approach of IKONOS-2 imagery for land cover mapping to assist flood risk and flood damage assessment. *International Journal of Applied Earth Observation and Geoinformation*, *4*(3), 217–229. https://doi.org/10.1016/S0303-2434(03)00003-5

van Genderen, J. L., & Lock, B. F. (1977). TESTING LAND-USE MAP ACCURACY. *Photogrammetric Engineering and Remote Sensing*, *43*(9). https://trid.trb.org/view/59678

Vanselow, K. A., & Samimi, C. (2014). Predictive Mapping of Dwarf Shrub Vegetation in an Arid High Mountain Ecosystem Using Remote Sensing and Random Forests. *Remote Sensing*, *6*(7), 7. https://doi.org/10.3390/rs6076709

Verburg, P. H., Kok, K., Pontius, R. G., & Veldkamp, A. (2006). Modeling Land-Use and Land-Cover Change. In E. F. Lambin & H. Geist (Eds.), *Land-Use and Land-Cover Change: Local Processes and Global Impacts* (pp. 117–135). Springer. https://doi.org/10.1007/3-540-32202-7_5

Vincent, P., Larochelle, H., Lajoie, I., Bengio, Y., & Manzagol, P.-A. (2010). Stacked Denoising Autoencoders: Learning Useful Representations in a Deep Network with a Local Denoising Criterion. *The Journal of Machine Learning Research*, *11*, 3371–3408.

Virk, R., & King, D. (2006). Comparison of Techniques for Forest Change Mapping Using Landsat Data in Karnataka, India. *Geocarto International*, *21*(4), 49–57. https://doi.org/10.1080/10106040608542402

Vitousek, P. M., Mooney, H. A., Lubchenco, J., & Melillo, J. M. (1997). Human Domination of Earth's Ecosystems. *Science*, *277*(5325), 494–499. https://doi.org/10.1126/science.277.5325.494

Vogels, M. F. A., de Jong, S. M., Sterk, G., & Addink, E. A. (2017). Agricultural cropland mapping using black-and-white aerial photography, Object-Based Image Analysis and Random Forests. *International Journal of Applied Earth Observation and Geoinformation*, *54*, 114–123. https://doi.org/10.1016/j.jag.2016.09.003

Volpi, M., & Tuia, D. (2017). Dense semantic labeling of sub-decimeter resolution images with convolutional NNs. *IEEE Transactions on Geoscience and Remote Sensing*, *55*(2), 881–893. https://doi.org/10.1109/TGRS.2016.2616585

Voss, M., & Sugumaran, R. (2008). Seasonal Effect on Tree Species Classification in an Urban Environment Using Hyperspectral Data, LiDAR, and an Object- Oriented Approach. *Sensors*, *8*(5), 5. https://doi.org/10.3390/s8053020

Waldhoff, G., Lussem, U., & Bareth, G. (2017). Multi-Data Approach for remote sensing-based regional crop rotation mapping: A case study for the Rur catchment, Germany. *International Journal of Applied Earth Observation and Geoinformation*, *61*, 55–69. https://doi.org/10.1016/j.jag.2017.04.009

Wali, E., Tasumi, M., & Moriyama, M. (2020). Combination of Linear Regression Lines to Understand the Response of Sentinel-1 Dual Polarization SAR Data with Crop Phenology—Case Study in Miyazaki, Japan. *Remote Sensing*, *12*(1), 1. https://doi.org/10.3390/rs12010189

Walker, R. (2004). Theorizing Land-Cover and Land-Use Change: The Case of Tropical Deforestation. *International Regional Science Review*, *27*(3), 247–270. https://doi.org/10.1177/0160017604266026

Wang, C., Jia, M., Chen, N., & Wang, W. (2018). Long-Term Surface Water Dynamics Analysis Based on Landsat Imagery and the Google Earth Engine Platform: A Case Study in the Middle Yangtze River Basin. *Remote Sensing*, *10*(10), 10. https://doi.org/10.3390/rs10101635

Wang, D., Lin, H., Chen, J., Zhang, Y., & Zeng, Q. (2010). Application of Multitemporal ENVISAT ASAR data to agricultural area mapping in the Pearl River Delta. *International Journal of Remote Sensing*, *31*(6), 1555–1572. https://doi.org/10.1080/01431160903475258

Wang, F., & Xu, Y. J. (2010). Comparison of remote sensing change detection techniques for assessing hurricane damage to forests. *Environmental Monitoring and Assessment*, *162*(1), 311–326. https://doi.org/10.1007/s10661-009-0798-8

Wang, H., Li, X., Han, R., & Ge, Y. (2006). [Variability of vegetation growth season in different latitudinal zones of North China: A monitoring by NOAA NDVI and MSAVI]. *Ying yong sheng tai xue bao = The journal of applied ecology*, *17*(12), 2236–2240.

Wang, H., Zhao, Y., Pu, R., & Zhang, Z. (2015). Mapping Robinia Pseudoacacia Forest Health Conditions by Using Combined Spectral, Spatial, and Textural Information Extracted from IKONOS Imagery and Random Forest Classifier. *Remote Sensing*, *7*(7), 7. https://doi.org/10.3390/rs70709020

Wang, L., & Qu, J. J. (2009). Satellite remote sensing applications for surface soil moisture monitoring: A review. *Frontiers of Earth Science in China*, *3*(2), 237–247. https://doi.org/10.1007/s11707-009-0023-7

Wang, L., Xu, X., Dong, H., Gui, R., & Pu, F. (2018). Multi-Pixel Simultaneous Classification of PolSAR Image Using Convolutional NNs. *Sensors*, *18*(3), 3. https://doi.org/10.3390/s18030769

Wang, M., Zhang, H., Sun, W., Li, S., Wang, F., & Yang, G. (2020). A Coarse-to-Fine Deep Learning Based Land Use Change Detection Method for High-Resolution Remote Sensing Images. *Remote Sensing*, *12*(12), 12. https://doi.org/10.3390/rs12121933

Wang, P., Zhang, H., & Patel, V. M. (2017). SAR Image Despeckling Using a Convolutional NN. *IEEE Signal Processing Letters*, *24*(12), 1763–1767. https://doi.org/10.1109/LSP.2017.2758203

Wang, S.-L., Xu, X.-R., Sun, Y.-X., Liu, J.-L., & Li, H.-B. (2013). Heavy metal pollution in coastal areas of South China: A review. *Marine Pollution Bulletin*, *76*(1), 7–15. https://doi.org/10.1016/j.marpolbul.2013.08.025

Wang, X., Xiao, X., Zou, Z., Chen, B., Ma, J., Dong, J., Doughty, R. B., Zhong, Q., Qin, Y., Dai, S., Li, X., Zhao, B., & Li, B. (2020). Tracking annual changes of coastal tidal flats in China during 1986–2016 through analyses of Landsat images with Google Earth Engine. *Remote Sensing of Environment*, *238*, 110987. https://doi.org/10.1016/j.rse.2018.11.030

Wang, X., Zhao, X., Zhang, Z., Yi, L., Zuo, L., Wen, Q., Liu, F., Xu, J., Hu, S., & Liu, B. (2016). Assessment of soil erosion change and its relationships with land use/cover change in China from the end of the 1980s to 2010. *CATENA*, *137*, 256–268. https://doi.org/10.1016/j.catena.2015.10.004

Wang, Y., He, C., Liu, X., & Liao, M. (2018). A Hierarchical Fully Convolutional Network Integrated with Sparse and Low-Rank Subspace Representations for PolSAR Imagery Classification. *Remote Sensing*, *10*(2), 2. https://doi.org/10.3390/rs10020342

Wang, Y., Li, Z., Zeng, C., Xia, G.-S., & Shen, H. (2020). An Urban Water Extraction Method Combining Deep Learning and Google Earth Engine. *IEEE Journal of Selected Topics in Applied Earth Observations and Remote Sensing*, *13*, 769–782. https://doi.org/10.1109/JSTARS.2020.2971783

Wang, Z., Liu, C., & Huete, A. (2003). From AVHRR-NDVI to MODIS-EVI: Advances in vegetation index researc. *Acta Ecologica Sinica*, *23*(5), 979–987.

Wang, Z., Yang, X., Lu, C., & Yang, F. (2018). A scale self-adapting segmentation approach and knowledge transfer for automatically updating land use/cover change databases using high spatial resolution images. *International Journal of Applied Earth Observation and Geoinformation*, *69*, 88–98. https://doi.org/10.1016/j.jag.2018.03.001

Wardlow, B. D., & Egbert, S. L. (2008). Large-area crop mapping using time-series MODIS 250 m NDVI data: An assessment for the U.S. Central Great Plains. *Remote Sensing of Environment*, *112*(3), 1096–1116. https://doi.org/10.1016/j.rse.2007.07.019

Wardlow, B. D., Egbert, S. L., & Kastens, J. H. (2007). Analysis of time-series MODIS 250 m vegetation index data for crop classification in the U.S. Central Great Plains. *Remote Sensing of Environment*, *108*(3), 290–310. https://doi.org/10.1016/j.rse.2006.11.021

Waske, B., Fauvel, M., Benediktsson, J. A., & Chanussot, J. (2009). Machine learning techniques in remote sensing data analysis. In L. B. Gustavo Camps-Valls (Ed.), *Kernel Methods for Remote Sensing Data Analysis* (p.). Wiley and Sons. https://doi.org/10.1002/9780470748992.ch1

Weih, R., & Riggan, N. (2010). Object-based classification vs. Pixel-based classification: Comparitive importance of multi-resolution imagery. *International Archives of the Photogrammetry, Remote Sensing and Spatial Information Sciences - ISPRS Archives*, *38*.

Weis, M., Müller, S., Liedtke, C.-E., & Pahl, M. (2005). A framework for GIS and imagery data fusion in support of cartographic updating. *Information Fusion*, *6*(4), 311–317. https://doi.org/10.1016/j.inffus.2004.08.001

Weng, Q. (2001). A remote sensing?GIS evaluation of urban expansion and its impact on surface temperature in the Zhujiang Delta, China. *International Journal of Remote Sensing*, *22*(10), 1999–2014. https://doi.org/10.1080/713860788

Weng, Q. (2012). Remote sensing of impervious surfaces in the urban areas: Requirements, methods, and trends. *Remote Sensing of Environment*, *117*, 34–49. https://doi.org/10.1016/j.rse.2011.02.030

Weng, Q., Mao, Z., Lin, J., & Liao, X. (2018). Land-use scene classification based on a CNN using a constrained extreme learning machine. *International Journal of Remote Sensing*, *39*(19), 6281–6299. https://doi.org/10.1080/01431161.2018.1458346

Whiteside, T. G., Boggs, G. S., & Maier, S. W. (2011). Comparing object-based and pixel-based classifications for mapping savannas. *International Journal of Applied Earth Observation and Geoinformation*, *13*(6), 884–893. https://doi.org/10.1016/j.jag.2011.06.008

Whitman, R. T., Park, M. B., Ambrose, S. M., & Hoel, E. G. (2014). Spatial indexing and analytics on Hadoop. *Proceedings of the 22nd ACM SIGSPATIAL International Conference on Advances in Geographic Information Systems*, 73–82. https://doi.org/10.1145/2666310.2666387

Wiegand, C. L., Richardson, A. J., Escobar, D. E., & Gerbermann, A. H. (1991). Vegetation indices in crop assessments. *Remote Sensing of Environment*, *35*(2), 105–119. https://doi.org/10.1016/0034-4257(91)90004-P

Wilmanski, M., Kreucher, C., & Lauer, J. (2016). Modern approaches in deep learning for SAR ATR. *Algorithms for Synthetic Aperture RaDAR Imagery XXIII*, *9843*, 195–204. https://doi.org/10.1117/12.2220290

Wilson, J. S., Clay, M., Martin, E., Stuckey, D., & Vedder-Risch, K. (2003). Evaluating environmental influences of zoning in urban ecosystems with remote sensing. *Remote Sensing of Environment*, *86*(3), 303–321. https://doi.org/10.1016/S0034-4257(03)00084-1

Witharana, C., & Civco, D. L. (2014). Optimizing multi-resolution segmentation scale using empirical methods: Exploring the sensitivity of the supervised discrepancy measure Euclidean distance 2 (ED2). *ISPRS Journal of Photogrammetry and Remote Sensing*, *87*, 108–121. https://doi.org/10.1016/j.isprsjprs.2013.11.006

World Bank Group. (n.d.). [Text/HTML]. World Bank Group - International Development, Poverty, & Sustainability. Retrieved January 1, 2023, from https://www.worldbank.org/en/home

Wright, C., & Gallant, A. (2007). Improved wetland remote sensing in Yellowstone National Park using classification trees to combine TM imagery and ancillary environmental data. *Remote Sensing of Environment*, *107*(4), 582–605. https://doi.org/10.1016/j.rse.2006.10.019

Wu, Q., Zhong, R., Zhao, W., Fu, H., & Song, K. (2017). A comparison of pixel-based decision tree and object-based Support Vector Machine methods for land-cover classification based on aerial images and airborne LiDAR data. *International Journal of Remote Sensing*, *38*(23), 7176–7195. https://doi.org/10.1080/01431161.2017.1371864

Wu, S., Mickley, L. J., Kaplan, J. O., & Jacob, D. J. (2012). Impacts of changes in land use and land cover on atmospheric chemistry and air quality over the 21st century. *Atmospheric Chemistry and Physics*, *12*(3), 1597–1609. https://doi.org/10.5194/acp-12-1597-2012

Wulder, M. A., Coops, N. C., Roy, D. P., White, J. C., & Hermosilla, T. (2018). Land cover 2.0. *International Journal of Remote Sensing*, *39*(12), 4254–4284. https://doi.org/10.1080/01431161.2018.1452075

Wyawahare, M., Kulkarni, P., Kulkarni, A., Lad, A., Majji, J., & Mehta, A. (2020). Agricultural Field Analysis Using Satellite Surface Reflectance Data and Machine Learning Technique. In M. Singh, P. K. Gupta, V. Tyagi, J. Flusser, T. Ören, & G. Valentino (Eds.), *Advances in Computing and Data Sciences* (pp. 439–448). Springer. https://doi.org/10.1007/978-981-15-6634-9_40

Xavier, A. C., & Vettorazzi, C. A. (2004). Mapping leaf area index through spectral vegetation indices in a subtropical watershed. *International Journal of Remote Sensing*, *25*(9), 1661–1672. https://doi.org/10.1080/01431160310001620803

Xie, G., & Niculescu, S. (2021). Mapping and Monitoring of Land Cover/Land Use (LCLU) Changes in the Crozon Peninsula (Brittany, France) from 2007 to 2018 by Machine Learning Algorithms (Support Vector Machine, Random Forest, and Convolutional NN) and by Post-classification Comparison (PCC). *Remote Sensing*, *13*(19), 19. https://doi.org/10.3390/rs13193899

Xie, G., & Niculescu, S. (2022). Mapping Crop Types Using Sentinel-2 Data Machine Learning and Monitoring Crop Phenology with Sentinel-1 Backscatter Time Series in Pays de Brest, Brittany, France. *Remote Sensing*, *14*(18), 18. https://doi.org/10.3390/rs14184437

Xie, G., Niculescu, S., Lam, C., & Seveno, E. (2019). Machine learning methods and classification of vegetation in Brest, France. *Remote Sensing Technologies and Applications in Urban Environments IV*, *11157*, 105–114. https://doi.org/10.1117/12.2533436

Xie, H., Wang, S., Liu, K., Lin, S., & Hou, B. (2014). Multilayer feature learning for polarimetric synthetic RaDAR data classification. *2014 IEEE Geoscience and Remote Sensing Symposium*, 2818–2821. https://doi.org/10.1109/IGARSS.2014.6947062

Xie, Y., Sha, Z., & Yu, M. (2008). Remote sensing imagery in vegetation mapping: A review. *Journal of Plant Ecology*, *1*(1), 9–23. https://doi.org/10.1093/jpe/rtm005

Xiong, Y., Huang, S., Chen, F., Ye, H., Wang, C., & Zhu, C. (2012). The Impacts of Rapid Urbanization on the Thermal Environment: A Remote Sensing Study of Guangzhou, South China. *Remote Sensing*, *4*(7), 7. https://doi.org/10.3390/rs4072033

Xu, F., Li, Z., Zhang, S., Huang, N., Quan, Z., Zhang, W., Liu, X., Jiang, X., Pan, J., & Prishchepov, A. V. (2020). Mapping Winter Wheat with Combinations of Temporally Aggregated Sentinel-2 and Landsat-8 Data in Shandong Province, China. *Remote Sensing*, *12*(12), 12. https://doi.org/10.3390/rs12122065

Xu, H., Wang, X., & Xiao, G. (2000). A remote sensing and GIS integrated study on urbanization with its impact on arable lands: Fuqing City, Fujian Province, China. *Land Degradation & Development*, *11*(4), 301–314. https://doi.org/10.1002/1099-145X(200007/08)11:4<301::AID-LDR392>3.0.CO;2-N

Xu, Z., Zhou, Y., Wang, S., Wang, L., Li, F., Wang, S., & Wang, Z. (2020). A Novel Intelligent Classification Method for Urban Green Space Based on High-Resolution Remote Sensing Images. *Remote Sensing*, *12*(22), 22. https://doi.org/10.3390/rs12223845

Xue, J., & Su, B. (2017). Significant Remote Sensing Vegetation Indices: A Review of Developments and Applications. *Journal of Sensors*, *2017*, 1–17. https://doi.org/10.1155/2017/1353691

Yan, J., Wang, L., Song, W., Chen, Y., Chen, X., & Deng, Z. (2019). A time-series classification approach based on change detection for rapid land cover mapping. *ISPRS Journal of Photogrammetry and Remote Sensing*, *158*, 249–262. https://doi.org/10.1016/j.isprsjprs.2019.10.003

Yang, C., Wu, G., Ding, K., Shi, T., Li, Q., & Wang, J. (2017). Improving Land Use/Land Cover Classification by Integrating Pixel Unmixing and Decision Tree Methods. *Remote Sensing*, *9*(12), 12. https://doi.org/10.3390/rs9121222

Yang, J., Guo, J., Yue, H., Liu, Z., Hu, H., & Li, K. (2019). CDnet: CNN-Based Cloud Detection for Remote Sensing Imagery. *IEEE Transactions on Geoscience and Remote Sensing*, *57*(8), 6195–6211. https://doi.org/10.1109/TGRS.2019.2904868

Yang, X., & Lo, C. P. (2002). Using a time series of satellite imagery to detect land use and land cover changes in the Atlanta, Georgia metropolitan area. *International Journal of Remote Sensing*, *23*(9), 1775–1798. https://doi.org/10.1080/01431160110075802

Yang, X. X. (2021). *Urban Remote Sensing: Monitoring, Synthesis and Modeling in the Urban Environment*. John Wiley & Sons.

Yin, G., Verger, A., Descals, A., Filella, I., & Peñuelas, J. (2022). A Broadband Green-Red Vegetation Index for Monitoring Gross Primary Production Phenology. *Journal of Remote Sensing*, *2022*. https://doi.org/10.34133/2022/9764982

Yin, H., Prishchepov, A. V., Kuemmerle, T., Bleyhl, B., Buchner, J., & Radeloff, V. C. (2018). Mapping agricultural land abandonment from spatial and temporal segmentation of Landsat time series. *Remote Sensing of Environment*, *210*, 12–24. https://doi.org/10.1016/j.rse.2018.02.050

Yin, J., Wang, T., Du, Y., Liu, X., Zhou, L., & Yang, J. (2022). SLIC Superpixel Segmentation for Polarimetric SAR Images. *IEEE Transactions on Geoscience and Remote Sensing*, *60*, 1–17. https://doi.org/10.1109/TGRS.2020.3047126

Yoo, C., Han, D., Im, J., & Bechtel, B. (2019). Comparison between convolutional NNs and random forest for local climate zone classification in mega urban areas using Landsat images. *ISPRS Journal of Photogrammetry and Remote Sensing*, *157*, 155–170. https://doi.org/10.1016/j.isprsjprs.2019.09.009

Yu, B., & Shang, S. (2017). Multi-Year Mapping of Maize and Sunflower in Hetao Irrigation District of China with High Spatial and Temporal Resolution Vegetation Index Series. *Remote Sensing*, *9*(8), 8. https://doi.org/10.3390/rs9080855

Yu, J., Wu, J., & Sarwat, M. (2015). GeoSpark: A cluster computing framework for processing large-scale spatial data. *Proceedings of the 23rd SIGSPATIAL International Conference on Advances in Geographic Information Systems*, 1–4. https://doi.org/10.1145/2820783.2820860

Yuping, M., Shili, W., Li, Z., Yingyu, H., Liwei, Z., Yanbo, H., & Futang, W. (2008). Monitoring winter wheat growth in North China by combining a crop model and remote sensing data. *International Journal of Applied Earth Observation and Geoinformation*, *10*(4), 426–437. https://doi.org/10.1016/j.jag.2007.09.002

Zabalza, J., Ren, J., Zheng, J., Zhao, H., Qing, C., Yang, Z., Du, P., & Marshall, S. (2016). Novel segmented stacked autoencoder for effective dimensionality reduction and feature extraction in hyperspectral imaging. *Neurocomputing*, *185*, 1–10. https://doi.org/10.1016/j.neucom.2015.11.044

Zabuawala, S., Nguyen, H., Wei, H., & Yadegar, J. (2009). Fusion of LIDAR and aerial imagery for accurate building footprint extraction. *Image Processing: Machine Vision Applications II*, *7251*, 337–347. https://doi.org/10.1117/12.806141

Zafari, A., Zurita-Milla, R., & Izquierdo-Verdiguier, E. (2019). Evaluating the Performance of a Random Forest Kernel for Land Cover Classification. *Remote Sensing*, *11*(5), 5. https://doi.org/10.3390/rs11050575

Zeng, H., Wu, B., Zhang, N., Tian, F., Phiri, E., Musakwa, W., Zhang, M., Zhu, L., & Mashonjowa, E. (2019). Spatiotemporal Analysis of Precipitation in the Sparsely Gauged Zambezi River Basin Using Remote Sensing and Google Earth Engine. *Remote Sensing*, *11*(24), 24. https://doi.org/10.3390/rs11242977

Zeng, T., Wang, L., Zhang, Z., Wen, Q., Wang, X., & Yu, L. (2019). An Integrated Land Cover Mapping Method Suitable for Low-Accuracy Areas in Global Land Cover Maps. *Remote Sensing*, *11*(15), 15. https://doi.org/10.3390/rs11151777

Zhang, A., Sun, G., Ma, P., Jia, X., Ren, J., Huang, H., & Zhang, X. (2019). Coastal Wetland Mapping with Sentinel-2 MSI Imagery Based on Gravitational Optimized Multilayer Perceptron and Morphological Attribute Profiles. *Remote Sensing*, *11*(8), 8. https://doi.org/10.3390/rs11080952

Zhang, C., Pan, X., Li, H., Gardiner, A., Sargent, I., Hare, J., & Atkinson, P. M. (2018). A hybrid MLP-CNN classifier for very fine resolution remotely sensed image classification. *ISPRS Journal of Photogrammetry and Remote Sensing*, *140*, 133–144. https://doi.org/10.1016/j.isprsjprs.2017.07.014

Zhang, C., Pattey, E., Liu, J., Cai, H., Shang, J., & Dong, T. (2018). Retrieving Leaf and Canopy Water Content of Winter Wheat Using Vegetation Water Indices. *IEEE Journal of Selected Topics in Applied Earth Observations and Remote Sensing*, *11*(1), 112–126. https://doi.org/10.1109/JSTARS.2017.2773625

Zhang, C., Wei, S., Ji, S., & Lu, M. (2019a). Detecting Large-Scale Urban Land Cover Changes from Very High Resolution Remote Sensing Images Using CNN-Based Classification. *ISPRS International Journal of Geo-Information*, *8*(4), 4. https://doi.org/10.3390/ijgi8040189

Zhang, C., Wei, S., Ji, S., & Lu, M. (2019b). Detecting Large-Scale Urban Land Cover Changes from Very High Resolution Remote Sensing Images Using CNN-Based Classification. *ISPRS International Journal of Geo-Information*, *8*(4), 4. https://doi.org/10.3390/ijgi8040189

Zhang, F., Du, B., & Zhang, L. (2016). Scene Classification via a Gradient Boosting Random Convolutional Network Framework. *IEEE Transactions on Geoscience and Remote Sensing*, *54*(3), 1793–1802. https://doi.org/10.1109/TGRS.2015.2488681

Zhang, F., & Zhou, G. (2019). Estimation of vegetation water content using hyperspectral vegetation indices: A comparison of crop water indicators in response to water stress treatments for summer maize. *BMC Ecology*, *19*(1), 18. https://doi.org/10.1186/s12898-019-0233-0

Zhang, L., Ma, W., & Zhang, D. (2016). Stacked Sparse Autoencoder in PolSAR Data Classification Using Local Spatial Information. *IEEE Geoscience and Remote Sensing Letters*, *13*(9), 1359–1363. https://doi.org/10.1109/LGRS.2016.2586109

Zhang, L., Zhang, L., & Du, B. (2016). Deep Learning for Remote Sensing Data: A Technical Tutorial on the State of the Art. *IEEE Geoscience and Remote Sensing Magazine*, *4*(2), 22–40. https://doi.org/10.1109/MGRS.2016.2540798

Zhang, S., Li, C., Qiu, S., Gao, C., Zhang, F., Du, Z., & Liu, R. (2020). EMMCNN: An ETPS-Based Multi-Scale and Multi-Feature Method Using CNN for High Spatial Resolution Image Land-Cover Classification. *Remote Sensing*, *12*(1), 1. https://doi.org/10.3390/rs12010066

Zhang, W., Liu, H., Wu, W., Zhan, L., & Wei, J. (2020). Mapping Rice Paddy Based on Machine Learning with Sentinel-2 Multitemporal Data: Model Comparison and Transferability. *Remote Sensing*, *12*(10), 10. https://doi.org/10.3390/rs12101620

Zhao, X., Xia, H., Pan, L., Song, H., Niu, W., Wang, R., Li, R., Bian, X., Guo, Y., & Qin, Y. (2021). Drought Monitoring over Yellow River Basin from 2003–2019 Using Reconstructed MODIS Land Surface Temperature in Google Earth Engine. *Remote Sensing*, *13*(18), 18. https://doi.org/10.3390/rs13183748

Zhong, Z., Li, J., Clausi, D. A., & Wong, A. (2020). Generative Adversarial Networks and Conditional Random Fields for Hyperspectral Image Classification. *IEEE Transactions on Cybernetics*, *50*(7), 3318–3329. https://doi.org/10.1109/TCYB.2019.2915094

Zhou, K., Ming, D., Lv, X., Fang, J., & Wang, M. (2019). CNN-Based Land Cover Classification Combining Stratified Segmentation and Fusion of Point Cloud and Very High-Spatial Resolution Remote Sensing Image Data. *Remote Sensing*, *11*(17), 17. https://doi.org/10.3390/rs11172065

Zhou, T., Pan, J., Zhang, P., Wei, S., & Han, T. (2017). Mapping Winter Wheat with Multitemporal SAR and Optical Images in an Urban Agricultural Region. *Sensors*, *17*(6), 6. https://doi.org/10.3390/s17061210

Zhou, W., Ming, D., Lv, X., Zhou, K., Bao, H., & Hong, Z. (2020). SO–CNN based urban functional zone fine division with VHR remote sensing image. *Remote Sensing of Environment*, *236*, 111458. https://doi.org/10.1016/j.rse.2019.111458

Zhou, X., & Wang, Y.-C. (2011). Spatial–temporal dynamics of urban green space in response to rapid urbanization and greening policies. *Landscape and Urban Planning*, *100*(3), 268–277. https://doi.org/10.1016/j.landurbplan.2010.12.013

Zhou, Y., Wang, H., Xu, F., & Jin, Y.-Q. (2016). Polarimetric SAR Image Classification Using Deep Convolutional NNs. *IEEE Geoscience and Remote Sensing Letters*, *13*(12), 1935–1939. https://doi.org/10.1109/LGRS.2016.2618840

Zhu, L., Liu, X., Wu, L., Tang, Y., & Meng, Y. (2019). Long-Term Monitoring of Cropland Change near Dongting Lake, China, Using the LandTrendr Algorithm with Landsat Imagery. *Remote Sensing*, *11*(10), 10. https://doi.org/10.3390/rs11101234

Zhu, N., Liu, X., Liu, Z., Hu, K., Wang, Y., Tan, J., Huang, M., Zhu, Q., Ji, X., Jiang, Y., & Guo, Y. (2018). Deep learning for smart agriculture: Concepts, tools, applications, and opportunities. *International Journal of Agricultural and Biological Engineering*, *11*(4), 4. https://doi.org/10.25165/ijabe.v11i4.4475

Zhu, X. X., Tuia, D., Mou, L., Xia, G.-S., Zhang, L., Xu, F., & Fraundorfer, F. (2017). Deep Learning in Remote Sensing: A Comprehensive Review and List of Resources. *IEEE Geoscience and Remote Sensing Magazine*, *5*(4), 8–36. https://doi.org/10.1109/MGRS.2017.2762307

Zhu, Z., Wang, S., & Woodcock, C. E. (2015). Improvement and expansion of the Fmask algorithm: Cloud, cloud shadow, and snow detection for Landsats 4–7, 8, and Sentinel 2 images. *Remote Sensing of Environment*, *159*, 269–277. https://doi.org/10.1016/j.rse.2014.12.014

Zhu, Z., & Woodcock, C. E. (2012). Object-based cloud and cloud shadow detection in Landsat imagery. *Remote Sensing of Environment*, *118*, 83–94. https://doi.org/10.1016/j.rse.2011.10.028

Zimudzi, E., Sanders, I., Rollings, N., & Omlin, C. (2019). Segmenting mangrove ecosystems drone images using SLIC superpixels. *Geocarto International*, *34*(14), 1648–1662. https://doi.org/10.1080/10106049.2018.1497093

Zou, X., & Mõttus, M. (2017). Sensitivity of Common Vegetation Indices to the Canopy Structure of Field Crops. *Remote Sensing*, *9*(10), 10. https://doi.org/10.3390/rs9100994

Titre : Méthodes d'apprentissage automatique et les changements de l'occupation du littoral du Pays de Brest

Mots clés : télédétection, occupation du sol, apprentissage automatique, apprentissage profond, littoral

Résumé : En tant que zone côtière, le Pays de Brest a été reconnu comme une source essentielle de production alimentaire, un centre d'activités socio-économiques ainsi qu'un écosystème unique et un réservoir de biodiversité. Cependant, le Pays de Brest souffre d'une vulnérabilité environnementale et des impacts des activités humaines, en particulier le Pays de Brest a connu changements d'occupation des sols (LULCC) importants depuis les années 1990 en raison de l'augmentation de la population et de l'expansion urbaine. Il est donc essentiel de développer une solide compréhension de l'occupation du sol (LULC) et de surveiller les LULCC qui se produisent au fil du temps dans le Pays de Brest. Les technologies de télédétection sont aujourd'hui l'outil le plus utilisé pour la cartographie de LULC et la détection des LULCC, notamment grâce au développement d'algorithmes de traitement avancés, et à l'arrivée de la dernière génération d'images satellites ces dernières années.

Dans ce contexte, l'objectif de ce travail est de produire une méthodologie robuste, spécifique et reproductible qui se concentre sur une approche comparative des méthodes de *machine learning* (ML) adaptées aux zones côtières pour le suivi rentable des LULC et l'évaluation des changements impactant le Pays de Brest. De plus, l'étude a été réalisée à travers trois cas d'étude spécifiques au Pays de Brest : 1) classification du couvert végétal en utilisant les methodes ML dans la ville de Brest, 2) cartographie et suivi des changements d'occupation et d'utilisation des sols dans la presqu'ile de Crozon (Bretagne, France) de 2007 à 2018 par des algorithmes ML et par comparaison post-classification, et 3) cartographie des types de cultures avec des données optiques Sentinel-2 et ML méthodes, et suivi de la phénologie des cultures avec les séries temporelles de rétrodiffusion Sentinel-1 dans le Pays de Brest, Bretagne, France.

Title : Machine Learning methods and Land Use/Land Cover (LULC) in the coastal Pays de Brest

Keywords : remote sensing, land cover, land use, machine learning, deep learning, coastal area

Abstract : As a coastal area, Pays de Brest have been recognized as an essential sources of food production, a center of socio-economic activities as well as an unique ecosystem and a repository of biodiversity. However, the coastal Pays de Brest suffers from environmental vulnerability and the impacts of human activities, especially the Pays de Brest has experienced significant land use and land cover changes (LULCC) since the 1990s due to rising population and urban expansion. It is therefore critical to develop a solid understanding of land use and land cover (LULC) and to monitor LULCC that occur over time in Pays de Brest. Remote sensing technologies are the most widely used tool for LULC mapping and LULCC detection nowadays, especially with the development of advanced processing algorithms, and the arrival of the latest generation of satellite imagery in recent years. With this context, the objective of this work is to produce a robust, specific, and reproducible methodology that focuses on a comparative approach to machine learning (ML) methods adapted to coastal areas for the cost-effective monitoring of LULC and the assessment of changes impacting Pays de Brest. Moreover, the study was carried out through three specific study cases in Pays de Brest: 1) ML methods and classification of vegetation in Brest, France, 2) mapping and monitoring of LULCC in the Crozon Peninsula (Brittany, France) from 2007 to 2018 by ML algorithms and by post-classification comparison, and 3) mapping crop types using Sentinel-2 optical satellite data ML algorithms and monitoring crop phenology with Sentinel-1 backscatter time series in pays de Brest, Brittany, France.